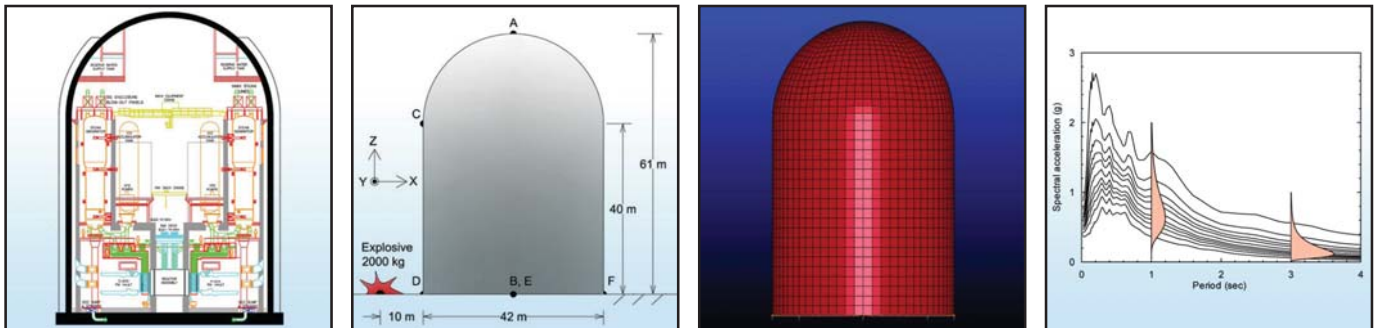


# Performance Assessment of Conventional and Base-Isolated Nuclear Power Plants for Earthquake and Blast Loadings

by  
Yin-Nan Huang, Andrew S. Whittaker  
and Nicolas Luco



Technical Report MCEER-08-0019

October 28, 2008

## NOTICE

This report was prepared by the University at Buffalo, State University of New York as a result of research sponsored by MCEER through a grant from the Earthquake Engineering Research Centers Program of the National Science Foundation under NSF award number EEC-9701471 and other sponsors. Neither MCEER, associates of MCEER, its sponsors, the University at Buffalo, State University of New York, nor any person acting on their behalf:

- a. makes any warranty, express or implied, with respect to the use of any information, apparatus, method, or process disclosed in this report or that such use may not infringe upon privately owned rights; or
- b. assumes any liabilities of whatsoever kind with respect to the use of, or the damage resulting from the use of, any information, apparatus, method, or process disclosed in this report.

Any opinions, findings, and conclusions or recommendations expressed in this publication are those of the author(s) and do not necessarily reflect the views of MCEER, the National Science Foundation, or other sponsors.

## **Performance Assessment of Conventional and Base-Isolated Nuclear Power Plants for Earthquake and Blast Loadings**

by

Yin-Nan Huang,<sup>1</sup> Andrew S. Whittaker<sup>2</sup> and Nicolas Luco<sup>3</sup>

Publication Date: October 28, 2008

Submittal Date: June 28, 2008

Technical Report MCEER-08-0019

Task Number 10.4.2

NSF Master Contract Number EEC 9701471

- 1 Post-doctoral Research Associate, Department of Civil, Structural and Environmental Engineering, University at Buffalo, State University of New York
- 2 Professor, Department of Civil, Structural and Environmental Engineering, University at Buffalo, State University of New York
- 3 Research Structural Engineer, U.S. Geological Survey

MCEER

University at Buffalo, State University of New York

Red Jacket Quadrangle, Buffalo, NY 14261

Phone: (716) 645-3391; Fax (716) 645-3399

E-mail: [mceer@buffalo.edu](mailto:mceer@buffalo.edu); WWW Site: <http://mceer.buffalo.edu>

---

## **NTIS DISCLAIMER**

- ❖ This document has been reproduced from the best copy furnished by the sponsoring agency.

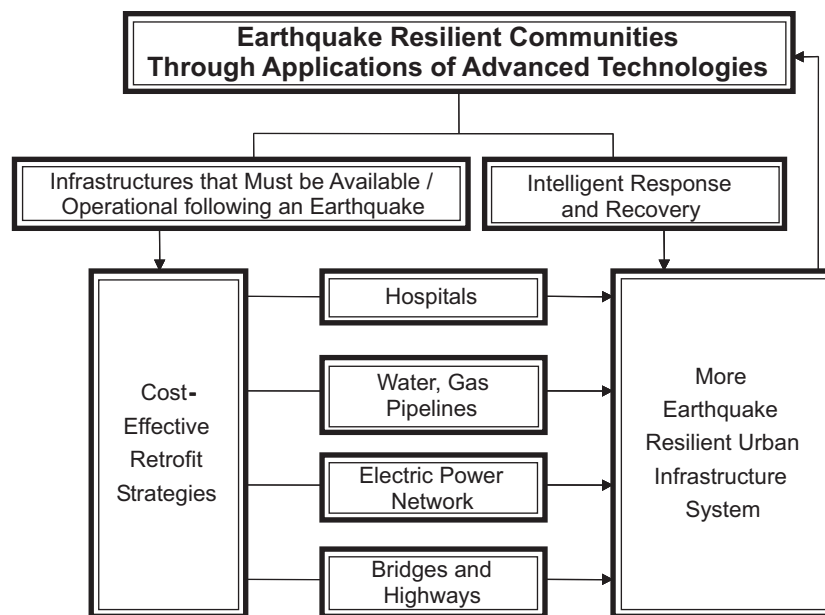
## Preface

The Multidisciplinary Center for Earthquake Engineering Research (MCEER) is a national center of excellence in advanced technology applications that is dedicated to the reduction of earthquake losses nationwide. Headquartered at the University at Buffalo, State University of New York, the Center was originally established by the National Science Foundation in 1986, as the National Center for Earthquake Engineering Research (NCEER).

Comprising a consortium of researchers from numerous disciplines and institutions throughout the United States, the Center's mission is to reduce earthquake losses through research and the application of advanced technologies that improve engineering, pre-earthquake planning and post-earthquake recovery strategies. Toward this end, the Center coordinates a nationwide program of multidisciplinary team research, education and outreach activities.

MCEER's research is conducted under the sponsorship of two major federal agencies: the National Science Foundation (NSF) and the Federal Highway Administration (FHWA), and the State of New York. Significant support is derived from the Federal Emergency Management Agency (FEMA), other state governments, academic institutions, foreign governments and private industry.

MCEER's NSF-sponsored research objectives are twofold: to increase resilience by developing seismic evaluation and rehabilitation strategies for the post-disaster facilities and systems (hospitals, electrical and water lifelines, and bridges and highways) that society expects to be operational following an earthquake; and to further enhance resilience by developing improved emergency management capabilities to ensure an effective response and recovery following the earthquake (see the figure below).



A cross-program activity focuses on the establishment of an effective experimental and analytical network to facilitate the exchange of information between researchers located in various institutions across the country. These are complemented by, and integrated with, other MCEER activities in education, outreach, technology transfer, and industry partnerships.

*The study presented in this report assesses the performance of conventional and base isolated Nuclear Power Plant (NPP) reactor buildings subjected to earthquakes and blast loadings. Three base isolation systems, including Friction Pendulum, lead-rubber and low damping rubber bearings, are studied. This report proposes a new procedure for probabilistic seismic risk assessment of structures. The proposed procedure is built on the methodology presented in the ATC-58 Guidelines and the Zion method. The procedure improves the Zion method by using fragility curves defined in terms of structural response parameters instead of ground motion parameters, providing a more suitable technique for the assessment of damage and failure of NPP components. The seismic performance assessment confirms the ability of base isolation systems to reduce spectral demands on secondary systems. Procedures for reducing the construction cost of secondary systems in isolated reactor buildings are also presented. Response-history analyses of conventional and base isolated reactor buildings to external blast loads are performed. The spectral demands on the secondary systems in the base isolated reactor building due to air blast loadings are greater than for a conventional reactor building, but much smaller than the demands associated with the safe shutdown earthquake loading. The base isolation systems are effective at filtering out high acceleration-high frequency ground shock loading.*

## ABSTRACT

Nuclear power plants (NPPs) and spent nuclear fuel (SNF) are required by code and regulations to be designed for a family of extreme events, including very rare earthquake shaking, loss of coolant accidents, and tornado-borne missile impacts. Blast loading due to malevolent attack became a design consideration for NPPs and SNF after the terrorist attacks of September 11, 2001. The studies presented in this report assess the performance of sample conventional and base isolated NPP reactor buildings subjected to seismic effects and blast loadings. The response of the sample reactor building to tornado-borne missile impacts and internal events (e.g., loss of coolant accidents) will not change if the building is base isolated and so these hazards were not considered.

The sample NPP reactor building studied in this report is composed of containment and internal structures with a total weight of approximately 75,000 tons. Four configurations of the reactor building are studied, including one conventional fixed-base reactor building and three base-isolated reactor buildings using Friction Pendulum™, lead rubber and low damping rubber bearings.

The seismic assessment of the sample reactor building is performed using a new procedure proposed in this report that builds on the methodology presented in the draft *ATC-58 Guidelines* and the widely used Zion method, which uses fragility curves defined in terms of ground-motion parameters for NPP seismic probabilistic risk assessment. The new procedure improves the Zion method by using fragility curves that are defined in terms of structural response parameters since damage and failure of NPP components are more closely tied to structural response parameters than to ground motion parameters. Alternate ground motion scaling methods are studied to help establish an optimal procedure for scaling ground motions for the purpose of seismic performance assessment. The proposed performance assessment procedure is used to evaluate the vulnerability of the conventional and base-isolated NPP reactor buildings. The seismic performance assessment confirms the utility of seismic isolation at reducing spectral demands on secondary systems. Procedures to reduce the construction cost of secondary systems in isolated reactor buildings are presented.

A blast assessment of the sample reactor building is performed for an assumed threat of 2000 kg of TNT explosive detonated on the surface with a closest distance to the reactor building of 10 m.

The air and ground shock waves produced by the design threat are generated and used for performance assessment. The air blast loading to the sample reactor building is computed using a Computational Fluid Dynamics code Air3D and the ground shock time series is generated using an attenuation model for soil/rock response. Response-history analysis of the sample conventional and base isolated reactor buildings to external blast loadings is performed using the hydrocode LS-DYNA. The spectral demands on the secondary systems in the isolated reactor building due to air blast loading are greater than those for the conventional reactor building but much smaller than those spectral demands associated with Safe Shutdown Earthquake shaking. The isolators are extremely effective at filtering out high acceleration, high frequency ground shock loading.



## ACKNOWLEDGEMENTS

The research presented in this report was supported in part by the Multidisciplinary Center for Earthquake Engineering Research (MCEER) through grants from the Earthquake Engineering Centers Program of the National Science Foundation (NSF), Award Number EEC-9701471, and the State of New York. The opinions expressed in report are those of the authors and do not reflect the views of the sponsors or the Research Foundation of the State University of New York. No guarantee regarding the results, findings, and recommendations are offered by MCEER, NSF or the State of New York.

Dr. Ayman Saady and Mr. Medhat Elgohary of Atomic Energy Canada Limited (AECL) provided invaluable information on NPP reactor building construction. Professors Michael Constantinou and Gilberto Mosqueda reviewed the manuscript in its dissertation format. Mr. Ronald Hamburger, S.E., provided counsel on the topic of selecting and scaling earthquake ground motions. Mr. Graeme Ballantyne helped develop a finite element model for the sample containment vessel. Dr. David Ritzel provided valuable insight into CFD and hydrocode analysis and air-blast computations in the near field. Dr. Timothy Rose, formerly of Cranfield University, generously provided his CFD code, Air3D, for the air-blast computations. The authors gratefully acknowledge this assistance.



# TABLE OF CONTENTS

Chapter	Title	Page
<b>1</b>	<b>INTRODUCTION .....</b>	<b>1</b>
1.1	Hazard Assessment of Nuclear Power Plants.....	1
1.2	Seismic Performance Assessment .....	1
1.2.1	Conventional and Base Isolated Nuclear Power Plants.....	1
1.2.2	Seismic Performance-Based Design of Buildings.....	2
1.3	Blast Assessment.....	4
1.4	Objectives.....	5
1.5	Organization of the Report .....	5
<b>2</b>	<b>SAMPLE NPP REACTOR BUILDINGS .....</b>	<b>7</b>
2.1	Conventional Reactor Building .....	7
2.2	Base Isolated Reactor Building .....	7
2.3	Key Secondary Systems .....	11
<b>3</b>	<b>METHODOLOGIES FOR SEISMIC PERFORMANCE</b>	
	<b>ASSESSMENT .....</b>	<b>13</b>
3.1	Introduction .....	13
3.2	Conventional Methodology for Seismic Performance Assessment of NPPs .....	14
3.2.1	Seismic Probabilistic Risk Assessment.....	14
3.2.1.1	Introduction .....	14
3.2.1.2	Seismic Hazard Analysis.....	16
3.2.1.3	Component Fragility Evaluation .....	17
3.2.1.4	Plant-System and Accident-Sequence Analysis.....	18
3.2.1.5	Consequence Analysis.....	22
3.2.2	Development of Fragility Curves .....	22
3.2.2.1	Fragility Model.....	22
3.2.2.2	Developing Fragility Curves .....	26
3.3	A New Procedure for Seismic Performance Assessment of NPPs.....	29
3.3.1	Introduction .....	29
3.3.1.1	A Shortcoming of the Conventional Methodology .....	29
3.3.1.2	Overview of the New Procedure .....	30
3.3.2	Types and Products of Performance Assessment.....	31
3.3.2.1	Intensity-Based Assessment.....	31
3.3.2.2	Scenario-Based Assessment.....	32

## TABLE OF CONTENTS (CONT'D)

<b>Chapter</b>	<b>Title</b>	<b>Page</b>
3.3.2.3	Time-Based Assessment.....	32
3.3.3	Methodology for Performance Assessment.....	33
3.3.3.1	Step 1: Perform Plant-System and Accident-Sequence Analysis and Develop Component Fragility Curves.....	33
3.3.3.2	Step 2: Characterize Earthquake Shaking .....	34
3.3.3.3	Step 3: Simulate Structural Response.....	35
3.3.3.4	Step 4: Assess Damage of NPP Components.....	37
3.3.3.5	Step 5: Compute the Risk.....	39
3.3.4	Scaling Earthquake Ground Motions for Nonlinear Response-History Analysis.....	43
3.3.4.1	Intensity-Based Assessment .....	43
3.3.4.2	Scenario-Based Assessment.....	44
3.3.4.3	Time-Based Assessment.....	48
<b>4</b>	<b>SCALING GROUND MOTIONS FOR PERFORMANCE ASSESSMENT .....</b>	<b>51</b>
4.1	Introduction .....	51
4.2	State of the Art .....	51
4.2.1	Probabilistic Seismic Hazard Analysis and Uncertainties in Spectral Demands.....	51
4.2.2	Existing Procedures for Selecting and Scaling Ground Motions .....	52
4.2.3	Recent Studies .....	54
4.2.4	Epsilon Scaling and the Conditional Mean Spectrum.....	54
4.3	Scaling Ground Motions for Response-History Analysis .....	60
4.3.1	Optimal Scaling Procedure.....	60
4.3.2	Numerical Models.....	60
4.3.3	Near-Fault and Far-Field Seed Ground Motions.....	61
4.3.3.1	Dataset.....	61
4.3.3.2	Epsilon and Spectral Shape .....	61
4.3.4	Existing Procedures for Scaling Ground Motions.....	73
4.3.4.1	Method 1: Geometric-Mean Scaling of Pairs of Ground Motions (Bins 1a and 2a).....	73
4.3.4.2	Method 2: Spectrum Matching (Bins 1b and 2b) .....	76
4.3.4.3	Method 3: $Sa(T_i)$ Scaling (Bins 1c and 2c) .....	79

## TABLE OF CONTENTS (CONT'D)

<b>Chapter</b>	<b>Title</b>	<b>Page</b>
4.3.5	The Distribution-Scaling Method Using Spectrum-Matched Motions .....	84
4.3.5.1	Introduction .....	84
4.3.5.2	Response-History Analysis Using the D-scaling Method .....	88
4.3.5.3	Modification Factors .....	105
4.3.5.4	Response-History Analysis Using the D-Scaling Method and the Modified Stripes .....	106
4.3.6	The D-scaling Method Using Actual Earthquake Records .....	110
4.3.6.1	The Scaling Procedure.....	110
4.3.6.2	Response-History Analysis Results.....	121
<b>5</b>	<b>SEISMIC PERFORMANCE ASSESSMENT OF THE SAMPLE NPP REACTOR BUILDINGS.....</b>	<b>127</b>
5.1	Introduction .....	127
5.2	Intensity-Based Assessment of the Conventional Reactor Building .....	128
5.2.1	Safe Shutdown Earthquake .....	128
5.2.1.1	Procedures in Design Guidelines .....	128
5.2.1.2	The Target Design Spectrum for this Study .....	132
5.2.2	Selection and Scaling of Ground Motions.....	134
5.2.2.1	Ground Motions from Tables 4.1 and 4.2 .....	134
5.2.2.2	Ground Motions generated by SGMS .....	135
5.2.3	Development of Fragility Curves for the Secondary Systems in the Sample NPP.....	136
5.2.3.1	Demand Parameter, Median and Logarithmic Standard Deviations .....	136
5.2.3.2	Fragility Curves.....	142
5.2.4	Probability of Unacceptable Performance.....	146
5.2.4.1	Fault Tree and Nonlinear Response-History Analysis .....	146
5.2.4.2	Calculation of Probability of Unacceptable Performance .....	147
5.3	Scenario-Based Assessment of the Conventional and Base Isolated Reactor Building.....	159
5.3.1	Introduction .....	159
5.3.2	Scaling of Ground Motions .....	162
5.3.3	Analysis Results .....	164
5.3.4	Probability of Unacceptable Performance.....	173
5.3.4.1	Model 1 .....	173
5.3.4.2	Models 2, 3 and 4 .....	178

## TABLE OF CONTENTS (CONT'D)

Chapter	Title	Page
5.3.4.3	Results Using Modified Mean Fragility Curves.....	179
5.4	Time-Based Assessment of the Conventional and Base Isolated Reactor Building.....	180
5.4.1	Hazard Curves .....	180
5.4.2	Scaling of Ground Motions .....	182
5.4.2.1	Model 1 .....	182
5.4.2.2	Models 2, 3 and 4 .....	184
5.4.3	Analysis Results .....	187
5.4.4	Frequency of Unacceptable Performance.....	203
5.4.4.1	Mean Fragility Curves.....	203
5.4.4.2	Mean Fragility Curves Modified by $R_a$ .....	208
<b>6</b>	<b>BLAST ASSESSMENT OF THE SAMPLE NPP REACTOR BUILDINGS .....</b>	<b>209</b>
6.1	Introduction .....	209
6.2	Blast Loading on Structures .....	210
6.2.1	Air Shock.....	210
6.2.2	Ground Shock.....	216
6.3	Blast Loading for the Sample Reactor Buildings .....	222
6.3.1	Introduction .....	222
6.3.2	Blast Threat .....	222
6.3.3	Air Blast Loading .....	223
6.3.3.1	Air3D Model .....	223
6.3.3.2	Pressure Histories .....	227
6.3.4	Ground Shock.....	233
6.4	Blast Assessment of the Sample Reactor Buildings.....	234
6.4.1	Introduction .....	234
6.4.2	LS-DYNA Models for Conventional and Base-Isolated Reactor Buildings .....	236
6.4.3	Response of the Sample Reactor Buildings Subjected to Air Blast Loading .....	238
6.4.3.1	Globe Response.....	238
6.4.3.2	Local Response.....	240
6.4.4	Response of the Sample Reactor Buildings Subjected to Ground Shock.....	242
6.4.4.1	Global Response.....	242
6.4.4.2	Local Response.....	246
6.5	Closing Remarks .....	248

## TABLE OF CONTENTS (CONT'D)

Chapter	Title	Page
<b>7</b>	<b>SUMMARY AND CONCLUSIONS.....</b>	<b>251</b>
7.1	Introduction .....	251
7.2	Scaling of Ground Motions .....	252
7.2.1	Summary .....	252
7.2.2	Conclusions .....	253
7.3	Seismic Performance Assessment .....	254
7.3.1	Summary .....	254
7.3.2	Conclusions .....	255
7.4	Blast Assessment.....	256
7.4.1	Summary .....	256
7.4.2	Conclusions .....	257
<b>8</b>	<b>REFERENCES .....</b>	<b>259</b>
<b>Appendix A</b>	<b>CHARACTERISTICS OF THE LOGNORMAL DISTRIBUTION.....</b>	<b>269</b>
<b>Appendix B</b>	<b>CORRELATED VECTORS FOR PERFORMANCE ASSESSMENT .....</b>	<b>273</b>
B.1	Introduction .....	273
B.2	Algorithm .....	273
B.3	Matlab Code .....	275
<b>Appendix C</b>	<b>NUMBER OF GROUND MOTION RECORDS FOR INTENSITY-BASED ASSESSMENT .....</b>	<b>277</b>
C.1	Introduction .....	277
C.2	Relationship Between $n$ , $X$ , $Z$ and $\beta_Y$ .....	277
C.3	Numbers of Ground Motions Used in the Response Analysis for Intensity-Based Assessment .....	279
<b>Appendix D</b>	<b>EPSILON AND SPECTRAL SHAPE OF 147 NEAR-FAULT RECORDS .....</b>	<b>281</b>
D.1	Near-fault Ground Motion Dataset.....	281
D.2	Epsilon ( $\varepsilon$ ) and Spectral Shape for All Records in the Dataset .....	281
D.3	An Example of Selecting Ground Motions Using $M_w$ , $r$ and $\varepsilon$ .....	284
<b>Appendix E</b>	<b>GEOMETRIC-MEAN SCALING METHOD.....</b>	<b>309</b>

## TABLE OF CONTENTS (CONT'D)

<b>Chapter</b>	<b>Title</b>	<b>Page</b>
<b>Appendix F</b>	<b>PERFORMANCE ASSESSMENT CONSIDERING VARIATIONS IN ISOLATOR MECHANICAL PROPERTIES .....</b>	<b>317</b>
F.1	Treatment of Uncertainty of Isolator Properties for Performance Assessment .....	317
F.2	Impact of Choice of Isolator Properties on the Results of a Performance Assessment .....	318
<b>Appendix G</b>	<b>AIR BLAST LOADS ON SIMPLE AND COMPLEX OBJECTS .....</b>	<b>323</b>
G.1	Introduction .....	323
G.2	Simple Objects .....	323
G.2.1	Two-Dimensional Case .....	323
G.2.2	Three-Dimensional Cases.....	324
G.3	Complex Objects .....	325



## LIST OF FIGURES

Figure	Title	Page
1.1	A blast risk assessment process model .....	4
2.1	Sample NPP reactor building and the corresponding stick model .....	8
2.2	Node numbers for the stick models for the sample NPP reactor building.....	9
2.3	Assumed properties of the LR and Coulomb-friction-FP bearings .....	9
2.4	The influence of $a$ on the velocity dependence of the coefficient of sliding friction .....	11
2.5	Secondary systems in the sample NPP reactor building.....	12
3.1	Seismic probabilistic risk analysis for NPPs .....	15
3.2	Sample hazard curves for an Eastern United States site.....	18
3.3	Sample event and fault trees of NPP accident-sequence analysis .....	20
3.4	Sample fragility curves and probability density function for core melt .....	23
3.5	Sample risk curves.....	24
3.6	Family of fragility curves at 95%, 50% and 5% confidence levels and HCLFP.....	25
3.7	A sample force-displacement relationship of low-rise reinforced concrete walls.....	28
3.8	Sample cumulative distribution function for the probability of unacceptable performance of a NPP .....	32
3.9	Sample cumulative distribution function for the annual frequency of core melt of a NPP .....	33
3.10	A model for shear-displacement backbone curve for reinforced concrete wall segments .....	36
3.11	A sample fragility curve for a secondary system in NPPs .....	39
3.12	Seismic hazard curve and time-based loss calculations .....	42
3.13	Spectral accelerations for 11 sample ground motions for intensity-based assessment.....	44
3.14	Calculation of spectral accelerations given a lognormal distribution.....	47
3.15	Spectral accelerations for 11 sample ground motions for scenario-based assessment.....	47
3.16	Calculation of spectral accelerations given a mean hazard curve .....	48
3.17	Spectral accelerations for 11 sample ground motions at intensities 1 and 8 .....	50
4.1	Sample seismic hazard curves .....	53
4.2	A sample response spectrum (Agrarias station, the 1979 Imperial Valley earthquake) and the 84th, 50th and 16th percentiles of spectra predicted by the attenuation relationship of Abrahamson and Silva (1997) for soil sites.....	56
4.3	Sample uniform hazard spectrum and CMS- $\epsilon$ .....	59
4.4	The CMS- $\epsilon$ and the mean response spectra of record sets selected using Methods 1 through 4.....	59

## LIST OF FIGURES (CONT'D)

Figure	Title	Page
4.5	Mean annual frequency of exceeding various levels of maximum story drift ratio .....	59
4.6	A flow chart for determining the type of spectral shape .....	71
4.7	Spectral accelerations and the regression results for five sample ground motions .....	72
4.8	Elastic acceleration spectra (84th, 50th and 16th percentiles), $\sigma$ and $\beta$ for all ground motion bins and attenuation relationships .....	77
4.9	The impact of geometric mean scaling of pairs of ground motions for the $\theta$ and $\beta$ of spectral acceleration for the selected NF and FF ground motions .....	78
4.10	Eighty-fourth, 50th and 16th percentiles, $\sigma$ and $\beta$ of spectral displacement for Bins 1a and 1b ground motions .....	80
4.11	Eighty-fourth, 50th and 16th percentiles, $\sigma$ and $\beta$ of spectral displacement for Bins 2a and 2b ground motions .....	81
4.12	Eighty-fourth, 50th and 16th percentiles, $\sigma$ and $\beta$ of spectral displacement for Bins 1a and 1c ground motions .....	82
4.13	Eighty-fourth, 50th and 16th percentiles, $\sigma$ and $\beta$ of spectral displacement for Bins 2a and 2c ground motions .....	83
4.14	From hazard curves to a design spectrum .....	85
4.15	The stripes in D-scaling method: a) a sample probability density function (pdf) from Figure 4.14b, b) the cumulative distribution function corresponding to the pdf in Figure 4.15a, c) the stripes of spectral acceleration generated by D-scaling method with 1-second spectral ordinates from Figure 4.15b .....	87
4.16	Eleven stripes (target spectra) from the D-scaling method with $\theta$ and $\beta$ from Bin 2a ground motions .....	91
4.17	Eighty-fourth, 50th and 16th percentiles of $\Theta_{d,7}$ , $B_{d,7}$ and $84TH_{d,7}$ for Bin 1d; and $\theta_{a,50}$ , $\beta_{a,50}$ and $84th_{a,50}$ for Bin 1a motions .....	92
4.18	Eighty-fourth, 50th and 16th percentiles of $\Theta_{d,11}$ , $B_{d,11}$ and $84TH_{d,11}$ for Bin 1d; and $\theta_{a,50}$ , $\beta_{a,50}$ and $84th_{a,50}$ for Bin 1a motions .....	93
4.19	Eighty-fourth, 50th and 16th percentiles of $\Theta_{d,21}$ , $B_{d,21}$ and $84TH_{d,21}$ for Bin 1d; and $\theta_{a,50}$ , $\beta_{a,50}$ and $84th_{a,50}$ for Bin 1a motions .....	94
4.20	Eighty-fourth, 50th and 16th percentiles of $\Theta_{d,7}$ , $B_{d,7}$ and $84TH_{d,7}$ for Bin 2d; and $\theta_{a,50}$ , $\beta_{a,50}$ and $84th_{a,50}$ for Bin 2a motions .....	95
4.21	Eighty-fourth, 50th and 16th percentiles of $\Theta_{d,11}$ , $B_{d,11}$ and $84TH_{d,11}$ for Bin 2d; and $\theta_{a,50}$ , $\beta_{a,50}$ and $84th_{a,50}$ for Bin 2a motions .....	96
4.22	Eighty-fourth, 50th and 16th percentiles of $\Theta_{d,21}$ , $B_{d,21}$ and $84TH_{d,21}$ for Bin 2d; and $\theta_{a,50}$ , $\beta_{a,50}$ and $84th_{a,50}$ for Bin 2a motions .....	97

## LIST OF FIGURES (CONT'D)

Figure	Title	Page
4.23	Confidence levels for $0.9 \leq R_{\Theta_{d,7}}, R_{B_{d,7}}$ or $R_{84TH_{d,7}} \leq 1.1$ and $0.9 \leq R'_{\Theta_{d,7}}, R'_{B_{d,7}}$ or $R'_{84TH_{d,7}} \leq 1.1$ for Bin 1d ground motions.....	99
4.24	Confidence levels for $0.9 \leq R_{\Theta_{d,11}}, R_{B_{d,11}}$ or $R_{84TH_{d,11}} \leq 1.1$ and $0.9 \leq R'_{\Theta_{d,11}}, R'_{B_{d,11}}$ or $R'_{84TH_{d,11}} \leq 1.1$ for Bin 1d ground motions.....	100
4.25	Confidence levels for $0.9 \leq R_{\Theta_{d,21}}, R_{B_{d,21}}$ or $R_{84TH_{d,21}} \leq 1.1$ and $0.9 \leq R'_{\Theta_{d,21}}, R'_{B_{d,21}}$ or $R'_{84TH_{d,21}} \leq 1.1$ for Bin 1d ground motions.....	101
4.26	Confidence levels for $0.9 \leq R_{\Theta_{d,7}}, R_{B_{d,7}}$ or $R_{84TH_{d,7}} \leq 1.1$ and $0.9 \leq R'_{\Theta_{d,7}}, R'_{B_{d,7}}$ or $R'_{84TH_{d,7}} \leq 1.1$ for Bin 2d ground motions.....	102
4.27	Confidence levels for $0.9 \leq R_{\Theta_{d,11}}, R_{B_{d,11}}$ or $R_{84TH_{d,11}} \leq 1.1$ and $0.9 \leq R'_{\Theta_{d,11}}, R'_{B_{d,11}}$ or $R'_{84TH_{d,11}} \leq 1.1$ for Bin 2d ground motions.....	103
4.28	Confidence levels for $0.9 \leq R_{\Theta_{d,21}}, R_{B_{d,21}}$ or $R_{84TH_{d,21}} \leq 1.1$ and $0.9 \leq R'_{\Theta_{d,21}}, R'_{B_{d,21}}$ or $R'_{84TH_{d,21}} \leq 1.1$ for Bin 2d ground motions.....	104
4.29	$\theta_{a,50}/\theta_{\Theta_{d,21}}, \beta_{a,50}/\theta_{B_{d,21}}, C_{\theta}$ and $C_{\beta}$ for Bin 1d ground motions .....	107
4.30	$\theta_{a,50}/\theta_{\Theta_{d,21}}, \beta_{a,50}/\theta_{B_{d,21}}, C_{\theta}$ and $C_{\beta}$ for Bin 2d ground motions .....	108
4.31	Eighty-fourth, 50th and 16th percentiles of $\Theta_{e,11}, B_{e,11}$ and $84TH_{e,11}$ for modified Bin 1e motions; and $\theta_{a,50}, \beta_{a,50}$ and $84th_{a,50}$ for Bin 1a motions.....	111
4.32	Eighty-fourth, 50th and 16th percentiles of $\Theta_{e,21}, B_{e,21}$ and $84TH_{e,21}$ for modified Bin 1e motions; and $\theta_{a,50}, \beta_{a,50}$ and $84th_{a,50}$ for Bin 1a motions.....	112
4.33	Eighty-fourth, 50th and 16th percentiles of $\Theta_{e,11}, B_{e,11}$ and $84TH_{e,11}$ for modified Bin 2e motions; and $\theta_{a,50}, \beta_{a,50}$ and $84th_{a,50}$ for Bin 2a motions.....	113
4.34	Eighty-fourth, 50th and 16th percentiles of $\Theta_{e,21}, B_{e,21}$ and $84TH_{e,21}$ for modified Bin 2e motions; and $\theta_{a,50}, \beta_{a,50}$ and $84th_{a,50}$ for Bin 2a motions.....	114
4.35	Confidence levels for $0.9 \leq R_{\Theta_{e,11}}, R_{B_{e,11}}$ or $R_{84TH_{e,11}} \leq 1.1$ and $R_{\Theta_{e,11}}, R_{B_{e,11}}$ or $R_{84TH_{e,11}} \geq 0.9$ for Bin 1e ground motions.....	115
4.36	Confidence levels for $0.9 \leq R_{\Theta_{e,21}}, R_{B_{e,21}}$ or $R_{84TH_{e,21}} \leq 1.1$ and $R_{\Theta_{e,21}}, R_{B_{e,21}}$ or $R_{84TH_{e,21}} \geq 0.9$ for Bin 1e ground motions .....	116
4.37	Confidence levels for $0.9 \leq R_{\Theta_{e,11}}, R_{B_{e,11}}$ or $R_{84TH_{e,11}} \leq 1.1$ and $R_{\Theta_{e,11}}, R_{B_{e,11}}$ or $R_{84TH_{e,11}} \geq 0.9$ for Bin 2e ground motions.....	117
4.38	Confidence levels for $0.9 \leq R_{\Theta_{e,21}}, R_{B_{e,21}}$ or $R_{84TH_{e,21}} \leq 1.1$ and $R_{\Theta_{e,21}}, R_{B_{e,21}}$ or $R_{84TH_{e,21}} \geq 0.9$ for Bin 2e ground motions .....	118
4.39	$\theta_{a,50}/\theta_{\Theta_{e,21}}, \beta_{a,50}/\theta_{B_{e,21}}$ and $84th_{a,50}/\theta_{84TH_{e,21}}$ for Bin 1e ground motions.....	119
4.40	$\theta_{a,50}/\theta_{\Theta_{e,21}}, \beta_{a,50}/\theta_{B_{e,21}}$ and $84th_{a,50}/\theta_{84TH_{e,21}}$ for Bin 2e ground motions.....	120
4.41	Eighty-fourth, 50th and 16th percentiles of $\Theta_{f,11}, B_{f,11}$ and $84TH_{f,11}$ for Bin 1f; and $\theta_{a,50}, \beta_{a,50}$ and $84th_{a,50}$ for Bin 1a motions .....	122

## LIST OF FIGURES (CONT'D)

Figure	Title	Page
4.42	Eighty-fourth, 50th and 16th percentiles of $\Theta_{f,11}$ , $B_{f,11}$ and $84TH_{f,11}$ for Bin 2f; and $\theta_{a,50}$ , $\beta_{a,50}$ and $84th_{a,50}$ for Bin 2a motions.....	123
4.43	Confidence levels for $0.8 \leq R_{\Theta_{f,11}}, R_{B_{f,11}}$ or $R_{84TH_{f,11}} \leq 1.2$ and $0.8 \leq R_{\theta_{f,11}}, R_{\beta_{f,11}}$ or $R_{84TH_{f,11}} \leq 1.5$ for Bin 1f motions .....	125
4.44	Confidence levels for $0.8 \leq R_{\Theta_{f,11}}, R_{B_{f,11}}$ or $R_{84TH_{f,11}} \leq 1.2$ and $0.8 \leq R_{\theta_{f,11}}, R_{\beta_{f,11}}$ or $R_{84TH_{f,11}} \leq 1.5$ for Bin 2f motions .....	126
5.1	Development of the SSE spectrum (USNRC 1997).....	130
5.2	Horizontal design response spectrum of USNRC Regulatory Guide 1.60 for a damping ratio of 5%, normalized to a peak ground acceleration of 1 g.....	130
5.3	The URS for the sample NPP reactor building for a MAFE of $10^{-5}$ .....	132
5.4	The spectra established using a) the performance-based procedure; b) the attenuation model of McGuire et. al. (2001), magnitude of 5.5, distance of 20 km and PGA of 0.351 g; and c) the Regulatory Guide 1.60 with PGA of 0.351 g.....	134
5.5	The URS for the sample NPP and the median spectra of the two bins of 11 ground motions randomly selected from Tables 4.1 and 4.2 and scaled to the URS at a period of 0.14 second.....	135
5.6	Deaggregation of $S_{1-2.5}$ and $S_{5-10}$ at an annual frequency of exceedance of $10^{-5}$ for the sample NPP site .....	137
5.7	The URS for the sample NPP and the response spectra of the 11 ground motions generated by SGMS and scaled to the URS at a period of 0.14 second.....	138
5.8	The URS for the sample NPP and the median spectrum of the 11 ground motions generated by SGMS and scaled to the URS at a period of 0.14 second.....	138
5.9	Floor spectral accelerations at Nodes 201, 1009 and 216 computed using the linear response-history analysis of Section 5.2.3.1 .....	140
5.10	Fragility curves for the secondary systems at Nodes 201, 1009 and 216.....	144
5.11	Floor response spectra for the design of secondary systems at Nodes 1009 and 216 .....	145
5.12	A fault tree for the unacceptable performance of the sample NPP.....	146
5.13	Floor spectral accelerations at Nodes 201, 1009 and 216 computed using non-linear response-history analyses for the intensity-based assessment of Model 1 .....	148
5.14	AFSA at Nodes 201, 1009 and 216 generated using 1) response-history analysis, and 2) the procedure of Appendix B for the intensity-based assessment of Model 1 .....	150
5.15	Distributions of the probability of unacceptable performance for Analyses 1a and 1b for the intensity-based assessment of Model 1 .....	152

## LIST OF FIGURES (CONT'D)

<b>Figure</b>	<b>Title</b>	<b>Page</b>
5.16	Distributions and arithmetic means of the probability of unacceptable performance for Analyses 1a, 1c and 1d for the intensity-based assessment of Model 1 .....	153
5.17	Median and mean fragility curves for the secondary systems at Nodes 201, 1009 and 216 .....	154
5.18	Distributions of the probability of unacceptable performance for Analyses 2 and 3a for the intensity-based assessment of Model 1 .....	155
5.19	Definition of confidence level .....	156
5.20	Distributions of the probability of unacceptable performance for Analyses 3a, b, c, e and g for the intensity-based assessment of Model 1 .....	157
5.21	Medians and dispersions of the probability of unacceptable performance for Analysis 3 for the intensity-based assessment of Model 1 as a function of the number of row vectors of the DP matrix .....	157
5.22	Distributions of the probability of unacceptable performance for Analyses 1d and 3 for the intensity-based assessment of Model 1 .....	158
5.23	Deaggregation of the 2-second seismic hazard at a annual frequency of exceedance of $2 \times 10^{-4}$ for the sample NPP site (USGS 2008).....	160
5.24	Median spectral accelerations predicted by Campbell (2003) for three magnitude-distance pairs: (5.3, 7.5 km), (6.3, 37.5 km) and (7.3 and 538 km) .....	161
5.25	Spectral accelerations of the 11 scaled SGMS ground motions and the 11 target spectral ordinates for scenario-based assessment.....	163
5.26	Median, 84th and 16th percentiles of spectral accelerations a) predicted by Campbell (2003) for $M= 5.3$ and $r= 7.5$ km, and b) of the 11 scaled SGMS ground motions for scenario-based assessment.....	164
5.27	Floor spectral accelerations at Nodes 201, 1009 and 216 in the X direction for the scenario-based assessment of Models 1, 2, 3 and 4.....	165
5.28	Floor spectral accelerations at Nodes 201, 1009 and 216 in the Y direction for the scenario-based assessment of Models 1, 2, 3 and 4.....	166
5.29	AFSA at Nodes 201 and 216 in the X direction generated using 1) response-history analyses, and 2) the procedure of Appendix B for the scenario-based assessment of Models 1, 2, 3 and 4 .....	170
5.30	AFSA at Nodes 201 and 216 in the Y direction generated using 1) response-history analyses, and 2) the procedure of Appendix B for the scenario-based assessment of Models 1, 2, 3 and 4 .....	171

## LIST OF FIGURES (CONT'D)

Figure	Title	Page
5.31	AFSA at Nodes 201 and 216 generated using 1) response-history analyses, and 2) the procedure of Appendix B for the scenario-based assessment of Models 2, 3 and 4 .....	172
5.32	Distributions of the probability of unacceptable performance for Analyses 1a and 1b for the scenario-based assessment of Model 1 .....	173
5.33	Distributions of the probability of unacceptable performance for Analyses 2 and 3a for the scenario-based assessment of Model 1 established a) from sorting the realizations and b) using a lognormal distribution .....	175
5.34	Distributions of the probability of unacceptable performance for Analyses 3a, b, c, e and g for the scenario-based assessment of Model 1 .....	176
5.35	Medians and dispersions of the probability of unacceptable performance for Analysis 3 for the scenario-based assessment of Model 1 as a function of the number of row vectors of the DP matrix .....	176
5.36	Distributions of the probability of unacceptable performance for Analyses 1b and 3 for the scenario-based assessment of Model .....	177
5.37	Probability of unacceptable performance as a function of $R_a$ for the scenario-based assessment of Models 2, 3 and 4 using 2000 row vectors .....	177
5.38	Probability of unacceptable performance as a function of $R_a$ for the scenario-based assessment of Models 2, 3 and 4 using 200,000 row vectors .....	178
5.39	Seismic hazard curves at periods of 0.1, 0.14, 1 and 2 seconds for the sample NPP Site .....	181
5.40	Computation of target spectral ordinates for scaling ground motions for the time-based assessment of Model 1 .....	184
5.41	Response spectra of the ground motions in Bins TC1 and TC8 .....	186
5.42	Computation of target spectral ordinates for scaling ground motions for the time-based assessment of Models 2, 3 and 4 .....	187
5.43	Response spectra of the ground motions in Bins TI1 and TI8 .....	188
5.44	Floor spectral accelerations at Nodes 201, 1009 and 216 in the X direction from the response-history analyses of 1) Model 1 subjected to the Bin TC1 motions, and 2) Models 2, 3 and 4 subjected to the Bin TI1 motions .....	189
5.45	Floor spectral accelerations at Nodes 201, 1009 and 216 in the Y direction from response-history analyses of 1) Model 1 subjected to the Bin TC1 motions, and 2) Models 2, 3 and 4 subjected to the Bin TI1 motions .....	190

## LIST OF FIGURES (CONT'D)

<b>Figure</b>	<b>Title</b>	<b>Page</b>
5.46	AFSA at Nodes 201 and 216 in the X direction generated using 1) response-history analyses, and 2) the procedure of Appendix B for 1) Model 1 subjected to the Bin TC1 ground motions, and 2) Models 2, 3 and 4 subjected to the Bin TI1 ground motions .....	191
5.47	AFSA at Nodes 201 and 216 in the Y direction generated using 1) response-history analyses, and 2) the procedure of Appendix B for 1) Model 1 subjected to the Bin TC1 ground motions, and 2) Models 2, 3 and 4 subjected to the Bin TI1 ground motions .....	192
5.48	AFSA at Nodes 201 and 216 generated using 1) response-history analyses, and 2) the procedure of Appendix B for Models 2, 3 and 4 subjected to the Bin TI1 ground motions .....	193
5.49	Floor spectral accelerations at Nodes 201, 1009 and 216 in the X direction from response-history analyses of 1) Model 1 subjected to the Bin TC8 motions, and 2) Models 2, 3 and 4 subjected to the Bin TI8 motions .....	194
5.50	Floor spectral accelerations at Nodes 201, 1009 and 216 in the Y direction from response-history analyses of 1) Model 1 subjected to the Bin TC8 motions, and 2) Models 2, 3 and 4 subjected to the Bin TI8 motions .....	195
5.51	AFSA at Nodes 201 and 216 in the X direction generated using 1) response-history analyses, and 2) the procedure of Appendix B for 1) Model 1 subjected to the Bin TC8 ground motions, and 2) Models 2, 3 and 4 subjected to the Bin TI8 ground motions .....	196
5.52	AFSA at Nodes 201 and 216 in the Y direction generated using 1) response-history analyses, and 2) the procedure of Appendix B for 1) Model 1 subjected to the Bin TC8 ground motions, and 2) Models 2, 3 and 4 subjected to the Bin TI8 ground motions .....	197
5.53	AFSA at Nodes 201 and 216 generated using 1) response-history analyses, and 2) the procedure of Appendix B for Models 2, 3 and 4 subjected to the Bin TI8 ground motions .....	198
5.54	Median of AFSA at Nodes 201, 1009 and 216 as a function of ground motion bin for the time-based assessments of Models 1, 2, 3 and 4 .....	204
5.55	Logarithmic standard deviation ( $\beta$ ) of AFSA at Nodes 201, 1009 and 216 as a function of ground motion bin for the time-based assessments of Models 1, 2, 3 and 4 .....	205

## LIST OF FIGURES (CONT'D)

Figure	Title	Page
5.56	Annual frequency of unacceptable performance as a function of $R_a$ using 2000 row vectors .....	208
6.1	Sample pressure results for an Air3D analysis for a surface detonation of 2000 kg of TNT .....	213
6.2	Mapping in Air3D for the sample reactor building .....	214
6.3	A sample shape function for ground shock simulation .....	221
6.4	TSWG threat chart.....	224
6.5	Blast analysis for the sample NPPs .....	225
6.6	Location of a sample monitoring point in the Air3D model for the sample reactor building.....	226
6.7	Pressure histories at Points A, C and D of Figure 6.5 for the blast analysis of the sample NPP .....	228
6.8	Pressure histories of Figure 6.7 with the same scale for the Y axis .....	228
6.9	Pressure contour plots for the blast analysis of Section 6.3.3 at the instant of 6.57 msec after detonation.....	229
6.10	Pressure contour plots for the blast analysis of Section 6.3.3 at the instant of 18 msec after detonation.....	230
6.11	Pressure contour plots for the blast analysis of Section 6.3.3 at the instant of 154 msec after detonation.....	231
6.12	Actual and simplified pressure histories at Point D of Figure 6.5.....	232
6.13	Translational load history for the sample NPP containment building .....	232
6.14	Normalized power spectrum for ground shock simulation .....	233
6.15	Acceleration, velocity and displacement histories used in the ground shock analysis of the sample reactor buildings.....	235
6.16	LS-DYNA model for the conventional reactor building .....	237
6.17	LS-DYNA model for the base-isolated reactor building.....	238
6.18	Base shear histories for the conventional and base-isolated reactor buildings subjected to the air blast loading of Section 6.3.3 .....	239
6.19	Acceleration history at the base slab of the containment structure for the base-isolated reactor building subjected to the air blast loading of Section 6.3.3 .....	241
6.20	FFT magnitude of the acceleration history of Figure 6.19 .....	241



## LIST OF FIGURES (CONT'D)

Figure	Title	Page
6.21	Acceleration histories and floor spectral accelerations at Nodes 201, 1009 and 216 for the base-isolated reactor building subjected to the air blast loading of Section 6.3.3.....	243
6.22	Base shear histories for the containment vessel of the conventional and base-isolated reactor buildings subjected to the ground shock of Figure 6.15.....	244
6.23	Base shear histories for the internal structure in the conventional and base-isolated reactor buildings subjected to the ground shock of Figure 6.15.....	245
6.24	Acceleration history at the base slab of the base-isolated containment structure subjected to the ground shock of Figure 6.15.....	246
6.25	Acceleration histories below and above the isolators for the base-isolated containment structure subjected to the ground shock of Figure 6.15.....	246
6.26	Acceleration histories and floor spectral accelerations at Nodes 201, 1009 and 216 for the conventional and base-isolated reactor buildings subjected to the ground shock of Figure 6.15.....	247
6.27	Floor spectral accelerations at Nodes 201, 1009 and 216 at frequencies of 5 through 100 Hz for the conventional reactor building subjected to the ground shock of Figure 6.15.....	248
A.1	Characteristics of a lognormal distribution .....	271
B.1	Generation of vectors of correlated demand parameters (Yang 2006).....	276
C.1	A standardized normal distribution .....	280
D.1	Good-of-fit test for the distribution of $\varepsilon$ .....	303
D.2	Geometric-mean spectra for the records in the period bins P1 through P5 and the $\varepsilon$ bins of (2, 1), (1, 0), (0, -1) and (-1, -2).....	304
D.3	Spectral accelerations predicted by Chiou-Youngs NGA relationship for a moment magnitude of 6.8, a site-to-source distance of 1.6 km and $\varepsilon$ of 1.5, 0 and -1.5, and the corresponding CMS for $\varepsilon$ of 1.5 and -1.5 .....	305
D.4	The correlation coefficient used to generate the CMS of Figure D.3.....	305
D.5	UHS, CMS and the geomean spectral accelerations for sample earthquake records for a rock site at 122.2°W, 37.8°N and earthquake shaking return periods of 2475, 475 and 108 years.....	306
D.6	Deaggregation of 1-second seismic hazard with 2% probability of exceedance in 50 years for a rock site at 122.2°W, 37.8°N .....	307

## LIST OF FIGURES (CONT'D)

<b>Figure</b>	<b>Title</b>	<b>Page</b>
D.7	Deaggregation of 1-second seismic hazard with 10% probability of exceedance in 50 years for a rock site at 122.2°W, 37.8°N .....	307
D.8	Deaggregation of 1-second seismic hazard with 50% probability of exceedance in 75 years for a rock site at 122.2°W, 37.8°N .....	308
E.1	Median spectral accelerations for the ground motions bins E0, E1 and E2 and the target spectral accelerations for Bins E1 and E2 .....	315
F.1	Floor spectral accelerations at Nodes 201, 1009 and 216 in the X direction for the scenario-based assessment of Models 2, 3, 4 and 5 .....	320
F.2	Floor spectral accelerations at Nodes 201, 1009 and 216 in the Y direction for the scenario-based assessment of Models 2, 3, 4 and 5 .....	321
F.3	Probability of unacceptable performance as a function of the median-capacity ratio of fragility curves using Analysis 3e of Section 5.3.4.1 for the scenario-based assessment of Models 2, 3, 4 and 5 .....	322
G.1	Blast analysis of Section G.2.1 for a 30×30 m object .....	327
G.2	Pressure contour plots for the blast analysis of Section G.2.1 .....	328
G.3	Translational load histories for the analysis of Section G.2.1 .....	332
G.4	Blast analysis of Section G.2.2 for a 30×30×20 m object .....	333
G.5	Distribution of pressure monitors on the front surface of the object of Figure G.4 .....	333
G.6	Translational load histories for the analysis of Figure G.4 with R= 30 meters .....	334
G.7	Translational load histories for the analysis of Figure G.4 with R= 15 meters .....	334
G.8	Pressure histories for the analysis of Figure G.4 with R= 15 meters at locations 1, 2 and 3 of Figure G.5.....	335
G.9	Interaction of a shock front with a cylinder (Baker 1973) .....	336
G.10	Pressure contour plot for the blast analysis of Section G.3 .....	337
G.11	Sample pressure results for the analysis of Section G.3 at 0.9 msec after detonation .....	341
G.12	Translational load histories for the analysis of Section G.3 .....	341

## LIST OF TABLES

Table	Title	Page
2.1	Description of response-history-analysis models .....	10
2.2	Node numbers and elevations for the supports of the key secondary systems in the internal structure of the sample NPP building .....	12
3.1	Logarithmic standard deviation for the factors of safety for mechanical equipment (Kennedy and Ravindra 1984).....	29
3.2	A sample matrix of demand parameters .....	37
3.3	Values of $\eta_i$ for generating a distribution of $S_{ai}(T_1)$ .....	45
4.1	Near-field ground motions .....	64
4.2	Far-field ground motions.....	65
4.3	Parameters for the seed motions NF11 through NF20 .....	66
4.4	Epsilon ( $\varepsilon$ ) and spectral shape of the near-fault ground motions of Table 4.1 .....	67
4.5	Epsilon ( $\varepsilon$ ) and spectral shape of the far-field ground motions of Table 4.2.....	69
4.6	Numbers of the NF and FF ground motions in the $\varepsilon$ bins at periods of 0.2, 0.5, 1, 2 and 4 seconds.....	70
4.7	Period bins for the computation of spectral shape.....	70
4.8	Types of spectral shape .....	71
4.9	Numbers of the NF and FF ground motions as a function of the period bins of Table 4.7 and the types of spectral shape of Table 4.8.....	73
4.10	Ground motion bins.....	74
4.11	$\alpha_i$ for the D-scaling method.....	89
5.1	Calculations of the URS of Figure 5.3 .....	133
5.2	AFSA at Nodes 201, 1009 and 216 of Model 1 computed using the linear response-history analysis of Section 5.2.3.1.....	141
5.3	Logarithmic standard deviations for developing fragility curves used in this report .....	142
5.4	AFSA at Nodes 201, 1009 and 216 for intensity-based assessment of Model 1.....	145
5.5	The values of AFSA associated with a 1% and a 10% probability of failure for the median fragility curves of Figure 5.10 .....	146
5.6	Analyses 1, 2 and 3 for the intensity-based assessment of Model 1.....	149

## LIST OF TABLES (CONT'D)

<b>Table</b>	<b>Title</b>	<b>Page</b>
5.7	Statistics of Analysis 3 for the intensity-based assessment of Model 1 .....	158
5.8	Target spectral accelerations for scenario-based assessment at a period of 0.14 second .....	162
5.9	AFSA at Nodes 201, 1009 and 216 for scenario-based assessment of Model 1 .....	167
5.10	AFSA at Nodes 201, 1009 and 216 for scenario-based assessment of Model 2 .....	167
5.11	AFSA at Nodes 201, 1009 and 216 for scenario-based assessment of Model 3 .....	168
5.12	AFSA at Nodes 201, 1009 and 216 for scenario-based assessment of Model 4 .....	168
5.13	Median and logarithmic standard deviation of AFSA at Nodes 201, 1009 and 216 for scenario-based assessment .....	169
5.14	Analyses 1, 2 and 3 for the scenario-based assessment of Model 1 .....	174
5.15	Statistics of Analysis 3 for the scenario-based assessment of Model 1 .....	174
5.16	Seismic hazard curves at periods of 0.14 and 2 seconds for the sample NPP site .....	182
5.17	Spectral accelerations and MAFEs ( $\lambda_i$ ) at the boundaries of spectral intervals on the seismic hazard curves of Figure 5.40 and Figure 5.42.....	185
5.18	Mean annual frequency (MAF) for the eight spectral intervals in time-based assessment.....	185
5.19	AFSA at Nodes 201, 1009 and 216 of Model 1 subjected to the Bin TC1 ground motions.....	199
5.20	AFSA at Nodes 201, 1009 and 216 of Model 2 subjected to the Bin TI1 ground motions .....	199
5.21	AFSA at Nodes 201, 1009 and 216 of Model 3 subjected to the Bin TI1 ground motions .....	200
5.22	AFSA at Nodes 201, 1009 and 216 of Model 4 subjected to the Bin TI1 ground motions .....	200
5.23	AFSA at Nodes 201, 1009 and 216 of Model 1 subjected to the Bin TC8 ground motions.....	201
5.24	AFSA at Nodes 201, 1009 and 216 of Model 2 subjected to the Bin TI8 ground motions .....	201
5.25	AFSA at Nodes 201, 1009 and 216 of Model 3 subjected to the Bin	

## LIST OF TABLES (CONT'D)

<b>Table</b>	<b>Title</b>	<b>Page</b>
	TI8 ground motions .....	202
5.26	AFSA at Nodes 201, 1009 and 216 of Model 4 subjected to the Bin TI8 ground motions .....	202
5.27	Computation of annual frequency of unacceptable performance of Model 1 using 2,000 row vectors.....	207
5.28	Computation of annual frequency of unacceptable performance of Models 2, 3 and 4 using 200,000 row vectors .....	207
6.1	PPA, PPV and PPD predicted by Smith and Hetherington (1994), TM5-1300 (DoA 1991) and Westine (1978) for a surface explosion of 2000 kg of TNT at a distance of 31 m.....	219
6.2	PPA, PPV and PPD predicted by TM5-1300 (DoA 1991), Westine (1978) and Wu and Hao (1995) for a surface explosion on granite of 2000 kg of TNT at a distance of 31 m .....	222
6.3	Parameters for ground shock simulation .....	233
6.4	Drifts and base shears of the conventional and base-isolated containment vessels subjected to the blast loading of Section 6.3 .....	240
6.5	Peak floor accelerations and AFSA at Nodes 201, 1009 and 216 for the conventional and base-isolated reactor buildings subjected to the blast loading of Section 6.3.....	242
6.6	Arrival times for air blast and ground shock waves at Points D, E and F of Figure 6.5 .....	249
B.1	A Matlab code for generating correlated vectors of demand parameters.....	275
C.1	Sample values for $\beta_Y$ , $Z$ , $X$ , and $n$ per (C.7) .....	280
D.1	Earthquake ground motion record pairs from PEER NGA Database.....	287
D.2	Epsilon ( $\varepsilon$ ) and spectral shape for the records of Table D.1 .....	292
D.3	Number of records from Table D.1 in $\varepsilon$ bins at periods of 0.2, 0.5, 1, 2 and 4 seconds.....	301
D.4	Number of records from Table D.1 as a function of the period bin and type of spectral shape .....	301

## LIST OF TABLES (CONT'D)

Table	Title	Page
D.5	Spectral accelerations and governing events of 1-second seismic hazard with return periods of 2475, 475 and 108 years for a rock site at 122.2°W, 37.8°N .....	302
D.6	Ground motion bins D1 through D4.....	302
E.1	Spectral accelerations for the ground motion bins E0 and E1 at periods of 0.3, 0.6 and 2 seconds .....	312
E.2	Spectral accelerations for the ground motion bins E0 and E2 at periods of 0.3, 0.6 and 2 seconds .....	312
E.3	Median ( $\theta$ ) and $\beta$ for spectral accelerations for all bins of ground motion .....	313
E.4	Normalized median spectral accelerations for all ground motion bins .....	314
E.5	Variation in scale factor $a$ as a function of spectrum matching periods.....	314
F.1	Ratios of median AFSA of Models 5 and 2 and those of Models 5 and 3 in the X direction for the scenario-based assessment .....	319
G.1	Peak reflected overpressures, impulses and arrival times for the pressure histories of Figure G.8a.....	326

# CHAPTER 1

## INTRODUCTION

### 1.1 Hazard Assessment of Nuclear Power Plants

Nuclear power plants (NPPs) and spent nuclear fuel (SNF) facilities are required by code and regulations to be designed for a family of extreme events, including very rare earthquake shaking, loss of coolant accidents, and tornado-borne missile impacts. The terrorist attacks of September 11, 2001, added another extreme event to the family, namely, attack by improvised explosive devices and military munitions.

This report explores the opportunities afforded to designers of NPPs and SNF facilities by the use of seismic isolation systems. Prior studies have shown that the use of seismic or base isolation can substantially reduce demands on primary structural components in buildings, bridges and mission-critical infrastructure, but little attention has been focused on the secondary or nonstructural systems despite the fact that such systems often represent 80+% of the capital investment. This report addresses this oversight and focuses to the large part on such systems.

Improvements in structural systems to respond to one hazard have resulted in the past in poorer performance when subjected to other hazards. One example is the conflict between earthquake shaking and blast loading, where a reduction in mass will generally lead to better seismic performance and poorer blast performance. Given that NPPs have been designed in the past for earthquake shaking, loss of coolant accidents and tornado-borne missile loadings, the focus of this report is on the possible conflicts between seismic improvements in the form of base isolation and the impact of such improvements on the blast tolerance of nuclear structures.

### 1.2 Seismic Performance Assessment

#### *1.2.1 Conventional and Base Isolated Nuclear Power Plants*

The U.S. Nuclear Regulatory Commission (USNRC) Regulatory Guide RG 1.165 (USNRC 1997) specifies that the Safe Shutdown Earthquake (SSE) for the seismic design of safety-related nuclear structures be based on a 5% damped response spectrum with a median return period of 100,000 years (or a median annual probability of exceedance of  $1 \times 10^{-5}$ ). For many NPP and SNF sites in the U.S., earthquake shaking associated with the SSE will result in high seismic acceleration demands in the stiff NPP structural systems and extremely high demands on the safety-related secondary systems.

Seismic isolation systems can substantially mitigate these high demands on primary structural components and secondary mechanical, electrical and piping systems, by reducing the natural frequency of the NPP structure (Huang et al. 2007a) and can enable direct reductions in overnight capital cost and standardization of NPP and SNF facility designs and simplified design and regulatory review, facilitate design certification and the granting of early site permits and construction and operating licenses, and enhance NPP and SNF safety at lower capital cost.

Although seismic isolation is widely used to protect mission-critical infrastructure, there are only 6 applications to NPPs: four in France and two in South Africa (Buckle et al. 1987). To identify the utility of seismic isolation to reduce seismic risk in NPPs, a probabilistic study was performed that assessed the seismic performance of sample conventional and base isolated NPPs. This report presents the results of this study.

Seismic Probabilistic Risk Assessment (SPRA) was developed in 1981 and subsequently accepted by the United States Nuclear Regulatory Commission (USNRC) to be used in NPP Individual Plant Examination of External Events (IPEEE). The traditional SPRA procedure is improved in this report (Chapters 3 and 5) to assess the performance of conventional and base isolated NPPs. The improvements are based in part on the next generation tools being developed for seismic performance-based design of buildings. The following subsection briefly introduces the development of performance-based earthquake engineering (PBEE).

### ***1.2.2 Seismic Performance-Based Design of Buildings***

Force-based approaches have been used in the United States for the design of buildings for more than eight decades (ATC 1995). The structural and non-structural damages observed during the 1989 Loma Prieta and 1994 Northridge earthquakes motivated expert practitioners and researchers to reassess these traditional approaches and to develop the first-generation tools for PBEE, such as those documented in FEMA 273 and 274 (FEMA 1997), FEMA 356 (FEMA 2000b) and ASCE/SEI 41-06 (ASCE 2006). The deterministic assessment procedures in those documents provided relations between structural response indices (such as story drifts and inelastic member deformations) and performance levels (such as immediate occupancy, life safety and collapse prevention) and shifted the focus of assessment from forces to displacements and deformations. FEMA 350 (FEMA 2000a), which was drafted as part of the SAC Steel Project, extended the first generation tools through the use of probabilistic assessment procedures.



Another focus of PBEE is the performance of secondary or non-structural systems in buildings. Astrella and Whittaker (2004) proposed a change on the design paradigm for performance-based design recognizing that nonstructural components and contents (NCCs) represent the greatest investment in most buildings (NIBS 1997, Taghavi and Miranda 2003). Traditionally, NCCs have been overlooked in the preliminary design of a building: they are usually designed and detailed after the structural framing has been finalized. Such a procedure can not minimize either the seismic demands on NCCs or the total capital cost of a building. Astrella and Whittaker recommended that the performance-based design process should focus first and foremost on the most significant investments in the building, namely, the NCCs.

In contrast to the first-generation tools for PBEE, where performance assessments are performed using a deterministic approach, the ATC-58 project is developing next-generation tools and guidelines for performance-based seismic design and assessment using a probability framework, which can incorporate the inherent uncertainties and variabilities in seismic hazard, structural and non-structural responses, damage states and repair costs in the assessment process. The 35% draft *Guidelines for Seismic Performance Assessment of Buildings* (termed the *draft ATC-58 Guidelines* hereafter), presents the assessment procedures developed to date in the ATC-58 project, which can estimate the probability of a building exceeding a given performance level for a given intensity of shaking, magnitude-distance pair, and shaking over time (ATC 2007). Performance levels are defined in terms of direct economic loss, casualties and downtime, and are fundamentally different from those used in the first-generation PBEE tools.

One key issue in the seismic performance assessment procedure is the selection and scaling of ground motions for response-history analysis. Ground motions used in response-history analysis need to be selected and scaled to properly represent the seismic hazard selected for a performance assessment so that one can properly capture the *distribution* (both median and dispersion) of structural responses and accordingly estimate the probability of the building exceeding a given performance level for the selected seismic hazard. The *draft ATC-58 Guidelines* use scaling procedures different from those presented in other design codes. The scaling procedures of the *Guidelines* were established in the large part based on the research results presented in this report. Detailed information for these scaling procedures and their technical basis are presented in Chapters 3 and 4 of this report, respectively.

### 1.3 Blast Assessment

Methodologies for risk assessment for blast loading have been developed for buildings, bridges and infrastructures. A typical example is shown in Figure 1.2, which illustrates the risk assessment process recommended in FEMA 452 for mitigating terrorist attacks against buildings (FEMA 2005).

In FEMA 452, risk is defined by the product of a threat rating, asset value and vulnerability rating. As shown in Figure 1.2, the risk assessment process begins with a threat assessment, which identifies, defines and quantifies the design basis threats. Step 2 identifies the value of a building's assets that need to be protected. Step 3 evaluates the potential vulnerability of the critical assets against the identified threats. The risk for each critical asset is determined in Step 4. The final step is to consider mitigation options for the major risks identified in Step 4.

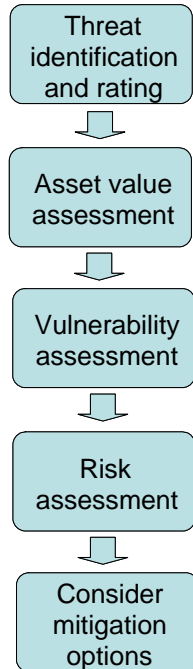


**Figure 1.1. A blast risk assessment process model (from FEMA 452)**

The vulnerability assessment is the link in the methodology that connects threat, asset value and the resultant level of risk and provides a basis for determining the risk mitigation method. Chapter 6 of this report focuses on the blast assessment of NPPs. The design blast threat was assumed to be a surface detonation involving conventional high explosive that generated both air blast and ground shock waves. The responses of both the conventional and base isolated NPPs are investigated to determine whether the

use of seismic protective devices increases the vulnerability of a NPP to air blast and ground shock loadings.

## **1.4 Objectives**

This report develops performance assessments for the sample conventional and base isolated NPPs subjected to seismic and blast loads. For seismic performance assessment, a new procedure is proposed for the seismic performance assessments of NPPs. The proposed assessment procedure has a focus on secondary (nonstructural) systems in the sample NPP because the costs associated with analysis, design, construction, testing and regulatory approval of secondary systems can dominate the cost of NPPs. For blast loading, the focus is on the vulnerability of the NPP containment vessel against an external terrorist bomb threat, assuming that physical security systems will prevent terrorist attacks inside the reactor building.

Based on the background information presented in Sections 1.1 and 1.3, the objectives of the studies performed in this report include:

1. Developing a seismic performance assessment methodology for NPPs.
2. Evaluating the impact of scaling ground motions on the results of response-history analysis and recommending a scaling procedure for performance assessments of mission critical structures.
3. Assessing the performance of the sample conventional and base isolated NPPs subjected to intensity-, scenario- and time-based seismic hazards with a focus on the secondary systems in the sample reactor building.
4. Assessing the performance of the sample conventional and base isolated reactor buildings subjected to air blast and ground shock loadings.

## **1.5 Organization of the Report**

Chapter 2 introduces the sample NPP reactor building, both conventionally constructed and equipped with base isolation systems, together with the key secondary systems in the reactor building.

Chapter 3 describes two procedures for seismic performance assessment of NPPs. One is the seismic probability risk assessment (SPRA) conducted for the seismic review of NPPs since the mid-1970s (Reed and Kennedy 1994) and the second is the proposed procedure that builds on the procedure presented in

the *draft ATC-58 Guidelines* and that used for NPPs to date. In this report, the latter procedure is used to analyze the sample reactor building.

Chapter 4 introduces the state-of-art on the selection and scaling of ground motions and investigates five scaling methods using a series of single-degree-of-freedom nonlinear response-history analyses. The scaling procedure used in the *draft ATC-58 Guidelines* was established based on the results of the study presented in Chapter 4.

Chapter 5 presents the seismic performance assessments for the sample conventional and base isolated NPPs using the proposed procedure introduced in Chapter 3 with a focus on the secondary systems. The benefit associated with the use of base isolation systems in reducing seismic risk is identified.

Chapter 6 presents potential blast threats for NPPs, identifies the air blast and ground shock loading histories for a target threat and presents the numerical responses of the conventional and base isolated NPPs for the target threat.

Chapter 7 presents the key conclusions of the studies reported in this report.

Seven appendices provide supplemental information to the body of the report. Appendix A presents the basic characteristics of the lognormal distribution, which is used in this report to describe fragility curves and the distribution of peak structural responses. Appendix B presents a statistical procedure used in the *draft ATC-58 Guidelines* to manipulate a small-size demand-parameter matrix into a large-size and statistically consistent matrix. This procedure allows the performance assessment to be performed using a small number of response-history analyses. Appendix C provides the technical background related to the number of ground motions for the intensity-based assessment described in Chapter 3. Appendix D presents the values of two ground motion parameters defined in Chapter 4,  $\varepsilon$  and spectral shape, for a large set of near-fault ground motions. Appendix E provides detailed information for the geometric-mean scaling method, which is evaluated in Chapter 4. Appendix F addresses the impact of uncertainty and randomness in the mechanical properties of seismic isolators on the performance of secondary systems in base isolated NPPs. Appendix G provides examples of computational fluid dynamics (CFD) analysis of simple and complex objects to illustrate why CFD or hydrocodes must be used to compute the air blast loading environment on NPPs.

## CHAPTER 2

### SAMPLE NPP REACTOR BUILDINGS

#### 2.1 Conventional Reactor Building

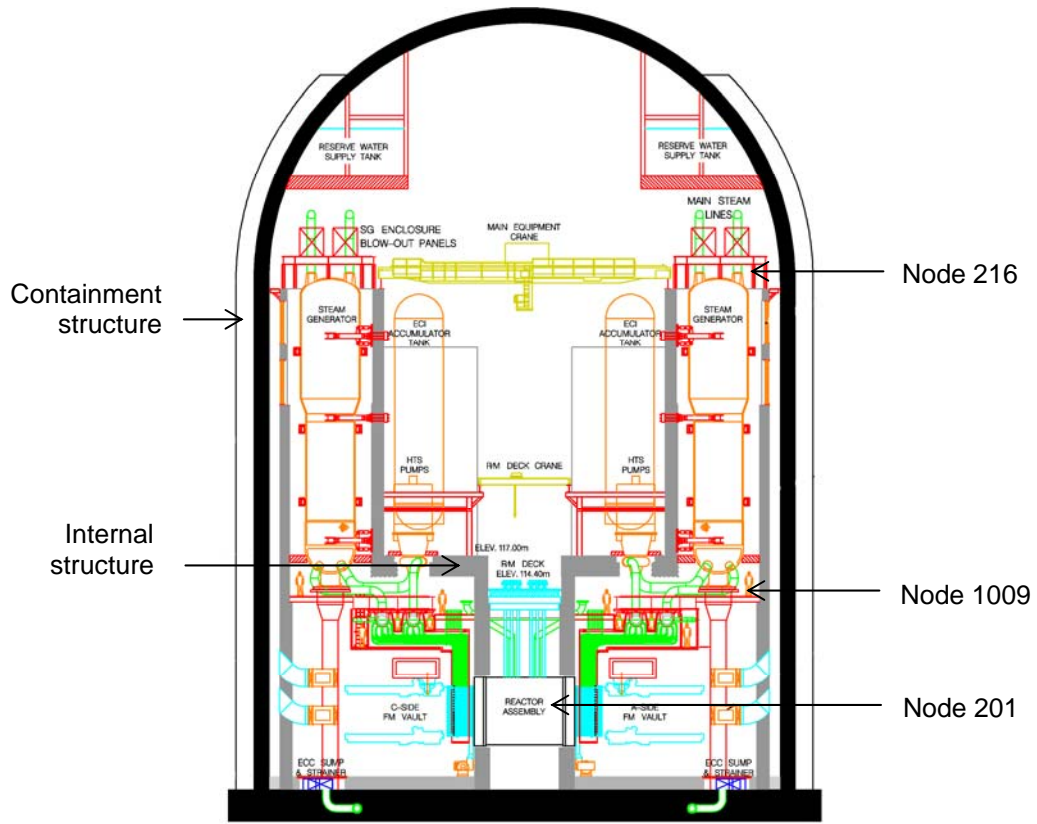
Figure 2.1a shows a cutaway view of a NPP reactor building of conventional construction. A lumped-mass stick model of this reactor building was developed in the computer code SAP2000 Nonlinear (CSI 2002) for the purpose of response-history analysis. The model, shown in Figure 2.1b, is composed of two *sticks*: one representing the containment structure and the other representing the internal structure. The two sticks are structurally independent and are connected only at the base. The mechanical properties of the frame elements that compose each stick were provided by a NPP supplier. The properties were back-calculated from analysis of the 3-D reactor building using industry-standard procedures. Figure 2.2 presents the node numbers assigned for the containment and internal structures of the sample NPP.

The mass of the structure and the secondary systems was lumped at discrete locations at key levels in the reactor building. The discrete masses were connected to the frame elements through rigid links to account for torsional effects. The total height of the containment structure is 59.5 meters and its first mode period is approximately 0.2 second. The thickness of the post-tensioned concrete cylindrical wall of the containment structure is about 1 meter. The height of the internal structure is 39 meters; the first mode period of the internal structure in both horizontal directions is approximately 0.14 second. The total weight of the NPP reactor building is approximately 75,000 tons.

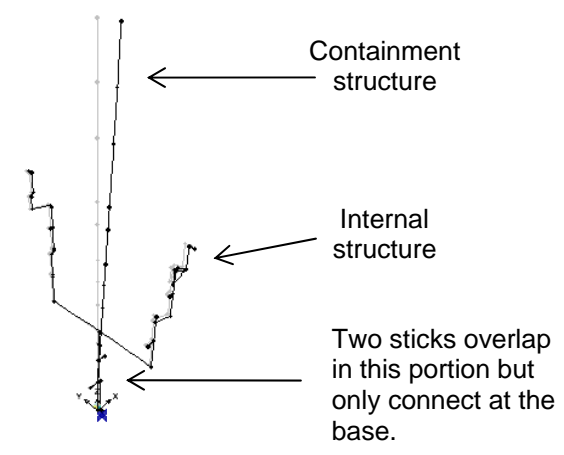
#### 2.2 Base Isolated Reactor Building

In addition to the model for the conventional NPP, three numerical models of base isolated reactor buildings were also developed in SAP2000 Nonlinear to study the influence of seismic isolation on demands on secondary systems in the sample NPP reactor building. Model 1 is for the conventionally framed NPP reactor building. Models 2 and 3 include representations of Friction Pendulum<sup>TM</sup> (FP) bearings and lead-rubber (LR) bearings, respectively. Low damping rubber (LDR) bearings and linear viscous dampers (LVD) are included in Model 4. Table 2.1 lists the properties of the protective systems for each model. Bilinear plasticity elements were used to model the LR bearings. Figure 2.3 shows the key variables defining the bilinear hysteresis loop. For FP bearings, the velocity dependence of the coefficient of sliding friction is given by (Constantinou et al. 1999, Fenz 2005)

$$\mu = \mu_{\max} - (\mu_{\max} - \mu_{\min}) \cdot e^{-aV} \quad (2.1)$$

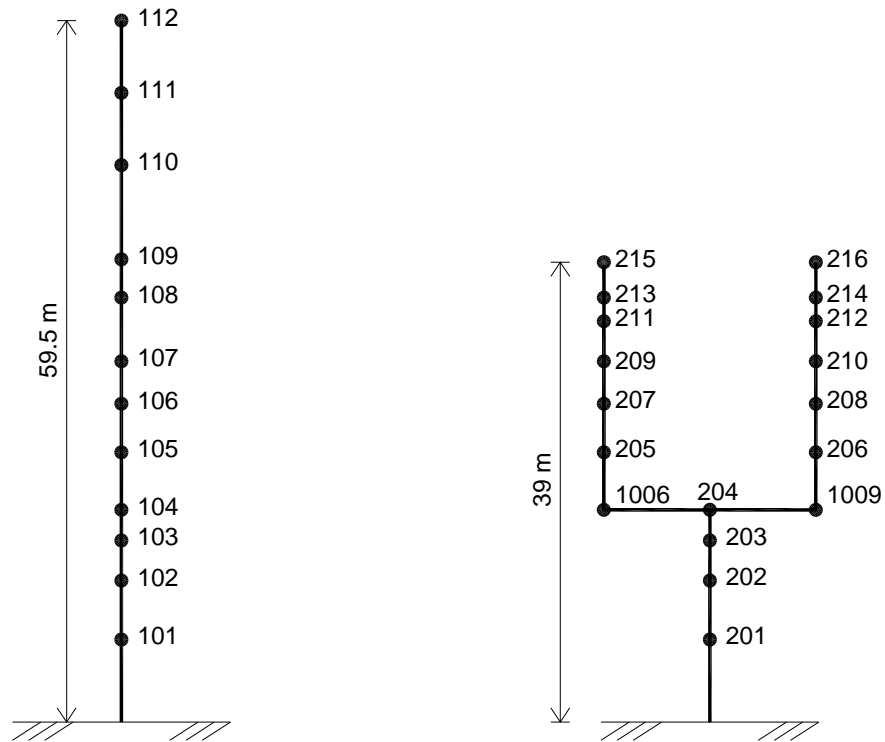


a. a cutaway view of the sample NPP reactor building



b. First mode shape of the stick model for the sample NPP in SAP2000

**Figure 2.1. Sample NPP reactor building and the corresponding stick model**



a. Stick model for the containment structure

b. Stick model for the internal structure

**Figure 2.2. Node numbers for the stick models for the sample NPP reactor building**

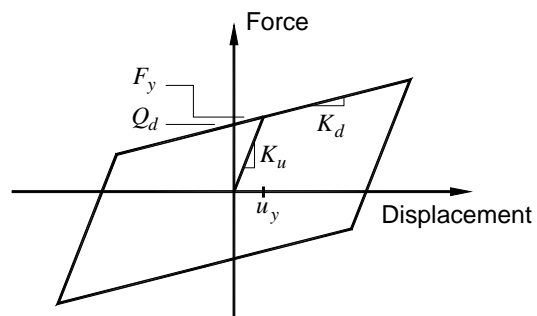


**Figure 2.3. Assumed properties of the LR and Coulomb-friction-FP bearings**

**Table 2.1. Description of response-history-analysis models**

Model no.	Protective system	Description <sup>1</sup>
1	None	First mode periods of the containment and internal structures, in each horizontal direction, are (0.22 sec, 0.21 sec) and (0.14 sec, 0.13 sec), respectively
2	Friction Pendulum <sup>TM</sup> (FP)	$\mu_{\max} = 0.06$ ; $\mu_{\min} = 0.03$ ; $a = 55 \text{ sec/m}$ ; $T_d = 2 \text{ seconds}$ ; $u_y = 1 \text{ mm}$
3	Lead Rubber (LR)	$Q_d = 0.06W$ ; $T_d = 2 \text{ seconds}$ ; $K_u = 10 K_d$
4	Low Damping Rubber (LDR) and Linear Viscous Damper (LVD)	$T_i = 2 \text{ seconds}$ ; $\xi_i = 0.10$

where  $\mu$  is the coefficient of sliding friction, varying between  $\mu_{\max}$  and  $\mu_{\min}$  (obtained at high and very small velocities, respectively),  $a$  is a velocity-related parameter, and  $V$  is the sliding velocity. Figure 2.4 shows the velocity dependence of  $\mu$  for a typical FP PTFE-type composite material in contact with polished stainless steel for a typical contact (normal) pressure of approximately 41 MPa (6 ksi). For this pressure,  $\mu_{\max} = 6\%$ ,  $\mu_{\min} = 3\%$ , and  $a=55 \text{ sec/m}$ . A value of  $a=55 \text{ sec/m}$  was adopted for the study describe herein. The influence of  $a$  on the velocity dependence of  $\mu$  is shown in Figure 2.4 for  $a=40, 55$  and  $100 \text{ sec/m}$ .<sup>2</sup>

The characteristic strength,  $Q_d$  of Figure 2.3, was set equal to 6 percent of the supported weight  $W$  for the LR bearings and  $\mu_{\max}$  was set equal to 6 percent for the FP bearings, where for Coulomb friction,  $Q_d = \mu_{\max}W$ . The second-slope period (related to  $K_d$  of Figure 2.3 through the supported weight) was assigned a value of 2 seconds for the LR and FP bearings. The LDR bearings were modeled as linear elements. The dynamic properties of Model 4 include an isolated period of 2 seconds and an added viscous damping ratio of 10% of critical<sup>3</sup>.

<sup>1</sup> See Figure 2.3 for definitions of  $Q_d$ ,  $K_d$  and  $K_u$  and Figure 2.4 and (2.1) for those of  $\mu_{\max}$ ,  $\mu_{\min}$  and  $a$ ;  $T_d$  is related to  $K_d$  through the supported weight;  $T_i$  is the isolated period for the LDR isolation systems based on a rigid superstructure;  $\xi_i$  is the damping contributed by LVDs.

<sup>2</sup> The hysteresis loop for the FP bearing will converge to the bilinear loop shown in the Figure 2.3 for Coulomb friction ( $a = \infty$ ).

<sup>3</sup> For design of a seismically isolated NPP, the analyst would have to address possible variations in the mechanical properties over the service life of the plant. See Appendix F for more information on this topic.



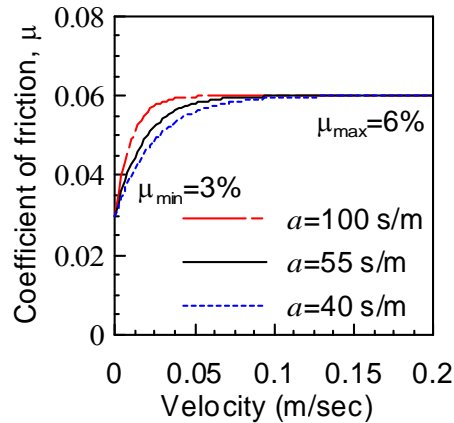


**Figure 2.4. The influence of  $a$  on the velocity dependence of the coefficient of sliding friction**

### 2.3 Key Secondary Systems

The seismic performance assessments performed in this study focus on the secondary systems in the sample NPP reactor building. Figure 2.5 illustrates the distribution of several important secondary systems in the sample reactor building. Most of these secondary systems are attached to the internal structure. Six key secondary systems in the internal structure were identified by the NPP supplier (Saady 2006) and listed in Table 2.2, including reactor assembly, steam generator, emergency coolant injection (ECI) tank, piping, heat transport system and maintenance crane.

In a typical seismic probabilistic risk assessment (SPRA) for a NPP, the capacity of a secondary system, measured in terms of resistance to undesirable response or failure, is characterized by a high-confidence-of-low-probability-of-failure (HCLPF) value. In a plant assessment, the HCLPF value is used in seismic capacity walkdowns to screen out the seismically robust elements and determine those elements that need further assessment. SPRA and the calculation of HCLPF values is introduced in Chapter 3.

The seismic demands on secondary systems in NPPs are generally characterized using floor response spectra. Table 2.2 presents the node numbers and elevations (above the base of the reactor building) for the supports of the six key secondary systems in the sample reactor building. The supports distribute at elevations of 7, 18 and 39 m. In Chapter 5, the floor response spectral demands at these locations with respect to different levels of seismic hazards are computed using response-history analysis for seismic performance assessments.

**Table 2.2. Node numbers and elevations for the supports of the key secondary systems in the internal structure of the sample NPP building**

Secondary system	Node number	Elevation (m)
Reactor assembly	201	7
Steam generator	1006, 1009	18
Emergency Coolant Injection (ECI) tank	1006, 1009	18
Main piping system	215, 216	39
Heat transport system	1006, 1009	18
Maintenance crane	215, 216	39

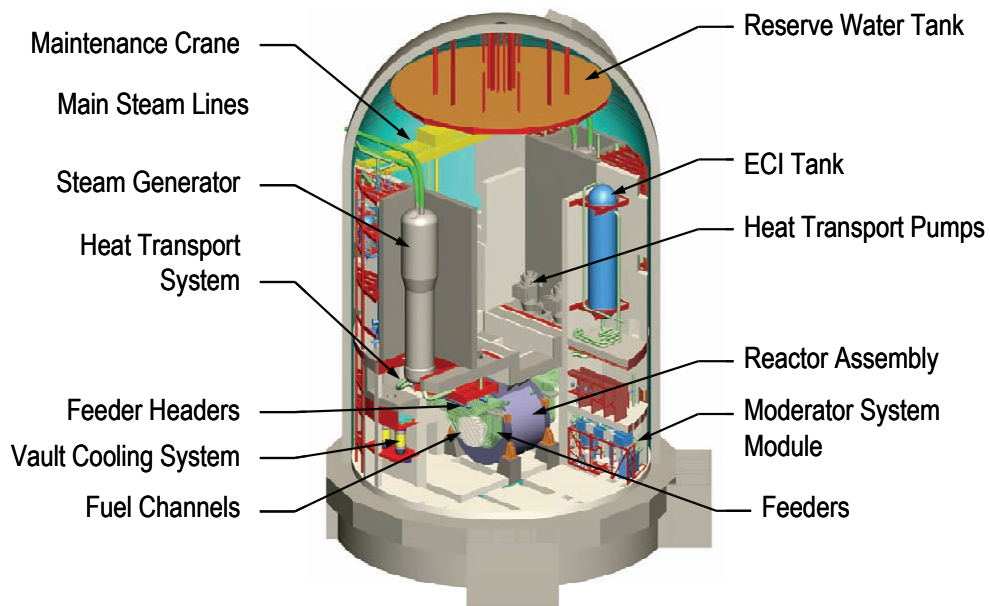


**Figure 2.5. Secondary systems in the sample NPP reactor building**

# CHAPTER 3

## METHODOLOGIES FOR SEISMIC PERFORMANCE ASSESSMENT

### 3.1 Introduction

In 1991, the United States Nuclear Regulatory Commission (NRC) issued Supplement 4 to Generic Letter No. 88-20 (USNRC 1991a) asking nuclear power plant utilities to perform an Individual Plant Examination of External Events (IPEEE) and also issued NUREG-1407 (USNRC 1991b) to help guide the IPEEE. The five external events were 1) earthquakes, 2) internal fires, 3) high winds and tornadoes, 4) external floods and 5) transportation and nearby facility accidents. NUREG-1407 identified Seismic Probabilistic Risk Assessment (SPRA) as an acceptable methodology for the examination of earthquakes. SPRA provides a formal process in which the randomness and uncertainty in seismic input, structure response and material capacity is considered in the computation of risk.

NUREG/CR-2300 (USNRC 1983) provides the general guidance for performing SPRA for NPPs. The guideline describes two SPRA methods: 1) Zion and 2) the Seismic Safety Margin Research Program (SSMRP). The Zion method was first developed and applied in the Oyster Creek probabilistic risk assessment and later improved and applied in 1981 to estimate seismic risk for the Zion Plant (Pickard, Lowe, and Garrick, Inc., et al. 1981). The SSMRP method was developed in an NRC-funded project termed “the Seismic Safety Margin Research Program (SSMRP)” at the Lawrence Livermore National Laboratory (LLNL) (Smith et al. 1981). The SSMRP method requires extensive component and system modeling as well as a detailed seismic response analysis and is generally not used in practice (Reed and Kennedy 1994). Only the Zion method is discussed in this chapter.

The SPRA procedure uses component fragility curves to characterize the probability of failure for a component as a function of a demand parameter. Reed and Kennedy (1994) present a methodology for developing fragility curves for use in a SPRA. In the Zion method and Reed and Kennedy (1994), the component fragility curves are defined in terms of *ground-motion* parameters, such as peak ground acceleration and spectral acceleration at a given period, although the failure of a component has a much improved correlation to *response* parameters, such as floor spectral acceleration and story drift.

The Zion method can be improved using fragility curves defined using structural response parameters. Procedures for seismic performance assessment of buildings have been developed in the ATC-58 project and proposed in the 35% draft *Guidelines for Seismic Performance Assessment of Buildings* (ATC 2007) (termed the *draft ATC-58 Guidelines* hereafter). The procedures also involve the use of fragility curves but the curves are defined using structural response parameters. These procedures in the *draft ATC-58 Guidelines* provide a robust technical basis for developing an alternative procedure for seismic probabilistic risk assessment for NPPs.

This chapter presents two methodologies for seismic performance assessment of NPPs. Section 3.2 presents the conventional SPRA procedure for NPPs with a focus on the development of component fragility curves. The information presented in Section 3.2 is based mostly on NUREG/CR-2300 and Reed and Kennedy (1994). Section 3.3 presents new assessment procedures developed in part on the procedures set forth in the *draft ATC-58 Guidelines*.

## **3.2 Conventional Methodology for Seismic Performance Assessment of NPPs**

### **3.2.1 Seismic Probabilistic Risk Assessment**

#### *3.2.1.1 Introduction*

The objective of SPRA is to estimate the frequency of occurrence of accidents induced by earthquakes for different levels of damage, including property damage, core melt, radiation release and off-site consequences (e.g., early deaths and latent cancer fatalities).

A SPRA includes the following four steps:

1. Seismic hazard analysis
2. Component fragility evaluation
3. Plant-system and accident-sequence analysis
4. Consequence analysis

**Figure 3.1** illustrates the steps in a SPRA and the relationship between each step. In Step 1, the frequencies of exceedance for different earthquake intensities are characterized for the NPP site. In Step 2, a family of fragility curves is developed for each structural and nonstructural components in the NPP. In Step 3, event trees and fault trees are developed to determine all

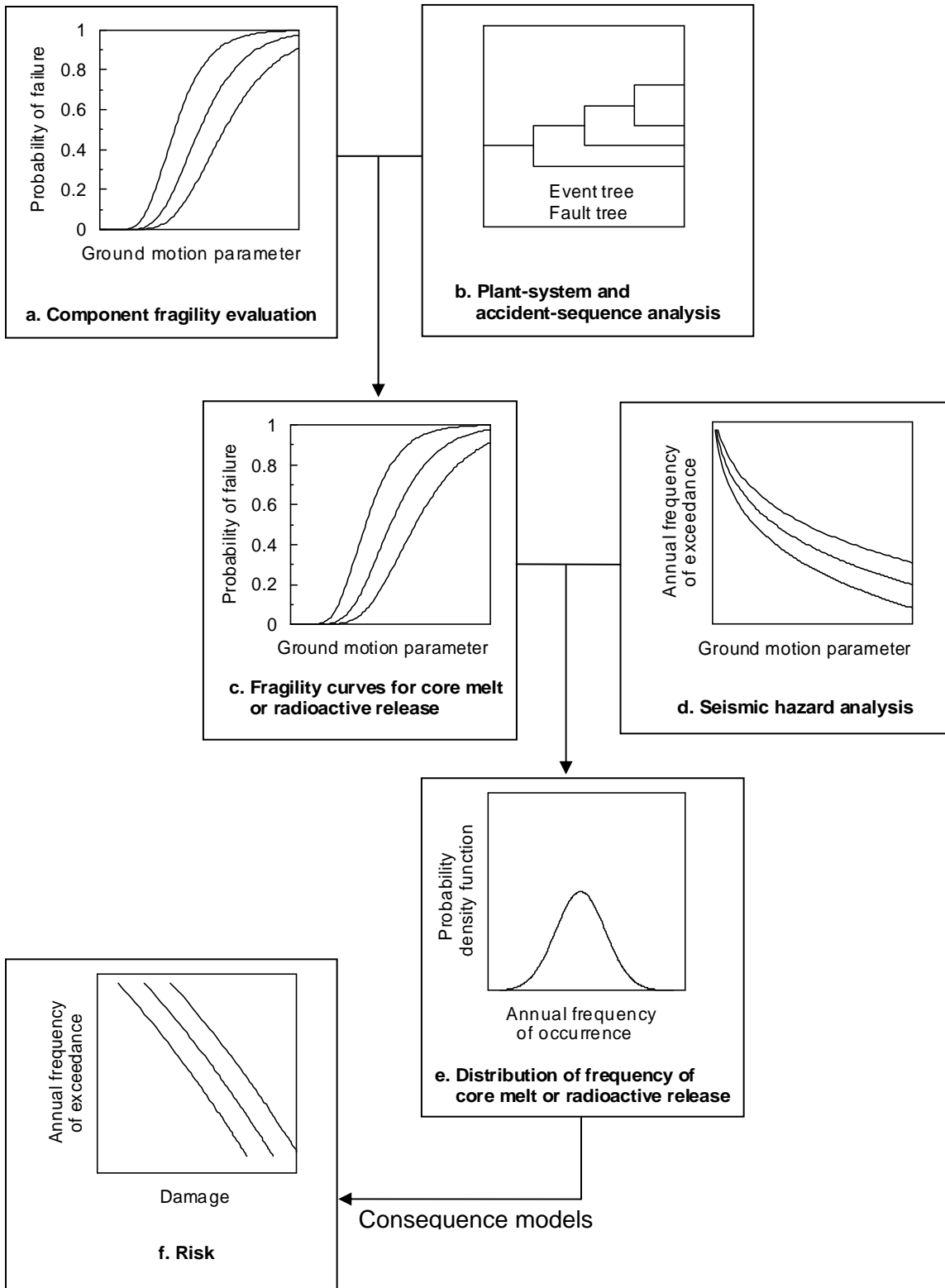


**Figure 3.1. Seismic probabilistic risk analysis for NPPs (modified from Reed and Kennedy 1994)**

possible sequences and likelihood of a failure event, such as core melt and radiation release. The component fragility curves of Step 2 (panel a of **Figure 3.1**) and the accident sequences identified in Step 3 (panel b) are used to compute the fragility curves for the failure event, i.e., the probability of occurrence of the failure event for a given earthquake intensity (panel c). The fragility curves for the failure event and the hazard curves developed in Step 1 (panel d) are integrated over the entire range of earthquake intensity considered in the analysis to estimate the distribution of the frequency of the failure event (panel e). In the final step, the frequency of the failure event is used as input for consequence models to estimate the frequencies of exceeding a given value of damage, such as fatalities and dollar loss (panel f). More information for each step is described in the following subsections.

#### *3.2.1.2 Seismic Hazard Analysis*

The seismic hazard used in a SPRA is characterized using Probabilistic Seismic Hazard Analysis (PSHA). A PSHA generates a family of hazard curves, which describe the frequency of exceedance for a ground-motion parameter (e.g., peak ground acceleration and spectral acceleration at a given period) at a specific site. The steps for performing PSHA for a NPP site are:

1. Identify the sources of earthquakes with potential to generate significant shaking at the site.
2. Evaluate the earthquake history of the region to determine the recurrence relationships of earthquakes for each source.
3. Select or develop attenuation relationships to estimate the distribution of the selected ground-motion parameter at the site for all possible earthquake events.
4. Integrate the information gathered in Steps 1 through 3 to compute the frequency of the selected ground-motion parameter exceeding a given target value. Repeat Step 4 with different target values to generate the hazard curve at the site.

The use of steps 1 through 4 captures the inherent randomness in the selected ground-motion parameter and generates a single hazard curve. However, the uncertainties in some factors, such as maximum earthquake magnitude, the geometry of the source and the choice of attenuation relationships, are not considered. Such uncertainties can be included in PSHA using a logic tree, which allows the use of alternative hypotheses for the uncertain factors mentioned above, assigns

a weighting factor for each combination of hypotheses to represent the likelihood of the combination, and results in a family of hazard curves. More information on the implementation of logic trees in PSHA can be found in McGuire (2004). Figure 3.2 presents a family of sample hazard curves for an eastern US site as well as the mean curve of the family. Each curve in the family (except the mean curve) has an associated weighting factor and the sum of all weighting factors is one. The mean hazard curve of the family is determined using the weighting factors and each curve in the family. For example, the weighting factor for each of the 10 hazard curves in Figure 3.2 (termed  $w_i$ ) is 0.1 and the annual frequencies of exceedance of the 10 curves at a spectral acceleration (at a period of zero second or PGA in this case) of 1.0 g (termed  $\lambda_{i,1g}$ ) are 2.88E-5, 4.18E-6, 1.69E-6, 6.80E-7, 3.07E-7, 1.39E-7, 7.02E-8, 2.83E-8, 5.77E-9 and 3.70E-10. The annual frequency of exceedance of the mean hazard curve at a PGA of 1.0 g (termed  $\bar{\lambda}_{1g}$ ) is 3.59E-6, computed using the following equation:

$$\bar{\lambda}_{1g} = \sum_{i=1}^{10} w_i \bar{\lambda}_{i,1g} \quad (3.1)$$

Some of these values are identified in the figure.

### 3.2.1.3 Component Fragility Evaluation

Panel a of **Figure 3.1** represents the component fragility analysis. As described in Section 3.1, a component fragility curve characterizes the probability of failure of the component as a function of a demand parameter. In the Zion method and Reed and Kennedy (1994), a ground-motion parameter was used as the demand parameter to develop fragility curves.

Similar to the hazard analysis, a set of fragility curves will be developed for a component with a probabilistic weighting factor assigned to each curve to consider the randomness and uncertainty in the capacity and demand<sup>1</sup> of the component in risk computation. More information for the development of component fragility curves and the treatment of randomness and uncertainty in the curves is introduced in Section 3.2.2.

---

<sup>1</sup> Generally speaking, a fragility curve characterizes the *capacity* of a component. However, since the curve is defined as a function of a ground-motion parameter for the case discussed herein, the variability in the structural response (i.e., the *demand* of the component) for a given ground-motion intensity should be included in the development of fragility curves.

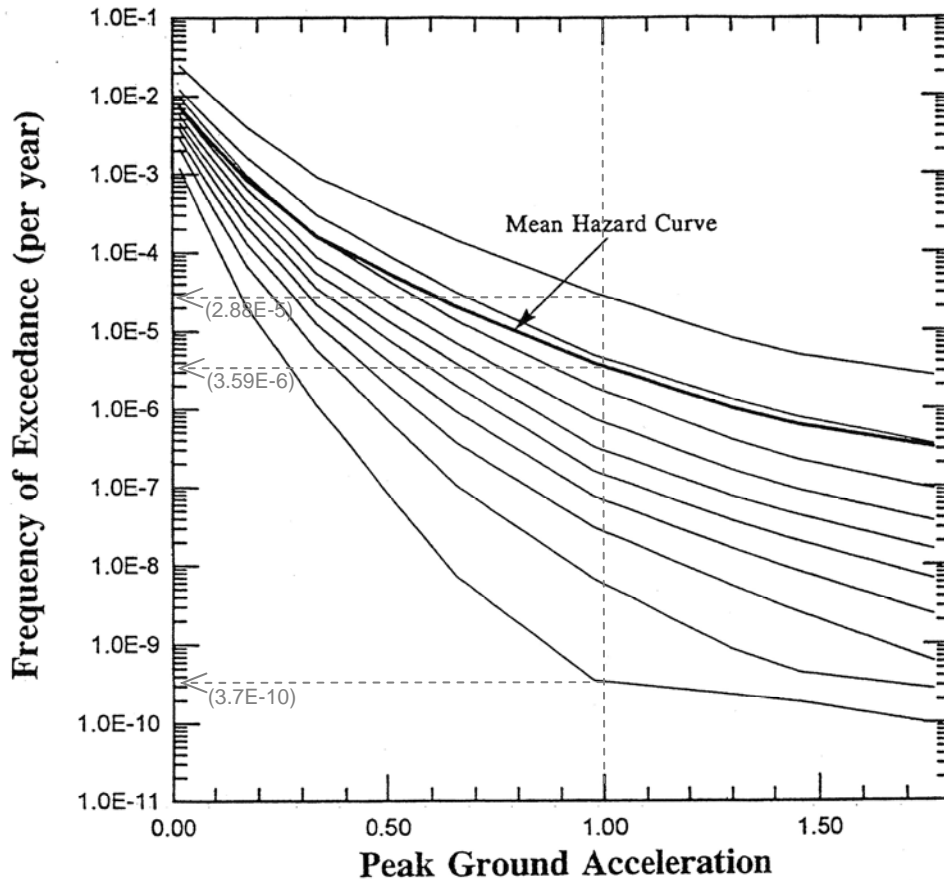


**Figure 3.2. Sample hazard curves for an Eastern United States site (Reed and Kennedy 1994)**

#### 3.2.1.4 Plant-System and Accident-Sequence Analysis

Panel b of **Figure 3.1** represents the plant-system and accident-sequence analysis. The purpose of this analysis is to determine the frequencies of the occurrence of failure events (e.g., core melt and radiation release). A NPP includes a series of systems to prevent the overheating of fuel and to control potential releases of radioactivity from the fuel (e.g., the emergency core cooling system (ECCS)). For a potential accidental release of radioactivity to the environment to occur, a series of failures in the safety systems must occur first.

This analysis requires the identification of a) earthquake-induced initiating events (e.g., loss-of-coolant accident (LOCA) and reactor vessel rupture) that might cause core melt and radiation releases, and b) the accident sequences resulting from the initiating events. Since the initiating events will activate various mitigating and safety systems in the reactor building, the occurrence of the initial events does not trigger failure. All possible sequences started by the initiating event



need to be considered in the computation of the frequency of the failure event. A robust way to identify all possible accident sequences is to use event trees.

### *Event Trees*

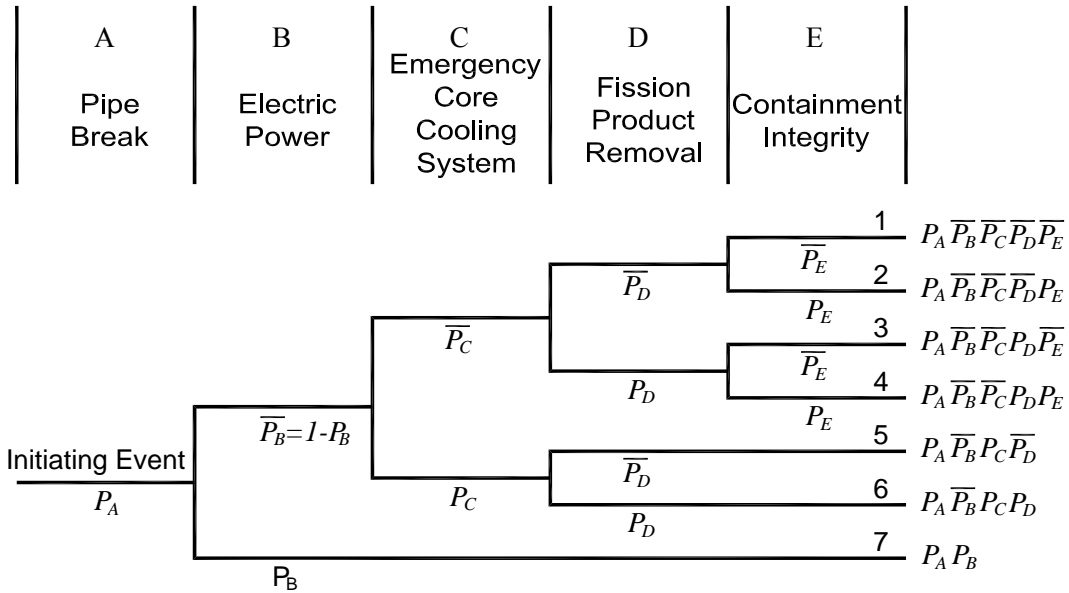
The use of event trees is a logic method for identifying the various possible outcomes of an initiating event. A sample event tree is shown in Figure 3.3a where the initiating event is the break of a large pipe and the failure event is radiation release (USNRC 1975, Reed and Kennedy 1994). Four safety systems, which might affect the accident sequences started by the initiating event, are presented at the top of Figure 3.3a and ordered in the time sequence in which they participate in the process. The initiating event is termed Event A. The failures of the four safety systems were termed Events B through E, respectively. All branches in the figure, except that for the initiating event, appear in pairs. The upper branches represent success of the safety systems and the lower branches represent failure. The event tree includes seven sequences. The probability of occurrence of each sequence is presented at the end of the event tree assuming the five events are independent and the probability of occurrence of each event ( $P_A$  through  $P_E$ ) is known. The sequences corresponding to the radiation release can be identified based on the success or failure of each safety system in each sequence<sup>2</sup>. The probability of the radiation release for the initiating event can then be computed. Results from all initiating events should be combined to compute the probability of the radiation release.

### *Fault Trees*

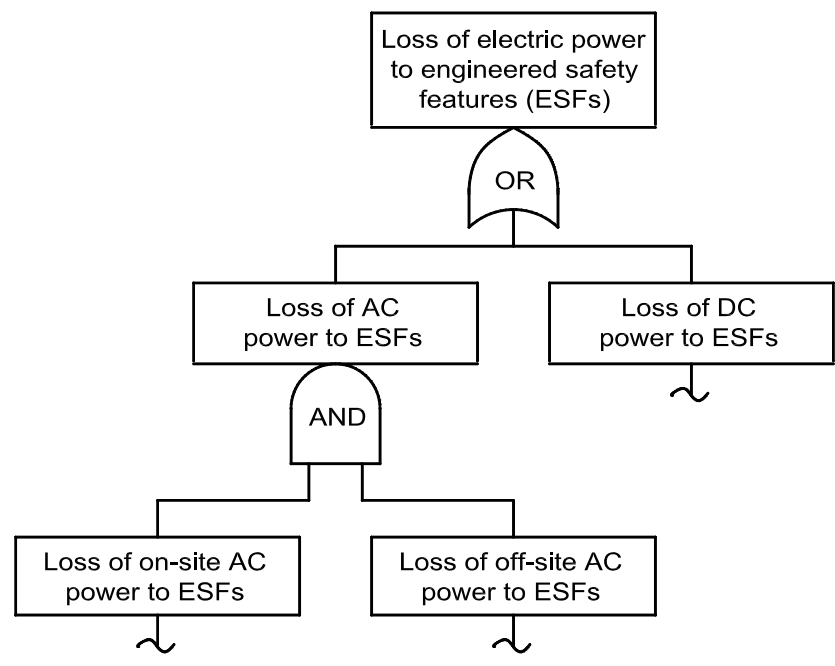
The computation described in the previous paragraph requires the values of  $P_A$  through  $P_E$  as shown in Figure 3.3a. These values can be estimated using the fault tree method. In the method, a fault tree is developed for each of the events in an event tree to compute the probability of the event. A fault tree identifies the various combinations and sequences of other failures leading to a given failure. The logic of the method is essentially the reverse of that for event trees.

---

<sup>2</sup> Not all seven sequences identified in Figure 3.3a result in the occurrence of the failure event. In this case, the top-most branch is a sequence where the radiation release does not occur while all other sequences will result in the radiation release. Note that the event tree shown in Figure 3.3a is a *reduced* tree, where the unnecessary sequences has been eliminated. For example, if station electric power fails, none of the other safety systems can operate since their operation requires electricity.



a. Sample event tree



b. Sample fault tree for Event B

**Figure 3.3. Sample event and fault trees of NPP accident-sequence analysis (USNRC 1975, Reed and Kennedy 1994)**

Figure 3.3b shows an example of a partial fault tree for Event B of Figure 3.3a (USNRC 1975; Reed and Kennedy 1994). In Figure 3.3b, an “OR” gate defines the failure of the event right above the gate as the failure of one or more of the events immediately below the gate and an “AND” gate defines the failure of the event right above the gate as the failure of all events immediately below the gate. The branches of the fault tree keep proceeding downward until reaching the most basic failure events (for example, the failure of a structural or nonstructural component), for which the fragility data exist to characterize their failure probabilities at a given earthquake intensity. Using the probabilities of the basic failure events and the sequences identified in the fault tree, the probability of the top event of the fault tree can be estimated given an intensity of earthquake shaking.

Through the event and fault trees, the fragility data of structural and nonstructural components in a NPP are used to compute the probabilities of failure events (core melt and radiation release). Since the component fragility curves provide information at different earthquake intensities, the fragility curves for the failure events can be developed by repeating the analysis at different earthquake intensities (see panels a, b and c of **Figure 3.1**). Moreover, in a SPRA, a family of fragility curves is developed for a component (see Section 0). The use of alternate component fragility curves in the analysis described herein will result in different fragility curves for the failure event of interest. Figure 3.4a presents a family of sample core-melt fragility curves, which were generated for the Zion PRA. Again, each curve was assigned a probabilistic weighting factor and the sum of the values of the factors is 1.

#### *Frequencies of Failure Events*

Once the hazard curves for the site and the fragility curves for a failure event are obtained, two curves, one from each of the two sets, are selected to compute the frequency of the failure event,  $\lambda_f$ , using the following equation:

$$\lambda_f = - \int P_{f|a} \frac{d\lambda}{da} da \quad (3.2)$$

where  $P_{f|a}$  represents the fragility curve, which characterizes the probability of the occurrence of the failure event given a value of the parameter  $a$ ; and  $\lambda$  represents the seismic hazard curve. The range of integration should be wide enough to cover all the earthquake intensities with significant contributions to  $\lambda_f$ . The use of (3.2) requires that the fragility and seismic hazard

curves be a function of the same parameter: the reason why fragility curves were developed as a function of a ground-motion parameter in the Zion method and Reed and Kennedy (1994).

The distribution of  $\lambda_f$  can be identified using different combinations of hazard and fragility curves (see panels c, d and e of Figure 3.1). For example, assume that the 10 hazard curves of Figure 3.2 and the 5 fragility curves of Figure 3.4a are used in a SPRA to compute the frequency of exceedance ( $\lambda_f$ ) of core melt. Each of the hazard curves is integrated with each of the fragility curves using (3.2). A total of 50 values of  $\lambda_f$  are generated and the probability of each value is determined by multiplying the probabilistic weighting factors associated with the two curves used in each integration. The distribution of  $\lambda_f$  can thus be estimated from the 50 realizations and the associated probabilities. Figure 3.4b presents a density function for core melt developed in the Zion SPRA.

#### *3.2.1.5 Consequence Analysis*

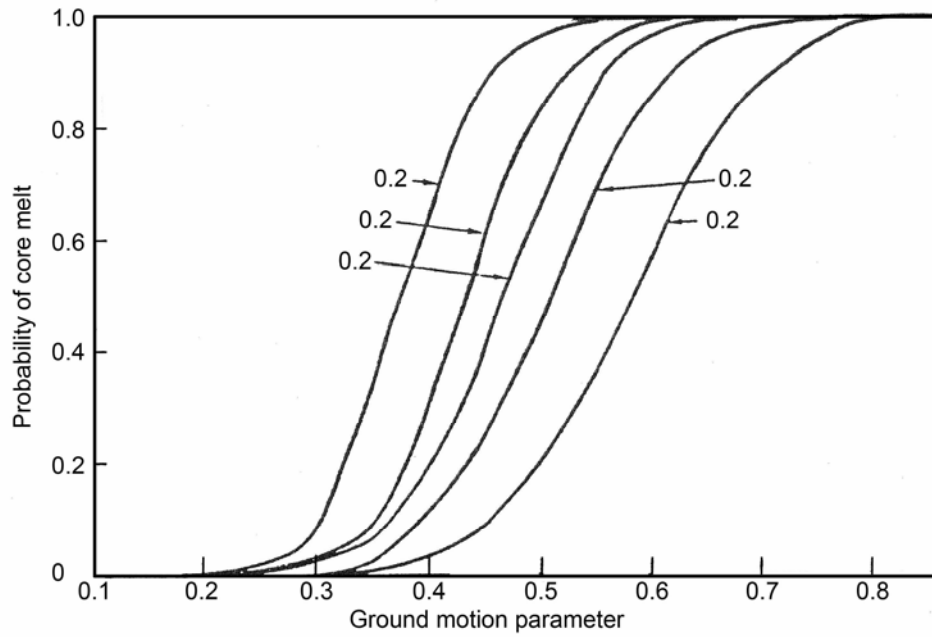
The objective of a consequence analysis is to estimate the public consequences that result from radiation release. The consequences of a given radiation release depend upon how the radioactivity is dispersed in the environment, the number of people and amount of property exposed, and the effects of radiation exposure on people and contamination of property (USNRC 1975). Various types of consequence models, such as atmospheric dispersion, population, evacuation and health effects and property damage, are needed to quantify the effects of seismic events and the risk of damage. The products of a consequence analysis are risk curves, such as those shown in Figure 3.5. The curves characterize the frequency of exceedance of a given damage, including the number of fatalities and the property damage in terms of dollars.

### **3.2.2 Development of Fragility Curves**

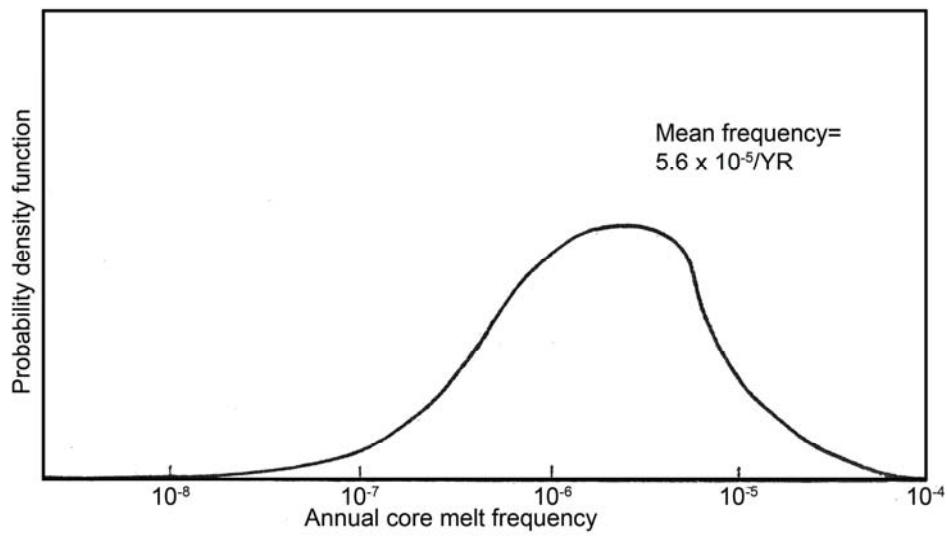
#### *3.2.2.1 Fragility Model*

Seismic fragility curves for structural and nonstructural components in NPPs are needed in a SPRA to estimate the frequencies of occurrence of initiating events and the failures of different safety systems. The lognormal distribution has become the most widely used distribution for developing fragility curves. Appendix A introduces the characteristics of the lognormal distribution.

A lognormal distribution for a random variable can be fully defined by two parameters, the median and logarithmic standard deviation. The latter parameter represents the dispersion in the



a. A family of sample fragility curves for core melt



b. Sample probability density function for core melt

**Figure 3.4. Sample fragility curves and probability density function for core melt (Reed and Kennedy 1994)**

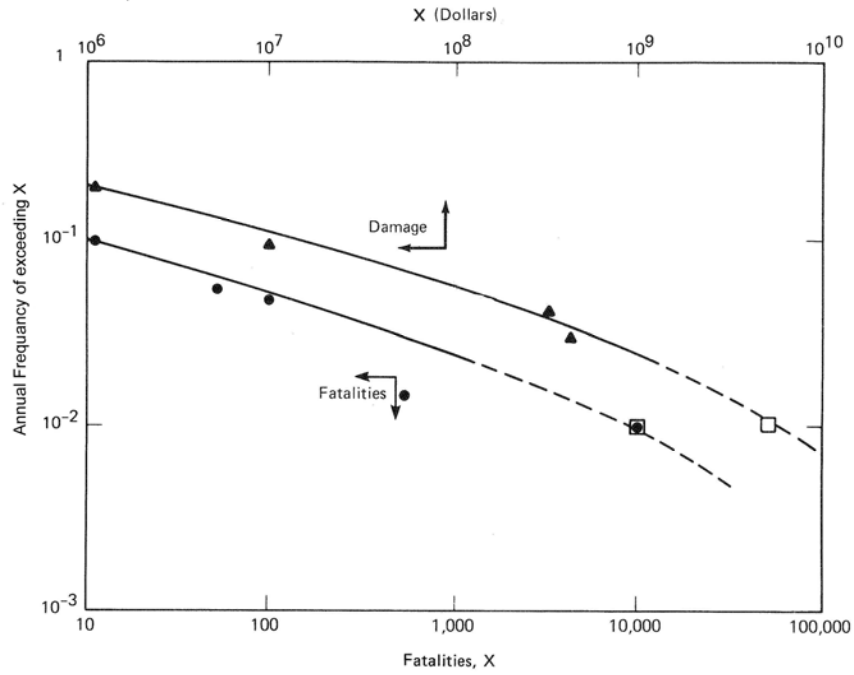


**Figure 3.5. Sample risk curves (USNRC 1975)**

variable. The sources of the dispersion are distinguished into two types for developing fragility curves for structural and nonstructural components in NPPs: 1) *uncertainty*, for the variability due to the lack of knowledge for the procedure and variables used in the analysis process, for example, the variability in the strength of a shear wall, which could be tested to eliminate the uncertainty; and 2) *randomness*, for the variability that is inherent in the used variables and cannot be practically reduced, for example, the variability in structure response for a given value of peak ground acceleration.

To consider the two types of variability separately, a double lognormal model was adopted for the Zion method and in Reed and Kennedy (1994) to express the capacity of a component. The model is

$$A = \bar{A} \cdot \varepsilon_r = \hat{a} \cdot \varepsilon_u \cdot \varepsilon_r \quad (3.3)$$

where  $A$  is the random variable for the capacity of the component and the capacity is defined in terms of a ground-motion parameter, such as PGA or spectral acceleration at a given period;  $\bar{A}$ , which is equal to  $\hat{a}\varepsilon_u$ , is a random variable for the median capacity of the component;  $\hat{a}$  is a deterministic value representing the median of  $\bar{A}$ ; and  $\varepsilon_u$  and  $\varepsilon_r$  are two lognormally distributed random variables with medians both equal to one and logarithmic standard deviations of  $\beta_u$  and

$\beta_r$ , respectively. Variables  $\varepsilon_u$  and  $\varepsilon_r$  represent the uncertainty and randomness in  $A$ , respectively. In this model, the median capacity of the component is considered uncertain.

The upper panel of Figure 3.6 presents the probability density function of  $\bar{A}$ : a lognormal distribution with median  $\hat{a}$  and logarithmic standard deviation  $\beta_u$ . The area of the gray zone in the figure,  $Q$ , represents the probability (confidence level) that the median capacity of the component exceeds a given value  $\bar{a}$ . For example, the value of  $Q$  associated with  $\hat{a}$  (median of  $\bar{A}$ ) is 0.5 since the probability of  $\bar{A}$  being greater than  $\hat{a}$  is 50%. The relationship between  $\bar{a}$  and  $Q$  is given by:

$$\bar{a} = \hat{a} \cdot e^{-\Phi^{-1}(Q) \cdot \beta_u} \quad (3.4)$$

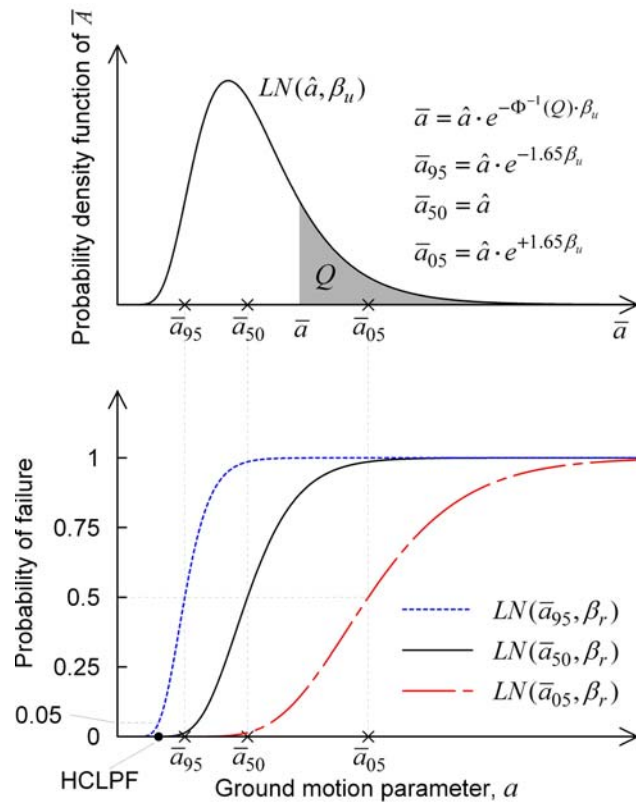


**Figure 3.6. Family of fragility curves at 95%, 50% and 5% confidence levels and HCLFP**

where  $\Phi$  is the standardized normal distribution function. The values of  $\Phi^{-1}(0.95)$ ,  $\Phi^{-1}(0.5)$  and  $\Phi^{-1}(0.05)$  are 1.65, 0 and -1.65, respectively. The estimations of the median capacity associated with exceedance probabilities of 95%, 50% and 5% are identified in Figure 3.6 as  $\bar{a}_{95}$ ,  $\bar{a}_{50}$  and  $\bar{a}_{05}$ . The fragility curves for the component (associated with various confidence levels)

can then be computed using the logarithmic standard deviation for randomness  $\beta_r$  and each of  $\bar{a}_{95}$ ,  $\bar{a}_{50}$  and  $\bar{a}_{05}$ . The resultant fragility curves are shown in the lower panel of Figure 3.6.

The fragility curves generated using this procedure, such as those shown in Figure 3.6, can be expressed by the following equation:

$$f = \Phi\left(\frac{\ln a - \ln \bar{a}}{\beta_r}\right) \quad (3.5)$$

where  $f$  is the probability of failure of the component for a given ground-motion intensity,  $a$ . Substituting (3.4) into (3.5) gives

$$f = \Phi\left(\frac{\ln \frac{a}{\hat{a}} + \Phi^{-1}(Q) \cdot \beta_u}{\beta_r}\right) \quad (3.6)$$

In a SPRA, the value of  $a$  associated with 95% confidence of a 5% probability of failure (i.e.,  $Q = 0.95$  and  $f = 0.05$ ) is defined as the high-confidence-of-low-probability (HCLPF) capacity, as shown in Figure 3.6. HCLPF values need to be computed for components that are not screened out during the plant walkdown to evaluate their safety during an earthquake event. Solving (3.6) for  $a$  with  $Q = 0.95$  and  $f = 0.05$  leads to the HCLPF capacity shown below:

$$HCLPF = \hat{a} \cdot e^{-1.65(\beta_r + \beta_u)} \quad (3.7)$$

Given a set of  $\hat{a}$ ,  $\beta_u$  and  $\beta_r$ , one can use (3.6) to generate a family of fragility curves with different confidence levels and use (3.7) to determine the HCLPF capacity for a component in a NPP. A method for estimating  $\hat{a}$ ,  $\beta_u$  and  $\beta_r$  is described in the following subsection.

### 3.2.2.2 Developing Fragility Curves

The fragility parameters,  $\hat{a}$ ,  $\beta_u$  and  $\beta_r$ , are estimated using an intermediate random variable known as the factor of safety,  $F$ , with median  $\hat{f}$  and logarithmic standard deviations for randomness and uncertainty  $\beta_{F,r}$  and  $\beta_{F,u}$ , respectively. The factor of safety,  $F$ , is defined as the ratio of the actual seismic capacity of the component of interest to the actual seismic response (demand) due to the safe-shutdown-earthquake (SSE) shaking. The relationship between  $\hat{a}$  and  $\hat{f}$  is

$$\hat{a} = \hat{f} \cdot a_{SSE} \quad (3.8)$$



where  $a_{SSE}$  is the SSE shaking level specified for design. All parameters in (3.8) are defined in terms of the ground-motion parameter chosen for the development of fragility curves. Dispersions  $\beta_{F,r}$  and  $\beta_{F,\mu}$  are used in (3.6) as  $\beta_u$  and  $\beta_r$ , respectively, for developing the fragility curves.

For structural components,  $F$  is modeled as follows:

$$F = F_C F_{RS} = F_S F_\mu F_{RS} \quad (3.9)$$

where  $F_C$  is the capacity factor, equal to the product of  $F_S$  and  $F_\mu$ ;  $F_{RS}$  is the structure-response factor, used to address the variability in spectral shape, damping, modeling, soil-structure interaction, structural analysis method, ground-motion simulation, etc.;  $F_S$  is the strength factor, defined by the ratio of ultimate strength to the demand calculated for  $a_{SSE}$ ; and  $F_\mu$  is the inelastic energy-absorption factor, accounting the capability of structural components to absorb seismic energy through yielding without losing their function<sup>3</sup>.

For equipment in NPPs,  $F$  is modeled as:

$$F = F_C F_{RE} F_{RS} = F_S F_\mu F_{RE} F_{RS} \quad (3.10)$$

---

<sup>3</sup> The inelastic energy-absorption factor,  $F_\mu$ , has been defined as a function of the ductility ratio,  $\mu$ : the ratio of maximum displacement to displacement at yield. The relationship between  $F_\mu$  and  $\mu$  was developed using a bilinear force-displacement relationship. Kennedy and Ravindra (1984) proposed a median value for  $F_\mu$  of 2.0 for low-rise reinforced concrete shear walls for a ductility ratio of 3. This value for  $F_\mu$  is likely too high based on the data of Gulec et al. (2008). Consider Figure 3.7 that presents a force-displacement relationship for a sample low-rise reinforced concrete shear wall (Synge 1980, Gulec et al. 2008). The force-displacement behavior for the wall is far from bilinear and the wall undergoes a rapid loss of strength and stiffness with cyclic loading. If maximum shear strength is to be used as the marker for the loss of intended function (resistance to earthquake effects),  $F_\mu$  should likely be set equal to 1.0. Importantly, such walls are often required to provide radiation shielding for which residual crack widths must be small. Given that crack widths are often significant at story drifts approaching that associated with maximum strength, a more appropriate damage state might be linked to wall shear stress, perhaps of the order of  $6\sqrt{f'_c}$ . More research is needed to develop recommendations for the distribution (both median and dispersion) of  $F_\mu$  or an alternate factor for NPP components.

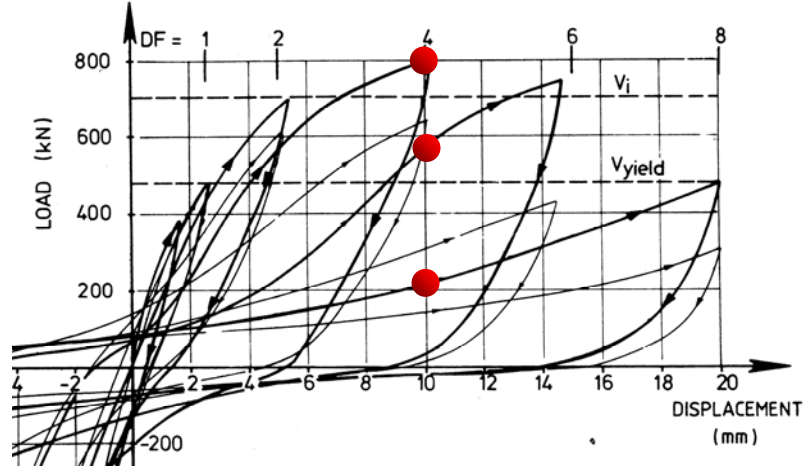


**Figure 3.7. A sample force-displacement relationship of low-rise reinforced concrete walls (Synge 1980, Gulec et al. 2008)**

where  $F_C$  (or the product of  $F_S$  and  $F_\mu$ ) represents the ratio of the acceleration level at which the equipment loses its intended function to the acceleration level specified for design;  $F_S$  and  $F_\mu$  are similar to those for (3.9), except for equipment;  $F_{RE}$  is the equipment response factor and defined by the ratio of equipment response used in design to the realistic equipment response for SSE shaking; and  $F_{RS}$  is the structural response factor as defined in (3.9).

The median, randomness and uncertainty of each random variable in (3.9) and (3.10) are estimated using structural analysis or component testing. The results are then combined to compute  $\hat{f}$ ,  $\beta_{F,r}$  and  $\beta_{F,u}$  using the properties of the lognormal distribution. For example,  $\hat{f}$ ,  $\beta_{F,r}$  and  $\beta_{F,u}$  for  $F$  in (3.10) can be computed as follows:

$$\hat{f} = \hat{f}_C \cdot \hat{f}_{RE} \cdot \hat{f}_{RS} \quad (3.11)$$

$$\beta_{F,r} = (\beta_{C,r}^2 + \beta_{RE,r}^2 + \beta_{RS,r}^2)^{1/2} \quad (3.12)$$

$$\beta_{F,u} = (\beta_{C,u}^2 + \beta_{RE,u}^2 + \beta_{RS,u}^2)^{1/2} \quad (3.13)$$

where  $\hat{f}_C$ ,  $\hat{f}_{RE}$  and  $\hat{f}_{RS}$  are the medians of the random variables  $F_C$ ,  $F_{RE}$ ,  $F_{RS}$  in (3.10), respectively;  $\beta_{C,r}$ ,  $\beta_{RE,r}$  and  $\beta_{RS,r}$  are the logarithmic standard deviations for randomness in  $F_C$ ,  $F_{RE}$  and  $F_{RS}$ , respectively; and  $\beta_{C,u}$ ,  $\beta_{RE,u}$  and  $\beta_{RS,u}$  are the logarithmic standard deviations for uncertainty in  $F_C$ ,  $F_{RE}$  and  $F_{RS}$ , respectively. Table 3.1 presents representative values of  $\beta_{X,r}$  and  $\beta_{X,u}$  for mechanical equipment in NPPs (Kennedy and Ravindra 1984). The performance assessment performed in this report for the sample NPP defined in Chapter 2 focuses on the

secondary systems in the NPP. The values of Table 3.1 will be used to define the fragility curves for the key secondary systems in the sample NPP.

**Table 3.1. Logarithmic standard deviation for the factors of safety for mechanical equipment (Kennedy and Ravindra 1984)**

Item	$\beta_r$	$\beta_u$
Capacity factor, $F_C$	0.10-0.18	0.22-0.32
Building response factor, $F_{RS}$	0.20-0.32	0.18-0.33
Equipment response factor, $F_{RE}$	0.18-0.25	0.18-0.25

Once the values of  $\hat{f}$ ,  $\beta_{F,r}$  and  $\beta_{F,u}$  are determined,  $\hat{a}$ ,  $\beta_u$  and  $\beta_r$  for a structural element or a piece of equipment in NPPs can be obtained and used in (3.6) and (3.7) for developing fragility curves and HCLPF values.

### 3.3 A New Procedure for Seismic Performance Assessment of NPPs

#### 3.3.1 Introduction

##### 3.3.1.1 A Shortcoming of the Conventional Methodology

The methodology for risk analysis described in Section 3.2 involves the use of component fragility curves developed using ground-motion parameters. Both the capacity of the component and the response (demand) of the structure are required to generate such curves. For two similar components at two different positions of a structure, the methodology might produce two significantly different fragility curves due to different demands on the two components.

Damage and failure of structural and nonstructural components in NPPs (as well as in buildings) are more closely tied to structural response parameters (e.g., story drift and floor spectral acceleration) than to ground-motion parameters. The use of structural response parameters in developing component fragility curves reduces the dispersion in the curves and enables the use of a fragility database for structural and nonstructural components in NPPs since the curves are independent of the structural geometry of the NPP. However, the procedure presented in Section 3.2 must be adjusted to compute the frequency of a failure event using fragility curves defined by structural response parameters since the use of (3.2) requires that the fragility and hazard curves be defined in terms of the same parameter.

The *draft ATC-58 Guidelines* provide a basis to improve the risk-assessment procedure presented in Section 3.2 for NPPs. The ATC-58 project is developing next-generation tools and guidelines for performance assessment of *buildings*, with a focus on measuring performance in terms of direct economic loss, casualties and downtime. The *draft ATC-58 Guidelines* present procedures for performance assessment using a probabilistic framework, which provides a robust methodology to integrate hazard curves, component fragility curves and consequence functions and to capture the dispersions in each of these elements for evaluating the performance of a building. Importantly, the fragility curves used in the analysis are defined in terms of structural response parameters.

In Section 3.3, a new procedure for assessing the performance of NPPs is proposed by incorporating the methodology presented in the *draft ATC-58 Guidelines* with the procedure presented in Section 3.2 and **Figure 3.1**. The proposed procedure enables the use of *structural-response-based* fragility curves in the risk computation and is used in Chapter 5 of this report to evaluate the seismic performance of the sample NPP reactor buildings.

#### *3.3.1.2 Overview of the New Procedure*

The proposed procedure includes the following five steps:

1. Perform plant-system and accident-sequence analysis and develop component fragility curves.
2. Characterize earthquake hazards.
3. Simulate structural response.
4. Assess damage of NPP components.
5. Compute the risk.

Step 1, which is the same as those shown in panels a and b of **Figure 3.1**, requires the user to develop the fragility curves for the structural and nonstructural components of the NPP, as well as the event trees and fault trees for unacceptable performance, such as core melt and radiation release. Step 2 involves the characterization of the seismic hazard. Step 3 involves response-history analysis of the NPP subjected to the seismic hazard of Step 2 to estimate the accelerations, forces, displacements and deformations that serve as demands on the NPP's components and

contents. Damage of the structural and nonstructural components is assessed in Step 4 using the demands computed in Step 3 and fragility curves developed in Step 1. Step 5 involves the computation of seismic risk using the results of Step 4 and the event trees and fault trees developed in Step 1. More information on each step is provided in Section 3.3.3.

In the *draft ATC-58 Guidelines*, seismic performance can be evaluated using one or more of three characterizations of seismic hazard: a user-specified *intensity* of earthquake shaking, a user-specified *scenario* of earthquake magnitude and site-to-source distance, and a *time-based* representation considering all possible earthquakes. The three types of assessments are adopted in the proposed procedure. Each type of assessment is introduced in Section 3.3.2.

A key issue in the proposed procedure is how to properly scale ground motions to represent the seismic hazard for intensity-, scenario- and time-based assessments. Section 3.3.4 summarizes an acceptable scaling method in the *draft ATC-58 Guidelines* for each of the three assessments. These scaling methods are also used in the proposed procedure to assess the seismic performance of NPPs. The technical basis of these scaling methods is provided in Chapter 4.

### **3.3.2 Types and Products of Performance Assessment**

#### **3.3.2.1 Intensity-Based Assessment**

An intensity-based performance assessment estimates the probability of unacceptable performance, given that the NPP experiences a specific intensity of shaking. The ground shaking intensity can be represented by a Safe Shutdown Earthquake (SSE) response spectrum or other design spectra. This type of assessment could be used to answer questions like: 1) What is the probability of core melt if the NPP experiences a SSE? and 2) What is the probability of radiation release, if the NPP experiences a ground shaking represented by a site-specific spectrum with a peak ground acceleration of 0.5 g?

If a single fragility curve is developed for each component in the NPP, the product of the intensity-based assessment is a single value of the probability of unacceptable performance, which is similar to a single point on one fragility curve presented in panel a of Figure 3.4. If a family of fragility curves is developed for each component in the NPP and used for analysis, the product is a distribution of the probability of unacceptable performance, which is similar to the distribution characterized by the family of fragility curves presented in panel a of Figure 3.4 at a given ground-motion intensity. The identified distribution can be presented as a probability

density function (similar to that presented in panel b of Figure 3.4 except the parameter for the X axis should be probability of unacceptable performance) or a cumulative distribution function, such as that shown in Figure 3.8, where the median probability of unacceptable performance is 0.3.

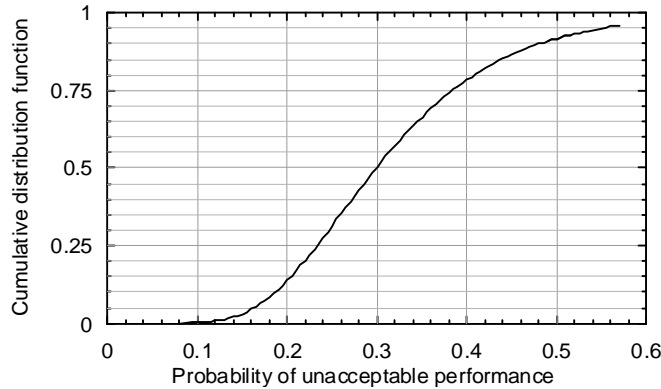


**Figure 3.8. Sample cumulative distribution function for the probability of unacceptable performance of a NPP**

### 3.3.2.2 Scenario-Based Assessment

A scenario-based performance assessment estimates the probability of unacceptable performance, given that a NPP experiences a specific earthquake, defined as a combination of earthquake magnitude and distance of the site from the part of the fault on which the earthquake occurs. This type of assessment could be used to answer the following question: What is the probability of core melt from an M 6 earthquake and ten kilometers from the NPP site?

For a scenario-based assessment, the seismic hazard is characterized by a distribution of spectral demand predicted by an attenuation relationship for the scenario case of interest. The product of a scenario-based assessment is similar to that of an intensity-based assessment.

### 3.3.2.3 Time-Based Assessment

A time-based assessment estimates the annual frequency of unacceptable performance of a NPP, considering all potential earthquakes that may occur. A time-based assessment could be used to answer the following type of question: What is the mean annual frequency of earthquake-induced radiation release for a NPP in Santa Barbara, California?

A time-based assessment is performed as a series of intensity-based assessments with different target spectral intensities determined from a seismic hazard curve. Probabilities of unacceptable performance are developed for intensities of earthquake shaking that span the intensity range of interest and then integrated (summed) over the hazard curve to compute the annual frequency of unacceptable performance. If a single fragility curve is developed for each component in the NPP and single hazard curve is used in the analysis, the product of the time-based assessment is a single value of the annual frequency of unacceptable performance. If a family of fragility curves is developed for each component in the NPP and used in the analysis, the product is a distribution of the annual frequency of unacceptable performance, which can be presented as a probability density function, such as that presented in panel b of Figure 3.4, or a cumulative distribution function, such as that shown in Figure 3.9, where the median annual frequency of unacceptable performance is  $2 \times 10^{-5}$ .

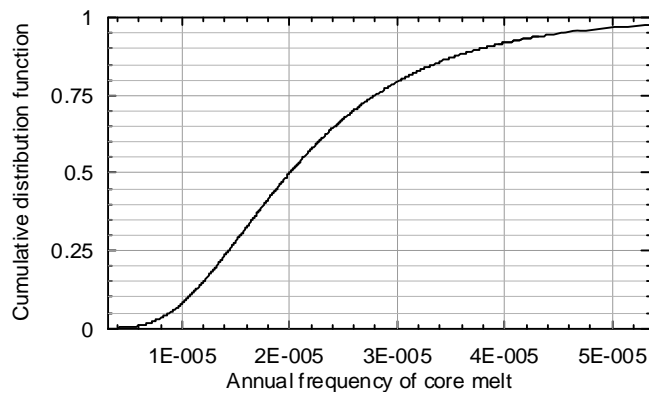


**Figure 3.9. Sample cumulative distribution function for the annual frequency of core melt of a NPP**

### 3.3.3 Methodology for Performance Assessment

#### 3.3.3.1 Step 1: Perform Plant-System and Accident-Sequence Analysis and Develop Component Fragility Curves

The first step is to perform plant-system and accident-sequence analysis and develop component fragility curves using response parameters.

As described in Section 3.2.1.4, the computation of unacceptable performance requires identification of all earthquake-induced initiating events. An event tree is developed for each initiating event to identify all meaningful accident sequences started by the event. A fault tree is

developed for each event included in the event trees to determine the probability of occurrence of the event. Fragility data are required in the proposed performance-assessment procedure for all basic failure events at the lowest levels of the fault trees (e.g., the failure of a structural or nonstructural component).

Event trees and fault trees provide a systematic method to consider the inter-dependency between different NPP systems and components. For example, the fault tree shown in panel b of Figure 3.3 presents the first few steps regarding the loss of electric power to engineered safety features (ESFs). The power to ESFs relies on both AC and DC power because the AC provides the energy for the ESFs but the DC is required by the control systems that turn on the AC (USNRC 0975). The loss of either AC or DC power will cause the loss of electric power to ESFs. This dependency between systems is captured in the fault tree by coupling the loss of AC and DC power to the top event using an “OR” gate.

#### 3.3.3.2 Step 2: Characterize Earthquake Shaking

A primary input into the performance assessment process is the definition of the earthquake effects that cause the unacceptable performance of NPPs. In the most general case, earthquake hazards can include ground shaking, ground fault rupture, liquefaction, lateral spreading and land sliding. Each of these can have different levels of severity, or intensity. Generally, as the intensity of these hazards increases, so does the potential for damage and risk. Given that nuclear structures would not be located at sites prone to ground fault rupture, liquefaction, lateral spreading and land sliding, such hazards are not described further herein.

Section 3.3.4 summarizes an acceptable procedure in the *draft ATC-58 Guidelines* for selecting and scaling ground motions for nonlinear response analysis to represent the seismic hazard for each of the intensity-, scenario- and time-based assessments. The product of the procedure in this step is a set of 11 (or more) pairs of ground motions for intensity- and scenario-based assessments and 8 (or more) sets of 11 (or more) pairs of ground motions for time-based assessments.

The ATC-58 recommendation of 11 minimum pairs is for performance assessment of regular low-rise buildings, with the minimum number being selected a) to estimate the median story drifts and floor accelerations in code-compliant structures within  $\pm 20\%$  of the *true* median with 75% when subjected to a family of ground motions scaled to a given first mode spectral acceleration (see Appendix C, Section C.3), b) recognizing the limited number of appropriate pairs of seed



ground motions, and c) to limit the computational endeavor. Herein, 11 pairs of ground motions are used to describe the procedure only.

### 3.3.3.3 Step 3: Simulate Structural Response

The third step is to perform nonlinear response-history analysis of the NPP for ground shaking consistent with the seismic hazard of Step 2. It is not possible to calculate precise values of seismic demands for a NPP since both the mechanical characteristics of the structure and the earthquake shaking are highly uncertain. Instead, it is necessary to predict a statistical distribution of the likely values of demands, considering the possible variation in earthquake intensity, ground motion characteristics and structural modeling uncertainty.

The variations in earthquake intensity and ground motion characteristics are addressed by appropriate selection and scaling of ground motion histories (see Section 3.3.4). Uncertainty in the structural models can be directly or indirectly included in the performance assessment. The indirect method involves increasing the dispersion in the computed responses (e.g., drift, acceleration, force) from analysis of a *best estimate* numerical model by a default value based on expert judgment or (prior) large-scale nonlinear response analysis of archetype NPP structures. Appendix B presents the indirect method.

A direct method for accounting for uncertainty in the structural models involves response-history analysis using multiple numerical models constructed using alternate formulations (epistemic uncertainty) and plausible distributions in material properties (aleatory randomness). For example, Figure 3.10 presents a force-displacement backbone curve for reinforced concrete wall segments with shear-dominant behavior (Wallace 2007). Assume that the nonlinear response-history analysis can be performed using a numerical model that adopts the backbone curve of Figure 3.10. The nominal shear strength  $V_n$  can be estimated from the geometry of the wall section, the compressive strength of concrete ( $f'_c$ ) and reinforcement yield stress ( $f_y$ ) using shear strength prediction equations, such as those provided in ACI 318-08 (ACI 2008), Barda et al., (1977) and ASCE/SEI 43-05 (ASCE 2005). The values of  $f'_c$  and  $f_y$  can be described with probability distributions. All other parameters defining the backbone curve, such as c, d and e, are also uncertain. Different combinations of c, d, e,  $f'_c$ ,  $f_y$  and shear strength prediction equation will result in alternate backbone curves. Uncertainty in the structural model could be included in the performance assessment by the analysis of a large family of NPP models with each model associated with a combination of c, d, e,  $f'_c$ ,  $f_y$  and shear strength prediction equation. This

procedure is extended simply to seismically isolated NPPs by expanding the family of NPP models to consider variations in isolator properties over the lifespan of the power plant. Appendix F provides supplemental information on this topic.

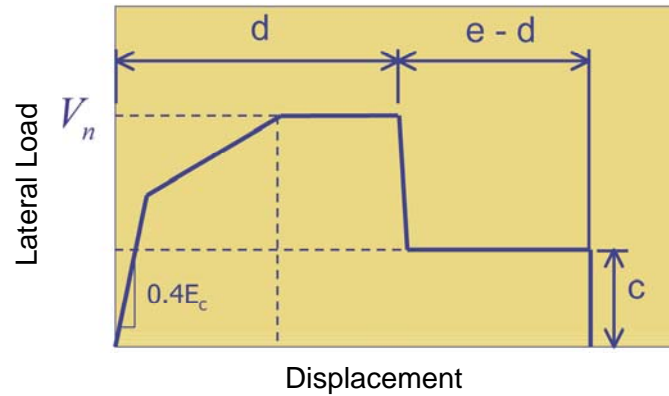


**Figure 3.10. A model for shear-displacement backbone curve for reinforced concrete wall segments (Wallace 2007)**

In Step 3, users are required to identify a list of demand parameters that can be used to estimate damage to structural and nonstructural components in NPPs, for example, peak story drifts, peak floor accelerations and floor spectral acceleration. The demand parameters should include all of the response parameters used in Step 1 for developing the component fragility curves. Each nonlinear response-history analysis will produce a value for each of the identified demand parameters and thus enable the construction of a vector of demand parameters. The analyses using the 11 (or more) ground motions developed in Step 2 for all the models developed in Step 3 will result in a matrix of demand parameters. The product of the procedure in this step is a demand-parameter matrix for intensity- and scenario-based assessments and 8 (or more) demand-parameter matrices for time-based assessments. The number of columns in the demand-parameter matrix depends on the numbers of demand parameters used in the performance assessment. The number of rows in the demand-parameter matrix is equal to the product of the number of numerical models and the number of ground motion pairs (11 minimum). For a time-based assessment, the number of the demand-parameter matrices is equal to the number of the ground-motion sets developed in Step 2.

Table 3.2 presents a sample demand-parameter matrix for an intensity-based assessment of the sample NPP (Model 1, as defined in Chapter 2). Three demand parameters are used in this example: the average floor spectral acceleration (over 5 through 33 Hz) at Nodes 201, 1009 and

216 of Model 1. Each row vector includes the values of the three demand parameters per each nonlinear response-history analysis for the intensity-based assessment. In this case, the failure events at the end of the branches of the fault tree for the unacceptable performance of interest are assumed to be the failure of the secondary systems supported at Nodes 201, 1009 and 216. The distributions in each demand parameter are then used to assess the damage of the secondary systems supported at those nodes and estimate the probability of unacceptable performance.

**Table 3.2. A sample matrix of demand parameters**

GM No.	Floor spectral acceleration (g)		
	Node 201	Node 1009	Node 216
1	0.99	1.28	2.60
2	0.79	1.09	2.05
3	0.78	1.24	2.25
4	1.06	1.49	2.89
5	0.74	1.02	1.93
6	0.91	1.34	2.17
7	0.67	0.96	1.83
8	0.78	1.02	1.98
9	0.95	1.16	2.09
10	0.65	0.93	1.88
11	1.03	1.28	2.34

As noted previously, a time-based assessment is performed as a series of intensity-based assessments spanning a wide range of target spectral intensities. Eight (or more) demand-parameter matrices (one per target spectral intensity) are required in this step for time-based assessment. The demand-parameter matrices are then used to assess the damage of the NPP components and estimate the annual frequency of unacceptable performance of the NPP.

#### *3.3.3.4 Step 4: Assess Damage of NPP Components*

In Step 4, the response data from the structural analysis of Step 3 is used together with the component fragility curves to assess the possible distribution of damage to structural and nonstructural components of a NPP. Each analysis in Step 3 will produce a vector of response

quantities that can be applied as demands to one or more structural and nonstructural components in the NPP. Structural and nonstructural component fragility curves are then used to characterize damage for the demands computed by the analysis.

In the *draft ATC-58 Guidelines*, the damage of a building component is measured using several damage states, for the purpose of loss computation. Each damage state is associated with a consequence function, which characterizes the relationship between the damage state and loss (for example, repair costs, downtime and casualties). Rather than estimating the repair cost, the focus of the assessment procedure proposed herein is to determine the probability or annual frequency of unacceptable performance (such as core melt or radiation release) of a NPP subjected to different seismic hazards. Therefore, only one damage state is used in the proposed procedure and the NPP component is considered to have either passed or failed. A component passes if it maintains its functionality during and after the earthquake and does not trigger other undesirable events. The component fails if it cannot function properly or its damage results in the occurrence of the unacceptable performance. The probability of failure of the component is characterized by fragility curves that plot the probability of failure as a function of a structural response parameter.

An example for assessing NPP component damage is presented herein using the fragility curve shown in Figure 3.11 for a sample secondary system. Assume a response-history analysis has identified that the location of the secondary system has a floor spectral acceleration of 2 g at the period of the secondary system. Per Figure 3.11, the probability of failure is 32% at a floor spectral acceleration of 2 g. A random number generator that generates random numbers uniformly distributed between 0 and 1 can be used to select the damage state for the secondary system. If the realization generated by the random generator is smaller or equal to 0.32, the secondary system is considered to have failed; and if the realization is greater than 0.32, the secondary system is considered safe. For a given response-history analysis, this procedure needs to be performed for all basic events at the lowest levels of the fault trees to determine the success or failure of each basic event.

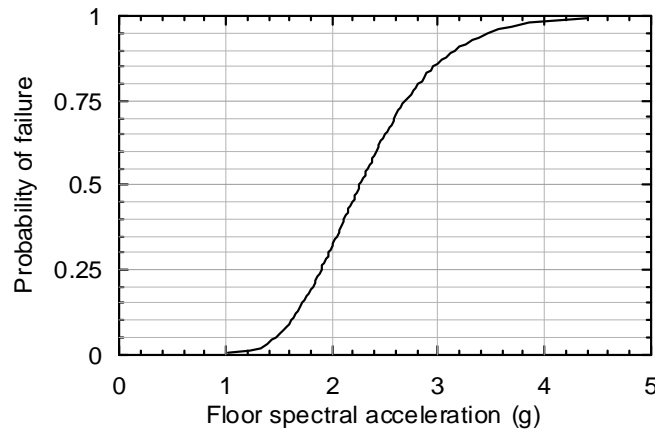


**Figure 3.11. A sample fragility curve for a secondary system in NPPs**

### 3.3.3.5 Step 5: Compute the Risk

#### *The Treatment of Variability: Monte Carlo Procedures*

The purpose of Step 5 is to determine the probability or annual frequency of unacceptable performance of a NPP for a given seismic hazard (characterized by a design spectrum in an intensity-based assessment, an attenuation relationship in a scenario-based assessment or a seismic hazard curve in a time-based assessment).

The procedure for performance (risk) assessment should consider the variability existing in the factors that affect risk, including 1) earthquake intensity, 2) structural response (as measured by demand parameters) for a given earthquake intensity, and 3) component damage (as measured by the damage state) for a given structural response. Monte Carlo type procedures are used in the proposed assessment procedure to address uncertainty. In Monte Carlo analysis, the three factors listed above are assumed to be random variables, each with a specific probability distribution. The distribution of earthquake intensity is used to scale ground motions for the nonlinear response-history analysis; the distribution of structural responses is preserved in the demand-parameter matrix, such as that shown in Table 3.2; and the distribution of the damage state (i.e., the fragility curve) is used to determine whether a NPP component fails or not for a set of simulation results (i.e., a row vector in the demand-parameter matrix).

The use of Monte Carlo procedures requires a large set (100s) of simulations so that the probability and annual frequency of the unacceptable performance can be estimated with high

confidence. The large set of simulations can be generated by two procedures, 1) directly by a large number of analyses using alternate numerical models of the NPP structure, or 2) indirectly by statistical manipulation of the results of a smaller number of analyses of a best estimate numerical model of the NPP structure. The *draft ATC-58 Guidelines* presents one acceptable procedure, which is summarized in Appendix B of this report, for generating a large number of simulations through statistical manipulation of a relatively small number of structural analyses (ATC 2007; Yang et al. 2006). The Yang et al. procedure is extended in Appendix B to address the uncertainty associated with the use of a best estimate numerical model.

For example, the demand-parameter matrix of Table 3.2 has 3 columns (representing 3 demand parameters) and 11 row vectors (from 11 nonlinear response-history analyses). The procedure of Appendix B can be used to generate a new demand-parameter matrix with a large number of row vectors based on the values in the original demand-parameter matrix computed using a best estimate numerical model. The mean vector and covariance matrix of the natural logarithm of the new demand-parameter matrix will be the same as those of the natural logarithm of the original matrix. The enlarged demand-parameter matrix should have a minimum of 200 row vectors.<sup>4</sup>

#### *Intensity- and Scenario-Based Assessments*

For a row vector of the demand-parameter matrix, the success or failure of each basic event<sup>5</sup> presented at the lowest level of a fault tree is determined in Step 4. The success or failure of the top event of each fault tree can then be determined following the logic of the fault tree. The fault tree presented in panel b of Figure 3.3 is used as an example to describe the process herein. If the distribution of failure among the basic events of the fault tree causes the loss of both on-site and off-site AC power to ESFs (the third level of the tree), the loss of AC power to ESFs (the second level of the tree) will occur and the top event, the loss of electric power to ESFs, will also occur because of the “OR” gate between the first and second levels of the tree.

---

<sup>4</sup> A series of analyses are presented in Chapter 5 to study the reliability of the use of 200 row vectors for the different types of performance assessment and the impact of the number of row vectors on the distribution of the probability of unacceptable performance.

<sup>5</sup> Since the events in a fault tree are “failure” events, the failure of an event is referred to the occurrence of that event.

The procedure described above is performed for all 200 row vectors of the demand-parameter matrix for a given earthquake intensity. The number of the row vectors associated with a failure of the top event is computed and termed  $n_{FTE}$ . The occurrence probability of the top event of the fault tree, termed  $P_{TE}$ , is determined by the ratio of  $n_{FTE}$  to 200. This analysis is repeated for all fault trees developed in Step 1. The occurrence probability of an event in an event tree (for example,  $P_A$  through  $P_E$  shown in panel a of Figure 3.3) is then determined by the value of  $P_{TE}$  for the corresponding fault tree. The probability of unacceptable performance for each initiating event identified for the unacceptable performance is computed using the corresponding event tree<sup>6</sup> and the results for all initiating events are probabilistically combined<sup>7</sup> to obtain the total probability of the unacceptable performance for the NPP subjected to the earthquake intensity under consideration.

For intensity- and scenario-based assessments, a single realization for the probability of the unacceptable performance is computed if the failure probability of each NPP component is characterized using a single fragility curve. If a family of fragility curves is used for each NPP component to consider the variability in component capacity, a number of realizations can be obtained using different combinations of component fragility curves. The key difference between the intensity- and scenario-based assessments is that a single design response spectrum is used to characterize the seismic hazard for a intensity-based assessment and a distribution of earthquake shaking conditioned on a given earthquake magnitude and site-to-source distance is used for a scenario-based assessment.

### *Time-Based Assessment*

---

<sup>6</sup> An example is presented herein using the event tree shown in panel a of Figure 3.3. The event tree identifies seven possible accident sequences, of which the occurrence probabilities are presented at the end of the branches. Among the seven sequences, Sequences 2 through 7 will cause the release of radiation and Sequence 1 will not. The probability of the radiation release due to the initiating event, pipe break, is the sum of the occurrence probabilities of Sequences 2 through 7.

<sup>7</sup> For example, assume a) an unacceptable performance has only two initiating events, Events 1 and 2; b) the two events are independent of each other; and c) the probabilities of the unacceptable performance initiating by Events 1 and 2 for a given seismic intensity are  $P_1$  and  $P_2$ , respectively. The total probability of the unacceptable performance is  $P_1 + P_2 - P_1P_2$ .

As described earlier, the seismic hazard for a time-based assessment is characterized using seismic hazard curves. A sample seismic hazard curve is shown in Figure 3.12, where the annual frequency of exceeding an earthquake intensity,  $\lambda(e)$ , is plotted versus the earthquake intensity,  $e$ , where the typical earthquake intensity is spectral acceleration at the first mode period of the structure of interest.

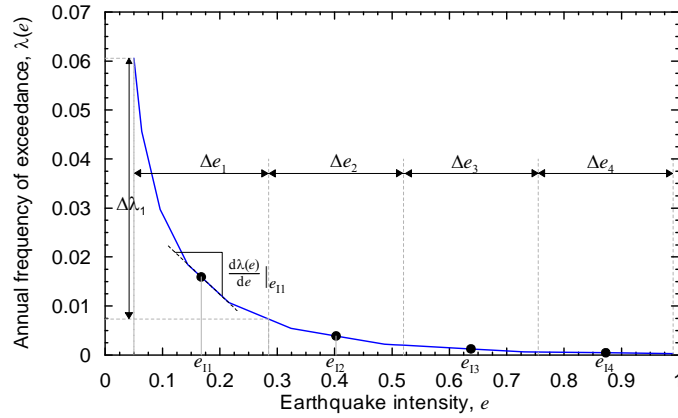


**Figure 3.12. Seismic hazard curve and time-based loss calculations**

For a given hazard curve, the spectral range of interest is split into  $n$  equal intervals,  $\Delta e_i$ , and the midpoint intensity in each interval is  $e_{i1}$ , and the annual frequency of earthquake intensity in the range  $\Delta e_i$  is  $\Delta \lambda_i$ . Equal intervals are used herein in the absence of information that would support the use of unequal intervals. Figure 3.12 defines  $\Delta e_i$ ,  $e_{i1}$  and  $\Delta \lambda_i$  for the sample hazard curve and  $n = 4$ . (The small value of  $n$  is chosen to simplify the figure. A procedure presented in the *draft ATC-58 Guidelines* and summarized in Section 3.3.4 of this report has recommended that  $n$  be equal or greater than 8).

For a time-based assessment, a series of  $n$  intensity-based assessments are performed at  $e_{11}$  through  $e_{n1}$ , where the user-selected range of earthquake intensity is from no damage (small  $e$ ) through collapse (larger  $e$ ). Earthquake intensity at intensity  $e_{11}$  is assumed to represent all shaking in the interval  $\Delta e_1$ , and so on. The product of the  $n$  intensity-based assessments is  $n$  realizations for the probability of the unacceptable performance (one per each intensity-based assessment). Equation (3.14) is used to calculate the annual frequency of the unacceptable performance,  $\lambda_f$ , for the NPP:

$$\lambda_f = \sum_{i=1}^n P_i \cdot \Delta \lambda_i \quad (3.14)$$



where  $P_i$  is the probability of the unacceptable performance for the  $i$ -th intensity-based assessment and  $\Delta\lambda_i$  has been defined earlier. A time-based assessment can generate either a single value or a distribution of  $\lambda_f$ , depending on whether a single or a family of fragility curve(s) is used for each NPP component analyzed in the assessment.

### **3.3.4 Scaling Earthquake Ground Motions for Nonlinear Response-History Analysis**

#### **3.3.4.1 Intensity-Based Assessment**

Section 3.3.4 presents a set of ground-motion scaling methods recommended in the *draft ATC-58 Guidelines* for nonlinear response-history analysis for intensity-, scenario- and time-based assessment. The set of scaling methods is adopted in the proposed performance-assessment procedure for NPPs. The *draft ATC-58 Guidelines* provides two bins of 50 ground motions for use in response-history analysis: Bin 1 for near-fault sites and Bin 2 for far-field sites. Detailed information for the two bins of ground motions is provided in Chapter 4.

The seismic hazard for intensity-based assessment is characterized by a user-specified 5%-damped, elastic horizontal acceleration response spectrum. The recommended scaling procedure for intensity-based assessment is intended to capture the *median* structural response, given a specific spectral demand at the fundamental period of the structure. The dispersion in spectral demand is not considered in the scaling procedure although some dispersion in structural response is preserved.

The procedure for scaling ground motions for intensity-based assessment involves the following steps:

1. Select a response spectrum.
2. Determine the target spectral acceleration at the fundamental period of the structure,  $S_a(T_1)$ .
3. Randomly select at least 11 ground motions<sup>8</sup> from Bin 1 or Bin 2 based on the seismologic information of the site and amplitude scale each ground motion to the target  $S_a(T_1)$ .

---

<sup>8</sup> Both intensity- and scenario-based assessments involve the use of at least 11 ground motions for the response-history analysis. The number of ground motions used in the analysis depends on the required

Figure 3.13 presents spectra for 11 sample ground motions and scaled using the above procedure for a building with fundamental period of 1.14 seconds and  $S_a(T_1)$  equal to 0.51 g. Note that the dispersion at periods other than 1.14 seconds are non-zero.

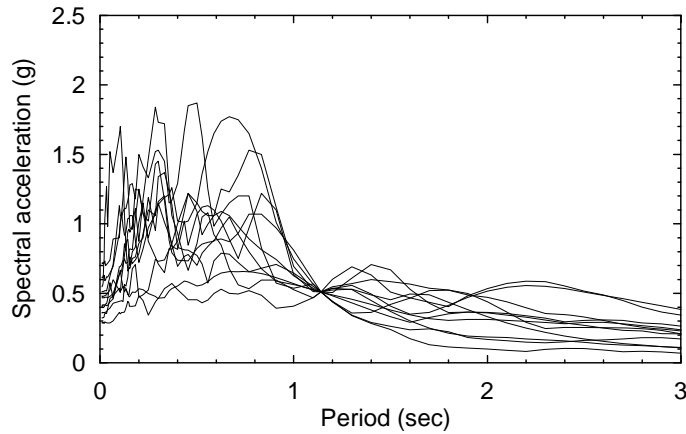


**Figure 3.13. Spectral accelerations for 11 sample ground motions for intensity-based assessment**

#### 3.3.4.2 Scenario-Based Assessment

The seismic hazard representations used for scenario-based assessment are the median,  $\theta$ , and dispersion,  $\beta$ , of spectral acceleration for a given (magnitude, distance) pair computed using an attenuation relationship or relationships.

Ground-motion scaling procedures for scenario-based assessments must consider the distribution (i.e., both  $\theta$  and  $\beta$ ) of spectral demand for the target scenario. In the *draft ATC-58 Guidelines*, at least 11 values of spectral acceleration are required to characterize the distribution of seismic demand at the fundamental period of the building. For the case using 11 target spectral accelerations:

$$S_{ai}(T_1) = \theta \cdot e^{\beta \eta_i} \quad i = 1, 11 \quad (3.15)$$

where  $S_a(T_1)$  is the  $i$ th target spectral acceleration at the fundamental period of the structure and values of  $\eta_i$  are as listed in Table 3.3.

---

accuracy and confidence in the estimates of structural responses. The technical basis for the use of 11 ground motions is provided in Chapter 4 and Appendix C of this report.

**Table 3.3. Values of  $\eta_i$  for generating a distribution of  $S_{ai}(T_1)$**

I	$\eta_i$
1	-1.69
2	-1.10
3	-0.75
4	-0.47
5	-0.23
6	0
7	0.23
8	0.47
9	0.75
10	1.10
11	1.69

Figure 3.14 illustrates this process for a scenario earthquake having median spectral acceleration of 0.3 g and dispersion equal to 0.4. The figure shows the cumulative probability distribution represented by this median and dispersion. Horizontal lines across the plot divide the distribution into eleven regions, each having a probability of occurrence of 9.09%. For each region, the midpoint value of the probability of exceedance is shown by  $\odot$  with values of 4.55%, 13.64%, 22.73%, 31.82%, 40.91%, 50%, 59.09%, 68.18%, 77.27%, 86.36% and 95.45%. A dashed horizontal line is drawn across the plot from the vertical axis to intersect the cumulative distribution function and dropped vertically to the horizontal axis, where spectral acceleration values of .153 g, .193 g, .222 g, 0.248 g, 0.274 g, 0.300 g, 0.329 g, 0.362 g, 0.405 g, 0.465 g and 0.590 g, respectively, can be read off. These values are the same as those computed by (3.15) using  $\theta = 0.3$  and  $\beta = 0.4$ .

The procedure for scaling 11 ground motions for scenario-based assessment involves the following steps:

1. Select the magnitude and site-to-source distance for the scenario event.
2. Select an appropriate attenuation relationship (or relationships) for the region, site soil type and source characteristics.

3. Determine the median spectral acceleration demand,  $\theta$ , and its dispersion,  $\beta$ , at the fundamental period of the structure using the attenuation relationship(s) of step 2.
4. Compute 11 target values of spectral acceleration,  $S_a(T_i)$ ,  $i = 1, 11$ , using  $\theta$  and  $\beta$  from step 3 and (3.15).
5. Select 11 ground motions from Bin 1 or Bin 2.<sup>9</sup>
6. Amplitude scale one of the 11 ground motions to one of the 11 target spectral accelerations of step 4; repeat the selection and scaling process 10 times for the remaining 10 target values of spectral acceleration so as to fully populate the distribution of  $S_a(T_i)$ .

---

<sup>9</sup> Huang et al. (2007) shows that randomly selecting ground motions from Bin 1 or Bin 2 might cause the median spectral shape of the scaled ground motions to be significantly different from the shape of the median spectrum predicted by an attenuation relationship for a given pair of magnitude and distance. Given that losses might accrue at periods less than the first mode period (i.e., higher modes), it would be better to select ground motions for scenario-based analysis per the magnitude and distance pair for the scenario event of interest. Baker and Cornell (2005 and 2006) and the results presented in Appendix D of this report show that the ground-motion randomness index,  $\varepsilon$ , is an indicator of spectral shape. Selecting ground motions without consideration of  $\varepsilon$  may result in conservative estimates in structural responses for structures subjected to earthquake shaking associated with a value of  $\varepsilon$  greater than 1. Epsilon can be included in a scenario-based assessment by selecting and scaling ground motions using the value of  $\varepsilon$  associated with each target spectral ordinate. Multiple ground motions will likely be required for a target spectral ordinate. More research is needed to develop such a procedure.

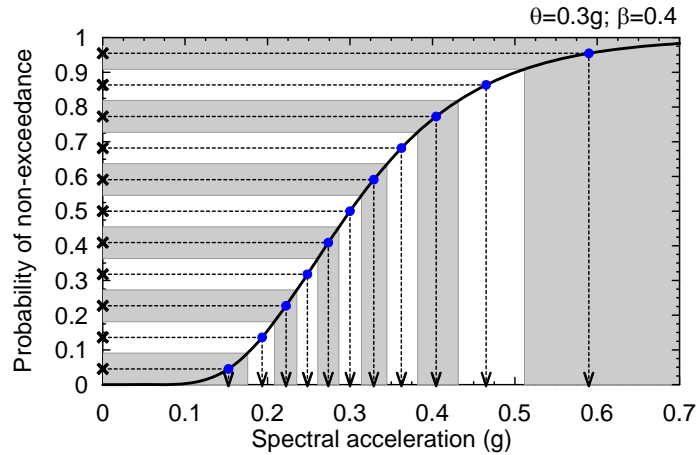


**Figure 3.14. Calculation of spectral accelerations given a lognormal distribution**

Figure 3.15 presents acceleration spectra for 11 sample ground motions scaled using the procedure proposed in the *draft ATC-58 Guidelines* for a building with a fundamental period of 1.14 seconds. The 11 target spectral ordinates shown in Figure 3.15 were computed using (3.15) with  $\theta = 0.41$  g and  $\beta = 0.64$ , where the median and dispersion were computed using the Chiou-Young Next Generation Attenuation relationship (Chiou and Young 2006) for  $M_W = 7$ ,  $r = 1$  km, strike-slip faulting and a shear wave velocity of 760 m/s.

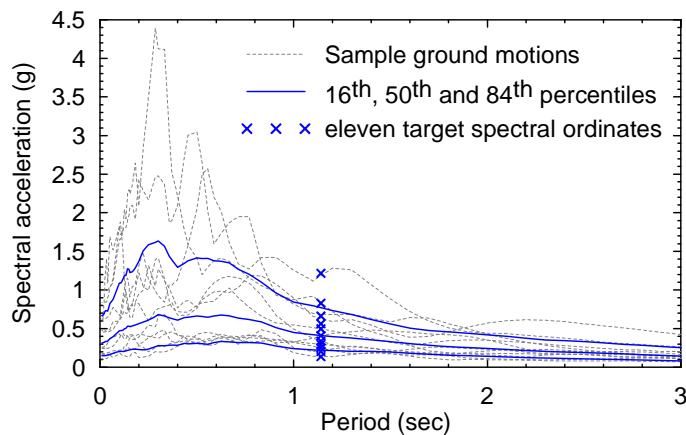


**Figure 3.15. Spectral accelerations for 11 sample ground motions for scenario-based assessment**

### 3.3.4.3 Time-Based Assessment

Earthquake shaking for time-based assessment is characterized by a seismic hazard curve that plots spectral acceleration at a user-specified period versus the annual frequency of exceeding (MAFE) that value of spectral acceleration. A sample curve is presented in Figure 3.16.

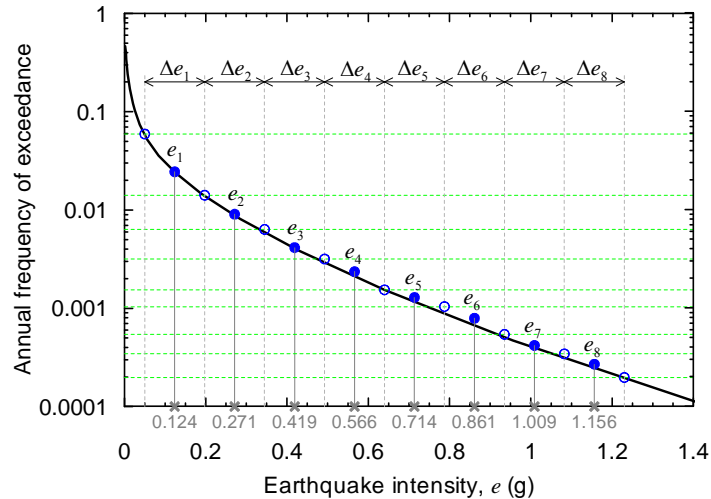


**Figure 3.16. Calculation of spectral accelerations given a mean hazard curve**

In the *draft ATC-58 Guidelines*, time-based assessment is performed as a series of intensity-based assessments. The principal contributions to probable loss for regular buildings are assumed to accumulate in the range of spectral demand between 0.05 g and the spectral acceleration corresponding to an annual frequency of exceedance of 0.0002. The lower bound on this range (0.05 g) is assumed to cause no damage to either structural or nonstructural components and the upper bound is assumed sufficient to have a high probability of triggering collapse in modern code-compliant buildings. This range of spectral demand is then split into at least 8 equal intervals and the midpoint values (intensity) of spectral acceleration in each interval is assumed to represent shaking across the entire interval.

The range of the spectral demand recommended in the *draft ATC-58 Guidelines* is inappropriate for the time-based assessment of NPPs since the MAFE for the SSE shaking (about  $10^{-5}$ ) is smaller than 0.0002. The range of spectral demand for the time-based assessment should be selected to cover all significant risk. The upper bound of spectral demand must be greater than the design level (the spectral demand associated with a MAFE of  $10^{-5}$ ). Chapter 5 of this report discusses this issue in more detail.

The seismic hazard curve shown in Figure 3.16 illustrates the calculations of 8 target spectral accelerations. The range of spectral acceleration was selected as  $0.05 g^{10}$  to  $1.23 g$ , where  $1.23 g$  is the spectral acceleration (at a given period) corresponding to an annual frequency of exceedance of  $0.0002$ . This range of spectral acceleration was split into eight equal intervals,  $\Delta e_i$ , of  $0.1475$ . The midpoint value in each interval characterizes a target spectral demand for the scaling of ground motions. The 8 target spectral accelerations are identified in the figure by the symbol  $x$  with values of  $0.124 g$ ,  $0.271 g$ ,  $0.419 g$ ,  $0.566 g$ ,  $0.714 g$ ,  $0.861 g$ ,  $1.009 g$  and  $1.156 g$ .

The *draft ATC-58 Guidelines* provides two methods for time-based assessment. Method 1 scales ground motions to the target spectral accelerations characterized by the mean seismic hazard curve, when this is available. Method 2 considers the distribution of spectral accelerations at a selected annual frequency of exceedance and can be used when both the median hazard curve and the dispersion in the hazard curve (due to the epistemic uncertainty) are available. Only the procedure for Method 1 is presented herein.

Method 1 uses a mean seismic hazard curve computed at the fundamental period of the building. The procedure for scaling ground motions to 8 intensity levels for time-based assessment of buildings involves the following steps:

1. Develop a mean seismic hazard curve at the fundamental period of the structure that is appropriate for the soil type at the building site.
2. Compute the spectral acceleration from the mean seismic hazard curve of step 1 for an annual frequency of exceedance =  $0.0002$  and denote that spectral acceleration as  $S_a^{\max}$ .
3. Split the range of spectral acceleration,  $0.05$  to  $S_a^{\max} g$ , into 8 equal intervals; identify the midpoint spectral acceleration in each interval.

---

<sup>10</sup> Although  $0.05 g$  might be a reasonable lower bound for building structures, it is likely far too small for conventional nuclear structures.

4. For *each* of the 8 midpoint spectral accelerations,  $S_{ai}(T_1)$ ,  $i = 1, 8$ , randomly<sup>11</sup> select eleven ground motions from either Bin 1 or Bin 2 and amplitude scale each ground motion to  $S_{ai}(T_1)$  for response calculations.

Figure 3.17 presents spectra for 11 sample ground motions, scaled by the procedure described above, for intensities 1 and 8 per Figure 3.16.

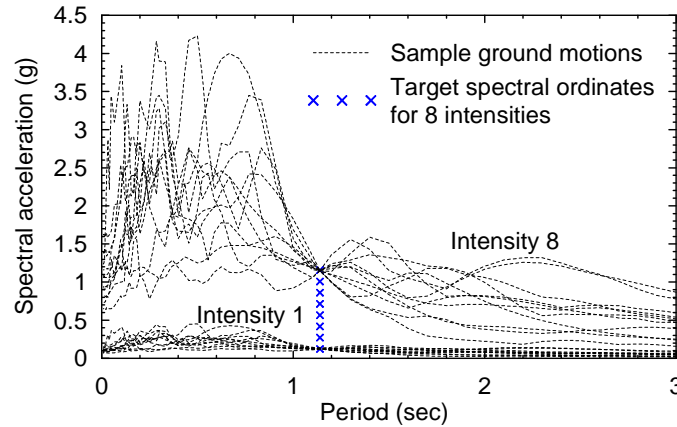


**Figure 3.17. Spectral accelerations for 11 sample ground motions at intensities 1 and 8**

For time-based assessment of NPPs, Steps 2, 3 and 4 presented above should be adjusted as follows:

2. Determine the upper and lower bounds of spectral accelerations (denoted as  $S_a^{\max}$  and  $S_a^{\min}$ ) using the mean seismic hazard curve of step 1. The range should be wide enough to capture all significant risk. Possible values of  $S_a^{\max}$  and  $S_a^{\min}$  are the spectral accelerations associated with mean annual frequencies of exceedance of  $10^{-6}$  and  $10^{-4}$ , respectively.
3. Split the range of spectral acceleration,  $S_a^{\min}$  to  $S_a^{\max}$  g, into 8 equal intervals; identify the midpoint spectral acceleration in each interval.
4. For *each* of the 8 midpoint spectral accelerations,  $S_{ai}(T_1)$ ,  $i = 1, 8$ , select eleven ground motions based on the combination of magnitude, distance and  $\varepsilon$  appropriate for  $S_{ai}(T_1)$  and amplitude scale each ground motion to  $S_{ai}(T_1)$  for response calculations.

---

<sup>11</sup> The 50% draft of the ATC-58 Guidelines that will be published at the end of 2008 will include rules that require consideration of spectral shape for  $\varepsilon \geq 1$ .



# CHAPTER 4

## SCALING GROUND MOTIONS FOR PERFORMANCE ASSESSMENT

### 4.1 Introduction

The procedures used to select and scale earthquake ground motions for nonlinear response-history analysis directly affect the distributions of demand on structural and nonstructural components. Section 3.3.4 presented procedures for intensity-, scenario- and time-based assessments, which have been adopted in the 35% draft ATC-58 *Guidelines for the Seismic Performance Assessment of Buildings* (ATC 2007), but did not provide the technical basis for the ground-motion scaling procedures. The information presented in this chapter identifies the impact of different scaling procedures on the results of response-history analysis for the purpose of performance assessments.

Section 4.2 describes the state-of-art in the selection and scaling of ground motions for response-history analysis. Five procedures are introduced. Section 4.3 presents results for a series of nonlinear response-history analyses using the five scaling procedures. The advantages and disadvantages of each procedure are identified.

### 4.2 State of the Art

#### 4.2.1 *Probabilistic Seismic Hazard Analysis and Uncertainties in Spectral Demands*

Probabilistic seismic hazard analysis (PSHA) has been used to characterize ground motion for the design of conventional buildings and NPPs. The United States Geological Survey (USGS) has developed seismic hazard maps based on PSHA for the design of conventional structures in the United States. The United States Nuclear Regulatory Commission (USNRC) developed Regulatory Guide 1.165 (USNRC 1997) that presents PSHA-based rules to establish Safe Shutdown Earthquake (SSE) shaking for the design of NPPs.

Uncertainty and randomness in the calculation of spectral demands for a given mean annual frequency of exceedance is captured explicitly by PSHA. The product of PSHA is a family of hazard curves that are typically presented as the relationship between annual frequency of exceedance and spectral acceleration at a given period. Sample hazard data are shown in Figure 4.1 (Abrahamson and Bommer 2005). This figure presents zero-period acceleration (ZPA) hazard

curves for a site in southern Nevada; the minimum annual frequency of exceedance is  $10^{-8}$ . Aleatory variability is included in each of the curves presented in this figure. Epistemic (model) uncertainty is represented by the dispersion in the spectral demand at a given annual frequency of exceedance<sup>1</sup>. Median, mean and four fractile (from 5th to 95th) hazard curves are shown in the figure, capturing the epistemic uncertainty. For an annual frequency of exceedance of  $10^{-5}$  (return period of 100,000 years), the ZPA demand distributes from 0.5g (5%) to 2.5g (95%). Uniform hazard spectra (UHS) are developed for a given fractile (or mean) by computing spectral ordinates across a range of periods for a given annual frequency of exceedance.

#### **4.2.2 Existing Procedures for Selecting and Scaling Ground Motions**

Current codified procedures for response-history analysis involve scaling ground motions to match a uniform hazard spectrum using one of two methods: 1) amplitude and/or frequency scaling single-component ground motions to exactly match a target spectrum, a procedure developed originally for analysis of (elastic) nuclear power plant structures, and 2) amplitude scaling pairs of ground motions so that the average value of the square root of the sum of the squares of the 5-percent damped spectral ordinates is not less than 1.3 times the 5-percent damped target spectrum for periods from  $0.2 T_1$  to  $1.5 T_1$  (FEMA 2004, ASCE 2006), where  $0.2 T_1$  represents an estimate of the second mode period and  $1.5 T_1$  is an estimate of the degraded first mode period (accounting for damage to the framing system). The second method was developed in its original form in the early 1990s for the nonlinear analysis of seismically isolated buildings

---

<sup>1</sup> Two types of uncertainty are considered in the calculation of hazard curves: *aleatory variability*, which characterizes the inherent variability of the earthquake magnitude ( $M$ ), site-to-source distance ( $r$ ), and spectral demand for a given pair of  $M$  and  $r$  considered in the integration of seismic hazard, and *epistemic uncertainty*, which characterizes the scientific uncertainty of the models for the style of faulting, maximum magnitude, recurrence laws and attenuation relationships (usually considered using logic trees). Aleatory variability results in a hazard curve given a set of assumptions for the models whereas epistemic uncertainty defines the probabilities for alternative hazard curves from different assumptions (Abrahamson and Bommer 2005; McGuire et al. 2005). One must be careful to distinguish between the dispersion in spectral acceleration for a *scenario event* and the dispersion in spectral acceleration computed using *PSHA* for a given return period: the former can be determined from the standard deviation reported in attenuation relationships whereas the latter must be determined using different models to include both aleatory variability and epistemic uncertainty.

(with a slightly modified period range from that indicated above). Historically, either three or seven pairs of ground motions have been used for response analysis, based in part on rules adopted for the analysis of nuclear structures in the 1970s. If three pairs are used, assessment is based on the maxima of peak component actions and deformations. If seven pairs are used, assessment is based on the average of each maximum response.

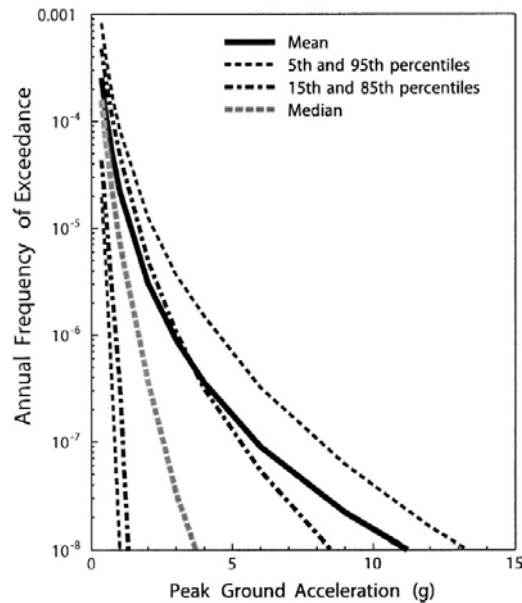


**Figure 4.1. Sample seismic hazard curves (adopted from Abrahamson and Bommer 2005)**

Other procedures have been developed for scaling pairs of earthquake ground motions for response analysis. One procedure that was developed for the offshore oil industry and used for the SAC Steel Project by Somerville et al. (1997) involves amplitude scaling a pair of ground motions by a single factor to minimize the sum of the squared errors between target spectral values and the geometric mean of the spectral ordinates for the pair, where the user selects the periods (frequencies) for the calculation. This procedure preserves spectral shape and the correlation between the components in the pair of motions; it is studied in Section 4.3.4.1.

Seed ground motions for response-history analysis have traditionally been selected (at least for the analysis of seismically isolated structures) on the basis that the magnitude(s), site-to-source distance(s) and source mechanisms are compatible with the design-basis or maximum considered earthquake. More recently, the practice has been to de-aggregate the uniform hazard spectrum (or spectra) at the first mode period of the structure ( $T_1$ ), determine the modal magnitude ( $M$ ) and

site-to-source distance ( $r$ ) pair, and select recorded ground motions corresponding to the modal  $[M, r]$  pair and local site conditions.

#### **4.2.3 Recent Studies**

Recent publications have reported on the selection and scaling of ground motions for response-history analysis, including Shome et al. (1998), Carballo and Cornell (2000), Baker and Cornell (2005), Iervolino and Cornell (2005), Huang et al. (2006) and Haselton and Baker (2006). Conclusions of these studies are described below.

Shome et al. (1998) proposed a ground-motion scaling method to predict the median response of nonlinear oscillators. The method involves scaling ground motions to a selected spectral acceleration at the first mode period of the building ( $S_a(T_1)$ ). They concluded that neither three nor seven pairs of scaled ground motions are sufficient to produce reliable median estimates of displacement response. Appendix C describes the scaling method in some detail.

For far-field ground motions, Shome et al. (1998), Baker and Cornell (2005) and Iervolino and Cornell (2005) showed that the choice of seed motions based on controlling  $[M, r]$  pairs (selected by deaggregating the hazard curve) did not have significant effect on structural response after the seed motions were amplitude scaled to a specified spectral acceleration, at the first mode period of the building. They recommended that any requirement that seed ground motions be selected on the basis of controlling  $[M, r]$  pairs be set aside.

Carballo and Cornell (2000) selected a set of 63 ground motion records in the range of moment magnitude from 6.7 to 7.3 and closest distance to the rupture zone from 10 to 30 km and generated two sets of 63 spectrally matched ground motions using frequency- and time-domain techniques. The spectrum for each of the artificial accelerograms was then matched to the median spectrum of the 63 original records. Carballo and Cornell observed that the use of spectrally matched ground motions results in un-conservatively biased displacement demands in highly nonlinear framing systems compared to the results for the original ground motions. Huang et al. (2006) confirmed this observation using bilinear SDOF oscillators and 20 near-fault ground motions developed for the SAC Steel project.

#### **4.2.4 Epsilon Scaling and the Conditional Mean Spectrum**

Much recent discussion on scaling ground motions for shaking with very low annual frequencies of exceedance has centered on the ground-motion randomness index known as epsilon ( $\varepsilon$ ).

Epsilon is defined as the number of logarithmic standard deviations by which the underlying logarithmic spectral acceleration  $[\ln(x_{s_a})]$  deviates from the median value, where the median and the logarithmic standard deviation of spectral acceleration (denoted as  $\theta_{s_a}$  and  $\beta_{s_a}$ , respectively) are predicted by an attenuation relationship (McGuire 1995; Baker and Cornell 2005; Haselton and Baker 2006):

$$\varepsilon = \frac{\ln(x_{s_a}) - \ln(\theta_{s_a})}{\beta_{s_a}} \quad (4.1)$$

Figure 4.2 shows a sample calculation of  $\varepsilon$ . The dotted line in the figure is the spectral acceleration for a sample ground motion recorded at a deep soil site in the 1979 Imperial Valley earthquake with  $M=6.5$  and  $r=12.9$  km. The 84th, 50th (median) and 16th percentile spectral accelerations predicted by the attenuation relationship of Abrahamson and Silva (1997) for the site are also shown in Figure 4.2. The three fractile spectra correspond to  $\varepsilon = +1$  (84th percentile),  $=0$  (50th percentile, median) and  $=-1$  (16th percentile), respectively, at all periods. At a period of 0.2 second, the attenuation relationship predicts  $\theta_{s_a} = 0.5g$  and  $\beta_{s_a} = 0.69$ , respectively. The spectral acceleration for the sample motion is 0.35g; the resulting value of  $\varepsilon$  is -0.36. For the same ground motion, magnitude and distance pair, and attenuation relationship,  $\varepsilon$  is +0.78 at a period of 2 seconds. Epsilon is often presented as a component of hazard-curve deaggregation (an  $[M, r, \varepsilon]$  triple) to identify the departure of the spectral ordinates computed using probabilistic seismic hazard analysis (PSHA) from those calculated using the controlling  $[M, r]$  pair and an attenuation relationship or relationships. For such a calculation,  $\ln(x_{s_a})$  is the natural logarithm of the spectral acceleration computed by PSHA<sup>2</sup>.

---

<sup>2</sup> A value of  $\varepsilon$  is generated for each  $[M, r]$  pair and attenuation relationship used in the PSHA for the given  $\ln(x_{s_a})$ . USGS reports the modal value of  $\varepsilon$  in the peak  $[M, r]$  bin.

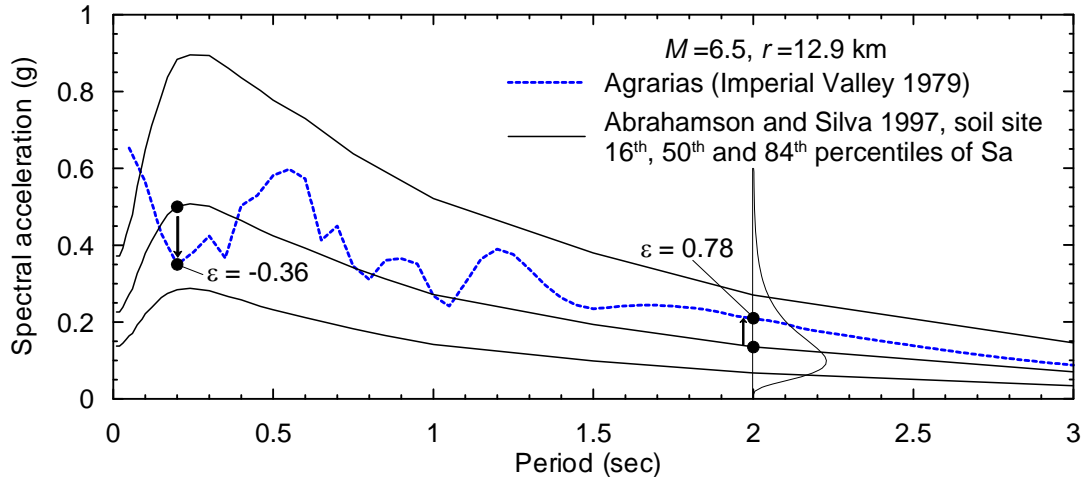


**Figure 4.2. A sample response spectrum (Agrarias station, the 1979 Imperial Valley earthquake) and the 84th, 50th and 16th percentiles of spectra predicted by the attenuation relationship of Abrahamson and Silva (1997) for soil sites**

Baker and Cornell (2005) proposed that the effect of  $\varepsilon$  on structural response given  $S_a(T_1)$  is greater than that of either magnitude or distance because  $\varepsilon$  is an indicator of spectral shape. Baker and Cornell (2005, 2006) and Haselton and Baker (2006) concluded that a positive value of  $\varepsilon$  at a given period tends to indicate a relative peak in the acceleration response spectrum at that period.

UHS and its two-point representation have been widely used for the design of buildings (ICC 2000, FEMA 2004, ASCE 2006). Cornell (2006) and Baker and Cornell (2006) have reflected on the utility of UHS for design and have observed:

- a) If the spectral ordinates of a UHS are governed by multiple scenario events, the spectral shape of the UHS will not represent the spectral shape for any of the governing events, regardless of the return period of the UHS.
- b) For long-return-period earthquake shaking, the spectral ordinates of a UHS are usually associated with a high value of  $\varepsilon$  values across a wide range of period<sup>3</sup>: for the case where

---

<sup>3</sup> Harmsen (2001) noted that  $\varepsilon > 2$  for modal events for sites on the West Coast of the United States and a 2% probability of exceedance in 50 years, which means that less than 23 of 1000 earthquakes of the controlling  $[M, r]$  pair will produce shaking more severe, as measured by spectral ordinates, than the spectral demand predicted by PSHA.

the spectral ordinate of a record attains the UHS ordinate at a given period, the spectrum of the record is unlikely to have values as large as those of the UHS across a wide range of period.

These observations result from the fact that the UHS spectral ordinates are computed independently. Baker and Cornell (2005, 2006) introduced a Conditional Mean Spectrum, which considers  $\varepsilon$  at the fundamental period and the correlation of spectral demands at different periods, for selecting and scaling ground motions to represent very rare earthquake shaking. The proposed spectrum was termed CMS- $\varepsilon$  and computed using the following equation:

$$\mu_{\ln Sa(T_2) | \ln Sa(T_1) = \ln Sa(T_1)^*} = \mu_{\ln Sa}(\bar{M}, \bar{R}, T_2) + \sigma_{\ln Sa}(\bar{M}, T_2) \rho_{\ln Sa(T_1), \ln Sa(T_2)} \cdot \bar{\varepsilon}(T_1) \quad (4.2)$$

where  $Sa(T_1)$  and  $Sa(T_2)$  are spectral accelerations at periods  $T_1$  and  $T_2$ ;  $T_1$  is the fundamental period of the structure;  $Sa(T_1)^*$  is the value of  $Sa(T_1)$  corresponding to a given annual frequency of exceedance;  $\bar{M}$ ,  $\bar{R}$  and  $\bar{\varepsilon}$  are the mean magnitude ( $M$ ), distance ( $R$ ) and  $\varepsilon$  values, respectively, that produce  $Sa(T_1)^*$ ;  $\mu_{\ln Sa(T_2) | \ln Sa(T_1) = \ln Sa(T_1)^*}$  is the mean of  $\ln Sa(T_2)$  given that  $\ln Sa(T_1) = \ln Sa(T_1)^*$ ;  $\mu_{\ln Sa}$  and  $\sigma_{\ln Sa}$  are the mean and standard deviation of  $\ln Sa$ , respectively, obtained from a ground motion attenuation relationship; and  $\rho_{\ln Sa(T_1), \ln Sa(T_2)}$  is the correlation coefficient of  $\ln Sa(T_1)$  and  $\ln Sa(T_2)$ . A CMS- $\varepsilon$  is constructed by changing the value of  $T_2$  in (4.2). Figure 4.3 presents a sample UHS with 2% probability of exceedance in 50 years for a site in Van Nuys, California, and a CMS- $\varepsilon$  with  $Sa(T_1 = 0.8s) = 1.6$  g determined by the sample UHS, where the value of  $Sa(T_1 = 0.8s)$  corresponds to a value of 2.1 for  $\bar{\varepsilon}$ . The UHS has greater spectral ordinates than the CMS- $\varepsilon$  at all periods other than  $T_1$ , which is a typical relationship between a UHS and CMS- $\varepsilon$  at a low annual frequency of exceedance.

To evaluate the influence of different ground-motion-selection procedures on predicting the probability of building collapse, Baker and Cornell (2006) performed a series of nonlinear response analyses using four selection methods:

1. Method 1 (AR method): Records were randomly selected without attempting to match any specific properties, such as  $M$ ,  $R$  and  $\varepsilon$ .
2. Method 2 (MR-BR method): Records were selected with their values of  $M$  and  $R$  representative of the site hazard.

3. Method 3 ( $\varepsilon$ -BR method): Records were selected with their values of  $\varepsilon$  representative of the site hazard.
4. Method 4 (CMS- $\varepsilon$  method): Records were selected that had a minimum sum of squared differences between their spectrum and the CMS- $\varepsilon$  across a wide range of period after scaling the records to match the target  $Sa(T_1)$ . No direct attempt was made to match the  $M$ ,  $R$  and  $\varepsilon$ .

Baker and Cornell (2006) selected 4 sets of 40 records using each of the four methods. All 40 records in each set were amplitude-scaled to each of 12  $Sa(T_1)$  levels between 0.1 and 4 g. Twelve bins of scaled ground motions for a given ground-motion selection method were used as inputs for non-linear response-history analysis of a seven-storey reinforced concrete building to develop the drift hazard curve for the building and the given selection method. The numerical model for the building had an elastic first-mode period of 0.8 second and used non-linear elements with strength and stiffness degradation in both shear and bending. Figure 4.4 shows the mean response spectra of the record sets selected using each of the four methods for  $Sa(T_1) = 1.6$  g together with the CMS- $\varepsilon$  for Method 4, which was presented in Figure 4.3. The mean spectra of the records of Methods 3 and 4 are close to the CMS- $\varepsilon$  and that of the MR-BR records are much greater than the CMS- $\varepsilon$  at almost all periods other than 0.8 second. Figure 4.5 presents the drift hazard curve (more specifically, the mean annual frequency of exceeding a given maximum story-drift ratio) for each method. Methods 1 and 2 produce much greater estimated probabilities of exceedance than the other two methods at large story-drift-ratio levels; the results from Methods 3 and 4 are nearly identical. Baker and Cornell repeated the analysis of Figure 4.5 but using a different integration approach and concluded that a) Methods 3 and 4, unlike Methods 1 and 2, produced unbiased (integration-approach-independent) drift hazard curves, and b) the CMS- $\varepsilon$  is a more appropriate target than UHS for record selection. Some of these observations are evaluated below using a set of near-fault ground motions; results are presented in Appendix D.



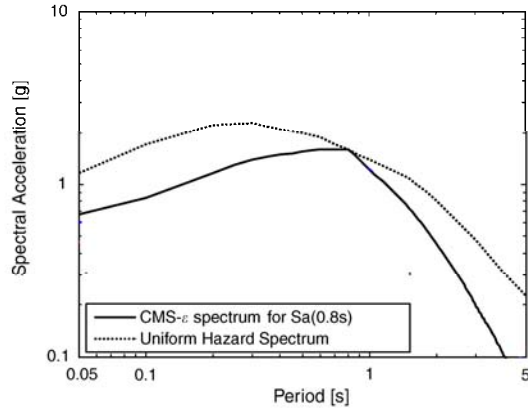


Figure 4.3. Sample uniform hazard spectrum and CMS- $\varepsilon$  (Baker and Cornell 2006)

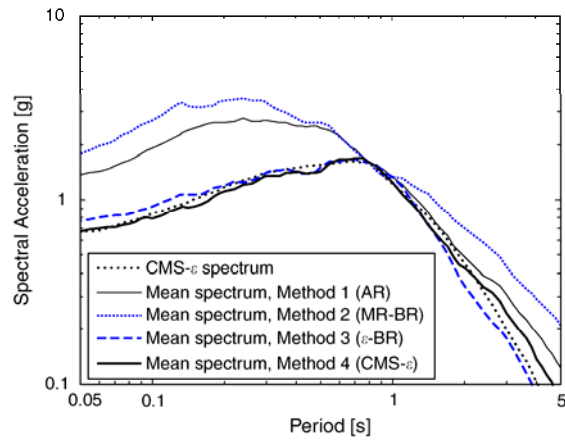


Figure 4.4. The CMS- $\varepsilon$  and the mean response spectra of record sets selected using Methods 1 through 4 (Baker and Cornell 2006)

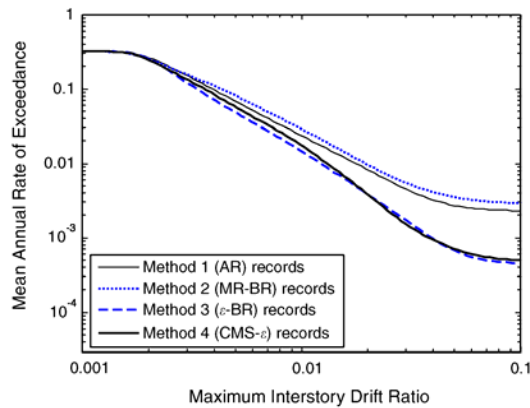


Figure 4.5. Mean annual frequency of exceeding various levels of maximum story drift ratio (Baker and Cornell 2006)

### 4.3 Scaling Ground Motions for Response-History Analysis

#### 4.3.1 *Optimal Scaling Procedure*

An optimal procedure for scaling earthquake ground motions for performance-based loss assessments should

- preserve the distribution in the earthquake shaking for the selected characterization of the hazard (spectrum,  $[M, r]$  pair, or annual probability of exceedance of a spectral ordinate) for the site of interest
- confidently estimate the distribution of seismic demand for nonlinear structural and nonstructural systems using as small a number of ground motions as possible
- be independent of structural period, enabling losses to be computed for a) a range of structural systems with one set of scaled motions, and b) structural and nonstructural components and systems in a building
- be appropriate for near-fault and far-field sites across the United States
- be applicable across a wide range of mean annual frequency of exceedance

A series of nonlinear response-history analyses were performed for three existing and two new ground-motion scaling procedures. Response data were evaluated using the criteria described above. The advantages and disadvantages of each procedure are presented below.

#### 4.3.2 *Numerical Models*

A large number of bilinear single-degree-of-freedom (SDOF) models were analyzed. Yield strengths were set at infinity,  $0.40W$ ,  $0.20W$ ,  $0.10W$  and  $0.06W$  to represent, albeit simplistically, conventional and isolated ( $0.06W$ ) construction, where  $W$  is the reactive weight of the structure. For the oscillators with yield strengths of  $0.10W$  and larger, the elastic period ranged between 0.05 second and 2 seconds; for the oscillator with a yield strength of  $0.06W$ , the post-yield (isolated) period ranged between 2 and 4 seconds. The ratio of post-yield to elastic stiffness was set to 0.1 for all oscillators.

The use of bilinear SDOF oscillators will limit the utility of the results and observations presented below to low-rise, code-conforming, regularly configured buildings whose displacement response

(and thus damage) is dominated by one mode of response. The development of optimal procedures for selecting and scaling ground motions for assessment of loss in taller buildings and/or non-conforming buildings will require analysis of a large family of linear and nonlinear multiple degree of freedom (MDOF) models and considerations of strength and stiffness deterioration. Some initial studies are under way (Goulet et al., 2008).

### **4.3.3 Near-Fault and Far-Field Seed Ground Motions**

#### *4.3.3.1 Dataset*

Response-history analysis was performed using both near-fault (NF) and far-field (FF) earthquake histories. Table 4.1 and Table 4.2 list the two sets of 25 pairs of seed ground motions used in this study. The moment magnitude for the ground motions in the NF bin ranges between 6.2 and 7.3 and the site-to-source distance ranges between 1 and 17.5 km. There are a limited number of U.S. near-fault records and so records from Japan, Turkey, Chile, and Taiwan were used to augment the U.S. dataset. The first ten pairs of ground motions in the NF set were developed in the SAC Steel Project for a firm-soil site in Los Angeles and a 2% probability of exceedance in 50 years (Somerville et al. 1997). The ground motions in the FF bin were chosen from the list presented in Iervolino and Cornell (2005) with moment magnitudes ranging between 6.3 and 7.1 and site-to-source distances ranging between 20 and 50 km. The records in the FF bin are from California earthquakes and were chosen to avoid directivity (pulse-type effects). All 50 pairs of records are for NEHRP Site Class C-D soils (FEMA 2004). Aside from the 10 pairs of SAC ground motions in the NF set, all ground motions were assembled from the Pacific Earthquake Engineering Research (PEER) Center Strong Motion Database, which can be found at <http://peer.berkeley.edu/smcat>.

#### *4.3.3.2 Epsilon and Spectral Shape*

Baker and Cornell (2005) reported that epsilon ( $\varepsilon$ ) and spectral shape have significant effect on the response of structures. These two parameters are studied herein using the ground motions of Table 4.1 and Table 4.2.

The calculation of  $\varepsilon$  requires the use of attenuation relationships. The United States Geological Survey (USGS) is using three attenuation relationships to generate the 2008 seismic hazard maps for the Western United States: 1) Boore and Atkinson (2008), 2) Campbell and Bozorgnia (2008), and 3) Chiou and Youngs (2008). The three attenuation relationships are products of the PEER

Next Generation Attenuation (NGA) of Ground Motions Project and were developed to predict spectral demand for shallow crustal earthquakes in the Western United States.

For each seed motion and periods of 0.2, 0.5, 1, 2 and 4 seconds, the value of  $\varepsilon$  was computed using each of the three NGA relationships described above. The values of the ground-motion parameters required in the NGA relationships were extracted from the NGA flatfile ([http://peer.berkeley.edu/products/nga\\_project.html](http://peer.berkeley.edu/products/nga_project.html)) for seed motions NF1 through NF10, NF21 through NF50 and all motions in the FF bin. However, since the SAC ground motions were modified to make their response spectra appropriate for NEHRP Site Class D, a value of 270 m/s for the shear wave velocity, rather than the values extracted from the NGA flatfile, was used for NF1 through NF10. NF11 through NF20 are synthetic motions. For these motions, the values of the ground-motion parameters used for computing  $\varepsilon$  are tabulated in Table 4.3. For each seed motion and each period, the three values of  $\varepsilon$  for the three NGA relationships were averaged and presented in the columns 2 through 6 of Table 4.4 and Table 4.5 for the NF and FF bins, respectively. Table 4.6 defines 8 bins per the value of  $\varepsilon$  and presents the number of seed motions in each bin at each period of 0.2, 0.5, 1, 2 and 4 seconds. Most of the values of  $\varepsilon$  shown in Table 4.4 and Table 4.5 range between -1 and 2.

Five period bins are defined in Table 4.7 to investigate the spectral shapes of the seed ground motions over a wide period range. Periods  $T_L$  and  $T_U$  are the lower- and upper-bound periods, respectively, for each bin. The period range between  $T_L$  and  $T_U$  was equally divided into four sections by  $T_A$ ,  $T_M$  and  $T_B$  in a logarithmic scale:

$$\frac{T_U}{T_B} = \frac{T_B}{T_M} = \frac{T_M}{T_A} = \frac{T_A}{T_L} = \sqrt{2} \quad (4.3)$$

The median periods,  $T_M$ , are 0.2, 0.5, 1, 2 and 4 for Bins P1 through P5, respectively, and  $T_L$ ,  $T_A$ ,  $T_B$  and  $T_U$  for each bin can be determined by  $T_M$  and (4.3).

The shape of the acceleration spectrum for each seed motion and each period bin was tagged as one of five types: 1) a straight line, 2) a descending curve, 3) an ascending curve, 4) convex, and 5) concave. For many of the records, the type of spectral shape was ambiguous and the procedure below was used to determine systematically the shape of the acceleration spectrum:

1. For a given time series and a given period bin, determine the 99 periods that equally divide the period range between  $T_L$  and  $T_U$  into 100 intervals in a logarithmic scale.
2. Compute the spectral accelerations for the given time series at  $T_L$ ,  $T_U$  and the 99 periods of step 1.
3. Perform the least-squares regression analysis for the 101 spectral accelerations computed in step 2 using a second-order linear model:

$$y(T) = aT^2 + bT + c \quad (4.4)$$

where  $y$  is the regression result;  $T$  is period; and  $a$ ,  $b$  and  $c$  are regression coefficients.

4. Define  $\bar{y}$  as the average of the maximum and minimum values of  $y(T)$  and  $T_L \leq T \leq T_U$ . If all  $y(T)$  with  $T_L \leq T \leq T_U$  vary between  $\pm 0.1\bar{y}$ , the spectral shape is classified as Type 1. If not, go to step 5.
5. If  $T_A \leq -b/2a \leq T_B$  and  $a > 0$ , the spectral shape is classified as Type 5. If  $T_A \leq -b/2a \leq T_B$  and  $a < 0$ , the spectral shape is classified as Type 4. If not, go to step 6.
6. If  $y'(T_M) > 0$ , the spectral shape is classified as Type 3. If not, the spectral shape is classified as Type 2.

Figure 4.6 presents a flow chart for the procedure described above. Table 4.8 summarizes the five types of spectral shape. Spectral accelerations for five sample ground motions selected from Table 4.1 and the corresponding regression results are shown in Figure 4.7 to illustrate the procedure for determining the type of spectral shape. Equation (4.4) represents a parabolic curve with the maximum or minimum value occurring at  $T = -b/2a$ . If  $T_A \leq -b/2a \leq T_B$ , the spectral shape is classified as either convex (Type 4, see Figure 4.7d) or concave (Type 5, see Figure 4.7e), depending on the sign of  $a$ . If the value of  $-b/2a$  falls outside the range  $T_A$  to  $T_B$ , the spectral shape is identified as either a descending curve (Type 2, see Figure 4.7b) or an ascending curve (Type 3, see Figure 4.7c), depending on the sign of  $y'(T_M)$ , the slope of the regression curve at  $T_M$ .

**Table 4.1. Near-field ground motions**

No.	Event	Station	$M^*$	$r^*$
NF1, NF2	Kobe 1995	jma	6.9	3.4
NF3, NF4	Loma Prieta 1989	lgpc	7.0	3.5
NF5, NF6	Northridge 1994	rrs	6.7	7.5
NF7, NF8	Northridge 1994	sylm	6.7	6.4
NF9, NF10	Tabas 1974	tab	7.4	1.2
NF11, NF12	Elysian Park 1 (simulated)	st04	7.1	17.5
NF13, NF14	Elysian Park 2 (simulated)	st10	7.1	10.7
NF15, NF16	Elysian Park 3 (simulated)	st13	7.1	11.2
NF17, NF18	Palos Verdes 1 (simulated)	st03	7.1	1.5
NF19, NF20	Palos Verdes 2 (simulated)	st06	7.1	1.5
NF21, NF22	Cape Mendocino 04/25/92 18:06	89156 Petrolia	7.1	9.5
NF23, NF24	Chi-Chi 09/20/99	TCU053	7.6	6.7
NF25, NF26	Chi-Chi 09/20/99	TCU056	7.6	11.1
NF27, NF28	Chi-Chi 09/20/99	TCU068	7.6	1.1
NF29, NF30	Chi-Chi 09/20/99	TCU101	7.6	11.1
NF31, NF32	Chi-Chi 09/20/99	TCUWGK	7.6	11.1
NF33, NF34	Duzce 11/12/99	Duzce	7.1	8.2
NF35, NF36	Erzinkan 03/13/92 17:19	95 Erzinkan	6.9	2.0
NF37, NF38	Imperial Valley 10/15/79 23:16	5057 El Centro Array #3	6.5	9.3
NF39, NF40	Imperial Valley 10/15/79 23:16	952 El Centro Array #5	6.5	1
NF41, NF42	Imperial Valley 10/15/79 23:16	942 El Centro Array #6	6.5	1
NF43, NF44	Kobe 01/16/95 20:46	Takarazu	6.9	1.2
NF45, NF46	Morgan Hill 04/24/84 04:24	57191 Halls Valley	6.2	3.4
NF47, NF48	Northridge 1/17/94 12:31	24279 Newhall	6.7	7.1
NF49, NF50	Northridge 1/17/94 12:31	0637 Sepulveda VA	6.7	8.9

\*  $M$  = moment magnitude;  $r$  = closest site-to-fault-rupture distance

**Table 4.2. Far-field ground motions**

No.	Event	Station	$M^*$	$r^*$
FF1, FF2	Cape Mendocino 04/25/92 18:06	89509 Eureka—Myrtle & West	7.1	44.6
FF3, FF4	Cape Mendocino 04/25/92 18:06	89486 Fortuna—Fortuna Blvd	7.1	23.6
FF5, FF6	Coalinga 1983/05/02 23:42	36410 Parkfield—Cholame 3W	6.4	43.9
FF7, FF8	Coalinga 1983/05/02 23:42	36444 Parkfield—Fault Zone 10	6.4	30.4
FF9, FF10	Coalinga 1983/05/02 23:42	36408 Parkfield—Fault Zone 3	6.4	36.4
FF11, FF12	Coalinga 1983/05/02 23:42	36439 Parkfield—Gold Hill 3E	6.4	29.2
FF13, FF14	Imperial Valley 10/15/79 23:16	5052 Plaster City	6.5	31.7
FF15, FF16	Imperial Valley 10/15/79 23:16	724 Niland Fire Station	6.5	35.9
FF17, FF18	Imperial Valley 10/15/79 23:16	6605 Delta	6.5	43.6
FF19, FF20	Imperial Valley 10/15/79 23:16	5066 Coachella Canal #4	6.5	49.3
FF21, FF22	Landers 06/28/92 11:58	22074 Yermo Fire Station	7.3	24.9
FF23, FF24	Landers 06/28/92 11:58	12025 Palm Springs Airport	7.3	37.5
FF25, FF26	Landers 06/28/92 11:58	12149 Desert Hot Springs	7.3	23.2
FF27, FF28	Loma Prieta 10/18/89 00:05	47524 Hollister—South & Pine	6.9	28.8
FF29, FF30	Loma Prieta 10/18/89 00:05	47179 Salinas—John & Work	6.9	32.6
FF31, FF32	Loma Prieta 10/18/89 00:05	1002 APEEL 2—Redwood City	6.9	47.9
FF33, FF34	Northridge 01/17/94 12:31	14368 Downey—Co Maint Bldg	6.7	47.6
FF35, FF36	Northridge 01/17/94 12:31	24271 Lake Hughes #1	6.7	36.3
FF37, FF38	Northridge 01/17/94 12:31	14403 LA—116th St School	6.7	41.9
FF39, FF40	San Fernando 02/09/71 14:00	125 Lake Hughes #1	6.6	25.8
FF41, FF42	San Fernando 02/09/71 14:00	262 Palmdale Fire Station	6.6	25.4
FF43, FF44	San Fernando 02/09/71 14:00	289 Whittier Narrows Dam	6.6	45.1
FF45, FF46	San Fernando 02/09/71 14:00	135 LA—Hollywood Stor Lot	6.6	21.2
FF47, FF48	Superstitt Hills (A) 11/24/87 05:14	5210 Wildlife Liquef. Array	6.3	24.7
FF49, FF50	Superstitt Hills (B) 11/24/87 13:16	5210 Wildlife Liquef. Array	6.7	24.4

\*  $M$  = moment magnitude;  $r$  = closest site-to-fault-rupture distance

**Table 4.3. Parameters for the seed motions NF11 through NF20**

Parameter	Unit	Cases or values for the parameter	Description
Fault type	--	strike-slip fault	for NF17 through NF20
		reverse dip-slip fault	for NF11 through NF16
$V_{S30}$	m/s	270	Midpoint shear wave velocity for NEHRP Site Class D
$M_W$	--	per Table 4.1 and Table 4.2	Moment magnitude
$r$	km	per Table 4.1 and Table 4.2	Closest site-to-fault distance
$r_{JB}$	km	= $r$ for ss fault = 0 for ds fault	Joyner-Boore distance
Dip	degree	= 90° for ss fault = 45° for ds fault	--
$Z_{TOR}$	km	0	Depth to the top of the rupture
$Z_{2.5}$	km	2	Depth to the 2.5 km/s shear-wave velocity horizon. A factor for the shallow sediment and 3-D basin effects
$W$	km	15	Rupture width



**Table 4.4. Epsilon ( $\epsilon$ ) and spectral shape of the near-fault ground motions of Table 4.1**

No.	$\epsilon$					Type of spectral shape				
	0.2 s	0.5 s	1 s	2 s	4 s	P1	P2	P3	P4	P5
NF1	0.70	1.77	1.97	1.04	0.18	3	3	2	2	2
NF2	0.32	0.77	1.84	0.23	0.30	5	3	2	2	2
NF3	-1.40	-0.17	-0.47	-0.31	-0.13	5	4	2	2	2
NF4	-0.60	0.47	0.47	1.06	1.30	3	4	2	2	2
NF5	1.00	0.65	1.06	0.37	0.54	3	2	2	2	2
NF6	0.57	0.66	1.37	1.07	0.11	3	1	2	2	2
NF7	-0.12	0.26	-0.05	0.87	0.29	1	1	2	2	2
NF8	0.81	1.57	0.37	1.03	0.24	3	2	2	2	2
NF9	1.63	0.00	0.18	-0.35	-0.53	4	5	2	2	2
NF10	2.20	1.35	0.02	0.76	1.09	4	2	2	2	2
NF11	1.28	1.08	0.74	0.19	0.49	3	2	2	2	2
NF12	1.13	0.93	1.09	0.31	0.57	4	2	2	2	2
NF13	0.72	0.47	0.65	1.16	0.60	3	2	2	2	2
NF14	0.53	0.49	0.11	1.14	0.55	3	2	2	2	2
NF15	1.20	0.61	0.15	1.71	1.49	4	2	5	4	2
NF16	0.73	0.33	0.63	1.85	1.45	3	4	5	2	2
NF17	0.37	0.46	0.96	0.86	1.04	3	3	2	2	2
NF18	0.15	0.04	0.98	1.29	1.20	1	3	4	2	2
NF19	-0.01	0.43	0.23	0.00	-0.58	3	2	2	2	2
NF20	-0.32	-0.52	0.07	1.40	0.64	3	2	3	2	2
NF21	-0.73	0.06	0.66	0.04	0.17	1	4	2	2	2
NF22	-0.75	0.77	1.41	1.53	1.39	5	4	2	2	2
NF23	-2.03	-1.33	-1.06	-0.96	0.11	3	4	2	2	4
NF24	-1.35	-0.21	-0.69	-0.85	-0.70	3	2	2	2	2
NF25	-1.45	-0.96	-0.84	-0.96	-0.05	3	1	2	2	2
NF26	-1.34	-0.45	-0.57	-0.37	-0.63	3	2	2	2	2
NF27	-1.19	-1.26	-0.55	0.70	0.86	1	4	1	2	5
NF28	-0.98	0.00	0.17	0.58	1.52	3	2	2	2	2
NF29	-1.85	-1.11	-1.27	-1.56	-0.95	3	4	2	2	2
NF30	-0.72	-1.41	-1.68	-1.87	-0.60	4	2	2	2	2
NF31	0.02	-0.44	-0.10	-0.33	0.88	4	1	2	1	2
NF32	0.40	0.78	1.07	0.92	1.39	5	5	2	2	2
NF33	-0.92	0.25	-0.36	-0.78	0.18	3	2	2	2	2
NF34	0.49	-0.26	0.19	0.32	0.72	3	1	2	2	2
NF35	0.48	-0.22	-0.20	0.27	0.30	4	2	2	2	2
NF36	-0.32	-0.69	0.38	1.03	0.12	3	5	4	2	2
NF37	0.99	0.49	-0.07	0.85	0.61	4	2	2	2	2
NF38	0.79	0.30	-1.26	-1.01	0.74	4	2	2	5	4
NF39	0.89	0.63	-0.35	-0.30	-0.10	1	2	2	2	2
NF40	0.09	0.61	0.43	0.22	1.47	3	2	2	5	2
NF41	-0.24	-0.71	-0.09	0.05	0.19	5	5	2	2	2

No.	$\varepsilon$					Type of spectral shape				
	0.2 s	0.5 s	1 s	2 s	4 s	P1	P2	P3	P4	P5
NF42	-0.15	-0.30	-0.61	0.20	1.39	3	2	2	1	2
NF43	0.47	0.52	0.21	0.26	-0.73	4	4	2	2	2
NF44	0.75	1.10	0.07	-0.05	-1.55	4	4	2	2	2
NF45	-0.77	-0.16	-1.35	-2.62	-2.92	4	4	2	2	2
NF46	-0.60	0.07	0.15	-0.82	-1.35	4	4	2	2	2
NF47	0.53	0.54	0.47	0.14	0.23	3	2	2	2	2
NF48	0.75	1.05	1.20	0.92	0.89	3	4	2	2	2
NF49	0.17	0.62	1.14	0.45	-0.31	4	4	2	2	2
NF50	1.00	0.81	0.23	0.00	0.64	3	2	2	2	2

**Table 4.5. Epsilon ( $\epsilon$ ) and spectral shape of the far-field ground motions of Table 4.2**

No.	$\epsilon$					Spectral shape				
	0.2 s	0.5 s	1 s	2 s	4 s	P1	P2	P3	P4	P5
FF1	-0.15	0.10	0.19	1.16	0.41	3	2	2	2	2
FF2	-0.26	0.95	0.95	1.68	1.46	4	2	2	2	2
FF3	-1.60	-0.61	-0.25	0.82	0.83	4	1	2	2	2
FF4	-1.38	-0.71	-0.21	0.53	1.26	4	2	2	2	2
FF5	0.24	0.83	1.00	0.55	0.65	3	2	2	2	2
FF6	0.14	0.96	0.97	0.55	-0.06	3	4	2	2	2
FF7	-0.96	-0.17	1.59	2.11	1.85	3	1	4	2	2
FF8	-0.48	0.73	2.18	1.67	0.10	3	4	4	2	2
FF9	-0.17	1.91	2.18	1.89	1.49	3	4	2	2	2
FF10	0.30	1.45	2.68	2.10	1.05	3	4	4	2	2
FF11	-0.78	-0.13	0.32	0.88	0.43	3	2	2	2	2
FF12	-0.68	-0.66	-0.59	-0.25	-0.41	3	2	2	2	2
FF13	-0.58	-1.89	-2.34	-1.06	-1.15	4	2	2	2	2
FF14	-0.28	-1.25	-0.71	-0.88	-0.39	4	2	2	2	2
FF15	-0.07	-0.50	-0.86	-0.77	0.01	4	2	2	2	2
FF16	-0.02	0.10	0.24	-0.55	0.06	3	2	2	2	2
FF17	0.72	1.53	0.86	1.19	1.17	1	4	2	2	2
FF18	1.12	1.38	1.81	1.71	1.57	2	4	2	2	2
FF19	0.81	1.61	0.88	0.98	0.10	3	4	2	2	2
FF20	0.09	2.36	0.86	0.80	-0.34	3	4	2	2	2
FF21	0.13	0.55	0.82	0.17	0.63	4	2	4	2	2
FF22	0.09	0.90	1.50	0.89	0.87	3	1	4	2	2
FF23	-1.04	-1.53	0.19	-0.63	-0.87	2	5	4	2	2
FF24	-0.86	-0.47	0.13	0.20	-1.11	4	3	2	2	2
FF25	0.35	-0.15	0.15	-0.42	-1.71	3	2	2	2	2
FF26	-0.30	-0.21	0.77	0.31	-0.40	3	5	2	2	2
FF27	0.82	2.30	2.95	2.68	1.95	3	3	2	2	2
FF28	-0.16	1.47	1.34	1.17	1.94	3	4	2	2	2
FF29	-0.94	-0.74	-0.82	-0.55	0.81	1	2	2	2	2
FF30	-0.01	-0.51	-1.13	0.08	0.46	4	2	2	4	2
FF31	-0.19	0.78	2.65	0.47	0.37	5	3	4	2	2
FF32	-0.51	0.52	1.47	-0.08	-0.72	5	3	2	2	2
FF33	0.86	0.62	0.16	0.16	-0.40	3	2	2	2	2
FF34	1.48	0.66	0.32	0.54	-1.03	4	2	2	2	2
FF35	-0.32	0.37	1.50	-0.40	-0.20	3	2	2	2	2
FF36	-1.17	-0.18	0.99	-0.13	-0.36	4	1	2	2	2
FF37	0.42	0.89	-0.09	0.24	-0.81	5	4	2	2	2
FF38	0.81	0.77	0.33	0.22	-0.53	1	2	2	2	2
FF39	-0.48	0.77	2.00	0.77	-0.44	3	3	2	2	2
FF40	-0.76	-0.12	0.70	0.11	-0.78	1	4	2	2	2
FF41	0.30	0.56	0.77	1.31	-0.45	2	2	2	2	2

No.	$\varepsilon$					Spectral shape				
	0.2 s	0.5 s	1 s	2 s	4 s	P1	P2	P3	P4	P5
FF42	-0.05	-0.28	0.32	0.59	-0.80	4	2	2	2	2
FF43	0.66	-0.50	-0.85	-0.02	1.38	4	2	2	5	2
FF44	0.79	-0.01	-0.43	0.18	1.00	4	2	2	2	2
FF45	0.32	0.23	0.18	0.86	0.82	2	2	2	2	2
FF46	1.02	0.26	0.91	0.37	2.04	4	2	4	2	2
FF47	-0.20	-0.69	-0.84	0.25	0.08	2	2	2	2	2
FF48	-0.05	-0.30	-0.74	0.15	0.61	2	2	2	2	2
FF49	0.56	1.05	1.59	2.23	2.02	5	2	2	2	2
FF50	0.23	0.06	0.37	1.65	1.96	2	2	2	2	2

**Table 4.6. Numbers of the NF and FF ground motions in the  $\varepsilon$  bins at periods of 0.2, 0.5, 1, 2 and 4 seconds**

Bin	NF					FF				
	0.2 s	0.5 s	1 s	2 s	4 s	0.2 s	0.5 s	1 s	2 s	4 s
$\varepsilon \geq 3$	0	0	0	0	0	0	0	0	0	0
$3 > \varepsilon \geq 2$	1	0	0	0	0	0	2	6	4	2
$2 > \varepsilon \geq 1$	6	6	9	12	11	3	7	7	9	12
$1 > \varepsilon \geq 0$	22	27	23	22	25	19	20	24	25	16
$0 > \varepsilon \geq -1$	14	13	13	12	11	24	18	11	11	16
$-1 > \varepsilon \geq -2$	6	4	5	3	2	4	3	1	1	4
$-2 > \varepsilon \geq -3$	1	0	0	1	1	0	0	1	0	0
$\varepsilon < -3$	0	0	0	0	0	0	0	0	0	0

**Table 4.7. Period bins for the computation of spectral shape**

Bin	$T_L$ (sec)	$T_A$ (sec)	$T_M$ (sec)	$T_B$ (sec)	$T_U$ (sec)
P1	0.1	0.14	0.2	0.28	0.4
P2	0.25	0.35	0.5	0.71	1
P3	0.5	0.71	1	1.41	2
P4	1	1.41	2	2.83	4
P5	2	2.83	4	5.66	8

**Table 4.8. Types of spectral shape**

Type	Symbol	The shape of the regression curve
1	—	A curve with a small slope between $T_L$ and $T_U$ .
2	\	A descending curve between $T_A$ and $T_B$ .
3	/	An ascending curve between $T_A$ and $T_B$ .
4	∩	Convex with the maximum value between $T_A$ and $T_B$ .
5	∪	Concave with the minimum value between $T_A$ and $T_B$ .

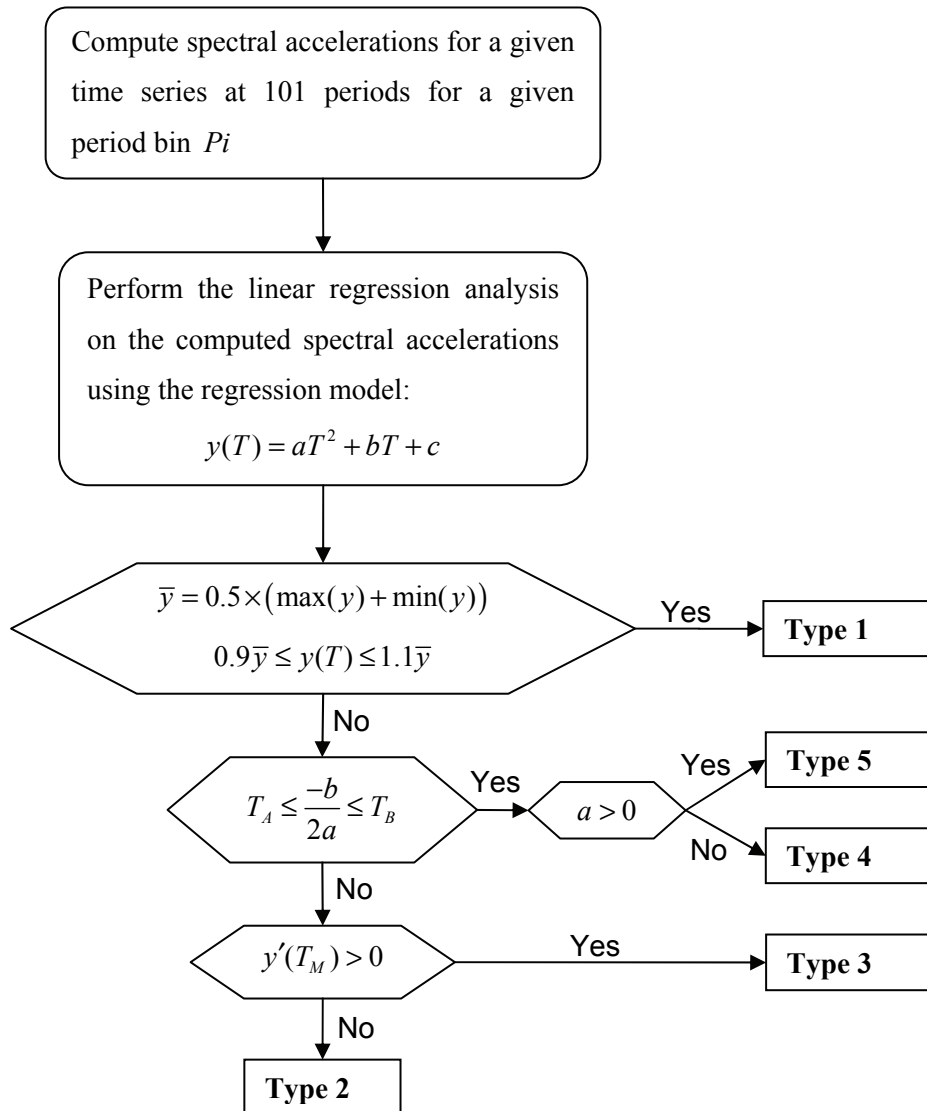
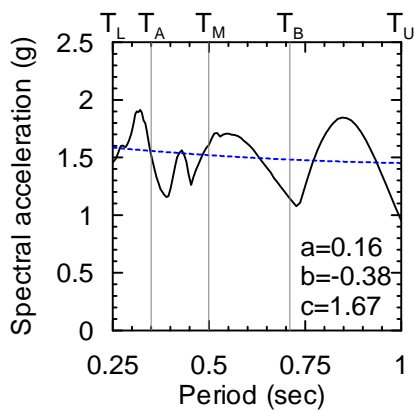
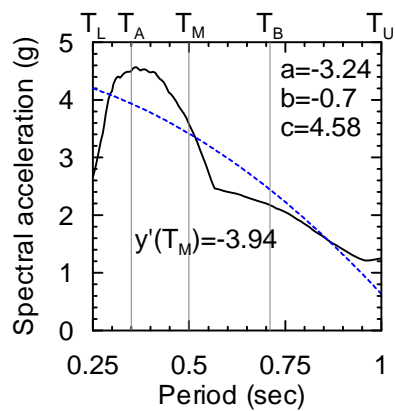


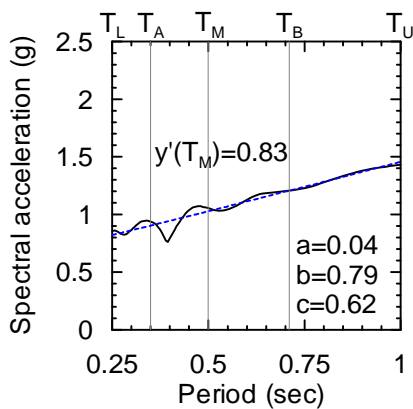
**Figure 4.6. A flow chart for determining the type of spectral shape**



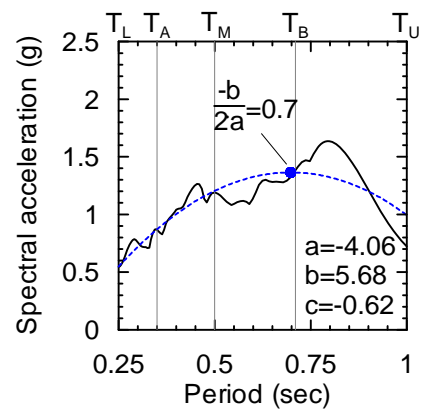
a. Type 1



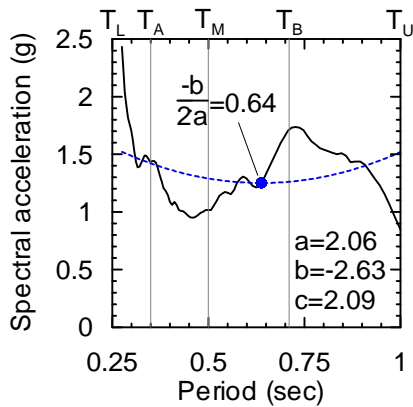
b. Type 2



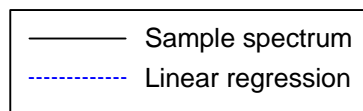
c. Type 3



d. Type 4



e. Type 5



f. legend

**Figure 4.7. Spectral accelerations and the regression results for five sample ground motions**

The types of spectral shape for the NF and FF seed motions are presented in columns 7 through 11 of Table 4.4 and Table 4.5, respectively.<sup>4</sup> Table 4.9 presents the numbers of the NF and FF seed motions for each type of spectral shape in each period bin. The spectral shapes for most records are classified as Type 2 for the period bins P3, P4 and P5 since spectral acceleration tends to decrease with period in the long period range.

**Table 4.9. Numbers of the NF and FF ground motions as a function of the period bins of Table 4.7 and the types of spectral shape of Table 4.8**

Type of spectral shape	NF					FF				
	P1	P2	P3	P4	P5	P1	P2	P3	P4	P5
1	5	5	1	2	0	4	4	0	0	0
2	0	23	44	45	47	7	28	42	48	50
3	26	4	1	0	0	20	5	0	0	0
4	14	14	2	1	2	15	11	8	1	0
5	5	4	2	2	1	4	2	0	1	0

#### 4.3.4 Existing Procedures for Scaling Ground Motions

##### 4.3.4.1 Method 1: Geometric-Mean Scaling of Pairs of Ground Motions (Bins 1a and 2a)

Method 1 involves amplitude scaling a pair of seed motions by a single factor to minimize the sum of the squared errors between the target spectral values and the geometric mean (square root of the product) of the spectral ordinates for the pair at periods of 0.3, 0.6, 1, 2 and 4 seconds. An example of the scaling process is presented in Appendix E. The resultant amplitude-scaled NF and FF motions are denoted herein as Bins 1a and 2a motions, respectively, as noted in Table 4.10. (Table 4.10 also lists the other 8 ground motion bins used in Section 4.3.)

Figure 4.8a shows the target spectrum for Bin 1a (NF) motions, which was developed by Somerville et al. (1997) from the USGS hazard maps for a 2% probability of exceedance in 50 years (denoted hereafter as 2/50) and a site in Los Angeles. The target spectrum for the Bin 2a

---

<sup>4</sup> A larger set of near-fault ground motions is introduced in Appendix D with 147 pairs of records selected from the database used to develop the NGA relationships. Epsilon and spectral shape for the set of records were reported in Appendix D as a reference for the use of the information in selecting ground motions for response-history analysis.

(FF) motions is shown in Figure 4.8b. The FF spectrum was generated by dividing the NF target spectrum by the short-period near-source factor  $N_a$  at periods of 0.3 and 0.6 second, and by the long-period near-source factor  $N_v$  at periods of 1, 2 and 4 seconds<sup>5</sup>. Values of 1.2 and 1.6 were selected for  $N_a$  and  $N_v$ , respectively, assuming a seismic source type A (as defined by the 1997 UBC) and a site-to-source distance of 5 km.

**Table 4.10. Ground motion bins**

Bin	Number of ground motions	Types of ground motions	Scaling method
Bin1a	50	NF	Geometric mean of pairs
Bin1b	50	NF	Spectrum-matching
Bin1c	50	NF	Shome and Cornell ( $Sa(T_1)$ )
Bin1d	--	NF	D-scaling
Bin1e	--	NF	D-scaling with modification factors
Bin1f	--	NF	D-scaling using earthquake records
Bin2a	50	FF	Geometric mean of pairs
Bin2b	50	FF	Spectrum-matching
Bin2c	50	FF	Shome and Cornell ( $Sa(T_1)$ )
Bin2d	--	FF	D-scaling
Bin2e	--	FF	D-scaling with modification factors
Bin2f	--	FF	D-scaling using earthquake records

This scaling procedure preserves some dispersion in the spectral demand at a given period and the irregular spectral shapes of the seed ground motions. Figure 4.8a and Figure 4.8b present the 16th, 50th and 84th percentiles of elastic spectral acceleration for Bins 1a and 2a, respectively. Figure 4.8c through Figure 4.8f present the  $\sigma$  and  $\beta$  of elastic spectral acceleration for Bins 1a and 2a<sup>6</sup>.

---

<sup>5</sup> Near-source factors  $N_a$  and  $N_v$  are presented in the 1997 Uniform Building Code (International Conference of Building Officials 1997) to account for near-fault (rupture directivity) effects in the short and long period ranges of the acceleration response spectrum, respectively.

<sup>6</sup> The statistical interpretation of the results presented in Section 4.3 assumed that spectral acceleration, spectral displacement and the maximum structural responses obtained from response-history analysis



Figure 4.8a and Figure 4.8b serve to identify a shortcoming with this scaling procedure, namely, a difference of about 0.3 g between the median (50th percentile) ordinate and target spectral ordinate at a period of 0.6 second. The scaling procedure minimizes the sum of the squared errors between the target spectral values and the geometric mean of the spectral ordinates for *each individual pair* of ground motions but doesn't minimize the sum of the squared errors between the target spectrum and the median spectrum for *all 50* ground motions.

The median ( $\theta$ ) spectral accelerations and dispersions ( $\beta$ ) of the ground motions in Bins 1a and 2a, before and after scaling, are plotted in Figure 4.9. The records were scaled with target values at a)  $T = 0.3$  second only, b)  $T = 0.3$  and 2 seconds, and c)  $T = 0.3, 0.6, 1, 2$  and 4 seconds. The median spectra for the original (or pre-scaled) motions and the three sets of the amplitude-scaled motions were normalized to the target spectrum at a period of 0.3 second to study the sensitivity of target spectral ordinates on the shape of the resultant median spectrum. Figure 4.9a and Figure 4.9c present the normalized median spectra and the target spectral values for the NF and FF motions, respectively. Figure 4.9b and Figure 4.9d show the dispersion  $\beta$  in the spectral acceleration for the four sets of NF and FF motions, respectively. Some key observations are:

- a. The shape of the median spectrum after geometric-mean scaling of pairs of ground motions is independent of the target spectral values and is nearly identical to the shape of the pre-scaled median spectrum: the normalized median spectra are identical (see Figure 4.9a and Figure 4.9c). The geometric-mean scaling method does not minimize the sum of the squared errors between the target and median spectra, resulting in the spectral difference seen in Figure 4.8a and Figure 4.8b at a period of 0.6 second. If the period range of interest is broad (for example, when the structure has a significant higher-mode effect) and different magnitude-distance pairs dominate the UHS for design across the subject period range, it will be difficult to select a set of ground motions whose median spectrum closely matches the target spectrum.
- b. Figure 4.9b and Figure 4.9d show that this scaling method reduces the dispersion in the spectral acceleration with respect to the pre-scaled motions. Whether sufficient dispersion is

---

were lognormally distributed. The values for the percentile results and other statistical parameters were estimated per Appendix A.

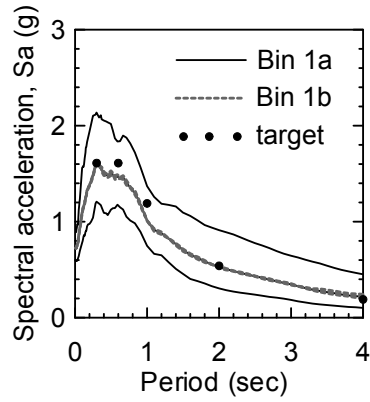
preserved by this method depends on the dispersion in either the attenuation relationships used to compute the spectral acceleration conditioned on magnitude and distance for a scenario-based assessment, or associated with a PSHA (capturing the epistemic or model uncertainty at different mean annual frequencies of exceedance) for a time-based assessment. The method will typically either underestimate or overestimate the target dispersion.

The ground motions of Bins 1a and 2a are assumed to reasonably represent the seismic hazard for 2/50 shaking at a NF site and a FF site in California, respectively. The median ( $\theta$ ) of and dispersion ( $\beta$ ) in the elastic spectral acceleration shown in Figure 4.8 for Bins 1a and 2a are assumed in this chapter to characterize the results of a PSHA for those two sites. The results of linear and nonlinear analysis using the 50 motions in Bins 1a and 2a are used to benchmark the results of other scaling methods and to determine the level of confidence associated with response analysis using fewer ground motions than 50.

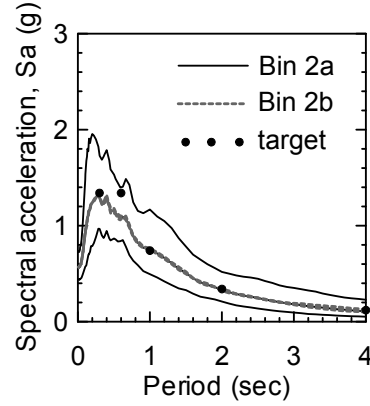
Figure 4.10 and Figure 4.11 present the 16th, 50th and 84th percentiles,  $\sigma$  and  $\beta$  of peak displacement for all oscillators of Section 4.3.2 and for Bins 1a and 2a, respectively. The dashed lines in the first row (a. through e.) of both figures identify the yield displacement for each oscillator. The value of  $\beta$  for the displacements shown in Figure 4.10 and Figure 4.11 varies mainly between 0.4 and 0.7.

#### 4.3.4.2 Method 2: Spectrum Matching (Bins 1b and 2b)

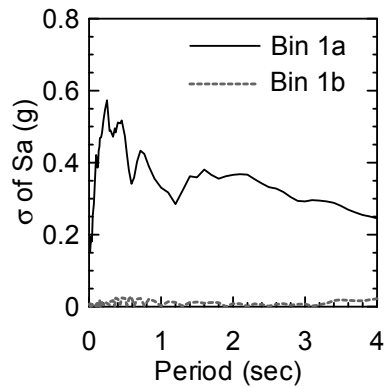
Spectrally matched ground motions are often used to compute seismic demands on structural framing systems. To judge the utility of using spectrum-matched ground motions for predicting the response of nonlinear SDOF framing systems (see Section 4.3.2), the NF and FF seed motions of Table 4.1 and Table 4.2 were modified to match the median spectrum of Bins 1a and 2a, respectively, using the computer code RSPMATCH (Abrahamson 1998). These bins of 50 spectrally matched motions are labeled as Bin 1b (NF) and Bin 2b (FF), respectively. The 16th, 50th and 84th percentiles of *elastic* spectral acceleration for these two bins are shown in Figure 4.8a and Figure 4.8b, respectively. The median spectral accelerations for Bins 1a and 1b and for Bins 2a and 2b are virtually identical. Figure 4.8c through Figure 4.8f present the dispersion ( $\sigma$  and  $\beta$ ) in the spectral accelerations for these four bins of ground motions. The dispersion in the bins of spectrally matched ground motions (Bins 1b and 2b) is negligible.



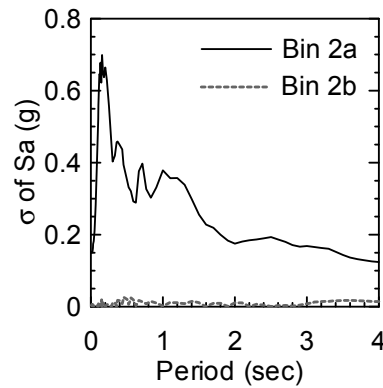
a. Sa: Bins 1a and 1b



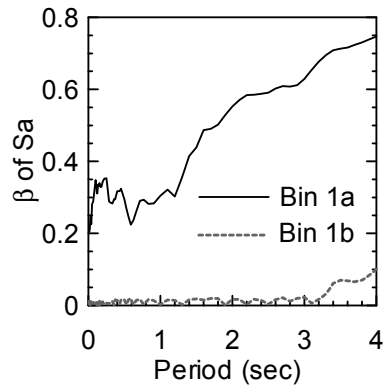
b. Sa: Bins 2a and 2b



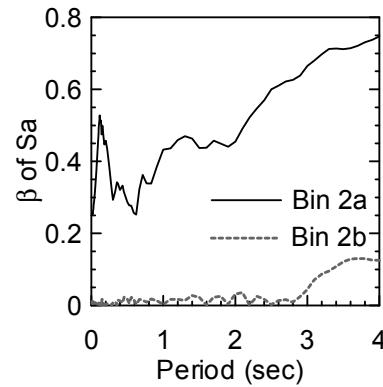
c.  $\sigma$  of Sa: Bins 1a and 1b



d.  $\sigma$  of Sa: Bins 2a and 2b



e.  $\beta$  of Sa: Bins 1a and 1b



f.  $\beta$  of Sa: Bins 2a and 2b

**Figure 4.8. Elastic acceleration spectra (84th, 50th and 16th percentiles),  $\sigma$  and  $\beta$  for ground motion bins 1a, 1b, 2a and 2b**

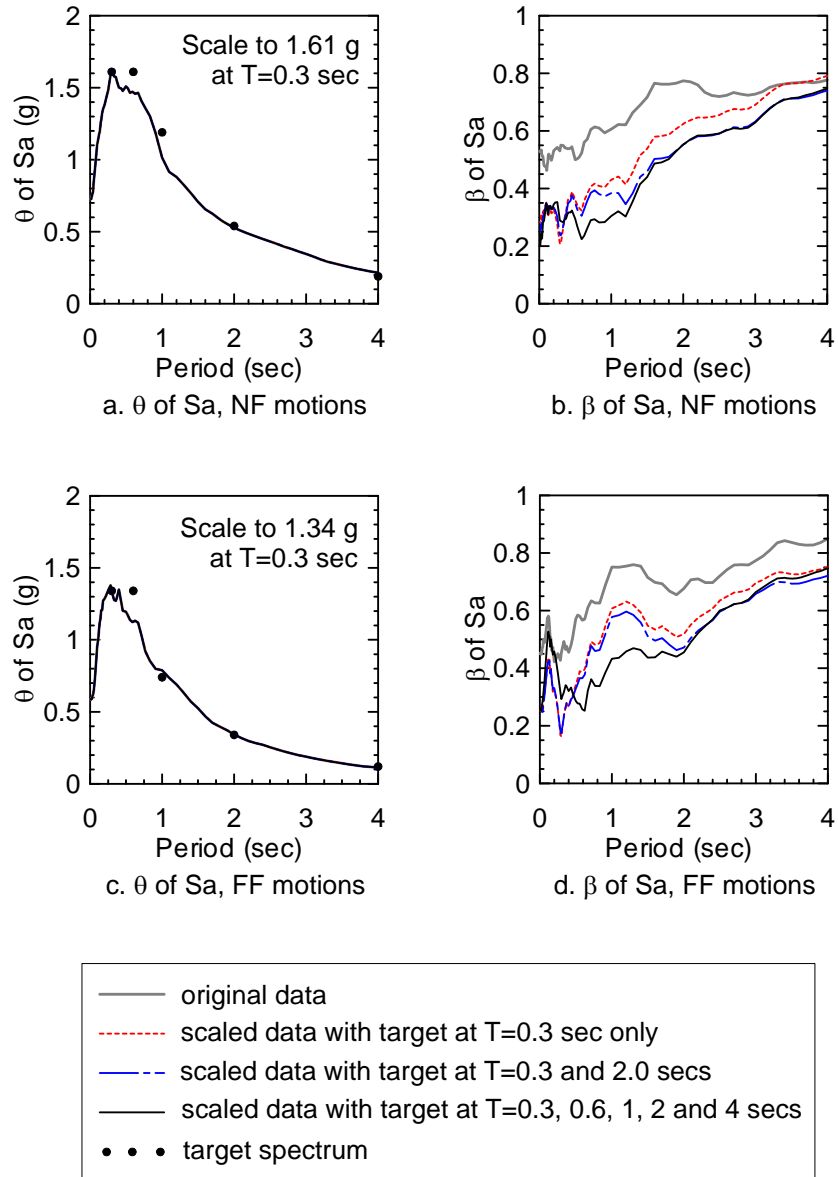


**Figure 4.9.** The impact of geometric mean scaling of pairs of ground motions for the  $\theta$  and  $\beta$  of spectral acceleration for the selected NF and FF ground motions

The 16th, 50th and 84th percentiles,  $\sigma$  and  $\beta$  of the elastic and inelastic peak displacement for Bins 1b and 2b are shown in Figure 4.10 and Figure 4.11, respectively, together with those for Bins 1a and 2a. The results indicate that the use of spectrally matched ground motions underestimate the median peak displacement demand in highly nonlinear systems and cannot capture the dispersion in the displacement response. For  $F_y = 0.06W$  (see Figure 4.10e and Figure 4.11e), the median responses are underestimated by 20% for the NF motions and 15% for the FF motions. This observation is similar to that of Carballo and Cornell (2000) for FF motions.

Earthquake ground motions that are spectrally matched to a target median spectrum should not be used for loss computations of SDOF systems because a) the median displacement response will be underestimated for all nonlinear systems, and b) the dispersion in the displacement response is underestimated by a wide margin for all systems, regardless of whether the response is linear or nonlinear.

#### 4.3.4.3 Method 3: $Sa(T_1)$ Scaling (Bins 1c and 2c)

Shome et al. (1998) proposed a method for scaling ground motions that involves amplitude scaling ground motion records to a specified spectral acceleration at the first mode period of the structure. Each of the 50 NF and 50 FF seed motions of Table 4.1 and Table 4.2, respectively, was scaled to match the median elastic spectral acceleration of Bins 1a and 2a, respectively, at many periods in the range of 0.05 to 4 seconds, where the oscillator period is based on the pre-yield (elastic) stiffness (including the oscillator with yield strength equal to  $0.06W$ ). These two bins of amplitude-scaled motions are labeled as Bin 1c (NF) and Bin 2c (FF), respectively. Figure 4.12 presents the 16th, 50th, 84th percentiles,  $\sigma$  and  $\beta$  of peak displacement for Bins 1a and 1c; Figure 4.13 presents results for Bins 2a and 2c. The dispersion in the elastic response ( $\beta$ ) for the Bin 1c and 2c motions is zero as seen in Figure 4.12k and Figure 4.13k, respectively: an expected result since all motions were matched to a specified spectral acceleration at each period. Some key observations are:

- a. Figure 4.12 and Figure 4.13 show that this scaling method produces unbiased estimates of the median displacement response even for the weakest oscillator ( $F_y = 0.06W$ ) for which the post-yield (stiffness) period dictates the displacement response.
- b. The dispersion ( $\beta$ ) in the peak displacement is not preserved for elastic or near-elastic systems: an expected result given that the dispersion in the ground motion was eliminated at

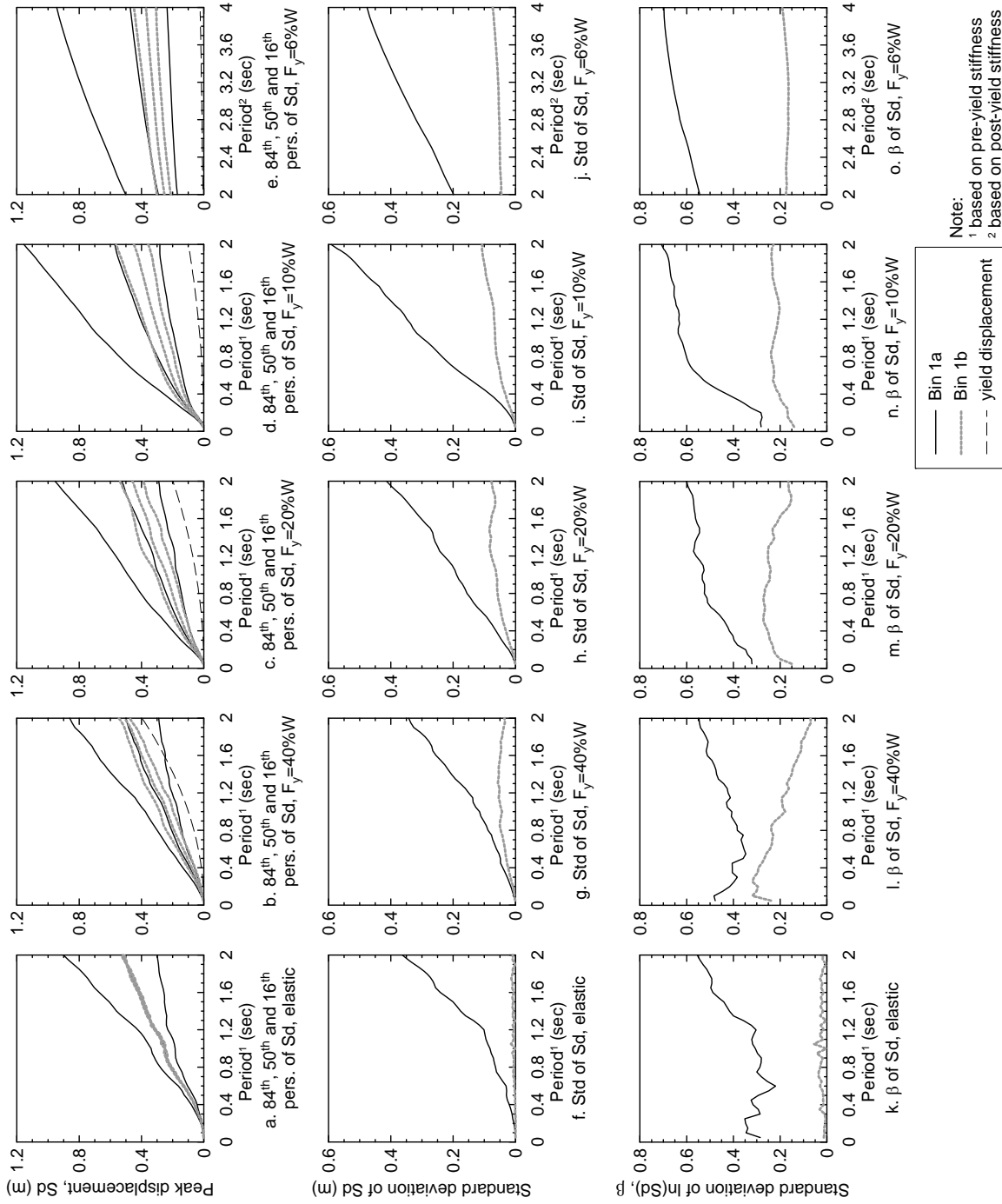


Figure 4.10. Eighty-fourth, 50th and 16th percentiles,  $\sigma$  and  $\beta$  of spectral displacement for Bins 1a and 1b ground motions

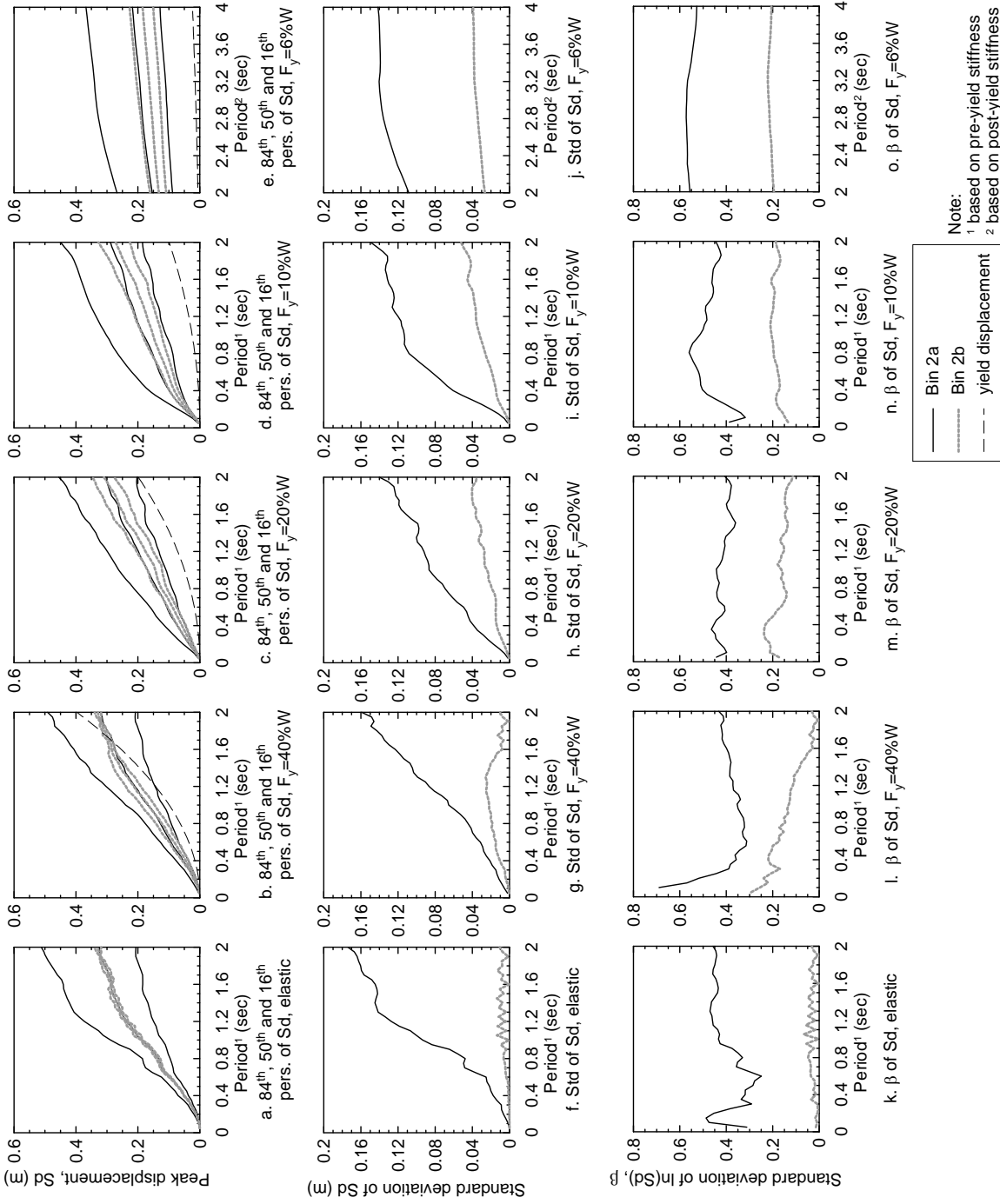


Figure 4.11. Eighty-fourth, 50th and 16th percentiles,  $\sigma$  and  $\beta$  of spectral displacement for Bins 2a and 2b ground motions

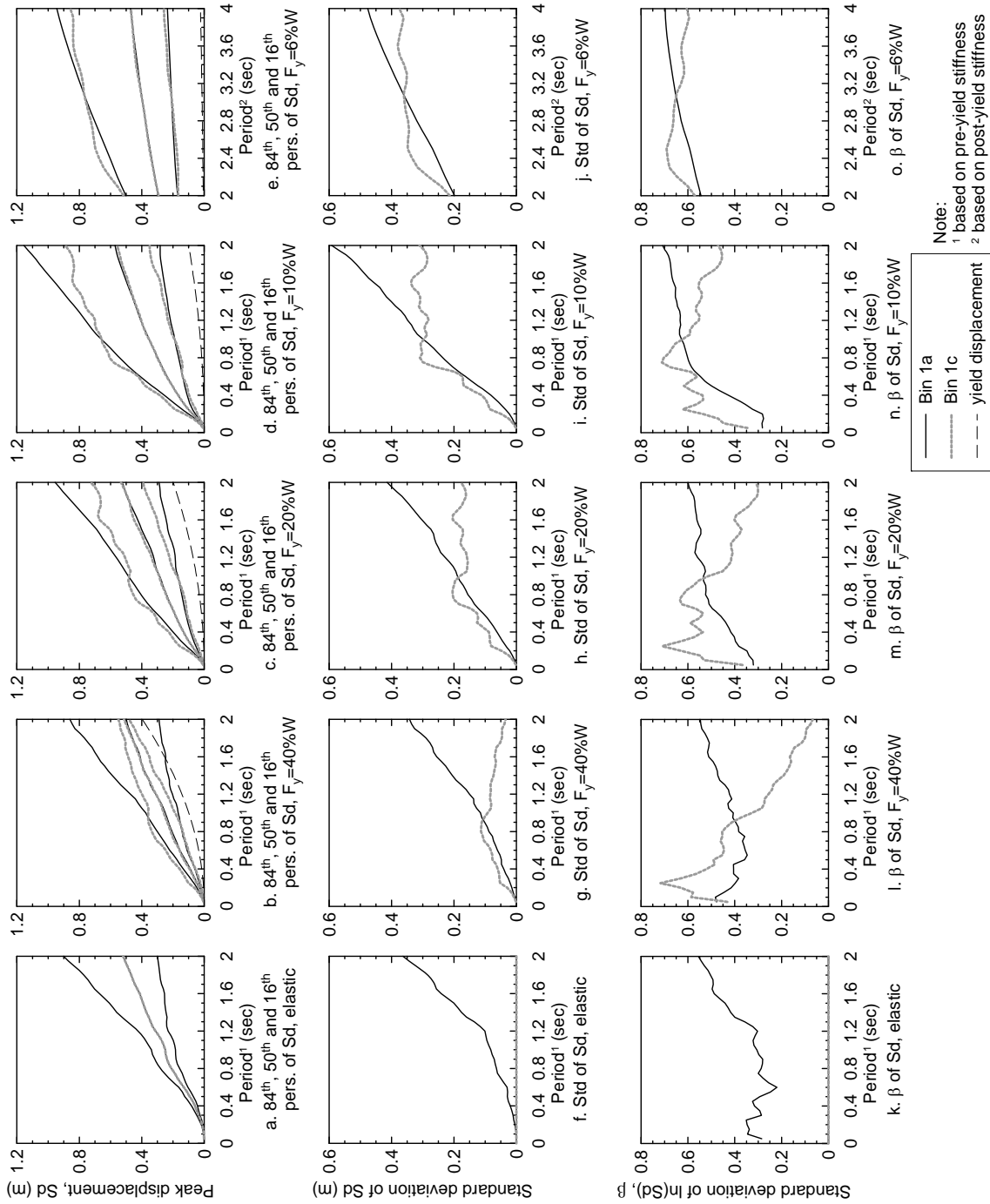


Figure 4.12. Eighty-fourth, 50th and 16th percentiles,  $\sigma$  and  $\beta$  of spectral displacement for Bins 1a and 1c ground motions



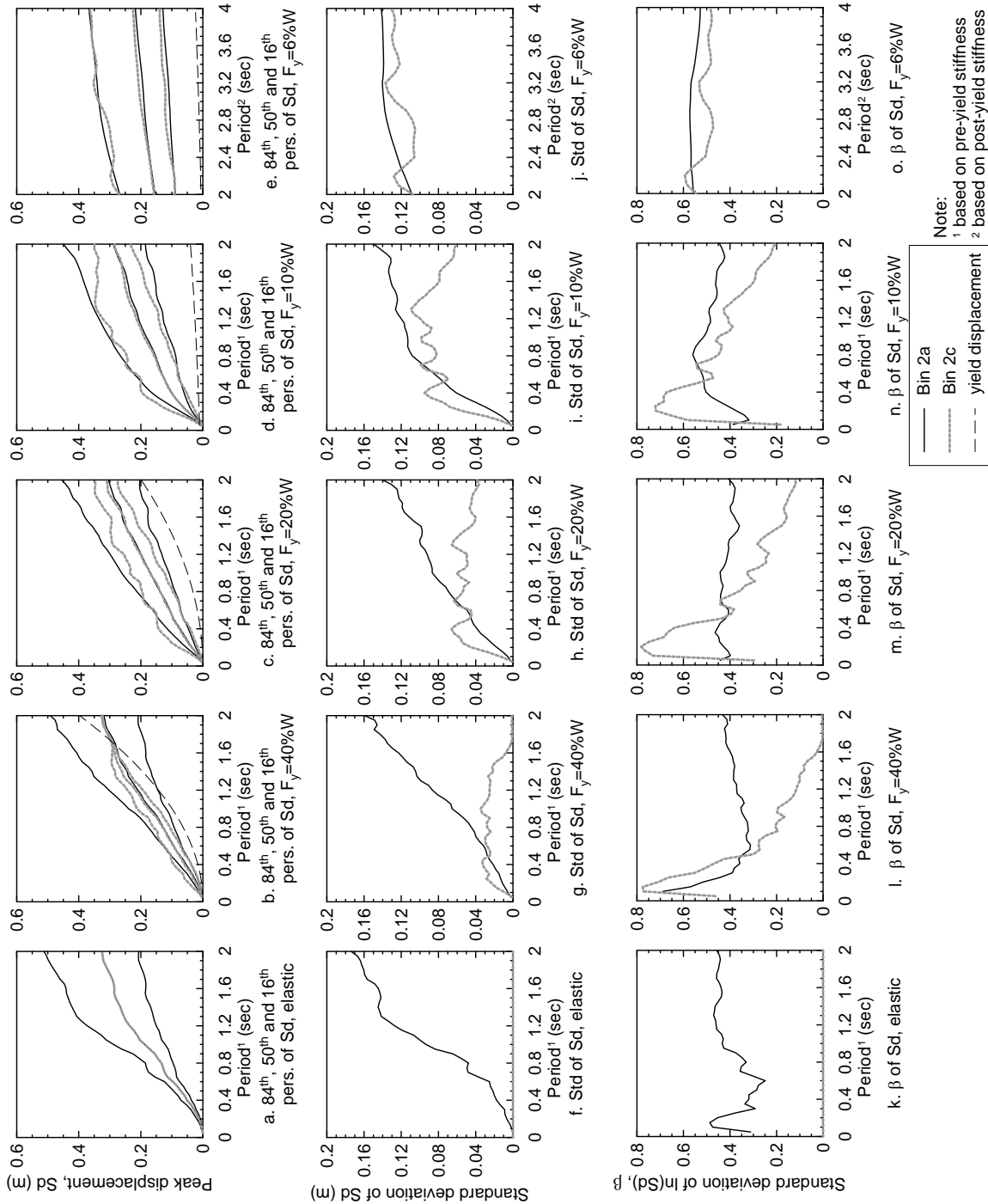


Figure 4.13. Eighty-fourth, 50th and 16th percentiles,  $\sigma$  and  $\beta$  of spectral displacement for Bins 2a and 2c ground motions

the natural period of the oscillator. The dispersion is smaller for the Bin 1c and 2c motions than for the Bin 1a and 2a motions, respectively, for oscillators with a small (displacement) ductility ratio and greater for the oscillators with a large ductility ratio. (For oscillators with  $F_y = 0.40W$ ,  $0.20W$  and  $0.10W$ , the ductility ratio decreases as the period of the oscillator increases.)

- c. The utility of the Shome et al. scaling method for loss assessment is unclear. If significant losses accumulate at periods other than the first mode period of the building frame, for example, at the second mode period of the building frame or at 10 to 20 Hz for the nonstructural components mounted at grade in the building, the scaling method will likely underestimate or overestimate the losses. Figure 4.12 and Figure 4.13 provide no information on seismic demands at periods remote from the first mode.

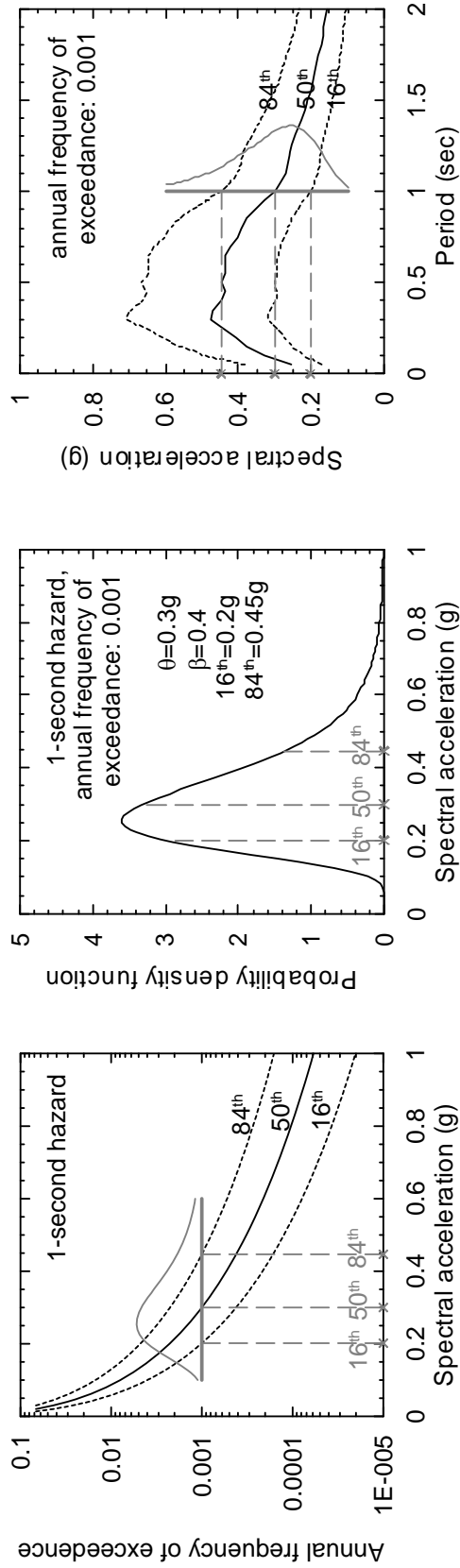
### **4.3.5 The Distribution-Scaling Method Using Spectrum-Matched Motions**

#### *4.3.5.1 Introduction*

None of the three ground motion scaling procedures introduced in Section 4.3.4 is optimal as defined in Section 4.3.1. None capture both the median ( $\theta$ ) and dispersion ( $\beta$ ) in spectral demand characterized by a PSHA or an attenuation relationship.

An alternate scaling procedure, Method 4, the distribution-scaling (D-scaling) method, is proposed herein. The D-scaling method produces  $m$  ground motions to match each of  $n$  stripes generated for a target UHS or a spectrum predicted by an attenuation relationship for a scenario case. For a target UHS, the values of  $\theta$  and  $\beta$  at each period are those returned by a PSHA and the chosen annual probability of exceedance. For a spectrum for a scenario case, the values of  $\theta$  and  $\beta$  at each period are those returned by an attenuation relationship for the given scenario. The key steps in the method are summarized below assuming the spectral stripes are generated for a given UHS. The procedure for an attenuation-relationship-based spectrum is similar to that for a UHS.

Figure 4.14a shows the 1-second-period spectral acceleration hazard for a site. Assume that the target annual frequency of exceedance is 0.001 (return period of 1000 years). The probability distribution of spectral acceleration at a period of 1 second is shown in Figure 4.14b with  $\theta = 0.3g$  and  $\beta = 0.4$ . For performance assessment and loss calculations, similar distributions ( $\theta$



- a. Sample 1-second hazard curves
- b. The probability density function of spectral acceleration using the data shown in Figure 4.14a for the annual frequency of exceedance of 0.001
- c. A sample spectrum with the 1-second spectral ordinates from the data shown in Figure 4.14a and Figure 4.14b

**Figure 4.14. From hazard curves to a design spectrum**

and  $\beta$ ) would be established across the entire period range. Figure 4.14c presents a sample spectrum that includes the data from Figure 4.14a and Figure 4.14b at period of 1 second.

Figure 4.14b is re-plotted as Figure 4.15a for the purpose of introducing *striping*. The cumulative distribution function (CDF) corresponding to Figure 4.15a is shown in Figure 4.15b. For the purpose of this example (only), the CDF in Figure 4.15b is divided into five regions, each with an equal probability of 0.2 (or 20%). The spectral acceleration corresponding to the midpoint of each region is identified by a horizontal dashed line. The five values of spectral acceleration characterize the distribution of spectral acceleration shown in the figure, namely,

- Region 1:  $0 \leq P(X < x_1) < 0.2$ ; for midpoint,  $P(X < x_1) = 0.1 \Rightarrow x_1 = 0.18 \text{ g}$
- Region 2:  $0.2 \leq P(X < x_2) < 0.4$ ; for midpoint,  $P(X < x_2) = 0.3 \Rightarrow x_2 = 0.24 \text{ g}$
- Region 3:  $0.4 \leq P(X < x_3) < 0.6$ ; for midpoint,  $P(X < x_3) = 0.5 \Rightarrow x_3 = 0.30 \text{ g}$
- Region 4:  $0.6 \leq P(X < x_4) < 0.8$ ; for midpoint,  $P(X < x_4) = 0.7 \Rightarrow x_4 = 0.37 \text{ g}$
- Region 5:  $0.8 \leq P(X < x_5) < 1.0$ ; for midpoint,  $P(X < x_5) = 0.9 \Rightarrow x_5 = 0.50 \text{ g}$

where  $P(X < x_i)$  is the probability of the random variable  $X$ , representing the 1-second spectral acceleration here, being smaller than the deterministic value  $x_i$ . The value of  $x_i$  can be obtained from the following equation:

$$x_i = \theta \cdot e^{\beta \cdot \Phi^{-1}(P_i)} \quad (4.5)$$

where  $\Phi^{-1}$  is inverse standardized normal distribution function and  $P_i$  is the midpoint cumulative probability for Region  $i$ . For example,  $x_1$  is obtained from

$$x_1 = 0.3 \cdot e^{0.4 \cdot \Phi^{-1}(0.1)} = 0.3 \cdot e^{0.4 \cdot (-1.28)} = 0.18 \quad (4.6)$$

This analysis is performed at each period in the spectrum and the midpoint spectral accelerations (at  $P = 0.1, 0.3, 0.5, 0.7$  and  $0.9$  in this example) at each period are used to develop a family of 5 spectra (or 5 stripes) such as that shown in Figure 4.15c, where the five spectral values calculated above at a period of 1 second period are indicated by crosses. Earthquake histories scaled to each of the stripes can then be used for performance assessment, noting that *much* of the epistemic

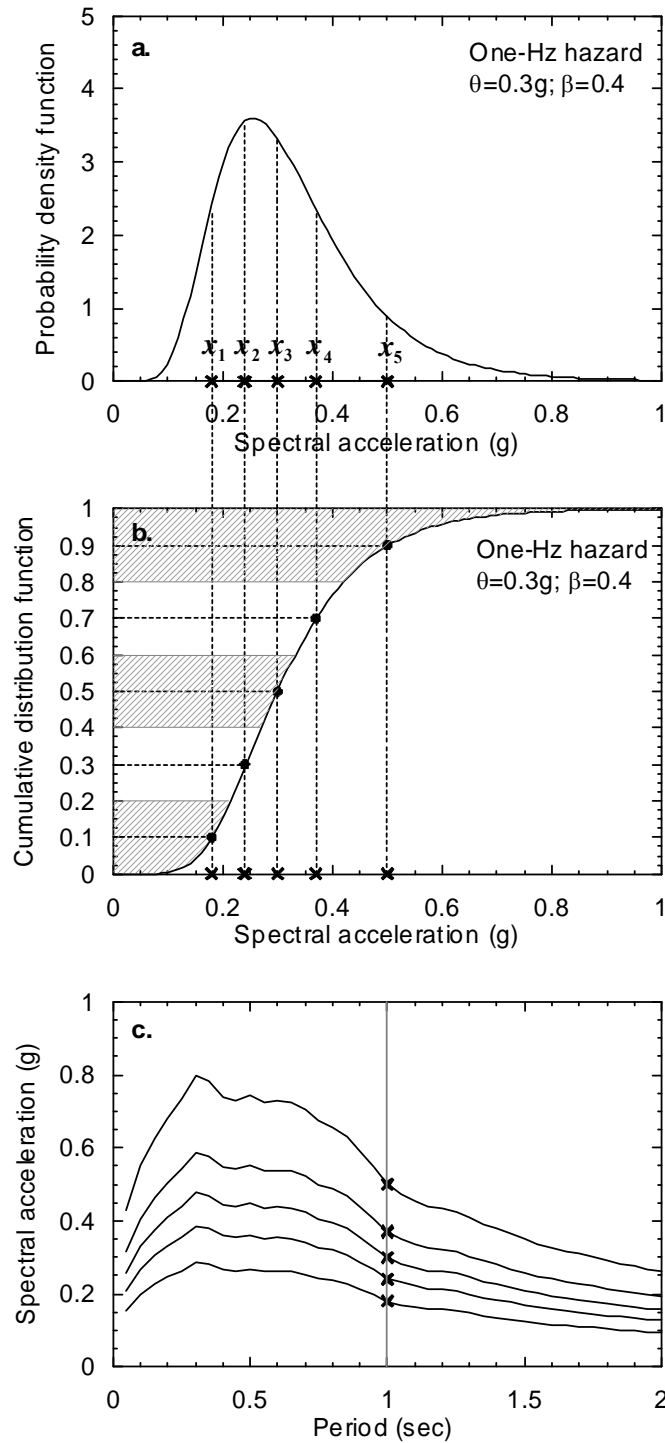


**Figure 4.15. The stripes in D-scaling method: a) a sample probability density function (pdf) from Figure 4.14b; b) the cumulative distribution function corresponding to the pdf in Figure 4.15a; c) the stripes of spectral acceleration generated by D-scaling method with 1-second spectral ordinates from Figure 4.15b**

uncertainty is directly captured using this procedure. Other questions that must be answered include:

1. How are the motions to be scaled to the stripes?
2. How many sets of motions (however scaled) must be generated for each stripe?
3. How many stripes are needed to capture the displacement response of linear and nonlinear systems?

It was assumed initially that motions would be spectrally matched to the stripes (question 1) and that one motion only would be used for each stripe (question 2). Ground motions were assumed to be spectrally matched to each stripe because of the seemingly intractable challenges associated with selecting one or more scaled ground motions records with spectral shapes that matched, in a general sense, those of the spectral stripe. The epistemic uncertainty is captured using the striping procedure (that explicitly addresses model uncertainty) but some of the aleatory variability is lost because the irregular (jagged) shape of the ground-motion spectrum is replaced by the smoothed shape of the spectral stripe. Importantly, because no two spectral stripes will have the same shape because the dispersion is period dependent, different seed ground motions might have to be used for matching to each stripe if spectral matching was not used. One ground motion per stripe was used herein to reduce the computational effort.

#### 4.3.5.2 Response-History Analysis Using the D-scaling Method

The numerical procedure for the D-scaling method involves two key steps:

1. Generate  $n$  stripes for the target spectrum (or spectra) using (4.7)

$$x_i(T_j) = \theta(T_j) \cdot e^{\beta(T_j)\alpha_i} \quad i = 1 \text{ to } n \quad (4.7)$$

where  $x_i(T_j)$  is the target spectral acceleration value of the  $i^{\text{th}}$  stripe at period  $T_j$ ;  $\theta(T_j)$  and  $\beta(T_j)$  are  $\theta$  and  $\beta$  of spectral acceleration determined from PSHA for the site and a chosen mean annual frequency of exceedance at period  $T_j$ ; and  $\alpha_i$  is from  $\Phi^{-1}(P_i)$  shown in (4.5). Some reference values of  $\alpha_i$  are tabulated in Table 4.11.

2. Generate a set of earthquake acceleration time series that spectrally match each of the stripes of step 1.

**Table 4.11.  $\alpha_i$  for the D-scaling method**

$i$	$\alpha_i$		
	$n=7$	$n=11$	$n=21$
1	-1.5	-1.7	-2
2	-0.8	-1.1	-1.5
3	-0.4	-0.75	-1.2
4	0	-0.5	-1
5	0.4	-0.3	-0.8
6	0.8	0	-0.6
7	1.5	0.3	-0.5
8	--	0.5	-0.4
9	--	0.75	-0.2
10	--	1.1	-0.1
11	--	1.7	0
12	--	--	0.1
13	--	--	0.2
14	--	--	0.4
15	--	--	0.5
16	--	--	0.6
17	--	--	0.8
18	--	--	1
19	--	--	1.2
20	--	--	1.5
21			2

Three sets (7, 11 and 21 stripes) of target acceleration spectra were generated using (4.7) and Table 4.11 with  $\theta$  and  $\beta$  from Bins 1a and 2a for NF and FF ground motions (as shown in Figure 4.8), respectively. Figure 4.16 illustrates the target spectra generated for 11 stripes and the FF (Bin 2a) motions. The distributions of spectral acceleration at periods of 1 and 3 seconds are shown in the figure. The 84th, 50th and 16th percentiles of spectral acceleration for these stripes distribute identically to those shown in Figure 4.8b for Bin 2a. To investigate the utility of this method for response-history analysis, some of the seed motions listed in Table 4.1 and Table 4.2 were spectrally matched to each of the stripes developed for the NF and FF ground motions using

RSPMATCH. The resulting sets were labeled as Bins 1d and 2d, respectively. Ten spectrally matched ground motions from different seed motions were generated for each of the  $n$  stripes, where  $n = 7, 11$  and  $21$ . One (of the ten) motions for each stripe was randomly selected for nonlinear response-history analysis for each of the SDOF oscillators in Section 4.3.2. Each trial of analysis produced  $n$  peak displacements for a given oscillator. These  $n$  peak displacements were assumed to be lognormally distributed;  $\theta$ ,  $\beta$  and the 84th percentile value of the  $n$  peak displacements were calculated as sample values for three random variables  $\Theta$ ,  $B$  and  $84TH$ , respectively. Ten thousand trials of analysis were performed with ten thousand different combinations of the 7, 11 and 21 ground motions to capture the distributions in  $\Theta$ ,  $B$  and  $84TH$  for each of the SDOF oscillators in Section 4.3.2.

Three parameters are defined below to aid in the presentation of the analysis results:

$$R_{\Theta_{d,n}} = \frac{\Theta_{d,n}}{\theta_{a,50}} \quad (4.8)$$

$$R_{B_{d,n}} = \frac{B_{d,n}}{\beta_{a,50}} \quad (4.9)$$

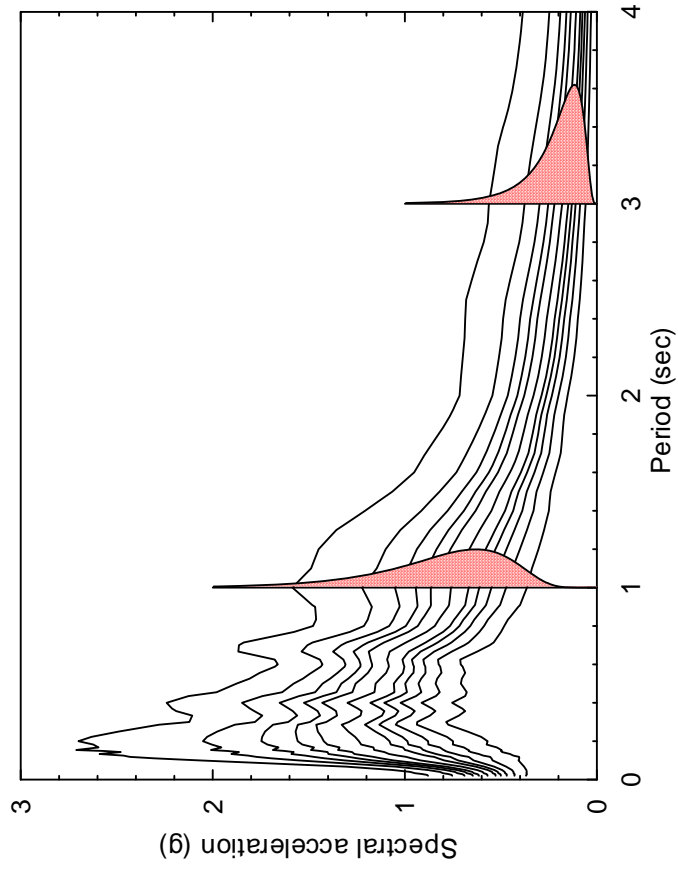
$$R_{84TH_{d,n}} = \frac{84TH_{d,n}}{84th_{a,50}} \quad (4.10)$$

where the three random variables,  $\Theta_{d,n}$ ,  $B_{d,n}$  and  $84TH_{d,n}$  are the  $\theta$ ,  $\beta$  and the 84th percentile of peak displacement estimated by the analysis with  $n$  ground motions from Bins 1d and 2d;  $\theta_{\Theta_{d,n}}$ ,  $\theta_{B_{d,n}}$  and  $\theta_{84TH_{d,n}}$  are the median values of random variables,  $\Theta_{d,n}$ ,  $B_{d,n}$  and  $84TH_{d,n}$ , respectively; and  $\theta_{a,50}$ ,  $\beta_{a,50}$  and  $84th_{a,50}$  are deterministic parameters for  $\theta$ ,  $\beta$  and the 84th percentile of peak displacement obtained from the analysis with all 50 ground motions in Bins 1a and 2a.

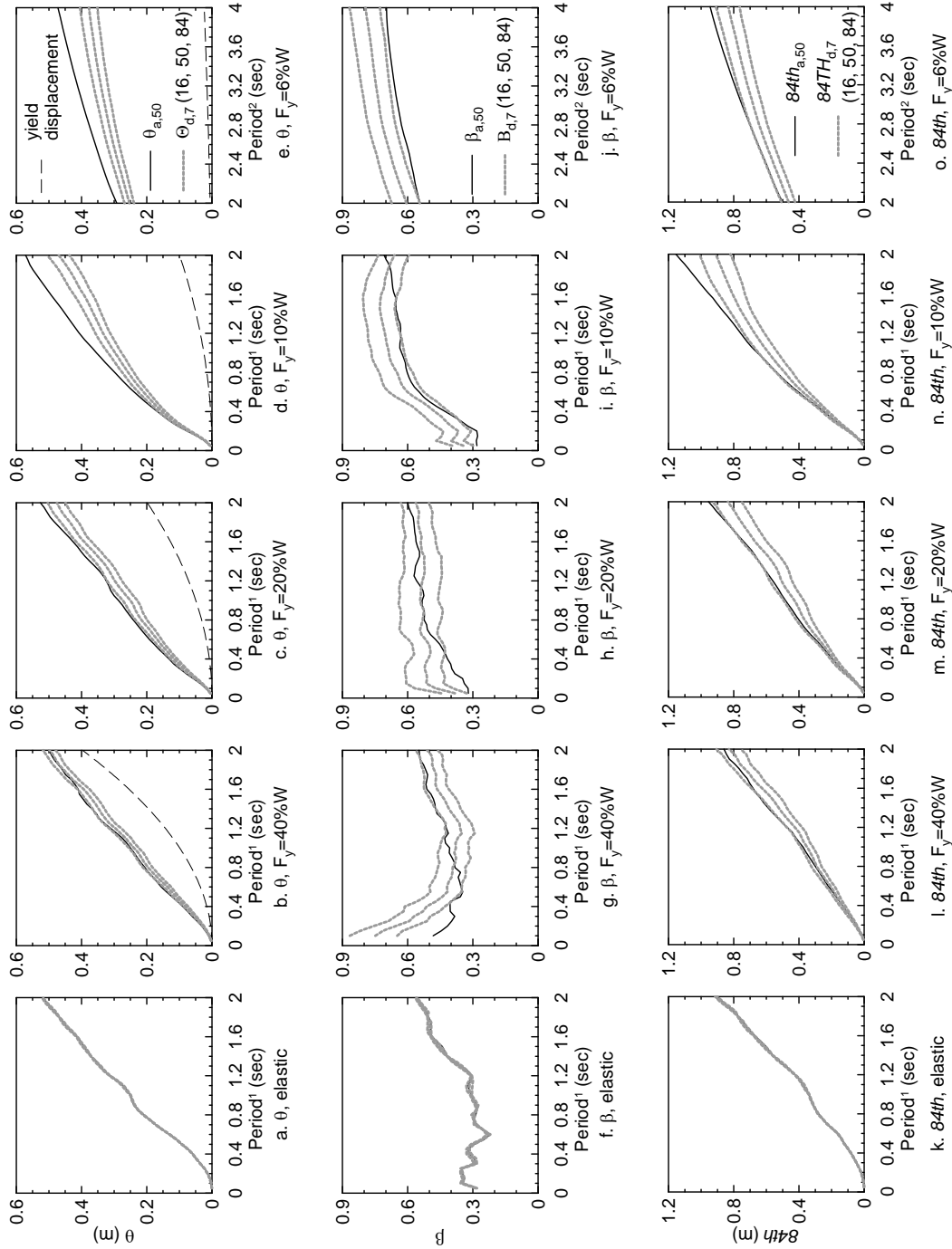
Figure 4.17 through Figure 4.19 present the 84th, 50th and 16th percentiles of  $\Theta_{d,n}$ ,  $B_{d,n}$  and  $84TH_{d,n}$  for  $n = 7, 11$  and  $21$ , respectively, and the Bin 1d motions. Figure 4.20 through Figure 4.22 present results for the Bin 2d motions. Some key observations are:

1. This method underestimates the median peak displacement for oscillators with  $F_y = 0.10W$  and  $0.06W$  by 10% to 20% for the Bin 1d motions and by 5% to 15% for the Bin 2d motions, and underestimates the 84th percentile displacements for the Bin 1d motions.



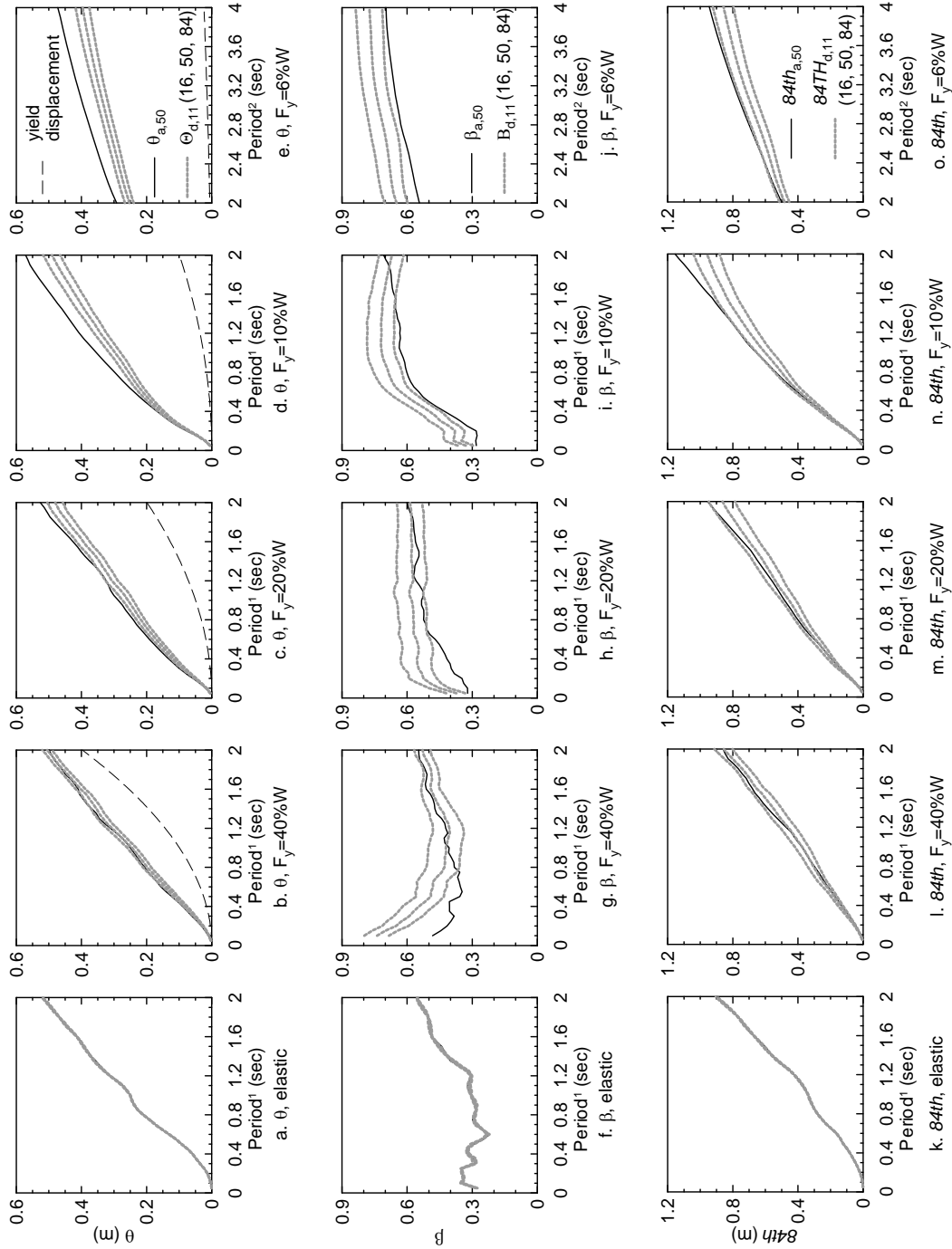


**Figure 4.16. Eleven stripes (target spectra) from the D-scaling method with  $\theta$  and  $\beta$  from Bin 2a ground motions**



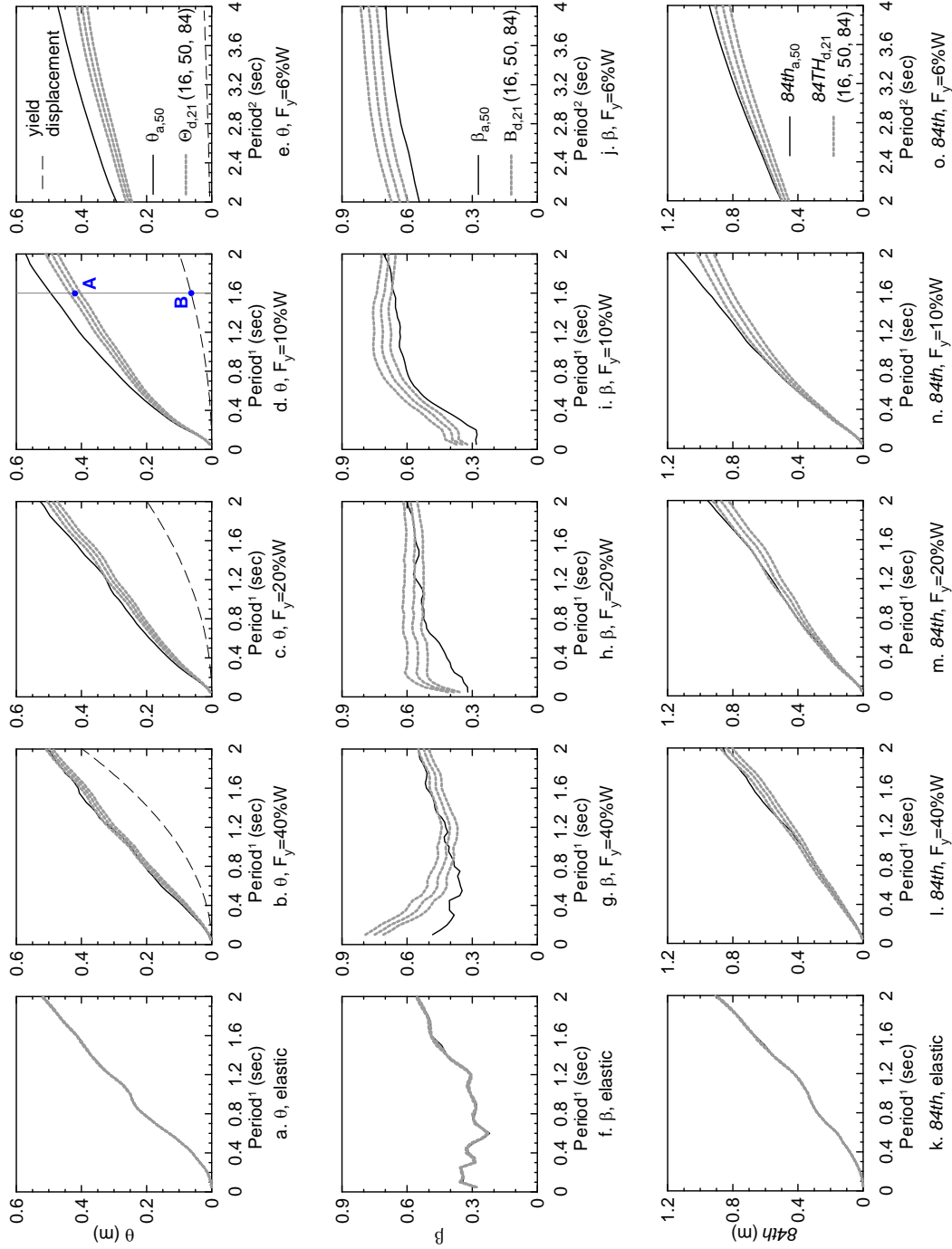
Note:  
<sup>1</sup> based on pre-yield stiffness  
<sup>2</sup> based on post-yield stiffness

Figure 4.17. Eighty-fourth, 50th and 16th percentiles of  $\Theta_{d,7}$ ,  $B_{d,7}$  and  $84TH_{d,7}$  for Bin 1d; and  $\theta_{a,50}$ ,  $\beta_{a,50}$  and  $84th_{a,50}$  for Bin 1a motions



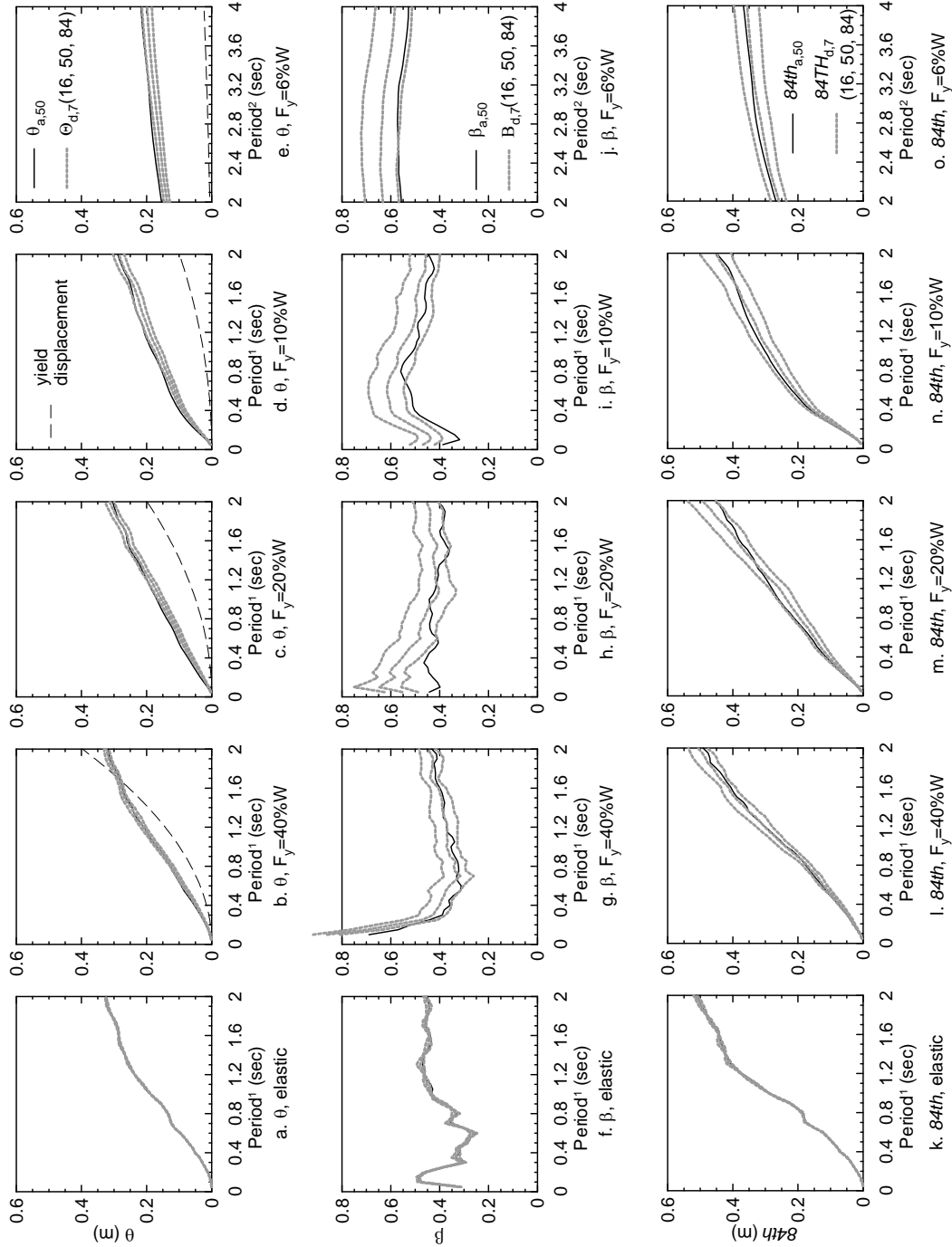
Note:  
<sup>1</sup> based on pre-yield stiffness  
<sup>2</sup> based on post-yield stiffness

Figure 4.18. Eighty-fourth, 50th and 16th percentiles of  $\theta_{d,11}$ ,  $B_{d,11}$  and  $84TH_{d,11}$  for Bin 1d; and  $\theta_{a,50}$ ,  $\beta_{a,50}$  and  $84th_{a,50}$  for Bin 1a motions



Note:  
<sup>1</sup> based on pre-yield stiffness  
<sup>2</sup> based on post-yield stiffness

Figure 4.19. Eighty-fourth, 50th and 16th percentiles of  $\theta_{d,21}$ ,  $B_{d,21}$  and  $84TH_{d,21}$  for Bin 1d; and  $\theta_{d,50}$ ,  $\beta_{d,50}$  and  $84th_{d,50}$  for Bin 1a motions



Note:  
<sup>1</sup> based on pre-yield stiffness  
<sup>2</sup> based on post-yield stiffness

Figure 4.20. Eighty-fourth, 50th and 16th percentiles of  $\theta_{d,7}$ ,  $B_{d,7}$  and  $84TH_{d,7}$  for Bin 2d,  $\theta_{d,50}$ ,  $\beta_{d,50}$  and  $84th_{d,50}$  for Bin 2a motions

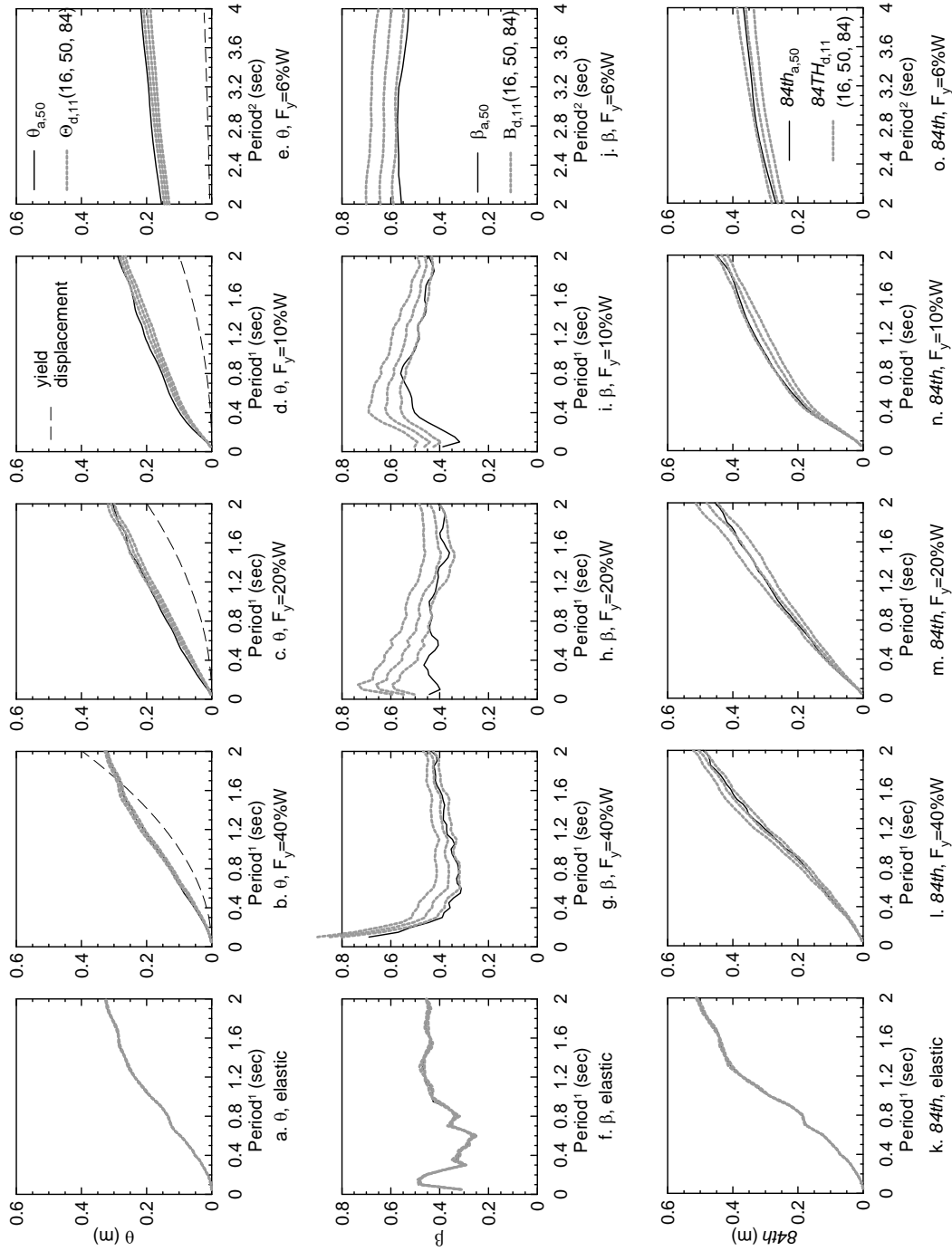


Figure 4.21. Eighty-fourth, 50th and 16th percentiles of  $\theta_{d,11}$ ,  $B_{d,11}$  and  $84TH_{d,11}$  for Bin 2d; and  $\theta_{a,50}$ ,  $\beta_{a,50}$  and  $84TH_{a,50}$  for Bin 2a motions

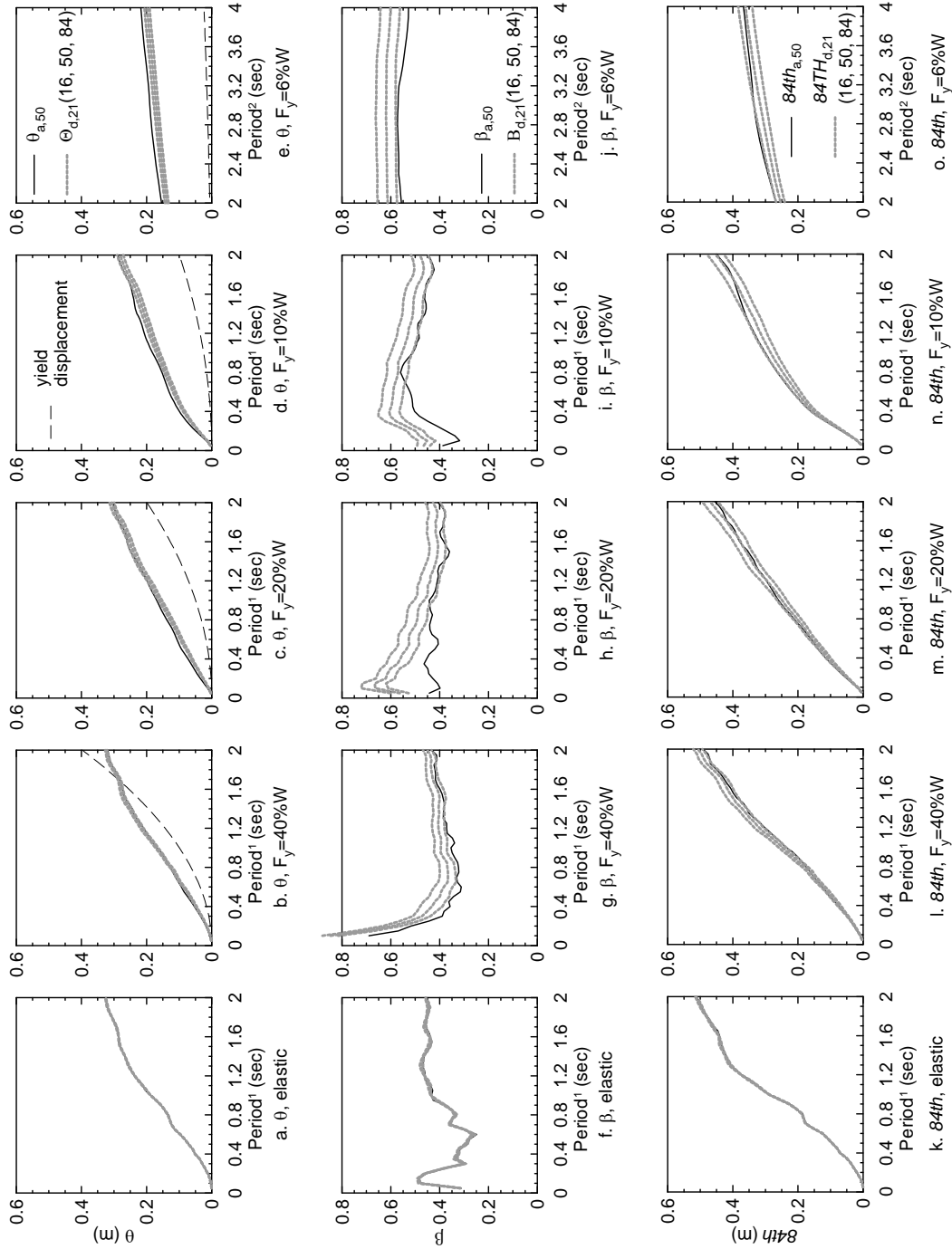


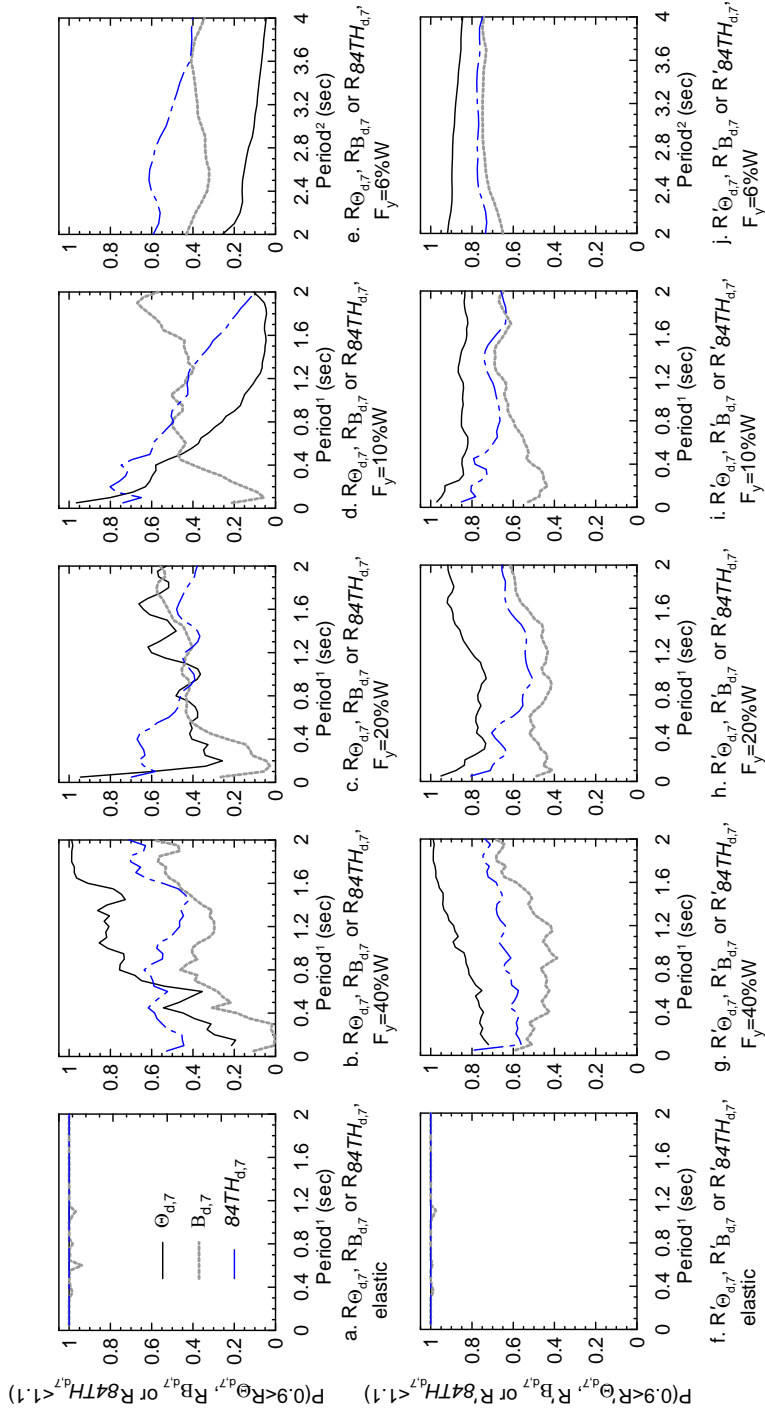
Figure 4.22. Eighty-fourth, 50th and 16th percentiles of  $\theta_{d,21}$ ,  $B_{d,21}$  and  $84TH_{d,21}$  for Bin 2a motions and  $\theta_{d,50}$ ,  $\beta_{d,50}$  and  $84th_{d,50}$  for Bin 2a motions

2. In most cases, the estimate for  $\beta$  is conservatively biased, especially for short-period structures.
3. The dispersions in  $\Theta_{d,n}$ ,  $B_{d,n}$  and  $84TH_{d,n}$  decrease as the number of ground motions used in the analysis increases.

Two sets of probabilities (confidence levels) are shown in Figure 4.23 through Figure 4.28. The first row in each of these figures presents five panels showing the probabilities that  $\Theta_{d,n}$ ,  $B_{d,n}$  and  $84TH_{d,n}$  lie between  $\pm 10\%$  of  $\theta_{a,50}$ ,  $\beta_{a,50}$  and  $84th_{a,50}$  [i.e.,  $P(0.9 \leq R_{\Theta_{d,n}}, R_{B_{d,n}}, R_{84TH_{d,n}} \leq 1.1)$ ], respectively. Figure 4.23 through Figure 4.25 are for Bin 1d motions and  $n = 7, 11$  and  $21$ , respectively. The confidence level is 100% for elastic systems because the striping method captures the median and dispersion of the seismic hazard and there is no bias or dispersion due to nonlinear response. Since this *striping* procedure produces biased estimates of median responses for nonlinear systems,  $\Theta_{d,7}$  approaches 1.0 only for near-elastic oscillators in panels b. through e. of the figures (i.e., only for periods of 1.8+ seconds for  $F_y = 0.4W$ ; see Figure 4.8a for periods associated with spectral accelerations smaller than 0.4 g). For highly nonlinear systems and the near-fault ground motions of Bin 1d, the confidence levels for  $0.9 \leq R_{\Theta_{d,n}}, R_{B_{d,n}}, R_{84TH_{d,n}} \leq 1.1$  are very low, even when 21 ground motions are used for the computation. Importantly, for weak nonlinear SDOF systems (such as seismic isolation systems, see Figure 4.23e), the level of confidence in the prediction of median displacement demands plus and minus 10% is extremely low because the use of spectrally matched motions systemically under predicts displacements by up to 20%: the level of confidence drops with an increase in  $n$  because the dispersion in the biased estimate decreases. Figure 4.26 through Figure 4.28 present data for Bin 2d motions and  $n = 7, 11$  and  $21$ , respectively. The trends are similar to those of Figure 4.23 through Figure 4.25, including  $\Theta_{d,7}$  approaching 1.0 only for near-elastic oscillators in panels b. through e. of the figures (i.e., only for periods of 1.0+ seconds for  $F_y = 0.4W$ ; see Figure 4.8b). For weak nonlinear systems (see Figure 4.26e, Figure 4.27e and Figure 4.28e), the level of confidence in the prediction of median displacement demands plus and minus 10% is low because the use of spectrally matched motions systemically under predicts displacements albeit not to the same degree as for near-fault motions.

The key shortcoming of the D-scaling method is that its use leads to an underestimate of median displacement response in SDOF systems and an overestimate of the dispersion. The low estimate of displacement response is due to the use of spectrally matched ground motions for each stripe.





Note:

<sup>1</sup> based on pre-yield stiffness

<sup>2</sup> based on post-yield stiffness

**Figure 4.23. Confidence levels for  $0.9 \leq R_{\Theta}, R_B$  or  $R_{84TH} \leq 1.1$  and  $0.9 \leq R'_{\Theta}, R'_B$  or  $R'_{84TH} \leq 1.1$  for Bin 1d ground**

**motions**

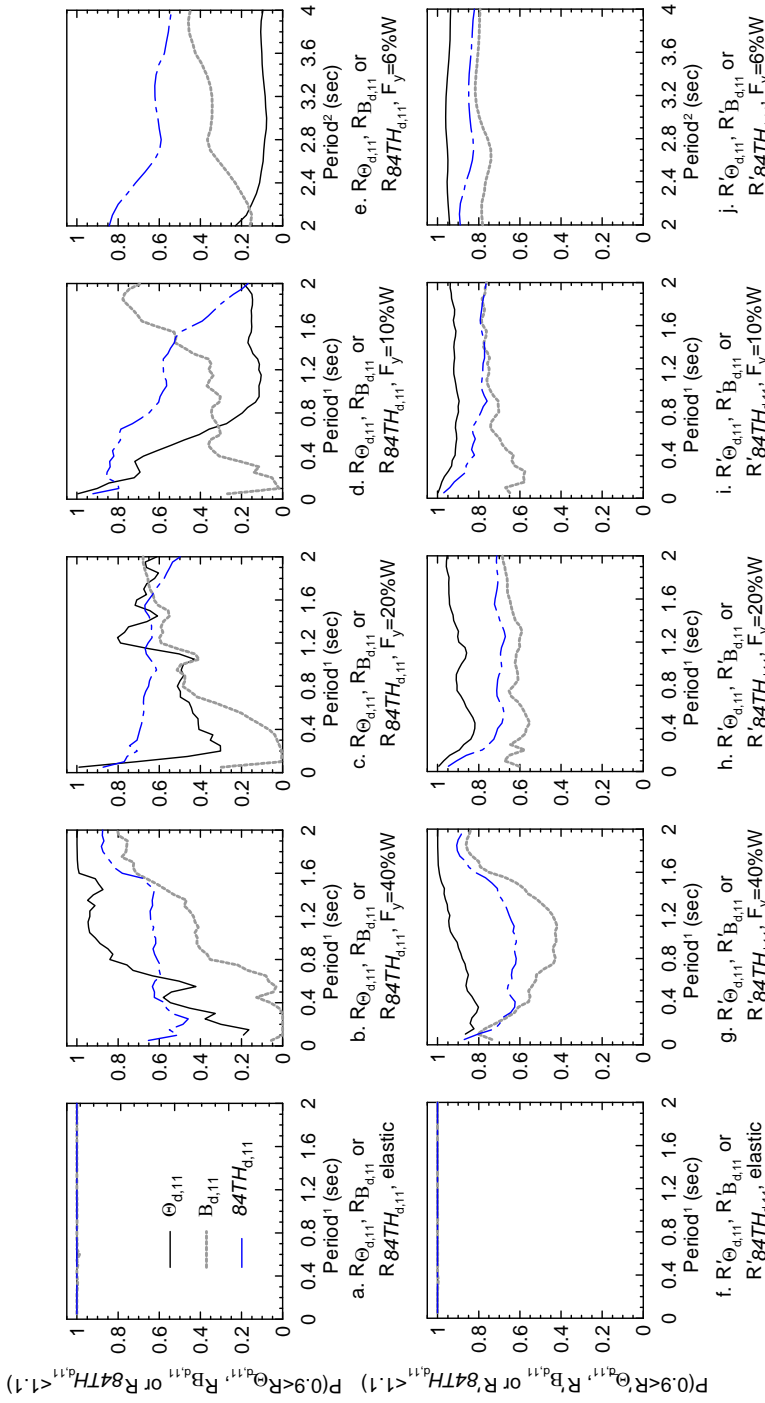
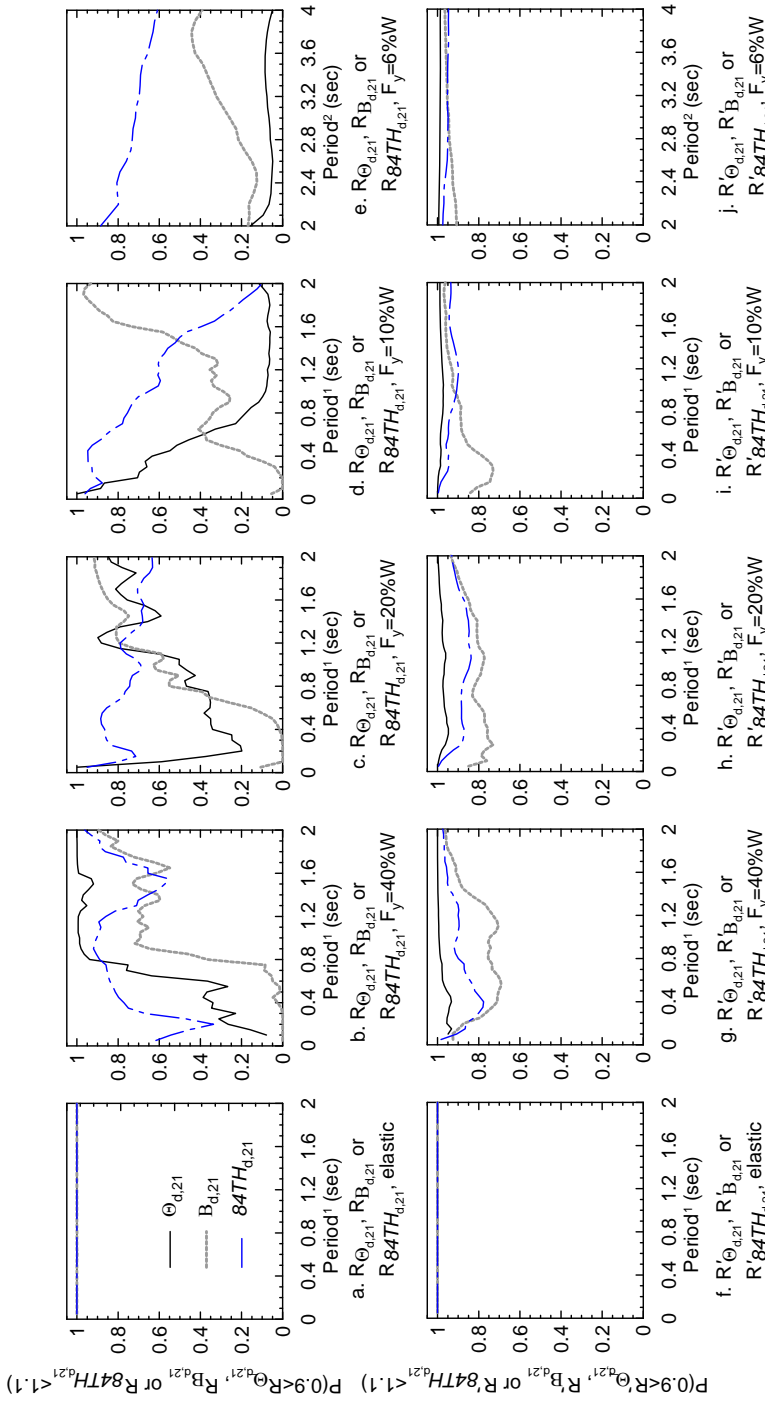


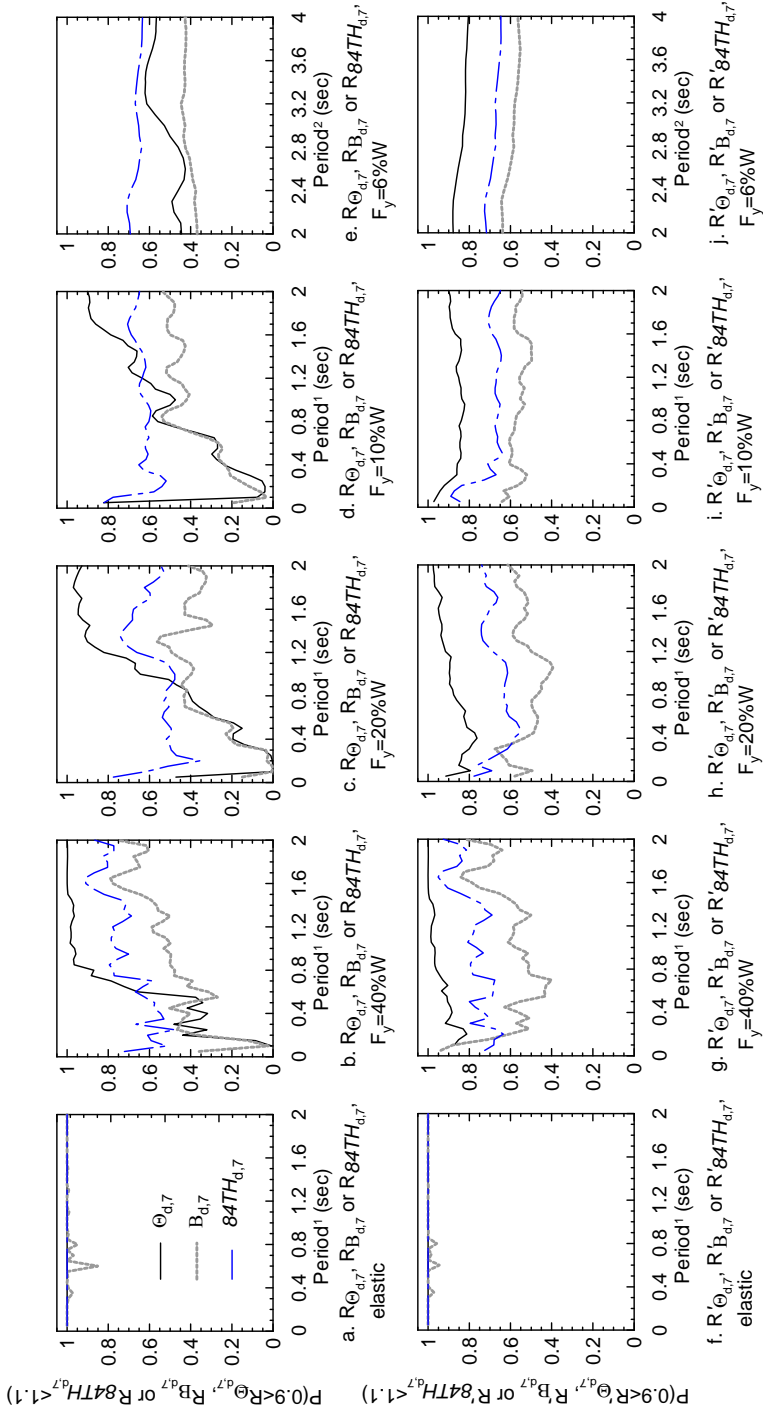
Figure 4.24. Confidence levels for  $0.9 \leq R_{\Theta_{d,11}}, R_{B_{d,11}}$  or  $R_{84TH_{d,11}} \leq 1.1$  and  $0.9 \leq R'_{\Theta_{d,11}}, R'_{B_{d,11}}$  or  $R'_{84TH_{d,11}} \leq 1.1$  for Bin 1d ground motions

Note:  
<sup>1</sup> based on pre-yield stiffness  
<sup>2</sup> based on post-yield stiffness



Note:  
<sup>1</sup> based on pre-yield stiffness  
<sup>2</sup> based on post-yield stiffness

Figure 4.25. Confidence levels for  $0.9 \leq R_{\Theta_{d,21}}, R_{B_{d,21}}$  or  $R_{84TH_{d,21}} \leq 1.1$  and  $0.9 \leq R'_{\Theta_{d,21}}, R'_{B_{d,21}}$  or  $R'_{84TH_{d,21}} \leq 1.1$  for Bin 1d ground motions

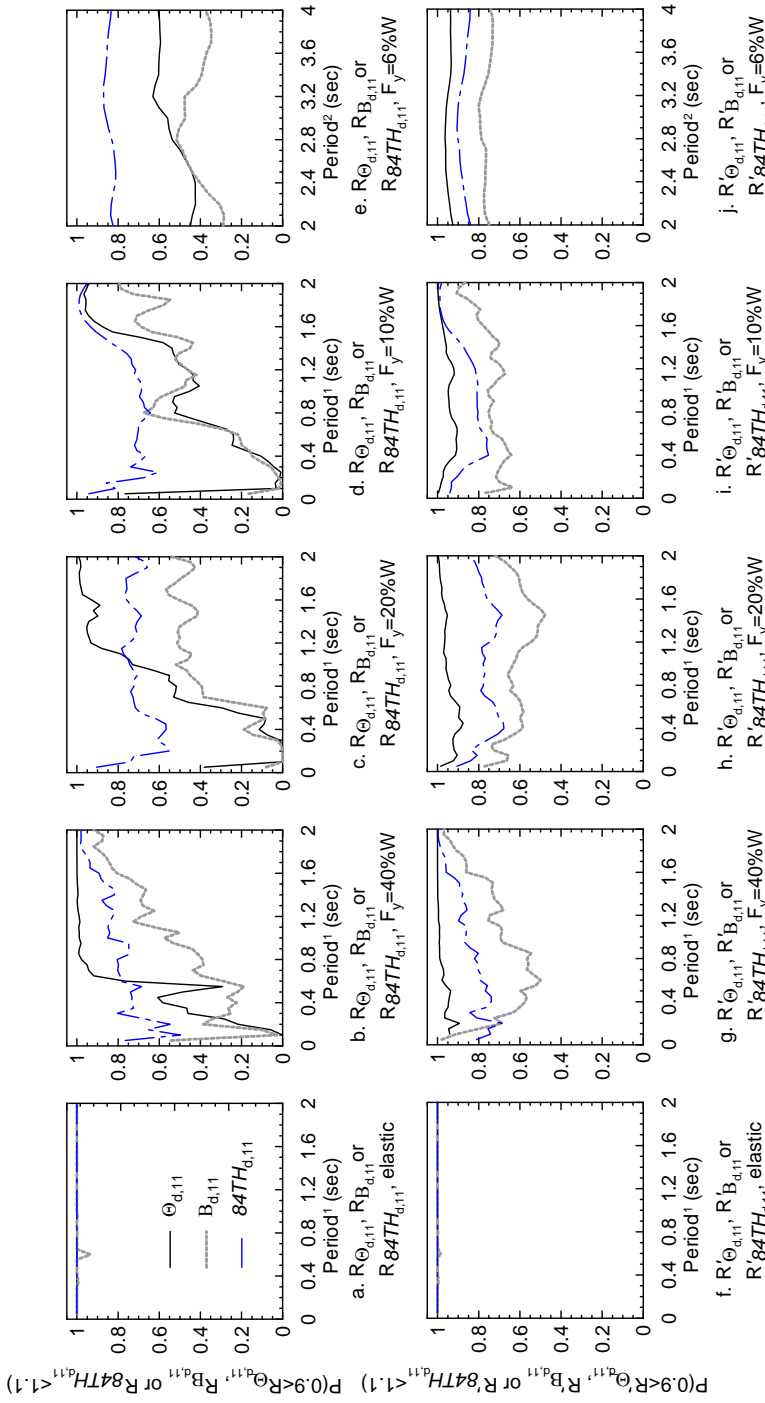


Note:

1 based on pre-yield stiffness

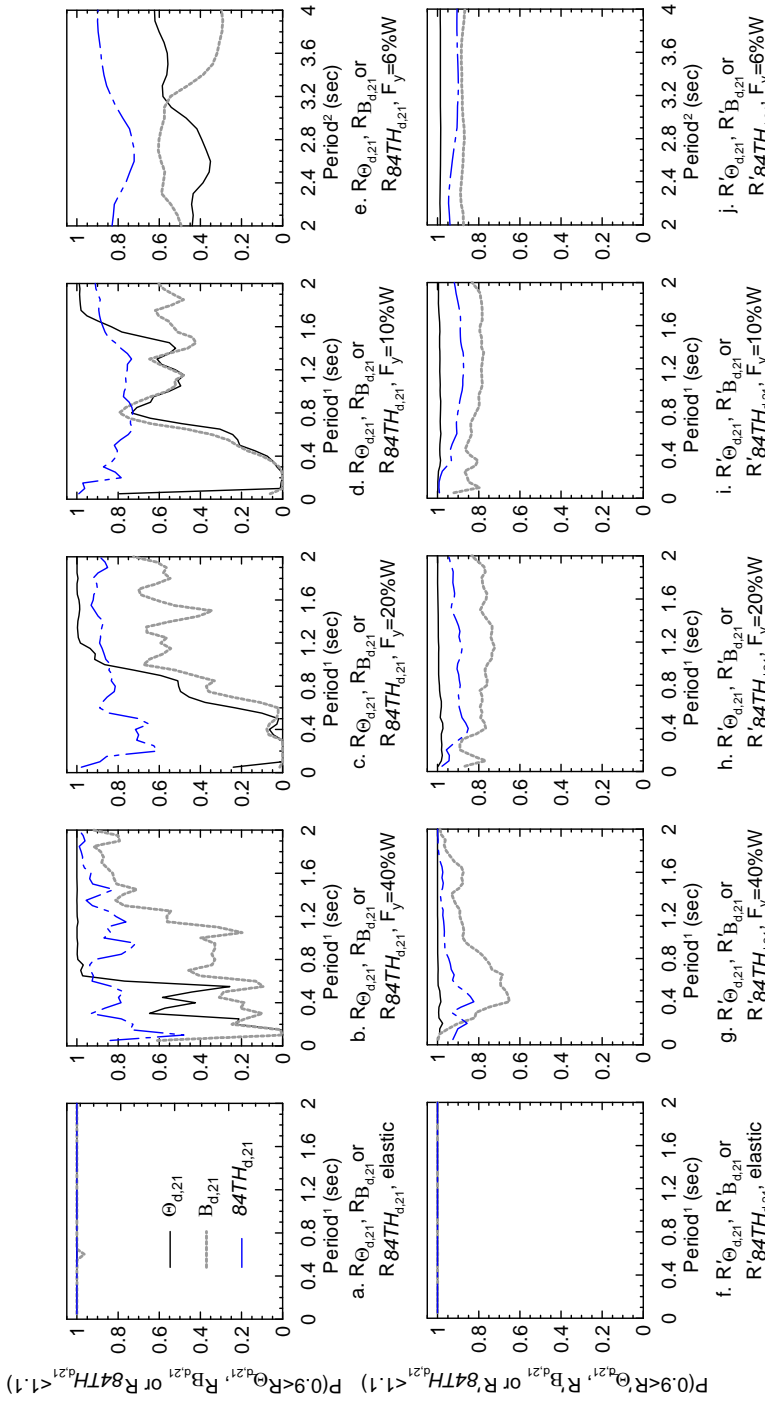
2 based on post-yield stiffness

Figure 4.26. Confidence levels for  $0.9 \leq R_{\Theta_{d,7}}, R_{B_{d,7}}$  or  $R_{84TH_{d,7}} \leq 1.1$  and  $0.9 \leq R'_{\Theta_{d,7}}, R'_{B_{d,7}}$  or  $R'_{84TH_{d,7}} \leq 1.1$  for Bin 2d ground motions



Note:  
<sup>1</sup> based on pre-yield stiffness  
<sup>2</sup> based on post-yield stiffness

Figure 4.27. Confidence levels for  $0.9 \leq R_{\Theta_{d,11}}, R_{B_{d,11}}$  or  $R_{84TH_{d,11}} \leq 1.1$  and  $0.9 \leq R'_{\Theta_{d,11}}, R'_{B_{d,11}}$  or  $R'_{84TH_{d,11}} \leq 1.1$  for Bin 2d ground motions



Note:  
<sup>1</sup> based on pre-yield stiffness  
<sup>2</sup> based on post-yield stiffness

**Figure 4.28. Confidence levels for  $0.9 \leq R_{\Theta}, R_B$  or  $R_{84TH} \leq 1.1$  and  $0.9 \leq R'_{\Theta}, R'_B$  or  $R'_{84TH} \leq 1.1$  for Bin 2d ground motions**

Section 4.3.5.3 addresses numerical corrections to the D-scaling method to achieve accurate estimates (medians and dispersions) of displacement response. An alternate procedure, intended to negate the need for modification factors, is presented in Section 4.3.6.

#### 4.3.5.3 Modification Factors

The ratios  $\theta_{a,50}/\theta_{\Theta_{d,21}}$  and  $\beta_{a,50}/\beta_{B_{d,21}}$  were calculated and plotted in Figure 4.29 and Figure 4.30 for Bins 1d and 2d, respectively, to develop correction factors to eliminate the bias in the estimate of  $\theta_{a,50}$  and  $\beta_{a,50}$  using the D-scaling method. The two ratios for oscillators were plotted as a function of the elastic period, ductility ratio ( $\mu$ ) and response modification coefficient ( $R$ ) for oscillators with  $F_y = 0.4W$ ,  $0.2W$  and  $0.1W$ , where  $\mu$  is the ratio of  $\theta_{\Theta_{d,21}}$  and the yield displacement of the oscillator (e.g., see Points A and B in Figure 4.19d), and  $R$  is the ratio of the median elastic spectral acceleration (shown in Figure 4.8) and  $F_y/W^7$ . For  $F_y = 0.06W$ , the ratios were plotted as function of the second-slope period only because they were approximately constant and independent of  $T$ ,  $\mu$  and  $R$ .

Based on the trends seen in these figures, expressions for  $C_\theta$  and  $C_\beta$  are proposed below to modify the  $\theta$  and  $\beta$  of (4.7) for generating the stripes associated with a target spectrum:

$$x_i(T_j) = \theta'(T_j) \cdot e^{\beta'(T_j)\alpha_i} = C_\theta \theta(T_j) \cdot e^{C_\beta \beta(T_j)\alpha_i} \quad i=1 \text{ to } n \quad (4.11)$$

For conventional structures and near-fault ground motions:

$$C_\theta = -0.004R^2 + 0.06R + 0.94 \quad 1 \leq R \leq 10 \quad (4.12)$$

$$C_\beta = \begin{cases} 0.48T^2 - 0.19T + 0.67 & T \leq 1 \text{ sec} \\ 1.1R^{-0.08} & 1 \leq R \leq 10, \quad T > 1 \text{ sec} \end{cases} \quad (4.13)$$

For isolated structures and near-fault ground motions:

---

<sup>7</sup> Values of  $\mu$  in excess of 5 are likely impractical for conventional structures but information is presented here for larger values of  $\mu$  for the sake of completeness.

$$C_\theta = 1.15 \quad (4.14)$$

$$C_\beta = 0.88 \quad (4.15)$$

For conventional structures and far-field ground motions:

$$C_\theta = \begin{cases} -0.05T^2 - 0.01T + 1.13 & T \leq 0.7 \text{ sec} \\ 1 & 1 \leq R \leq 2, \quad T > 0.7 \text{ sec} \\ -0.0035R^2 + 0.05R + 0.92 & 2 \leq R \leq 10, \quad T > 0.7 \text{ sec} \end{cases} \quad (4.16)$$

$$C_\beta = \begin{cases} 0.67T^2 - 0.53T + 0.92 & T \leq 0.7 \text{ sec} \\ 0.004R^2 - 0.042R + 1.02 & 1 \leq R \leq 10, \quad T > 0.7 \text{ sec} \end{cases} \quad (4.17)$$

For isolated structures and far-field ground motions:

$$C_\theta = 1.1 \quad (4.18)$$

$$C_\beta = 0.9 \quad (4.19)$$

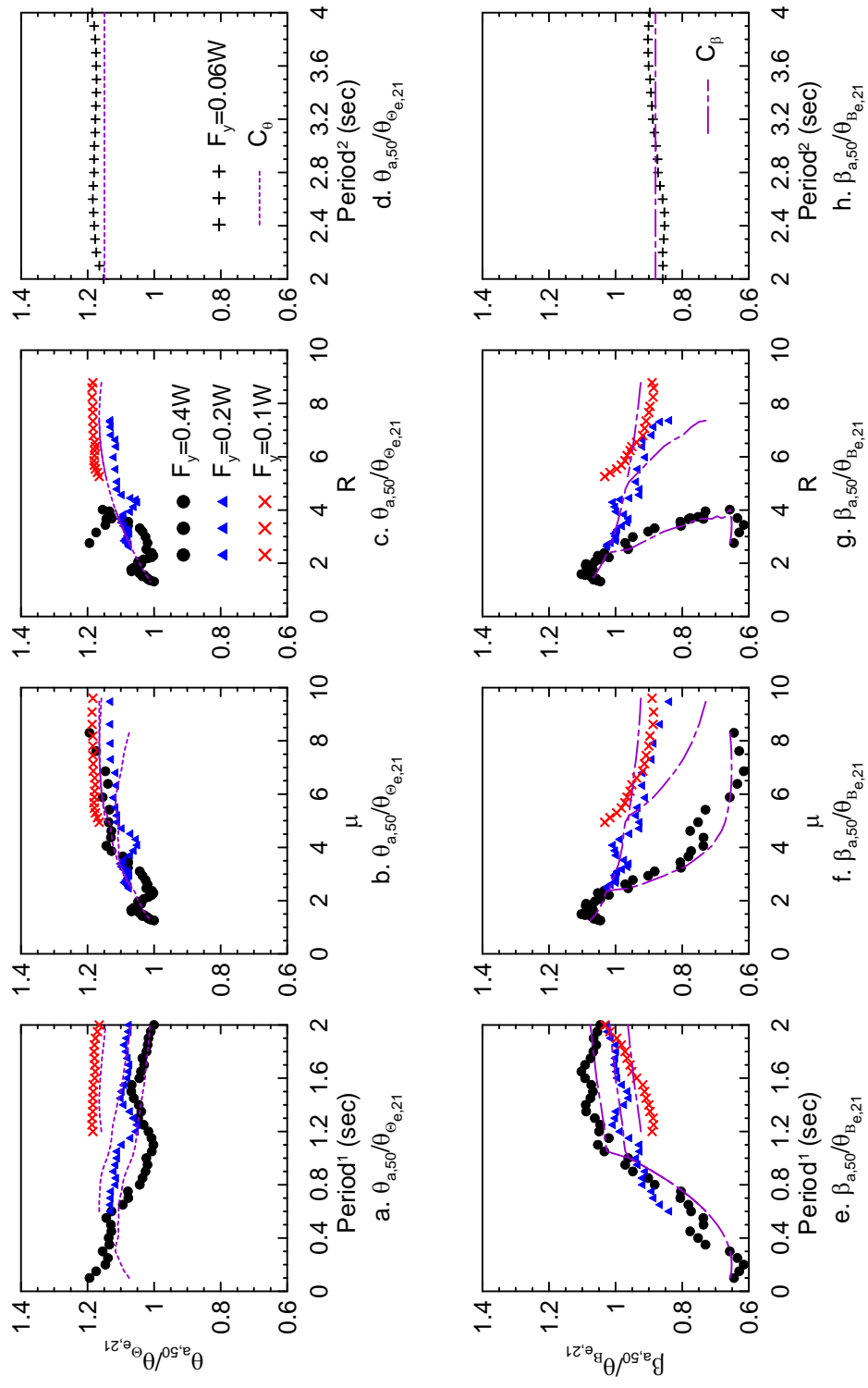
The modification factors  $C_\theta$  and  $C_\beta$  are plotted in Figure 4.29 and Figure 4.30 to permit a comparison with the raw data. The trends are captured well by these factors but considerable scatter remains.

Note again that the ratios  $\theta_{a,50}/\theta_{\theta_{d,21}}$  and  $\beta_{a,50}/\theta_{\beta_{d,21}}$  are characterizations of structural (displacement) response whereas the factors  $C_\theta$  and  $C_\beta$  are used to modify the hazard (response spectra) with goal of producing either unbiased or slightly conservative estimates of  $\theta_{a,50}$  and  $\beta_{a,50}$ .

#### 4.3.5.4 Response-History Analysis Using the D-Scaling Method and the Modified Stripes

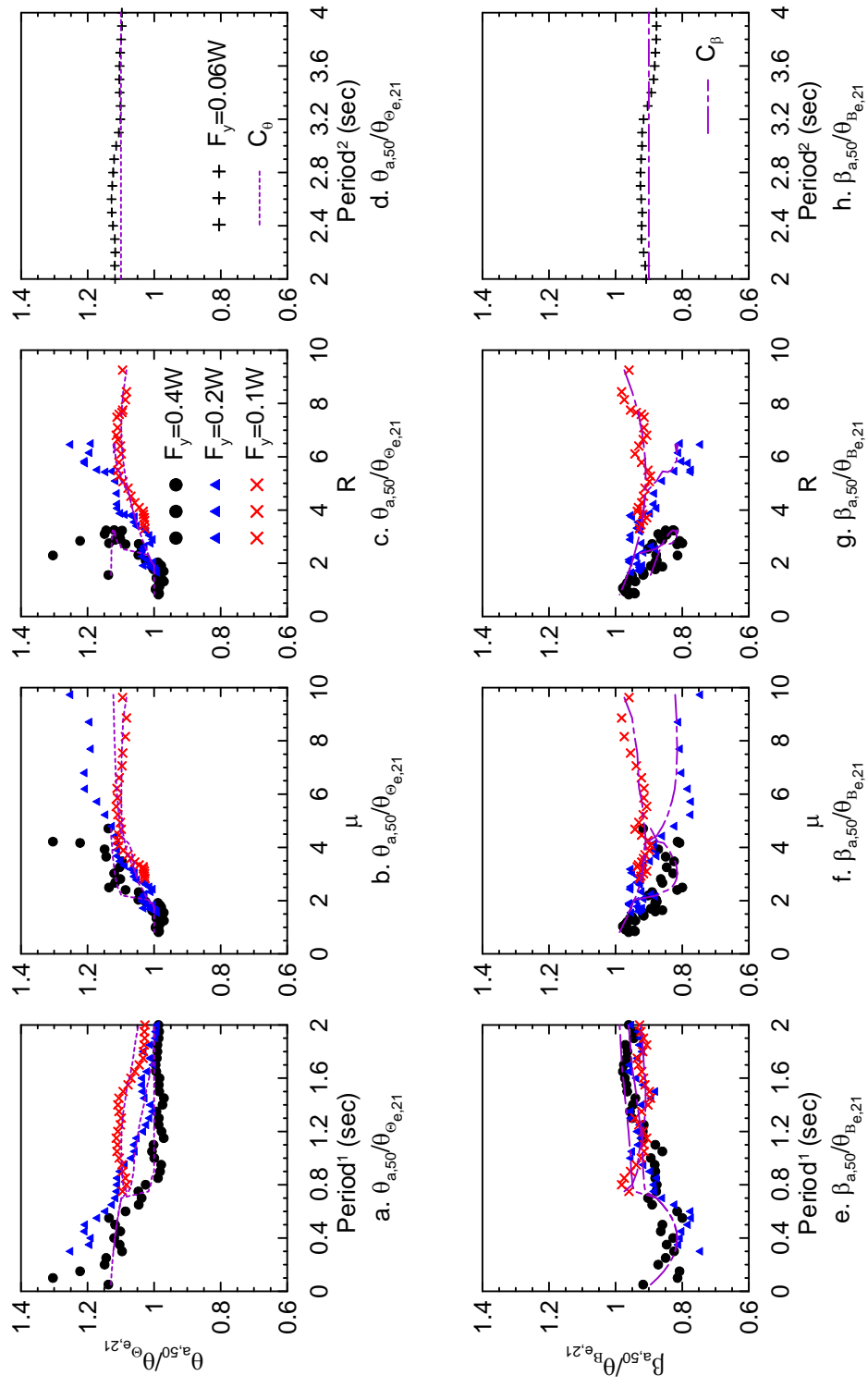
To verify the utility of the modification factors  $C_\theta$  and  $C_\beta$ , ground motions similar to those in Bins 1d and 2d were generated for two sets of stripes ( $n = 11, 21$ ) of target acceleration spectra using (4.11) and the proposed equations for  $C_\theta$  and  $C_\beta$ . The resulting sets of motions were labeled as Bin 1e and Bin 2e for NF and FF ground motions, respectively. Response-history analysis similar to that conducted using Bins 1d and 2d was performed using the Bin 1e and 2e ground motions. Equations (4.8) through (4.10) were used to present results of the analysis; the subscript  $e$  denotes analysis using the Bin 1e and 2e ground motions.





Note:  
<sup>1</sup> based on pre-yield stiffness  
<sup>2</sup> based on post-yield stiffness

**Figure 4.29.**  $\theta_{a,50}/\theta_{e,21}$ ,  $\beta_{a,50}/\theta_{B_e,21}$ ,  $C_\theta$  and  $C_\beta$  for Bin 1d ground motions



Note:  
<sup>1</sup> based on pre-yield stiffness  
<sup>2</sup> based on post-yield stiffness

**Figure 4.30.**  $\theta_{a,50}/\theta_{e,21}$ ,  $\beta_{a,50}/\theta_{B_e,21}$ ,  $C_\theta$  and  $C_\beta$  for Bin 2d ground motions

Figure 4.31 and Figure 4.32 show the 84th, 50th and 16th percentiles of  $\Theta_{e,n}$ ,  $B_{e,n}$  and  $84TH_{e,n}$  for  $n = 11$  and  $21$ , respectively, for the Bin 1e motions. Figure 4.33 and Figure 4.34 present the same information for Bin 2e motions. The vertical thin line in each of the plots separates the data into two parts:  $\mu > 10$  and  $\mu < 10$ , noting that the equations for  $C_\theta$  and  $C_\beta$  were derived assuming that values of  $\mu$  and  $R$  were smaller than 10. For the oscillators with  $F_y = 0.40W$ ,  $0.20W$  and  $0.10W$ , the results show that the prior unconservative (low) estimates of  $\theta_{a,50}$  are greatly improved with the use of the factors  $C_\theta$  and  $C_\beta$ . The estimate of  $\theta_{a,50}$  for the Bin 1e motions and oscillators with  $F_y = 0.1W$  and  $T = 0.2$  through  $0.9$  second (see Figure 4.31c) is underestimated but  $\mu > 10$  is assumed to be impractical in this period range. The estimate of  $\beta_{a,50}$  is still conservative but the significant overestimate of  $\beta_{a,50}$  by the Bin 1d motions in the short period range (see Figure 4.18g, Figure 4.18h and Figure 4.18i) is greatly reduced with the use of the modification factors. The estimate of  $84th_{a,50}$  is slightly conservative for the Bin 1e motions and almost unbiased for the Bin 2e motions. For the oscillators with  $F_y = 0.06W$ , the use of  $C_\theta$  and  $C_\beta$  produces unbiased estimates for  $\theta_{a,50}$ ,  $\beta_{a,50}$  and  $84th_{a,50}$ . These results indicate that the D-scaling method (including the modification factors) can be used to estimate both the median and dispersion in the displacement response of nonlinear (single-degree-of-freedom) framing systems. A question that remains is how many stripes are needed to capture the median and 84th percentile responses with a high degree of confidence?

The panels in the first row of Figure 4.35 and Figure 4.36 show the confidence levels for  $0.9 \leq R_{\Theta_{e,11}}, R_{B_{e,11}}, R_{84TH_{e,11}} \leq 1.1$  and  $0.9 \leq R_{\Theta_{e,21}}, R_{B_{e,21}}, R_{84TH_{e,21}} \leq 1.1$ , respectively, for Bin 1e ground motions. Identical data are presented in first row of Figure 4.37 and Figure 4.38 for Bin 2e ground motions. A thin vertical line in each of the panels separates the results for  $\mu < 10$  and  $\mu > 10$ . Data for  $\mu > 10$  is presented for information only; the discussion below focuses solely on cases for which  $\mu < 10$ . The confidence levels for  $0.9 \leq R_{\Theta_{e,n}}, R_{B_{e,n}}, R_{84TH_{e,n}} \leq 1.1$  still vary widely and between 0.2 and 1. Some notable exceptions are a) for isolated structures ( $F_y = 0.06W$ ) and 21 spectral stripes (see Figure 4.36d and Figure 4.38d), the confidence levels exceed 90% for the estimates of  $\theta_{a,50}$  and  $84th_{a,50}$  and 80% for the estimate of  $\beta_{a,50}$ ; and b) for  $F_y = 0.40W$ ,  $0.20W$  and  $0.10W$  and  $\mu < 10$  (see Figure 4.37a through Figure 4.37c and Figure 4.38a through Figure 4.38c), the confidence levels exceed 90% for the estimate of  $\theta_{a,50}$ .

In most cases, the estimate of  $\theta_{a,50}$  has the highest confidence and that of  $\beta_{a,50}$  the lowest confidence because  $\Theta_{e,n}$  and  $B_{e,n}$  have the smallest and largest dispersions, respectively, of the three random variables  $\Theta_{e,n}$ ,  $B_{e,n}$  and  $84TH_{e,n}$ . This observation implies that the number of

stripes required to estimate  $\beta_{a,50}$  should be greater than that for  $\theta_{a,50}$  and  $84th_{a,50}$ . The reason that the confidence levels shown in the first row of Figure 4.35 through Figure 4.38 for  $F_y = 0.40W, 0.20W$  and  $0.10W$  vary widely is because the modification factors cannot totally eliminate the bias in the estimates of  $\theta_{a,50}$ ,  $\beta_{a,50}$  and  $84th_{a,50}$ ; many of the estimates are mildly conservative (high), especially for  $\beta_{a,50}$  (see the panels f and g in Figure 4.31 through Figure 4.34). To illustrate the influence of a mildly conservative bias on the confidence level, the probabilities for  $R_{\Theta_{e,n}}, R_{B_{e,n}}, R_{84TH_{e,n}} \geq 0.9$  are presented in the second row of panels in Figure 4.35 through Figure 4.38. The confidence levels are greatly increased by comparison with the companion oscillators in the first row of the figures. However, for selected oscillators in Figure 4.35e, Figure 4.35h, Figure 4.37e, Figure 4.37f and Figure 4.37h, the probability that  $R_{B_{e,11}} \geq 0.9$  is smaller than 0.9, which suggests that the dispersion in  $B_{e,11}$  should be reduced and that more than 11 stripes should be used to estimate  $\beta_{a,50}$  to reach a 90% confidence level.

The ratios of  $\theta_{a,50}/\theta_{\Theta_{e,21}}$ ,  $\beta_{a,50}/\theta_{B_{e,21}}$  and  $84th_{a,50}/\theta_{84TH_{e,21}}$  are shown in Figure 4.39 and Figure 4.40 for the Bin 1e and 2e ground motions, respectively, to illustrate that the estimations are not overly conservative. For the oscillators with  $F_y = 0.40W, 0.20W$  and  $0.10W$ , the ratios of  $\theta_{a,50}/\theta_{\Theta_{e,21}}$  and  $84th_{a,50}/\theta_{84TH_{e,21}}$  distribute between 0.9 and 1.05 and the ratio of  $\beta_{a,50}/\theta_{B_{e,21}}$  distributes between 0.8 and 1.05. For the oscillators with  $F_y = 0.06W$ , all three ratios are approximately equal to 1.

On the basis of the results presented in Figure 4.31 through Figure 4.40, median and 84th percentile nonlinear displacement demands can be estimated plus or minus 10 percent, with 90% confidence, using ground motions scaled by the D-scaling method (with modification factors) and at least 11 spectral stripes; 21 stripes are needed to compute the corresponding value of  $\beta$ , larger than minus 10%, with 90% confidence.

### **4.3.6 The D-scaling Method Using Actual Earthquake Records**

#### **4.3.6.1 The Scaling Procedure**

Modification factors were developed in Section 4.3.5.3 to enable a robust calculation of median and fractile displacement responses in nonlinear SDOF systems. The modification factors are needed to eliminate the systemic under prediction of displacement responses that result from the spectral matching of ground motions to the stripes associated with the target response spectrum.

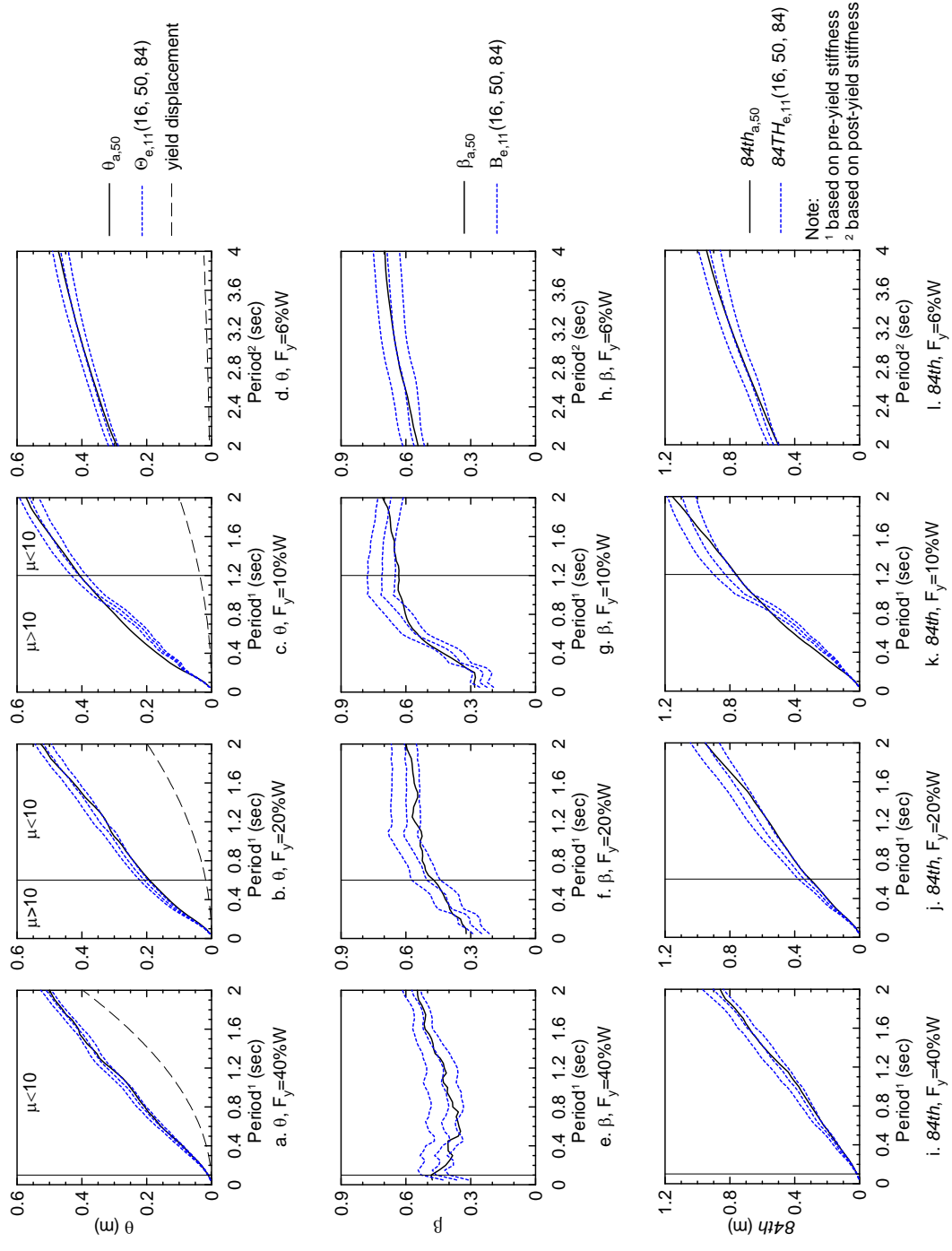


Figure 4.31. Eighty-fourth, 50th and 16th percentiles of  $\theta_{e,11}$ ,  $\beta_{e,11}$  and 847th $_{e,11}$  for modified Bin 1e motions; and  $\theta_{a,50}$ ,  $\beta_{a,50}$  and 84th $_{a,50}$  for Bin 1a motions

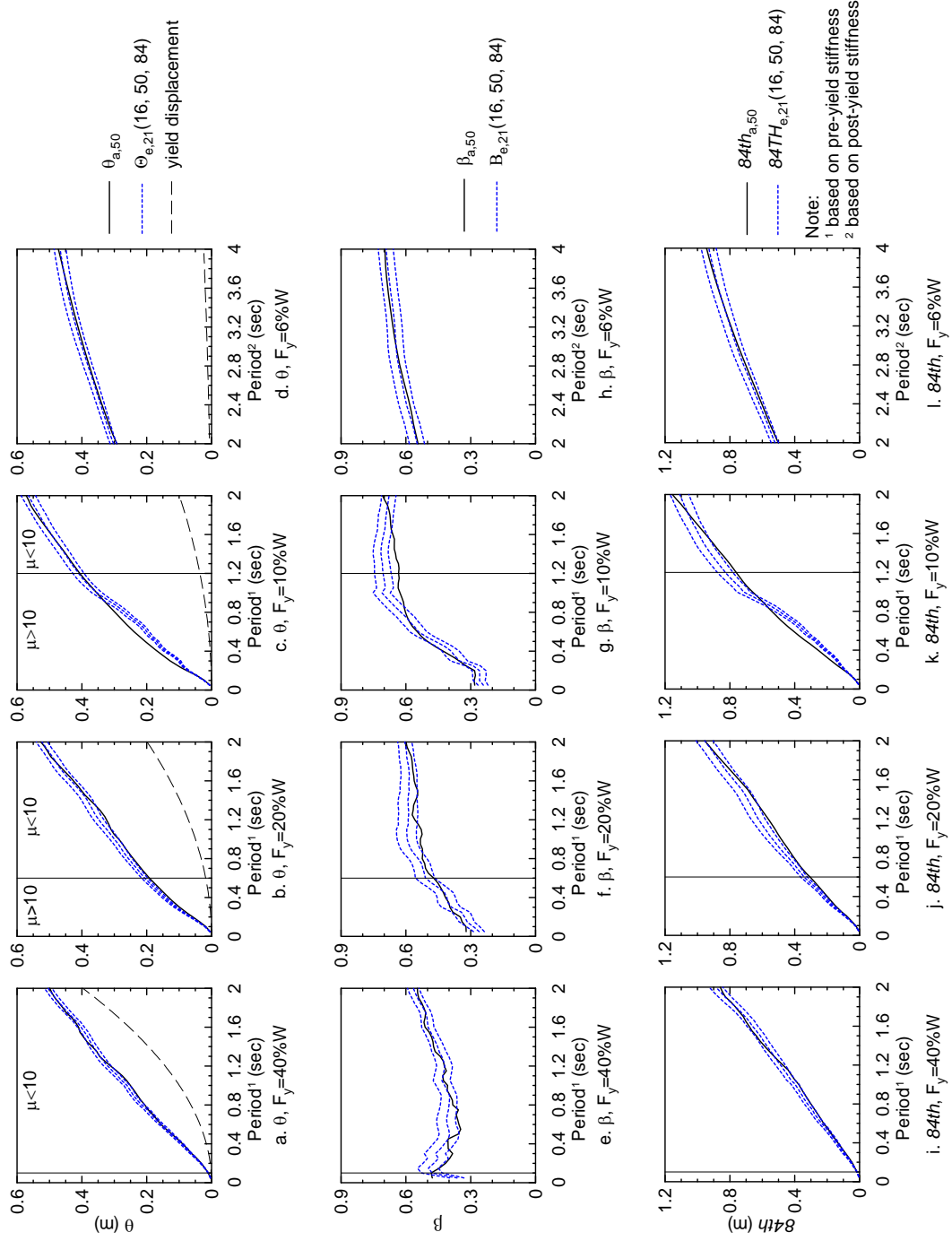


Figure 4.32. Eighty-fourth, 50th and 16th percentiles of  $\theta_{e,21}$ ,  $B_{e,21}$  and  $84TH_{e,21}$  for modified Bin 1e motions; and  $\theta_{a,50}$ ,  $\beta_{a,50}$  and  $84th_{a,50}$  for Bin 1a motions

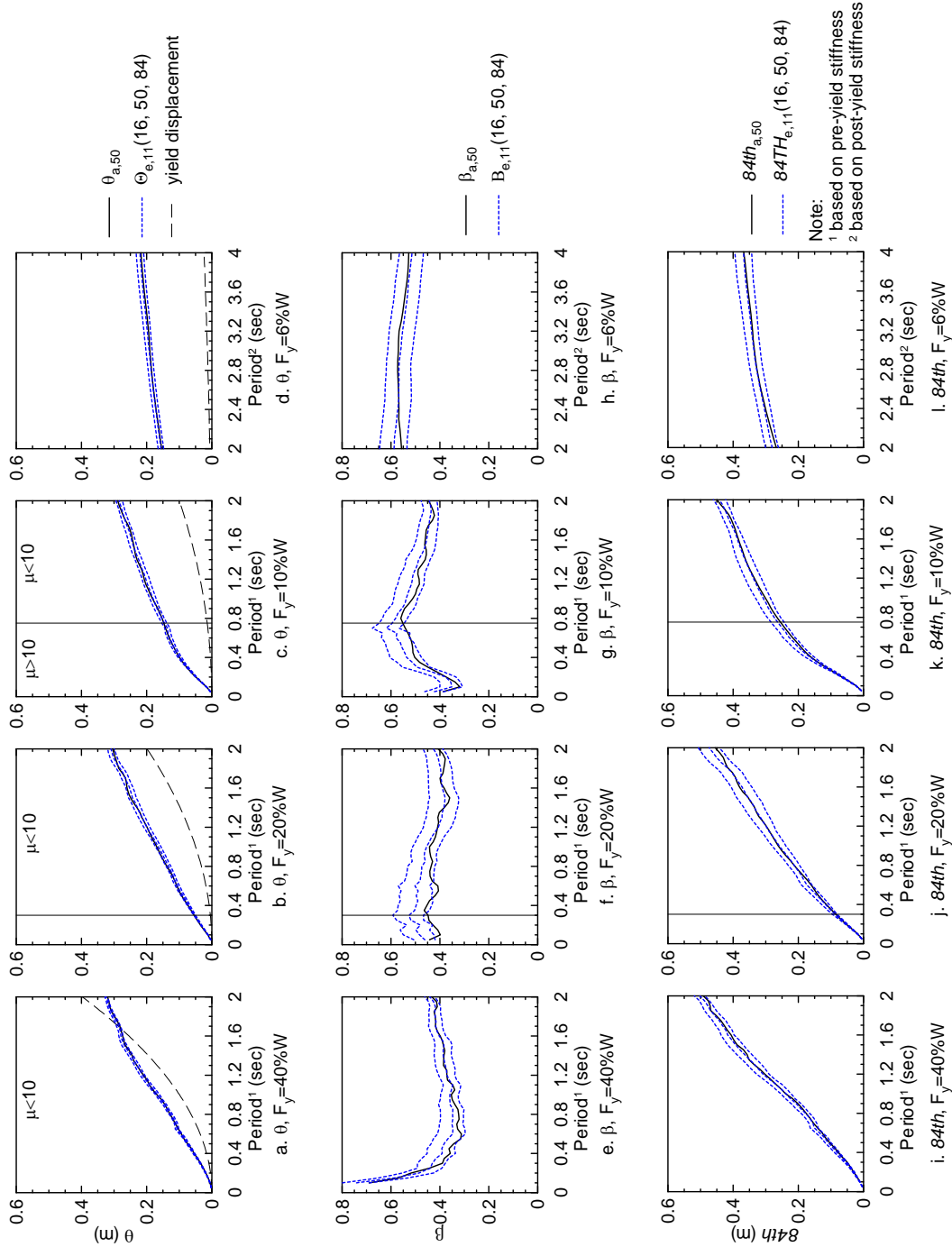


Figure 4.33. Eighty-fourth, 50th and 16th percentiles of  $\theta_{e,11}$ ,  $B_{e,11}$  and  $84TH_{e,11}$  for modified Bin 2e motions; and  $\theta_{a,50}$ ,  $\beta_{a,50}$  and  $84th_{a,50}$  for Bin 2a motions

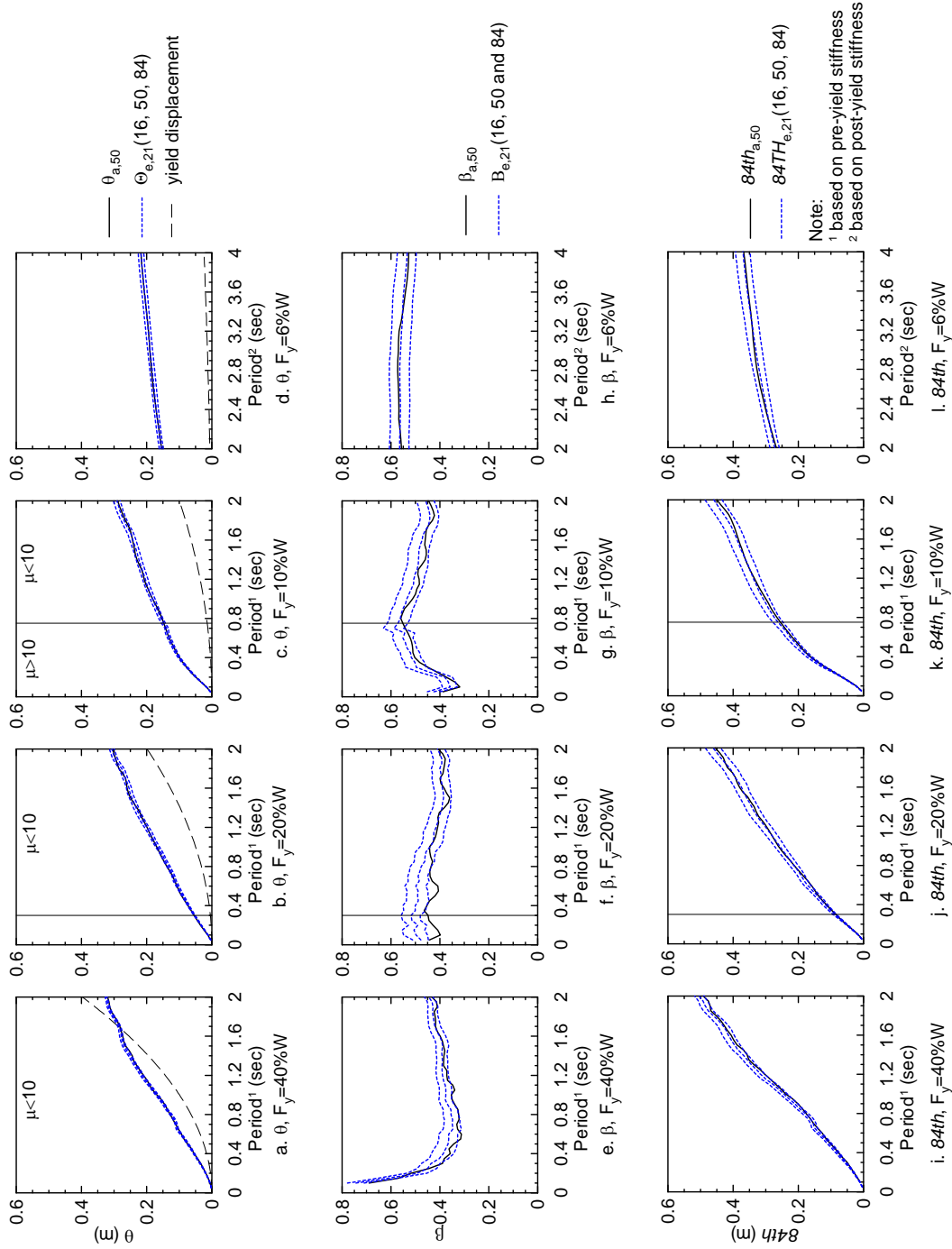
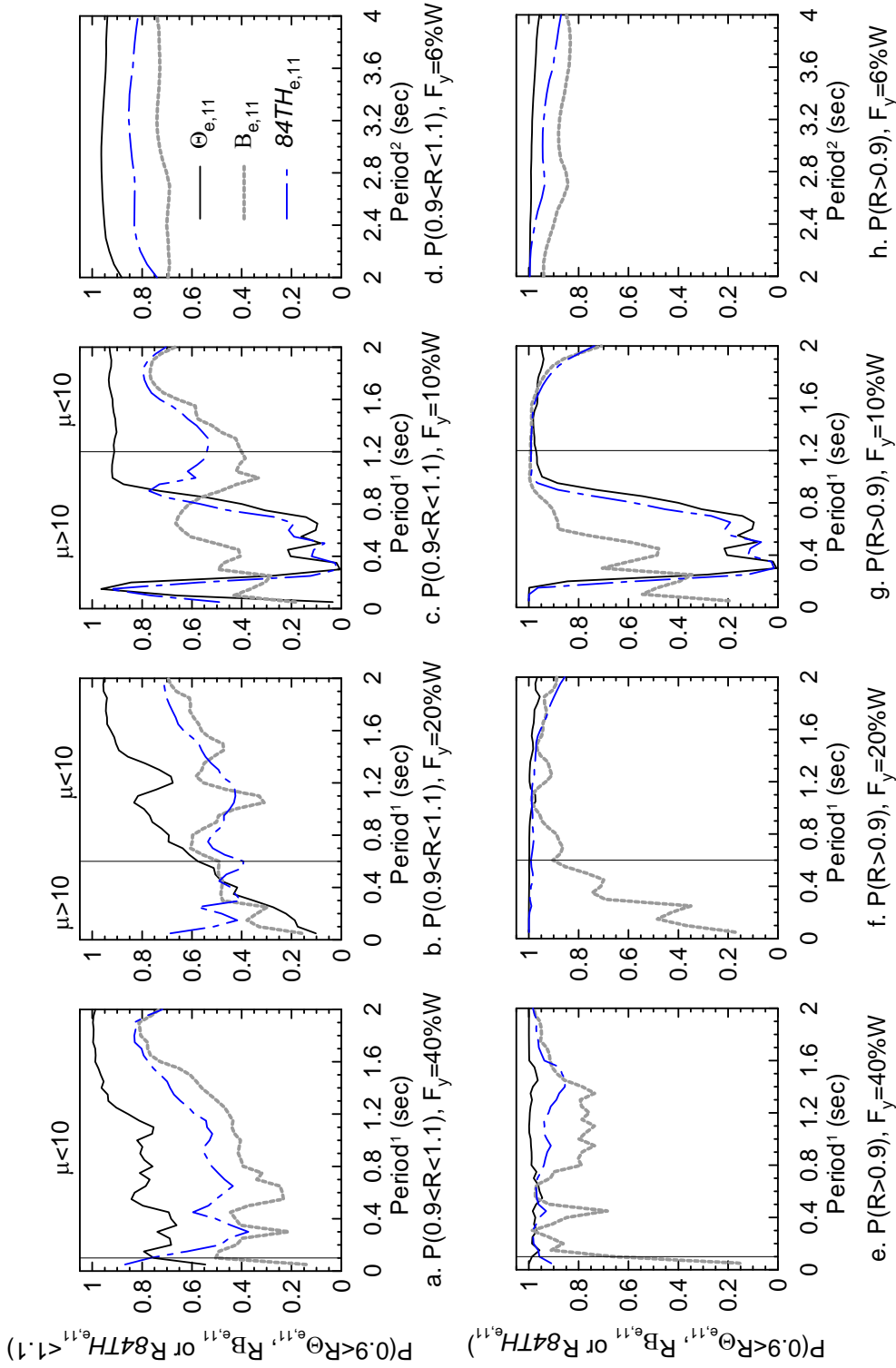


Figure 4.34. Eighty-fourth, 50th and 16th percentiles of  $\theta_{e,21}$ ,  $\beta_{e,21}$  and  $84TH_{e,21}$  for modified Bin 2e motions; and  $\theta_{a,50}$ ,  $\beta_{a,50}$  and  $84th_{a,50}$  for Bin 2a motions





Note:

<sup>1</sup> based on pre-yield stiffness

<sup>2</sup> based on post-yield stiffness

Figure 4.35. Confidence levels for  $0.9 \leq R_{e,11} < 1.1$  and  $R_{B, e,11}$  or  $R_{84TH_{e,11}} \geq 0.9$  for Bin 1e ground motions

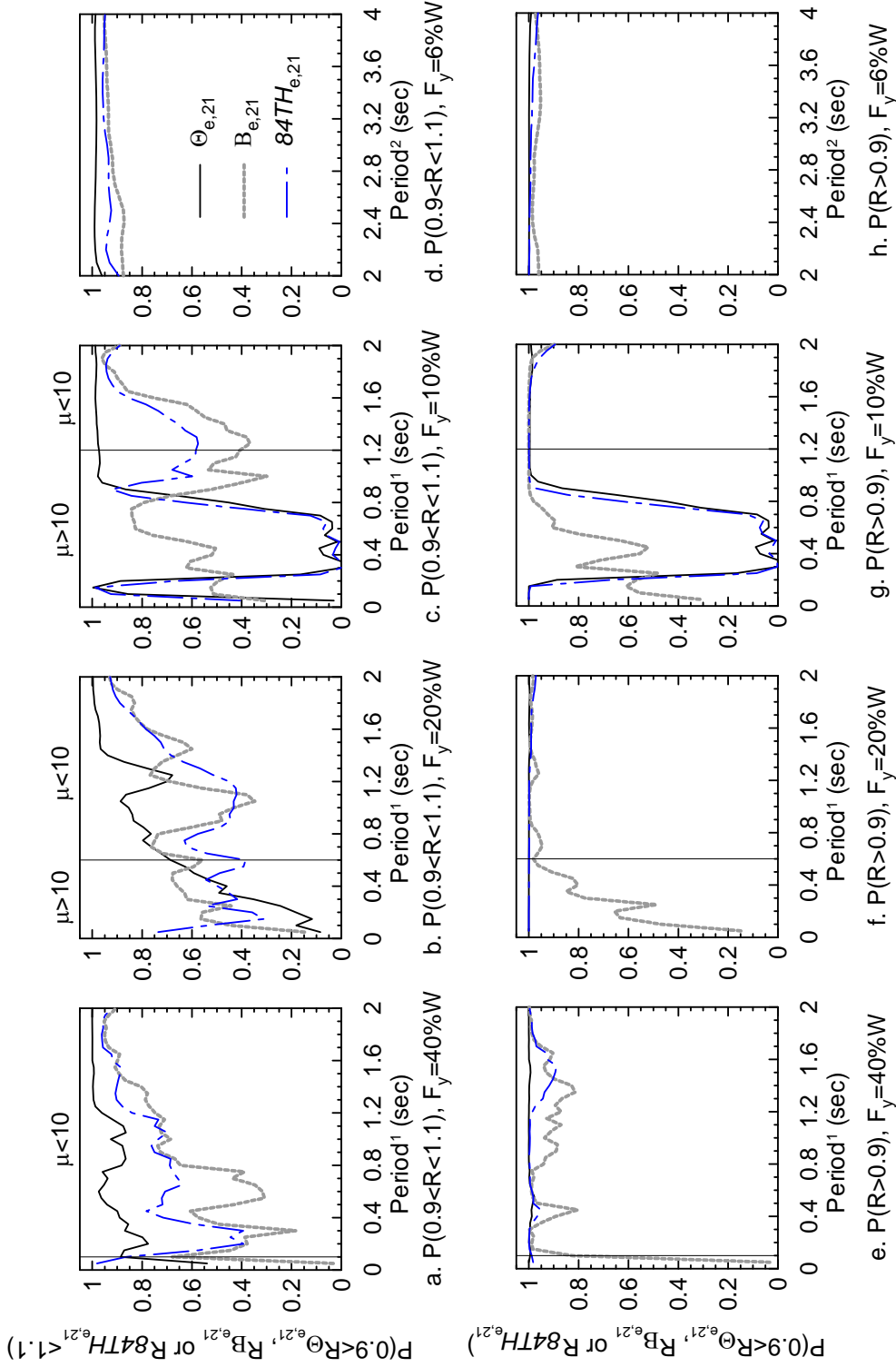
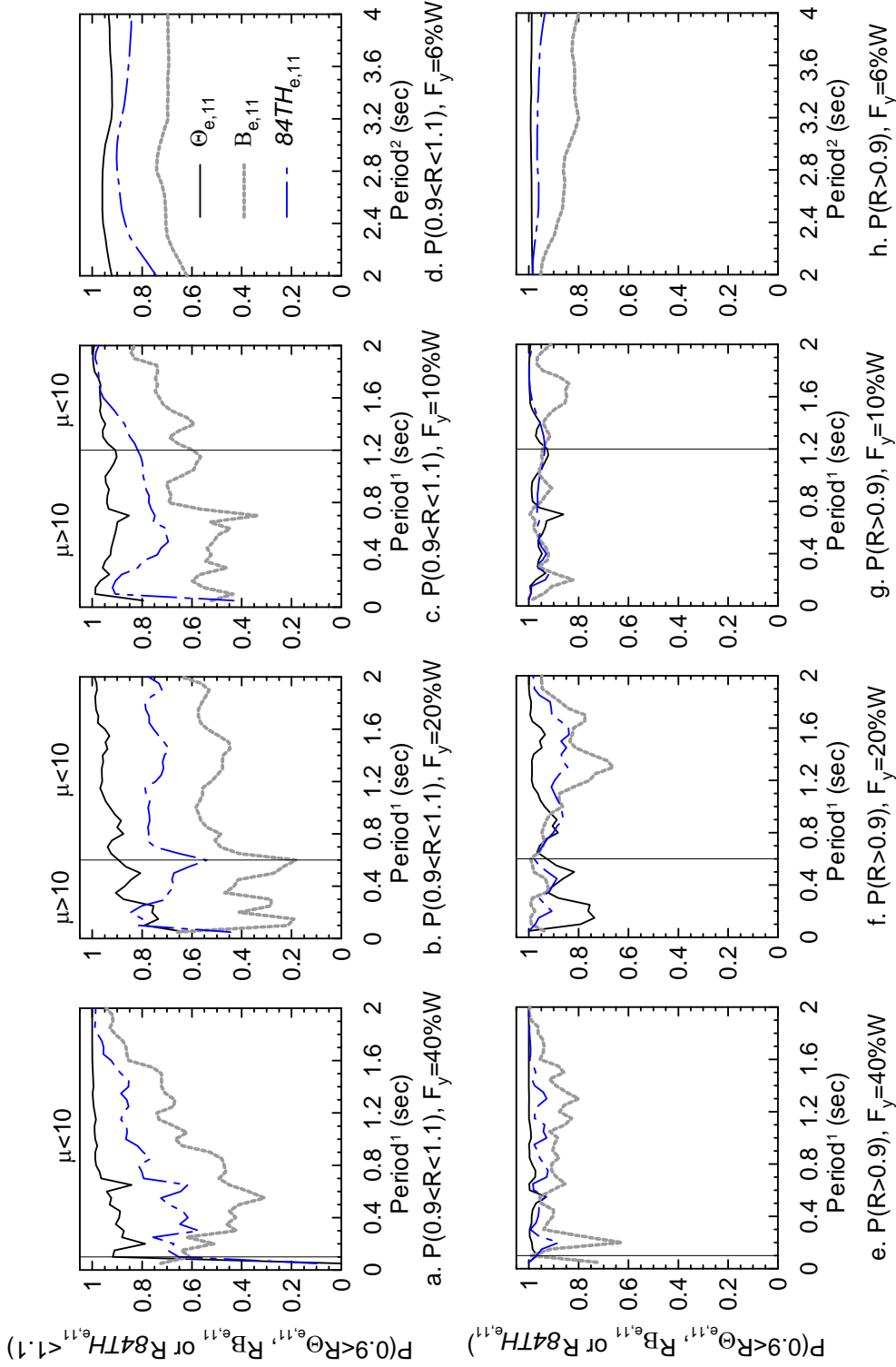


Figure 4.36. Confidence levels for  $0.9 \leq R_{\Theta_{e,21}}, R_{B_{e,21}}, \text{ or } R_{84TH_{e,21}} \leq 1.1$  and  $R_{\Theta_{e,21}} \geq 0.9$  for Bin 1e ground motions

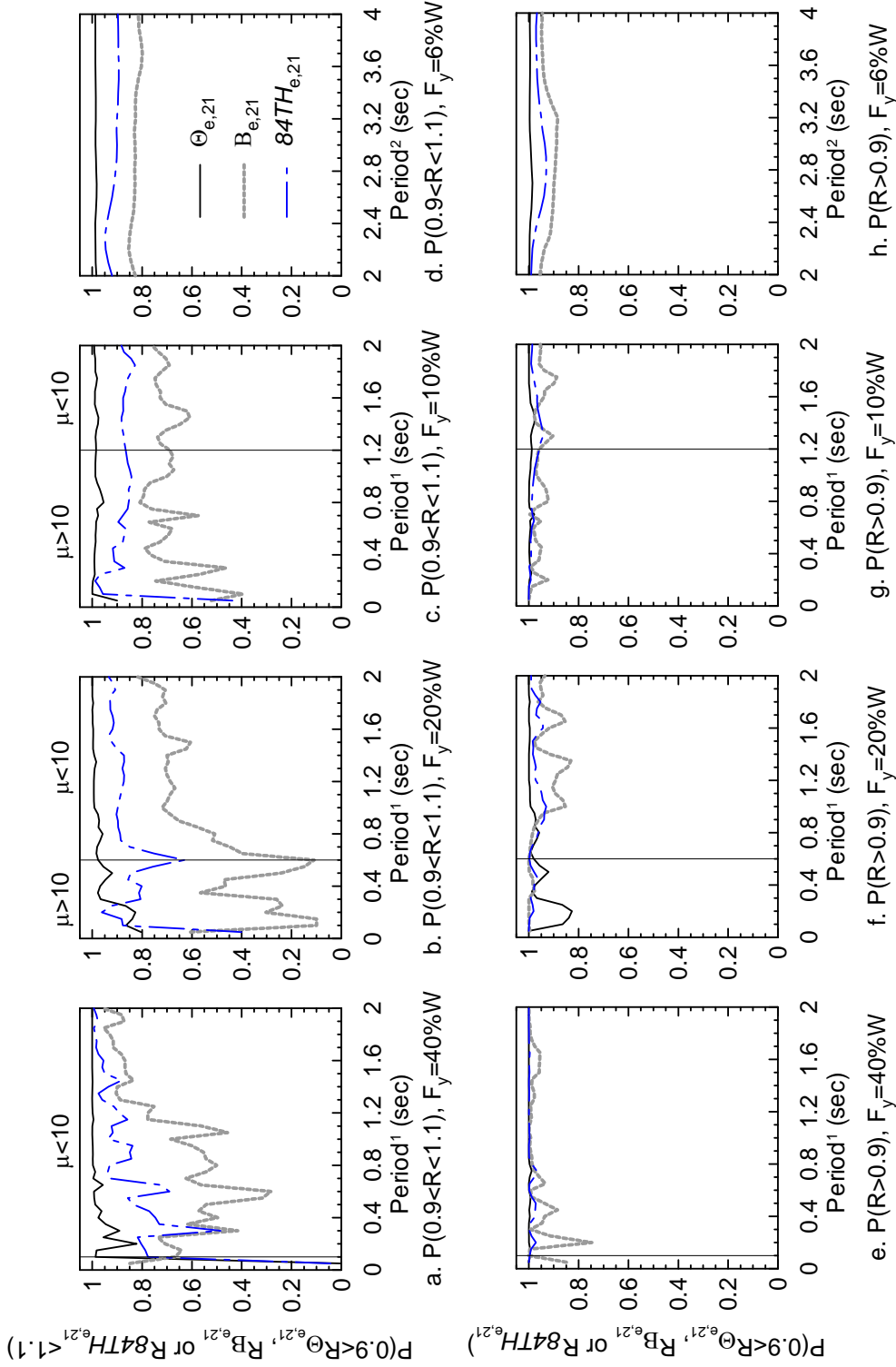


Note:

<sup>1</sup> based on pre-yield stiffness

<sup>2</sup> based on post-yield stiffness

Figure 4.37. Confidence levels for  $0.9 \leq R_{e,11} < 1.1$  and  $R_{B,11}$  or  $R_{84TH_{e,11}} \geq 0.9$  for Bin 2e ground motions

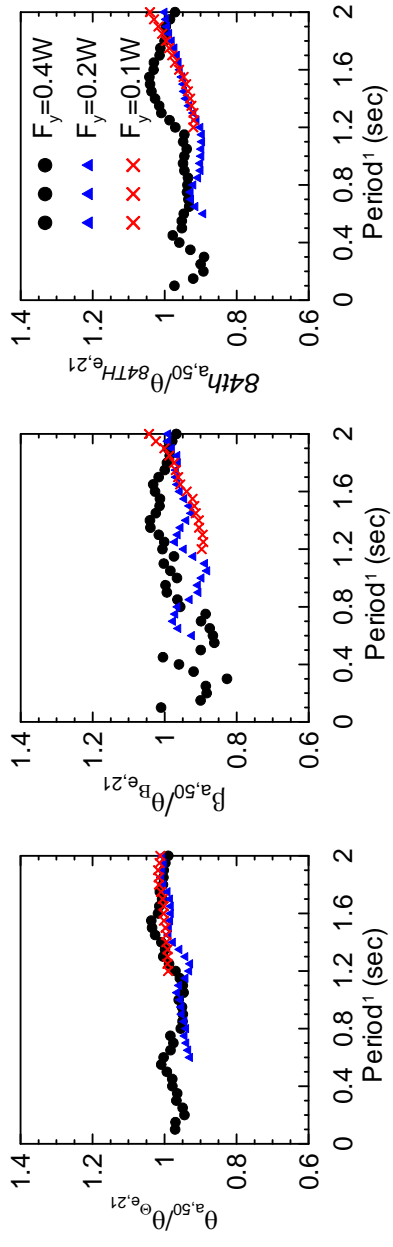


Note:

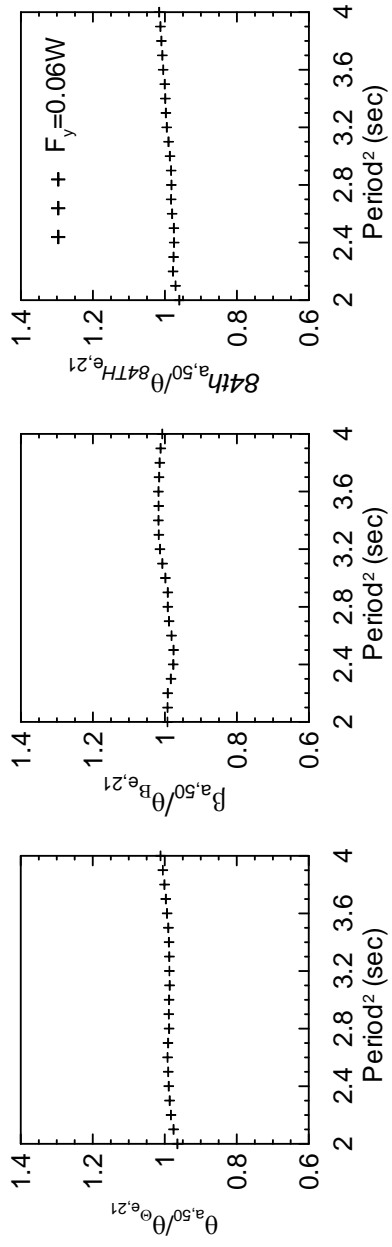
<sup>1</sup> based on pre-yield stiffness

<sup>2</sup> based on post-yield stiffness

Figure 4.38. Confidence levels for  $0.9 \leq R_{\Theta_{e,21}}, R_{B_{e,21}}, \text{ or } R_{84TH_{e,21}} \leq 1.1$  and  $R_{\Theta_{e,21}} \geq 0.9$  for Bin 2e ground motions



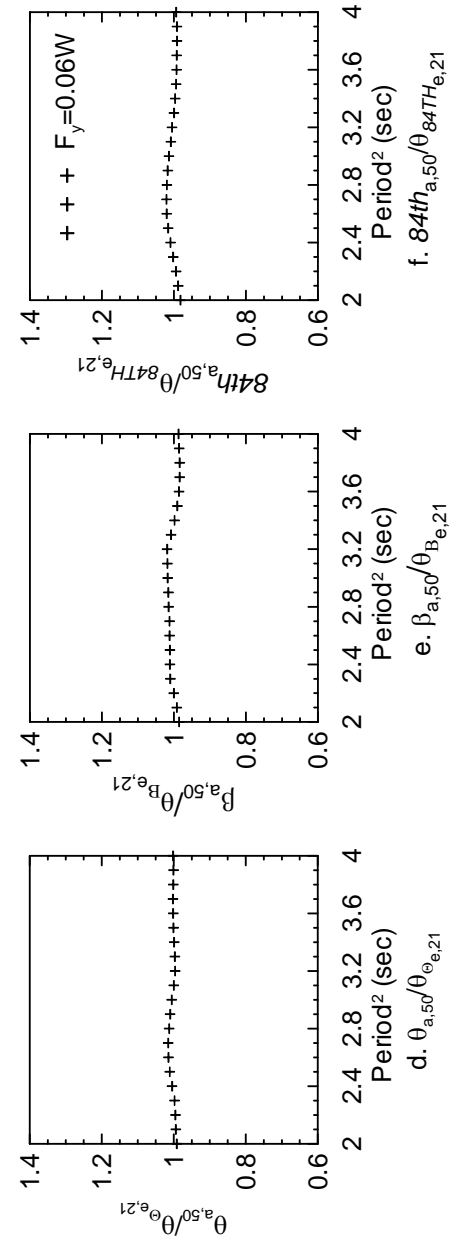
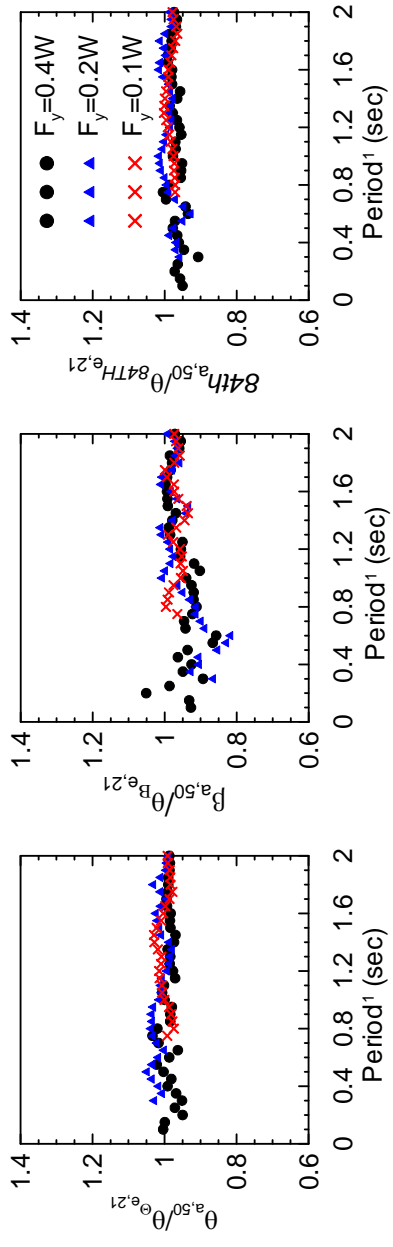
c.  $84th_{a,50}/\theta_{84TH_{e,21}}$



f.  $84th_{a,50}/\theta_{84TH_{e,21}}$

Note:  
<sup>1</sup> based on pre-yield stiffness  
<sup>2</sup> based on post-yield stiffness

Figure 4.39.  $\theta_{a,50}/\theta_{e,21}$ ,  $\beta_{a,50}/\theta_{B,e,21}$  and  $84th_{a,50}/\theta_{84TH_{e,21}}$  for Bin 1e ground motions



Note:  
 1 based on pre-yield stiffness  
 2 based on post-yield stiffness

**Figure 4.40.**  $\theta_{a,50}/\theta_{e,21}$ ,  $\beta_{a,50}/\beta_{e,21}$  and  $84th \theta_{a,50}/\theta_{84TH_{e,21}}$  for Bin 2e ground motions

An alternate procedure, which is intended to negate the need for modification factors by using actual earthquake records in the D-scaling method, is described below:

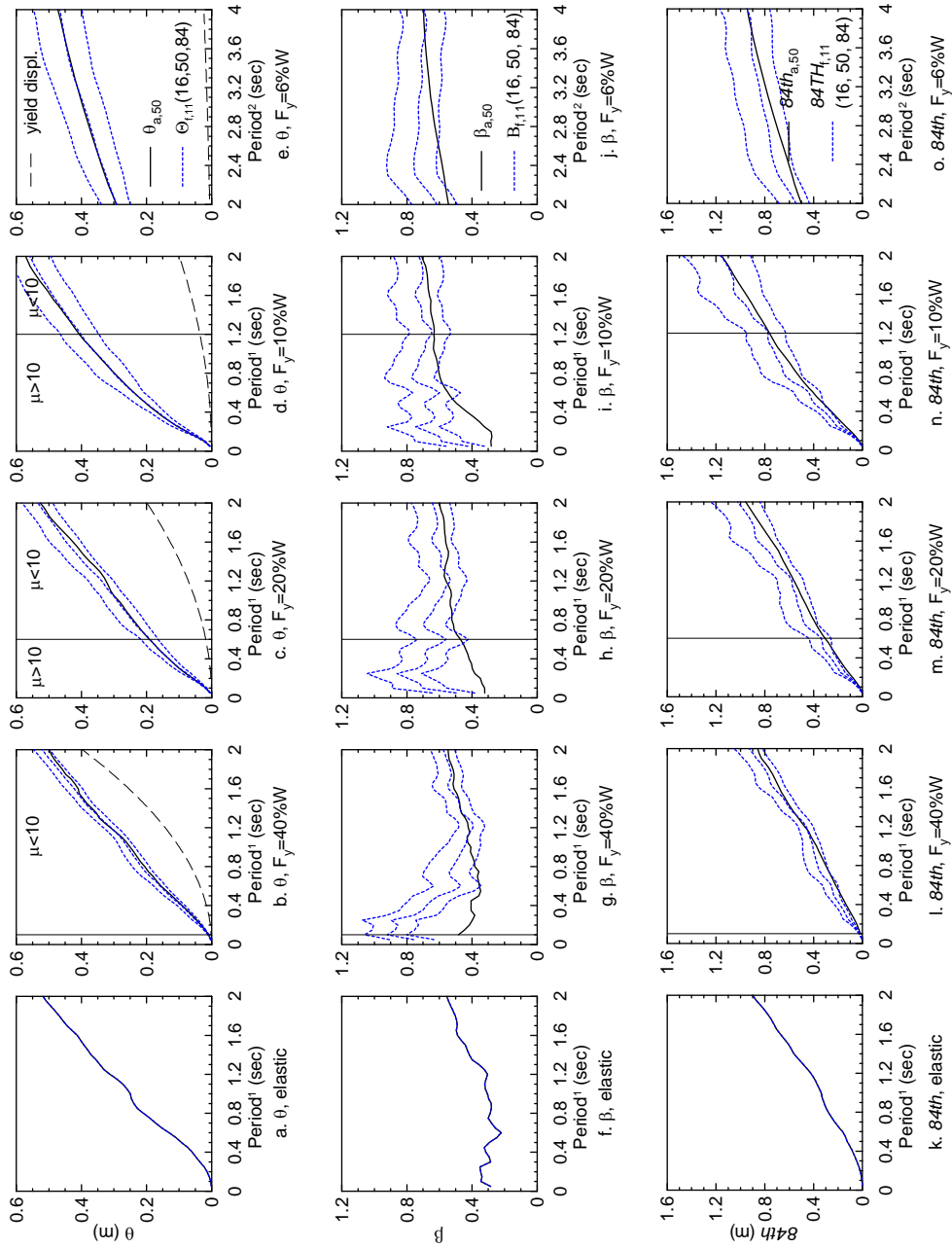
1. Generate  $n$  target spectral accelerations at the fundamental period of the analyzed structure,  $T_1$ , using (4.7).
2. Select  $n$  ground motions and calculate their spectral accelerations at period  $T_1$ .
3. Amplitude scale the  $n$  ground motions to the  $n$  target spectral ordinates: one ground motion for one target spectral value.

#### 4.3.6.2 Response-History Analysis Results

The procedure described in Section 4.3.6.1 is the same as that presented in Section 3.2.2 and has been used in the 35% draft ATC-58 Guidelines (ATC 2007) for the scenario- and time-based assessments with  $n$  equal to 11. The procedure and the use of 11 ground motions are evaluated below using analysis similar to those of Section 4.3.5.

The median ( $\theta$ ) and  $\beta$  from Bins 1a and 2a (as shown in Figure 4.8) were substituted into (4.7) to generate 11 target spectral ordinates at periods ranging between 0.05 to 4 seconds. For each analysis at each period (i.e., one trial), 11 ground motions were randomly selected from the 50 NF or FF seed motions, scaled to the 11 target spectral ordinates and then used for nonlinear analysis with the corresponding oscillator. The resulting sets of motions were labeled as Bin 1f and Bin 2f for NF and FF ground motions, respectively. Again, the period calculation was based on the pre-yield (elastic) stiffness of the oscillator, including the oscillator with yield strength equal to  $0.06W$ . Each trial produced 11 peak displacements for the oscillator, which were assumed to be lognormally distributed. The median, logarithmic standard deviation and the 84th percentile value of the 11 peak displacements were taken as sample values for three random variables  $\Theta_{f,11}$ ,  $B_{f,11}$  and  $84TH_{f,11}$ , respectively. Ten thousand trials of analysis were performed with ten thousand different combinations of the 11 ground motions to capture the distributions in  $\Theta_{f,11}$ ,  $B_{f,11}$  and  $84TH_{f,11}$  for each of the SDOF oscillators in Section 4.3.2.

Figure 4.41 and Figure 4.42 show the 16th, 50th and 84th percentiles of  $\Theta_{f,11}$ ,  $B_{f,11}$  and  $84TH_{f,11}$  together with  $\theta_{a,50}$ ,  $\beta_{a,50}$  and  $84th_{a,50}$  for NF and FF ground motions, respectively. The vertical line in the figures for  $F_y = 0.4W$ ,  $0.2W$  and  $0.1W$  denote  $\mu$  of 10. The results show that the proposed scaling procedure produces *unbiased* estimates of *median* displacement responses but



Note:  
<sup>1</sup> based on pre-yield stiffness  
<sup>2</sup> based on post-yield stiffness

Figure 4.41. Eighty-fourth, 50th and 16th percentiles of  $\theta_{f,11}$ ,  $B_{f,11}$  and  $84TH_{f,11}$  for Bin 1a motions  
 Bin 1a motions



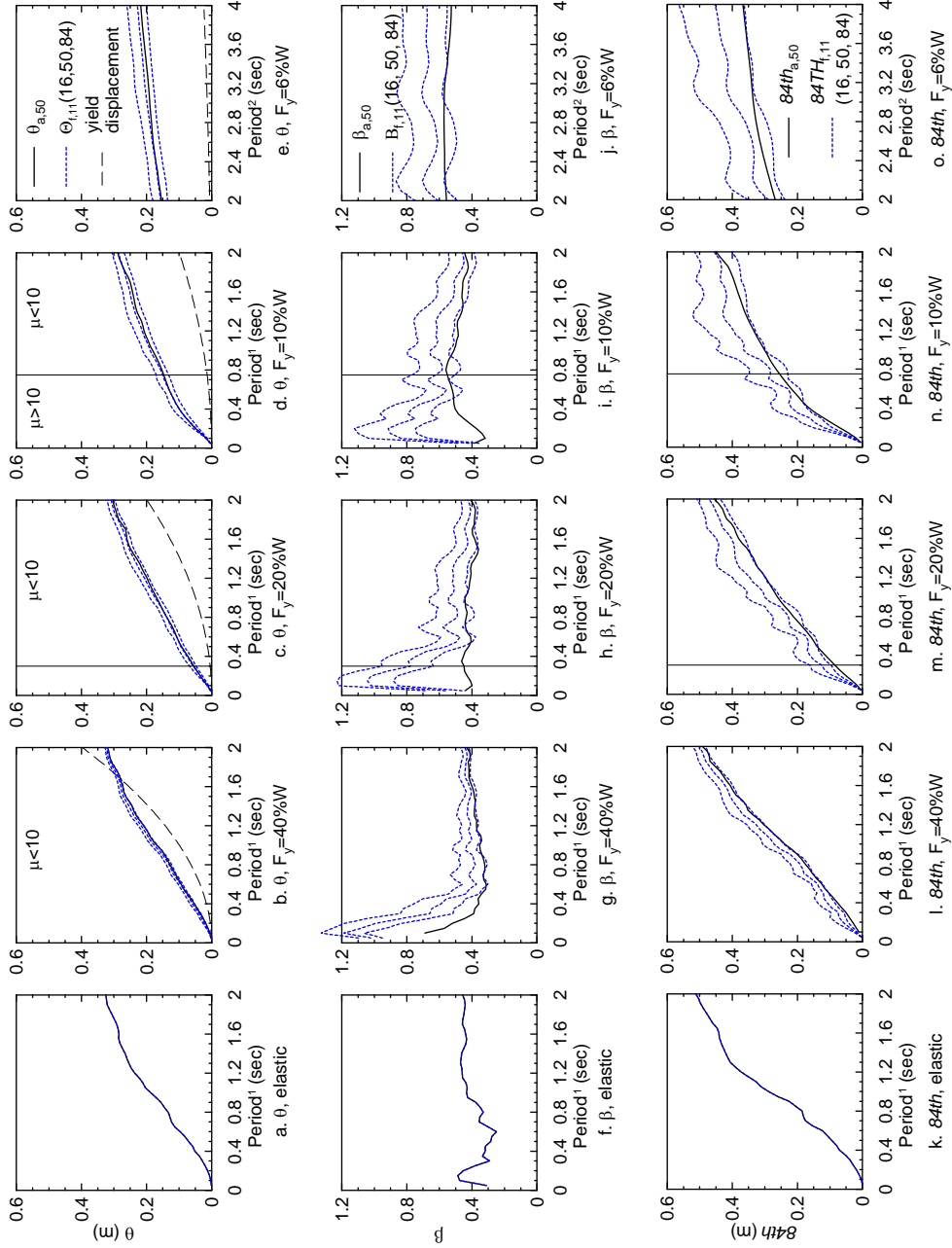
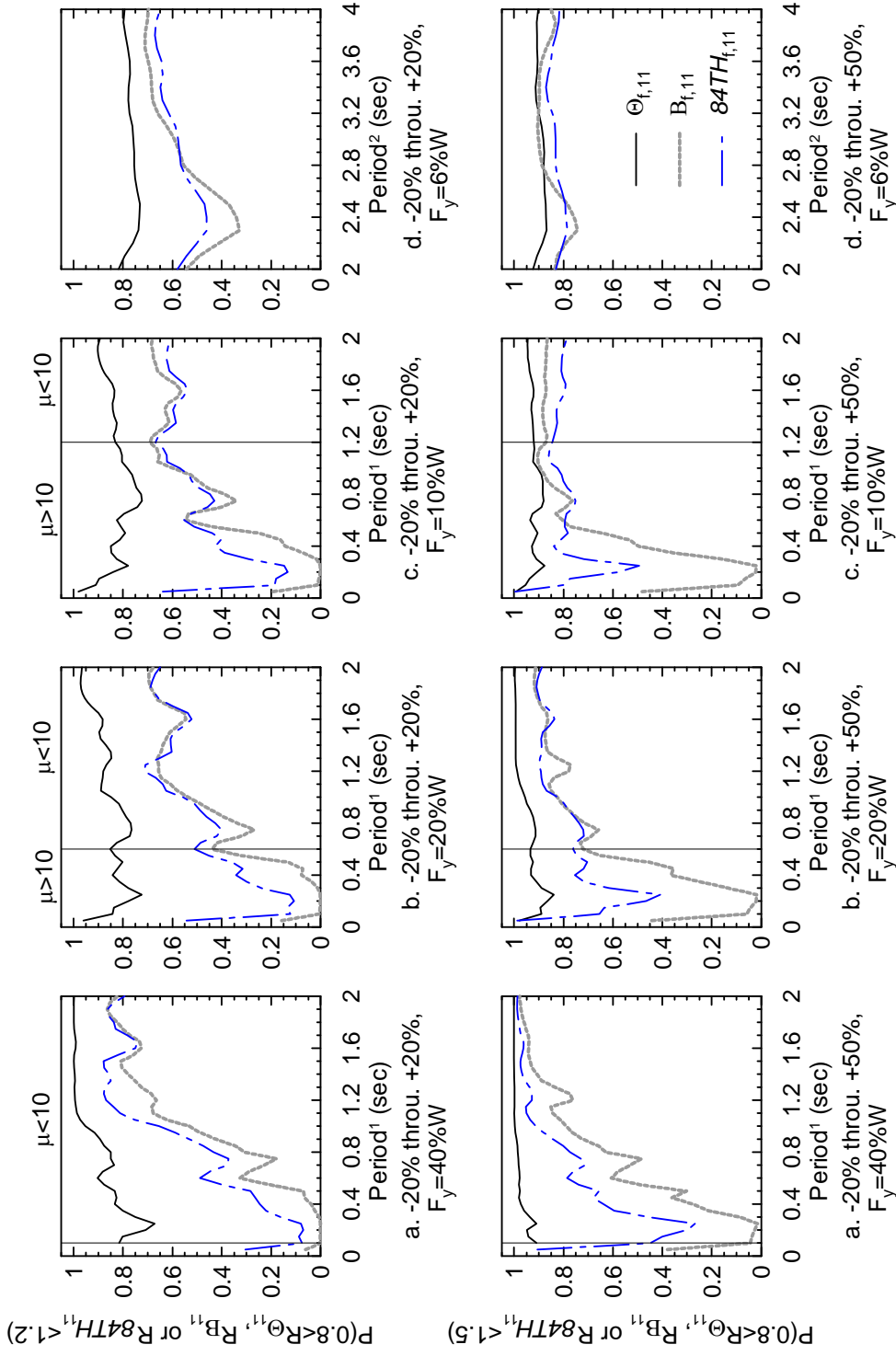


Figure 4.42. Eighty-fourth, 50th and 16th percentiles of  $\theta_{f,11}$ ,  $B_{f,11}$  and  $84TH_{f,11}$  for Bin 2f; and  $\theta_{a,50}$ ,  $\beta_{a,50}$  and  $84th_{a,50}$  for Bin 2a motions

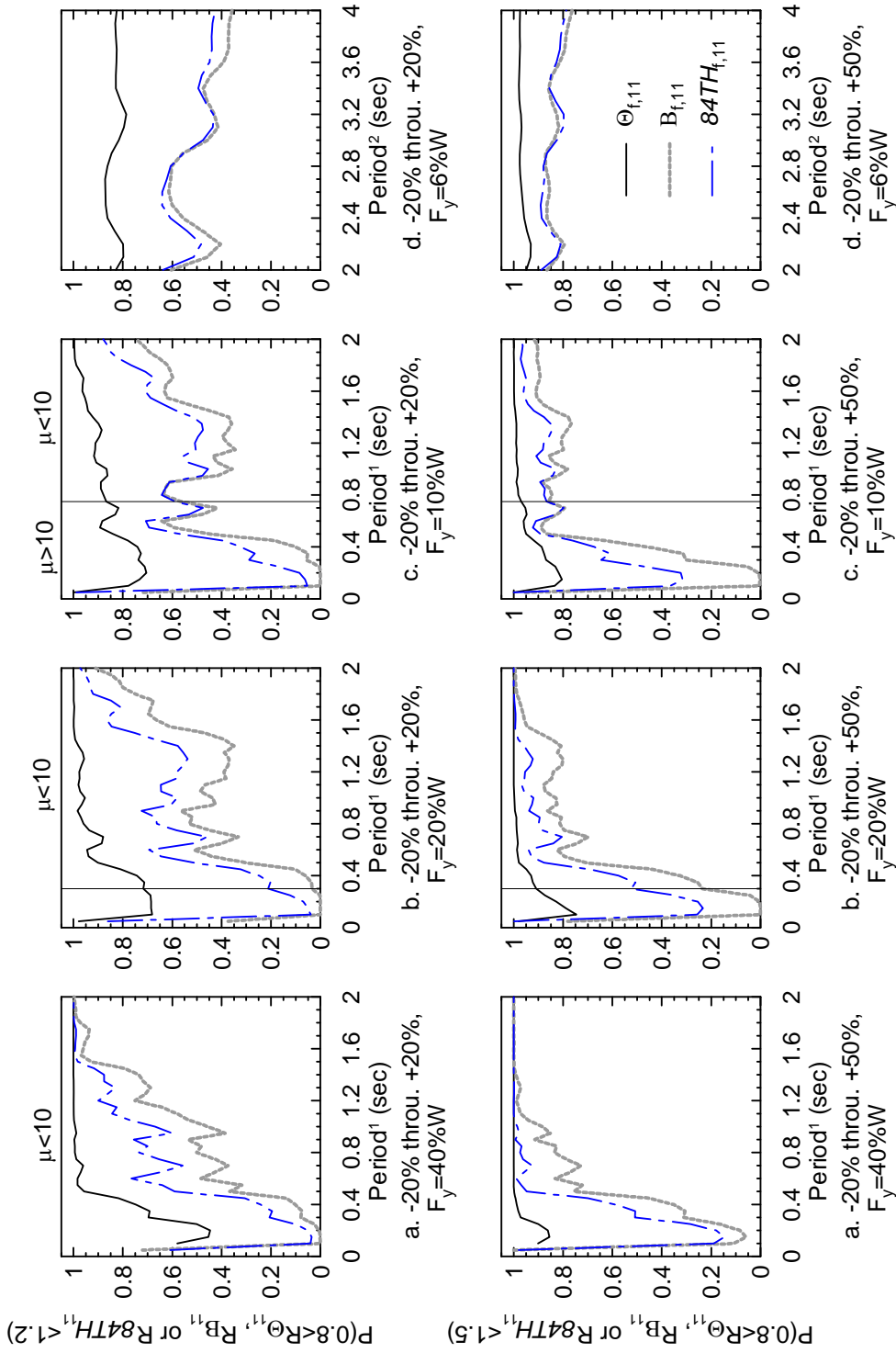
*overestimates* the *dispersions* and the *84th percentile* values for the nonlinear displacement responses (although the overestimate is insignificant for NF motions and  $F_y = 0.4W$ ,  $0.2W$  and  $0.1W$  at periods greater than 1 second).

Equations (4.8) through (4.10) were used to present results of the analysis; the subscript  $f$  denotes analysis using the Bin 1f and 2f ground motions. Two sets of probabilities are shown in Figure 4.43 and Figure 4.44. The first row in these figures presents four panels showing the probabilities that  $\Theta_{f,11}$ ,  $B_{f,11}$  and  $84TH_{f,11}$  lie between  $\pm 20\%$  of  $\theta_{a,50}$ ,  $\beta_{a,50}$  and  $84th_{a,50}$ , respectively, for nonlinear displacement response. For the cases with  $\mu$  smaller than 10, the confidence levels for  $\Theta_{f,11}$  to lie between  $\pm 20\%$  of  $\theta_{a,50}$  are greater than 80% for most oscillators except for the Bin 1f motions,  $F_y = 0.4W$  and elastic periods less than 0.4 second and for the Bin 2f motions,  $F_y = 0.4W$  and  $0.2W$  and elastic periods less than 0.5 second. For low ductility systems such as  $F_y = 0.4W$  and elastic periods greater than 1 second, the confidence levels for  $\Theta_{f,11}$  to lie between  $\pm 20\%$  of  $\theta_{a,50}$  are greater than 95%. The confidence levels for  $B_{f,11}$  and  $84TH_{f,11}$  to lie between  $\pm 20\%$  of  $\beta_{a,50}$  and  $84th_{a,50}$ , respectively, mostly vary between 40% and 80% because  $B_{f,11}$  and  $84TH_{f,11}$  overestimate  $\beta_{a,50}$  and  $84th_{a,50}$ . To illustrate the influence of this conservative bias, the probabilities for  $0.8 \leq R_{\Theta_{f,11}}, R_{B_{f,11}}, R_{84TH_{f,11}} \leq 1.5$  are presented in the second row of panels in Figure 4.43 and Figure 4.44. The confidence levels for  $B_{f,11}$  and  $84TH_{f,11}$  are greater than 80% in this range except for the Bin 1f motions,  $F_y = 0.4W$  and elastic periods less than 1 second and for the Bin 2f motions,  $F_y = 0.4W$  and elastic periods less than 0.5 second, where the overestimates produced by  $B_{f,11}$  and  $84TH_{f,11}$  are substantial. Increasing the number of ground motions beyond 11 will not eliminate the conservative bias in  $B_{f,11}$  and  $84TH_{f,11}$  but will reduce the dispersions in the two random variables and increase the confidence levels shown in Figure 4.43 and Figure 4.44.



Note:  
<sup>1</sup> based on pre-yield stiffness  
<sup>2</sup> based on post-yield stiffness

Figure 4.43. Confidence levels for  $0.8 \leq R_{\Theta}, R_B, \text{ or } R_{84TH_{f,11}} \leq 1.2$  and  $0.8 \leq R_{\Theta}, R_B, \text{ or } R_{84TH_{f,11}} \leq 1.5$  for Bin 1f motions



Note:  
<sup>1</sup> based on pre-yield stiffness  
<sup>2</sup> based on post-yield stiffness

Figure 4.44. Confidence levels for  $0.8 \leq R_{\Theta_{f,11}}, R_{B_{f,11}} \text{ or } R_{84TH_{f,11}} \leq 1.2$  and  $0.8 \leq R_{\Theta_{f,11}}, R_{B_{f,11}} \text{ or } R_{84TH_{f,11}} \leq 1.5$  for Bin 2f motions

# CHAPTER 5

## SEISMIC PERFORMANCE ASSESSMENT OF THE SAMPLE NPP REACTOR BUILDINGS

### 5.1 Introduction

The key product of the proposed performance assessment procedures for intensity- and scenario-based assessments is a mean probability of unacceptable performance. For a time-based assessment, the key product is a mean annual frequency of unacceptable performance. For a given NPP and earthquake shaking intensity, the probability of unacceptable performance is a random variable with a distribution that is a function of the demand parameters, fragility curves, and fault trees and event trees used for the assessment. The procedures proposed in this report seek to predict an unbiased estimate of the mean probability or frequency.

This chapter presents procedures for and results of seismic performance assessments of the four NPP models (Models 1 through 4) developed in Chapter 2. The four models were developed to represent a conventionally constructed NPP (Model 1) and three base isolated NPPs, where the isolators used are Friction Pendulum<sup>TM</sup> type sliding bearings (Model 2), lead-rubber bearings (Model 3) and low damping rubber bearings equipped with a supplemental damping system (Model 4). The three goals of the chapter are 1) to provide examples for the assessment procedures proposed in Chapter 3 for conventional and base isolated NPPs, 2) to evaluate the reliability of several key steps in the procedure for computing the probability of unacceptable performance, and 3) to identify the utility of base isolation to reduce the annual frequency of unacceptable performance of NPPs.

Uncertainty in the mechanical properties of the superstructure and isolator models was not considered for the analysis reported herein although the procedures can easily accommodate such uncertainty as described in Chapter 3. Best estimate mechanical properties were used to define the models.

The intensity-, scenario- and time-based assessments are presented in Sections 5.2, 5.3 and 5.4, respectively. The scenario- and time-based assessments were performed for Models 1 through 4. The intensity-based assessment was performed for Model 1 only. Each section includes the characterization of seismic hazard, scaling of ground motions, results of response-history analysis

and the computation of either a mean probability of unacceptable performance or a mean annual frequency of unacceptable performance.

## **5.2 Intensity-Based Assessment of the Conventional Reactor Building**

### **5.2.1 Safe Shutdown Earthquake**

#### *5.2.1.1 Procedures in Design Guidelines*

The seismic hazard for intensity-based assessment of the sample NPP is characterized by a Safe Shutdown Earthquake (SSE). This subsection introduces two procedures in use at this time for characterizing SSE shaking.

#### *USNRC Regulatory Guide 1.165*

Title 10, Chapter I, of the Code of Federal Regulations (denoted as 10 CFR) presents requirements binding on all persons and organizations who receive a license from U. S. Nuclear Regulatory Commission (NRC) to operate nuclear facilities (USNRC 2004). Appendix S of 10 CFR, Section 50 requires that the safety-related structures, systems, and components (SSCs) for a NPP must be designed to remain functional and within applicable stress, strain, and deformation limits for a SSE. Section 100.23 of 10 CFR requires that the SSE be characterized through an appropriate analysis, such as a probabilistic seismic hazard analysis (PSHA) or suitable sensitivity analysis, to include the uncertainty inherent in ground motions.

The NRC Regulatory Guide 1.165 (USNRC 1997) includes a *hazard-based* procedure that is acceptable to the NRC staff and satisfies the requirements of 10 CFR 100.23 for determining the SSE spectrum. The procedure includes following steps:

1. Perform a PSHA for the NPP site.
2. Compute the deaggregation results of the seismic hazard identified in 1.
3. Determine the controlling earthquakes.
4. Compute the spectral demands for the controlling earthquakes of 3.
5. Determine the shape and magnitude of the SSE spectrum based on the results of 4.

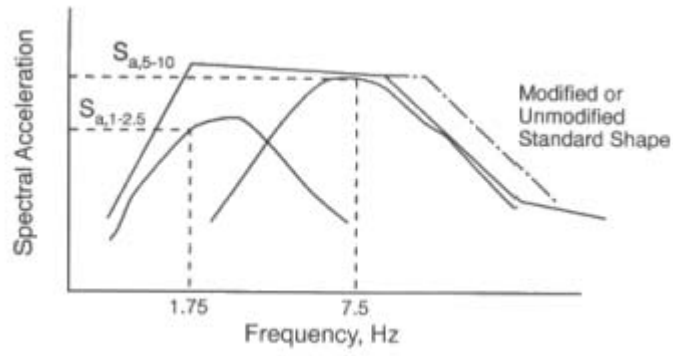
In Step 1, a site-specific PSHA is performed to compute the five-percent damping seismic hazard curves at 1, 2.5, 5 and 10 Hz for the NPP site. The spectral ordinates for the average of 5 and 10 Hz (denoted as  $S_{5-10}$ ) and for the average of 1 and 2.5 Hz (denoted as  $S_{1-2.5}$ ) are determined using the median hazard curves for the four frequencies at a annual frequency of exceedance of  $10^{-5}$ , which is termed the reference probability in Regulatory Guide 1.165.

In Step 2, the seismic hazard is deaggregated for each of the four spectral ordinates at 1, 2.5, 5 and 10 Hz identified in Step 1. The deaggregation results for each spectral ordinate include the values of median annual exceeding probability for 5 magnitude bins ranging between 5 and 7+ and for 7 distance bins ranging between 0 and 300+ km. The deaggregation results for 1 and 2.5 Hz are averaged and denoted herein as  $D_{1-2.5}$ ; and those for 5 and 10 Hz are averaged and denoted herein as  $D_{5-10}$ .

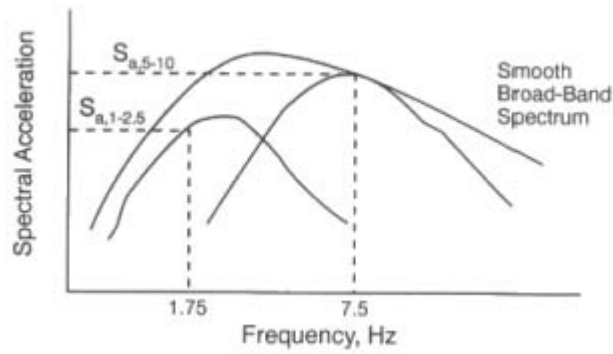
In Step 3, the controlling earthquake is determined by the mean magnitude-distance pair of  $D_{5-10}$ . If the contribution to the hazard for distances of 100 km or greater in  $D_{1-2.5}$  exceeds 5%, a second controlling earthquake must be developed to identify a distant and larger event that may control the spectral demand in the long-period range of a design spectrum. The second controlling earthquake is determined by the mean magnitude-distance pair identified from the data of  $D_{1-2.5}$  for distances greater than 100 km.

In Step 4, attenuation relationships appropriate for the source and the NPP site under consideration are used to develop a median site-specific spectral shape for each controlling earthquake. The median spectral shape for the first controlling earthquake is amplitude scaled to  $S_{5-10}$  at a frequency of 7.5 Hz. If a second controlling earthquake is developed, its median spectral shape is amplitude scaled to  $S_{1-2.5}$  at a frequency of 1.75 Hz.

In the final step, the SSE spectrum is established by enveloping the site-specific spectrum (or spectra if two controlling earthquakes are used). The appropriate spectral shape can be the site-specific spectral shape developed for the controlling earthquakes, a standard broad-band spectral shape (see panel a of Figure 5.1), or a smooth broad-band spectral shape (see panel b of Figure 5.1). Figure 5.2 presents a standard broad-band spectrum: the design spectrum defined in Regulatory Guide 1.60 (USAEC 1973), which was commonly used to establish the SSE spectrum before Regulatory Guide 1.165 was issued.



a. Use of a standard shape



b. Use of a specific smooth shape

**Figure 5.1. Development of the SSE spectrum (USNRC 1997)**

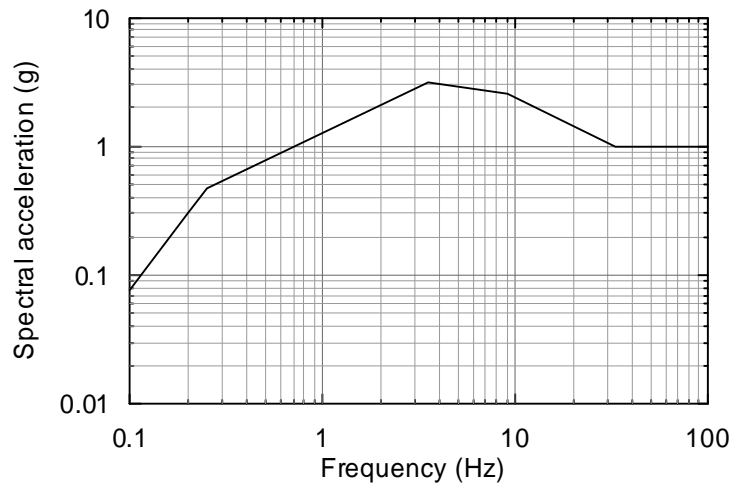


**Figure 5.2. Horizontal design response spectrum of USNRC Regulatory Guide 1.60 for a damping ratio of 5%, normalized to a peak ground acceleration of 1 g (USAEC 1973)**



ASCE Standard 43-05

An alternative procedure for establishing a SSE spectrum uses the *performance-based* approach defined in ASCE Standard 43-05 (ASCE 2005). Instead of developing a *hazard-consistent* design spectrum, this procedure seeks to generate a *risk-consistent* spectrum, where each of the spectral ordinates represents the same frequency of unacceptable seismic performance.

In ASCE Standard 43-05, the uniform-risk spectrum (URS) is developed by scaling the ordinates of a uniform-hazard spectrum (UHS) by period-dependent scale factors, SF:

$$\text{URS} = \text{UHS} \times \text{SF} \quad (5.1)$$

$$\text{SF} = \text{larger of } \left\{ 1, 0.6 \cdot A_R^{0.8} \right\} \quad (5.2)$$

where  $A_R$  is a factor related to the slope of the hazard curve and defined by the ratio of ground motion intensities corresponding to a ten-fold reduction in the annual frequency of exceedance used to develop the UHS, namely, if the annual frequency of exceedance for the UHS in (5.1) is  $H$ , the use of the URS in design will result in an annual frequency of unacceptable performance of  $0.1H$ .

The technical basis for the procedure is provided in Kennedy and Short (1994). The risk (or the mean annual frequency of unacceptable performance) is computed using:

$$P_F = -\int_0^\infty \frac{d\lambda(a)}{da} P_{F|a} da \quad (5.3)$$

where  $\lambda(a)$  represents a seismic hazard curve that plots the mean annual frequency of exceed a specified ground motion parameter versus that parameter (e.g., spectral acceleration at 1 Hz) and  $P_{F|a}$  is a fragility curve, representing the conditional probability of unacceptable performance given a level of ground motion. Both the seismic hazard curve and the fragility curve are defined in terms of a ground motion parameter,  $a$ . A combination of  $\lambda(a)$  and  $P_{F|a}$  will determine a value of  $P_F$ . Kennedy and Short (1994) performed a series of parametric studies to characterize the relationship between the hazard,  $\lambda(a)$ , and the risk,  $P_F$ . They showed that the ratio of hazard to risk is about 10 (see above) if the seismic demand for the design of NPPs is determined by (5.1) and (5.2).

### 5.2.1.2 The Target Design Spectrum for this Study

The hypothetical NPP analyzed in this report is sited near Richmond, Virginia, in the Eastern United States. The target design spectrum used for the intensity-based assessment is a URS prepared for an Early Site Permit (ESP) report for a nearby NPP site. Figure 5.3 presents the URS, which was established using the performance-based approach described in Section 5.2.1.1.

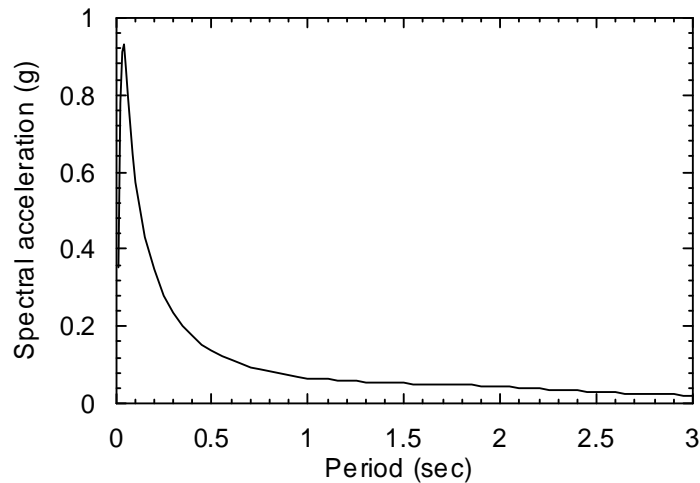


**Figure 5.3. The URS for the sample NPP reactor building for a MAFE of  $10^{-5}$**

The calculations for the URS of Figure 5.3 at periods of 0.01, 0.04, 0.1, 0.2, 0.4, 1 and 2 seconds are summarized in Table 5.1 using the data presented in the ESP report. In Table 5.1, the spectral accelerations corresponding to the mean annual frequencies of exceedance (MAFE) of  $10^{-4}$  and  $10^{-5}$  are reported; the values of  $A_R$  are the ratio of the spectral ordinates for MAFE of  $10^{-5}$  to  $10^{-4}$ ; the SF values are calculated using (5.2); and each spectral ordinate for URS in the sixth column is the product of the values in the second and fifth columns. Since the values in the second column (spectral accelerations for a MAFE of  $10^{-4}$ ) are used to establish the URS, the URS of Figure 5.3 corresponds to an annual frequency of unacceptable performance of  $10^{-5}$ . Table 5.1 also presents the spectral ordinates of the UHS with a MAFE of  $5 \times 10^{-5}$ . The URS is more similar to the UHS with a MAFE of  $5 \times 10^{-5}$  than to that with a MAFE of  $10^{-5}$ .

Table 5.1 presents calculations for seven spectral ordinates for the SEE spectrum. In the ESP report, the attenuation relationship of McGuire et al. (2001) for CEUS sites was used to generate a

realistic spectral shape for the URS.<sup>1</sup> The dotted line in Figure 5.4 presents the median spectrum predicted by the attenuation relationship of McGuire et al. (2001) using a moment magnitude of 5.5, a site-to-source distance of 20 km and a PGA of 0.351 g<sup>2</sup>. The magnitude-distance pair used herein was identified using the average deaggregation results for 5- and 10-Hz hazard curves at a MAFE of  $5 \times 10^{-5}$ . The URS of Figure 5.3, which is re-plotted in Figure 5.4 using a solid line, was established by scaling the dotted line using period-dependent scale factors. The scale factor at each of the seven periods of 0.01, 0.04, 0.1, 0.2, 0.4, 1 and 2 seconds was determined as the ratio of the URS spectral ordinate of Table 5.1 to the spectral ordinate of the dotted line. The scale factors for the intermediate periods were based on linear interpolation of the seven scale factors at the seven periods. For example, the spectral ordinates of the dotted line at 0.04 and 0.1 second are 0.841 and 0.569 g, respectively, and scaled by the factors of 1.11 and 1.01 to be 0.93 and 0.574 g, respectively. The spectral ordinate of the dotted line at an intermediate period between 0.04 and 0.1 second was scaled by a factor between 1.11 and 1.01 depending on the distance between the intermediate period and 0.04 (or 0.1) second.

**Table 5.1. Calculations of the URS of Figure 5.3**

Period (sec)	UHS (MAFE= $10^{-4}$ ) (g)	UHS (MAFE= $10^{-5}$ ) (g)	$A_R$	SF	URS (g)	UHS (MAFE= $5 \times 10^{-5}$ ) (g)
0.01	0.214	0.753	3.52	1.64	0.351	--
0.04	0.569	1.990	3.50	1.63	0.930	--
0.1	0.373	1.216	6.26	1.54	0.574	0.547
0.2	0.235	0.735	3.13	1.49	0.350	0.339
0.4	0.120	0.364	3.03	1.46	0.175	0.170
1	0.046	0.134	2.89	1.40	0.065	0.065
2	0.030	0.094	3.17	1.51	0.045	--

<sup>1</sup> This step is not required in the performance-based approach of ASCE Standard 43-05, which only involves the scaling of a UHS using period-dependent factors to develop a URS.

<sup>2</sup> Rather than predicting the spectral acceleration for a given scenario case, the attenuation relationship of McGuire et al. (2001) predicts the ratio of spectral acceleration at a given period to peak ground acceleration. The dotted line presented in Figure 5.4 was back-calculated from the predicted ratio using a PGA of 0.351 g: the spectral ordinate of the URS at a period of 0.01 second.

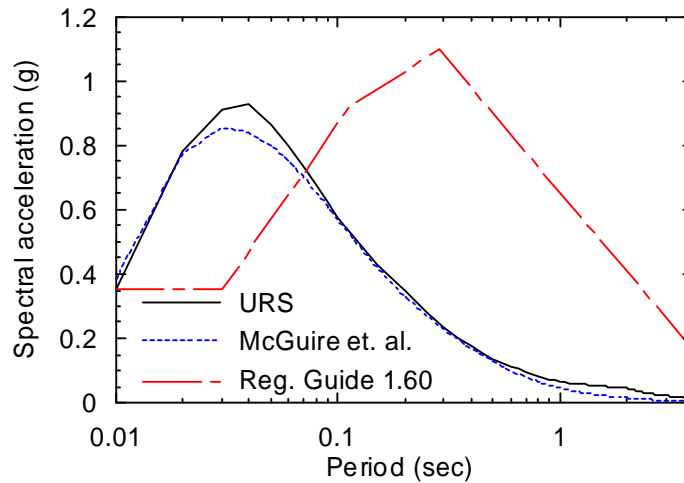


**Figure 5.4. The spectra established using a) the performance-based procedure; b) the attenuation model of McGuire et al. (2001), magnitude of 5.5, distance of 20 km and PGA of 0.351 g; and c) the Regulatory Guide 1.60 with PGA of 0.351 g**

Figure 5.4 also presents the spectrum of Regulatory Guide 1.60 with the PGA scaled to 0.351 g. The URS has significantly greater demand than the scaled spectrum of Regulatory Guide 1.60 at periods smaller than 0.07 second, which is a period range of importance to secondary systems in NPPs. Figure 5.4 shows that the spectral shape of Regulatory Guide 1.60 is inappropriate for the sample NPP site of this study.

## 5.2.2 Selection and Scaling of Ground Motions

### 5.2.2.1 Ground Motions from Tables 4.1 and 4.2

The scaling procedure of Section 3.3.4.1 was used to scale the ground motions for the intensity-based assessment of the sample NPP. Two bins of eleven ground motions were randomly selected from the ground motions of Tables 4.1 and 4.2, respectively, and scaled to the URS at the first mode period of the internal structure of the sample NPP (=0.14 second). Figure 5.5 presents the median spectra of the two bins of ground motions and the URS. The shapes of the median spectra of the two bins greatly differ from that of the URS. The median spectra of the two bins have significantly smaller high-frequency demands than the URS and much greater spectral demands at periods greater than 0.14 second.

One important reason for the difference in spectral shapes evident in Figure 5.5 is the different characteristics of East and West Coast ground motions in the United States. All of the ground

motions in Table 4.2 are West Coast records and most ground motions in Table 4.1 were recorded at or modified for West Coast sites. Another bin of ground motions, which are more appropriate for East Coast sites, is introduced in the following subsection.

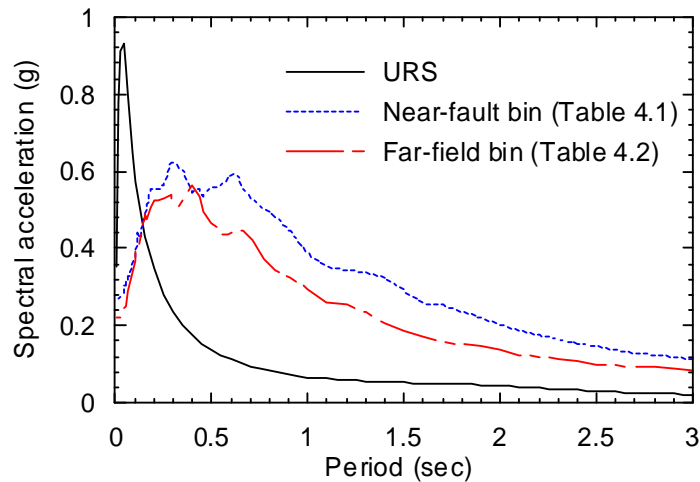


**Figure 5.5.** The URS for the sample NPP and the median spectra of the two bins of 11 ground motions randomly selected from Tables 4.1 and 4.2 and scaled to the URS at a period of 0.14 second

#### 5.2.2.2 Ground Motions generated by SGMS

Earthquake histories from large magnitude events in the Central and Eastern United States (CEUS) have not been recorded. The computer code “Strong Ground Motion Simulation (SGMS)” (Halldorsson 2004) was used to generate CEUS-type ground motions for response-history analysis. The SGMS code is based on the Specific Barrier Model, which provides a complete and self-consistent description of the heterogeneous earthquake faulting process and can be applied both in the near-fault and far-field regions (Halldorsson and Papageorgiou 2006). The specific barrier model has been calibrated to generate ground motions for different tectonic regimes and can capture the rich high-frequency content in CEUS ground motions (Halldorsson and Papageorgiou 2005).

The SGMS code requires the user to provide information for the site condition and the magnitude and distance for the scenario event of interest to simulate ground motions. It provides two soil types for the CEUS: generic very hard rock ( $\bar{V}_{30} = 2900$  m/s) and the NEHRP (FEMA 2004) B-C boundary ( $\bar{V}_{30} = 760$  m/s). The former was used herein based on the information from the

geotechnical survey presented in the ESP report. The controlling  $[M, r]$  pair for the ground motions can be determined by deaggregating the seismic hazard at the period of interest.

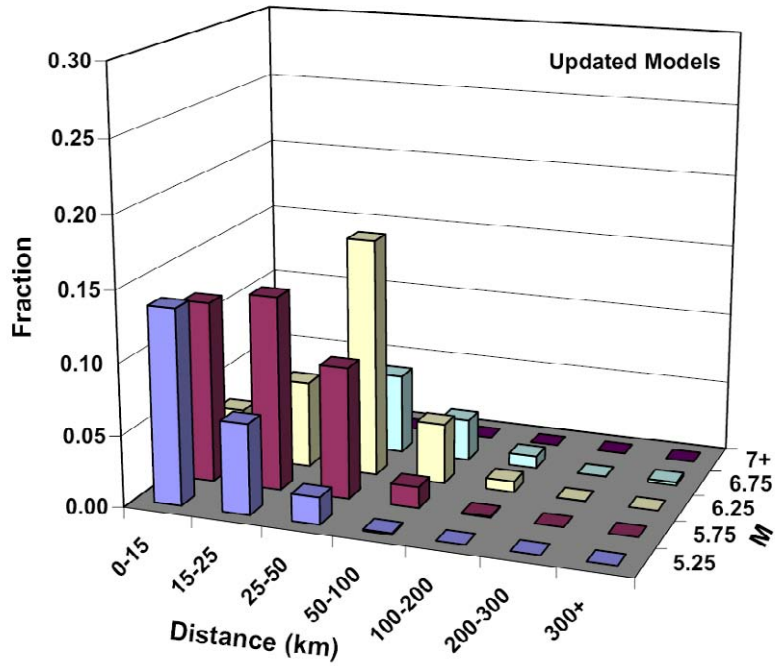
Figure 5.6, excerpted from the ESP report, presents deaggregation results for  $S_{1-2.5}$  and  $S_{5-10}$  (see Section 5.2.1.1) for the sample NPP site using the procedure described in Regulatory Guide 1.165. The spectral demands,  $S_{1-2.5}$  and  $S_{5-10}$ , were characterized from the seismic hazard curves for the sample NPP site at a MAFE of  $10^{-5}$ . The modal  $[M, r]$  pair (the  $[M, r]$  pair with the highest contribution to the seismic hazard) for  $S_{1-2.5}$  is  $M = 6.25$  and  $r = 25$  through 50 km as shown in Figure 5.6a and that for  $S_{5-10}$  is  $M = 5.25$  and  $r = 0$  through 15 km as shown in Figure 5.6b. The contribution of 100+ km earthquakes to the  $S_{1-2.5}$  hazard is less than 2% and thus the  $[M, r]$  pairs for those scenarios were not considered herein per USNRC Regulatory Guide 1.165.

Since the fundamental period of the internal structure of the sample NPP is 0.14 second, a magnitude of 5.3 and a distance of 7.5 km (the average of 0 and 15 km) was used in SGMS to generate ground motions for the NPP site. Eleven ground motions were generated using SGMS and scaled to the URS of Figure 5.3 at a period of 0.14 second. Figure 5.7 presents the response spectra for all 11 scaled ground motions generated using SGMS. Figure 5.8 presents the median spectrum of the 11 scaled ground motions and the URS. The two spectra in Figure 5.8 agree well with each other at periods smaller than 0.4 second. For periods greater than 0.4 second, the median spectral ordinates of the 11 scaled ground motions are smaller than the URS demands since the governing earthquakes for the short- and long-period spectral demands are controlled by different  $[M, r]$  pairs. The 11 scaled ground motions were used in the response-history analysis for intensity-based assessment of Model 1.

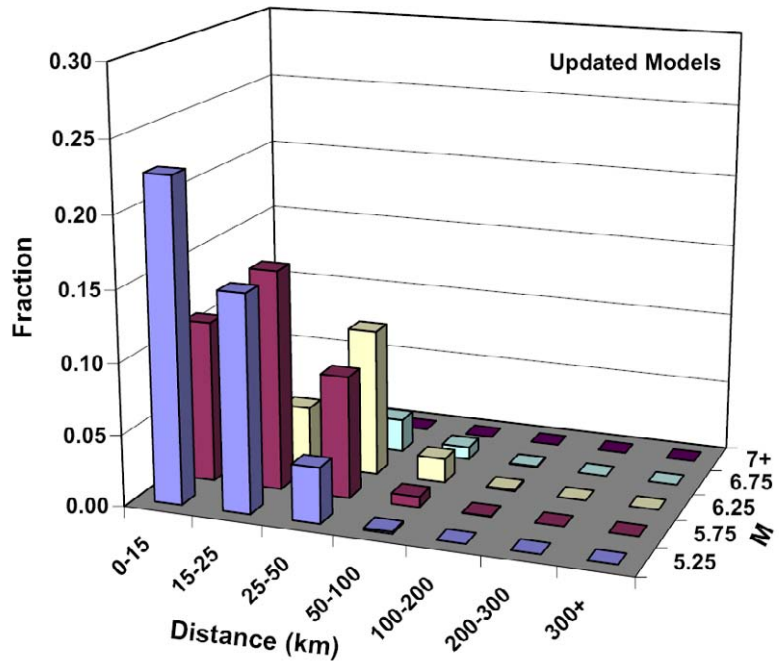
### ***5.2.3 Development of Fragility Curves for the Secondary Systems in the Sample NPP***

#### ***5.2.3.1 Demand Parameter, Median and Logarithmic Standard Deviations***

Due to the lack of fragility data for key NPP secondary systems in the open literature, sample fragility curves were developed for the secondary systems identified in Chapter 2 and used in the performance assessment presented in this chapter. The demand parameter, median ( $\hat{a}$ ) and logarithmic standard deviations ( $\beta_r$  and  $\beta_u$ ) for the sample fragility curves are introduced in this subsection. Section 5.2.3.2 presents the developed fragility curves and evaluates their appropriateness.



a. Deaggregation of  $S_{1-2.5}$  (1 and 2.5 Hz)



b. Deaggregation of  $S_{5-10}$  (5 and 10 Hz)

Figure 5.6. Deaggregation of  $S_{1-2.5}$  and  $S_{5-10}$  at an annual frequency of exceedance of  $10^{-5}$  for the sample NPP site

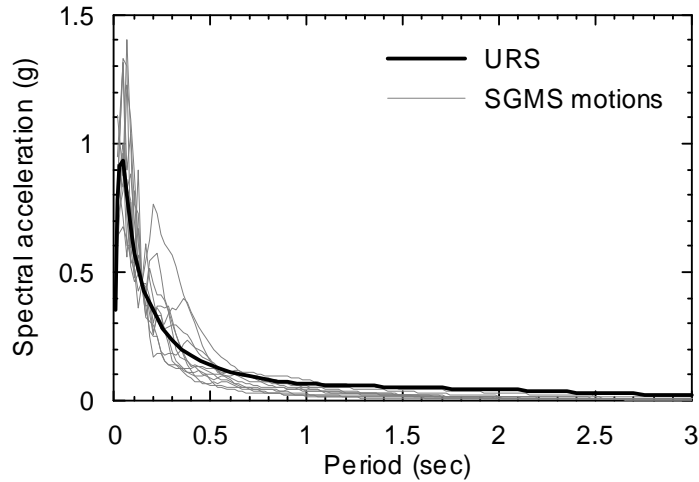


**Figure 5.7.** The URS for the sample NPP and the response spectra of the 11 ground motions generated by SGMS and scaled to the URS at a period of 0.14 second

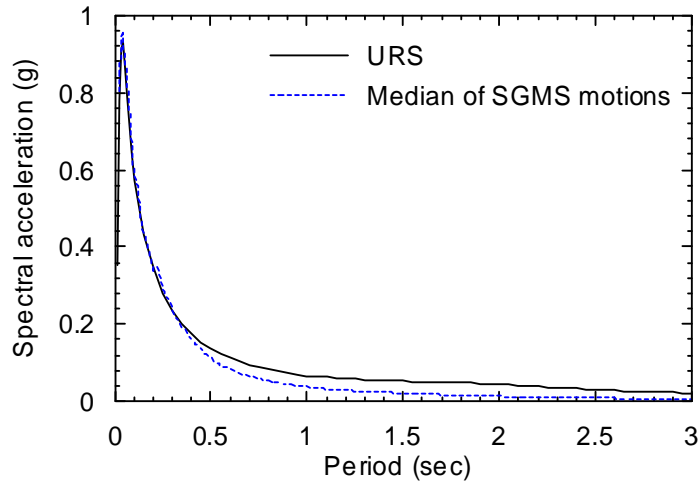


**Figure 5.8.** The URS for the sample NPP and the median spectrum of the 11 ground motions generated by SGMS and scaled to the URS at a period of 0.14 second

#### *Demand Parameter*

The demand parameter used to develop fragility curves for the secondary systems in the sample NPP is Average Floor Spectral Acceleration over 5 through 33 Hz, termed AFSA herein<sup>3</sup>, since the seismic demands on secondary systems in NPPs are characterized typically using a floor response spectrum and the frequencies of most secondary systems are in the range of 5 through 33

---

<sup>3</sup> The AFSA at a given node of the sample NPP for a response-history analysis is defined by the arithmetic mean of the 29 floor spectral ordinates at frequencies of 5 through 33 Hz with increments of 1 Hz.



Hz. (For a project specific application, any demand parameter could be used but fragility curves would have to be constructed for that parameter.)

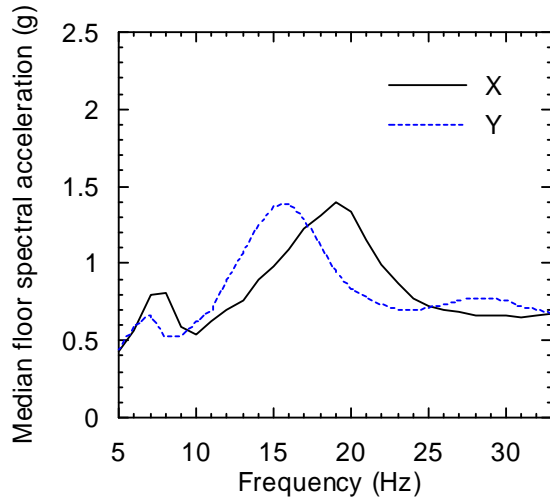
The six key secondary systems identified in Chapter 2 for the sample reactor building are supported at elevations of 7 m (Node 201), 18 m (Nodes 1006 and 1009) and 39 m (Nodes 215 and 216); see Table 2.1 for more information. This study focuses on the secondary systems supported at Nodes 201, 1009 and 216, due to the symmetrical shape of the sample NPP and the similar seismic demands at Nodes 1006 and 1009 and at Nodes 215 and 216.

Since fragility curves for the secondary systems were not available, curves were constructed using a HCLPF-based procedure based on demands from elastic analysis of the conventional NPP and dispersions from the studies of Kennedy and Ravindra (1984). The values of AFSA at Nodes 201, 1009 and 216 of Model 1 subjected to the 11 scaled SGMS ground motions of Figure 5.7 in the X and Y directions were computed first. The results of this set of response-history analyses are shown in Figure 5.9, where panels a, b and c present the median of the 11 floor spectral accelerations in the X and Y directions between 5 and 33 Hz at Nodes 201, 1009 and 216, respectively, and panel d presents the 84th, 50th and 16th percentiles of AFSA at the same nodes. Table 5.2 presents the 11 values of AFSA and the medians in the X and Y directions at each of the three nodes.

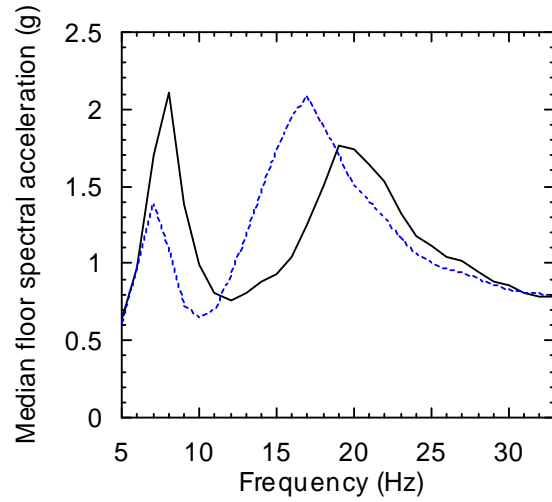
#### *Median and Logarithmic Standard Deviations*

A family of fragility curves was developed for the key secondary systems supported at each of Nodes 201, 1009 and 216 using (3.5), which requires a set of  $\hat{a}$ ,  $\beta_r$  and  $\beta_u$ . In this study, it was assumed that the secondary systems at a given node have the same fragility curves in the X and Y directions and are designed to have the HCLPF values equal to the median AFSA presented in the last row of Table 5.2. In Table 5.2, the median values in both the X and Y directions at a node are presented and the greater of the two was used in developing the fragility curves for the secondary systems at the node; that is, the HCLPF values of the secondary systems at Nodes 201, 1009 and 216 were assumed to be 0.84, 1.17 and 2.61 g, respectively. The values of  $\hat{a}$  were computed using (5.4), which is a rearrangement of (3.6):

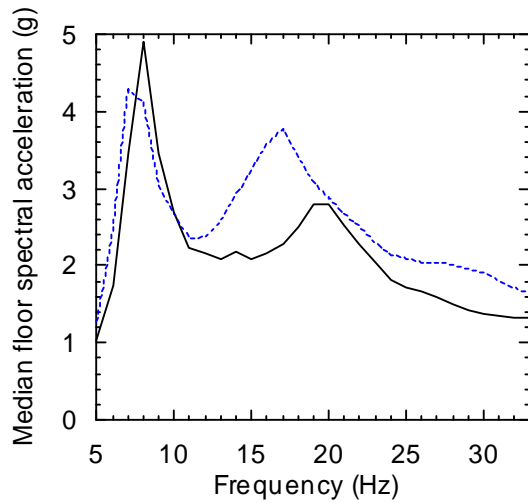
$$\hat{a} = \text{HCLPF} \cdot e^{1.65(\beta_r + \beta_u)} \quad (5.4)$$



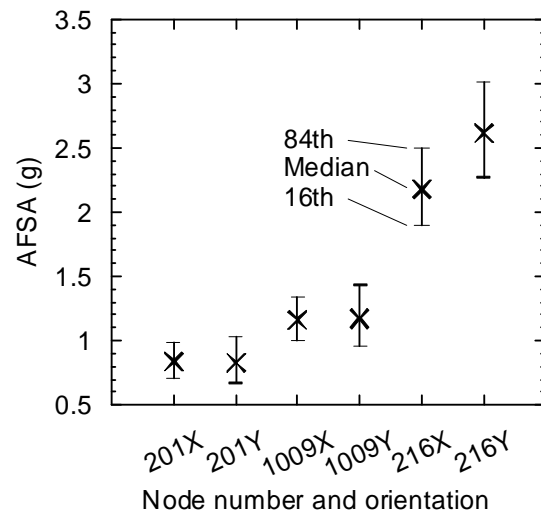
a. Median floor spectral accelerations, Node 201



b. Median floor spectral accelerations, Node 1009



c. Median floor spectral accelerations, Node 216



d. AFSA

**Figure 5.9. Floor spectral accelerations at Nodes 201, 1009 and 216 computed using the linear response-history analysis of Section 5.2.3.1**

**Table 5.2. AFSA at Nodes 201, 1009 and 216 of Model 1 computed using the linear response-history analysis of Section 5.2.3.1**

GM No.	AFSA in the X direction (g)			AFSA in the Y direction (g)		
	Node 201	Node 1009	Node 216	Node 201	Node 1009	Node 216
1	0.97	1.29	2.61	0.99	1.30	3.07
2	0.76	1.08	2.05	0.77	1.15	2.52
3	0.81	1.27	2.29	0.71	1.04	2.45
4	1.05	1.46	2.88	1.06	1.52	3.00
5	0.76	1.05	1.98	0.61	0.93	2.13
6	0.94	1.37	2.23	0.74	1.16	2.50
7	0.66	0.96	1.84	0.72	0.89	2.17
8	0.77	1.02	1.98	0.84	1.25	2.68
9	0.94	1.16	2.08	1.04	1.48	2.94
10	0.66	0.94	1.90	0.67	0.91	2.32
11	0.99	1.27	2.33	1.16	1.51	3.23
Median	0.84	1.16	2.18	0.83	1.17	2.61

The values of  $\beta_r$  and  $\beta_u$  can be computed using (3.12) and (3.13), respectively. However, since the fragility curves used herein are defined in terms of a response parameter and not a ground-motion parameter, the dispersion in structural response must not be included in  $\beta_r$  and  $\beta_u$ . The values of  $\beta_r$  and  $\beta_u$  used in this study were computed using the following equations:

$$\beta_r = (\beta_{C,r}^2 + \beta_{RE,r}^2)^{1/2} \quad (5.5)$$

$$\beta_u = (\beta_{C,u}^2 + \beta_{RE,u}^2)^{1/2} \quad (5.6)$$

where all the variables were defined in Chapter 3. The values of  $\beta_{C,r}$ ,  $\beta_{RE,r}$ ,  $\beta_{C,u}$  and  $\beta_{RE,u}$  used in this study are tabulated in Table 5.3, where each of the values is the middle point of the range recommended in Table 3.1 for a given variable. The resultant values of  $\beta_r$  and  $\beta_u$ , which are also presented in Table 5.3, are 0.26 and 0.34, respectively. The values of  $\hat{a}$  were then computed using (5.4) to be 2.26, 3.15 and 7.02 g at Nodes 201, 1009 and 216, respectively.

**Table 5.3. Logarithmic standard deviations for developing fragility curves used in this report**

$\beta_{C,r}$	$\beta_{RE,r}$	$\beta_r$
0.14	0.215	0.26
$\beta_{C,u}$	$\beta_{RE,u}$	$\beta_u$
0.27	0.215	0.34

### 5.2.3.2 Fragility Curves

Figure 5.10 presents the three families of fragility curves for the key secondary systems at Nodes 201, 1009 and 216. Each family of fragility curves includes 11 curves and each curve has an equal probability of occurrence. The fragility curves were computed using Equation (3.5), which is reproduced below:

$$f = \Phi \left( \frac{\ln \frac{a}{\hat{a}} + \Phi^{-1}(Q) \cdot \beta_u}{\beta_r} \right) \quad (5.7)$$

For a set of  $\hat{a}$ ,  $\beta_r$  and  $\beta_u$  and a value of  $\Phi^{-1}(Q)$ , a single curve can be determined. For example, the bold solid line in panel a of Figure 5.10 was determined by  $\hat{a} = 0.84$  g,  $\beta_r = 0.26$ ,  $\beta_u = 0.34$  and  $\Phi^{-1}(Q) = 0$ . The values of  $\alpha_i$  presented in Table 4.11 for  $n = 11$  were used in (5.7) for the values of  $\Phi^{-1}(Q)$  to develop the 11 fragility curves in each family of curves in Figure 5.10.

The appropriateness of the fragility curves of Figure 5.10 was evaluated using ASCE/SEI 43-05 (ASCE 2005), where the seismic design of NPP structural and nonstructural components is aimed at achieving both of the following performance criteria:

1. Less than about a 1% probability of unacceptable performance for the design basis earthquake.

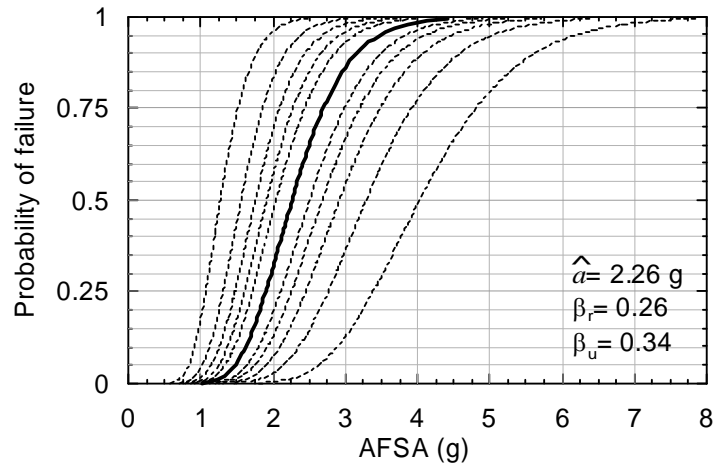
2. Less than about a 10% probability of unacceptable performance for shaking equal to 150% of the design basis earthquake shaking.

Table 5.5 presents the values of AFSA associated with a 1% and a 10% probability of failure for the median fragility curves of Figure 5.10 for Nodes 201, 1009 and 216. The AFSA demands at Nodes 201, 1009 and 216 for the design basis earthquake can be represented by the median values presented in the last row of Table 5.2. The median AFSA demands of Table 5.2 at Nodes 201, 1009 and 216 (i.e., 0.84, 1.17 and 2.61 g, respectively) are smaller than the AFSA values presented in Table 5.5 for a 1% probability of failure; the 150% of the median AFSA demands of Table 5.2 at Nodes 201, 1009 and 216 (i.e., 1.26, 1.76 and 3.92 g, respectively) are also smaller than the AFSA values presented in Table 5.5 for a 10% probability of failure. The fragility curves of Figure 5.10 satisfy the performance criteria described above.

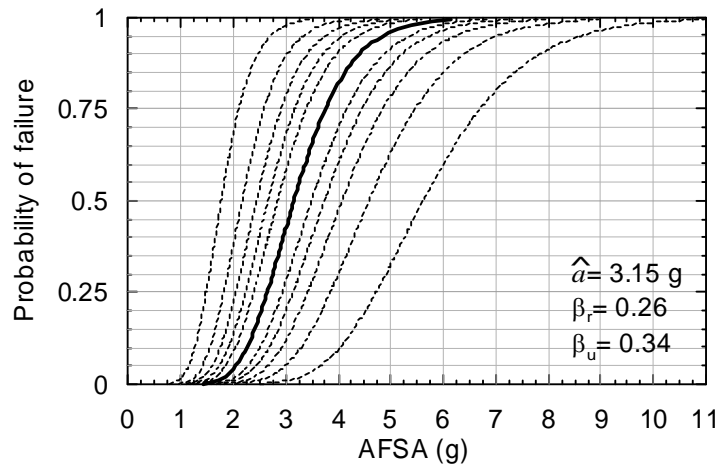
The fragility curves of Figure 5.10 were also evaluated using the information provided by the supplier of the sample NPP. Figure 5.11 presents the floor response spectra used by the supplier for the design of the secondary systems at Nodes 1009 and 216<sup>4</sup>. The spectra were developed using the URS of Figure 5.8 and period-dependent amplification factors and are more conservative than the floor spectra determined using response-history analysis. The AFSA values for the two spectra of Figure 5.11 computed using the procedure of Footnote 3 of this chapter are 1.68 g (Node 1009) and 3.42 g (Node 216). These two values are still smaller than the AFSA values of Table 5.5 for a 1% probability of failure and for Nodes 1009 and 216 (i.e., 1.72 and 3.83 g, respectively). One hundred and fifty percent of 1.68 g (= 2.52 g) is greater than 2.26 g (the AFSA value of Table 5.5 for a 10% probability of failure and for Node 1009) but only by 10%. One hundred and fifty percent of 3.42 g (= 5.13 g) is smaller than 5.83 g (the AFSA value of Table 5.5 for a 10% probability of failure and for Node 216). These results show that the fragility curves of Figure 5.10 reasonably represent the capacities of the secondary systems at Nodes 1009 and 216 if the design of those secondary systems is controlled by the seismic demand of Figure 5.11 and satisfies the two performance criteria described above.

---

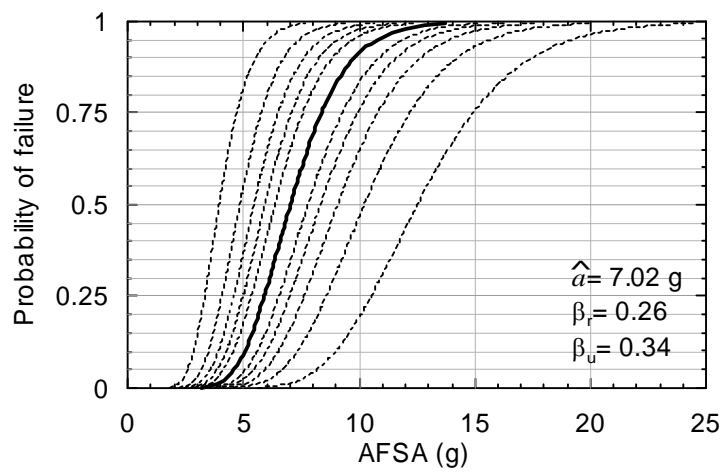
<sup>4</sup> The NPP supplier did not provide the design floor response spectrum at Node 201. Only Nodes 1009 and 216 are discussed herein.



a. Node 201



b. Node 1009



c. Node 216

Figure 5.10. Fragility curves for the secondary systems at Nodes 201, 1009 and 216

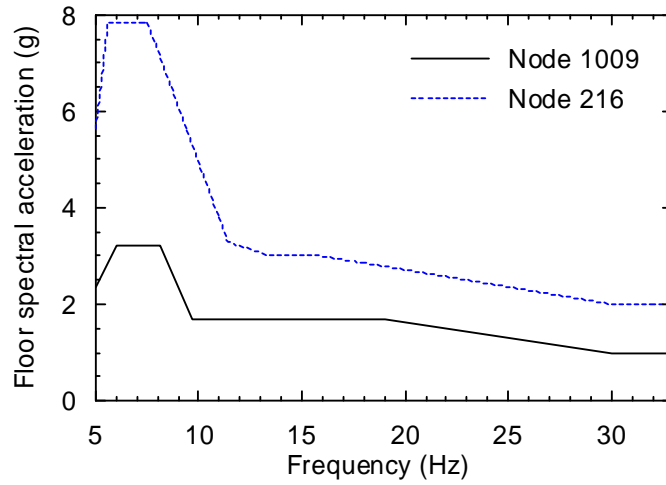


**Figure 5.11. Floor response spectra for the design of secondary systems at Nodes 1009 and 216**

**Table 5.4. AFSA at Nodes 201, 1009 and 216 for intensity-based assessment of Model 1**

GM No.	AFSA in the X direction (g)			AFSA in the Y direction (g)		
	Node 201	Node 1009	Node 216	Node 201	Node 1009	Node 216
1	0.99	1.28	2.60	1.00	1.30	3.01
2	0.79	1.09	2.05	0.78	1.15	2.48
3	0.78	1.24	2.25	0.73	1.01	2.44
4	1.06	1.49	2.89	1.02	1.49	2.93
5	0.74	1.02	1.93	0.61	0.90	2.08
6	0.91	1.34	2.17	0.75	1.12	2.45
7	0.67	0.96	1.83	0.75	0.91	2.19
8	0.78	1.02	1.98	0.84	1.24	2.67
9	0.95	1.16	2.09	1.04	1.47	2.93
10	0.65	0.93	1.88	0.67	0.89	2.32
11	1.03	1.28	2.34	1.18	1.54	3.24

**Table 5.5. The values of AFSA associated with a 1% and a 10% probability of failure for the median fragility curves of Figure 5.10**

Probability of failure	AFSA (g)		
	Node 201	Node 1009	Node 216
1%	1.23	1.72	3.83
10%	1.62	2.26	5.83

#### 5.2.4 Probability of Unacceptable Performance

##### 5.2.4.1 Fault Tree and Nonlinear Response-History Analysis

The unacceptable performance of the sample NPP evaluated in this study is defined by the fault tree of Figure 5.12. The unacceptable performance was defined as the failure of *any* of the secondary systems at Nodes 201, 1009 and 216 by using an “OR” gate in the fault tree.

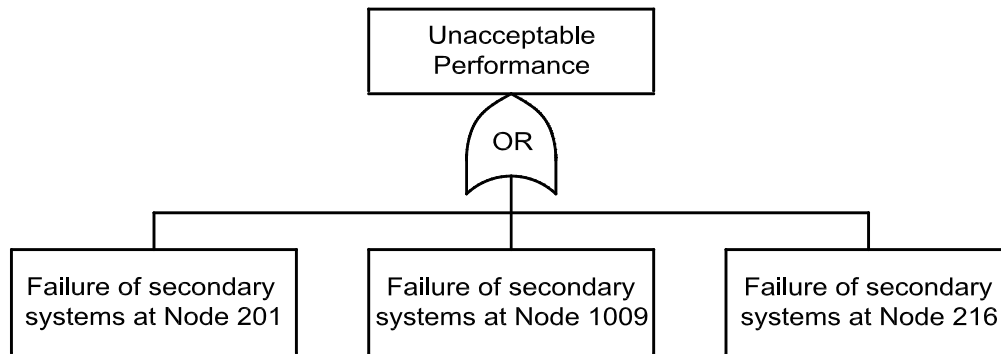


**Figure 5.12. A fault tree for the unacceptable performance of the sample NPP**

Nonlinear uni-directional response-history analyses of Model 1 subjected to the 11 scaled SGMS ground motions of Figure 5.7 in the X and Y directions were performed for the intensity-based assessment of Model 1. Bilinear shear hinges with 3% post-yield stiffness were assigned to all frame elements in the internal-structure stick. The containment structure was assumed to remain elastic because a) all the key secondary systems identified in Chapter 2 are supported at the internal structure; and b) containment structures are designed for large internal pressures (up to 500 kPa) resulting from a postulated accident, and seismic loadings generally do not control their



design. The yield forces of the bilinear shear hinges were estimated by  $0.5\sqrt{f'_c}A_s$  (Wood 1990), where  $f'_c$  is the compressive strength of concrete and a value of  $35 \text{ N/mm}^2$  was used in this study; and  $A_s$  is the shear area of each internal-structure stick in  $\text{mm}^2$  provided by the supplier of the sample NPP.

The results of this set of response-history analyses are shown in Figure 5.13, where panels a, b and c present the median of the 11 floor spectral accelerations in the X and Y directions between 5 and 33 Hz at Nodes 201, 1009 and 216, respectively, and panel d presents the 84th, 50th and 16th percentiles of AFSA at the three nodes. Table 5.4 presents the underlying demand-parameter matrix for the intensity-based assessment of Model 1: the eleven AFSA values at each of Nodes 201, 1009 and 216 in the X and Y directions.

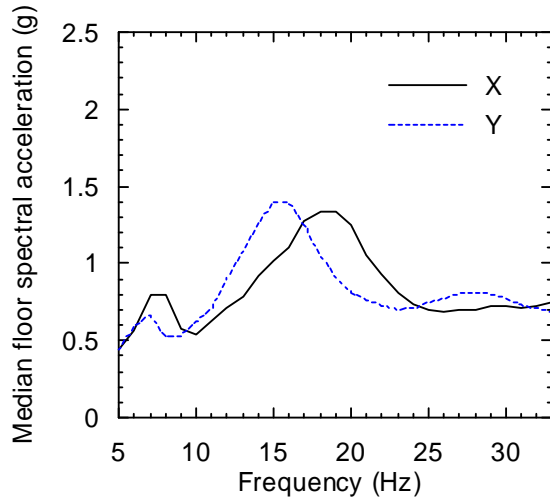
#### 5.2.4.2 Calculation of Probability of Unacceptable Performance

This subsection presents the procedure for and results of the calculation of the probability of unacceptable performance for Model 1 subjected to earthquakes with spectral acceleration of  $0.46 \text{ g}$  at a period of  $0.14 \text{ second}$ .

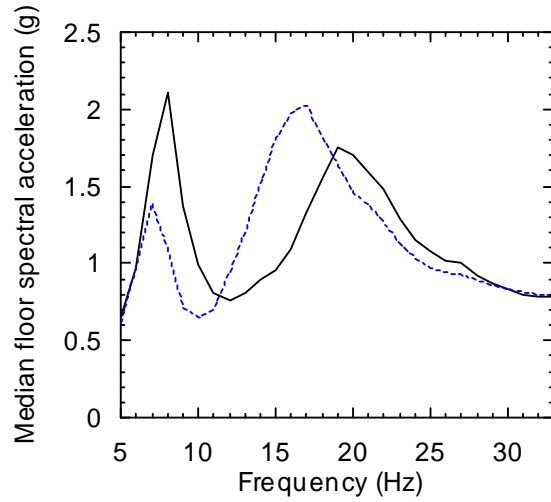
Analysis was performed to characterize the impact on the computed probability of unacceptable performance of alternate representations of fragility curves and number of row vectors in the demand-parameter matrix.

Analysis 1 involved the random selection of one fragility curve from a family of curves for each secondary system in the NPP to consider the epistemic variability in the median capacity of the secondary systems.

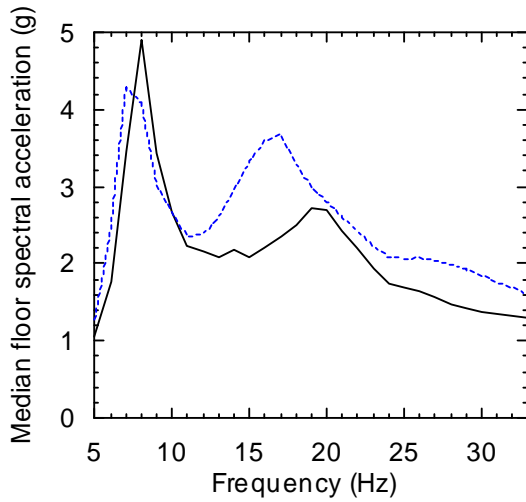
Probabilistic risk assessment for NPPs has routinely involved the use of either *mean* or *median* fragility curves for primary and secondary systems. Kennedy (1999) advocated for the use of mean fragility curves and noted that robust estimates of mean risk could be obtained by convolving the mean hazard curve with the mean fragility curves, where the fragility curves were defined by a ground motion parameter. This recommendation is evaluated herein but the fragility curves are defined in terms of demand parameters of floor acceleration and drift rather than a ground motion parameter. Analysis 2 used *median* secondary system fragility curves. Analysis 3 used *mean* fragility curves as recommended by Kennedy.



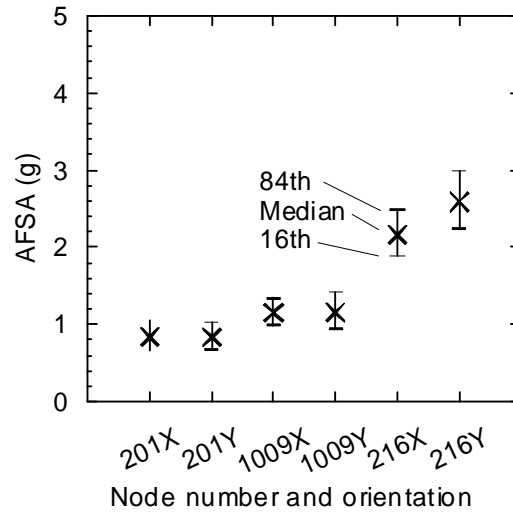
a. Median floor spectral accelerations, Node 201



b. Median floor spectral accelerations, Node 1009



c. Median floor spectral accelerations, Node 216



d. AFSA

**Figure 5.13. Floor spectral accelerations at Nodes 201, 1009 and 216 computed using non-linear response-history analyses for the intensity-based assessment of Model 1**

*Analysis 1*

Analysis 1 involved four parts: 1a through 1d. Table 5.6 summarizes the key variables for 1a through 1d, namely, a) the type/selection of the fragility curves, c) the number of fragility curves in a family, c) the number of row vectors in the demand-parameter matrix, and d) the number of trials used in the analysis.

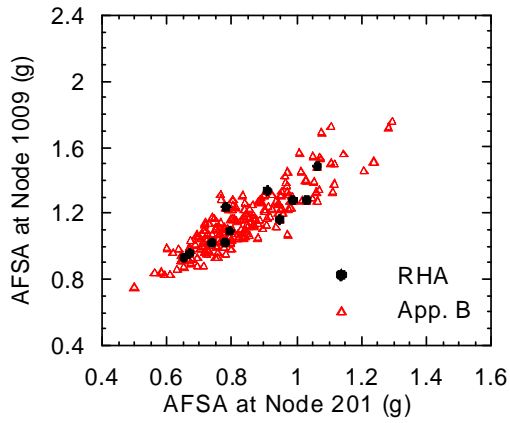
**Table 5.6. Analyses 1, 2 and 3 for the intensity-based assessment of Model 1**

Analysis		Fragility curve for each node	Number of fragility curves in a family	Number of row vectors <sup>1</sup>	Number of trials	Median <sup>2</sup>	Mean <sup>3</sup>
Analysis 1	a	Randomly selected	11	200	2000	0.040	0.061
	b		11	2000		0.037	0.060
	c		21	200		0.045	0.070
	d		201	200		0.040	0.079
Analysis 2		Median	--	200		0.005	0.004
Analysis 3	a	Mean	--	200		0.080	0.079

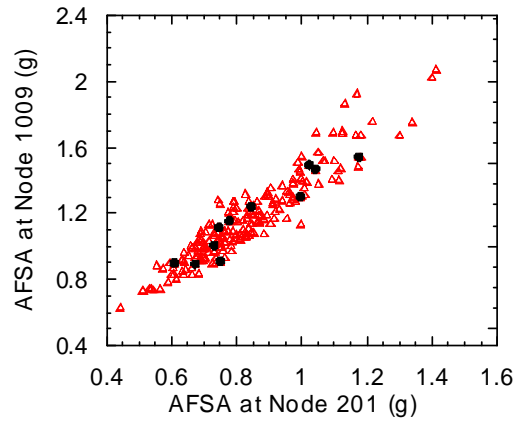
1. Number of row vectors in the demand-parameter matrix.
2. Median of the 2000 realizations for the probability of unacceptable performance from the 2000 trials.
3. Arithmetic mean of the 2000 realizations for the probability of unacceptable performance from the 2000 trials.

For Analysis 1a, the procedure of Appendix B was used to generate 200 sets of correlated AFSA values at Nodes 201, 1009 and 216 in each of the X and Y directions using the underlying demand-parameter matrix of Table 5.4. The results formed a 200×6 demand-parameter matrix. Figure 5.14 presents the distribution of AFSA obtained from the matrix developed from the results on response-history analysis and the matrix generated per Appendix B. The X- and Y-coordinates of each panel in Figure 5.14 are the AFSA values at any two of Nodes 201, 1009 and 216 in the X or Y directions. The results show that the AFSA values generated per Appendix B preserve a) the distribution of AFSA presented in each column of Table 5.4, and b) the correlation in AFSA between any two columns of Table 5.4.

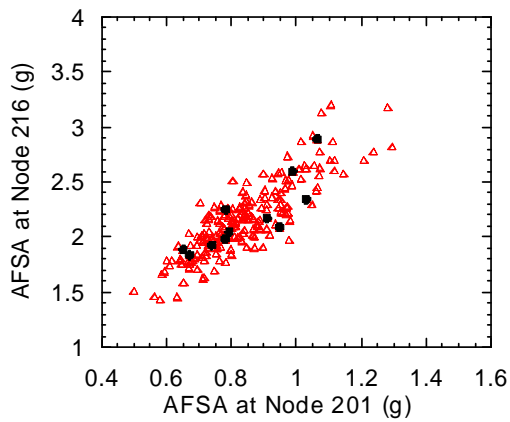
For each of the 6 AFSA values in a row vector of the demand-parameter matrix generated per Appendix B, the probability of failure of a secondary system can be computed from the corresponding fragility curve using the following steps: 1) a random number is generated using a generator that produces uniformly distributed random numbers between 0 and 1; 2) if the generated number is smaller than or equal to the probability of failure identified from the fragility curve, the secondary system is considered to have failed; and 3) if the generated number is greater than the probability of failure, the secondary system is considered to have passed (i.e., safe).



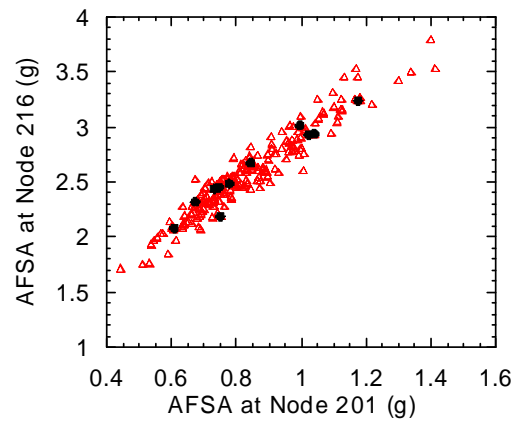
a. Node 201 vs. Node 1009, X dir.



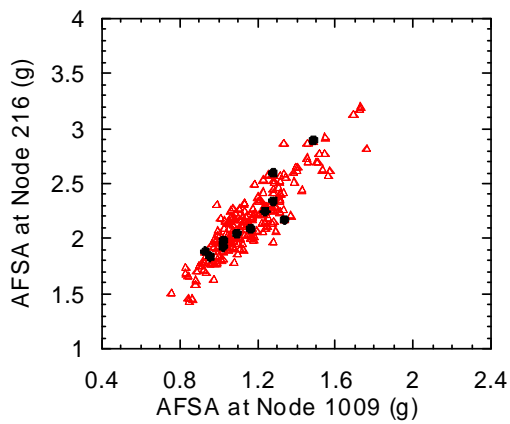
b. Node 201 vs. Node 1009, Y dir.



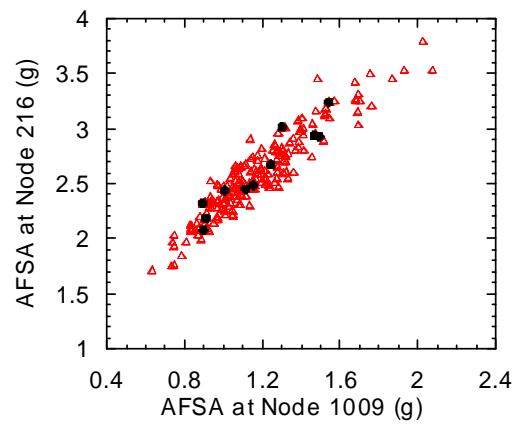
c. Node 201 vs. Node 216, X dir.



d. Node 201 vs. Node 216, Y dir.



e. Node 1009 vs. Node 216, X dir.



f. Node 1009 vs. Node 216, Y dir.

**Figure 5.14. AFSA at Nodes 201, 1009 and 216 generated using 1) response-history analysis and 2) the procedure of Appendix B for the intensity-based assessment of Model 1**

For example, as shown in Table 5.4, the AFSA value at Node 201 in the X direction for GM 1 is 0.99 g. Assume the bold solid curve in panel a of Figure 5.10 is selected for Node 201; the probability of failure for the secondary system supported at Node 201 with respect to an AFSA of 0.99 g can be identified from the curve to be 0.00075.<sup>5</sup> If the generated random number is greater than 0.00075, the secondary system at Node 201 is considered to be safe; if the number is smaller than 0.00075, the secondary system is considered to have failed. This analysis is then repeated for the other 5 values of AFSA in the set. The performance of Model 1 is considered unacceptable for this set of AFSA if any of the six values of AFSA produces a failure in the secondary system.

For Analysis 1a, the analysis described above was repeated using all 200 row vectors in the demand-parameter matrix and one fragility curve randomly selected from each of the three families of curves presented in Figure 5.10. A realization for the probability of unacceptable performance was computed as the ratio of the number of row vectors with unacceptable performance (see above) to 200. The analysis was repeated 2000 times using a newly generated demand-parameter matrix and combination of fragility curves to develop 2000 realizations for the distribution of the probability of unacceptable performance of Model 1 subjected to earthquake shaking with spectral acceleration of 0.46 g at a period of 0.14 second. The number 2000 was determined on a trial-and-error basis. An increase in the number of trials above 2000 did not alter the result.

The solid curve in Figure 5.15 is the cumulative distribution function (CDF) of the 2000 realizations. To develop the curve, the 2000 realizations were sorted from smallest to largest and assigned a probability from 1/2000 to 1.0 in increments of 1/2000. The slope of the CDF for Analysis 1a changes abruptly twice between probabilities of unacceptable performance of 0.05 and 0.12, which indicates that the underlying probability distribution has two peaks.

To study the impact of the choice of number of row vectors on the distribution of the probability of unacceptable performance, Analysis 1a was repeated but using demand-parameter matrices consisting of 2000 row vectors and denoted Analysis 1b. Results are presented in Figure 5.15

---

<sup>5</sup> This value is actual too small to be directly identified from Figure 5.10. In this example, the fragility curve is a cumulative lognormal distribution with a median of 2.26 g and a logarithmic standard deviation of 0.26. The probability of this distribution with respect to 0.99 g can be easily obtained using the function “LOGNORMDIST” in Excel or “logncdf” in Matlab.

using a dotted line. For the case studied herein, the increase in the number of row vectors from 200 to 2000 has negligible influence on the distribution.

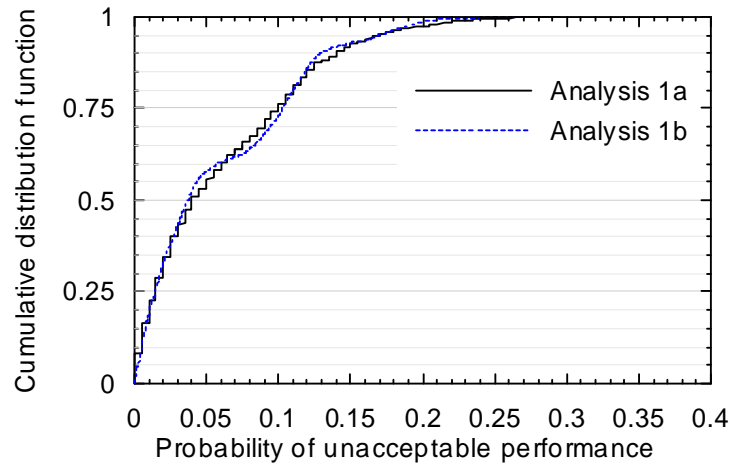


**Figure 5.15. Distributions of the probability of unacceptable performance for Analyses 1a and 1b for the intensity-based assessment of Model 1**

To study the impact of the number of fragility curves in a family, Analysis 1a (family of 11 curves) was repeated but using families of 21 (Analysis 1c) and 201 (Analysis 1d) curves for the secondary systems at Nodes 201, 1009 and 216. The 21 and 201 fragility curves in the families were developed using (5.7) and the same values of  $\hat{a}$ ,  $\beta_r$  and  $\beta_u$  as those used to develop the curves of Figure 5.10. The values of  $\Phi^{-1}(Q)$  for the 21 and 201 fragility curves in a family were determined using the procedure described in Section 4.3.5.1. Figure 5.16 presents the CDFs and arithmetic means of the 2000 realizations for Analyses 1a, 1c and 1d. The last two columns of Table 5.6 present the medians and arithmetic means, respectively, of the 2000 realizations for Analyses 1a through 1d.

The results of Figure 5.16 show that the notch in the curve for Analysis 1a vanishes as the number of fragility curves in a family increases to 201. The increase in the number of fragility curves in a family from 11 to 201 also increases the arithmetic mean of the 2000 realizations from 0.06 to about 0.079, which is used as the benchmark value for the probability of unacceptable performance for the intensity-based assessment of Model 1 since a further increase of the number of fragility curves in a family does not alter this value (0.079).

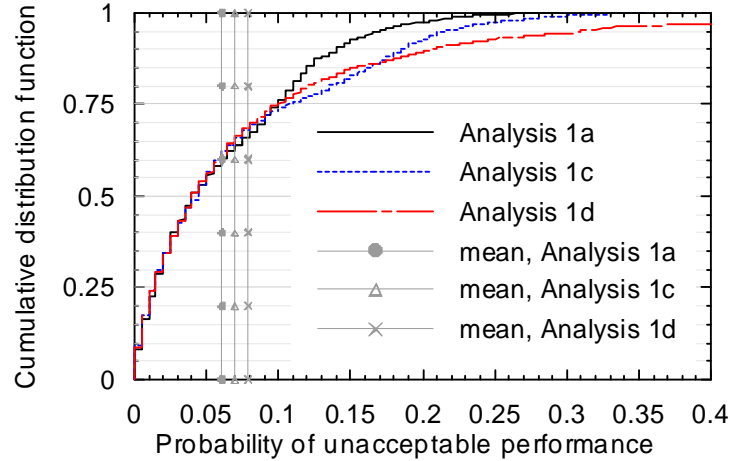


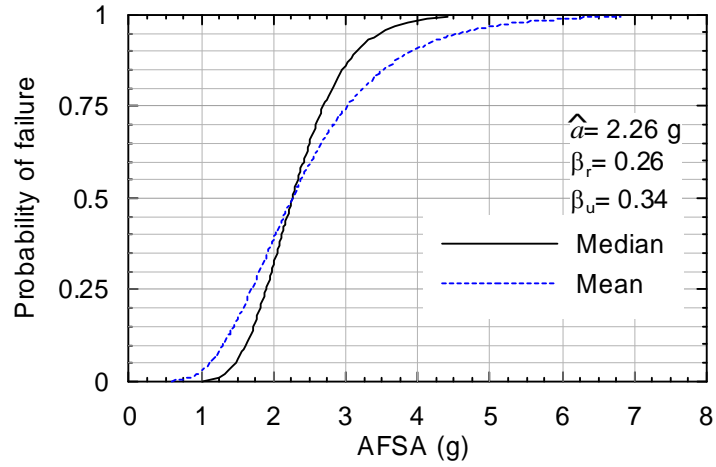
**Figure 5.16. Distributions and arithmetic means of the probability of unacceptable performance for Analyses 1a, 1c and 1d for the intensity-based assessment of Model 1**

### *Analyses 2 and 3*

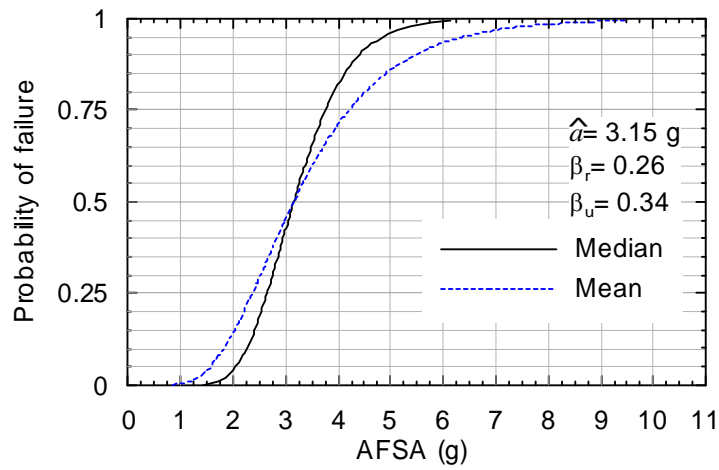
As presented previously, a family of fragility curves for a component in NPPs can be developed using parameters  $\hat{a}$ ,  $\beta_r$  and  $\beta_u$  defined using (5.4), (5.5) and (5.6), respectively. The median curve for a family of fragility curves is defined by a lognormal distribution with median and dispersion of  $\hat{a}$  and  $\beta_r$ , respectively, and the mean curve is defined by a lognormal distribution with median and dispersion of  $\hat{a}$  and  $\sqrt{\beta_r^2 + \beta_u^2}$ , respectively (Reed and Kennedy, 1994). In Figure 5.10, the solid bold curve in each panel represents the median curve for the corresponding family of fragility curves. The epistemic uncertainty  $\beta_u$  was used to consider the uncertainty in the median value of the fragility curve and not included in the median fragility curve.

Figure 5.17 presents the median and mean curves for the three families of fragility curves of Figure 5.10. In each panel of Figure 5.17, the mean curve has a lower probability of failure than the median curve at AFSA values greater  $\hat{a}$  than and higher probability of failure at AFSA values smaller than  $\hat{a}$ .

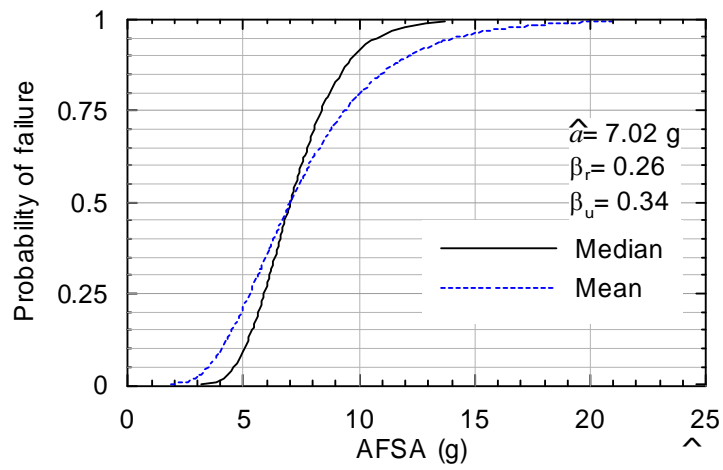
To study the impact of the use of median or mean fragility curves on the distribution of the probability of unacceptable performance, Analysis 1a was repeated but using the a) median (Analysis 2), and b) mean (Analysis 3a) curves of Figure 5.17 in each of the 2000 trials in lieu of randomly selected curves.



a. Node 201



b. Node 1009



c. Node 216

**Figure 5.17. Median and mean fragility curves for the secondary systems at Nodes 201, 1009 and 216**



Figure 5.18 presents the CDFs for the 2000 realizations of Analysis 2 and Analysis 3a. Two curves were developed for Analysis 3a: one established by sorting the 2000 realizations, and one by fitting a lognormal distribution to the data, where the median and dispersion were estimated from the same 2000 realizations using (A.5) and (A.6), respectively. The goodness-of-fit test shows that the distribution computed using the mean fragility curves is well represented by the lognormal distribution. The curve for Analysis 2 was established by sorting the 2000 realizations.

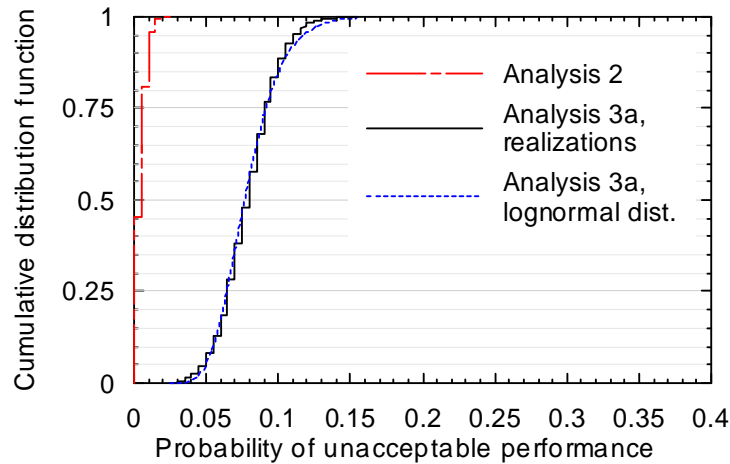


**Figure 5.18. Distributions of the probability of unacceptable performance for Analyses 2 and 3a for the intensity-based assessment of Model 1**

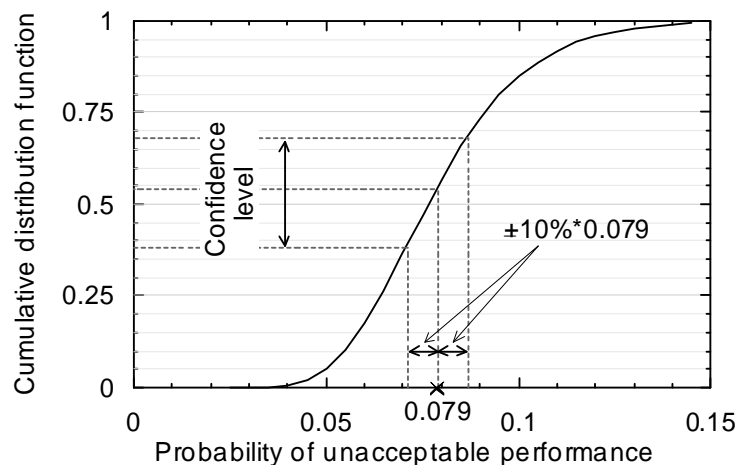
The arithmetic mean of the two sets of 2000 realizations for Analysis 2 and Analysis 3a are 0.004 and 0.079, respectively (see Table 5.6). This result is not surprising since the values of AFSA in the underlying demand-parameter matrix of Table 5.4 are much smaller than the value of  $\hat{a}$  for the corresponding family of fragility curves, where the probability of failure for the median curve is smaller than that for the mean curve.

The use of mean rather than median fragility curves is more appropriate for performance assessment since both aleatory randomness and epistemic uncertainty is considered. Importantly, the results presented in the shaded cells of Table 5.6 show that use of mean fragility curves (Analysis 3) will provide an unbiased estimate of the mean probability of unacceptable performance generated using a family of fragility curves (the benchmark Analysis 1d).

The results of Figure 5.18 for Analysis 3a raise one question: can Analysis 3a be performed for only one trial, instead of 2000, and reasonably estimate the benchmark value (Analysis 1d) for the

probability of unacceptable performance obtained using a family of fragility curves? To address this question, the confidence level for the realization from each trial of Analysis 3a to be within  $\pm 10\%$  of its mean value was computed. Figure 5.19 illustrates the definition of this confidence level using the CDF of Figure 5.18 for the lognormal distribution. The confidence level is defined by the difference between the values of CDF values associated with the probabilities of unacceptable performance of 0.071 ( $=0.9 \times 0.079$ ) and 0.087 ( $=1.1 \times 0.079$ ). For this example, the confidence level is 30%.

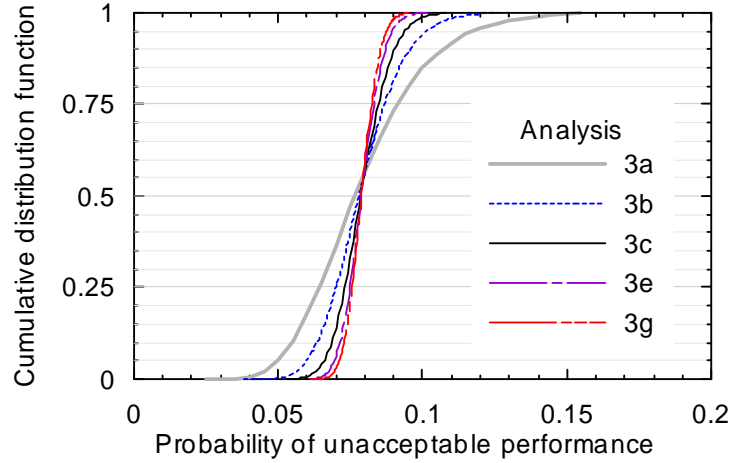
The confidence level of Figure 5.19 can be increased by reducing the dispersion in the realizations for Analysis 3a. A reduction in this dispersion can be achieved by increasing the number of row vectors in the demand-parameter matrix. To study the impact of the number of row vectors on the confidence level of the estimation using mean fragility curves, Analysis 3a was repeated using 500, 1000, 1500, 2000, 2500 and 3000 row vectors. These analyses were denoted Analyses 3b through 3g, respectively.



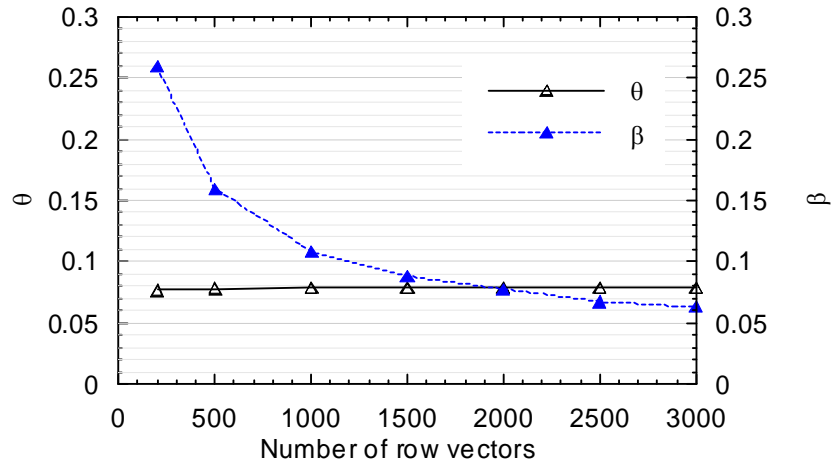
**Figure 5.19. Definition of confidence level**

Figure 5.20 presents the CDFs of the probability of unacceptable performance for Analyses 3a (200 rows), 3b (500 rows), 3c (1000 rows), 3e (2000 rows) and 3g (3000 rows) using the lognormal distributions, where the median ( $\theta$ ) and dispersion ( $\beta$ ) for each analysis were estimated from the 2000 realizations using (A.5) and (A.6), respectively. The medians and dispersions computed using (A.5) and (A.6) for Analyses 3a through 3g are presented in Figure 5.21 as a function of the number of row vectors. The results of Figure 5.21 show that the value of  $\theta$  is almost constant whereas the value of  $\beta$  decreases as the number of row vectors increases. Figure 5.22 present the CDFs of Figure 5.20 together with the CDF and mean value of the 2000

realizations for the benchmark Analysis 1d. The results for Analyses 3a through 3g provide an unbiased estimate of the mean value of the distribution for Analysis 1d but with different dispersions.



**Figure 5.20. Distributions of the probability of unacceptable performance for Analyses 3a, b, c, e and g for the intensity-based assessment of Model 1**



**Figure 5.21. Medians and dispersions of the probability of unacceptable performance for Analysis 3 for the intensity-based assessment of Model 1 as a function of the number of row vectors of the DP matrix**

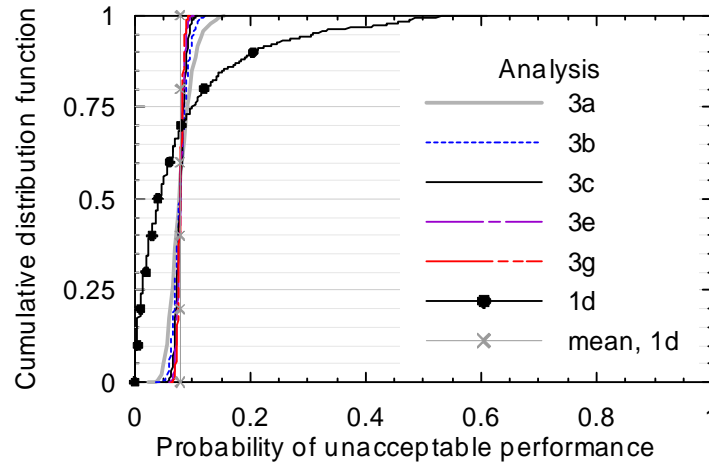


**Figure 5.22. Distributions of the probability of unacceptable performance for Analyses 1d and 3 for the intensity-based assessment of Model 1**

Table 5.7 summarizes the statistics for Analyses 3a through 3g, including the arithmetic mean, median (through counting), median (using (A.5)) and dispersion (using (A.6)) of the 2000 realizations for each analysis. In the table, the arithmetic means and the two medians for Analyses 3b through 3g are identical because the dispersions in the distribution of the 2000 realizations for each analysis are small. For such small dispersions, the differences between normal and lognormal distributions are insignificant.

**Table 5.7. Statistics of Analysis 3 for the intensity-based assessment of Model 1**

Analysis	3a	3b	3c	3d	3e	3f	3g
Number of row vectors	200	500	1000	1500	2000	2500	3000
Arithmetic mean	0.079	0.079	0.079	0.079	0.079	0.079	0.079
Median (counting)	0.080	0.078	0.079	0.079	0.080	0.079	0.079
Median (Equation A.5)	0.077	0.078	0.079	0.079	0.079	0.079	0.079
Dispersion (Equation A.6)	0.26	0.16	0.11	0.088	0.078	0.067	0.063
Confidence level	0.30	0.47	0.65	0.75	0.80	0.86	0.89

The confidence level defined in Figure 5.19 and listed in Table 5.7 increases as the number of row vectors increases. For this example, the demand-parameter matrix used for assessment involving mean fragility curves should consist of at least 2000 row vectors to achieve a confidence level of 80%.

## **5.3 Scenario-Based Assessment of the Conventional and Base Isolated Reactor Building**

### **5.3.1 Introduction**

Three scenario cases, involving moment magnitude and source-to-site distance pairs of (6.3 and 37.5 km), (5.3 and 7.5 km) and (7.3 and 538 km), were identified from the modal cases in panels a and b of Figure 5.6 and Figure 5.23, respectively. The results presented in Figure 5.6 were extracted from the ESP report for the sample NPP site and cover a period range from 0.1 to 1 second. The isolation systems of Models 2, 3 and 4 have an elastic (Model 4) or post-yield (Models 2 and 3) stiffness corresponding to a period of 2 seconds. Since deaggregation results were not presented in the ESP report for periods greater than 1 second, the deaggregation of the 2-second seismic hazard and a return period of 4975 years for the sample NPP site was generated using USGS interactive deaggregation tool (USGS 2008). Results are presented in Figure 5.23. The USGS interactive deaggregation tool does not provide information for a return period greater than 4975 years but does show that the modal events of the 2-second hazard at return periods of 975, 2475 and 4975 years at the sample NPP site are the same. Since the purpose is to identify an important magnitude-distance combination for the 2-second hazard at the sample NPP site, the modal event shown in Figure 5.6 was used although the return period of 4975 years is much smaller than 100,000 years.

Figure 5.24 presents the median spectral demands predicted using the attenuation relationship of Campbell (2003) for Eastern North America for the three scenario cases identified above. For clarity, panel a of Figure 5.24 presents the median spectral demands between periods of 0.01 and 1 second and panel b presents that between periods of 1 and 4 seconds. The magnitude-distance pair of (7.3, 538 km) has much smaller spectral demand than the other two pairs over the entire period range of Figure 5.24. The other two pairs have similar spectral demand in panel b whereas the pair of (5.3, 7.5 km) has much greater demand than the pair of (6.3, 37.5 km) in panel a at a period smaller than 0.6 second. The median spectral demands for the pairs of (6.3, 37.5 km) and (7.3, 538 km) are smaller than the URS demand of Table 5.1 and are less likely to cause significant damage in the sample NPP models than the pair of (5.3, 7.5 km). Therefore, the magnitude-distance pair of (5.3, 7.5 km) was selected for the scenario-based assessment of Models 1 through 4.

### Prob. Seismic Hazard Deaggregation

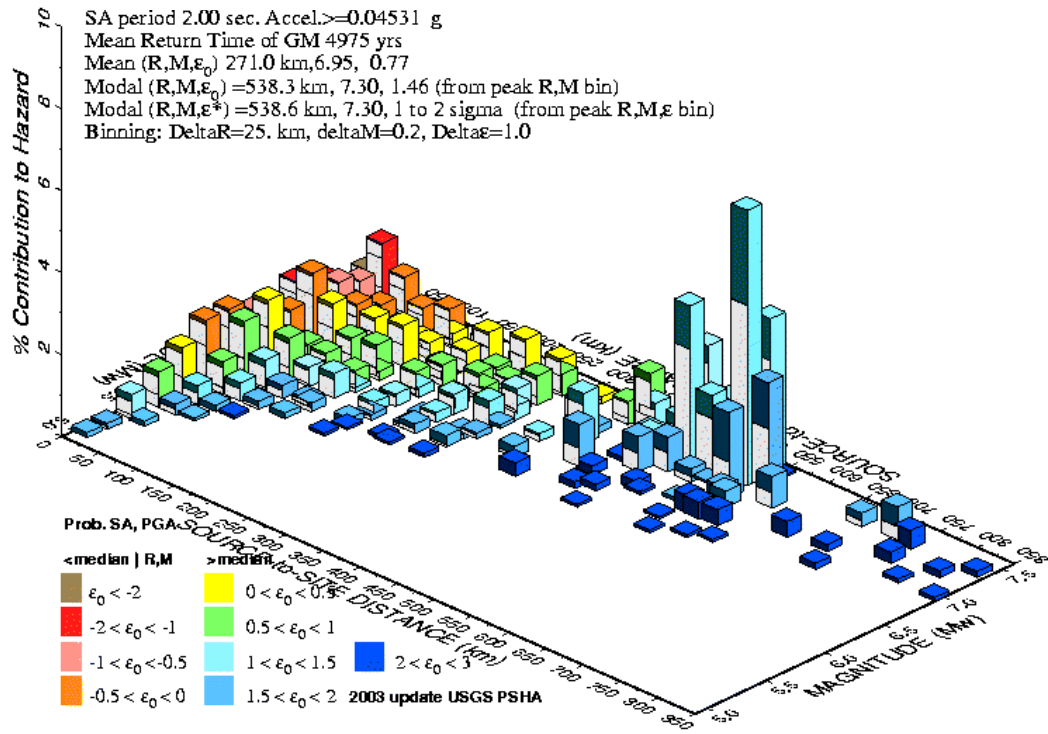
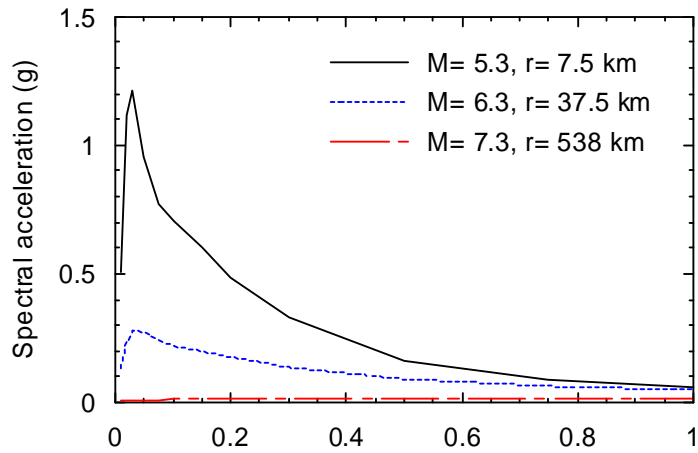
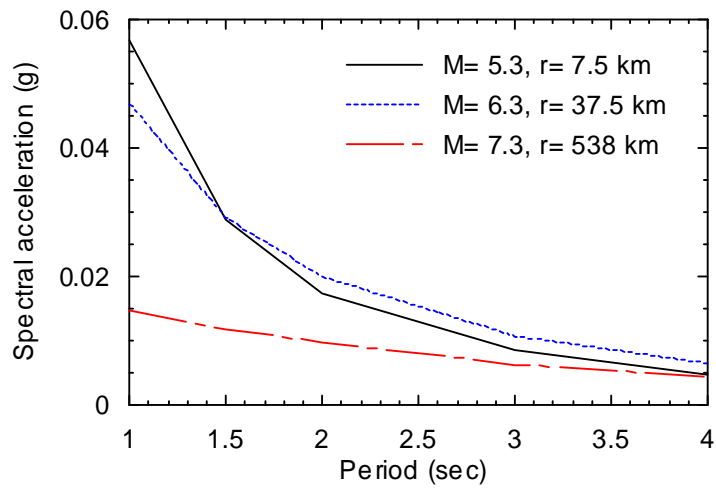


Figure 5.23. Deaggregation of the 2-second seismic hazard at an annual frequency of exceedance of  $2 \times 10^{-4}$  for the sample NPP site (USGS 2008)



a. Short period range



b. Long period range

**Figure 5.24. Median spectral accelerations predicted by Campbell (2003) for three magnitude-distance pairs: (5.3, 7.5 km), (6.3, 37.5 km) and (7.3 and 538 km)**

Supplemental analysis was performed to assess the influence of isolator yield displacement on the response of the isolated NPPs. The yield displacement was increased to 25 mm from the values for Models 2 and 3 in Table 2.1. Analysis results for this model, identified as Model 5, are presented in Appendix F. The impact on floor spectral acceleration of an increase in isolator yield displacement is identified in the appendix.

### 5.3.2 *Scaling of Ground Motions*

Based on the attenuation relationship of Campbell (2003), the median and logarithmic standard deviation of the spectral demand for the magnitude-distance pair of (5.3, 7.5 km) at a period of 0.14 second are 0.62 g and 0.62, respectively. Eleven target spectral ordinates were determined using the following equation:

$$S_{ai}(T = 0.14 \text{ s}) = 0.62 \cdot e^{0.62\alpha_i} \quad i = 1,11 \quad (5.8)$$

where the coefficient  $\alpha_i$  is given in Table 4.11. The eleven target spectral ordinates are listed in Table 5.8 and illustrated in Figure 5.25 using the symbol “⊕”.

**Table 5.8. Target spectral accelerations for scenario-based assessment at a period of 0.14 second**

No.	Spectral acceleration (g)
1	0.22
2	0.31
3	0.39
4	0.45
5	0.51
6	0.62
7	0.75
8	0.85
9	0.99
10	1.23
11	1.78



The eleven SGMS ground motions described in Section 5.2.2.2 were amplitude scaled to match the target spectral ordinates of Table 5.8 (one ground motion per target ordinate), as shown in Figure 5.25. Note that the eleven SGMS ground motions were originally generated for the magnitude-distance pair of (5.3, 7.5 km): the scenario case used in this section.

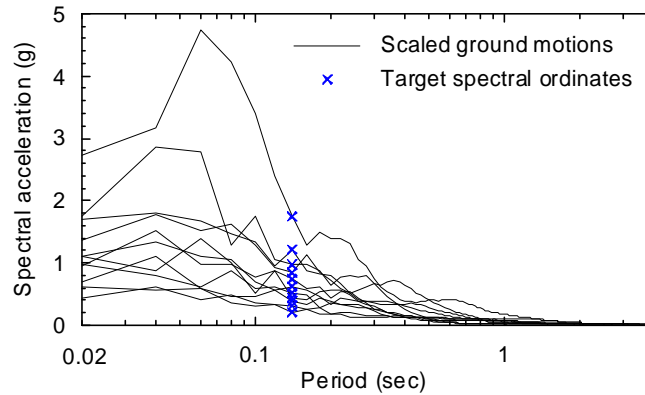


**Figure 5.25. Spectral accelerations of the 11 scaled SGMS ground motions and the 11 target spectral ordinates for scenario-based assessment**

Figure 5.26 presents the 84th, 50th and 16th percentiles of the spectral demands predicted by Campbell (2003) for the scenario case used herein and those of the 11 scaled SGMS ground motions shown in Figure 5.25 using normal scale (panel a) and log-log scale (panel b). The log-log scale was used so that the results at very short period (for example, smaller than 0.1 second) or with very small spectral demand (for example, smaller than 0.1 g) are clearly visible. The distribution of spectral demand of the 11 scaled SGMS ground motions agree well with that predicted by Campbell (2003) over a wide period range. This good agreement deemed a re-scaling of ground motions for Models 2, 3 and 4 unnecessary. The scaled ground motions of Figure 5.25 were used for the nonlinear response-history analyses for Models 1 through 4.

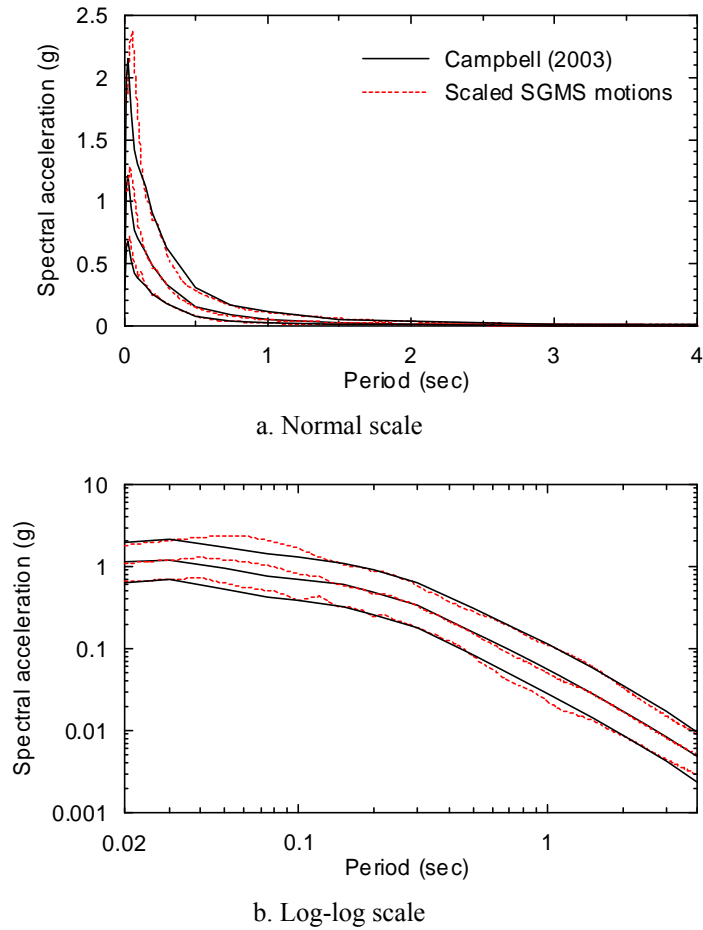
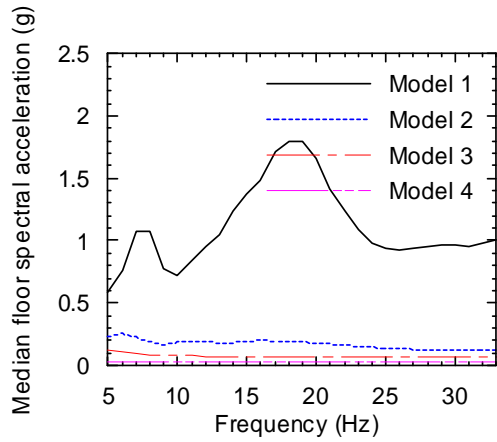


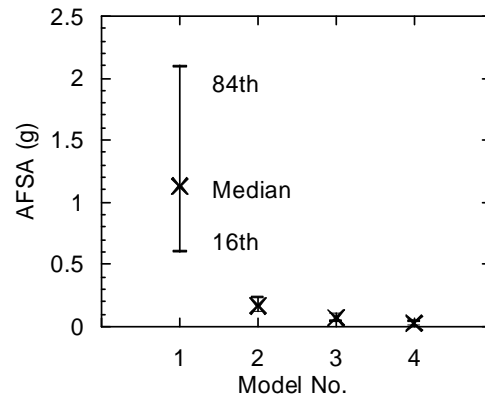
**Figure 5.26. Median, 84<sup>th</sup> and 16<sup>th</sup> percentiles of spectral accelerations a) predicted by Campbell (2003) for  $M= 5.3$  and  $r= 7.5$  km; and b) of the 11 scaled SGMS ground motions for scenario-based assessment**

### 5.3.3 Analysis Results

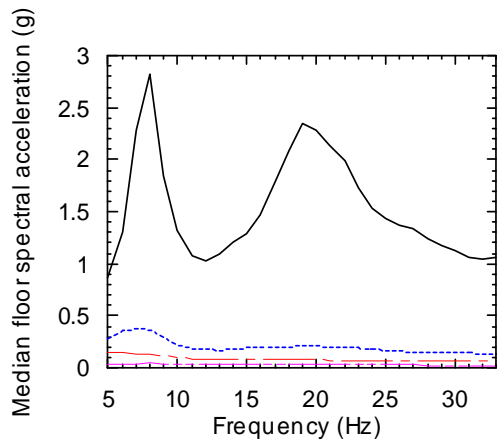
Nonlinear uni-directional response-history analyses were performed using each of Models 1 through 4 subjected to the 11 scaled SGMS ground motions of Figure 5.25 in the X and Y directions. Table 5.9 through Table 5.12 present the demand-parameter matrices for the scenario-based assessments of Models 1 through 4, respectively. Each matrix includes the eleven AFSA values at Nodes 201, 1009 and 216 in the X and Y directions, of which the median and logarithmic standard deviation are summarized in Table 5.13. Figure 5.27 presents the median of the eleven floor spectral accelerations between 5 and 33 Hz and the 84th, 50th and 16th percentiles of AFSA at Nodes 201, 1009 and 216 in the X direction. Figure 5.28 presents similar results in Y direction.



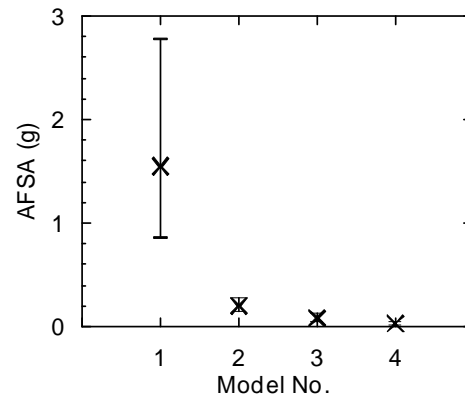
a. Median floor spectral accelerations, Node 201



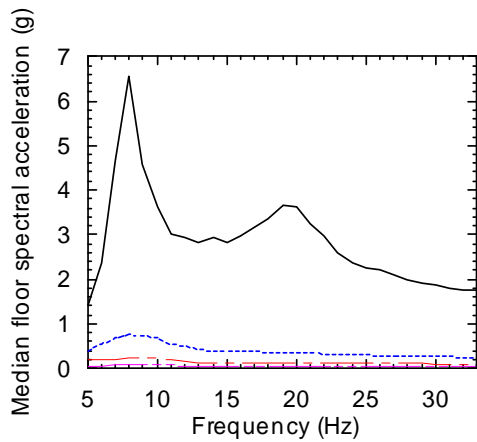
b. AFSA, Node 201



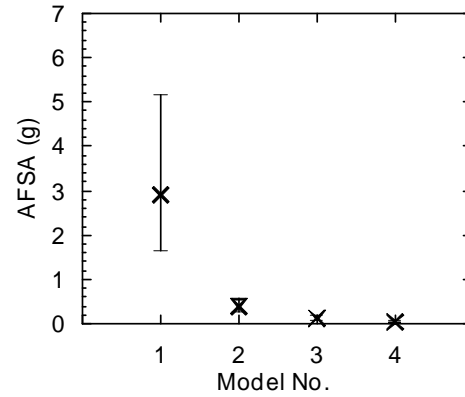
c. Median floor spectral accelerations, Node 1009



d. AFSA, Node 1009

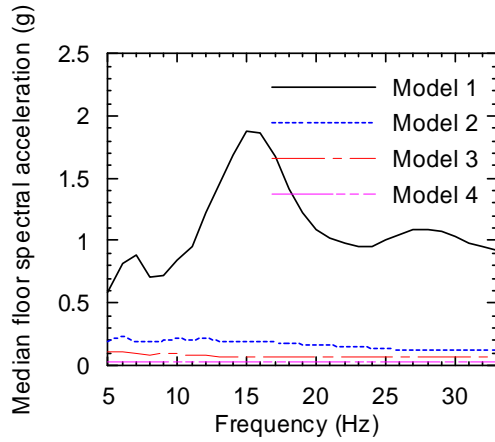


e. Median floor spectral accelerations, Node 216

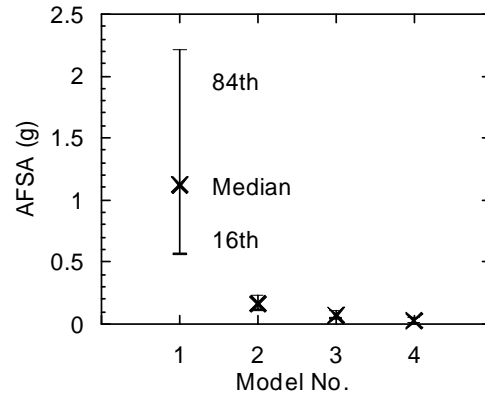


f. AFSA, Node 216

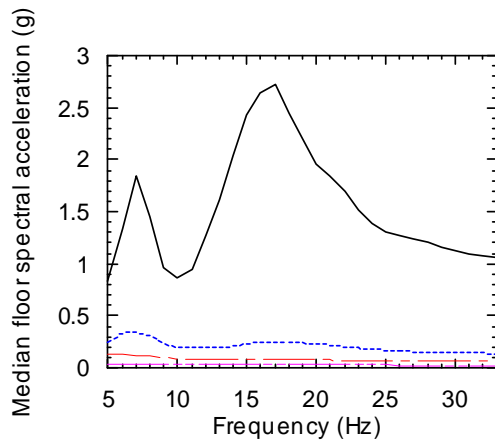
**Figure 5.27. Floor spectral accelerations at Nodes 201, 1009 and 216 in the X direction for the scenario-based assessment of Models 1, 2, 3 and 4**



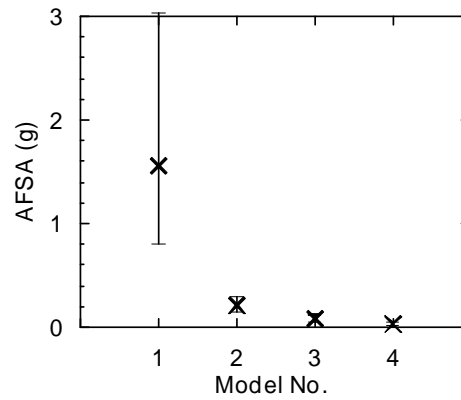
a. Median floor spectral accelerations, Node 201



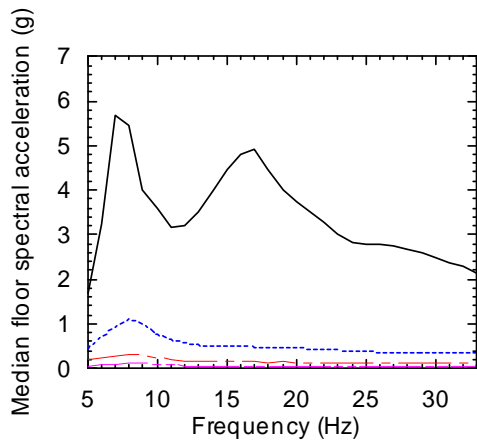
b. AFSA, Node 201



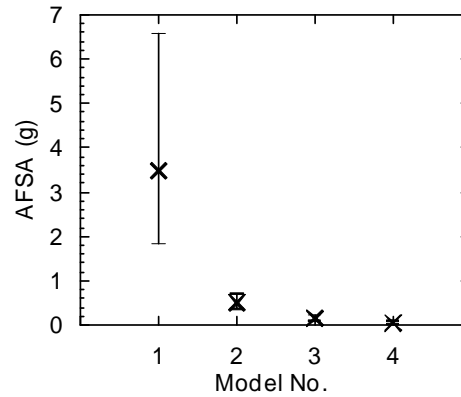
c. Median floor spectral accelerations, Node 1009



d. AFSA, Node 1009



e. Median floor spectral accelerations, Node 216



f. AFSA, Node 216

**Figure 5.28. Floor spectral accelerations at Nodes 201, 1009 and 216 in the Y direction for the scenario-based assessment of Models 1, 2, 3 and 4**

**Table 5.9. AFSA at Nodes 201, 1009 and 216 for scenario-based assessment of Model 1**

GM No.	AFSA in the X direction (g)			AFSA in the Y direction (g)		
	Node 201	Node 1009	Node 216	Node 201	Node 1009	Node 216
1	0.46	0.60	1.22	0.47	0.61	1.42
2	0.54	0.74	1.39	0.53	0.79	1.69
3	0.66	1.05	1.90	0.62	0.85	2.06
4	1.05	1.47	2.86	1.01	1.47	2.90
5	0.83	1.14	2.15	0.68	1.00	2.33
6	1.22	1.80	2.93	1.01	1.50	3.30
7	1.09	1.55	2.98	1.22	1.48	3.55
8	1.43	1.88	3.64	1.55	2.28	4.91
9	2.03	2.49	4.48	2.23	3.15	6.29
10	1.74	2.48	5.02	1.79	2.38	6.18
11	3.92	4.75	8.80	4.46	5.78	11.88

**Table 5.10. AFSA at Nodes 201, 1009 and 216 for scenario-based assessment of Model 2**

GM No.	AFSA in the X direction (g)			AFSA in the Y direction (g)		
	Node 201	Node 1009	Node 216	Node 201	Node 1009	Node 216
1	0.12	0.14	0.30	0.11	0.14	0.38
2	0.10	0.13	0.23	0.10	0.12	0.29
3	0.14	0.19	0.33	0.14	0.18	0.45
4	0.17	0.21	0.40	0.17	0.20	0.53
5	0.12	0.15	0.27	0.13	0.16	0.36
6	0.17	0.21	0.39	0.17	0.22	0.48
7	0.19	0.24	0.45	0.18	0.23	0.58
8	0.22	0.24	0.45	0.21	0.27	0.56
9	0.24	0.26	0.57	0.24	0.29	0.71
10	0.19	0.24	0.47	0.19	0.24	0.65
11	0.33	0.34	0.77	0.31	0.38	0.91

**Table 5.11. AFSA at Nodes 201, 1009 and 216 for scenario-based assessment of Model 3**

GM No.	AFSA in the X direction (g)			AFSA in the Y direction (g)		
	Node 201	Node 1009	Node 216	Node 201	Node 1009	Node 216
1	0.04	0.05	0.07	0.04	0.04	0.08
2	0.04	0.05	0.07	0.04	0.04	0.08
3	0.07	0.07	0.10	0.07	0.07	0.13
4	0.09	0.10	0.14	0.09	0.10	0.16
5	0.05	0.06	0.10	0.05	0.06	0.13
6	0.08	0.08	0.11	0.08	0.08	0.13
7	0.07	0.08	0.13	0.07	0.07	0.15
8	0.10	0.13	0.23	0.10	0.12	0.26
9	0.10	0.12	0.19	0.10	0.11	0.21
10	0.09	0.11	0.17	0.09	0.11	0.20
11	0.16	0.17	0.30	0.15	0.16	0.32

**Table 5.12. AFSA at Nodes 201, 1009 and 216 for scenario-based assessment of Model 4**

GM No.	AFSA in the X direction (g)			AFSA in the Y direction (g)		
	Node 201	Node 1009	Node 216	Node 201	Node 1009	Node 216
1	0.01	0.01	0.02	0.01	0.01	0.02
2	0.01	0.01	0.02	0.01	0.01	0.02
3	0.02	0.02	0.03	0.02	0.02	0.04
4	0.03	0.03	0.05	0.03	0.04	0.06
5	0.02	0.02	0.03	0.02	0.02	0.04
6	0.03	0.03	0.04	0.03	0.03	0.05
7	0.03	0.03	0.05	0.03	0.03	0.07
8	0.04	0.04	0.08	0.04	0.04	0.09
9	0.06	0.06	0.09	0.06	0.06	0.10
10	0.04	0.04	0.07	0.04	0.05	0.08
11	0.08	0.08	0.14	0.08	0.08	0.17

**Table 5.13. Median and logarithmic standard deviation of AFSA at Nodes 201, 1009 and 216 for scenario-based assessment**

Model No.	AFSA in the X direction (g)			AFSA in the Y direction (g)		
	Node 201	Node 1009	Node 216	Node 201	Node 1009	Node 216
Median						
1	1.13	1.55	2.91	1.12	1.56	3.47
2	0.17	0.21	0.40	0.17	0.21	0.51
3	0.07	0.09	0.13	0.07	0.08	0.15
4	0.03	0.03	0.05	0.03	0.03	0.06
Logarithmic standard deviation						
1	0.62	0.59	0.58	0.68	0.67	0.64
2	0.35	0.29	0.34	0.33	0.34	0.33
3	0.42	0.40	0.47	0.41	0.44	0.44
4	0.66	0.66	0.63	0.66	0.68	0.66

All three isolation systems analyzed herein greatly reduce the median floor spectral acceleration and AFSA demands of the sample NPP. For the AFSA demand, both the median and the difference between 84th and 16th percentiles are greatly reduced by the isolation systems. The logarithmic standard deviation of AFSA for the highly nonlinear systems (Models 2 and 3) is much smaller than that for the conventional NPP (see Table 5.13)<sup>6</sup>. One important issue for the seismic design of secondary systems for CEUS NPPs is the significant high-frequency spectral demand. The results presented herein clearly show that this issue can be effectively attenuated using base isolation.

The analysis of Figure 5.14 was repeated using the AFSA values of Table 5.9 through Table 5.12 to generate the 200 sets of AFSA values for each of Models 1 through 4. The relationships of the 200 AFSA values at Node 201 and those at Node 216 of Models 1 through 4 in the X direction are

---

<sup>6</sup> Note that the logarithmic standard deviations of AFSA for Models 2 and 3 presented in Table 5.13 are smaller than the dispersion in spectral acceleration. A simplified method for the estimate of dispersion in structural response is to use the square root of the sum of the square of the dispersion in spectral acceleration and the square of the dispersion in the structural response given a spectral acceleration. The results of Table 5.13 show that this simplified method is not appropriate in estimating the dispersion in AFSA for highly nonlinear systems, such as Models 2 and 3.

presented in panels a through d of Figure 5.29, respectively, and the results in Y direction are presented in Figure 5.30. The results at Node 1009 are not presented in Figure 5.29 and Figure 5.30 since the magnitude of the AFSA values at Node 1009 is generally between that at Nodes 201 and 216 (see Figure 5.27 and Figure 5.28) and the inclusion of the data at Node 1009 will not alter the conclusions. Each panel in Figure 5.29 and Figure 5.30 has the same scale for the X and Y axes to enable the direct comparison of the distribution of AFSA between the conventional and base isolated models. Significant reductions in the response *space* defined by the AFSA values at Nodes 201 and 216 can be identified for the base isolated models.

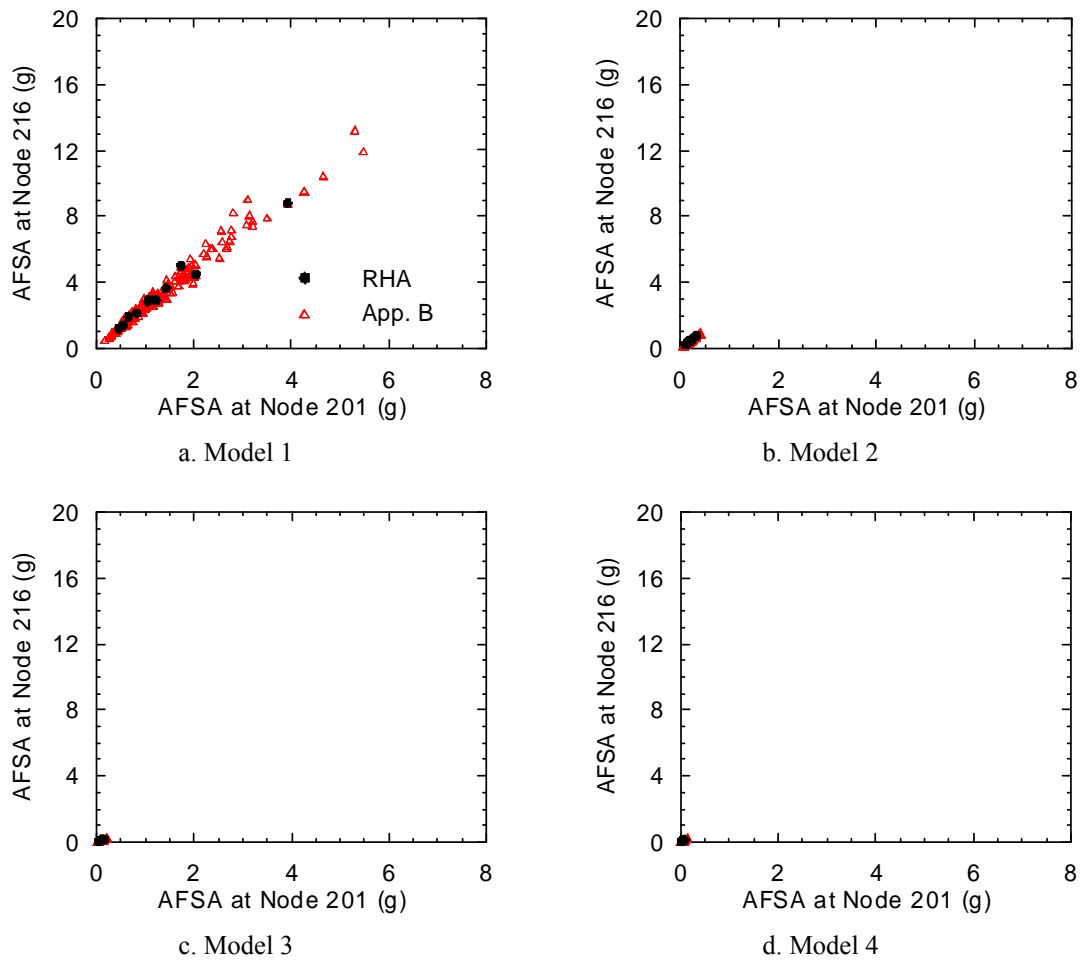


**Figure 5.29. AFSA at Nodes 201 and 216 in the X direction generated using 1) response-history analyses and 2) the procedure of Appendix B for the scenario-based assessment of Models 1, 2, 3 and 4**



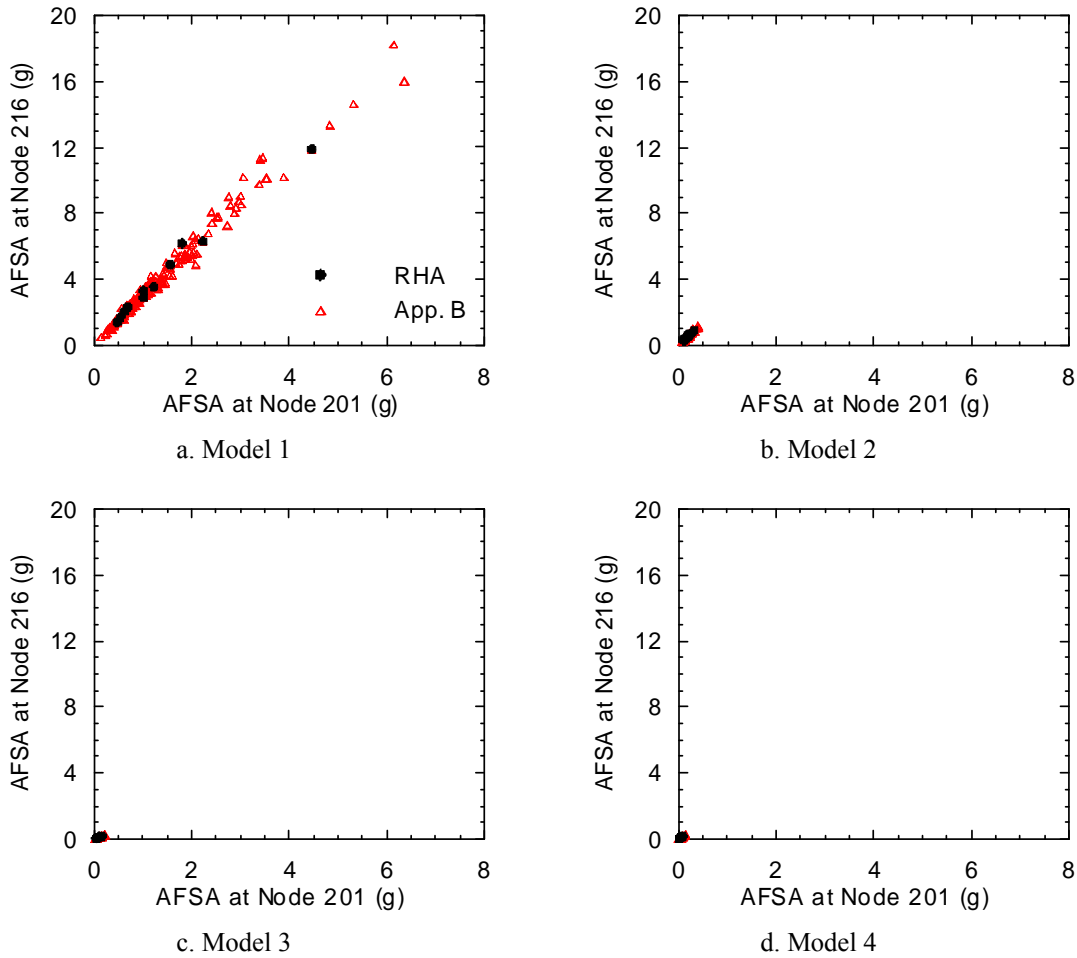
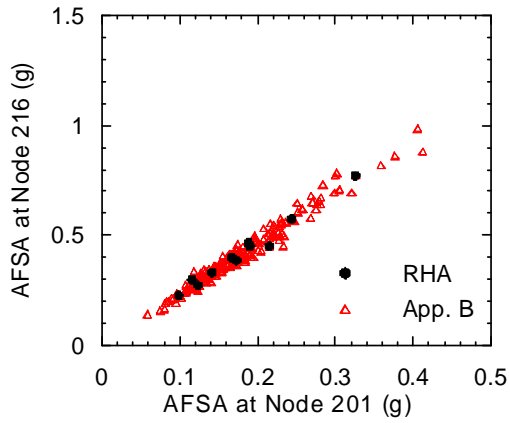
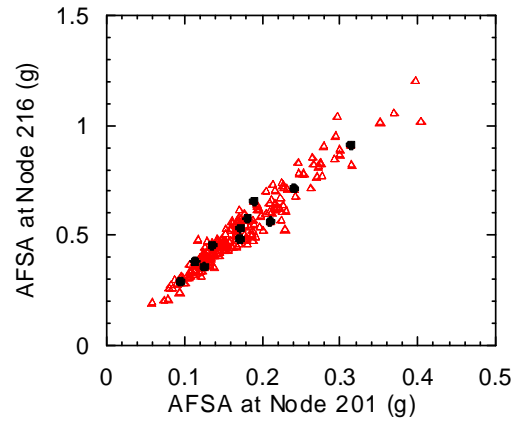


**Figure 5.30. AFSA at Nodes 201 and 216 in the Y direction generated using 1) response-history analyses and 2) the procedure of Appendix B for the scenario-based assessment of Models 1, 2, 3 and 4**

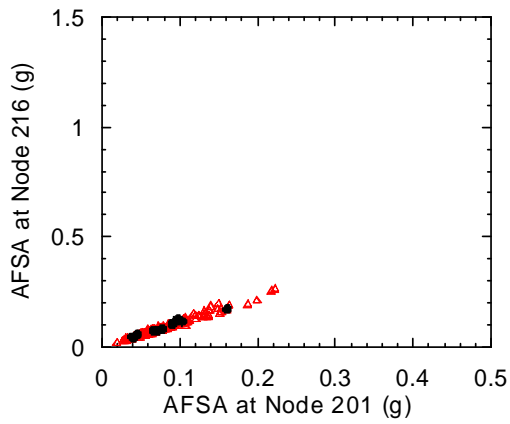
For clarity, the results of Figure 5.29 and Figure 5.30 for the base isolated models were re-plotted in Figure 5.31 using smaller scales in the X and Y axes. Figure 5.31 shows that a) the AFSA values generated per Appendix B have similar distributions to those computed using response-history analysis; and b) the response of Model 2 is greater than that of Models 3 and 4 in this case. Note that the isolation system of Model 2 has higher pre-yield stiffness than those of Models 3 and 4.



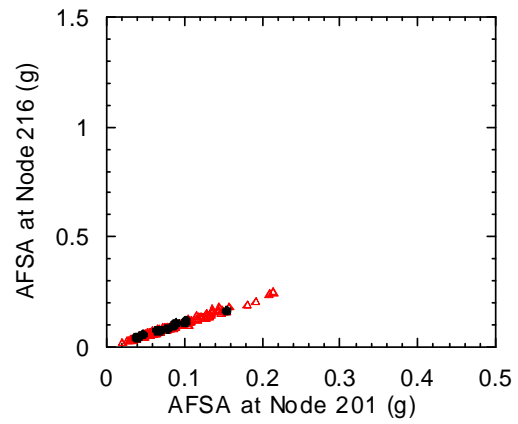
a. Model 2, X dir.



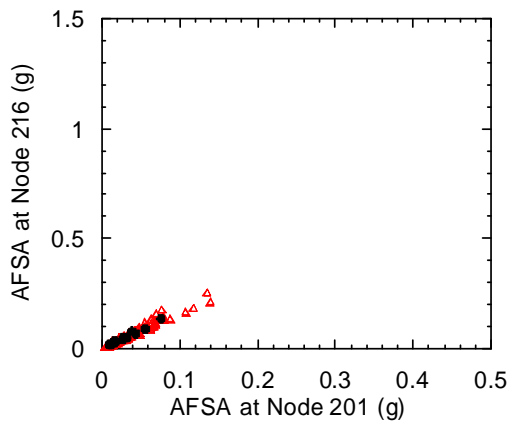
b. Model 2, Y dir.



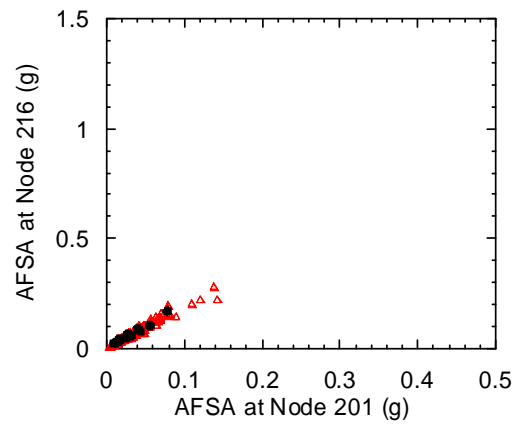
c. Model 3, X dir.



d. Model 3, Y dir.



e. Model 4, X dir.



f. Model 4, Y dir.

**Figure 5.31. AFSA at Nodes 201 and 216 generated using 1) response-history analyses and 2) the procedure of Appendix B for the scenario-based assessment of Models 2, 3 and 4**

### 5.3.4 Probability of Unacceptable Performance

#### 5.3.4.1 Model 1

The analyses of Table 5.6 and Table 5.7 were repeated using the underlying demand-parameter matrix of Table 5.9 to address the following questions for the scenario-based assessment of Model 1:

1. Are a family of 11 fragility curves and a demand-parameter matrix consisting of 200 row vectors sufficient to capture the distribution of the probability of unacceptable performance?
2. What is the impact of using median and mean fragility curves on estimating the probability of unacceptable performance?
3. Can the use of mean fragility curves provide an unbiased estimate of the mean probability of unacceptable performance estimated using a family of fragility curves? If so, what is the confidence level for the estimate using the mean fragility curve?

Results are presented in Table 5.14 and Table 5.15. Figure 5.32 presents the CDFs obtained by sorting the three sets of 2000 realizations for Analyses 1a, 1b and 1c. The three curves are nearly identical and have the same mean value of 0.51 (see Table 5.14). The use of 11 fragility curves at each node and 200 row vectors captures the distribution of unacceptable performance in this example and the mean value of the distribution ( $=0.51$ ) is used to benchmark the results for Analyses 2 and 3 below.

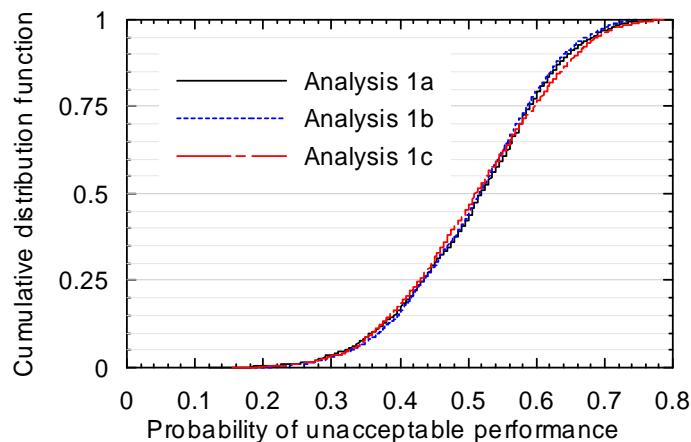


**Figure 5.32. Distributions of the probability of unacceptable performance for Analyses 1a and 1b for the scenario-based assessment of Model 1**

**Table 5.14. Analyses 1, 2 and 3 for the scenario-based assessment of Model 1**

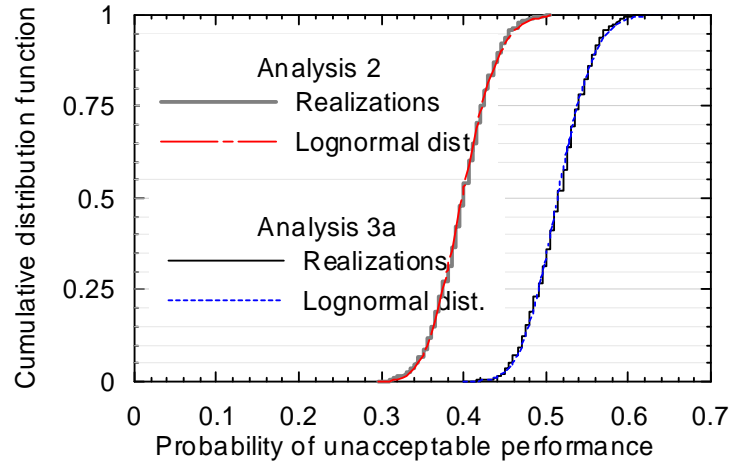
Analysis		Fragility curve for each node	Number of fragility curves in a family	Number of row vectors <sup>1</sup>	Number of trials	Median <sup>2</sup>	Mean <sup>3</sup>
Analysis 1	a	Randomly selected	11	200	2000	0.52	0.51
	b		11	2000		0.52	0.51
	c		21	200		0.51	0.51
Analysis 2		Median	--	200		0.40	0.40
Analysis 3	a	Mean	--	200		0.52	0.52

1. Number of row vectors in the demand-parameter matrix.
2. Median of the 2000 realizations for the probability of unacceptable performance from the 2000 trials.
3. Arithmetic mean of the 2000 realizations for the probability of unacceptable performance from the 2000 trials.

**Table 5.15. Statistics of Analysis 3 for the scenario-based assessment of Model 1**

Analysis	3a	3b	3c	3d	3e	3f	3g
Number of row vectors	200	500	1000	1500	2000	2500	3000
Arithmetic mean	0.52	0.52	0.51	0.52	0.51	0.52	0.52
Median (counting)	0.52	0.51	0.51	0.51	0.51	0.51	0.51
Median (Equation A.5)	0.51	0.51	0.51	0.51	0.51	0.51	0.51
Dispersion (Equation A.6)	0.068	0.043	0.031	0.025	0.022	0.020	0.018
Confidence level	0.86	0.98	1.00	1.00	1.00	1.00	1.00

Figure 5.33 presents the CDFs developed by sorting the two sets of 2000 realizations for Analyses 2 and 3a. The mean values of the CDFs are 0.4 and 0.52 for Analyses 2 and 3a, respectively (see Table 5.14). The mean value for Analysis 2 (using the median fragility curves) is smaller than that for Analysis 3a (using the mean fragility curves) since most ASFA values in the underlying demand-parameter matrix (Table 5.9) are smaller than the value of  $\hat{a}$  for the corresponding family of fragility curves, where the probability of failure for the median curve is smaller than that for the mean curve. Importantly, the mean value for Analysis 3a is almost identical to the benchmark value for the probability of unacceptable performance from Analysis 1.



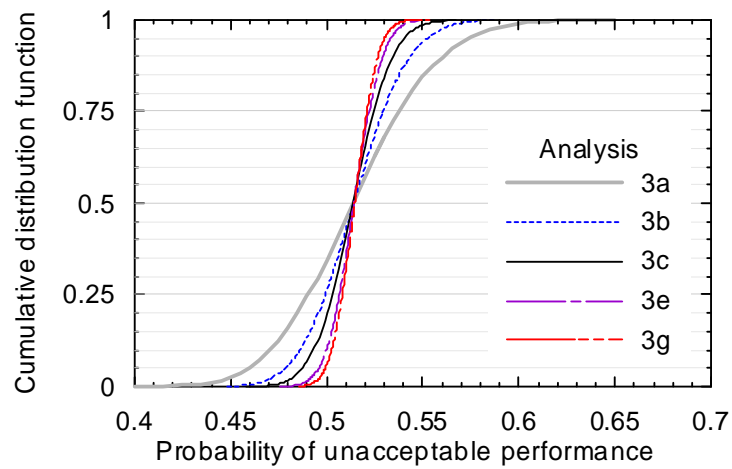
**Figure 5.33. Distributions of the probability of unacceptable performance for Analyses 2 and 3a for the scenario-based assessment of Model 1 established a) from sorting the realizations and b) using a lognormal distribution**

Figure 5.33 also presents goodness-of-fit tests, where the CDF developed by sorting the 2000 realizations for Analysis 2 (3a) is compared with the CDF of a lognormal distribution estimated from the 2000 realizations. The CDFs for Analyses 2 and 3a are well represented by lognormal distributions.

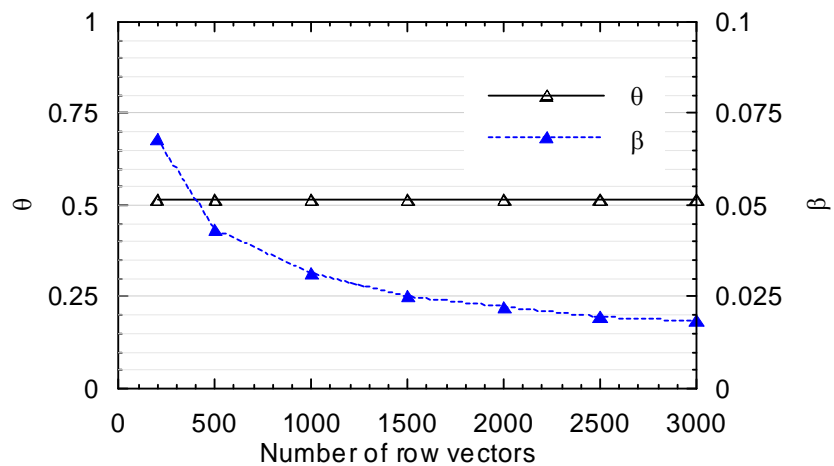
Analysis 3a was repeated using 500, 1000, 1500, 2000, 2500 and 3000 row vectors to study confidence levels. These analyses were denoted Analyses 3b through 3g, respectively. Results are presented in Figure 5.34 through Figure 5.38.

Figure 5.34 presents the CDFs of the probability of unacceptable performance for each of Analyses 3a (200 rows), 3b (500 rows), 3c (1000 rows), 3e (2000 rows) and 3g (3000 rows). The medians and dispersions computed using (A.5) and (A.6) for Analyses 3a through 3g are presented in Figure 5.35 as a function of the number of row vectors. The results of Figure 5.35 show that  $\theta$  is constant at 0.51 and the value of  $\beta$  decreases as the number of row vectors increases. All values of  $\beta$  are smaller than 0.08.

The CDFs of Figure 5.34 for Analysis 3 are re-plotted in Figure 5.36 together with the CDF of Figure 5.32 for Analysis 1b. All the curves have the same median value but different dispersions. The dispersion in the curve for Analysis 1b is greater than those in the curves for Analysis 3. Note that the purpose of Analysis 3 is to capture the mean value of the distribution for Analysis 1. The small dispersion in the results for Analysis 3 enables the analysis to be performed using only one trial, instead of repeating the analysis hundreds of times for a reliable estimation.



**Figure 5.34. Distributions of the probability of unacceptable performance for Analyses 3a, b, c, e and g for the scenario-based assessment of Model 1**



**Figure 5.35. Medians and dispersions of the probability of unacceptable performance for Analysis 3 for the scenario-based assessment of Model 1 as a function of the number of row vectors of the DP matrix**

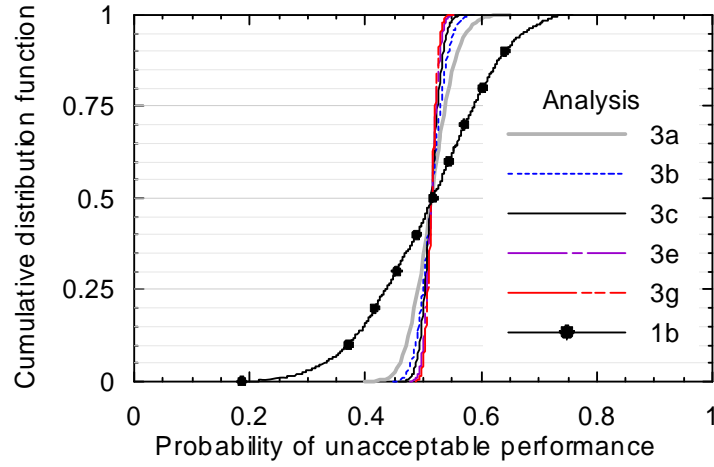


Figure 5.36. Distributions of the probability of unacceptable performance for Analyses 1b and 3 for the scenario-based assessment of Model

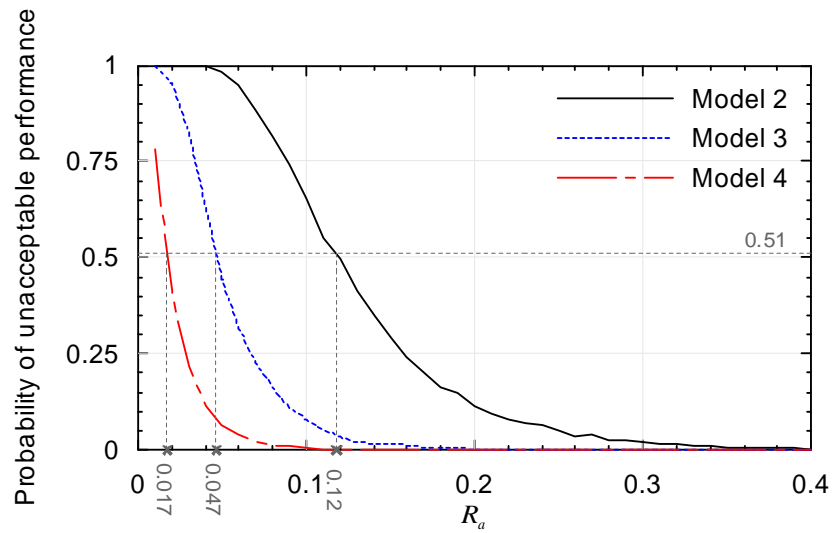
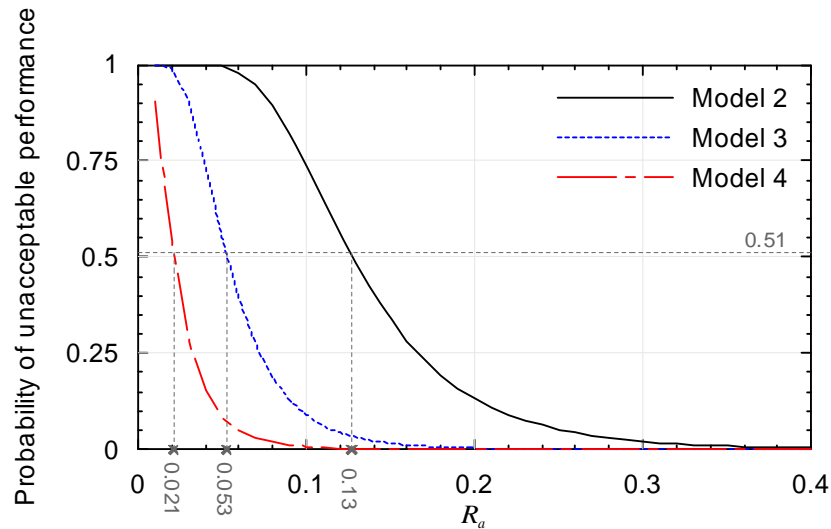


Figure 5.37. Probability of unacceptable performance as a function of  $R_a$  for the scenario-based assessment of Models 2, 3 and 4 using 2000 row vectors



**Figure 5.38. Probability of unacceptable performance as a function of  $R_a$  for the scenario-based assessment of Models 2, 3 and 4 using 200,000 row vectors**

Table 5.15 summarizes the statistics for Analyses 3a through 3g, including the arithmetic mean, median (through counting), median (using (A.5)) and dispersion (using (A.6)) of the 2000 realizations for each analysis. The trends in the values of mean (or median) and dispersion for Analysis 3 were discussed previously. The confidence levels listed in Table 5.15 increase as the number of row vectors increases. In this example, the use of 200 row vectors can achieve a confidence level of 86%; the use of 500+ row vectors almost guarantees the estimate of the probability of unacceptable performance to be within  $\pm 10\%$  of the benchmark value.

#### 5.3.4.2 Models 2, 3 and 4

The results presented in Sections 5.2.4.2 and 5.3.4.1 led to the observation that the mean value of the probability of unacceptable performance obtained using a family of fragility curves (Analysis 1) can be estimated without bias and with high confidence using the mean fragility curve of the family (Analysis 3). Accordingly, the probabilities of unacceptable performance for the scenario-based assessments of Models 2, 3 and 4 were computed using Analysis 3e with only one trial. No unacceptable performance was observed in any of the base isolated models. This does not mean that the probabilities of unacceptable performance for Models 2, 3 and 4 are zero since the probability of failure defined by any fragility curve of Figure 5.10 is not zero unless the value of ASFA is zero. If the probability of unacceptable performance is much smaller than 0.0005 ( $=1/2000$ ), many additional trials (row vectors) are required to capture such a small probability. To investigate this further, the analysis described above was repeated using 200,000 row vectors. Only one row vector for Model 2 resulted in unacceptable performance. Accordingly, the



probability of unacceptable performance for the scenario-based assessments of Models 2, 3 and 4 is smaller than  $5 \times 10^{-6}$ . (The corresponding value for the conventional NPP is 0.51.)

#### 5.3.4.3 Results Using Modified Mean Fragility Curves

Section 5.3.4.2 identified the utility of base isolation to reduce the probability of unacceptable performance of a conventional NPP assuming the secondary systems have the same capacities in the conventional and base isolated models. For secondary systems whose design is controlled by seismic demands, the use of base isolation can greatly reduce those demands, enable a more economic (lower strength) design for the systems and maintain a probability of unacceptable performance that is smaller than that in conventional NPPs.

To characterize the relationship between the degree of capacity reduction on secondary systems and the probability of unacceptable performance of base isolated NPPs, a parameter,  $R_a$ , is defined:

$$R_a = \frac{\hat{a}'}{\hat{a}} \quad (5.9)$$

where  $\hat{a}'$  is a deterministic value representing the reduced median capacity of the fragility curves. In this study,  $R_a$  was varied between 0.01 and 1.

Analysis 3e of Section 5.3.4.1 was repeated for each of Models 2, 3 and 4 using the updated fragility curves, which are similar to those presented in Figure 5.10, except that the median capacity for each family of fragility curves was reduced from  $\hat{a}$  to  $R_a \hat{a}$ .

For a given base isolated model and a given value of  $R_a$ , a value of the probability of unacceptable performance was computed per the procedure of Analysis 3e using only one trial. The results are presented in Figure 5.37 as a function of  $R_a$  and model number. Figure 5.37 also presents the probabilities of unacceptable performance identified in Section 5.3.4.1 for Model 1 and the value of  $R_a$  for each isolated NPP model that has a probability of unacceptable performance equal to that for Model 1; the values of  $R_a$  for this *equivalent* performance are 0.12, 0.047 and 0.017 for Models 2, 3 and 4, respectively. Although such small values of  $R_a$  likely have little practical significance since seismic demand is not the only factor controlling the design of a secondary system, these results show the advantages of base isolation, namely, enabling the design of secondary systems for far smaller seismic demands than for those in conventional (non-isolated) NPPs.

Analysis 3e above utilized 2000 row vectors. To verify the impact of the number of row vectors on the results, the above analysis was repeated using 200,000 row vectors. The results are presented in Figure 5.38. The differences in the results are insignificant. If the median values of the fragility curves are reduced, the probability of unacceptable performance increases and the use of a very large number of row vectors becomes unnecessary.

## **5.4 Time-Based Assessment of the Conventional and Base Isolated Reactor Building**

### **5.4.1 Hazard Curves**

Section 5.4 presents the time-based assessment of Models 1 through 4 and compares the annual frequency of unacceptable performance of the four models. A time-based assessment is performed as a series of intensity-based assessments except that the earthquake shaking is described by a seismic hazard curve. Figure 5.39 presents four seismic hazard curves at periods of 0.1, 0.14, 1 and 2 seconds. The 0.1- and 1-second curves were obtained from the ESP report for the sample NPP site and the other two curves were developed in this study for the use of the time-based assessment for Models 1 through 4 since the 0.14- and 2-second curves were not available in the ESP report.

Based on the UHS presented in Table 5.1 for a MAFE of  $10^{-5}$ , the spectral accelerations at periods of 0.14 and 2 seconds are 1.024 and 0.094 g, respectively. The value of 1.024 was determined from the linear interpolation of the spectral accelerations at 0.1 and 0.2 second. The 0.14- and 2-second hazard curves used in this study were assumed to have the same shapes as the 0.1- and 1-second curves, respectively, and generated by shifting the 0.1- and 1-second curves to spectral accelerations of 1.024 and 0.094 g, respectively, at a MAFE of  $10^{-5}$ . Table 5.16 lists the X and Y coordinates of the 0.14- and 2-second hazard curves used in this study.

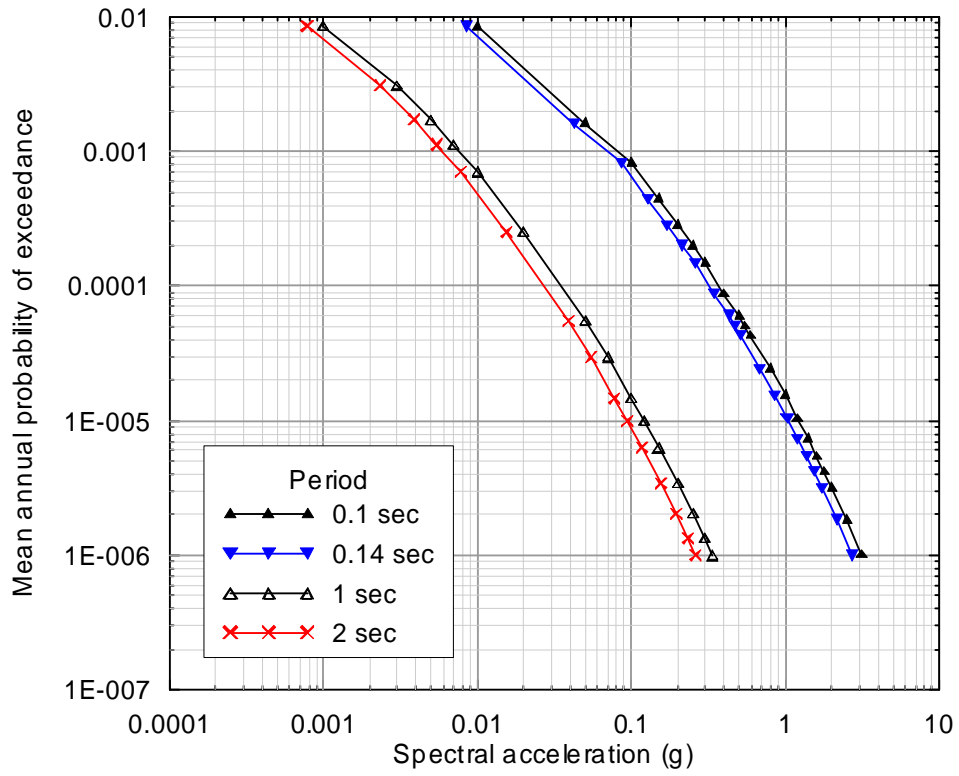


Figure 5.39. Seismic hazard curves at periods of 0.1, 0.14, 1 and 2 seconds for the sample NPP site

**Table 5.16. Seismic hazard curves at periods of 0.14 and 2 seconds for the sample NPP site**

T= 0.14 sec		T= 2 secs	
MAFE	Spectral acceleration (g)	MAFE	Spectral acceleration (g)
1.60E-03	4.28E-02	8.51E-03	7.79E-04
8.20E-04	8.56E-02	3.09E-03	2.34E-03
4.40E-04	1.28E-01	1.72E-03	3.89E-03
2.82E-04	1.71E-01	1.12E-03	5.47E-03
2.00E-04	2.15E-01	7.05E-04	7.79E-03
1.47E-04	2.58E-01	2.54E-04	1.55E-02
8.71E-05	3.41E-01	5.53E-05	3.91E-02
6.03E-05	4.29E-01	2.96E-05	5.45E-02
5.00E-05	4.68E-01	1.47E-05	7.79E-02
4.29E-05	5.10E-01	1.00E-05	9.40E-02
2.42E-05	6.80E-01	6.31E-06	1.17E-01
1.53E-05	8.56E-01	3.43E-06	1.55E-01
1.04E-05	1.02E+00	2.06E-06	1.95E-01
7.33E-06	1.20E+00	1.35E-06	2.33E-01
5.43E-06	1.37E+00	1.00E-06	2.62E-01
4.16E-06	1.54E+00	6.68E-07	3.12E-01
3.16E-06	1.71E+00	3.78E-07	3.90E-01
1.84E-06	2.15E+00	2.33E-07	4.67E-01
1.00E-06	2.68E+00	1.03E-07	6.23E-01

#### 5.4.2 Scaling of Ground Motions

##### 5.4.2.1 Model 1

The procedure of Section 3.3.4.3 was used to scale the 11 SGMS ground motions for the time-based assessment. In the *draft ATC-58 Guidelines*, the time-based assessment is performed in the range between 0.05 g and the spectral acceleration corresponding to a MAFE of  $2 \times 10^{-4}$  since the *Guidelines* is prepared for regular buildings. This range is not appropriate for NPPs since the MAFE for the SSE shaking (about  $10^{-5}$ ) is smaller than  $2 \times 10^{-4}$  and the upper bound spectral

acceleration for the time-based assessment should be higher than the design level to include all significant loss. In this study, the smallest MAFE of the 0.14-second hazard curve in Figure 5.39 ( $=10^{-6}$ ) was used to determine the upper bound of spectral acceleration for the time-based assessment of Model 1.

The 0.14-second hazard curve in Figure 5.39 is re-plotted in Figure 5.40, which illustrates the computation of the target spectral ordinates for scaling ground motions for the time-based assessment of Model 1. The range of spectral acceleration was selected as 0.05 g to 2.68 g, where the two spectral ordinates are associated with MAFEs of  $1.43 \times 10^{-3}$  and  $10^{-6}$ , respectively. (The appropriateness of this range will be evaluated at the end of Section 5.4 using the results of the time-based assessment.) The range of spectral acceleration was split into eight equal intervals and the midpoint value in each interval characterizes a target spectral demand for the scaling of ground motions. The second and third columns of Table 5.17 present the spectral accelerations and MAFEs ( $\lambda_i$ ), respectively, at the boundaries of the eight intervals. The eight target spectral ordinates are identified in the figure by the symbol “⊕” with values of 0.21, 0.54, 0.87, 1.2, 1.53, 1.86, 2.19 and 2.52 g. The Mean Annual Frequency (MAF,  $\Delta\lambda_i$ ) associated with each spectral interval, which is required for time-based assessment, is computed as the difference in the MAFEs at the boundaries of the interval. For example, the MAF associated with the first spectral interval, termed  $\Delta\lambda_1$ , is determined by the difference between  $\lambda_1$  ( $1.43\text{E-}03$ ) and  $\lambda_2$  ( $7.43\text{E-}05$ ) shown in the third column of Table 5.17. The values of  $\Delta\lambda_i$  for the eight spectral intervals for Model 1 are listed in the second column of Table 5.18.

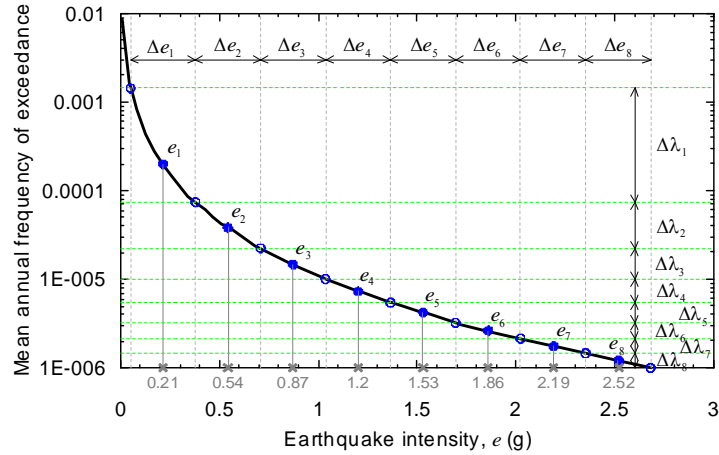


**Figure 5.40. Computation of target spectral ordinates for scaling ground motions for the time-based assessment of Model 1**

Eight bins of ground motions, termed Bins TC1 through TC8, used in the time-based assessment for Model 1 were developed by amplitude scaling the eleven SGMS ground motions to each of the eight target spectral ordinates identified in Figure 5.40 at a period of 0.14 second. Figure 5.41 presents the spectral accelerations of the ground motions in Bins TC1 and TC8 using a semi-log scale (panel a) and a log-log scale (panel b).

#### 5.4.2.2 Models 2, 3 and 4

The analysis of Figure 5.40 was repeated using the 2-second hazard curve of Figure 5.39 to determine the target spectral ordinates for scaling ground motions for the time-based assessments of the base isolated NPP models (i.e., Models 2, 3 and 4). The process is illustrated in Figure 5.42. To enable a comparison, the MAFE range for Model 1 ( $1.43 \times 10^{-3}$  to  $10^{-6}$ ) was used in Figure 5.42<sup>7</sup>. The eight target spectral ordinates are identified on the X axis of Figure 5.42 by the symbol “⊕” with values of 0.021, 0.052, 0.0844, 0.116, 0.148, 0.18, 0.212 and 0.244 g. The fourth and fifth columns of Table 5.17 present the spectral accelerations and MAFEs, respectively, at the boundaries of the eight spectral intervals determined in Figure 5.42. The values of  $\Delta\lambda_i$  for the eight spectral intervals are listed in the third column of Table 5.18.

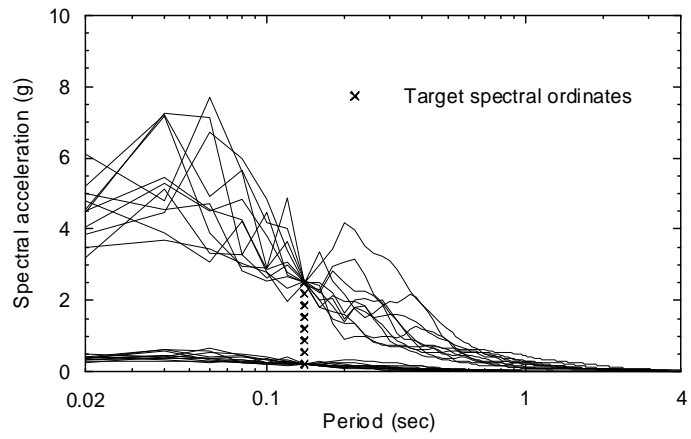
<sup>7</sup> The hazard curve of Figure 5.42 shows a problem of the spectral acceleration range recommended in the *draft ATC-58 Guidelines* for long-period or base isolated structures in CEUS: the MAFE associated with a spectral ordinate of 0.05 g is much smaller than  $2 \times 10^{-4}$ .

**Table 5.17. Spectral accelerations and MAFs ( $\lambda_i$ ) at the boundaries of spectral intervals on the seismic hazard curves of Figure 5.40 and Figure 5.42**

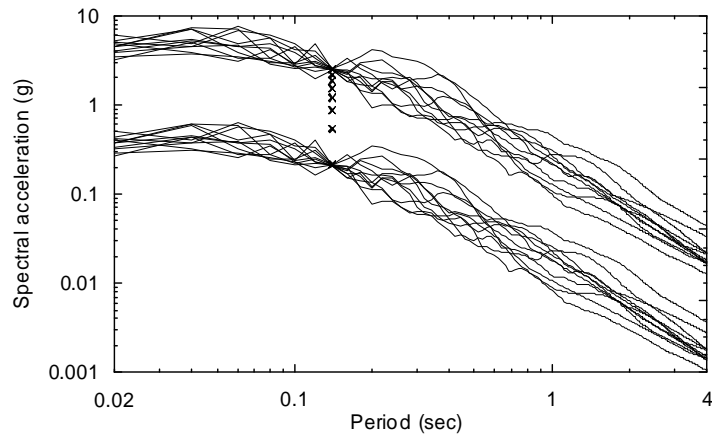
<i>i</i>	T= 0.14 sec		T= 2 secs	
	Spectral acceleration (g)	$\lambda_i$	Spectral acceleration (g)	$\lambda_i$
1	5.00E-02	1.43E-03	4.60E-03	1.42E-03
2	3.79E-01	7.43E-05	3.65E-02	6.52E-05
3	7.08E-01	2.25E-05	6.85E-02	1.95E-05
4	1.04E+00	1.01E-05	1.00E-01	8.78E-06
5	1.37E+00	5.47E-06	1.32E-01	4.93E-06
6	1.69E+00	3.23E-06	1.64E-01	3.06E-06
7	2.02E+00	2.15E-06	1.96E-01	2.04E-06
8	2.35E+00	1.46E-06	2.28E-01	1.43E-06
9	2.68E+00	1.00E-06	2.60E-01	1.02E-06

**Table 5.18. Mean annual frequency (MAF) for the eight spectral intervals in time-based assessment**

Interval	MAF, T= 0.14 sec	MAF, T= 2 sec
$\Delta\lambda_1$	1.35E-03	1.35E-03
$\Delta\lambda_2$	5.18E-05	4.57E-05
$\Delta\lambda_3$	1.24E-05	1.07E-05
$\Delta\lambda_4$	4.63E-06	3.85E-06
$\Delta\lambda_5$	2.23E-06	1.87E-06
$\Delta\lambda_6$	1.08E-06	1.03E-06
$\Delta\lambda_7$	6.90E-07	6.09E-07
$\Delta\lambda_8$	4.59E-07	4.05E-07



a. Log-normal scale



b. Log-log scale

**Figure 5.41. Response spectra of the ground motions in Bins TC1 and TC8**



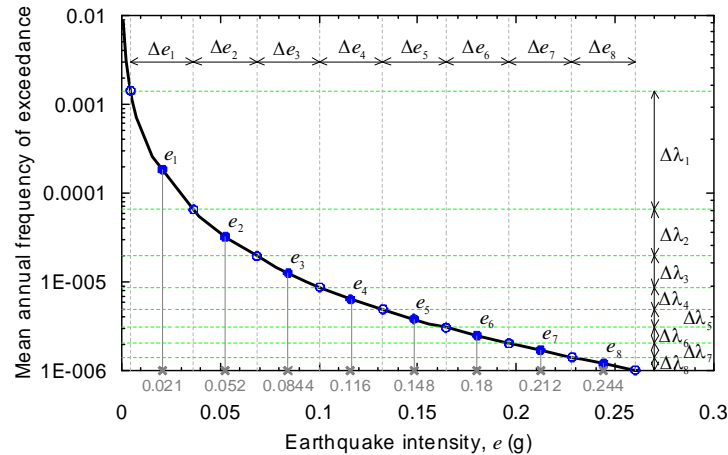


**Figure 5.42. Computation of target spectral ordinates for scaling ground motions for the time-based assessment of Models 2, 3 and 4**

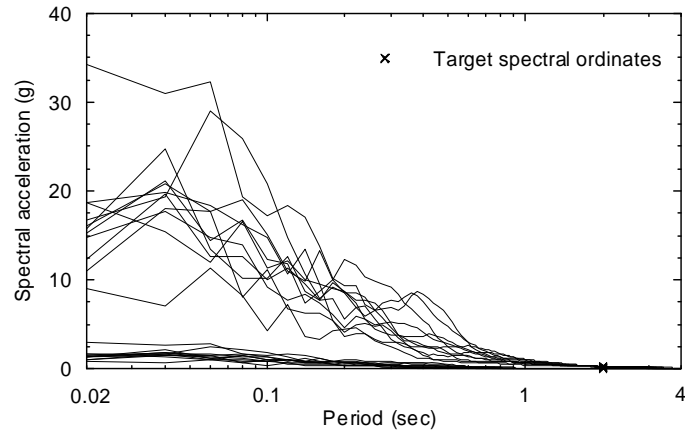
Eight bins of ground motions, termed Bins TI1 through TI8, used in the time-based assessment for Models 2, 3 and 4 were developed by amplitude scaling the eleven SGMS ground motions to each of the eight target spectral ordinates identified in Figure 5.42 at a period of 2 seconds. Figure 5.43 presents the spectral accelerations of the ground motions in Bins TI1 and TI8 using a semi-log scale (panel a) and a log-log scale (panel b).

### 5.4.3 Analysis Results

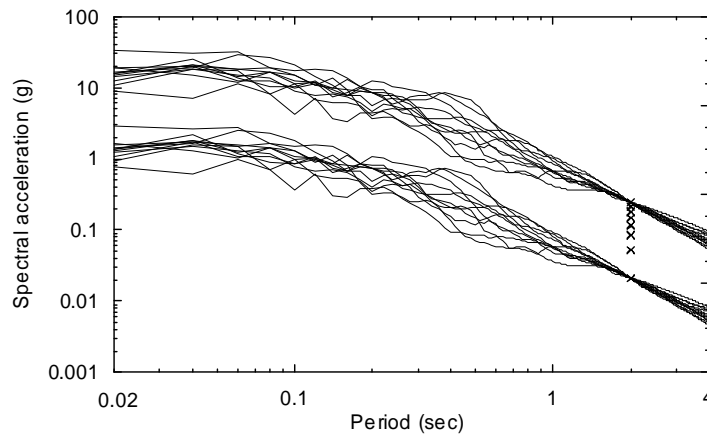
Nonlinear uni-directional response-history analyses were performed using Model 1 subjected to the Bins TC1 through TC8 ground motions and using Models 2, 3 and 4 subjected to the Bins TI1 through TI8 ground motions in the X and Y directions.

Figure 5.44 through Figure 5.48 and Table 5.19 through Table 5.22 present results for 1) Model 1 subjected to the Bin TC1 ground motions and 2) Models 2, 3 and 4 subjected to the Bin TI1 ground motions. Figure 5.44 presents the median of the 11 floor spectral accelerations between 5 and 33 Hz and the 84th, 50th and 16th percentiles of AFSA at Nodes 201, 1009 and 216 in the X direction. Figure 5.45 presents similar results in the Y direction. Table 5.19 through Table 5.22 present the demand parameter matrices for Models 1 through 4, respectively. Each parameter includes the eleven AFSA values at each of Nodes 201, 1009 and 216 in the X and Y directions. The analysis of Figure 5.14 was repeated using the AFSA values of Table 5.19 through Table 5.22 to generate the 200 sets of AFSA values for Models 1 through 4. Figure 5.46 and Figure 5.47 presents the relationships of the 200 AFSA values at Node 201 and those at Node 216 in the X and Y directions, respectively, with the same scale for the X axis and the same scale for the Y axis

to enable the direct comparison of the distributions of AFSA for the conventional and base isolated models. For clarity, the results of Figure 5.46 and Figure 5.47 for the base isolated models were re-plotted in Figure 5.48 using smaller scales for the X and Y axes.



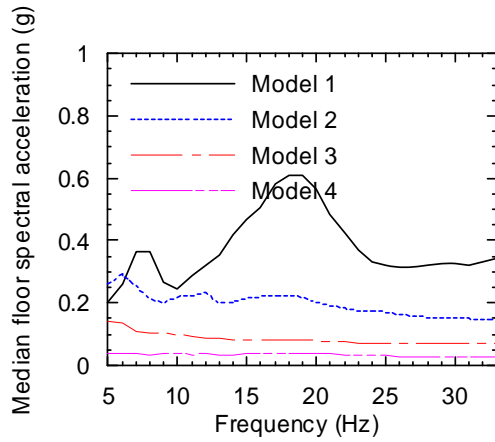
a. Log-normal scale



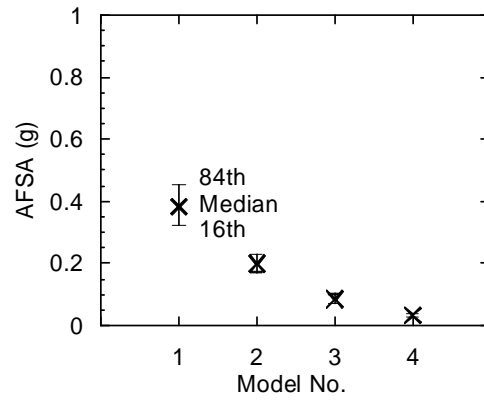
b. Log-log scale

**Figure 5.43. Response spectra of the ground motions in Bins TI1 and TI8**

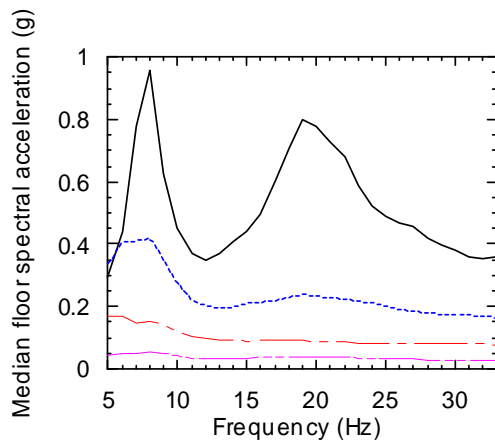
The presentation of Figure 5.44 through Figure 5.48 and Table 5.19 through Table 5.22 was repeated in Figure 5.49 through Figure 5.53 and Table 5.23 through Table 5.26 to present results for 1) Model 1 subjected to the Bin TC8 ground motions and 2) Models 2, 3 and 4 subjected to the Bin TI8 ground motions. The difference in the AFSA response between Models 1 and 2 is much more significant for the Bin 8 ground motions than for the Bin 1 ground motions since when Model 2 is subjected to ground motions with small intensity, its response is dominated by the high pre-yield stiffness of the isolators. (See Appendix F for a presentation on the influence of isolator pre-yield stiffness on floor acceleration response.)



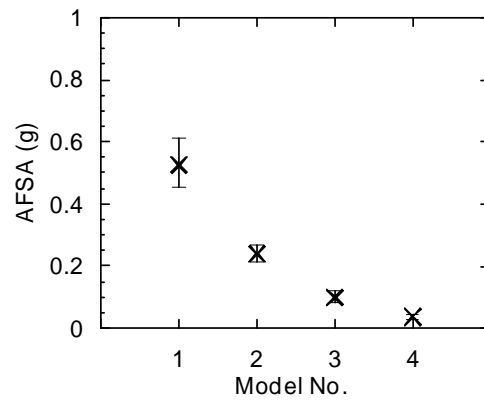
a. Median floor spectral accelerations, Node 201



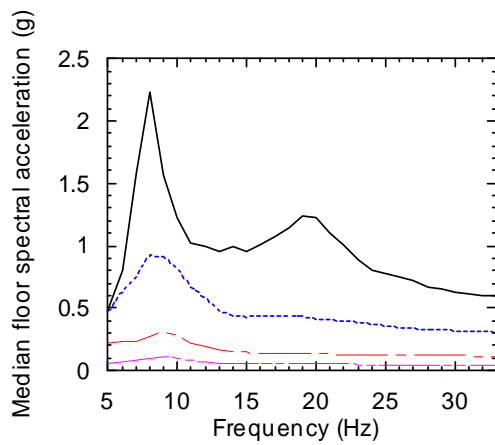
b. AFSA, Node 201



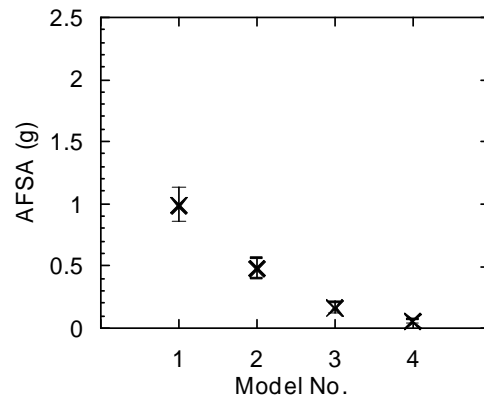
c. Median floor spectral accelerations, Node 1009



d. AFSA, Node 1009

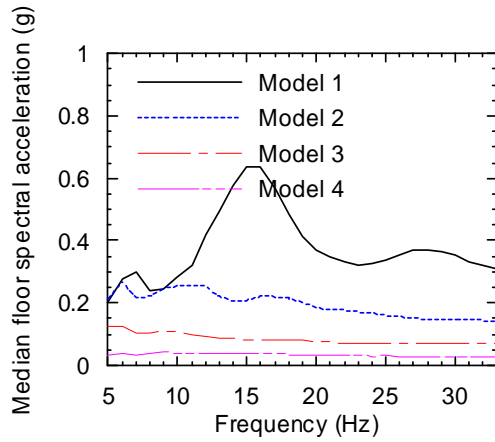


e. Median floor spectral accelerations, Node 216

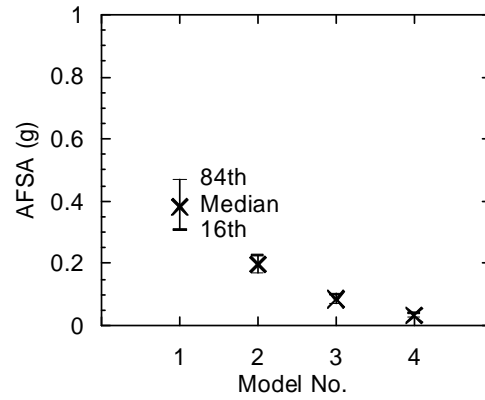


f. AFSA, Node 216

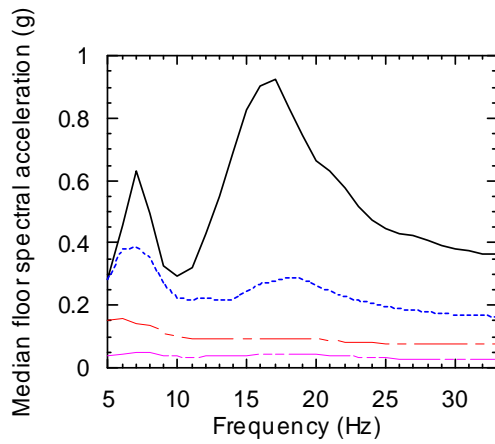
**Figure 5.44. Floor spectral accelerations at Nodes 201, 1009 and 216 in the X direction from the response-history analyses of 1) Model 1 subjected to the Bin TC1 motions and 2) Models 2, 3 and 4 subjected to the Bin TI1 motions**



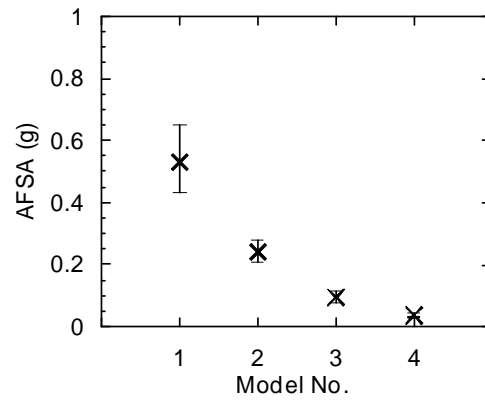
a. Median floor spectral accelerations, Node 201



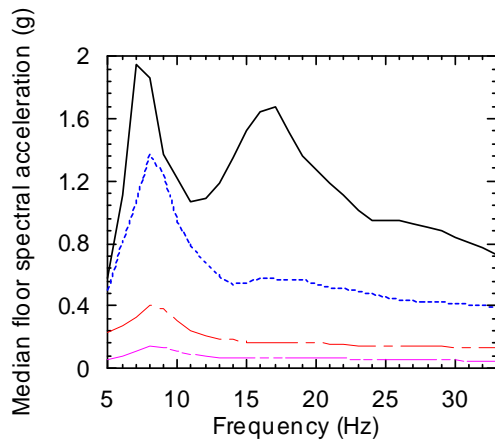
b. AFSA, Node 201



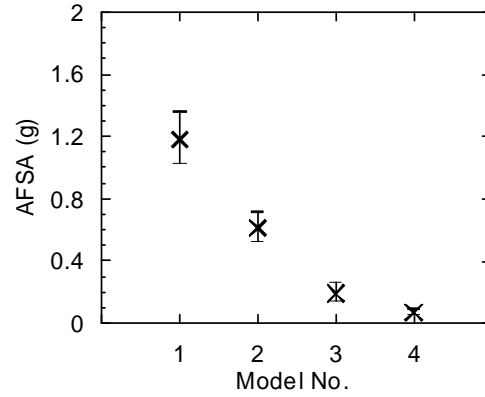
c. Median floor spectral accelerations, Node 1009



d. AFSA, Node 1009



e. Median floor spectral accelerations, Node 216



f. AFSA, Node 216

**Figure 5.45. Floor spectral accelerations at Nodes 201, 1009 and 216 in the Y direction from response-history analyses of 1) Model 1 subjected to the Bin TC1 motions and 2) Models 2, 3 and 4 subjected to the Bin TI1 motions**

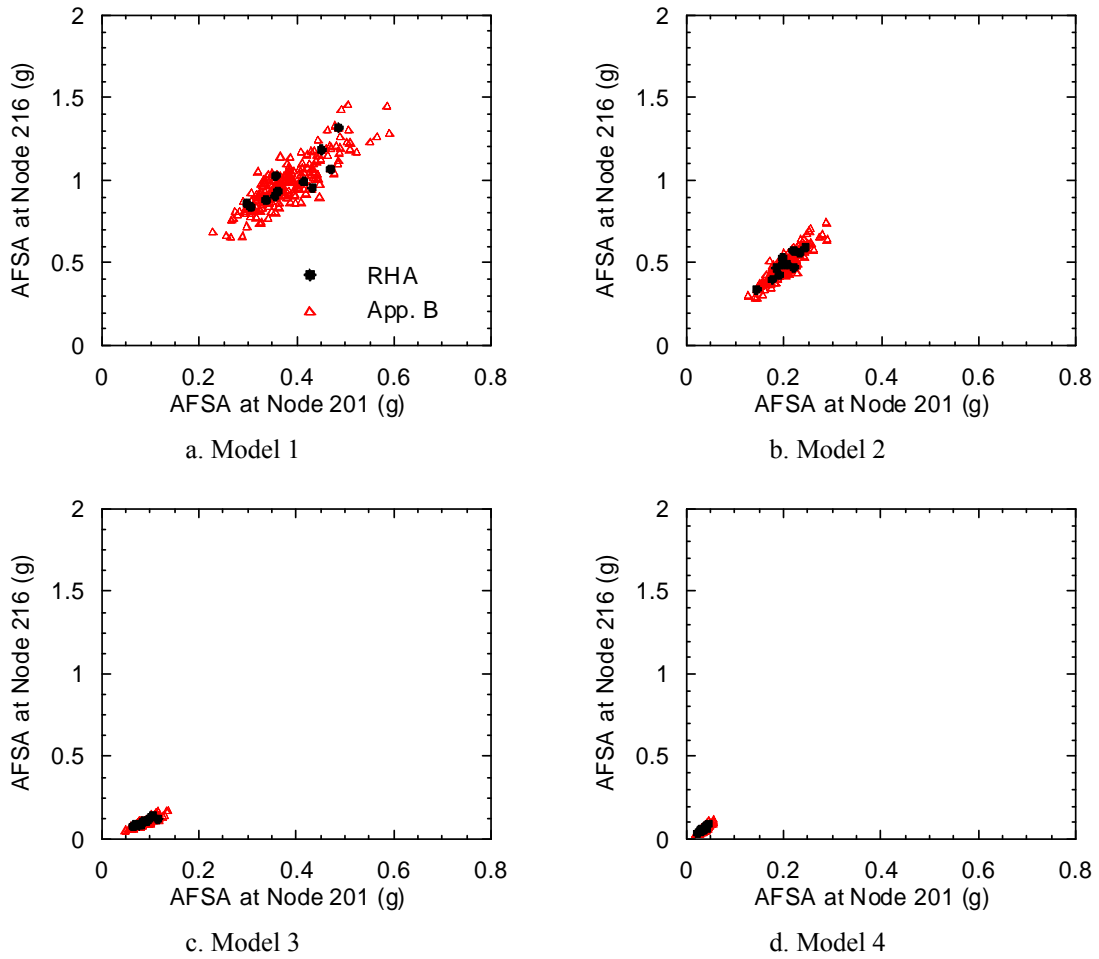


**Figure 5.46. AFSA at Nodes 201 and 216 in the X direction generated using 1) response-history analyses and 2) the procedure of Appendix B for 1) Model 1 subjected to the Bin TC1 ground motions and 2) Models 2, 3 and 4 subjected to the Bin TI1 ground motions**

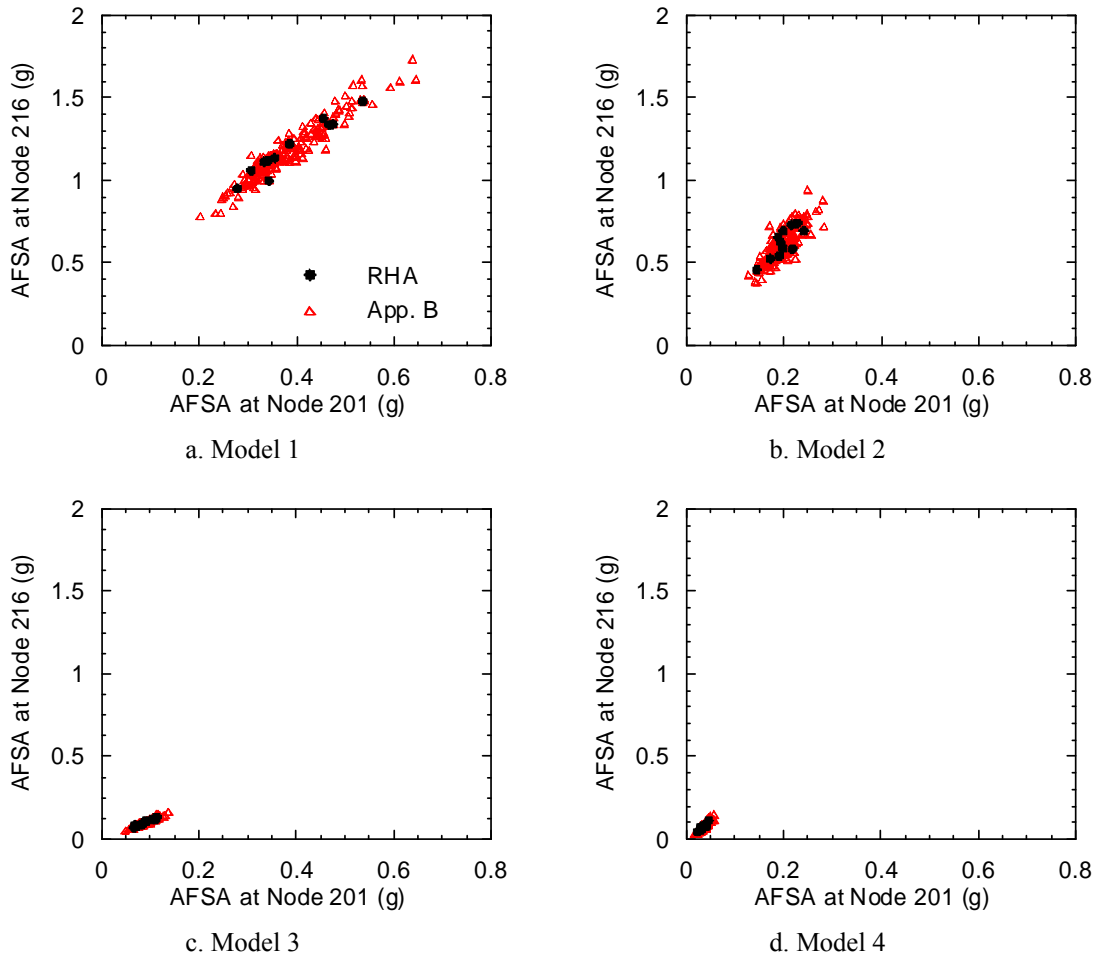


**Figure 5.47. AFSA at Nodes 201 and 216 in the Y direction generated using 1) response-history analyses and 2) the procedure of Appendix B for 1) Model 1 subjected to the Bin TC1 ground motions and 2) Models 2, 3 and 4 subjected to the Bin TI1 ground motions**

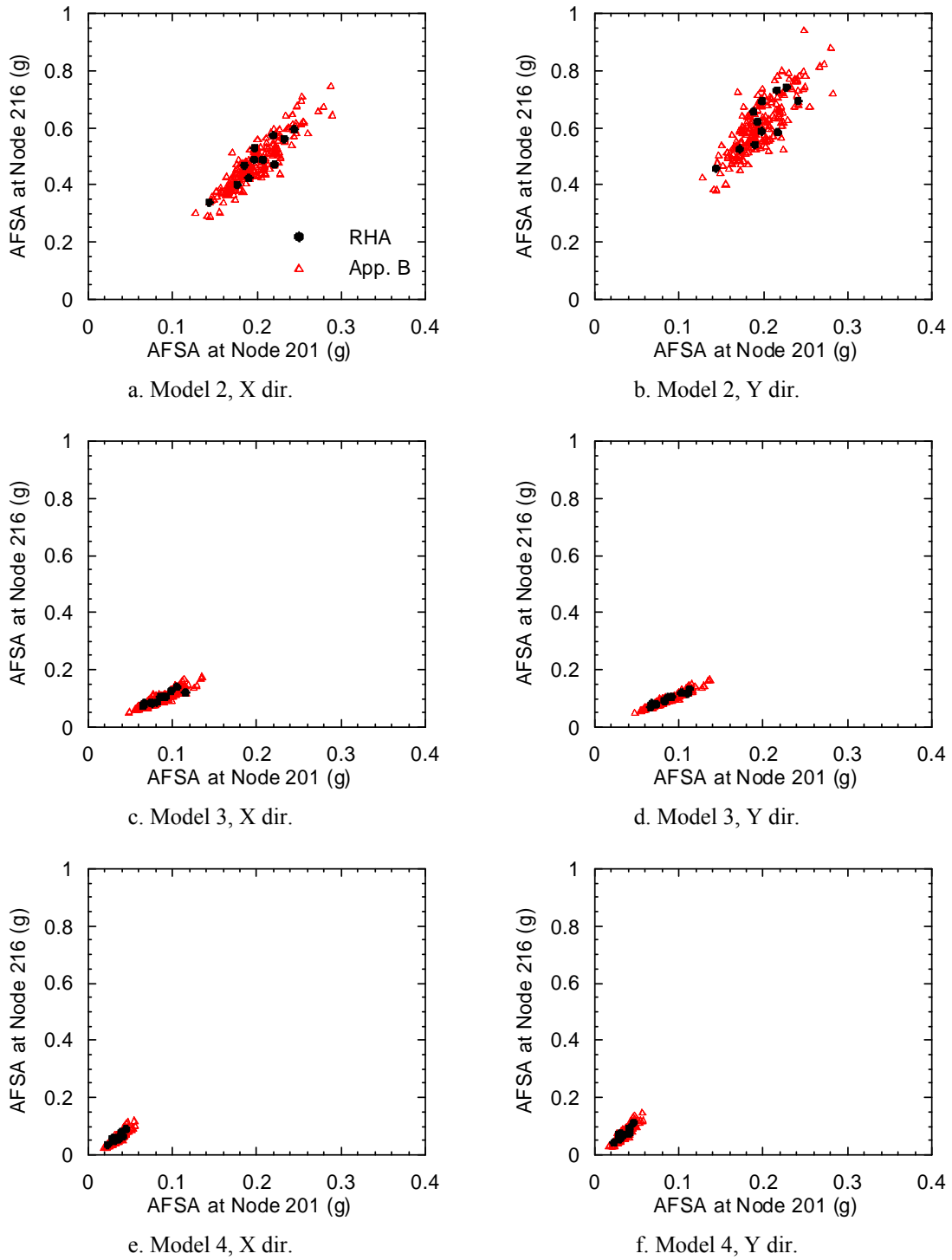
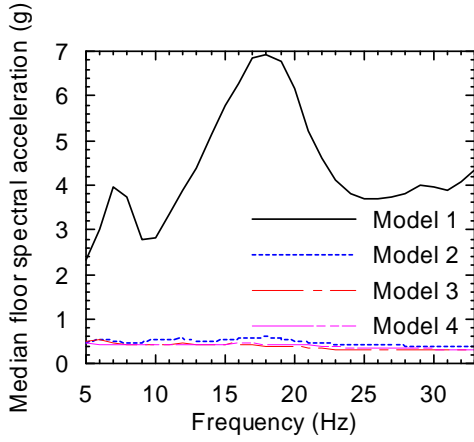
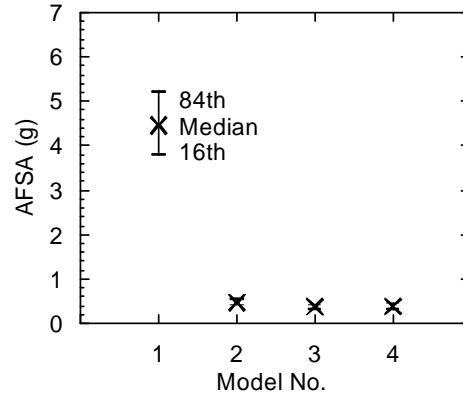


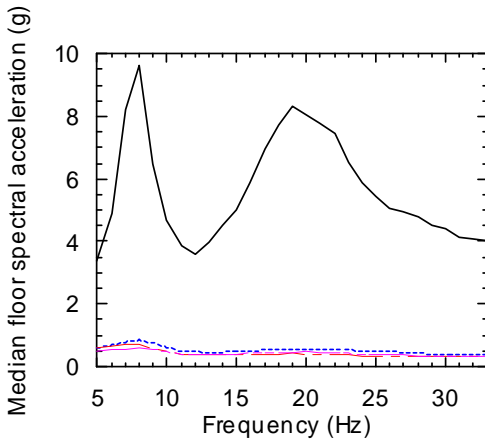
**Figure 5.48. AFSA at Nodes 201 and 216 generated using 1) response-history analyses and 2) the procedure of Appendix B for Models 2, 3 and 4 subjected to the Bin TII ground motions**



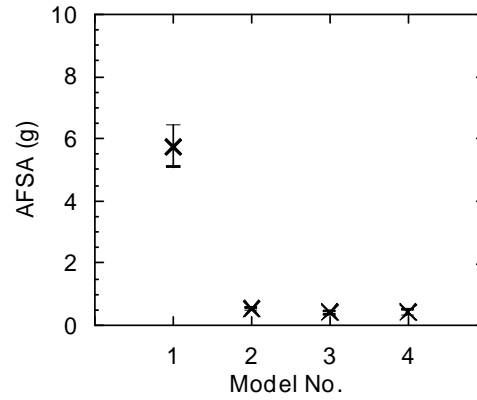
a. Median floor spectral accelerations, Node 201



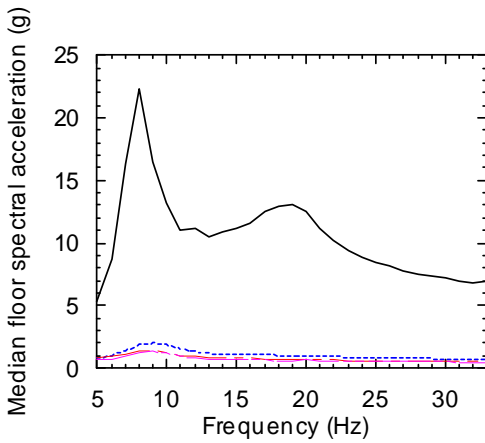
b. AFSA, Node 201



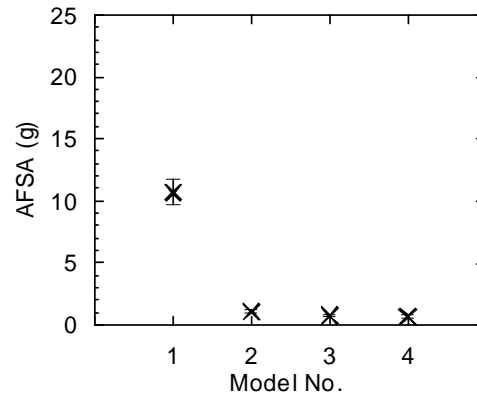
c. Median floor spectral accelerations, Node 1009



d. AFSA, Node 1009



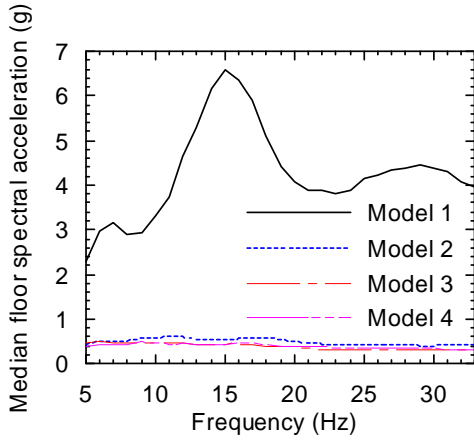
e. Median floor spectral accelerations, Node 216



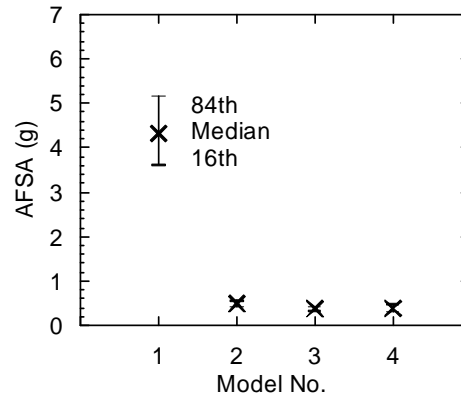
f. AFSA, Node 216

**Figure 5.49. Floor spectral accelerations at Nodes 201, 1009 and 216 in the X direction from response-history analyses of 1) Model 1 subjected to the Bin TC8 motions and 2) Models 2, 3 and 4 subjected to the Bin TI8 motions**

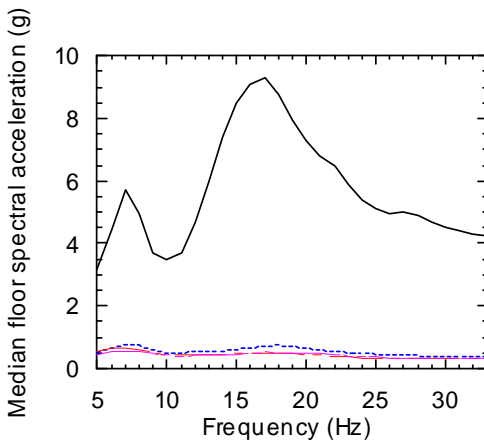




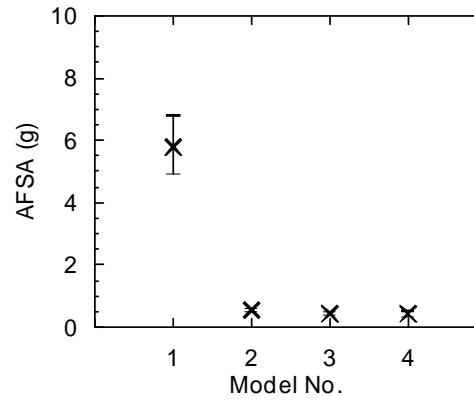
a. Median floor spectral accelerations, Node 201



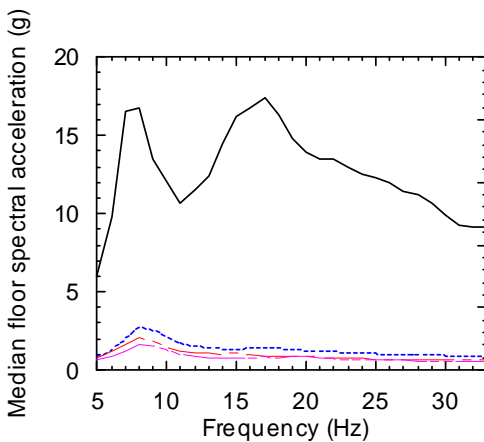
b. AFSA, Node 201



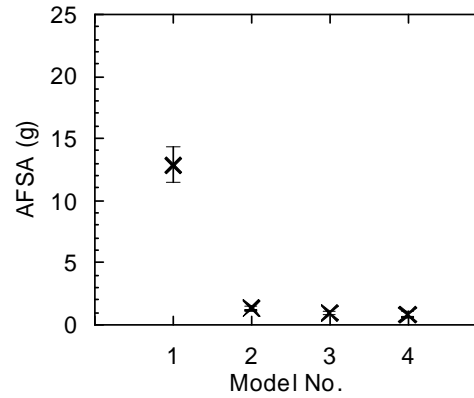
c. Median floor spectral accelerations, Node 1009



d. AFSA, Node 1009



e. Median floor spectral accelerations, Node 216



f. AFSA, Node 216

**Figure 5.50. Floor spectral accelerations at Nodes 201, 1009 and 216 in the Y direction from response-history analyses of 1) Model 1 subjected to the Bin TC8 motions and 2) Models 2, 3 and 4 subjected to the Bin TI8 motions**

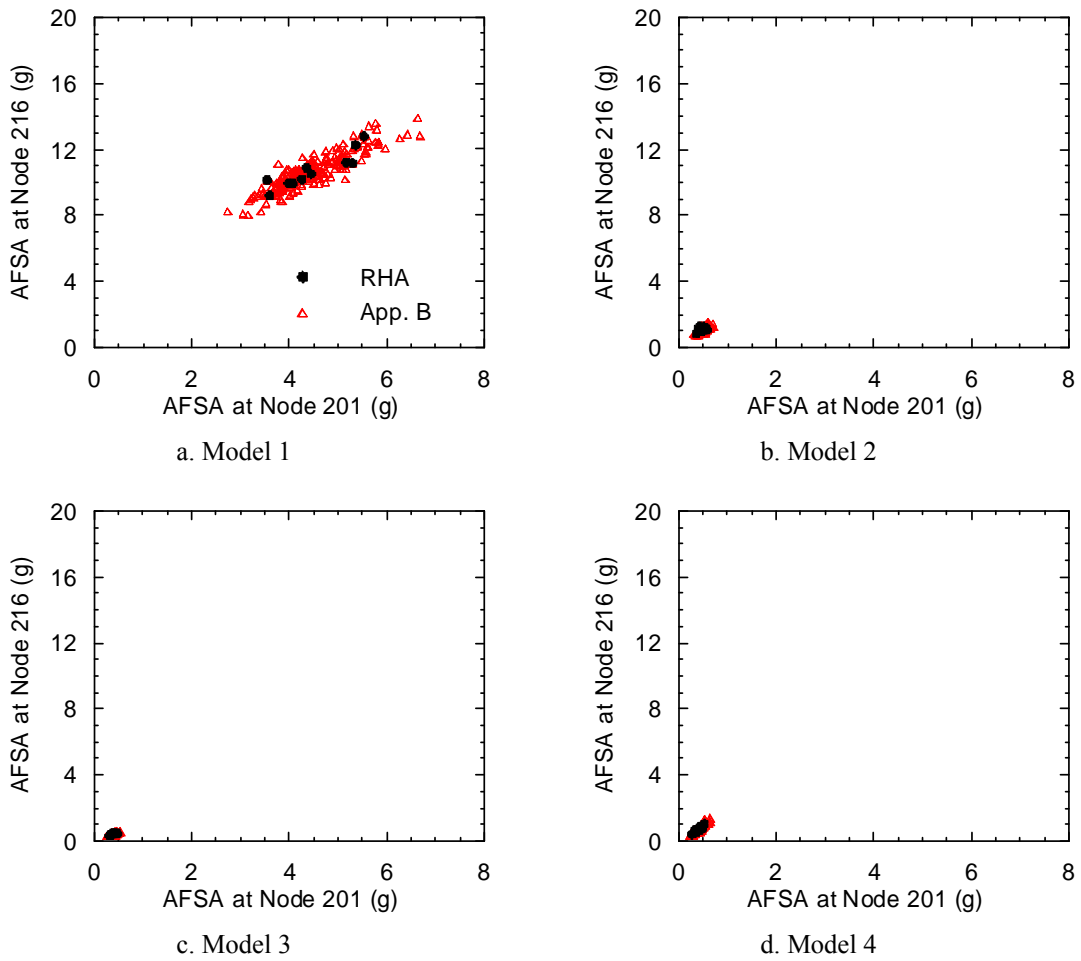


**Figure 5.51. AFSA at Nodes 201 and 216 in the X direction generated using 1) response-history analyses and 2) the procedure of Appendix B for 1) Model 1 subjected to the Bin TC8 ground motions and 2) Models 2, 3 and 4 subjected to the Bin TI8 ground motions**

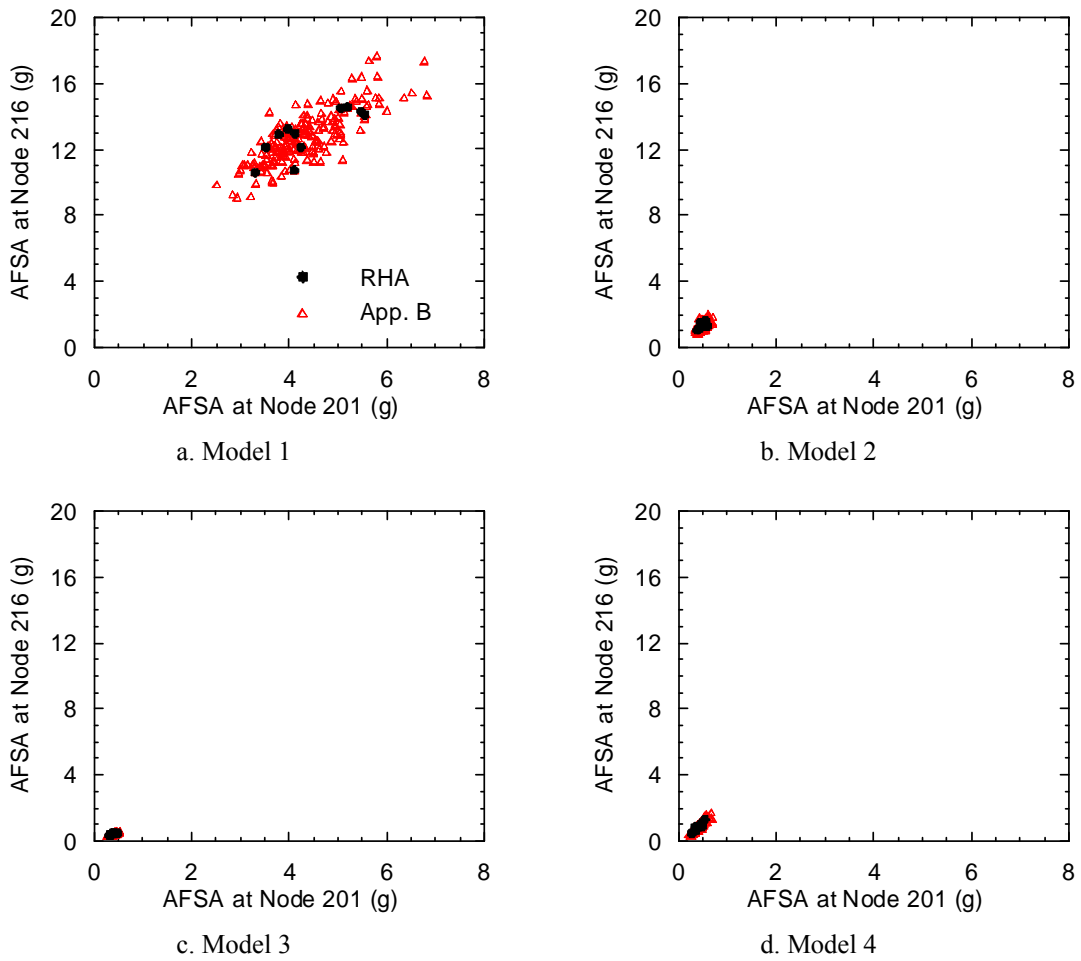


**Figure 5.52. AFSA at Nodes 201 and 216 in the Y direction generated using 1) response-history analyses and 2) the procedure of Appendix B for 1) Model 1 subjected to the Bin TC8 ground motions and 2) Models 2, 3 and 4 subjected to the Bin TI8 ground motions**

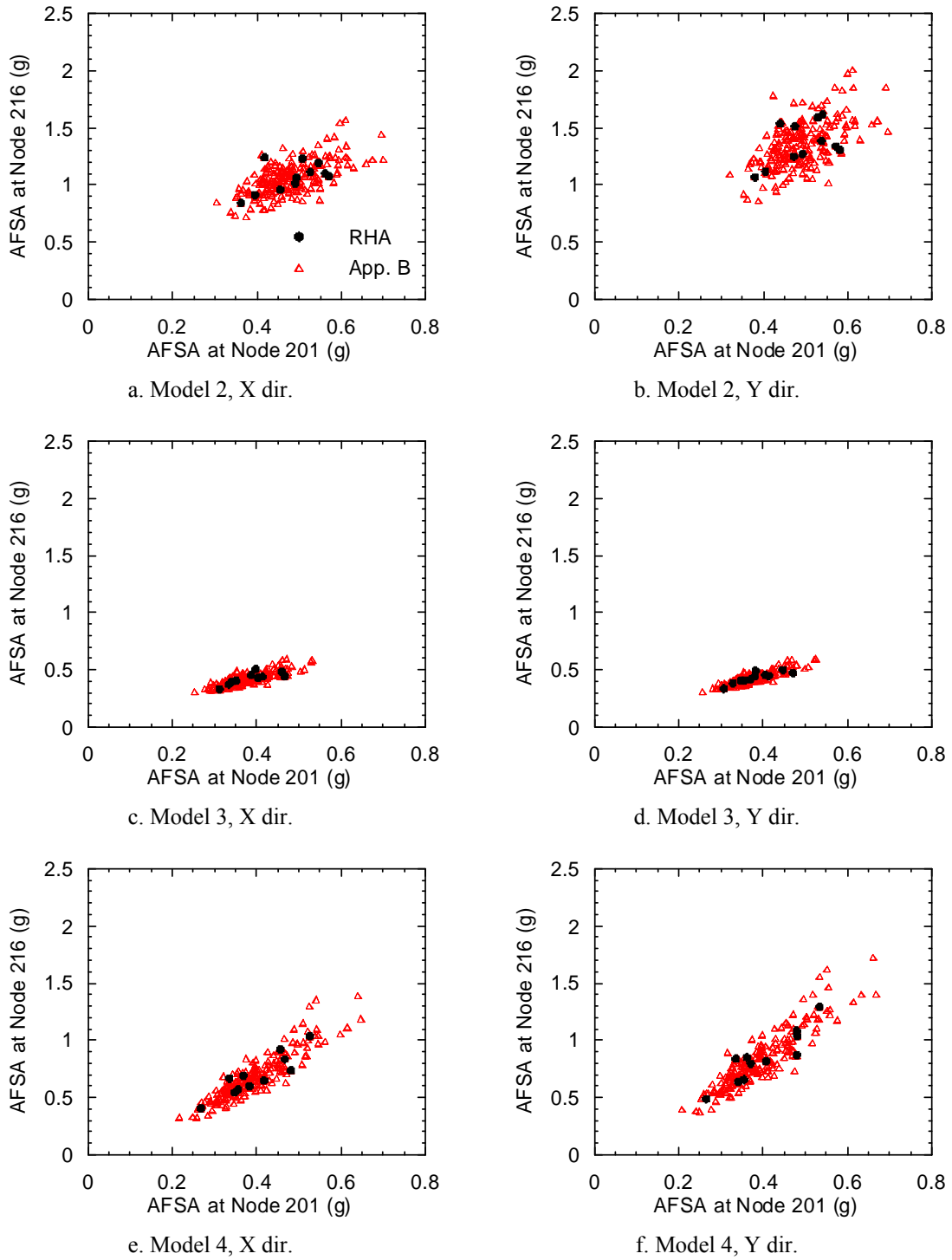


**Figure 5.53. AFSA at Nodes 201 and 216 generated using 1) response-history analyses and 2) the procedure of Appendix B for Models 2, 3 and 4 subjected to the Bin TI8 ground motions**

**Table 5.19. AFSA at Nodes 201, 1009 and 216 of Model 1 subjected to the Bin TC1 ground motions**

GM No.	AFSA in the X direction (g)			AFSA in the Y direction (g)		
	Node 201	Node 1009	Node 216	Node 201	Node 1009	Node 216
1	0.45	0.58	1.19	0.45	0.59	1.38
2	0.36	0.50	0.93	0.35	0.53	1.13
3	0.36	0.57	1.03	0.33	0.46	1.11
4	0.49	0.68	1.32	0.47	0.68	1.34
5	0.34	0.47	0.88	0.28	0.41	0.95
6	0.41	0.61	0.99	0.34	0.51	1.12
7	0.31	0.44	0.84	0.34	0.42	1.00
8	0.36	0.47	0.90	0.39	0.57	1.22
9	0.43	0.53	0.95	0.48	0.67	1.34
10	0.30	0.42	0.86	0.31	0.41	1.06
11	0.47	0.58	1.07	0.54	0.70	1.48

**Table 5.20. AFSA at Nodes 201, 1009 and 216 of Model 2 subjected to the Bin TII ground motions**

GM No.	AFSA in the X direction (g)			AFSA in the Y direction (g)		
	Node 201	Node 1009	Node 216	Node 201	Node 1009	Node 216
1	0.22	0.25	0.57	0.22	0.22	0.73
2	0.23	0.28	0.56	0.23	0.29	0.74
3	0.20	0.25	0.53	0.20	0.25	0.69
4	0.14	0.19	0.34	0.14	0.18	0.46
5	0.18	0.22	0.40	0.17	0.22	0.53
6	0.19	0.23	0.42	0.19	0.24	0.54
7	0.21	0.25	0.49	0.19	0.25	0.62
8	0.22	0.25	0.47	0.22	0.28	0.58
9	0.20	0.21	0.49	0.20	0.23	0.59
10	0.19	0.23	0.47	0.19	0.24	0.66
11	0.24	0.27	0.59	0.24	0.28	0.69

**Table 5.21. AFSA at Nodes 201, 1009 and 216 of Model 3 subjected to the Bin T11 ground motions**

GM No.	AFSA in the X direction (g)			AFSA in the Y direction (g)		
	Node 201	Node 1009	Node 216	Node 201	Node 1009	Node 216
1	0.09	0.11	0.19	0.08	0.09	0.21
2	0.11	0.14	0.28	0.11	0.13	0.36
3	0.09	0.11	0.16	0.09	0.11	0.21
4	0.07	0.08	0.11	0.07	0.08	0.13
5	0.07	0.08	0.16	0.07	0.08	0.21
6	0.08	0.09	0.12	0.08	0.09	0.15
7	0.08	0.08	0.14	0.07	0.08	0.17
8	0.10	0.13	0.23	0.10	0.12	0.26
9	0.07	0.07	0.12	0.07	0.07	0.13
10	0.09	0.11	0.16	0.09	0.10	0.20
11	0.12	0.12	0.18	0.11	0.12	0.20

**Table 5.22. AFSA at Nodes 201, 1009 and 216 of Model 4 subjected to the Bin T11 ground motions**

GM No.	AFSA in the X direction (g)			AFSA in the Y direction (g)		
	Node 201	Node 1009	Node 216	Node 201	Node 1009	Node 216
1	0.04	0.04	0.06	0.03	0.04	0.07
2	0.05	0.05	0.09	0.05	0.05	0.11
3	0.03	0.04	0.05	0.03	0.04	0.07
4	0.02	0.02	0.04	0.02	0.02	0.04
5	0.03	0.03	0.06	0.03	0.03	0.07
6	0.03	0.03	0.05	0.03	0.03	0.05
7	0.03	0.04	0.06	0.03	0.04	0.07
8	0.04	0.05	0.08	0.04	0.04	0.09
9	0.03	0.03	0.05	0.03	0.03	0.06
10	0.04	0.04	0.06	0.04	0.04	0.07
11	0.04	0.04	0.07	0.04	0.04	0.09

**Table 5.23. AFSA at Nodes 201, 1009 and 216 of Model 1 subjected to the Bin TC8 ground motions**

GM No.	AFSA in the X direction (g)			AFSA in the Y direction (g)		
	Node 201	Node 1009	Node 216	Node 201	Node 1009	Node 216
1	5.36	6.14	12.26	5.06	6.27	14.49
2	4.06	5.29	9.93	4.12	5.99	12.93
3	4.36	6.18	10.86	3.97	5.25	13.22
4	5.53	6.96	12.78	5.19	6.99	14.55
5	3.98	5.40	9.94	3.30	4.68	10.60
6	4.44	6.37	10.51	3.78	5.41	12.89
7	3.59	4.71	9.19	4.10	4.83	10.72
8	4.26	5.36	10.19	4.23	5.73	12.12
9	5.17	6.22	11.19	5.48	7.58	14.28
10	3.54	5.02	10.13	3.52	4.80	12.13
11	5.29	5.88	11.14	5.55	6.81	14.07

**Table 5.24. AFSA at Nodes 201, 1009 and 216 of Model 2 subjected to the Bin TI8 ground motions**

GM No.	AFSA in the X direction (g)			AFSA in the Y direction (g)		
	Node 201	Node 1009	Node 216	Node 201	Node 1009	Node 216
1	0.53	0.55	1.11	0.53	0.62	1.59
2	0.57	0.55	1.08	0.58	0.58	1.30
3	0.42	0.53	1.24	0.44	0.48	1.54
4	0.36	0.44	0.84	0.38	0.44	1.07
5	0.49	0.53	1.01	0.49	0.56	1.27
6	0.40	0.46	0.91	0.41	0.45	1.12
7	0.56	0.59	1.10	0.57	0.63	1.34
8	0.46	0.50	0.95	0.47	0.53	1.25
9	0.51	0.58	1.23	0.54	0.60	1.61
10	0.49	0.60	1.06	0.47	0.60	1.51
11	0.55	0.55	1.19	0.54	0.62	1.38

**Table 5.25. AFSA at Nodes 201, 1009 and 216 of Model 3 subjected to the Bin T18 ground motions**

GM No.	AFSA in the X direction (g)			AFSA in the Y direction (g)		
	Node 201	Node 1009	Node 216	Node 201	Node 1009	Node 216
1	0.41	0.44	0.85	0.41	0.45	1.17
2	0.47	0.44	0.82	0.47	0.47	1.04
3	0.39	0.46	0.86	0.38	0.44	1.10
4	0.31	0.33	0.67	0.31	0.34	0.78
5	0.34	0.40	0.74	0.36	0.41	1.01
6	0.34	0.40	0.73	0.35	0.41	0.95
7	0.33	0.37	0.67	0.33	0.38	0.89
8	0.40	0.43	0.66	0.40	0.46	0.84
9	0.35	0.40	0.71	0.37	0.41	0.94
10	0.40	0.50	0.79	0.38	0.49	1.11
11	0.46	0.48	0.91	0.45	0.50	1.02

**Table 5.26. AFSA at Nodes 201, 1009 and 216 of Model 4 subjected to the Bin T18 ground motions**

GM No.	AFSA in the X direction (g)			AFSA in the Y direction (g)		
	Node 201	Node 1009	Node 216	Node 201	Node 1009	Node 216
1	0.42	0.46	0.65	0.41	0.44	0.82
2	0.53	0.57	1.03	0.53	0.57	1.29
3	0.38	0.41	0.60	0.37	0.41	0.80
4	0.27	0.28	0.41	0.26	0.29	0.49
5	0.34	0.38	0.67	0.34	0.38	0.84
6	0.35	0.37	0.54	0.34	0.38	0.64
7	0.37	0.42	0.69	0.36	0.41	0.85
8	0.46	0.53	0.92	0.48	0.50	1.08
9	0.36	0.37	0.57	0.35	0.39	0.66
10	0.48	0.50	0.74	0.48	0.51	0.87
11	0.47	0.48	0.83	0.48	0.51	1.04



Figure 5.54 and Figure 5.55 present the medians and logarithmic standard deviations, respectively, of the AFSA values at Nodes 201, 1009 and 216 as a function of ground motion bin. Note that for a given bin number in Figure 5.54 and Figure 5.55, the ground motion bin used in the analysis for Model 1 (Bin TCx) is different from that used in the analysis for Models 2, 3 and 4 (Bin Tlx); and the median spectral acceleration for the Bin TCx ground motions is smaller than that for the Bin Tlx throughout the period range shown in Figure 5.41 and Figure 5.43.

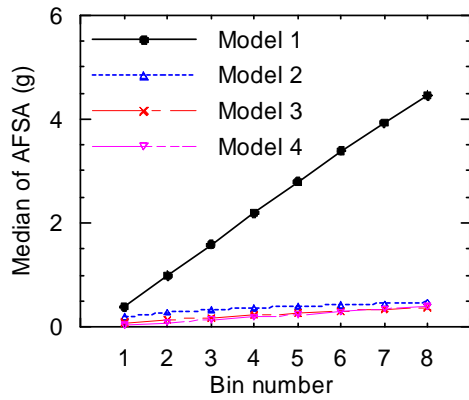
Figure 5.54 shows one advantage of the implementation of base isolation: as the intensity of the earthquake shaking increases, the increase in the AFSA response in the base isolated NPPs is much smaller than that in the conventional NPP. For example, in panel a of Figure 5.54, the median AFSA for Model 1 subjected to the ground motions of Bins TC1 and TC8 are 0.38 g and 4.45 g, respectively; and those for Model 2 subjected to the ground motions of Bins TI1 and TI8 are 0.20 g and 0.48 g, respectively. This observation explains why, for scenario-based assessment, the dispersion in AFSA for the conventional NPP model is much greater than that for the nonlinear base isolated NPPs: the ground motions used in scenario-based assessment are scaled to cover a wide range of spectral accelerations at the fundamental period of the structure and the increase of AFSA due to the increase of the spectral acceleration is much greater in the conventional NPP than in the base isolated NPPs.

Figure 5.55 shows that the dispersion ( $\beta$ ) in AFSA for the conventional NPP is not necessarily higher or lower than that for the base isolated NPPs when the ground motions are scaled to a given spectral acceleration at a given period. In general, the value of  $\beta$  decreases as the intensity of earthquake and the nonlinearity of the structure increase. Of the four models, the value of  $\beta$  for Model 3, which is the NPP equipped with LR bearings, is the most sensitive to the earthquake intensity.

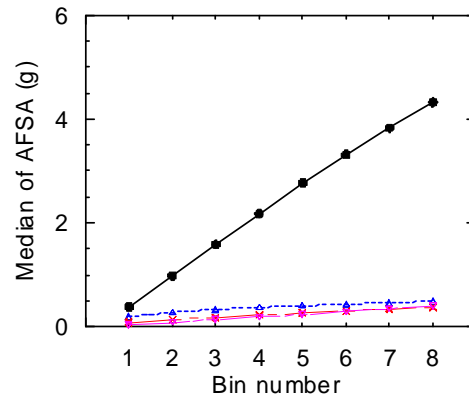
#### **5.4.4 Frequency of Unacceptable Performance**

##### **5.4.4.1 Mean Fragility Curves**

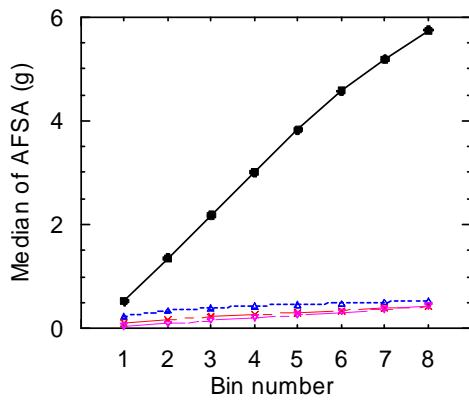
The results of Sections 5.2.4.2 and 5.3.4 show that the mean value of the distribution of the probability of unacceptable performance using a family of fragility curves can be estimated without bias and with high confidence by analysis using mean fragility curves and thousands of row vectors. This procedure was used below for the time-based assessments of Models 1 through 4.



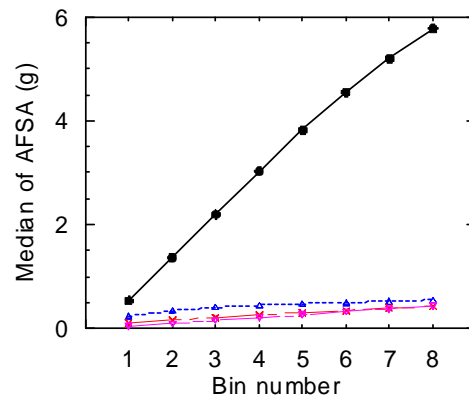
a. Node 201, X dir.



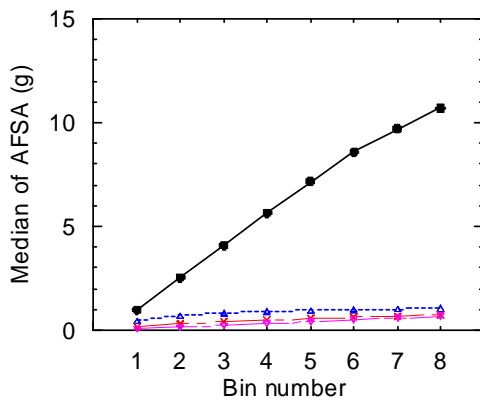
b. Node 201, Y dir.



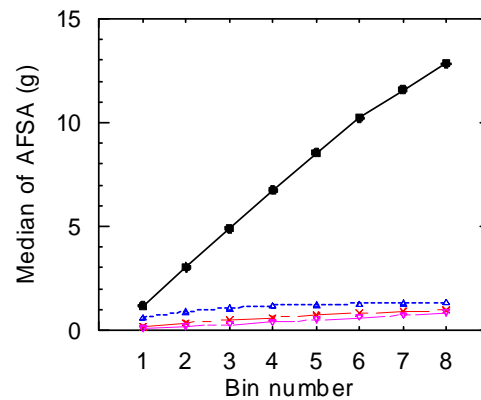
c. Node 1009, X dir.



d. Node 1009, Y dir.

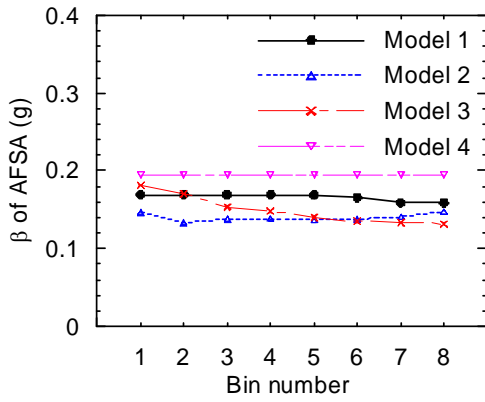


e. Node 216, X dir.

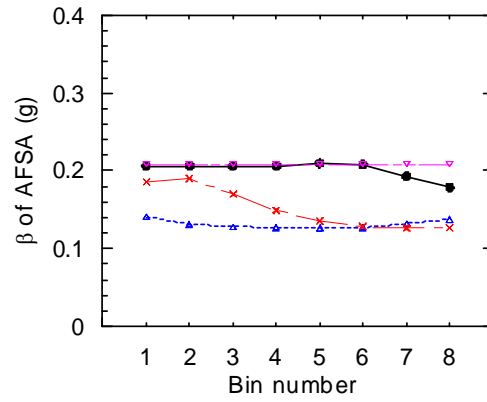


f. Node 216, Y dir.

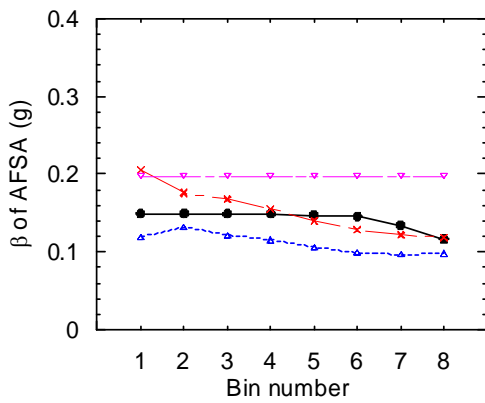
**Figure 5.54. Median of AFSA at Nodes 201, 1009 and 216 as a function of ground motion bin for the time-based assessments of Models 1, 2, 3 and 4**



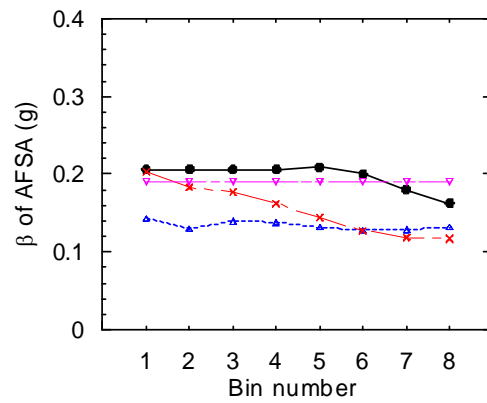
a. Node 201, X dir.



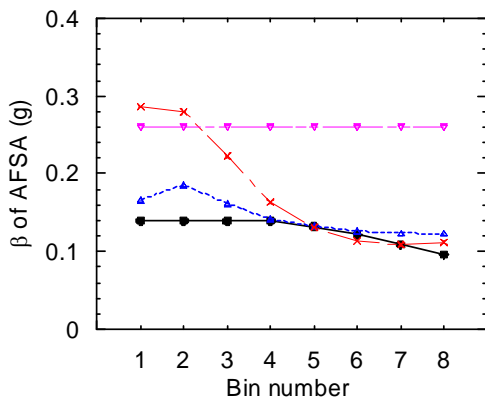
b. Node 201, Y dir.



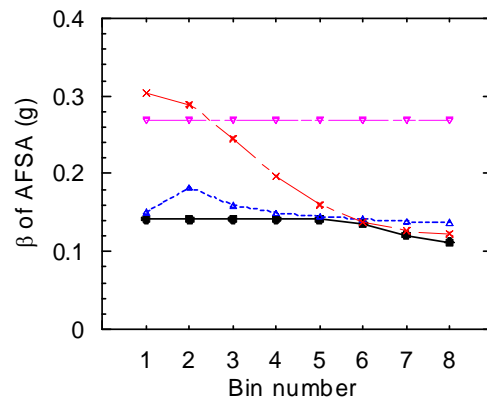
c. Node 1009, X dir.



d. Node 1009, Y dir.



e. Node 216, X dir.



f. Node 216, Y dir.

**Figure 5.55. Logarithmic standard deviation ( $\beta$ ) of AFSA at Nodes 201, 1009 and 216 as a function of ground motion bin for the time-based assessments of Models 1, 2, 3 and 4**

For Model 1, a single value of the probability of unacceptable performance was computed for each ground-motion bin using the mean fragility curves of Figure 5.17 and 2000 row vectors, which were generated using the underlying demand-parameter matrix for the corresponding ground-motion bin per the procedure of Appendix B. For Models 2, 3 and 4, a single value of the probability of unacceptable performance was computed for each model and ground-motion bin using the mean fragility curves of Figure 5.17 and 200,000 row vectors. For a given model, the product of the probability of unacceptable performance for each ground-motion bin ( $P_i$ ) and the MAF associated with the bin ( $\Delta\lambda_i$ ) was computed; the summation of the eight products was defined as the mean annual frequency of unacceptable performance for the model.

Table 5.27 summarizes the computation of the annual frequency of unacceptable performance of Model 1, including the values of  $\Delta\lambda_i$ ,  $P_i$  and  $\Delta\lambda_i \times P_i$  for ground-motion bins TI1 through TI8 and the annual frequency of unacceptable performance,  $2.55 \times 10^{-5}$ . Table 5.27 shows that the probability of unacceptable performance ( $P_i$ ) for Bin TI1 is 0 and that for each of Bins TI6, TI7 and TI8 is 1. The last column in Table 5.27 presents the contribution to the annual frequency of unacceptable performance from each intensity level, which can be used to evaluate the range of spectral acceleration selected for the time-based assessment. The ratio for Bin TI1 is 0, which deems a lower-bound spectral acceleration smaller than 0.05 g unnecessary. The ratio for Bin TI8 is 0.02 with  $P_i$  equal to 1, which implies that the upper-bound spectral acceleration is sufficient.

Table 5.28 summarizes the computation of the mean annual frequency of unacceptable performance of Models 2, 3 and 4. The mean annual frequencies of unacceptable performance of the three models are  $3.47 \times 10^{-9}$ ,  $4.25 \times 10^{-11}$  and  $1.64 \times 10^{-10}$ , respectively, and much smaller than that of Model 1 ( $2.55 \times 10^{-5}$ ).

**Table 5.27. Computation of annual frequency of unacceptable performance of Model 1 using 2,000 row vectors**

Ground-motion bin	$\Delta\lambda_i$	Probability of unacceptable performance, $P_i$	$\Delta\lambda_i \times P_i$	$\frac{\Delta\lambda_i \times P_i}{\sum_{i=1}^8 \Delta\lambda_i \times P_i}$
TC1	1.35E-03	0	0	0.00
TC2	5.18E-05	0.16	8.29E-06	0.32
TC3	1.24E-05	0.68	8.43E-06	0.33
TC4	4.63E-06	0.94	4.35E-06	0.17
TC5	2.23E-06	0.99	2.21E-06	0.09
TC6	1.08E-06	1	1.08E-06	0.04
TC7	6.90E-07	1	6.90E-07	0.03
TC8	4.59E-07	1	4.59E-07	0.02
Annual frequency of unacceptable performance $\sum_{i=1}^8 \Delta\lambda_i \times P_i$			2.55E-05	--

**Table 5.28. Computation of annual frequency of unacceptable performance of Models 2, 3 and 4 using 200,000 row vectors**

Ground-motion bin	$\Delta\lambda_i$	Probability of unacceptable performance, $P_i$			$\Delta\lambda_i \times P_i$		
		Model 2	Model 3	Model 4	Model 2	Model 3	Model 4
TI1	1.35E-03	0	0	0	0	0	0
TI2	4.57E-05	2.00E-05	0	0	9.15E-10	0	0
TI3	1.07E-05	6.00E-05	0	0	6.42E-10	0	0
TI4	3.85E-06	1.30E-04	0	0	5.00E-10	0	0
TI5	1.87E-06	2.15E-04	0	0	4.02E-10	0	0
TI6	1.03E-06	3.85E-04	0	5.00E-06	3.96E-10	0	5.14E-12
TI7	6.09E-07	4.90E-04	2.00E-05	1.05E-04	2.98E-10	1.22E-11	6.39E-11
TI8	4.05E-07	7.75E-04	7.50E-05	2.35E-04	3.13E-10	3.03E-11	9.51E-11
Annual frequency of unacceptable performance					3.47E-09	4.25E-11	1.64E-10

#### 5.4.4.2 Mean Fragility Curves Modified by $R_a$

The analyses of Section 5.3.4.3 were repeated using the AFSA results for the time-based assessments of Models 2, 3 and 4 to characterize the relationship between  $R_a$  and the mean annual frequency of unacceptable performance. The analyses were performed using 2000 row vectors<sup>8</sup>. The results are presented in Figure 5.56 as a function of  $R_a$  and models. Figure 5.56 also presents the mean annual frequencies of unacceptable performance identified in Table 5.27 for Model 1 and the value of  $R_a$  for each isolated NPP model that has an annual frequency of unacceptable performance equal to that for Model 1. The values of  $R_a$  for this equivalent performance are 0.31, 0.14 and 0.072 for Models 2, 3 and 4, respectively. The results of Figure 5.56 show that the use of base isolation enables secondary systems to be designed for smaller strengths than those in conventional NPPs and to achieve a lower annual frequency of unacceptable performance than that in a conventional NPP.

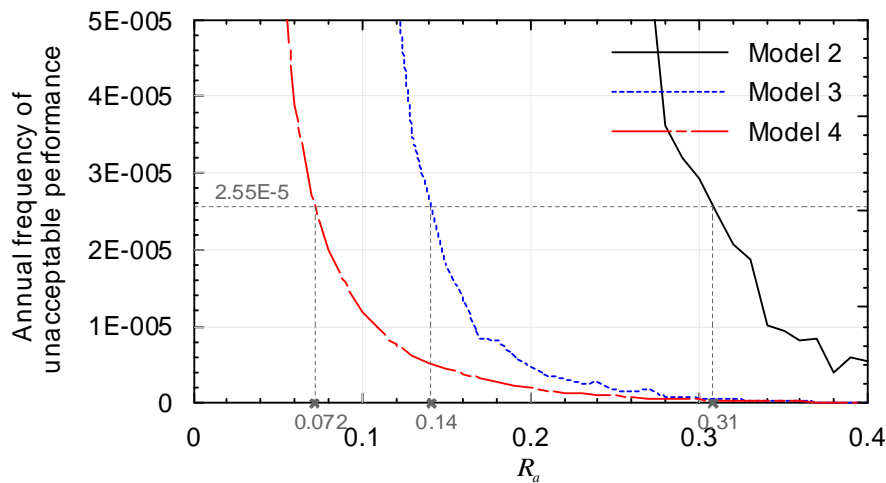


**Figure 5.56. Annual frequency of unacceptable performance as a function of  $R_a$  using 2000 row vectors**

---

<sup>8</sup> Another set of analyses similar to that presented in this subsection but using 20,000 row vectors was performed to ensure the use of 2000 row vectors was sufficient. The results for 20,000 row vectors are almost identical to those for 2000 row vectors.

## **CHAPTER 6**

# **BLAST ASSESSMENT OF THE SAMPLE NPP REACTOR BUILDINGS**

### **6.1 Introduction**

The response of the sample conventional and isolated reactor buildings to blast loadings is presented in this chapter of the report. The primary purpose of the study is to identify the impact of the implementation of seismic isolation bearings beneath the reactor building (for earthquake effects) on the blast vulnerability of the building to blast loadings.

The study, which is described in detail in the following sections, considers only detonations external to the containment vessel because it is assumed that access to the containment vessel is strictly controlled through the implementation of a layered physical security system, which would include vehicular barriers and physical inspection of all personnel and vehicles at some distance from the containment vessel. The impact of an internal explosion cannot be assessed on a generic basis and importantly, the vulnerability of the reactor building and its secondary systems would not be negatively impacted by the installation of seismic isolation bearings beneath the building.

The study considered air blast and ground shock loadings from conventional improvised explosive devices only. Loadings associated with the detonation of thermonuclear weapons have not been considered. Terrorist attack of reactor buildings through the use of aircraft similar to the attacks of 9/11/2001 is beyond the scope of this report, is indeed project specific, and has already been studied by the US Nuclear Regulatory Commission. The results of these studies have not been distributed to the public. Malevolent acts against reactor buildings using military munitions are also beyond the scope of this study. The US Department of Defense has detailed knowledge of the vulnerability of reinforced concrete structures to attack by bombs, missiles, rocket-propelled grenades and firearms. This classified knowledge could be used to assess the vulnerability of containment vessels to attack using military munitions. Again, the implementation of seismic isolation bearings beneath a reactor building will neither increase nor decrease the vulnerability of the vessel to such attacks.

The effects of external air blast loadings and blast-induced ground shock on structures must be assessed using global and local response metrics. An important global response metric is collapse. Collapse of a continuum such as a reinforced concrete containment vessel is extremely unlikely and

could only result from the destruction of much of the containment vessel, which would result in egregious damage to and likely failure of the internal structure and secondary systems. Instead, the global responses of the conventional and isolated reactor buildings are computed and compared. Local response metrics for reinforced concrete elements are spalling and breach.

Spalling of concrete is a result of the reflection of shock-induced compressive waves off the rear surface of a reinforced concrete component. The resultant tensile waves propagate back towards the impacted face. If the resultant tensile stresses exceed the tensile strength of the concrete, the concrete will spall. Breach results from the gross spalling of concrete such that a clear passage is opened from the front surface of the concrete to the rear surface. The US Department of Defense has developed knowledge and algorithms to compute the minimum thicknesses of concrete to prevent spalling and/or breach for a given charge weight and standoff distance. The minimum thickness is greater for spalling than breach. Again, the introduction of seismic isolation bearings below a reactor vessel will have no influence on the likelihood of spalling and/or breaching of a containment vessel.

Three sections are included in the rest of the chapter to present the analysis methodology, the target threat and the performance of the sample NPP. Section 6.2 describes the state-of-practice and -art for determining blast-induced loads on structures due to air shock (Section 6.2.1) and ground shock (Section 6.2.2). Section 6.3 introduces the assumed threat (weapon size and standoff distance) for the assessment sample reactor building as well as the corresponding air blast pressure histories and ground shock developed for the selected blast threat using the methodologies introduced in Section 6.2. Section 6.4 presents the results of the LS-DYNA analysis of the conventional and isolated reactor building for the pressure histories and ground shock of Section 6.3. Closing remarks are presented in Section 6.5 to summarize the analysis results and comment on the impact of the seismic isolation systems on the blast vulnerability of the sample reactor building.

## **6.2 Blast Loading on Structures**

### **6.2.1 Air Shock**

Computation of air blast wave parameters for analysis of the sample containment vessel can be performed using a number of procedures, namely,



1. The charts of TM5-1300 (DoA 1990), which utilize the equations of Kingery and Bulmash (1984), and empirical relationships for the influence of non-normal angles of incidence on reflected pressure and specific impulse
2. A DoD code such as CONWEP (Hyde 1993), which implements the procedures of TM5-1300, including the effects of clearing
3. A Computational Fluid Dynamics (CFD) code such as Air3D (Rose 2006) and STAR ([www.cd-adapco.com](http://www.cd-adapco.com)) or a hydrocode such as AUTODYN ([www.ansys.com](http://www.ansys.com)) and LSDYNA (LSTC 2003)

The first two procedures can be described as state-of-practice. The third procedure represents the state-of-art and this procedure was used to determine air-shock loads on the sample reactor buildings.

Air3D was used to compute reflected pressure histories at numerous monitoring points on the exterior surface of the containment vessel. A CFD code was used because the simplified procedures are incapable of capturing the complex loading environment associated with a conventional weapons detonation within a distance of less than the containment vessel diameter from the vessel. Appendix G presents introductory material on blast loads on simple and complex objects, respectively, to introduce the reader to blast loadings on structures and reinforce the need to use a CFD or hydrocode to establish the pressure and loading histories on complex structures such as containment vessels.

Identical to all CFD codes, Air3D solves the Eulerian conservation (momentum, mass and energy) equations in three dimensions. Rose (2006) provides detailed information on the numerical strategies adopted in Air3D.

The blast source model implemented in Air3D is based on the balloon analog developed by Ritzel and Matthews (1997), which in turn is based on the seminal work of Brode (1955, 1956, 1957). Such an approach is approximate in the fireball (expansion of the detonation products) and accurate in the mid-field (beyond the expansion of the detonation products but where complexities such as charge shape are important in terms of defining the flow field) and far-field (region of one-dimensional flow). The balloon is a statically pressurized volume of gas with the same blast energy potential as the charge. The blast is initiated by the instantaneous rupture of the balloon. Ritzel and Matthews demonstrated the utility of the analog by comparison of numerical and test data.

Brode equated the total blast energy potential of a pressurized volume of ideal gas to that of the total blast energy of a charge,  $E$ , as follows:

$$E = \frac{(P - P_0)V}{(\gamma - 1)} \quad (6.1)$$

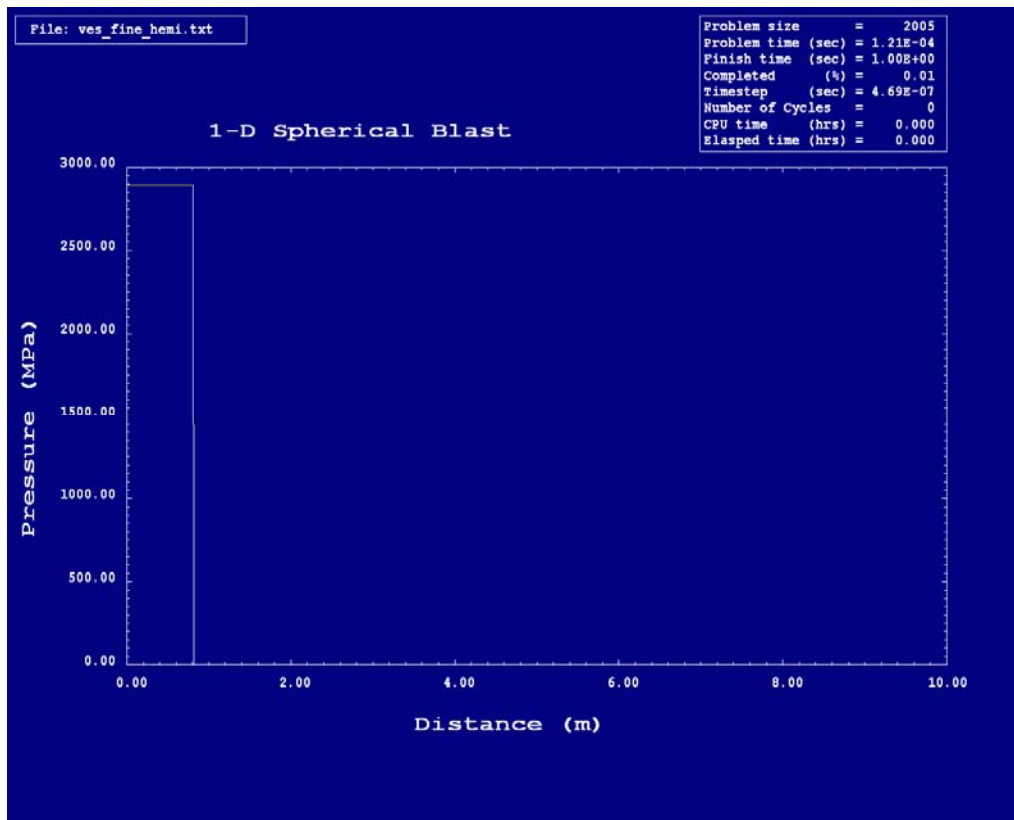
where  $P$  is the static pressure in the balloon prior to rupture,  $P_0$  is the ambient pressure (0.10 MPa, 1 atm),  $V$  is the volume of the balloon, and  $\gamma$  is the ratio of specific heats for the balloon gas (=1.4 for air at ambient pressure and temperature). For the Air3D analyses described herein, the volume of the spherical balloon was computed using the charge mass and an assumed charge mass density of  $1600 \text{ kg/m}^3$ ,  $\gamma = 1.4$ ,  $P_0 = 0.10 \text{ MPa}$ , and  $E = 4.52 \text{ MJ/kg}$  for TNT (Rose 2006).

Figure 6.1 shows the initial pressure condition of a sample 1D analysis for a 2000 kg charge detonated at the origin of the figure on a rigid reflecting surface ( $Z=0$ ). The input charge mass was increased by the standard multiplier of 1.8 to account for instantaneous reflection of the shock wave off the rigid surface, thereby increasing the effective charge mass to 3600 kg. The computed static pressure in the balloon prior to rupture was 2900 MPa and the radius of the balloon was 0.81 m. As a point of reference, the likely radius of the fireball for such a charge will range between 17 m (Ritzel 2008) and 23 m (Baker et al. 1983, Merrifield and Wharton 2000).

Air3D performs 3D analysis using a 3-stage process, whereby a 1D domain is solved and then mapped to the 2D domain, which, in turn, is solved before being mapped to a 3D domain. The geometry of the analysis is defined by the user through an input file.

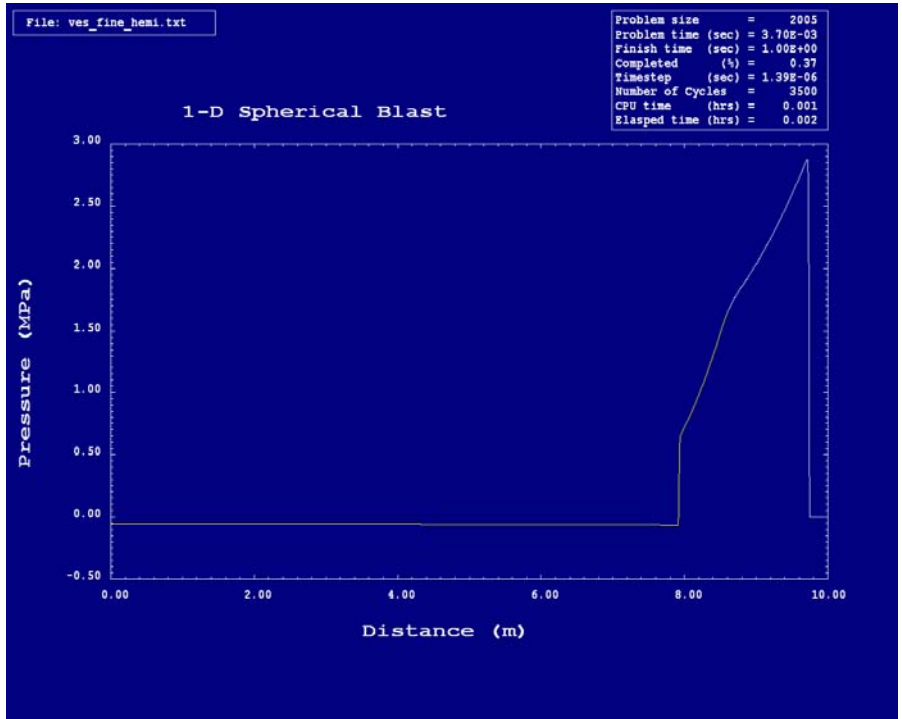
Figure 6.2 presents the mapping process of the Air3D analysis for the sample reactor building. Panels a and b of Figure 6.2 are for 1D and 2D analysis, respectively; panels c and d are for 3D analysis. The charge was detonated at ( $X=Y=Z=0$ ) of panels c and d; the closest distance to the containment vessel was 10 m. (The base of the containment vessel would be enveloped by the fireball for such an explosive.) For this analysis, the 1D Euler equations were first solved for the range of  $X=0$  through 10 m and  $Y=Z=0$ . The 1D analysis terminated when the shock wave reached an obstacle at  $X= 10$  m. Figure 6.2a presents the pressure contours immediately before the 1D analysis was terminated. The 1D results were then mapped to the 2D domain as shown in Figure 6.2b, where the radial distance ranged from 0 to 10 m. Since a 3D obstacle was placed in the path of the shock front, the 2D results were mapped immediately into 3D for further analysis. (The 2D

domain of Figure 6.2b is equivalent to  $Y=0$  in Figure 6.2c and  $X=0$  through 10 m in Figure 6.2d.) Note that the time step for which data are presented in panels b, c and d of Figure 6.2 are identical.

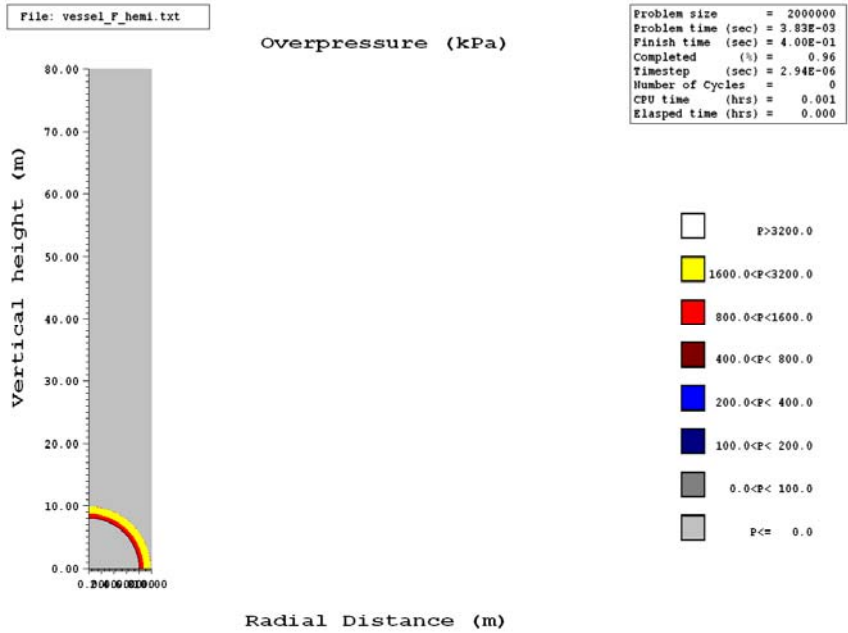


**Figure 6.1. Sample pressure results for an Air3D analysis for a surface detonation of 2000 kg of TNT**

Air3D input includes charge mass, problem geometry, cell size, and locations of monitoring points. The domain at a given stage of analysis is discretized on the basis of cell size. Alternate outer dimensions, cell size and monitoring points can be specified for the different stages of analysis. Reflective objects or obstacles are defined using the combination of cubic, spherical and cylindrical obstacles. (As shown in panels c and d of Figure 6.2, the sample reactor building was modeled in Air3D using overlapped spherical and a cylindrical obstacles.) Any cell with its midpoint bounded by the obstacle edges is considered empty and not included in the analysis. Air3D can output both pressure and temperature and histories at user-specified monitoring locations.

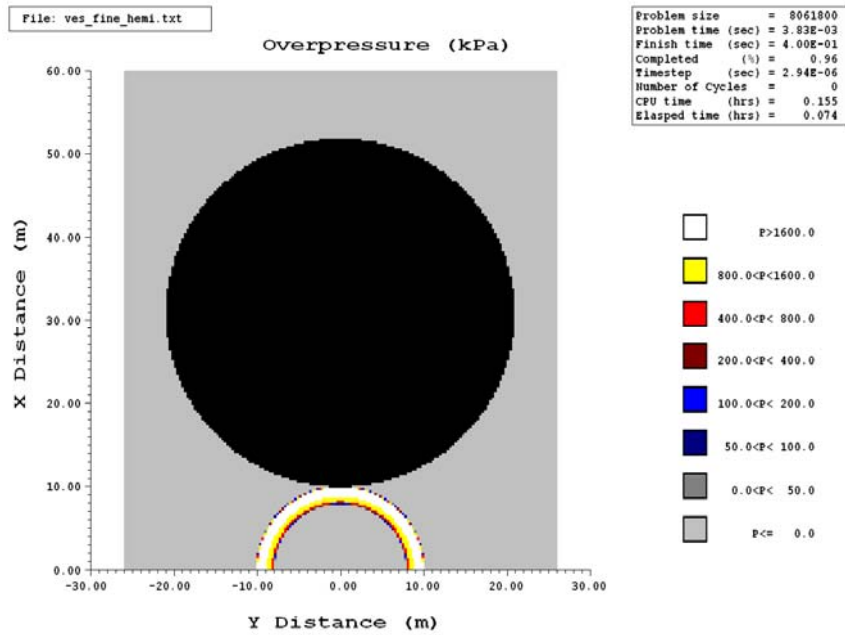


a. 1 D

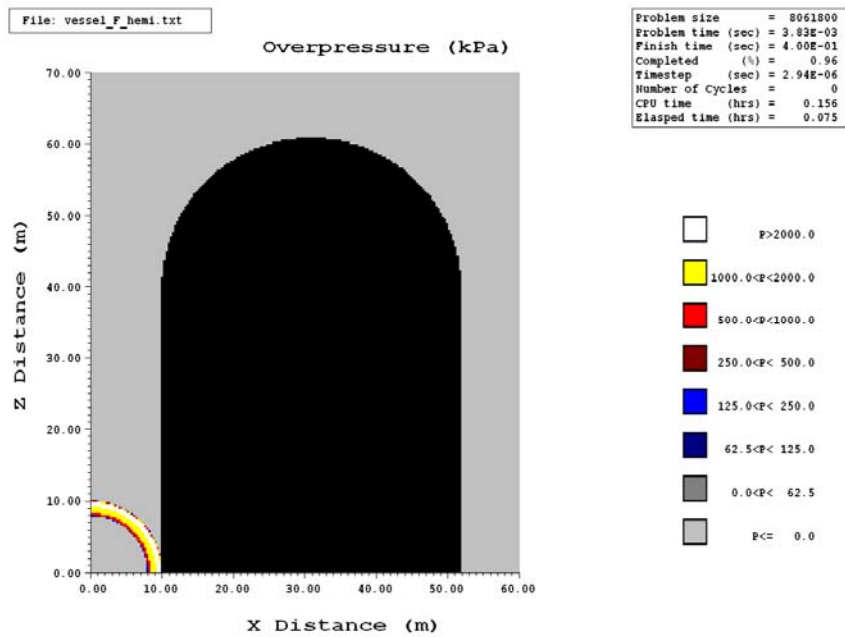


b. 2 D

Figure 6.2. Mapping in Air3D for the sample reactor building



c. Plan view, 3D



b. Elevation view, 3D

Figure 6.2 Mapping in Air3D for the sample reactor building (cont.)

### 6.2.2 Ground Shock

Sources of blast-induced ground shock include air burst, surface burst and buried burst. The detonation of an explosive in air will produce only weak levels of ground shock. The same detonation on the ground surface or below will generate much greater ground shock (Smith and Hetherington 1994).

The procedures for ground-shock analysis appear to be less advanced than those for air shock. The state-of-practice for ground-shock analysis of buried structures involves the following steps (Smith and Hetherington 1994):

1. Determine the design threat, including the charge size, the degree of coupling between the explosive and soil, soil properties and the distance from the charge.
2. Compute the corresponding soil particle movement parameters, such as peak particle displacement (PPD), peak particle velocity (PPV) and peak particle acceleration (PPA).
3. Convert particle movement parameters into loading parameters, such as peak incident overpressure and incident impulse. Smith and Hetherington (1994) provided the following equations for this conversion:

$$p_o = \rho \cdot C \cdot PPV \quad (6.2)$$

$$i_o = \rho \cdot C \cdot PPV \quad (6.3)$$

where  $p_o$  is the peak free-field pressure in  $\text{N/m}^2$ ;  $i_o$  is the free-field impulse in  $\text{N-s/m}^2$ ;  $\rho$  is the soil density in  $\text{kg/m}^3$  and  $C$  is the loading wave velocity defined below:

$$C = \begin{cases} c & \text{for fully saturated clays} \\ 0.6c + \left(\frac{n+1}{n-2}\right)PPV & \text{for saturated clays} \\ c + \left(\frac{n+1}{n-2}\right)PPV & \text{for sand} \end{cases} \quad (6.4)$$

where  $c$  is the seismic velocity<sup>1</sup> in m/s and  $n$  is a dimensionless soil-type dependent attenuation coefficient.; for a saturated clay,  $n = 1.5$  and for very a loose sand,  $n = 3.25$ .

4. Transform the incident overpressure and impulse to the corresponding reflected quantities using a factor of 1.5. Compute responses to the computed reflected overpressure and reflected impulse using standard SDOF procedures (e.g., Biggs 1964).

For above-ground (non buried) structures, the response of a structure to ground shock can be established by response-history analysis using one or more representative ground motion acceleration time series. Little information on the computation of acceleration time-series from ground shock loading has been published.

Research on ground shock has focused on the development of attenuation relationships for particle motion parameters (PPD, PPV, PPA). The remainder of this subsection introduces four ground-shock prediction models for surface and buried bursts.

*Smith and Hetherington (1994)*

Smith and Hetherington (1994) proposed that PPD and PPV associated with buried or partially buried charges with a scaled distance of  $5 \text{ m/kg}^{1/3}$  or less be computed using the following equations:

$$PPD = 60 \frac{f_c}{c} \left( \frac{2.52R}{M^{1/3}} \right)^{1-n} M^{1/3} \text{ (m)} \quad (6.5)$$

$$PPV = 48.8 f_c \left( \frac{2.52R}{M^{1/3}} \right)^{-n} \text{ (m/s)} \quad (6.6)$$

where  $M$  is the charge mass in kg;  $R$  is the distance from the explosive and measured in meters;  $f_c$  is a dimensionless coupling factor that varies as a function of the depth of burial of the explosive

---

<sup>1</sup> Smith and Hetherington (1994) defined *seismic* velocity as  $\sqrt{E/\rho}$ , where  $E$  is the modulus obtained from a uniaxial, unconfined compression test of a soil (rock) sample, with values ranging from less than 200 m/s for loose, dry sand to greater than 1500 m/s for saturated clays. This definition of seismic velocity is different from that for  $P$ - and  $S$ -wave velocities, which are computed as  $\sqrt{K/\rho}$  and  $\sqrt{G/\rho}$ , respectively, where  $K$  and  $G$  are the bulk and shear moduli of the soil (rock), respectively.

and equal to 0.4 for a surface blast;  $c$  is the seismic velocity (see footnote 1) in m/s and other parameters have been defined previously. Note that (6.5) and (6.6) are for peak particle motions at a radial distance  $R$  from the center of the explosive (and not necessarily on the ground surface).

*TM5-1300 (1991)*

TM5-1300 (DoA 1991) provides equations for PPA, PPV and PPD on the ground surface in the horizontal and vertical directions for dry soil, saturated soil and rock. The equations apply to TNT detonations at or near the ground surface. The equations for PPA, PPV and PPD in the horizontal direction are:

$$PPA = \begin{cases} 10,000/(W^{1/3}Z^2) & \text{for rock and saturated soil} \\ 5,000/(W^{1/3}Z^2) & \text{for dry soil} \end{cases} \quad (\text{g}) \quad (6.7)$$

$$PPV = 150/Z^{1.5} \quad \text{for all ground media} \quad (\text{in/sec}) \quad (6.8)$$

$$PPD = \begin{cases} 0.0125R^{1/3}W^{1/3}/Z^{1/3} & \text{for rock} \\ 0.17R^{1/3}W^{1/3}/Z^{2.3} & \text{for dry and saturated soil} \end{cases} \quad (\text{in}) \quad (6.9)$$

where  $W$  is charge weight in lbs;  $R$  is the distance from the explosive in feet; and  $Z$  is the scaled distance ( $= R/W^{1/3}$ ).

*Westine (1978)*

Equations (6.7) through (6.9) do not consider soil properties directly and assume that the relationships between  $W$ ,  $Z$  and ground shock parameters are logarithmically linear. Westine (1978) collected experimental test data in soil and rock with the dimensionless scaled energy factor  $E/\rho c_p^2 R^3$  (the variables are defined after (6.11)) ranged from  $4.4 \times 10^{-11}$  to  $4.4 \times 10^{-2}$  and developed nonlinear empirical attenuation relationships for radial PPV and PPD at a distance of  $R$  from the center of a buried charge (i.e., the explosive is fully coupled with ground). The attenuation relationships are:

$$\frac{PPD}{R} \left( \frac{P_0}{\rho c_p^2} \right)^{\frac{1}{2}} = \frac{0.04143 \left( \frac{E}{\rho c_p^2 R^3} \right)^{1.105}}{\tanh^{1.5} \left[ 18.24 \left( \frac{E}{\rho c_p^2 R^3} \right)^{0.2367} \right]} \quad (6.10)$$



$$\frac{PPV}{c_p} \left( \frac{P_0}{\rho c_p^2} \right)^{\frac{1}{2}} = \frac{6.169 \times 10^{-3} \left( \frac{E}{\rho c_p^2 R^3} \right)^{0.8521}}{\tanh \left[ 26.03 \left( \frac{E}{\rho c_p^2 R^3} \right)^{0.30} \right]} \quad (6.11)$$

where  $E$  is total explosive energy  $P_0$  is ambient (atmospheric) pressure;  $\rho$  is the mass density of soil or rock;  $c_p$  is the P-wave velocity, and all other variables have been defined previously. Since  $PPD/R$ ,  $PPV/c_p$ ,  $P_0/\rho c_p^2$  and  $E/\rho c_p^2 R^3$  are dimensionless, any consistent set of units can be used with (6.10) and (6.11).

Table 6.1 presents the values of PPA, PPV and PPD predicted by these three models for a surface detonation of 2000 kg of explosive at a distance of 31 m (the distance from the point of detonation to the center of the containment vessel). This combination of charge mass and distance is used for the ground shock analysis of the sample reactor building presented later in this chapter. Saturated clay was assumed for analysis. The seismic and P-wave velocities were each assumed to be 2000 m/s. For the model of Smith and Hetherington,  $n$  and  $f_c$  were set equal to 1.5 and 0.4, respectively. For the model of Westine, mass density was set equal to as 1800 kg/m<sup>3</sup> and the total energy release  $E$  in MJ was computed as the charge mass in kg multiplied by 4.52 MJ/kg. The results of (6.10) and (6.11) were multiplied by a coupling factor of 0.4 since the Westine model predicts peak particle motions for buried explosives. The results of Table 6.1 make it clear that PPV and PPD per Smith and Hetherington are much greater than those for TM5-1300 and Westine. The scatter in these sample results leads one to question the utility of computations using these simplified procedures and identifies the need for additional study to compute unbiased estimates of these variables.

**Table 6.1. PPA, PPV and PPD predicted by Smith and Hetherington (1994), TM5-1300 (DoA 1991) and Westine (1978) for a surface explosion of 2000 kg of TNT at a distance of 31 m**

Model	PPA (g)	PPV (m/s)	PPD (m)
Smith and Hetherington	--	1.26	0.06
TM5-1300	15.9	0.25	0.005
Westine*	--	0.3	0.002

\* The values for Westine have been multiplied by a factor of 0.4 to consider the degree of coupling between the explosive and ground.

*Wu and Hao (2005)*

Wu and Hao (2005) modeled simultaneous ground and air shock generated by surface explosions. They developed a numerical model to simulate the response of granitic rock to explosive loading and validated the model using field test results. Hydrocode models of air, granite and TNT were developed to simulate the ground shock and air blast pressure histories for different blast threats. Instead of providing attenuation relationships for PPD and PPV, Wu and Hao developed empirical relationships (using the simulation data) for parameters that they considered essential for developing ground shock acceleration histories, including arrival time, peak acceleration, load duration, the shape of the time series and the power spectrum of the ground shock. These relationships are described below. The authors note that the relationships are appropriate for stiff granite only, for which the P-wave velocity is approximately 5600 to 6000 m/s.

For PPA,

$$PPA = 3.979R^{-1.45}M^{1.07} \quad (\text{g}) \quad (6.12)$$

where  $R$  is the distance from the detonation in meters and  $M$  is the charge mass in kg. The arrival time of the ground shock,  $t_a$ , is given by:

$$t_a = 0.91R^{1.03}M^{-0.02}/c_p \quad (\text{s}) \quad (6.13)$$

where  $c_p$  is the P-wave velocity in granite. From their simulation data, Wu and Hao found that the power spectrum of blast-induced ground motions could be represented by the Tajimi-Kanai model, which has been widely used in earthquake engineering:

$$S(f) = \frac{1 + 4\zeta_g^2 f^2 / PF^2}{(1 - f^2 / PF^2)^2 + 4\zeta_g^2 f^2 / PF^2} S_0 \quad (6.14)$$

where  $S_0$  is the amplitude of a white-noise power spectrum or the scale factor of the spectrum;  $\zeta_g$  is a parameter governing the shape of the power spectrum and  $PF$  is the principal frequency of the ground shock, estimated as

$$PF = 465.62(R/M^{1/3})^{-0.13}, \quad 0.3 \leq R/M^{1/3} \leq 10 \quad (\text{Hz}) \quad (6.15)$$

Wu and Hao determined that the power spectrum shape of (6.14) computed using  $\zeta_g = 0.16$  agreed well with the shape of the power spectrum shape established by the simulations. They determined

that the envelope shape of a ground shock time series could be best modeled using the following equations:

$$\xi(t) = \begin{cases} 0 & t \leq 0 \\ \frac{t^2}{t_p^2} e^{-0.5(1-\frac{t^2}{t_p^2})} & t > 0 \end{cases} \quad (6.16)$$

$$t_p = 5.1 \times 10^{-4} R^{0.81} \quad (\text{s}) \quad (6.17)$$

where  $e$  is the base of the natural logarithm and  $t_p$  is the duration between the arrival of the shock wave and the occurrence of the peak acceleration. The peak value of  $\xi(t)$  in (6.16) is 1 at  $t = t_p$ . A sample envelope shape computed using (6.16) and (6.17) was presented in Figure 6.3 for  $R = 32$  m. This shape was also used to generate the ground shock time series for the response-history analyses of the containment vessels. The peak value of the shape of Figure 6.3 occurred at 8.2 msec as determined by (6.17).

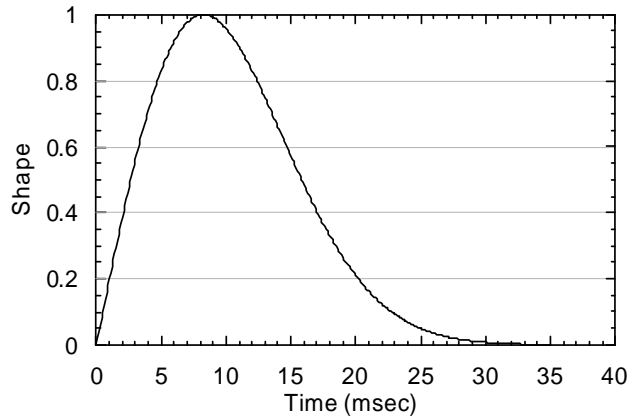


**Figure 6.3. A sample shape function for ground shock simulation**

The attenuation model of Wu and Hao (2005) was used herein to determine the ground shock parameters since it is the only model that provides sufficient information for simulating a ground acceleration history. The analysis of Table 6.1 was repeated but for a surface burst on granite. A  $P$ -wave velocity of granite of 5600 m/s was assumed. The results were presented in Table 6.2. The results for the model of Smith and Hetherington are not presented in Table 6.2 because a value for  $n$  is unavailable. The results for Westine are presented only for reference since the  $P$ -wave velocity for granite is beyond the range specified by Westine, namely, 150 m/s to 4600 m/s.

**Table 6.2. PPA, PPV and PPD predicted by TM5-1300 (DoA 1991), Westine (1978) and Wu and Hao (1995) for a surface explosion on granite of 2000 kg of TNT at a distance of 31 m**

Model	PPA (g)	PPV (m/s)	PPD (m)
TM5-1300	15.9	0.25	0.013
Westine*	--	(0.54)	(0.00078)
Wu and Hao	93.2	(0.38)**	(0.00038)**

\* The values for Westine (1978) were multiplied by 0.4 to consider coupling between the explosive and the ground.

\*\* The PPV and PPD are from the time series of Figure 6.15b and c, respectively.

The model of TM5-1300 does not require the user to input a seismic or *P*-wave velocity and so the TM5 results in Table 6.2 for PPA and PPV are identical to those in Table 6.1. For Westine's model, the mass density was set equal to 2600 kg/m<sup>3</sup>. The model of Wu and Hao (2005) does not predict PPV and PPD directly and so the acceleration time series was integrated to compute these peak values. The PPA of 93.2 g per Wu and Hao is much larger than that predicted by TM5-1300. The three models of Table 6.2 predict significantly different values of PPD values but somewhat similar values of PPV. As noted above, additional studies are needed to enable predictions of key soil response parameters for analysis of ground shock due to surface and buried detonations.

### **6.3 Blast Loading for the Sample Reactor Buildings**

#### **6.3.1 Introduction**

This section presents the air blast and ground shock loadings used for the response-history analysis for the sample reactor buildings. The air blast loading was computed using Air3D CFD code; the ground shock loading was generated using information presented in Wu and Hao (2005).

Section 6.3.2 introduces the assumed threat (weapon or charge size and standoff distance) for the assessment sample reactor building. Section 6.3.3 presents the Air3D models for the blast loading calculations (Section 6.3.3.1), and sample air blast loading histories at selected monitoring locations on the containment vessel (Section 6.3.3.2). Section 6.3.4 introduces the procedure for generating the ground shock and presents the acceleration, velocity and displacement histories of the ground shock used for the response-history analysis.

#### **6.3.2 Blast Threat**

This study considered blast loading from terrorist attack using conventional improvised explosive devices. In the United States, the Federal Bureau of Investigation (FBI) has the lead responsibility

for dealing with terrorism. The scale of improvised explosive devices spans many orders of magnitude. The Technical Services Working Group (TSWG) developed a threat chart, which is reproduced in Figure 6.4. Hand-delivered explosives range in size from a few pounds to 23 kg. Vehicle-borne threats can range in size up to 27,000 kg of explosive.

The design hazard for the threat analysis performed in this chapter was determined using the threat chart of Figure 6.4. The likelihood is low for a great amount of truck- or trailer-borne explosives to be detonated close to a NPP reactor building due to the strict security systems employed at nuclear power plants. The threat assumed for the assessment reported below was 2000 kg of hemispherical TNT explosive detonated on the surface, 10 m from the face of the sample reactor building.

The assessment presented below is separated into two parts: 1) air shock, and 2) ground shock. The air shock analysis assumes that the explosive is detonated on a near-rigid reflecting surface producing only limited ground shock and a small crater. The ground shock analysis assumes that the detonation results in ground shock and no air shock. A fully coupled hydrocode analysis involving a numerical model of the air, rock/soil and reactor building would be required to correctly partition the explosive effects between air and ground shock and to determine the response of the reactor building. Such analysis would be required on a project specific basis but was not attempted here as the goal was gain an understanding of the magnitude of the displacement and acceleration response of the conventional and isolated reactor buildings to blast loadings and to assess the impact of isolating the reactor building on its vulnerability to blast loadings.







### **6.3.3 Air Blast Loading**

#### *6.3.3.1 Air3D Model*

Figure 6.5 presents the layout for the Air3D analysis for the sample containment vessel. The height and diameter of the containment vessel are 61 and 42 m, respectively. Six points (A through F) are identified in the figure for the purpose of data presentation. Point A is at the top of the dome and Point B is at the center of the base slab, directly below Point A. Point D is at the base of the reactor building at the closest point on the containment vessel to the detonation. Point C is 40 m above Point D. Points E and F are at the base of the containment vessel, 90 and 180 degrees rotated from Point D, respectively.





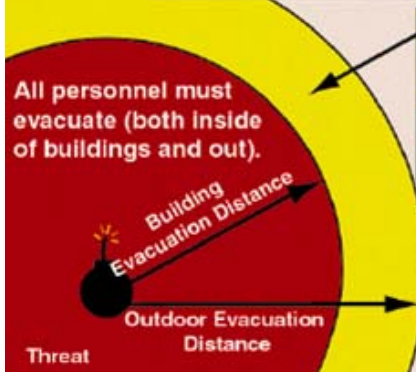
**Terrorist Bomb Threat Stand-Off**

THREAT	THREAT DESCRIPTION	EXPLOSIVES CAPACITY <sup>1</sup> (TNT EQUIVALENT)	BUILDING EVACUATION DISTANCE <sup>2</sup>	OUTDOOR EVACUATION DISTANCE <sup>3</sup>
	PIPE BOMB	5 LBS/ 2.3 KG	70 FT/ 21 M	850 FT/ 259 M
	BRIEFCASE/ SUITCASE BOMB	50 LBS/ 23 KG	150 FT/ 46 M	1,850 FT/ 564 M
	COMPACT SEDAN	500 LBS/ 227 KG	320 FT/ 98 M	1,500 FT/ 457 M
	SEDAN	1,000 LBS/ 454 KG	400 FT/ 122 M	1,750 FT/ 534 M
	PASSENGER/ CARGO VAN	4,000 LBS/ 1,814 KG	640 FT/ 195 M	2,750 FT/ 838 M
	SMALL MOVING VAN/DELIVERY TRUCK	10,000 LBS/ 4,536 KG	860 FT/ 263 M	3,750 FT/ 1,143 M

This card supersedes any previous undated versions 11/99



THREAT	THREAT DESCRIPTION	EXPLOSIVES CAPACITY <sup>1</sup> (TNT EQUIVALENT)	BUILDING EVACUATION DISTANCE <sup>2</sup>	OUTDOOR EVACUATION DISTANCE <sup>3</sup>
	MOVING VAN/ WATER TRUCK	30,000 LBS/ 13,608 KG	1,240 FT/ 375M	6,500 FT/ 1,982 M
	SEMI-TRAILER	60,000 LBS/ 27,216 KG	1,570 FT/ 475 M	7,000 FT/ 2,134 M



All personnel must either seek shelter inside a building (with some risk) away from windows and exterior walls, or move beyond the Outdoor Evacuation Distance.

Preferred area (beyond this line) for evacuation of people in buildings and mandatory for people outdoors.

<sup>1</sup> Based on maximum volume or weight of explosive (TNT equivalent) that could reasonably fit in a suitcase or vehicle.  
<sup>2</sup> Governed by the ability of an unstrengthened building to withstand severe damage or collapse.  
<sup>3</sup> Governed by the greater of fragment throw distance or glass breakage/falling glass hazard distance. Note that pipe and briefcase bombs assume cased charges which throw fragments farther than vehicle bombs.

Figure 6.4. TSWG threat chart

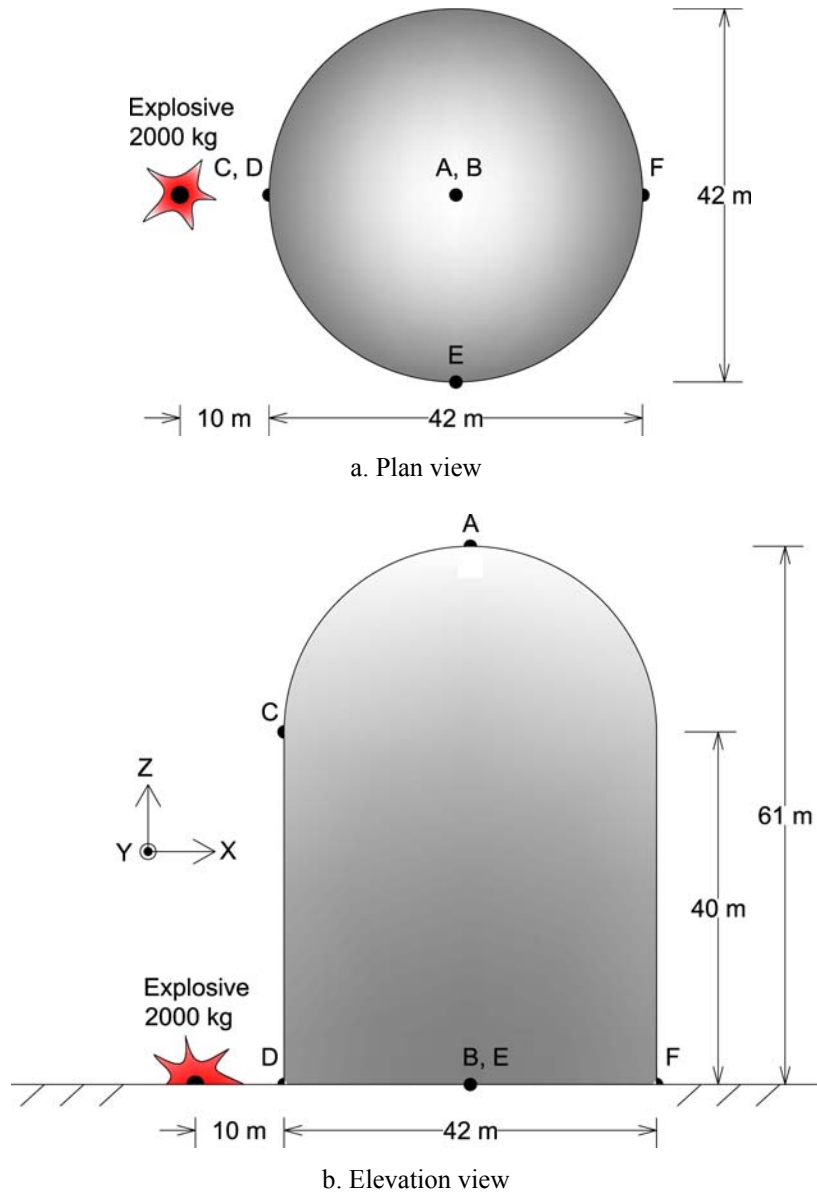


**Figure 6.5. Blast analysis for the sample NPPs**

In the Air3D model prepared for this study, the charge mass was multiplied by a factor of 1.8 (Smith and Hetherington 1994) to transform the blast effects from a free air burst to a hemispherical surface burst. The cell sizes for the 1-D, 2-D and 3-D analyses (see Section 6.2.1) were 0.005, 0.02 and 0.3 m, respectively, which correspond to scaled cell sizes of  $3.3 \times 10^{-4}$ ,  $1.3 \times 10^{-3}$  and  $2 \times 10^{-2}$   $\text{m}/\text{kg}^{1/3}$ , respectively. Although Rose (2006) recommends a scaled cell size of  $1 \times 10^{-3}$   $\text{m}/\text{kg}^{1/3}$ , a larger scaled size was used for the 3-D analysis herein. To verify the impact of cell size on the analysis results, the Air3D analysis described above was repeated using the same cell sizes for the 1-D and 2-D analyses but a cell size of 0.5 m for the 3-D analysis. The ratios of peak overpressure

and positive phase impulse for the two sets of analyses were computed at each of 2560 monitoring locations distributed around the containment vessel. The mean and standard deviation were 1.03 and 0.16, respectively, for the ratios of peak pressure and 1.02 and 0.05, respectively, for positive phase impulse. The use of the 0.3 m cell size for the 3-D analysis was considered appropriate.

The Air3D model included 2560 pressure monitoring points distributed over the exterior surface of the containment vessel, one per shell element of the LS-DYNA model of the vessel. Each monitoring point yielded a pressure history for the analysis of the vessel. The location of each monitoring point in the Air3D model was determined by the center of the corresponding shell element in the LS-DYNA (LSTC 2003) model with an offset of 0.24 m in the normal direction of the shell element away from the surface of the containment vessel.

In Air3D, a structure is modeled using obstacles. If the center of a cell is located inside an obstacle, the cell is set as *unused*. If a monitoring point is located in an unused cell, no pressure data will be generated at the monitoring point. Figure 6.6 shows a sample cell in the Air3D model for this study. The center of this cell is close to the surface of the dome and in the wall of the containment vessel. If a monitoring point is placed on the dome surface (for example, Point P of Figure 6.6), no pressure data will be obtained since the cell is set as unused. To collect pressure data, the monitoring point was shifted by 0.24 m in the direction normal to and outward from the surface of the containment vessel.

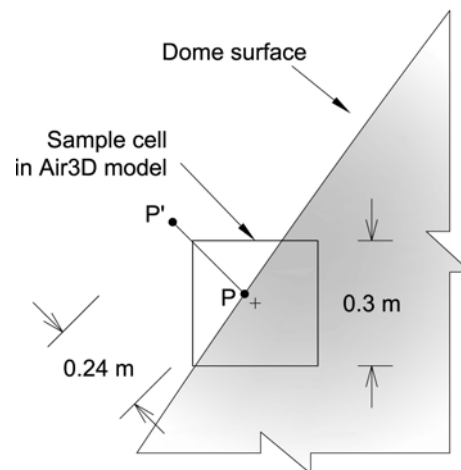


**Figure 6.6. Location of a sample monitoring point in the Air3D model for the sample reactor building**

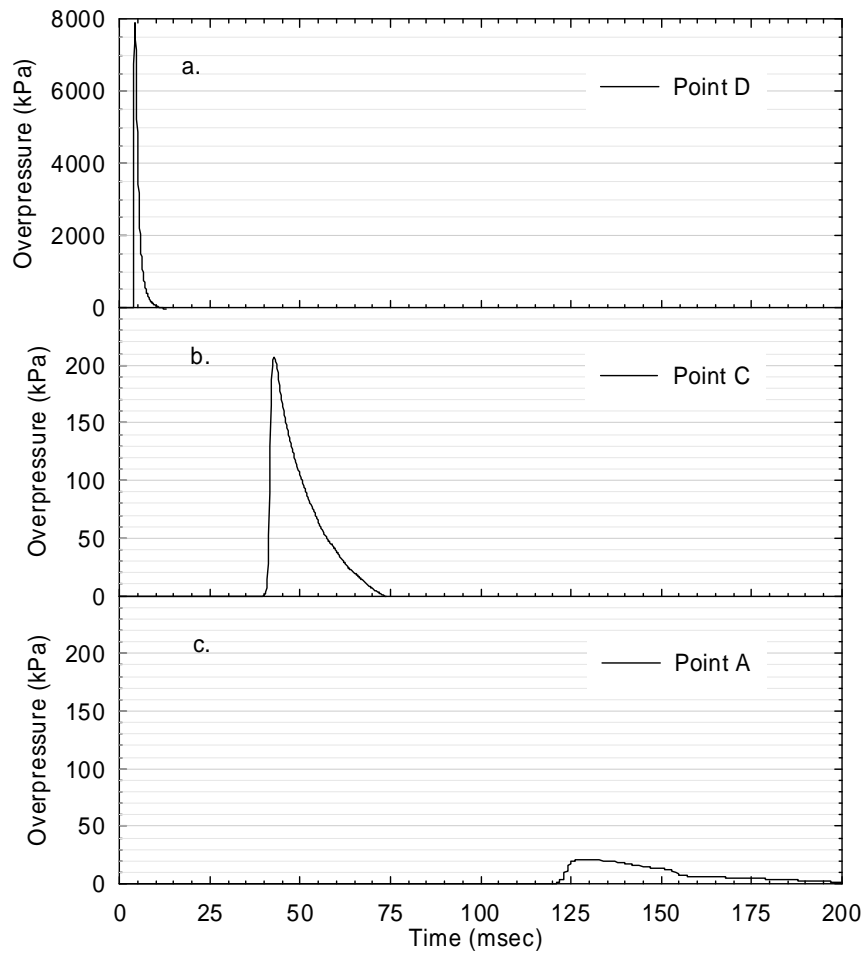


### 6.3.3.2 Pressure Histories

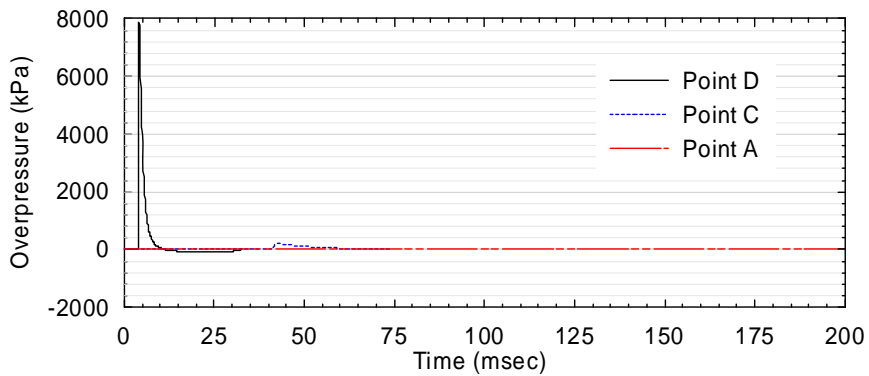
Figure 6.7 presents the pressure histories at Point D, C and A on the containment vessel (see Figure 6.5b) for the blast threat of Section 6.3.2. The peak reflected pressure drops rapidly as the distance and angle of incidence from the explosive to the monitoring point increase. The peak pressures at Points D, C and A were 7890, 207 and 22 kPa, respectively. The three pressure histories are re-plotted in Figure 6.8 using the same scale for the Y axis to show the great difference in peak pressure at the three points. The peak value of the curve for Point A cannot be observed in the figure since it is less than 0.3% of the peak pressure at Point D. The arrival time of the pressure at Points D, C and A are 3.8, 40.0 and 118.5 msec, respectively. The positive pressure loading at Point D vanishes before the shock wave reaches Point C, 40 m above Point D. The positive pressure loading at Point C vanishes before the shock wave reaches Point A. The simplified procedures that are widely used for the blast design of structures cannot capture the interaction of shock waves and complex geometries and the effect of different shock wave arrival times on global and local structural responses. The complex loading environment studied herein and the resultant structural responses can only be understood using hydrocode/CFD tools and response-history analysis.

Figure 6.9, Figure 6.10 and Figure 6.11 present the pressure contour plots of the Air3D analysis for the sample containment vessel and the assumed threat at 6.57, 18 and 154 msec, respectively, after the explosive was detonated at ( $X=Y=Z=0$ ). These figures show that the loading pattern on the containment vessel changes dramatically over the 154 msec. At  $t = 6.57$  msec, Point D on the containment vessel is subjected to a reflected overpressure of between 500 and 1000 kPa whereas the shock wave has yet to arrive at Points A and C. At  $t = 18$  msec, the shock wave distributes between the elevations of 8 and 27 m above the ground at the cutaway section of  $Y = 0$  (see Figure 6.10b). The positive overpressure at Point D has diminished substantially before the shock wave reaches Point C. At  $t = 154$  msec, the shock wave has passed the front side of the containment vessel (i.e., the side closer to the explosive) and reached the back side of the vessel.

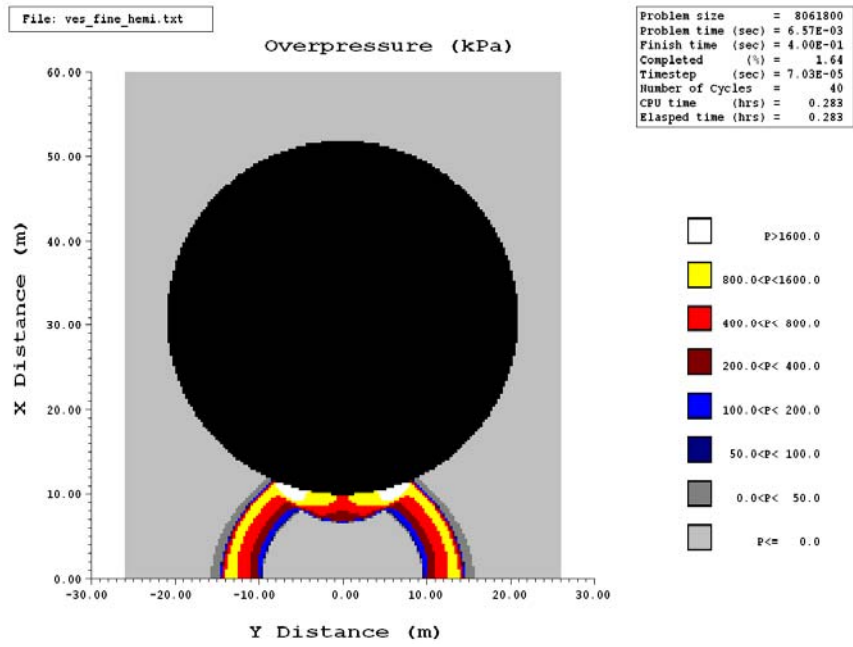
The solid curve in Figure 6.12 presents the pressure history at Point D from the Air3D analysis. The curve has a peak pressure ( $P_r$ ) of 7890 kPa, a positive phase impulse ( $i_r$ ) of 11400 kPa-msec and a positive phase duration of 7.5 msec. For the response-history analysis, the Air3D curves at every monitoring location were simplified to decay linearly from  $P_r$  to zero (see the dashed line in Figure 6.12). The simplified relationship has the same arrival time,  $P_r$  and  $i_r$  as the Air3D curve; the fictitious duration of the positive phase is set equal to  $2i_r/P_r$ , thereby preserving the peak reflected pressure and impulse.



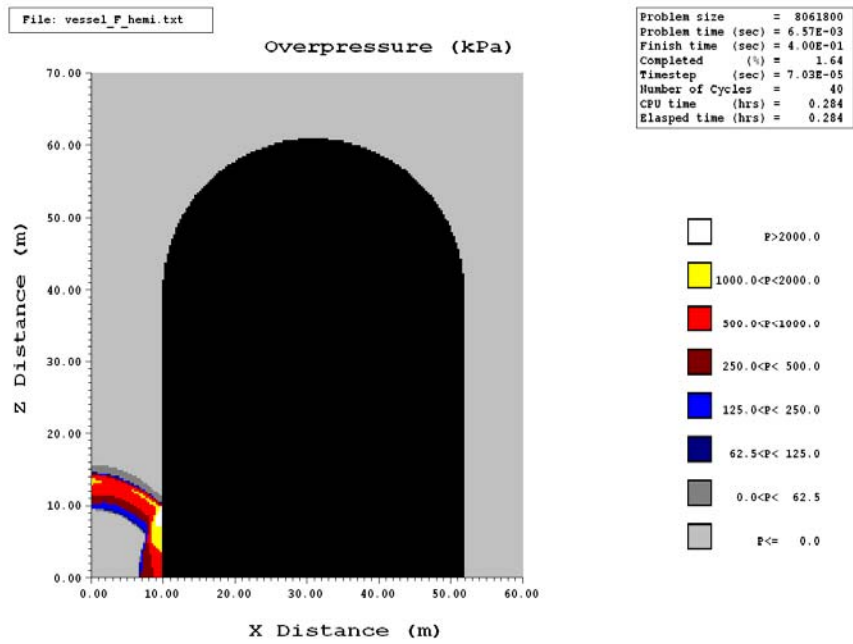
**Figure 6.7. Pressure histories at Points A, C and D of Figure 6.5 for the blast analysis of the sample NPP**



**Figure 6.8. Pressure histories of Figure 6.7 with the same scale for the Y axis**

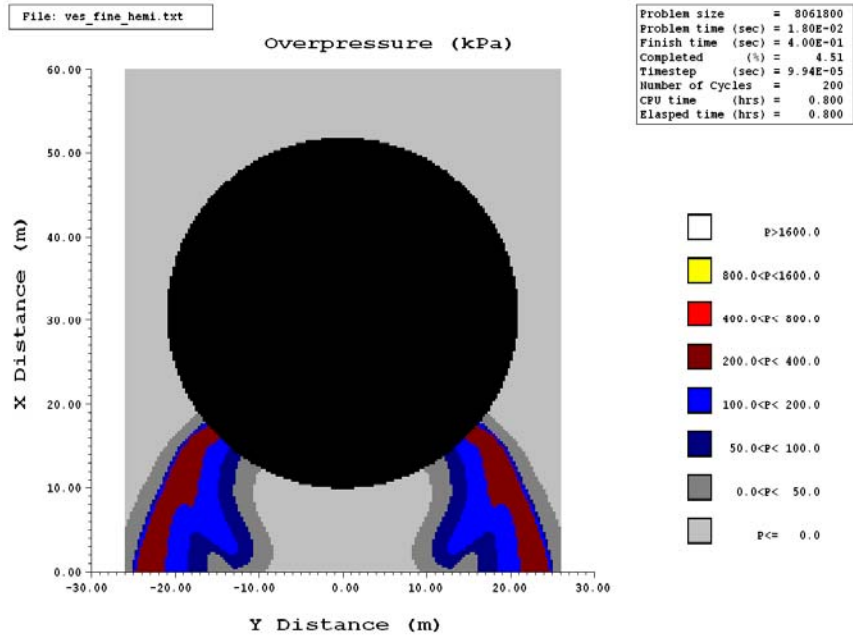


a. Plan view

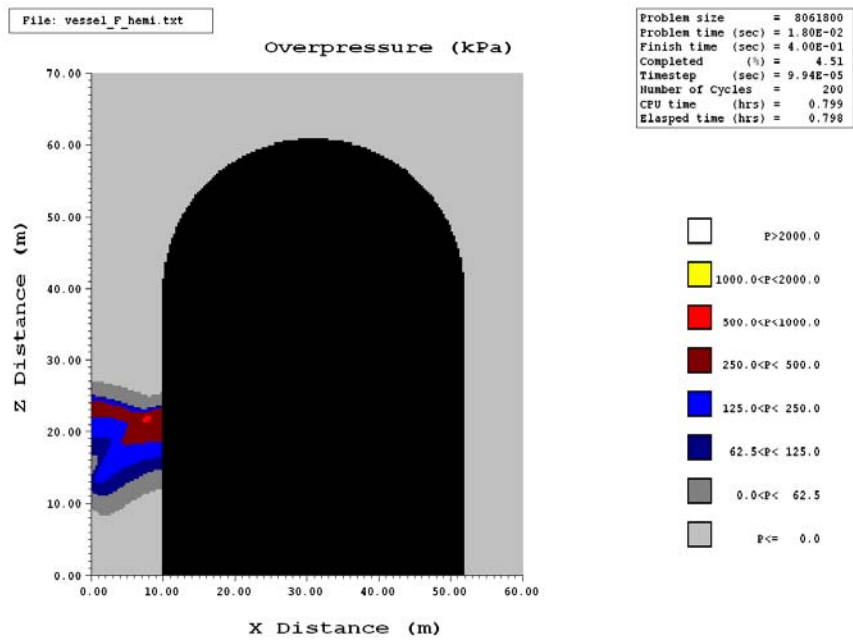


b. Elevation view

Figure 6.9. Pressure contour plots for the blast analysis of Section 6.3.3 at the instant of 6.57 msec after detonation

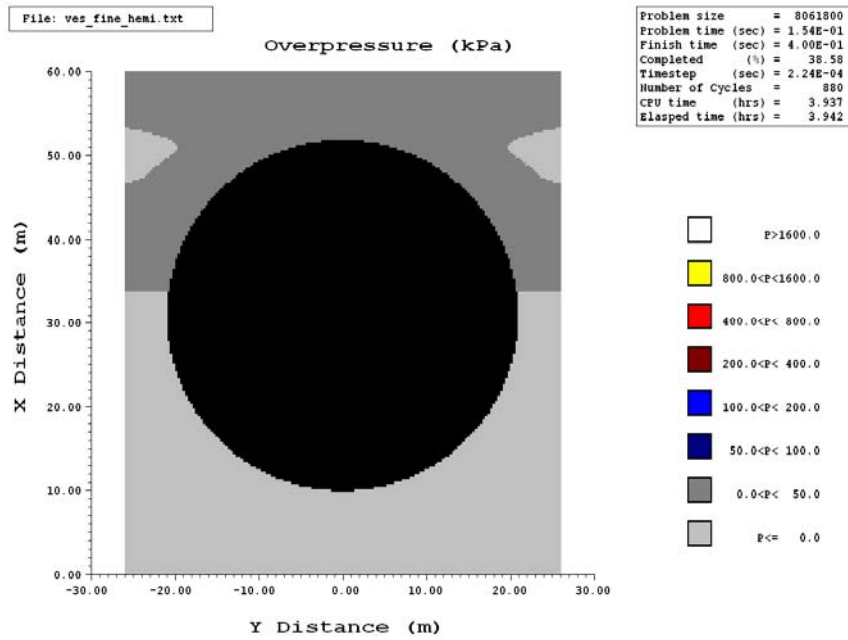


a. Plan view

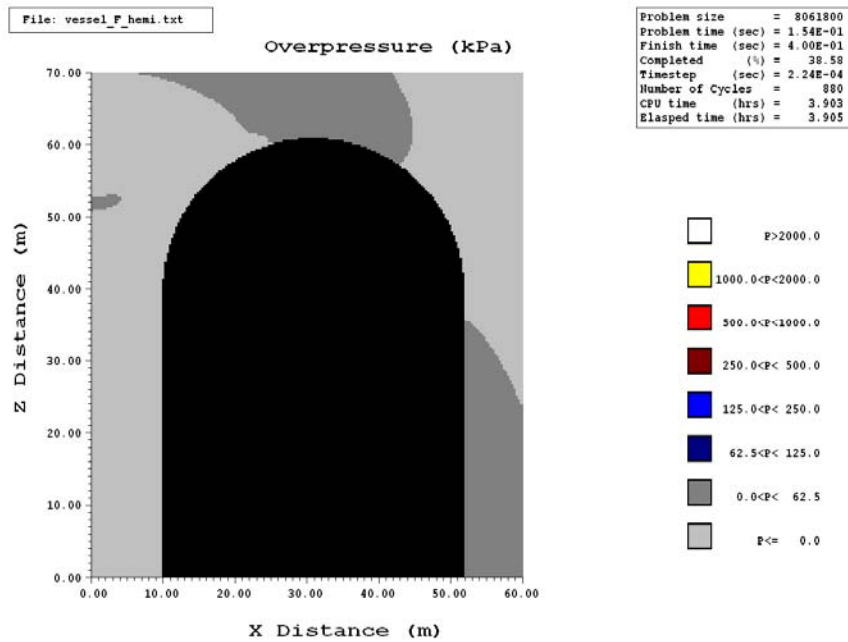


b. Elevation view

**Figure 6.10. Pressure contour plots for the blast analysis of Section 6.3.3 at the instant of 18 msec after detonation**

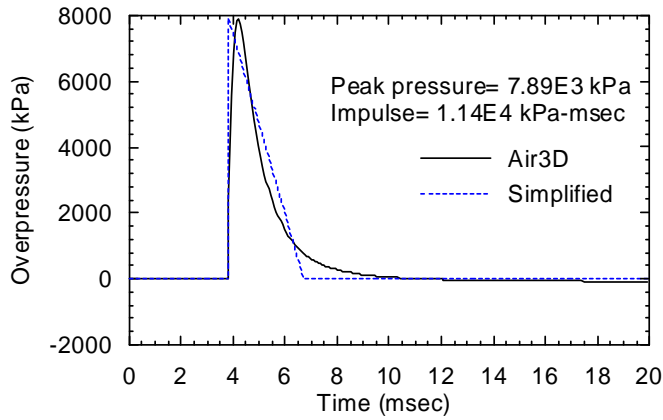


a. Plan view



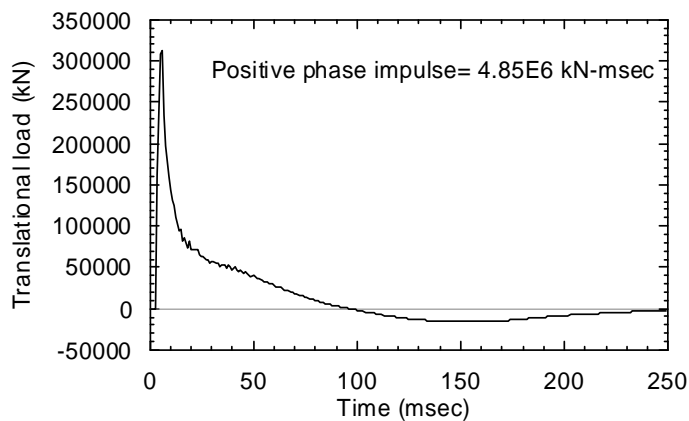
b. Elevation view

Figure 6.11. Pressure contour plots for the blast analysis of Section 6.3.3 at the instant of 154 msec after detonation



**Figure 6.12. Actual and simplified pressure histories at Point D of Figure 6.5**

Figure 6.13 presents the translational load history on the containment vessel in the X direction. This history was computed as the sum of the X components of the histories acting on the 2560 shell elements at every step in the time series; the arrival time of the shock wave at each monitoring location was preserved. The blast force history on a given shell element was computed using the triangular pressure function multiplied by the area of the shell element. The peak translational load and positive phase impulse of Figure 6.13 are  $3.13 \times 10^5$  kN (6 msec after detonation) and  $4.85 \times 10^6$  kN-msec, respectively. The minimum translational load in the X direction is  $-1.58 \times 10^4$  kN: a much smaller value in absolute terms than the peak load in the positive phase.



**Figure 6.13. Translational load history for the sample NPP containment building**

### 6.3.4 Ground Shock

An acceleration time series was generated to simulate the ground shock introduced by the blast threat selected for the sample conventional and isolated reactor buildings. Equations (6.12) through (6.17) were used to determine the parameters and functions required in ground shock simulation, including PPA, arrival time ( $t_a$ ), power spectral density function ( $S(f)$ ), principal frequency ( $PF$ ) and shape function ( $\xi(t)$ ). The intensity of the ground shock diminishes rapidly with distance, with amplitude at Point D (10 m from the detonation) being much greater than that on the opposite side of the containment vessel, 52 m from the detonation. For this study, an averaged distance of 31 m, equal to the distance between the point of detonation and the center of the base slab (Point B), was used for ground shock simulation. Table 6.3 summarizes the values of the parameters used for the ground shock simulation. Figure 6.14 and Figure 6.3 present the normalized power spectrum and the time-series shape function, respectively, for the ground shock simulation.

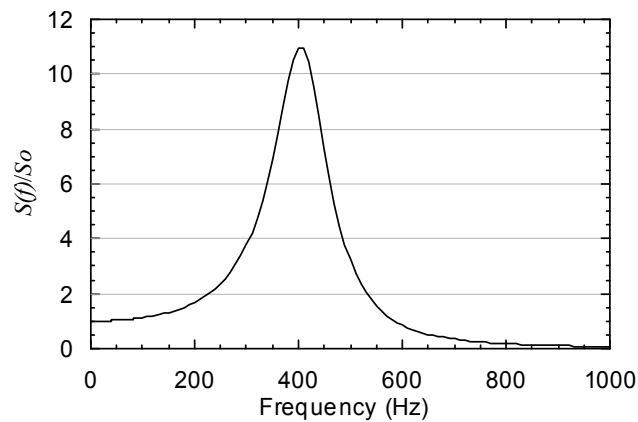


**Figure 6.14. Normalized power spectrum for ground shock simulation**

**Table 6.3. Parameters for ground shock simulation**

Parameter	Value
$\zeta_g$	0.16
$c_p$ (m/s)	5600
PPA (g)	93.2
$t_a$ (sec)	0.0048
$PF$ (Hz)	414.2
$t_p$	0.0082
$S_0$	0.03

The ground shock time series,  $a(t)$ , was assumed to be a Gaussian process (Soong and Grigoriu 1993) and was simulated using the following equation:

$$a(t) = \sum_i \xi_i(t) \sqrt{2S(f_i)\Delta f} \cos(2\pi f_i t + \Phi_i) \quad (6.18)$$

where  $\Phi_i$  is a random variable with an uniform distribution over  $(0, 2\pi)$ , representing the phase angle for each  $f_i$ . In this study, 590 values of  $f_i$  were used for the simulation, ranging between 0.01 and 1000 Hz. The resultant acceleration history is presented in Figure 6.15a. The acceleration history of Figure 6.15a was integrated with respect to time for the velocity and displacement histories, which are presented in panels b and c, respectively. The peak acceleration, velocity and displacement of Figure 6.15 are presented in the last row of Table 6.2 to enable a comparison of values with the procedures described previously.

## 6.4 Blast Assessment of the Sample Reactor Buildings

### 6.4.1 Introduction

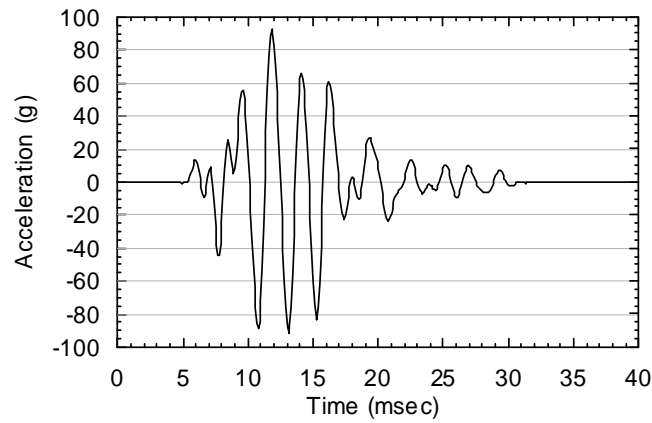
This section presents the results of the LS-DYNA analysis of the containment vessel for the air blast pressure histories and ground shock of Section 6.3. Per Section 6.1, the performance assessment presented here considers only conventional (non-nuclear) improvised explosive devices detonated on the ground and does not consider debris loadings, concrete breach or concrete spall, each of which would not be influenced by the installation of seismic isolators beneath the reactor building.

Section 6.4.2 presents the DYNA models used for the analysis of the conventional and isolated reactor buildings and introduces the models adopted for the reinforced concrete in the containment vessel and internal structure and for the seismic isolators.

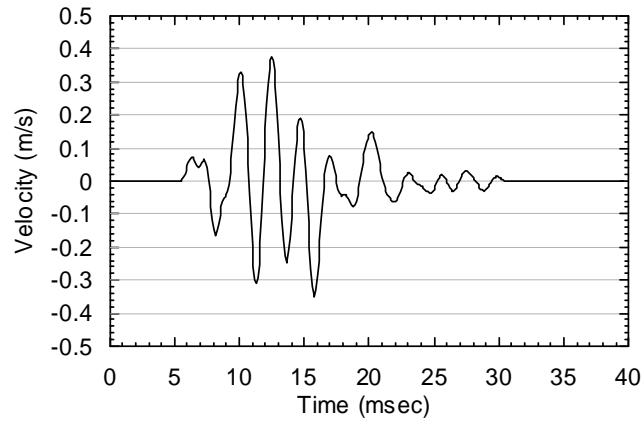
The global and local results of the DYNA analyses for the air blast loading are presented in Section 6.4.3. Global responses are measured using displacement and base shear of the containment vessel. Local responses are measured using peak floor accelerations and floor spectral accelerations at selected points on the internal structure. Since the internal structure of the conventional NPP is well-protected from the air blast loading, the discussion of local responses focuses on the base-isolated NPP only.

The global and local results of the DYNA analyses for the ground shock are presented in Section 6.4.4 using the same response parameters as in Section 6.4.3. Both conventional and base-isolated NPPs were investigated.

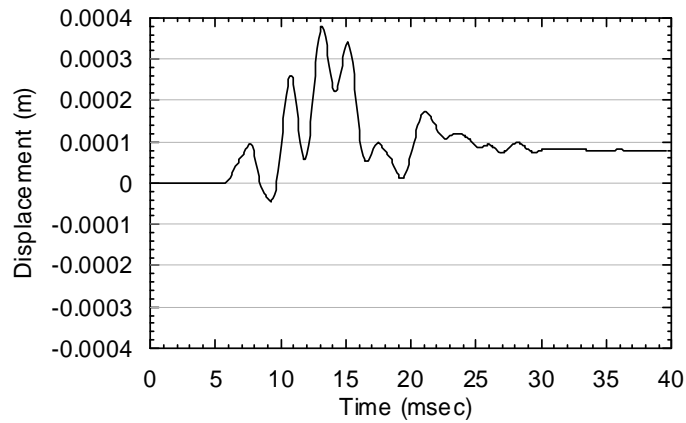




a. Acceleration



b. Velocity



c. Displacement

**Figure 6.15. Acceleration, velocity and displacement histories used in the ground shock analysis of the sample reactor buildings**

#### 6.4.2 *LS-DYNA Models for Conventional and Base-Isolated Reactor Buildings*

Two finite element models, representing the conventional and base-isolated reactor buildings, were developed using LS-DYNA (LSTC 2003) for response-history analyses due to air shock and ground shock loadings.

As described in Chapter 2, the sample reactor building structure consists of a containment vessel and an internal structure to which the secondary systems are attached. The containment vessel was modeled using 3584 four-node shell elements, of which 1024 were used for the base slab and 2560 were used for the dome and the wall. The thickness of the shell elements for the dome and wall of the containment vessel was 1.2 m and that for the base slab was 2.5 m. Elastic material properties were assigned to these shell elements with Young's modulus of 28,000 MPa and Poisson's ratio of 0.15. The mass density of the material for the dome and wall was set equal to 2709 kg/m<sup>3</sup> and to 8103 kg/m<sup>3</sup> for the base slab. These values of density were back-calculated using the mass data provided by the NPP supplier for each part of the sample reactor building. The density for the base slab is much higher than that for regular reinforced concrete and was adjusted upwards to account for the mass of the secondary systems supported by the base slab, the elements of the internal structure below an elevation of 3.5 m<sup>2</sup>, and part of the base slab not included in the model<sup>3</sup>. Figure 6.16a presents the LS-DYNA model of the containment vessel.

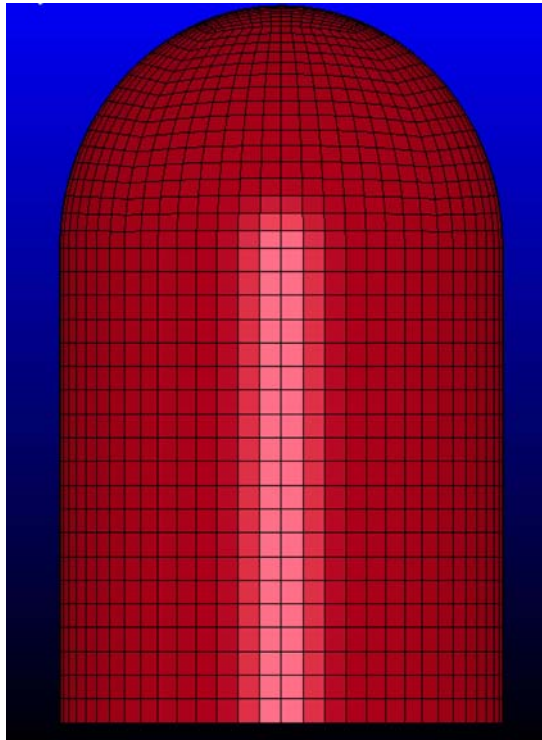
The internal structure of the sample reactor building was modeled as a lumped-mass stick, the same as that used in the SAP2000 model for the earthquake response-history analysis (see Figure 2.1b). The mass of the structural and nonstructural components of the internal structure was lumped at discrete nodes on the stick. Elastic beam elements were used for the stick model because preliminary simulations indicated that the shear demands produced by the blast loadings were much smaller than the shear capacities of the structural components in the internal structure<sup>4</sup>. Figure 6.16b presents the stick model for the internal structure in LS-DYNA.

---

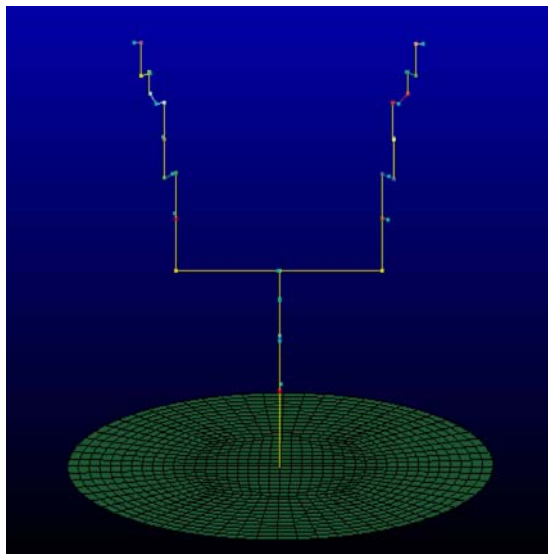
<sup>2</sup> The mass of the elements of the internal structure between elevations of 0 m and 3.5 m was lumped at the level of the base slab.

<sup>3</sup> The radius of the base slab is 25 m for the sample reactor building. The radius of the slab in the LS-DYNA model is 21 m. The true mass of the base slab was included in the LS-DYNA model by adjusting the density of the base slab concrete.

<sup>4</sup> This assumption was validated by the analysis results presented later. The shear capacities of the structural components for the internal stick were computed using  $0.5\sqrt{f'_c}A_s$  (see Section 5.2.4.1), where the shear areas of the components were provided by the supplier of the sample reactor building.



a. Containment vessel



b. Lumped-mass stick for the internal structure

**Figure 6.16. LS-DYNA model for the conventional reactor building**

To develop the finite element model for the base-isolated reactor building, bilinear springs were placed beneath the base slab of the conventional reactor building. The force-displacement relationship for the springs used herein was the same as that presented in Figure 2.3 and Table 2.1 for Model 3 (lead rubber bearing). In the LS-DYNA model for the base-isolated reactor building, the bearings were modeled using a beam element and the “nonlinear plastic discrete beam” material model, which can capture the effects of elasto-plastic and linear viscous behavior using six springs, one for each of the six local degrees of freedom. Figure 6.17 presents the model of the base-isolated reactor building.

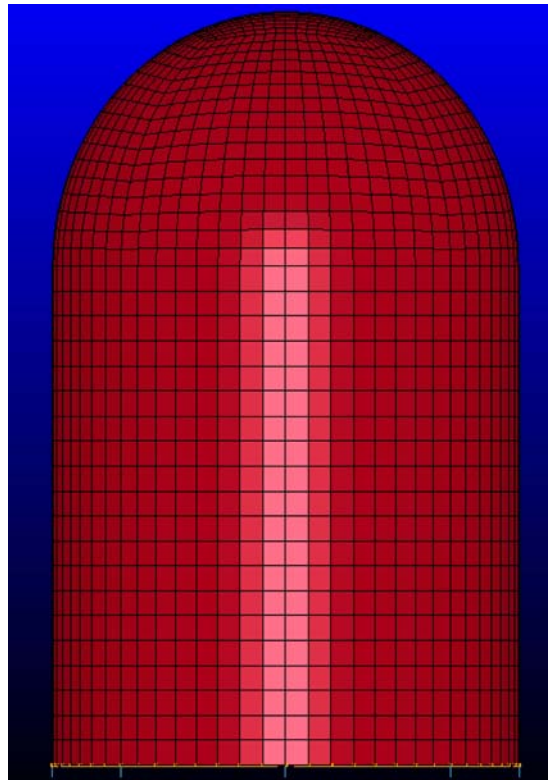


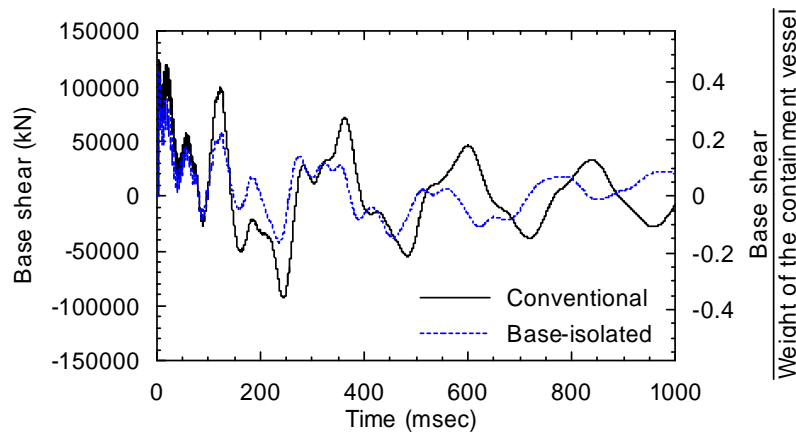
**Figure 6.17. LS-DYNA model for the base-isolated reactor building**

### **6.4.3 Response of the Sample Reactor Buildings Subjected to Air Blast Loading**

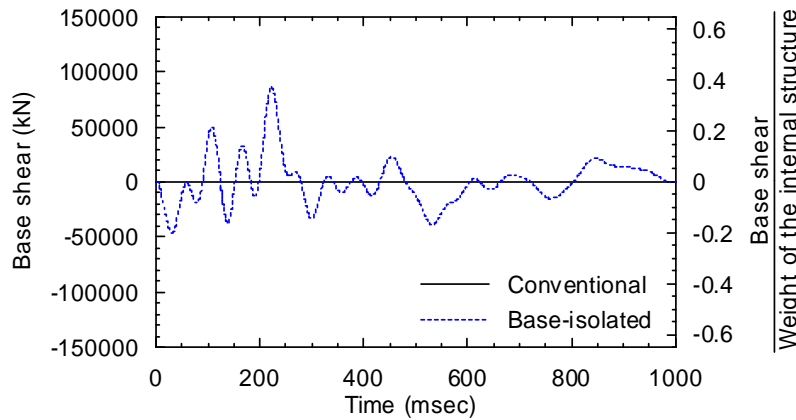
#### **6.4.3.1 Globe Response**

Figure 6.18 presents the base shear histories for the conventional and base-isolated reactor buildings subjected to the air blast loading of Section 6.3.3. Panels a and b of Figure 6.18 show the results for the containment vessel and internal structure, respectively. The base shear force history for the conventional containment vessel was computed using the horizontal reaction force history below the base slab since the base slab of the reactor building and the internal structure did not displace. The base shear force history

for the isolated containment vessel was computed using equilibrium of the base slab, where the sum of the inertial force of the slab, the horizontal shear forces in the bearings, the base shear force in the internal structure and the base shear force in the containment vessel must be zero at each time step. The base shear force for the internal structure was taken as the shear force in the lowest beam element in the internal stick, immediately above the base slab.



a. Containment vessel



b. Internal structure

**Figure 6.18. Base shear histories for the conventional and base-isolated reactor buildings subjected to the air blast loading of Section 6.3.3**

The peak base shear force in the conventional containment vessel was 125,000 kN (51% of the total weight of the containment vessel,  $0.51W_{con}$ ), which occurred at 5.7 msec, and very close to the time of the peak translational load (see Figure 6.14). The peak base shear for the base-isolated containment vessel was 115,000 kN ( $0.47W_{con}$ ): 92% of the peak base shear for the conventional reactor building. The peak base shear force for the internal structure in the base-isolated reactor building is 86,000 kN (37% of the total weight of the internal structure,  $0.37W_{int}$ ). As a point of reference, the shear strengths at the base of

the containment vessel and internal structure, computed using  $0.5\sqrt{f'_c}A_s$  (see Section 5.2.4.1) are 483,000 kN and 327,000 kN, respectively. The peak drift between Points A and B for the conventional and base-isolated reactor buildings subjected to the air blast loading of Section 6.3.3 are 6 and 4 mm, respectively. The peak global responses of this subsection are tabulated in Table 6.4. (Peak drift is used here as an indicator of global response. The peak local deformation of the wall of the containment vessel, with respect to the initial geometry, is 16 mm.)

**Table 6.4. Drifts and base shears of the conventional and base-isolated containment vessels subjected to the blast loading of Section 6.3**

Loading type	Drift (mm)		Base shear (kN)			
			Containment vessel		Internal structure	
	Conventional	Base-isolated	Conventional	Base-isolated	Conventional	Base-isolated
Air blast	6.0	4.0	125000	115000	0	86000
Ground shock	0.38	0.02	637000	410	69800	415

The analysis results for the base-isolated reactor building show that the maximum displacement in the isolators is 5.2 mm, which is smaller than the yield displacement of the isolators (=6.6 mm), and the vibration period of the reactor building was controlled by the initial stiffness of the isolators. (The fundamental period of the lead-rubber-bearing isolated containment vessel is 0.63 second if the isolator response is elastic.)

#### 6.4.3.2 Local Response

Figure 6.19 presents the acceleration history at the base slab of the containment structure for the base-isolated reactor building subjected to the air blast loading of Section 6.3.3. This time series determines the demands on the structural and nonstructural components of the internal structure. The peak acceleration of 0.44 g occurred at 5.7 msec after detonation. The acceleration history has a much higher frequency content in the transient phase of the loading (0 through 0.3 second) than in subsequent free-vibration phase (0.3 through 1 second). Figure 6.20 presents the Fast Fourier Transform of the acceleration history of Figure 6.19. Peaks in the Fourier spectrum are evident at frequencies of 8.5 Hz (the fundamental frequency of the internal structure) and 18 Hz (a modal frequency of the containment vessel).

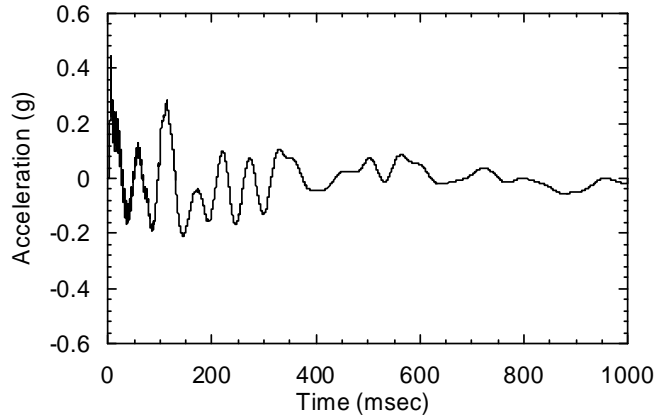


**Figure 6.19. Acceleration history at the base slab of the containment structure for the base-isolated reactor building subjected to the air blast loading of Section 6.3.3**

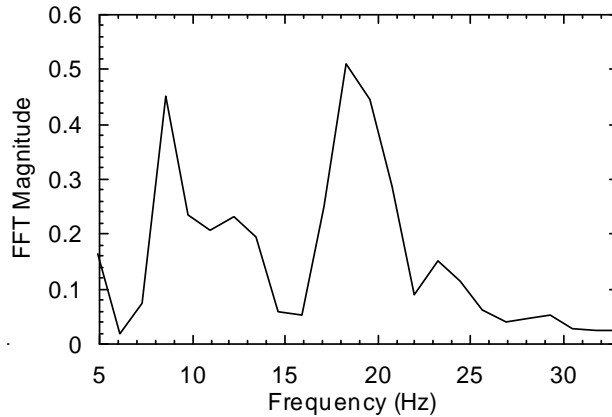


**Figure 6.20. FFT magnitude of the acceleration history of Figure 6.19**

Figure 6.21 presents the acceleration histories and floor spectral accelerations at Nodes 201, 1009 and 216 of Figure 2.2b: the three nodes on the internal structure used in Chapter 5 for seismic performance assessment. The peak accelerations at Node 201, 1009 and 216 are 0.24, 0.4 and 0.88 g, respectively. The floor spectral accelerations at the three nodes have peak values at frequencies close to 18 Hz. The AFSA values for the floor spectral accelerations at Nodes 201, 1009 and 216 are 0.45, 0.83 and 1.77, respectively; see Table 6.5. Table 6.5 also presents the ASFA-based HCLPF values assumed for the secondary systems at Node 201, 1009 and 216 (see Section 5.2.3) for the seismic performance assessment: 0.84, 1.17 and 2.61 g, respectively. These HCLFP values are greater than the ASFA demands for the secondary systems resulting from the air blast loading. The AFSA demands of 0.45, 0.83 and 1.77 g for the secondary systems at Nodes 201, 1009 and 216, respectively, are associated with probabilities of failure of  $2.7 \times 10^{-10}$ ,  $1.5 \times 10^{-7}$  and  $5.8 \times 10^{-8}$ , respectively, through the median fragility curves of Figure

5.10. (For example, the median fragility curve of Figure 5.10 at Node 201 is defined by a median and dispersion of 2.26 g and 0.26, respectively. The probability of failure for this curve at an AFSA = 0.45 g is  $2.7 \times 10^{-10}$ ).

**Table 6.5. Peak floor accelerations and AFSA at Nodes 201, 1009 and 216 for the conventional and base-isolated reactor buildings subjected to the blast loading of Section 6.3**

Response	Loading type	Structural system	Node number		
			201	1009	216
Peak floor acceleration (g)	Air blast	Base-isolated	0.24	0.40	0.88
	Ground shock	Conventional	1.26	0.54	0.91
		Base-isolated	0.007	0.011	0.11
AFSA (g)	Air blast	Base-isolated	0.45	0.83	1.77
	Ground shock	Conventional	0.33	0.28	0.59
		Base-isolated	0.0035	0.0044	0.011
HCLPF values for the secondary systems (g)			0.84	1.17	2.61

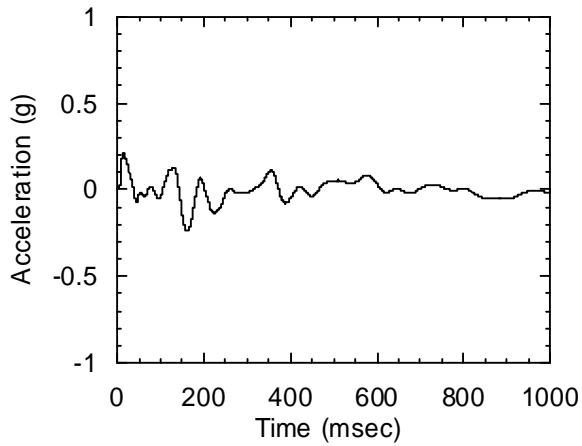
#### 6.4.4 Response of the Sample Reactor Buildings Subjected to Ground Shock

##### 6.4.4.1 Global Response

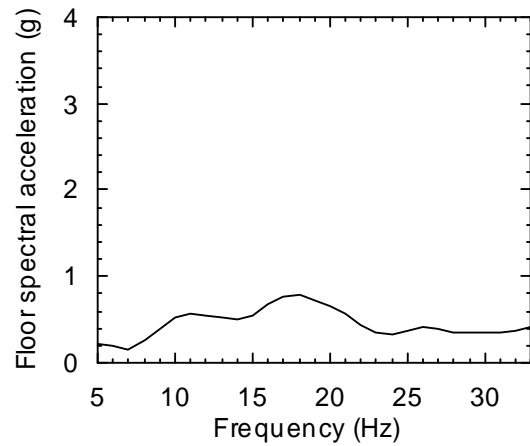
The base shear histories for the containment vessel and internal structure are presented in Figure 6.22 and Figure 6.23, respectively, for the conventional and base-isolated reactor buildings subjected to the ground shock of Section 6.3.4. The peak values of the four curves presented in Figure 6.22 and Figure 6.23 are presented in Table 6.4. The drift between Points A and B are presented also. Reductions by orders of magnitude due to the installation of the base isolation system are apparent.

Figure 6.22a shows that the peak base shear in the conventional containment vessel was more than twice its reactive weight, which is not a surprising result since the ground shock history had a PPA of 93.2 g and a *PF* of over 400 Hz (see Table 6.3 and Figure 6.15). These results need to be interpreted with caution because 1) studies are needed to verify the reliability of the ground shock model used herein (see Section 6.2.2), 2) the assumption of elastic response for a base shear of twice the reactive weight may not be valid, 3) the effects of vertical shaking due to ground shock have not been considered, and 4) the ground shock effects were considered as an in-phase loading at all support points beneath the base slab, rather than as a traveling wave, with an amplitude equal to that computed for the center of the base slab.

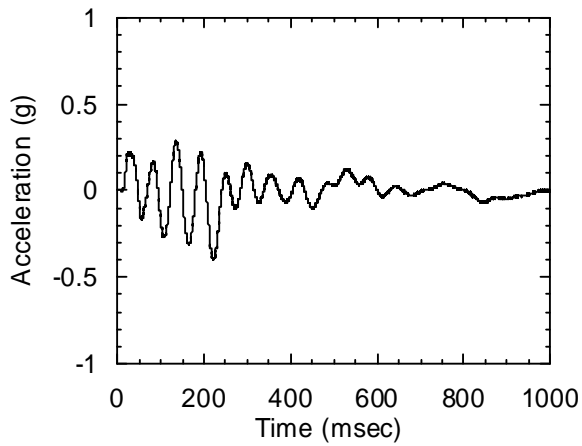




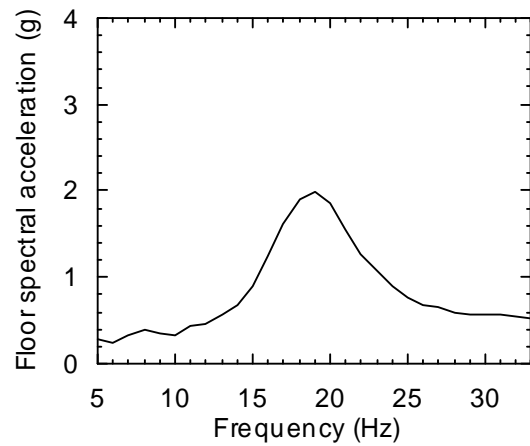
a. Acceleration history, Node 201



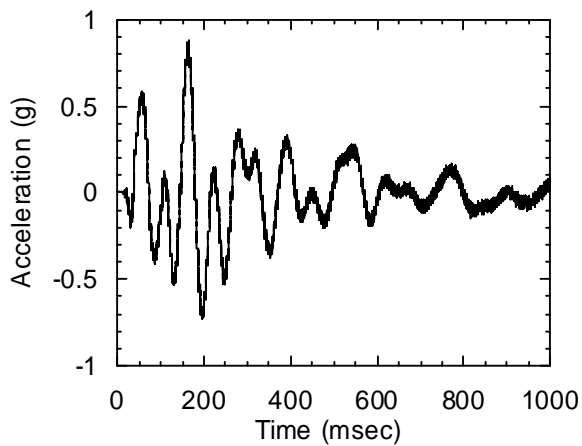
b. Floor spectral accelerations, Node 201



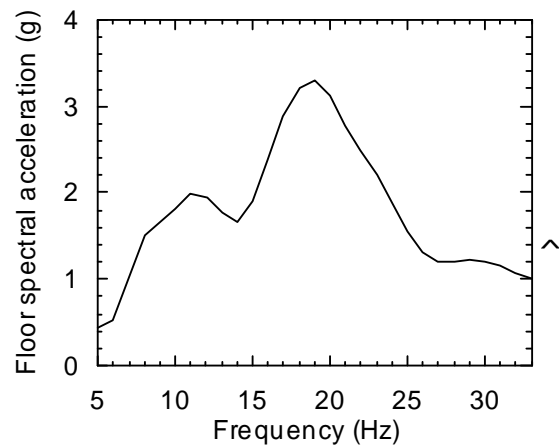
c. Acceleration history, Node 1009



d. Floor spectral accelerations, Node 1009

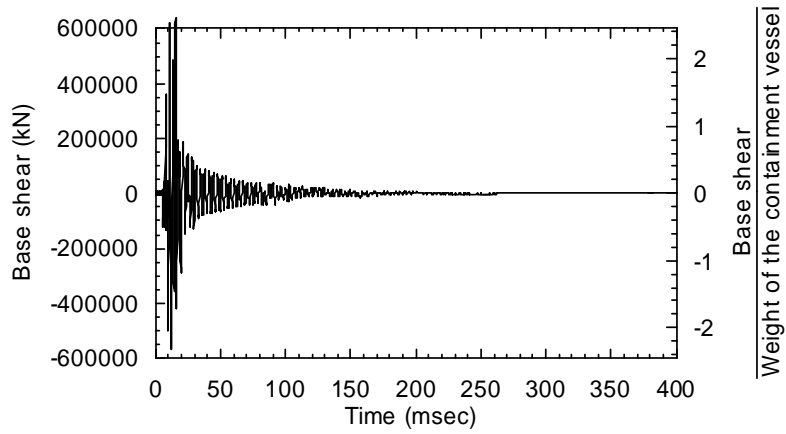


e. Acceleration history, Node 216

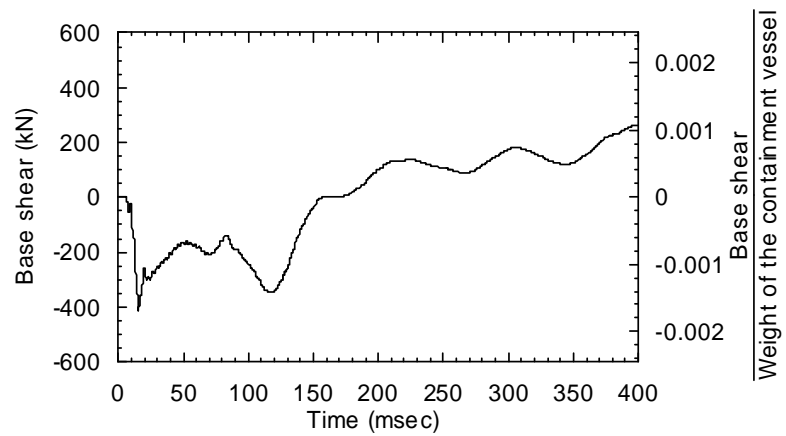


f. Floor spectral accelerations, Node 216

**Figure 6.21. Acceleration histories and floor spectral accelerations at Nodes 201, 1009 and 216 for the base-isolated reactor building subjected to the air blast loading of Section 6.3.3**

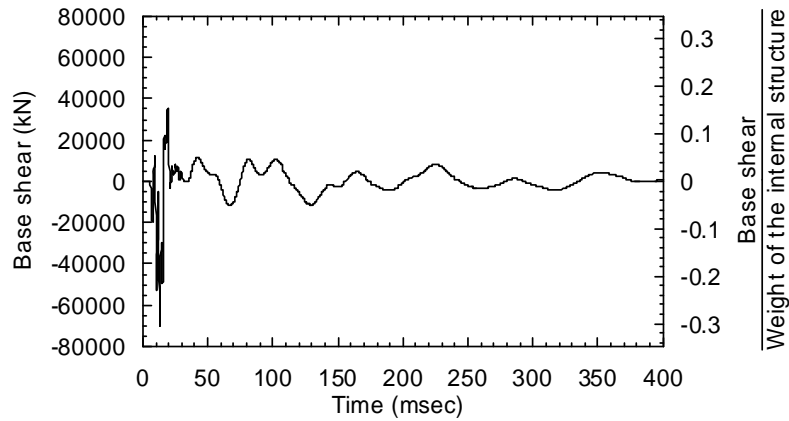


a. Conventional

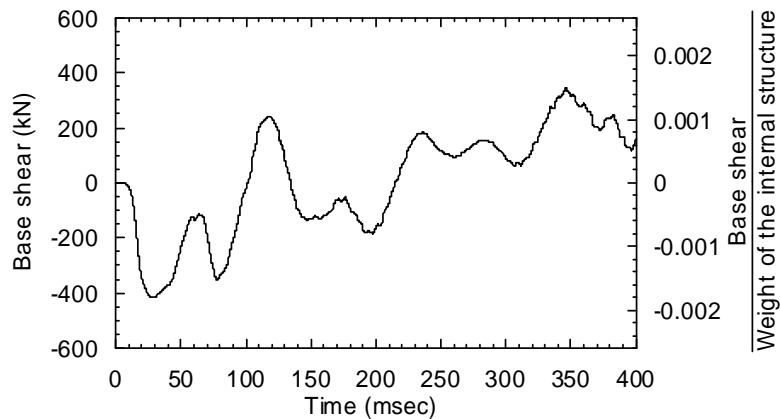


b. Isolated

**Figure 6.22. Base shear histories for the containment vessel of the conventional and base-isolated reactor buildings subjected to the ground shock of Figure 6.15**



a. Conventional



b. Isolated

**Figure 6.23. Base shear histories for the internal structure in the conventional and base-isolated reactor buildings subjected to the ground shock of Figure 6.15**

Figure 6.24 presents the acceleration history at the base slab of the isolated containment vessel. The peak acceleration is less than 0.01 g. Figure 6.25 presents the acceleration histories above and below the isolators. The accelerations above the isolators are too small to be observed.

The results presented in this section show that the performance of the isolated NPP is superior to that of the conventional NPP for ground shock loading.

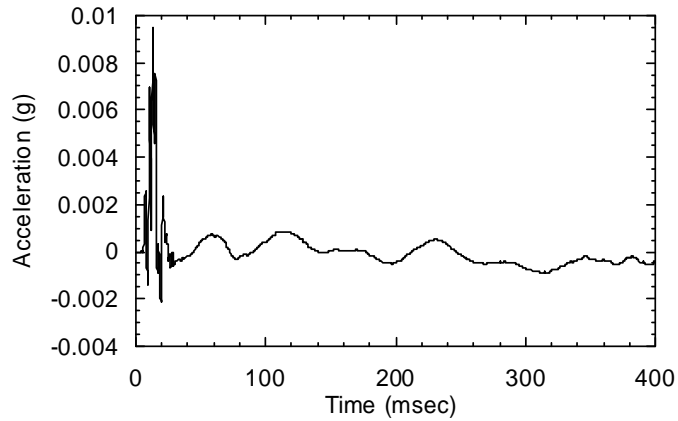


**Figure 6.24. Acceleration history at the base slab of the base-isolated containment structure subjected to the ground shock of Figure 6.15**

#### 6.4.4.2 Local Response

Figure 6.26 presents the acceleration histories and floor spectral accelerations at Nodes 201, 1009 and 216. The peak accelerations of the time series in panels a, c and e of Figure 6.26 and the AFSA of the spectra presented in panels b, d and f of Figure 6.26 are tabulated in Table 6.5. The demands on the secondary systems for the base-isolated NPP are much smaller than those for the conventional reactor building: an expected result due to the significant difference in the acceleration histories at the base slab of the conventional and isolated containment vessels (see Figure 6.25).

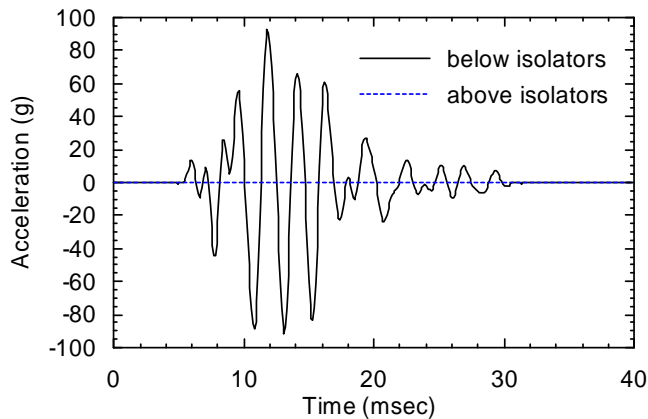
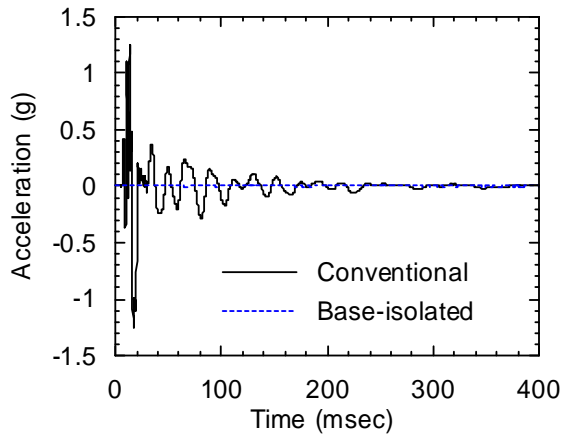
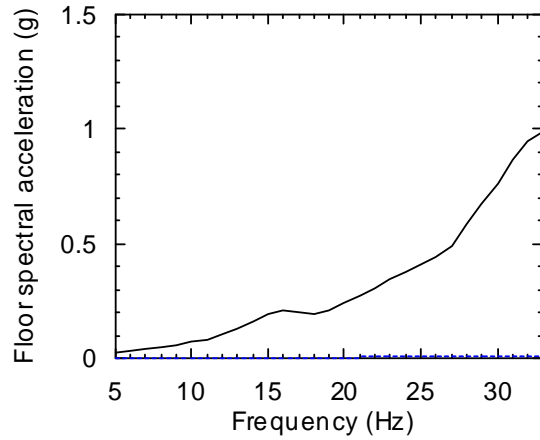


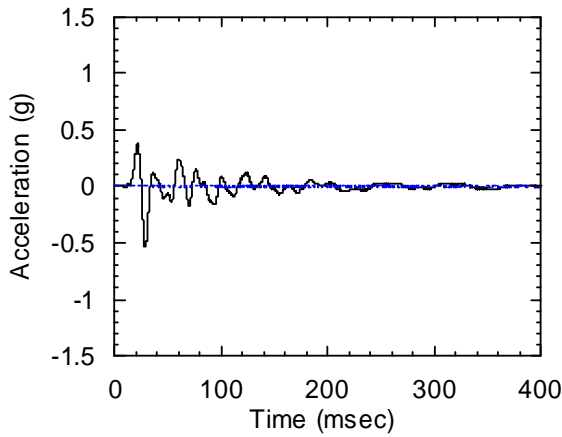
**Figure 6.25. Acceleration histories below and above the isolators for the base-isolated containment structure subjected to the ground shock of Figure 6.15**



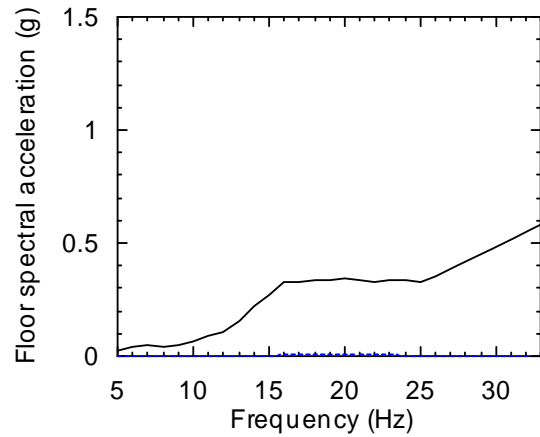
a. Acceleration history, Node 201



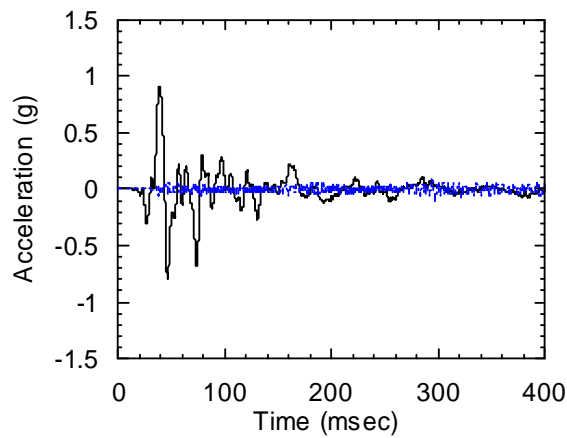
b. Floor spectral accelerations, Node 201



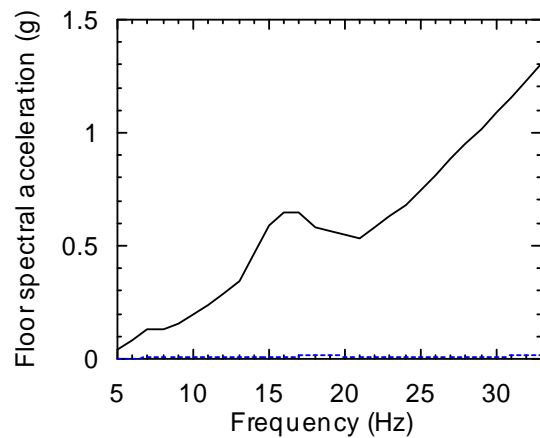
c. Acceleration history, Node 1009



d. Floor spectral accelerations, Node 1009



e. Acceleration history, Node 216



f. Floor spectral accelerations, Node 216

**Figure 6.26. Acceleration histories and floor spectral accelerations at Nodes 201, 1009 and 216 for the conventional and base-isolated reactor buildings subjected to the ground shock of Figure 6.15**

The AFSA values presented in Table 6.5 for ground shock loading of the conventional NPP are associated with insignificant probabilities of failure (smaller than  $10^{-10}$ ) using the median fragility curves of Figure 5.10. However, it must be noted that the spectral accelerations increase as the frequency increases as shown in Figure 6.26. The peak values of the three floor spectra of panels b, d, and f of Figure 6.26 for the conventional NPP occur at frequencies greater than 33 Hz due to the high-frequency content of the ground shock loading. These spectra are re-plotted in Figure 6.27 using a wider frequency range, namely, 5 to 100 Hz. The demands at frequencies above 50 Hz are much greater than those at frequencies lower than 33 Hz. The shape of the floor spectra of Figure 6.27 should be considered when designing secondary systems for blast-induced ground shock.

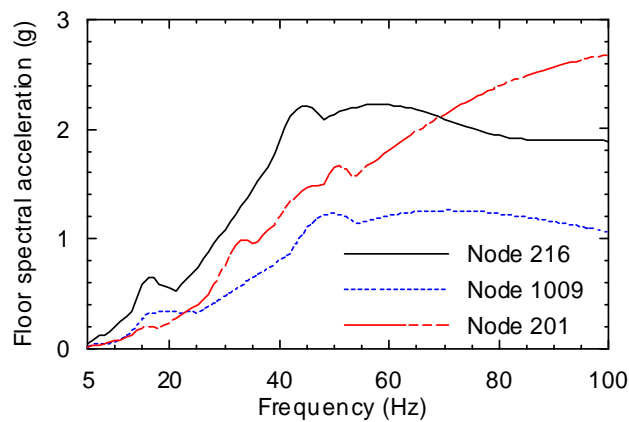


**Figure 6.27. Floor spectral accelerations at Nodes 201, 1009 and 216 at frequencies of 5 through 100 Hz for the conventional reactor building subjected to the ground shock of Figure 6.15**

## 6.5 Closing Remarks

The analysis results of Section 6.4 show that the installation of base isolation does not increase the vulnerability of the sample NPP to air blast loading and greatly improves the performance of the containment and internal structures subjected to ground shock. For air-blast analysis, the base-isolated containment vessel had a smaller base shear than the conventional containment vessel. The secondary systems attached to the internal structure in the base-isolated NPP experience floor spectral demands that are associated with extremely small probabilities of failure. The non-isolated containment vessel protected the secondary systems attached to the internal structure from the effects of air-blast loading (in part due to the assumption of base slab rigidity and restraint).

For short stand-off surface explosions such as the design threat analyzed herein, the air blast and ground shock loads will act simultaneously on the structure. Table 6.6 presents the arrival times for the air blast and ground shock waves induced by the design threat of Section 6.3.2 at Points D, E and F of Figure 6.5. The arrival times for the air blast shock front were obtained from the Air3D analysis of Section 6.3.3 and for the ground shock using (6.13). The results of Table 6.6 show that the ground shock front arrived at Point D earlier than the air blast shock front but the ground shock loading does not clear the containment vessel (Point F) before the shock front arrives at Point D. Based on these results, air shock and ground shock loadings should be imposed simultaneously on NPP buildings to assess the performance associated with near-field surface explosions.

The study presented herein was limited by a family of assumptions that were identified in Sections 6.2 through 6.4. Further research is needed to a) characterize the partitioning of blast induced energy between air and ground shock, and b) develop and validate by field experiments robust procedures to generate horizontal and vertical acceleration time series due to ground shock for common types of soils, clays and rock.

**Table 6.6. Arrival times for air blast and ground shock waves at Points D, E and F of Figure 6.5**

Loading type	Arrival time (msec)		
	Point D	Point E	Point F
Air blast	4	46	134
Ground shock	1.5	4.8	8.2





## CHAPTER 7

### SUMMARY AND CONCLUSIONS

#### 7.1 Introduction

The studies presented in this report assess the performance of sample conventional and base isolated NPP reactor buildings for seismic and blast loadings.

The sample conventional NPP reactor building is composed of containment and internal structures with a total weight of approximately 75,000 tons. A lumped-mass stick model of this reactor building, denoted as Model 1, was developed in the computer code SAP2000 Nonlinear. The first mode periods of the containment vessel and internal structures are 0.2 and 0.14 second, respectively. Numerical models for three base isolated reactor buildings, denoted as Models 2, 3 and 4, were also developed in SAP2000 Nonlinear by adding different link elements at the bottom of Model 1. The link elements in Models 2 through 4 represent Friction Pendulum™ (FP), lead rubber (LR) and low damping rubber (LDR) bearings, respectively, and have a second-slope stiffness (FP and LR) or elastic stiffness (LDR) associated with a period of 2 seconds. Model 4 also includes a representation of linear viscous dampers (LVD) to provide an added viscous damping ratio of 10% of critical.

The widely used Zion approach for NPP seismic probabilistic risk assessment uses fragility curves defined in terms of ground-motion parameters. A new procedure is proposed that builds on the methodology presented in the *draft ATC-58 Guidelines* and the Zion method. The new procedure improves the Zion method by using fragility curves defined using structural response parameters since damage and failure of NPP components are more closely tied to structural response parameters than to ground-motion parameters. The new performance assessment procedure was used to evaluate the vulnerability of the conventional (Model 1) and base isolated (Models 2, 3 and 4) NPP reactor buildings, each equipped with a small number of secondary systems installed at critical locations on the internal structure.

A key issue in the proposed procedure is the selection and scaling of ground motions for response-history analysis. A study was performed to help establish an optimal procedure for scaling ground motions for the purpose of seismic performance assessment. An optimal procedure for scaling earthquake ground motions should a) preserve the median and dispersion in the earthquake shaking for a given characterization of the hazard for the site of interest; b) address a wide range of periods, enabling losses to be computed for both

structural and nonstructural components; c) confidently estimate the distribution of seismic demand for nonlinear structural and nonstructural systems using as small a number of ground motions as possible; d) be appropriate for near-fault and far-field sites across the United States; and e) be applicable across a wide range of mean annual frequency of exceedance.

Although prior studies (e.g., Astrella and Whittaker 2004, Huang et al. 2007a) had shown that the implementation of base isolation substantially reduced demands on secondary systems (nonstructural components) in mission-critical infrastructure, no studies had been conducted to assess the impact of other natural and man-made hazards on base-isolated infrastructure. Two other hazards are tornado-borne missiles and detonation of improvised explosive devices. The impact of a tornado-borne missile on a containment vessel is a local loading with the primary concern being spalling or breach of the vessel; the implementation of base isolation will not change the vulnerability of the vessel. The detonation of a large mass of conventional high explosives could pose a threat to the global integrity of a base isolated containment vessel through air and ground shock loading. A study was performed to assess the vulnerability of conventional and isolated NPPs for an assumed threat. The methodology presented in the report could be used to assess vulnerability on a project-specific basis.

Sections 7.2, 7.3 and 7.4 present a summary and conclusions for a) the study for ground-motion scaling procedures, b) seismic performance assessments, and c) the blast assessment of the sample NPPs, respectively.

## **7.2 Scaling of Ground Motions**

### **7.2.1 Summary**

Five ground-motion scaling methods were investigated in this report using nonlinear single-degree of freedom models with yield strengths ranging from  $0.06W$  to infinity and periods ranging from 0.01 to 4 seconds; post-yield stiffness was set at 10% of the elastic stiffness. Two sets of 25 pairs of ground motions were used in the study: one set of near-fault motions and the other set of far-field motions.

The five methods of scaling ground motions investigated in the report were:

Method 1 amplitude scales the geometric mean of a pair of recorded ground motions by a single factor to minimize the sum of the squared errors between the target spectral values and the geometric mean of the spectral ordinates for the pair of motions.

Method 2 spectrally matches a single ground motion component to a target spectrum.

Method 3 involves the amplitude scaling of a single ground motion component to a specified value of spectral acceleration at the first mode period of the structural system.

Method 4 is termed the distribution scaling (D-scaling) method using spectrum-matched motions. The seismic hazard is characterized by period-dependent distributions of spectral acceleration across a wide range of periods. The distributions are either the results of a probabilistic seismic hazard analysis (facilitating the calculation of spectral demand at a user-defined annual frequency of exceedance) or computations using an attenuation relationship and a magnitude-distance pair. A series of spectral stripes are used to capture the distribution of the target spectral ordinates. One spectrally matched ground motion is generated for each stripe and used for response-history analysis.

Method 5, i.e., the D-scaling method using actual earthquake records, generates a series of target spectral ordinates at the first mode period of the structural system of interest using a distribution established from either probabilistic seismic hazard analysis at a user-defined annual frequency of exceedance or computations using an attenuation relationship and a magnitude-distance pair. One ground motion component is amplitude scaled to each of the target spectral ordinates.

Much of the recent discussion on scaling ground motions for shaking with very low annual frequencies of exceedance has centered on  $\epsilon$  and a conditional mean spectrum (Baker and Cornell 2005, 2006). A study was performed to investigate the impact of  $\epsilon$  on spectral shape using a) 25 pairs of NF and FF ground motions, and b) 147 pairs of near-fault ground motions from the NGA database.

### **7.2.2 Conclusions**

The key conclusions of the studies summarized in Section 7.2.1 are:

1. Method 1 preserves the irregular spectral shapes of recorded ground motion and some dispersion in the spectral demand. The shape of the median spectrum for a bin of ground motions scaled by this method is dominated by the pre-scaled shape of the median spectrum for the bin. If a wide range of periods must be addressed for analysis, and multiple magnitude-distance pairs dominate the uniform hazard spectrum at different periods across the range of interest, it will be difficult to select a bin of ground motions whose median spectrum closely matches the target spectrum.

2. Method 2 underestimates the median displacement demand in highly nonlinear systems and cannot capture the dispersion in the structural response because the scatter in the spectral ordinates is eliminated by the matching process. Earthquake ground motions that are spectrally matched to target median spectrum should not be used to characterize a distribution of seismic responses because the median displacement response will be underestimated for highly nonlinear systems and the dispersion in the displacement response will be underestimated by a wide margin for all systems, regardless of whether the response is linear or nonlinear.
3. Method 3 provides unbiased estimates of median responses of nonlinear systems and produces dispersions of the same order as or greater than those of Method 1 for nonlinear systems with ductility greater than 3 because the first mode period does not necessarily dictate the response of such systems. However, the method cannot capture the dispersion in response of elastic and near-elastic systems.
4. Method 4 underestimates median displacements in highly nonlinear systems because spectrally matched motions are used for analysis (identical to Method 2). The dispersion in response is captured well by Method 4, albeit conservatively biased in most cases. Modification factors for median responses and dispersions are derived as a function of ground motion type (near fault or far field), period and degree of inelastic response (measured herein by  $R$ ). Median and 84th percentile displacement responses are computed with high confidence if the correction factors are employed.
5. Method 5 produces unbiased estimates of median displacement responses but conservatively estimates the dispersions in the displacement responses.
6. Epsilon ( $\varepsilon$ ) has significant correlation with spectral shape and a conditional mean spectrum can reasonably represent the average spectral demand for a combination of  $M_w$ ,  $r$  and  $\varepsilon$ . For seismic hazard with very low annual frequencies of exceedance, selecting ground motions without considering  $\varepsilon$  may lead to a conservative estimates of performance.

### **7.3 Seismic Performance Assessment**

#### **7.3.1 Summary**

The proposed procedure for seismic performance assessment of NPPs can be used to perform three types of assessments: intensity-, scenario- and time-based assessments.

An intensity-based performance assessment estimates the probability of unacceptable performance, given that the NPP experiences a specific intensity of shaking. The ground shaking intensity can be represented by a Safe Shutdown Earthquake (SSE) response spectrum or other design spectra. A scenario-based performance assessment estimates the probability of unacceptable performance, given that a NPP experiences a specific earthquake, defined as a combination of earthquake magnitude and distance of the site from the fault on which the earthquake occurs. A time-based assessment estimates the annual frequency of unacceptable performance of a NPP, considering all potential earthquakes that may occur. A time-based assessment is performed as a series of intensity-based assessments with different target spectral intensities determined from a seismic hazard curve over a wide range of return period for ground motions.

The proposed procedure involves five steps. Step 1 is to perform plant-system and accident-sequence analysis for the target unacceptable performance, such as core melt and radiation release, and to develop component fragility curves using structural response parameters. Step 2 is to characterize earthquake shaking (see above). Step 3 is to perform nonlinear response-history analysis of models of the NPP for ground shaking consistent with the seismic hazard of Step 2. Step 4 is to assess the possible distribution of damage to structural and nonstructural components of the NPP using the component fragility curves of Step 1 and the response data of Step 3. Based on the damage distribution identified in Step 4 and the accident sequence determined in Step 1, Step 5 uses Monte Carlo procedures to determine the probability or annual frequency of unacceptable performance of the NPP for the seismic hazard of Step 2.

### **7.3.2 Conclusions**

In this report, an intensity-based assessment was performed for Model 1 and scenario- and time-based assessments were performed for Models 1 through 4 using the proposed procedure. The unacceptable performance was defined as the failure in any of the selected key secondary systems in the sample NPP. The key conclusions of these assessments are:

1. The proposed procedure enables the use of fragility curves defined using structural response parameters in the seismic performance assessment of NPPs. The procedure can be applied in a time-based assessment to evaluate the mean annual frequency of unacceptable performance of a NPP and also be used to assess the performance of a NPP subjected to an earthquake for a given intensity or scenario.

2. The use of base isolation greatly improves the seismic performance of the sample NPP reactor building. Model 1 has mean probabilities of unacceptable performance of 0.079 and 0.51 for the intensity- and scenario-based assessments, respectively, and a mean annual frequency of unacceptable performance of  $2.55 \times 10^{-5}$  for the time-based assessment. The probabilities of unacceptable performance for base isolated Models 2, 3 and 4 are each smaller than  $5.0 \times 10^{-6}$  for the scenario-based assessment and the mean annual frequencies of unacceptable performance for the three base isolated models are smaller than  $4.0 \times 10^{-9}$  for the time-based assessments.
3. The use of base isolation greatly reduces the seismic demand on the secondary systems. In the scenario-based assessment, the median seismic capacities of the secondary systems for the base isolated models could be reduced by at least 88% to achieve a probability of unacceptable performance equal to that for the conventional model. In the time-based assessment, the corresponding reduction is 69% to achieve an annual frequency of unacceptable performance equal to that for the conventional NPP. Although these percentages likely have little practical significance since the design of the secondary systems would be controlled by other demands, these results show the advantage of base isolation, namely, enabling a more economical design of secondary systems than in conventional NPPs.
4. The use of mean fragility curves for NPP components and a demand-parameter matrix of 1000+ row vectors can provide an unbiased estimate of the mean probability of unacceptable performance for the NPP with high confidence. The required number of row vectors in a demand-parameter matrix is a function of the required confidence level and the dispersion in the probability of unacceptable performance.

## **7.4 Blast Assessment**

### **7.4.1 Summary**

An assessment of the vulnerability of conventional and base isolated NPPs was performed for an assumed threat of 2000 kg of TNT explosive detonated on the surface with a closest distance to the reactor building of 10 m. Internal explosions were not considered because physical security systems should prevent the portage of large masses of explosive into a reactor building. (A 2000 kg weapon is similar in size to that which destroyed the Murrah Federal Building in 1995.) Both the air and ground shock waves produced by the design threat were generated and used for performance assessment. The complex loading environment for air blast was captured using the CFD code Air3D (Rose 2006) and a ground shock time series was

generated using information presented in Wu and Hao (2005). The air blast and ground shock loadings were analyzed separately for the response-history analysis of the sample reactor buildings because 1) the partition of the blast induced energy between air and ground shock is poorly understood and not documented in the literature, and 2) the existing models for soil/rock response to ground shock predict widely disparate results. Only the horizontal shaking effects of ground shock loading were considered.

Response-history analysis of the sample conventional (Model 1) and base isolated (Model 3) reactor buildings to external blast loadings was performed to identify the impact of the implementation of base isolation on the blast vulnerability of the NPP building. The vulnerability of the sample NPP buildings was assessed using a) global responses, including base shear force in the containment vessel, base shear force in the internal structure, and the drift of the containment vessel, and b) local responses, such as peak floor accelerations and floor spectral accelerations at selected points on the internal structure. The response-history analysis was performed using the hydrocode LS-DYNA (LSTC 2003). The key conclusions of this study are presented in the following subsection.

#### **7.4.2 Conclusions**

1. For air blast analysis, the base-isolated containment vessel had a smaller base shear and roof drift than the conventional containment vessel. The secondary systems attached to the internal structure in the conventional NPP were sheltered from the effects of air blast loading (in part because the base slab was assumed to be rigid and fixed to the subgrade). The secondary systems in the base isolated NPP experienced relatively low floor spectral demands and the probabilities of failure of these systems were extremely small.
2. Seismic isolation is an extremely effective strategy for protecting secondary systems against the effects of ground shock. The implementation of the isolators reduced the global and local responses by orders of magnitude.





## CHAPTER 8

### REFERENCES

- Aitchison, J., and Brown, J. A. C. (1957). *The lognormal distribution with special reference to its uses in economics*, Cambridge University Press, Cambridge.
- Abrahamson, N., and Silva, W. J. (1997). "Empirical response spectral attenuation relations for shallow crustal earthquakes." *Seismological research letters*, 68(1), 94-127.
- Abrahamson, N.A. (1998). "Non-stationary spectral matching program RSPMATCH." PG&E, Internal Report.
- Abrahamson, N. A., and Bommer, J. J. (2005). "Probability and uncertainty in seismic hazard analysis." *Earthquake Spectra*, 21(2), 603-607.
- ACI Committee 318. (2008). *Building code requirements for structural concrete (ACI 318-08) and commentary*, American Concrete Institute, Farmington Hills, Michigan.
- Aitchison, J., and Brown, J. A. C. (1957). *The lognormal distribution with special reference to its uses in economics*, Cambridge University Press, Cambridge.
- American Association of State Highway and Transportation Officials (AASHTO). (1999). "Guide specifications for seismic isolation design." American Association of State Highway and Transportation Officials, Washington, D.C.
- American Society of Civil Engineers (ASCE). (2005). "Seismic design criteria for structures, systems, and components in nuclear facilities." *ASCE/SEI 43-05*, American Society of Civil Engineers, Reston, Virginia.
- American Society of Civil Engineers (ASCE). (2006). "Minimum design loads for buildings and other structures." *ASCE/SEI 7-05*, American Society of Civil Engineers, Reston, Virginia.
- American Society of Civil Engineers (ASCE). (2007). "Seismic rehabilitation of existing buildings." *ASCE/SEI 41-06*, American Society of Civil Engineers, Reston, Virginia.
- Applied Technology Council (ATC). (1995). "A critical review of current approaches to earthquake-resistant design." *ATC-34*, Applied Technology Council, Redwood City, California.

- Applied Technology Council (ATC). (2007). "Guidelines for seismic performance assessment of buildings." *ATC-58 35% Draft*, Applied Technology Council, Redwood City, California.
- Astrella, M. J., and Whittaker, A. S. (2004). "Changing the paradigm for performance-based seismic design." *Proceedings*, International Workshop on Performance-Based Seismic Design, Bled, Slovenia.
- Baker, W. E., Cox, P. A., Westine, P. S., Kulesz, J. J., and Strehlow, R. A. (1983). *Explosion hazards and evaluation*, Elsevier Scientific Publishing Co., New York.
- Baker, J. W., and Cornell, C. A. (2005). "A vector-valued ground motion intensity measure consisting of spectral acceleration and epsilon." *Earthquake Engineering and Structural Dynamics*, 34(10), 1193-1217.
- Baker, J. W., and Cornell, C. A. (2006). "Spectral shape, epsilon and record selection." *Earthquake Engineering and Structural Dynamics*, 35(9), 1077-1095.
- Baker, J. W., and Jayaram, N. (2008). "Correlation of spectral acceleration values from NGA ground motions models," *Earthquake Spectra*, 24(1), 299-317.
- Barda, F., Hanson, J. M., and Corley, W. G. (1977). "Strength of low rise structural walls." *Reinforced Concrete Structures in Seismic Zones*, SP-53, American Concrete Institute, Farmington Hills, Michigan, 149-202.
- Benjamin, J. R., and Cornell, C. A. (1970). *Probability, statistics, and decision for civil engineers*, McGraw-Hill, Inc., New York.
- Boore, D. M., and Atkinson, G. M. (2008). "Ground-motion prediction equations for the average horizontal component of PGA, PGV, and 5%-Damped PSA at spectral periods between 0.01 s and 10.0 s." *Earthquake Spectra*, 24(1), 99-138.
- Brode, H. L. (1955). "Numerical solutions of spherical blast waves." *Journal of Applied Physics* 26(6), 766-775.
- Brode, H. L. (1956). "The blast wave in air resulting from a high temperature, high pressure sphere of air." *RM-1825-AEC*, Rand Corp., Santa Monica, California.
- Brode, H. L. (1957). "Theoretical solutions of spherical shock tube blasts." *RM-1974*, Rand Corp., Santa Monica, California.

- Buckle, I. G., Kelly, T. E., and Jones, L. R. (1987). "Basic concepts of seismic isolation and their application to nuclear structures." in *Seismic Engineering: Recent Advances in Design, Analysis, Testing and Qualification Methods*, American Society of Mechanical Engineers, PVP-Vol 127, 429-437.
- Carballo, J.E., and Cornell, C.A. (2000). "Probabilistic seismic demand analysis: spectrum matching and design." *Report No. RMS-41*, Department of Civil and Environmental Engineering, Stanford University.
- Campbell, K. W. (2003). "Prediction of strong ground motion using the hybrid empirical method and its use in the development of ground-motion (attenuation) relations in Eastern North America." *Bulletin of the Seismological Society of America*, 93, 1012-1033.
- Campbell, K. W., and Bozorgnia, Y. (2008). "NGA ground motion model for the geometric mean horizontal component of PGA, PGV, PGD and 5% damped linear elastic response spectra for periods ranging from 0.01 to 10 s." *Earthquake Spectra*, 24(1), 139-171.
- Chiou, B. S.-J., and Youngs, R. R. (2008). "A NGA model for the average horizontal component of peak ground motion and response spectra." *Earthquake Spectra*, 24(1), 173-215.
- Cornell, C. A. (2006). "Should uniform hazard spectra be used for design? How should design response spectra be determined considering uniform hazard spectra from design maps and hazard deaggregation data?" *Workshop Handouts*, Third ATC-35/USGS National Earthquake Ground-Motion Mapping Workshop, Applied Technology Council, San Mateo, California.
- Computers and Structures, Inc. (CSI). (2002). *SAP2000 user's manual – version 8.0*. Computers and Structures, Inc., Berkeley, California.
- Constantinou, M. C., Tsopeles, P., Kasalanati, A., and Wolff, E. D. (1999) "Property modification factors for seismic isolation bearings." *MCEER-99-0012*, Multidisciplinary Center for Earthquake Engineering Research, Buffalo, NY.
- Department of the Army (DoA). (1990). "Structures to resist the effects of accidental explosions." *Army TM 5-1300*, U.S. Department of the Army, Washington, D.C.

- Federal Emergency Management Agency (FEMA). (1997). "NEHRP recommended provisions for seismic regulations for new buildings and other structures." *FEMA 273 (Provisions) and 274 (Commentary)*, Federal Emergency Management Agency, Washington, D.C.
- Federal Emergency Management Agency (FEMA). (2000a). "Recommended seismic design criteria for new steel moment-frame buildings." *FEMA 350*, Federal Emergency Management Agency, Washington, D.C.
- Federal Emergency Management Agency (FEMA). (2000b). "Prestandard and commentary for the seismic rehabilitation of buildings." *FEMA 356*, Federal Emergency Management Agency, Washington, D.C.
- Federal Emergency Management Agency (FEMA). (2004). "NEHRP recommended provisions for seismic regulations for new buildings and other structures." *FEMA 450-1 (Provisions) and 450-2 (Commentary)*, Federal Emergency Management Agency, Washington, D.C.
- Federal Emergency Management Agency (FEMA). (2005). "Risk assessment: a how-to guide to mitigate potential terrorist attacks against buildings." *FEMA 452*, Federal Emergency Management Agency, Washington, D.C.
- Fenz, D. M. (2005). "Further development, testing and modeling of the axon seismic isolation system." *Master Thesis*, Department of Civil, Structural and Environmental Engineering, State University of New York, Buffalo, NY.
- Fenz, D. M., and Constantinou, M. C. (2008). "Spherical sliding isolation bearings with adaptive behavior: Theory." *Earthquake Engineering and Structural Dynamics*, 37(2), 163-183.
- Goulet, C. A., Watson-Lamprey, J., Baker, J., Haselton, C., and Luco, N. (2008). "Assessment of ground motion selection and modification (GMSM) methods for non-linear dynamic analyses of structures." Proceedings of the Fourth Geotechnical Earthquake Engineering and Soil Dynamics Conference, Sacramento, California.
- Gulec, C. K., Whittaker, A. S. and Stojadinovic, B. (2008). "Shear strength of squat rectangular reinforced concrete walls." *ACI Structural Journal*, 105(4), 488-497.
- Halldorsson, B. (2004). <<http://civil.eng.buffalo.edu/engseislab/products.htm>> Engineering Seismology Laboratory, State University of New York, Buffalo, New York.

- Halldorsson, B., and Papageorgiou, A. S. (2005). "Calibration of the specific barrier model to earthquakes of different tectonic regions." *Bulletin of the Seismological Society of America*, 93(3), 1099-1131.
- Halldorsson, B., and Papageorgiou, A. S. (2006). "Application of the specific barrier model to the simulation of earthquake strong ground motions." *Proceedings*, Eighth US National Conference on Earthquake Engineering, Earthquake Engineering Research Institute, San Francisco, California.
- Hamburger, R. O. (2003). "A vision of the ATC-58 Project, development of performance-based seismic guidelines." *Proceedings*, Programming Workshop on Performance-Based Design, Applied Technology Council, Redwood City, California.
- Harmsen, S. C. (2001). "Mean and modal  $\varepsilon$  in the deaggregation of probabilistic ground motion." *Bulletin of the Seismological Society of America*, 91(6), 1537-1552.
- Huang, Y.-N., Whittaker, A. S., and Constantinou, M. C. (2006). "Seismic demands on secondary systems in conventional and isolated nuclear power plants." *Proceedings*, Eighth US National Conference on Earthquake Engineering, Earthquake Engineering Research Institute, San Francisco, California.
- Huang, Y.-N., Whittaker, A. S., Constantinou, M. C. and Malushte S. (2007a). "Seismic demands on secondary systems in isolated nuclear power plants." *Earthquake Engineering and Structural Dynamics*, 36(12), 1741-1761.
- Huang, Y.-N., Whittaker, A. S., and Hamburger, R. O. (2007b). "Scaling earthquake ground motion records for performance-based assessment of buildings." *Proceedings*, 76th Annual Structural Engineers Association of California Convention, Lake Tahoe, California.
- Huang, Y.-N., Whittaker, A. S., and Hamburger, R. O. (2008a). "Linear analysis procedures for performance-based earthquake engineering." Paper in preparation, *Earthquake Spectra*.
- Huang, Y.-N., Whittaker, A., and Luco, N. (2008b). "Maximum spectral demands in the near-fault region." *Earthquake Spectra*, 24(1), 319-341.
- Hyde, D. W. (1993). "User's guide for microcomputer program CONWEP, application of TM5-855-1, fundamentals of protective design for conventional weapons." *Instruction Report SL-88-1*, Structures Laboratory, US Army Waterways Experiment Station, Vicksburg, Mississippi.

- Iervolino, I., and Cornell, C. A. (2005). "Record selection for nonlinear seismic analysis of structures." *Earthquake Spectra*, 21(3), 685-713.
- International Conference of Building Officials (ICBO). (1997). *Uniform Building Code*, Whittier, California.
- Kennedy, R. P., and K., R. M. (1984). "Seismic fragilities for nuclear power plant risk studies." *Nuclear Engineering and Design*, 79, 47-68.
- Kennedy, R. P., and Short, S. A. (1994). "Basis for seismic provisions of DOE-STD-1020." *UCRL-CR-111478*, U.S. Department of Energy, Washington, D.C.
- Kennedy, R. P. (1999). "Overview of Methods for Seismic PRA and Margin Analysis Including Recent Innovations." *Proceedings of the OECD-NEA Workshop on Seismic Risk*, Tokyo, Japan.
- Kingery, C. N., and Bulmash, G. (1984). "Air blast parameters from TNT spherical air burst and hemispherical surface burst." *ARBRL-TR-02555*, U. S. Army Ballistic Research Laboratory, Aberdeen Proving Ground, Maryland.
- Livermore Software Technology Corporation, Livermore (LSTC). (2003). *LS-DYNA keyword user's manual*, Livermore Software Technology Corporation, Livermore, California.
- Pickard, Lowe, and Garrick, Inc., and Westinghouse Electric Corporation, Fauske & Associates, Inc. (1981). "Zion Probabilistic Safety Study." prepared for Commonwealth Edison Company, Chicago.
- Reed, J. W., and Kennedy, R. P. (1994). "Methodology for developing seismic fragilities." *TR-103959*, Electric Power Research Institute.
- Ritzel, D. V., and Matthews, K. (1997). "An adjustable explosion-source model for CFD blast calculations." *Proceedings*, Twenty-First International Symposium on Shock Waves, Great Keppel Island, Australia.
- Ritzel, D. V. (2008). Personal communication to Andrew Whittaker.
- Rose, T. A. (2006). *A computational tool for airblast calculations -- Air3d version 9 users' guide*, Engineering Systems Department, Cranfield University, Shrivenham, United Kingdom.

- Taghavi, S., and Miranda, E. (2003). "Response assessment of nonstructural building elements." *PEER 2003/05*, Pacific Earthquake Engineering Research Center, Berkeley, California.
- McGuire, R. K. (1995). "Probabilistic seismic hazard analysis and design earthquakes: closing the loop." *Bulletin of the Seismological Society of America*, 85(5), 1275-1284.
- McGuire, R. K., Silva, W. J., and Costantino, C. J. (2001). "Technical basis for revision of regulatory guidance on design ground motions: hazard- and risk- consistent ground motion spectra guidelines." *NUREG/CR-6728*, U.S. Nuclear Regulatory Commission, Washington, D.C.
- McGuire, R. K. (2004). *Seismic hazard and risk analysis*, Earthquake Engineering Research Institute, Oakland, California.
- McGuire, R. K., Cornell, C. A., and Toro, G. R. (2005). "The case for using mean seismic hazard." *Earthquake Spectra*, 21(3), 879-886.
- Merrifield, R., and Wharton, R. (2000). "Measurement of the size, duration and thermal output of fireballs produced by a range of propellants." *Propellants, Explosives, Pyrotechnics*, 25(4), 179-185.
- National Institute of Building Sciences (NIBS). (1997). *Earthquake loss estimation technology – HAZUS; user's manual*. National Institute of Building Sciences, Washington, D.C.
- Saady, A. M. (2006). Personal communication.
- Shome, N., Cornell, C. A., Bazzurro, P., and Carballo, J. E. (1998). "Earthquakes, records, and nonlinear responses." *Earthquake Spectra*, 14(3), 469-500.
- Smith, P. D., Dong, R. G., Bernreuter, D. L., Bohn, M. P., Chuang, T. Y., Cummings, G. E., Johnson, J. J., Mensing, R. W., and Wells, J. E. (1981). "Seismic safety margins research program: phase 1 final report." *NUREG/CR 2015*, U.S. Nuclear Regulatory Commission, Washington, D.C.
- Smith, P. D., and Hetherington, H. J. (1994). *Blast and ballistic loading of structures*, Butterworth-Heinemann, Oxford, United Kingdom.
- Somerville, P., Smith, N., Punyamurthula, S., and Sun, J. (1997). "Development of ground motion time histories for phase 2 of the FEMA/SAC steel project." *Report SAC/BD-97/04*, SAC Joint Venture, Sacramento, California.

- Sturges, H. A. (1926). "The choice of a class interval." *Journal of the American Statistical Association*, 21, 65-66.
- Synge, A. J. (1980). "Ductility of squat shear walls." *Research Report 80-8*, Department of Civil Engineering, University of Canterbury, Christchurch, New Zealand.
- Thompson, A., Whittaker, A. S., Fenves, G. L., and Mahin, S. A. (2000). "Property modification factors for elastomeric bearings." *Proceedings*, Twelfth World Conference on Earthquake Engineering, Auckland, New Zealand.
- U.S. Atomic Energy Commission (USAEC). (1973). "Design response spectra for seismic design of nuclear power plants." *Regulatory Guide 1.60*, U.S. Atomic Energy Commission, Washington, D.C.
- U.S. Geological Survey (USGS). (2007). "Java ground motion parameter calculator - version 5.0.7." <<http://earthquake.usgs.gov/research/hazmaps/design/>>
- U.S. Geological Survey (USGS). (2008). "2002 Interactive Deaggregations." <<http://eqint.cr.usgs.gov/deaggint/2002/index.php>>
- U.S. Nuclear Regulatory Commission (USNRC). (1975). "Reactor safety study: an assessment of accident risks in U.S. commercial nuclear power plants." *NUREG 75/014*, U.S. Nuclear Regulatory Commission, Washington, D.C.
- U.S. Nuclear Regulatory Commission (USNRC). (1983). "PRA procedures guide." *NUREG/CR-2300*, U.S. Nuclear Regulatory Commission, Washington, D.C.
- U.S. Nuclear Regulatory Commission (USNRC). (1991a). "Individual plant examination of external events (IPEEE) for severe accident vulnerabilities." Generic Letter No. 88-20, Supplement 4, U.S. Nuclear Regulatory Commission, Washington, D.C.
- U.S. Nuclear Regulatory Commission (USNRC). (1991b). "Procedural and submittal guidance of individual plant examination of external events (IPEEE) for severe accident vulnerabilities." U.S. Nuclear Regulatory Commission, Washington, D.C.
- U.S. Nuclear Regulatory Commission (USNRC). (1997). "Identification and characterization of seismic sources and determination of safe shutdown earthquake ground motion." *Regulatory Guide 1.165*, U.S. Nuclear Regulatory Commission, Washington, D.C.



- U.S. Nuclear Regulatory Commission (USNRC). (2004). *NRC Regulations, Chapter 1, Title 10, Code of Federal Regulations*, U.S. Nuclear Regulatory Commission, Washington, D.C.
- Wallace, J. W. (2007). "Modeling issues for tall reinforced concrete core wall buildings." *The Structural Design of Tall and Special Buildings*, 16, 615-632.
- Westine, P. S. (1978). "Ground shock from the detonation of buried explosives." *Journal of Terramechanics*, 15(2), 69-79.
- Whittaker, A. S., Hamburger, R. O., and Huang, Y.-N. (2007). "Next-generation performance-based earthquake engineering." *Proceedings, First International Conference on Modern Design, Construction and Maintenance of Structures*, Hanoi, Vietnam.
- Wu, C., and Hao, H. (2005). "Modeling of simultaneous ground shock and airblast pressure on nearby structures from surface explosions." *International Journal of Impact Engineering*, 31(6), 699-717.
- Yang, T. Y. (2006). "Performance evaluation of innovative steel braces." *Ph.D. Dissertation*, University of California, Berkeley, Berkeley, California.
- Yang, T. Y., Moehle, J. P., Stojadinovic, B., and Der Kiureghian, A. (2006). "An application of PEER performance-based earthquake engineering methodology." *Proceedings, Eighth U.S. National Conference on Earthquake Engineering*, Earthquake Engineering Research Institute, San Francisco, California.



## APPENDIX A

### CHARACTERISTICS OF THE LOGNORMAL DISTRIBUTION

To illustrate the characteristics of the lognormal distribution, assume that  $Y$  is a lognormally distributed random variable, representing the peak seismic displacement of a 2-second oscillator. The distribution can be fully described with two parameters: the mean and standard deviation of the logarithm of  $Y$ ,  $m_{\ln Y}$  and  $\beta_Y$  ( $\sigma_{\ln Y}$ ), respectively. The mean of the logarithm of  $Y$ ,  $m_{\ln Y}$ , is equal to the logarithm of the median value of  $Y$ ,  $\ln \theta_Y$ . The median of  $Y$ ,  $\theta_Y$ , is more widely used than  $m_{\ln Y}$  because it is of the same scale as  $Y$ . The probability density function (pdf) of  $Y$  can be expressed by the following equation:

$$f_Y(y) = \begin{cases} \frac{1}{y\beta_Y\sqrt{2\pi}} \exp\left[-\frac{1}{2\beta_Y^2} \ln^2\left(\frac{y}{\theta_Y}\right)\right], & \text{for } y \geq 0 \\ 0, & \text{elsewhere} \end{cases} \quad (\text{A.1})$$

Figure A.1a and Figure A.1b present a sample lognormal probability density function (pdf) and probability (cumulative) distribution function (CDF) for  $Y$ , respectively. For the data of Figure A.1a and Figure A.1b,  $\theta_Y$  and  $\beta_Y$  are 0.69 m and 0.52, respectively. The 16th and 84th percentile values identified in the figure,  $y_{16th}$  and  $y_{84th}$ , represent the displacements corresponding to a 16% and an 84% probability of non-exceedance, respectively. Unlike the symmetric normal distribution, the pdf of the lognormal distribution is skewed: the median (i.e., 50th percentile, which is equivalent to the *mean* in a normal distribution) is smaller than the mean; the difference between  $y_{84th}$  and the median is greater than the difference between the median and  $y_{16th}$ ; and  $m_Y \pm \sigma_Y$  are no longer equivalent to  $y_{84th}$  and  $y_{16th}$  (as shown in Figure A.1a and Figure A.1b), where  $m_Y$  and  $\sigma_Y$  are the mean and standard deviation of  $Y$ .

Values of  $m_Y$  and  $\sigma_Y$  can be calculated from  $\theta_Y$  and  $\beta_Y$  as follows:

$$m_Y = \theta_Y \exp\left(\frac{\beta_Y^2}{2}\right) \quad (\text{A.2})$$

$$\sigma_Y^2 = m_Y^2 \left[ \exp(\beta_Y^2) - 1 \right] \quad (\text{A.3})$$

The dispersion  $\beta_Y$  is related to the coefficient of variation of  $Y$ ,  $\nu_Y$ , as

$$\beta_Y = \sqrt{\ln(v_Y^2 + 1)} \quad (\text{A.4})$$

The standard deviation  $\sigma_Y$  has the same scale as the underlying variable. For the lognormal distribution shown in Figure A.1b,  $\sigma_Y$  is 0.39 m, which is a little greater than one half of the difference in displacement between  $y_{84th}$  and  $y_{16th}$ : a relationship that changes with an increase in  $\beta_Y$ . The pdfs for lognormal distributions with the same median value (0.69 m) and four values of  $\beta_Y$  (0.2, 0.52, 1.0 and 2.1) are shown in Figure A.1c to illustrate the influence of  $\beta_Y$  on the shape of the lognormal distribution. For the (extreme) distribution with  $\beta_Y = 2.1$ ,  $m_Y$  is 6.26 m and  $\sigma_Y$  is 6.22 m; both values are greater than  $y_{84th}$  of 5.63 m. For small values of  $\beta_Y$ , the shape of the lognormal distribution approaches that of the normal distribution. For information, Figure A.1c presents the lognormal distribution for  $\theta_Y = 0.69$  m and  $\beta_Y = 0.2$  ( $m_Y = 0.7$  and  $\sigma_Y = 0.139$ ) and the normal distribution defined by the same mean and standard deviation, namely,  $m_Y = 0.7$  and  $\sigma_Y = 0.139$ .

In this report, values of  $\theta$  and  $\beta$  for peak seismic responses (acceleration or displacement)  $Y$ , computed from response-history analysis using  $n$  ground motions, were computed as follows:

$$\theta_Y = \exp\left(\frac{1}{n} \sum_{i=1}^n \ln y_i\right) \quad (\text{A.5})$$

$$\beta_Y = \sqrt{\frac{1}{n-1} \sum_{i=1}^n (\ln y_i - \ln \theta_Y)^2} \quad (\text{A.6})$$

where  $y_i$  is the peak displacement for the analysis subjected to the  $i^{\text{th}}$  ground motion. The 16th and 84th percentiles of  $Y$  can then be calculated using

$$y_{16th} = \theta_Y \cdot e^{-\beta_Y} \quad (\text{A.7})$$

$$y_{84th} = \theta_Y \cdot e^{\beta_Y} \quad (\text{A.8})$$

Note that  $\ln y_{16th}$  and  $\ln y_{84th}$  are equal to  $\ln \theta_Y \pm \beta_Y$  (i.e.,  $m_{\ln Y} \pm \sigma_{\ln Y}$ ) because  $\ln Y$  is normally distributed.

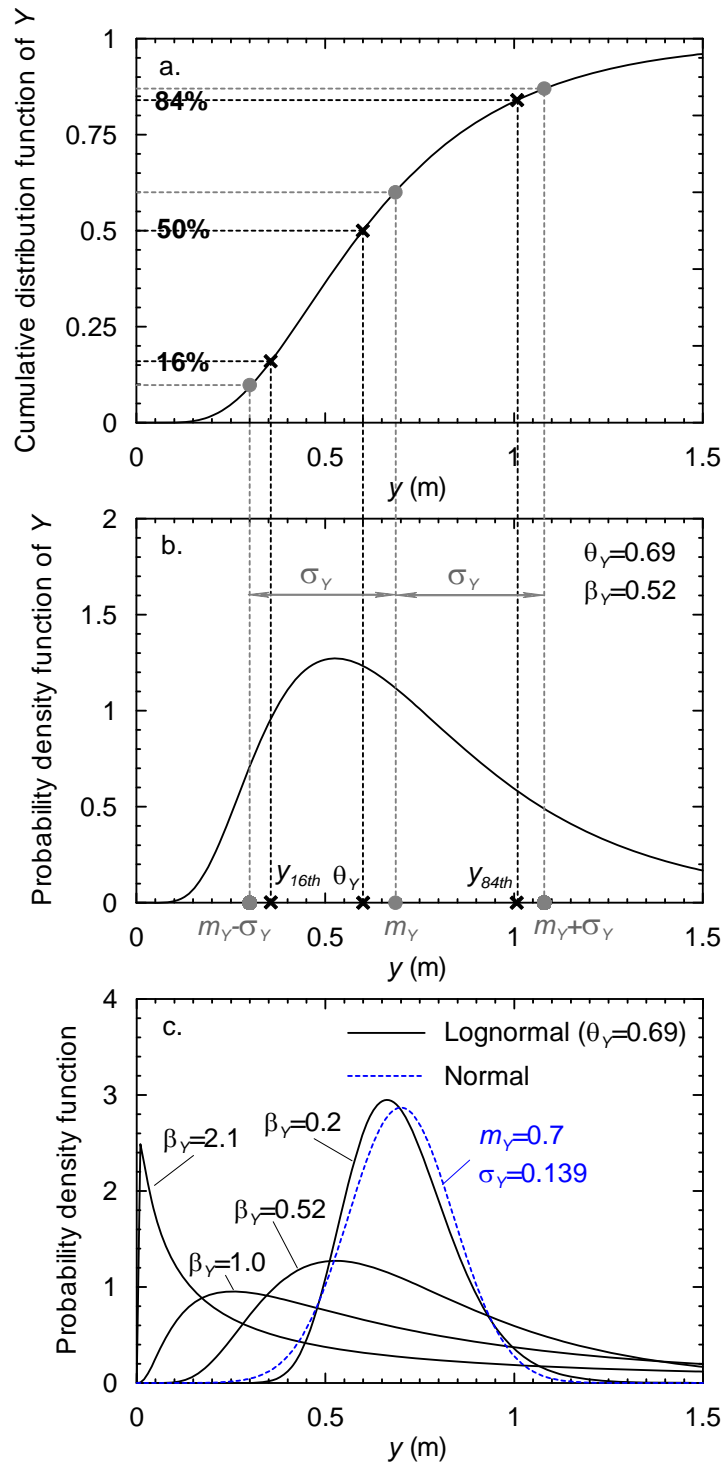


Figure A.1. Characteristics of a lognormal distribution



## APPENDIX B

### CORRELATED VECTORS FOR PERFORMANCE ASSESSMENT

#### B.1 Introduction

The procedure of performance assessment described in Section 3.3.3.5 of this report requires a large set (100s) of simulations so that the probability of the unacceptable performance can be estimated with high confidence. However, it is time-consuming to perform such a large number of response-history analyses. To address this issue, an algorithm was developed by Yang (2006) for the Pacific Earthquake Engineering Research (PEER) Center and is used in the *draft ATC-58 Guidelines*. In the algorithm, statistical relationships between the demand parameters developed using a small number (11 minimum) response-history analyses are manipulated to generate a family of 200+ statistically consistent vectors of demands to enable performance assessment using Monte Carlo methods.

The algorithm is described below and used in Chapter 5 to generate a large number of correlated vectors of demand parameters for Monte Carlo analysis. Section B.2 summarizes the algorithm. The algorithm is extended herein to accommodate uncertainty in structural modeling, which is discussed in Chapter 3 and Appendix F. Section B.3 presents the Matlab code used in this report.

#### B.2 Algorithm

For the purpose of illustrating the proposed performance assessment procedure and as implemented in the *draft ATC-58 Guidelines*, 11 response-history analyses are performed for each intensity of earthquake shaking. For each simulation, the peak absolute value of each demand parameter (e.g., floor spectral acceleration) is assembled into a  $1 \times n$  row vector, where  $n$  is the number of demand parameters. The 11 row vectors are catenated to form an  $11 \times n$  matrix (rows  $\times$  columns; simulations  $\times$  demand parameters). Each column presents 11 values of one demand parameter. The goal of the algorithm presented herein is to generate a  $200 \times n$  matrix, for which the mean vector and covariance matrix are equal to that of the  $11 \times n$  matrix developed from response-history analysis.

The  $11 \times n$  matrix of demand parameters generated using response-history analyses is denoted as  $\mathbf{X}$  herein. The entries in  $\mathbf{X}$  are assumed to be jointly lognormal. The natural logarithm of each entry in  $\mathbf{X}$  is computed to form an  $11 \times n$  matrix  $\mathbf{Y}$ . The entries in  $\mathbf{Y}$  are jointly normal and can be characterized by a

$1 \times n$  mean vector,  $\mathbf{M}_Y$ , a  $n \times n$  correlation coefficient matrix,  $\mathbf{R}_{YY}$ , and a  $n \times n$  diagonal matrix of standard deviations,  $\mathbf{D}_Y$ .

A  $200 \times n$  matrix of demand parameters,  $\mathbf{Z}$ , can be generated using the following equations:

$$\mathbf{Z}_i = [\mathbf{D}_Y \mathbf{L}_Y \mathbf{U}_i]^T + \mathbf{M}_Y \quad i = 1, 200 \quad (\text{B.1})$$

$$\mathbf{Z} = \begin{bmatrix} \mathbf{Z}_1 \\ \mathbf{Z}_2 \\ \vdots \\ \mathbf{Z}_{200} \end{bmatrix} \quad (\text{B.2})$$

where the matrix  $\mathbf{L}_Y$  is the transposed Cholesky decomposition<sup>1</sup> of  $\mathbf{R}_{YY}$ ;  $\mathbf{U}_i$  is a  $n \times 1$  vector with each element representing a normal distribution with a mean of 0 and a standard deviation of 1.0; and all other terms are defined above. Yang (2006) shows that  $\mathbf{Z}$  has the same statistical distribution as  $\mathbf{Y}$ .

The procedure used to generate the  $200 \times n$  matrix of demand parameters is summarized below. Steps 1, 3, 4, 6, 7 and 8 are from Yang. Steps 2 and 5 are proposed to address uncertainty in the structural models used for analysis.

1. Generate  $\mathbf{X}$  using the results of response-history analyses.
2. Input a value for the uncertainty in the structural model,  $\beta_m$ .
3. Take the natural logarithm of every entry in  $\mathbf{X}$  to form  $\mathbf{Y}$ .
4. Compute  $\mathbf{M}_Y$ ,  $\mathbf{D}_Y$  and  $\mathbf{L}_Y$  by sampling the  $11 \times n$  matrix,  $\mathbf{Y}$ .
5. Update each entry in  $\mathbf{D}_Y$ , as  $\mathbf{D}_{ii} = \sqrt{\mathbf{D}_{ii}^2 + \beta_m^2}$
6. Populate  $\mathbf{U}_i$  by random sampling each entry from a normal distribution with a mean of 0 and a standard deviation of 1.0.
7. Compute  $\mathbf{Z}$  per (B.1) and (B.2).

---

<sup>1</sup> If matrix  $\mathbf{K}$  is symmetric and positive-definite (e.g., a stiffness matrix), it can be decomposed into a lower triangular matrix,  $\mathbf{L}$ , the Cholesky triangle, and the transpose of the lower triangular matrix, such that  $\mathbf{K} = \mathbf{L}\mathbf{L}^T$ .



8. Take the exponential of every entry in  $\mathbf{Z}$  to form the  $200 \times n$  matrix of demand parameters.

The procedure of Yang is illustrated in Figure B.1; steps 2 and 5 are not shown.

### B.3 Matlab Code

The Matlab code presented in Table B.1 was used to generate correlated vectors of demand parameters, such as those shown in Figure 5.13. The file “DP.txt” used in the Matlab code includes the  $11 \times n$  matrix of demand parameters established using response-history analyses, such as that shown in Table 5.4, with one demand parameter per column and one simulation per row; the file “beta\_m.txt” includes the value for  $\beta_m$ ; and the file “n\_rows.txt” includes the number of the generated row vectors. For the algorithm presented in Section B.2, the value included in the file “n\_rows.txt”, that is, the number of the generated row vectors, should be 200.

**Table B.1. A Matlab code for generating correlated vectors of demand parameters**

```
% Develop underlying statistics of the response-history analysis
X=load('DP.txt');
Bm=load('beta_m.txt'); % modeling uncertainty
nr= load('n_rows.txt'); % number of the generated row vectors

Y=log(X);
My=(mean(Y))';
n=length(My);
Dy=diag(std(Y));
Dy=sqrt(Bm*Bm*eye(n)+Dy*Dy); % update Dy to include modeling uncertainty
Ryy=corrcoef(Y);
Ly=(chol(Ryy))';

% Generate correlated demand vectors using a Monte-Carlo technique
U=[];
for i=1:n
    U1=randn(nr,1);
    U=[U U1];
end

My=diag(My)*ones(n,nr);
Z=Dy*Ly*U'+My;
W=exp(Z');
```

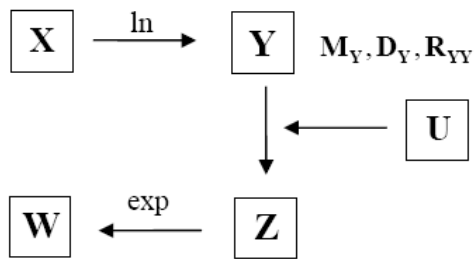


**Figure B.1. Generation of vectors of correlated demand parameters (Yang 2006)**

# APPENDIX C

## NUMBER OF GROUND MOTION RECORDS FOR INTENSITY-BASED ASSESSMENT

### C.1 Introduction

A procedure for scaling ground motions for an intensity-based assessment is to amplitude-scale a minimum of 11 recorded ground motions to a specified spectral acceleration at the first mode period of the building model,  $S_a(T_1)$ <sup>1</sup>. This scaling procedure is intended to bound the *median* displacement response with high confidence. No information is provided on the dispersion in the displacement response.

This appendix describes the technical basis for the use of 11 ground motions in the intensity-based assessment. The number of ground motions used in a response-history analysis ( $n$ ) is a function of the required accuracy of the estimate of the response (e.g.,  $1 \pm X$  of the *true* value) and the required confidence in the estimate (e.g.,  $Z\%$ ). Both  $X$  and  $Z$  are related to the dispersion,  $\beta_Y$ , in the displacement response given the scaling procedure. A relationship between  $n$ ,  $X$ ,  $Z$  and  $\beta_Y$  is derived in Section C.2. The values of  $X$ ,  $Z$  and  $\beta_Y$  used to determine  $n$  for intensity-based assessments is described in Section C.3.

### C.2 The Relationship Between $n$ , $X$ , $Z$ and $\beta_Y$

For a lognormally distributed random variable  $Y$  with a *true* median  $\theta_Y$  and *true* logarithmic standard deviation  $\beta_Y$ , the sample median can be estimated by

---

<sup>1</sup> This procedure has been adopted in the *draft ATC-58 Guidelines* for scaling ground motions for intensity-based assessment.

$$\hat{\Theta}_Y = \exp\left(\frac{1}{n} \sum_{i=1}^n \ln y_i\right) \quad (\text{C.1})$$

where  $y_i$  is a sample value for  $Y$  and  $n$  is the number of sample values used in the estimation. Assume that the natural logarithm of the estimator,  $\ln \hat{\Theta}_Y$ , is normally distributed; the mean and standard deviation of  $\ln \hat{\Theta}_Y$  (Aitchison and Brown 1957; Benjamin and Cornell 1970) are

$$E[\ln \hat{\Theta}_Y] = \ln \theta_Y \quad (\text{C.2})$$

$$\sigma[\ln \hat{\Theta}_Y] = \frac{\beta_Y}{\sqrt{n}} \quad (\text{C.3})$$

A standardized normal random variable  $U$  is defined by (C.4):

$$U[\ln \hat{\Theta}_Y] = \frac{\ln \hat{\Theta}_Y - \ln \theta_Y}{\beta_Y / \sqrt{n}} \quad (\text{C.4})$$

The distribution of  $U$  is shown in Figure C.1.

To estimate the median value within a range of  $\theta_Y(1 \pm X)$  with  $Z\%$  confidence:

$$U[\ln((1+X)\theta_Y)] = \Phi^{-1}\left(1 - \frac{\alpha}{2}\right) \quad (\text{C.5})$$

where  $\Phi^{-1}$  is the inverse standardized normal distribution function and  $\alpha = 1 - Z\%$ . Figure C.1 illustrates the calculation. Substituting (C.5) into (C.4) gives

$$\frac{\ln(1+X)}{\beta_Y / \sqrt{n}} = \Phi^{-1}\left(1 - \frac{\alpha}{2}\right) \quad (\text{C.6})$$

The number  $n$  is computed as

$$n = \left( \frac{\Phi^{-1}\left(1 - \frac{\alpha}{2}\right) \cdot \beta_Y}{\ln(1+X)} \right)^2 \quad (\text{C.7})$$

The first order term in the Taylor series of  $\ln(1+X)$  can be used to approximate  $\ln(1+X)$  in (C.7) when  $X$  is small and

$$n \approx \left( \frac{\Phi^{-1}\left(1 - \frac{\alpha}{2}\right) \cdot \beta_Y}{X} \right)^2 \quad (\text{C.8})$$

For  $Z = 95$  (approximately  $2\sigma$  in a normal distribution),  $\Phi^{-1}\left(1 - \frac{0.025}{2}\right) \approx 2$  and (C.8) yields the formula presented in Shome et al. (1998),

$$n = \frac{4\beta_Y^2}{X^2} \quad (\text{C.9})$$

Table C.1 provides sample values for  $\beta_Y$ ,  $Z$ ,  $X$  and  $n$  computed using (C.7).

### C.3 Numbers of Ground Motions for Intensity-Based Assessment

As shown in (C.7), the number  $n$  is a function of  $X$ ,  $Z$  and  $\beta_Y$ . For the intensity-based assessment described in Section C.1,  $\beta_Y$  is the dispersion in the displacement response resulting from analysis using ground motions scaled to a selected spectral acceleration at the first mode period.

Huang et al. (2008a) performed a series of nonlinear response-history analyses using 9 buildings of varying construction with first mode periods ranging between 0.2 and 2.5 seconds. One product of this study was an estimate of predicted dispersion in drift and acceleration response. The one hundred ground motion records listed in Tables 4.1 and 4.2 were scaled using the procedure described in Section C.1 and used for response-history analysis of the 9 buildings. The dispersion in displacement and acceleration responses computed by the analysis varied between 0.03 and 0.52, depending on period and extent of nonlinearity.

For  $X = 0.2$ ,  $Z = 75$ , and  $\beta = 0.52$ , the value of  $n$  per (C.7) is  $11^2$ . The use of more than 11 motions will improve the estimate of the median drift and acceleration responses whereas the use of fewer motions will result in poorer estimates.

---

<sup>2</sup> This calculation is the technical basis for determining the number of ground motions for intensity-based assessment in the *draft ATC-58 Guidelines*. The choice of  $X = 0.2$  and  $Z = 75$  was made by members of the ATC-58 Project Management Committee.

**Table C.1. Sample values for  $\beta_Y$ ,  $Z$ ,  $X$  and  $n$  per (C.7)**

$\beta_Y$	$Z$	$X$	$n$
0.5	75	0.1, 0.2, 0.3	36, 10, 5
	85	0.1, 0.2, 0.3	57, 16, 8
	95	0.1, 0.2, 0.3	106, 29, 14
0.55	75	0.1, 0.2, 0.3	44, 12, 6
	85	0.1, 0.2, 0.3	69, 19, 9
	95	0.1, 0.2, 0.3	128, 35, 17
0.6	75	0.1, 0.2, 0.3	52, 14, 7
	85	0.1, 0.2, 0.3	82, 22, 11
	95	0.1, 0.2, 0.3	152, 42, 20
0.65	75	0.1, 0.2, 0.3	62, 17, 8
	85	0.1, 0.2, 0.3	96, 26, 13
	95	0.1, 0.2, 0.3	179, 49, 24

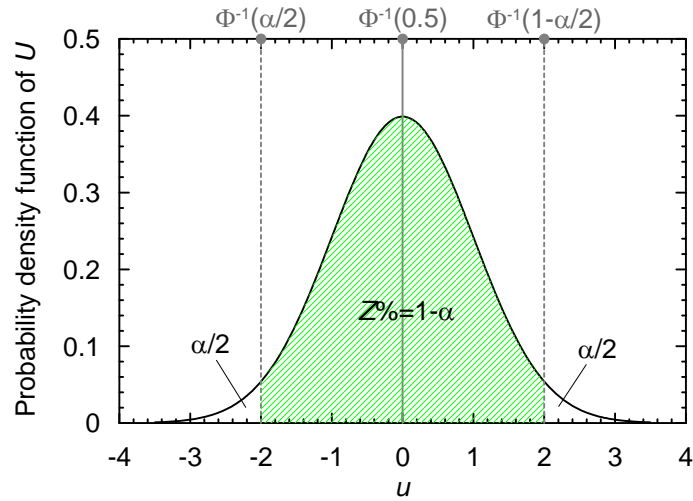


**Figure C.1. A standardized normal distribution**

## APPENDIX D

### EPSILON AND SPECTRAL SHAPE OF 147 NEAR-FAULT RECORDS

#### D.1 Near-fault Ground Motion Dataset

A near-fault ground-motion dataset is used in this appendix to study issues related to spectral shape and selection and scaling of earthquake ground motions. The dataset is a subset of that described in the PEER Next Generation Attenuation (NGA) Database Flatfile (see [http://peer.berkeley.edu/products/rep\\_nga\\_models.html](http://peer.berkeley.edu/products/rep_nga_models.html)). Each pair of time series in the Flatfile was rotated to be Strike-Normal (SN) and Strike-Parallel (SP) to the causative fault by members of the NGA project team. The dataset includes 147 pairs of ground motions from earthquakes with moment magnitude ( $M_w$ ) of 6.5 and greater, and with closest distance from the recording site to the ruptured area ( $r$ ) of 15 km and less. The 147 pairs of ground motions in the dataset are listed in Table D.1 together with the corresponding  $M_w$ ,  $r$  and average shear wave velocity in the top 30 meters ( $V_{s30}$ ).

#### D.2 Epsilon ( $\varepsilon$ ) and Spectral Shape for All Records in the Dataset

Table D.2 presents the values of  $\varepsilon$  at periods of 0.2, 0.5, 1, 2 and 4 seconds and the spectral-shape types per Table 4.8 for period bins P1 through P5 as defined in Table 4.7, for all records in Table D.1. The procedure used to develop the results of Table D.2 is the same as that used to develop Tables 4.4 and 4.5. Table D.3 presents the number of ground motions in each  $\varepsilon$  bin defined in the table at each period of interest; there are 294 ( $147 \times 2$ ) entries at each period. For a given period, the  $\varepsilon$  distributes approximately normally. Figure D.1 shows the results of a goodness-of-fit test for the distribution of  $\varepsilon$ . For a given period, the 294 sample values of  $\varepsilon$  shown in Table D.2 were sorted from smallest to largest and assigned a probability from 0.0034 ( $= 1/294$ ) to 1.00 in increments of 0.0034 for each of the sample values. This Cumulative Distribution Function (CDF) for the 294 sample values was then compared with that of a normal distribution with mean and standard deviation identified from the 294 sample values. Panels a through e of Figure D.1 present the results for 0.2, 0.5, 1, 2 and 4 seconds, respectively. The figures show that the normal distribution fits the distribution of  $\varepsilon$ . Figure D.1 also shows the values of mean and standard deviation identified from the sample data for each period. The values of the five standard deviations are very close to 1.0 and the mean values for 1, 2 and 3 seconds are approximately equal to zero. The mean values shown in Figure D.1 for periods of 0.2 and 0.5 second are smaller than zero, which means that the NGA relationships estimate conservatively biased spectral demands for the

ground motions of Table D.1 at 0.2 and 0.5 second: an observation similar to that reported by Huang et al. (2008b).

Table D.4 identifies the number of ground motions for each type of spectral shape in each period bin for a total of 294 entries per shape. The trend in Table D.4 is similar to that of Table 4.9, namely, the spectral shapes for most records are Type 2 for period bins P3, P4 and P5 because spectral acceleration tends to decrease with increasing period beyond 1 second.

The data presented in these tables are used below to evaluate the observations of Baker and Cornell (2005) who noted that 1) a positive value of  $\varepsilon$  tends to indicate a peak in spectral demand, 2) a negative value of  $\varepsilon$  tends to indicate a valley in spectral demand; and 3) if ground motions are scaled to a given value of spectral acceleration at a given period ( $Sa(T_1)$ ), records with a positive value of  $\varepsilon$  at the period produce systematically smaller displacement demands in linear and nonlinear multiple degree of freedom (MDOF) systems than records with a negative value of  $\varepsilon$ .

Twenty bins of ground motions from Table D.3, namely, the four  $\varepsilon$  bins of (2, 1), (1, 0), (0, -1) and (-1, -2) and five periods (0.2, 0.5, 1, 2 and 4 seconds) were used to study the observations of Baker and Cornell. Each ground motion in a given bin (e.g., 92 motions in the  $1 > \varepsilon \geq 0$ , 0.5-second bin) was amplitude-scaled to a spectral ordinate of 1 g at the period associated with the bin. The geometric mean of the spectral acceleration for all scaled ground motions in the bin was then computed (the square root of the product of the spectral acceleration for each record in the bin) and results are presented in Figure D.2. Note that the ordinates of the geometric-mean spectrum (hereafter termed a geomean spectrum) will be equal to those of the median spectrum if the spectral accelerations for a set of ground motions at a period distribute lognormally.

The results presented in Figure D.2 clearly show the impact of  $\varepsilon$  on spectral shape. Consider first the results for a period of 0.5 second presented in panel b. The ( $2 > \varepsilon \geq 1$ ) geomean spectrum peaks at 0.5 second but the other spectra do not. A relative<sup>1</sup> valley is seen for the ( $-1 > \varepsilon \geq -2$ ) geomean spectrum. Relative peaks and valleys are seen in Figure D.2c, Figure D.2d and Figure D.2e for the ( $2 > \varepsilon \geq 1$ ) and  $-1 > \varepsilon \geq -2$  geomean spectra, respectively. It is clear from the panels of Figure D.2 and the observed large differences in the geomean spectra as a function of  $\varepsilon$ , that spectral shape and  $\varepsilon$  should be

---

<sup>1</sup> Herein, *relative* peak and *relative* valley are defined with respect to adjacent spectral ordinates after correction for the average slope in the vicinity of the period in question.



important considerations in the selection and scaling of earthquake ground motions: the scaling of negative  $\varepsilon$  motions to positive  $\varepsilon$  spectral demands will result in conservative (over) predictions of response. The influence of magnitude and distance on the difference in spectral shape is not addressed here and is the subject of current study.

Baker and Cornell (2005) characterized spectral shape using the Conditional Mean Spectrum (CMS) as described in Section 4.2.4. Figure D.3a shows the spectral demands computed using the Chiou-Youngs NGA relationship (Chiou and Youngs 2006) for  $M_w$  6.8,  $r$  equal to 1.6 km and  $\varepsilon$  of 0 and 1.5, and a CMS conditioned to the spectral ordinate of the dotted line ( $\varepsilon = 1.5$ ) at a period of 1 second. The CMS was computed using the exponential of (4.2), which is reproduced below:

$$\mu_{\ln Sa(T_2) | \ln Sa(T_1) = \ln Sa(T_1)^*} = \mu_{\ln Sa}(\bar{M}, \bar{r}, T_2) + \sigma_{\ln Sa}(\bar{M}, T_2) \rho_{\ln Sa(T_1), \ln Sa(T_2)} \cdot \bar{\varepsilon}(T_1) \quad (D.1)$$

where all variables were defined in Chapter 4. For computing the CMS shown in Figure D.3a,  $\mu_{\ln Sa}$  and  $\sigma_{\ln Sa}$  were computed again using the Chiou-Youngs NGA relationship; the value of  $\bar{\varepsilon}(T_1)$  is 1.5; and  $\rho_{\ln Sa(T_1), \ln Sa(T_2)}$  was computed using the correlation-coefficient model of Baker and Jayaram (2008). If  $\rho_{\ln Sa(T_1), \ln Sa(T_2)}$  in (D.1) is zero, that is, the value of  $\varepsilon$  at a given period  $T_2$  is uncorrelated with that at  $T_1$  (1 second herein), the CMS in Figure D.3a will become the solid line ( $\varepsilon = 0$ ). If  $\rho_{\ln Sa(T_1), \ln Sa(T_2)}$  is 1, that is, the value of  $\varepsilon$  at a given period is linearly dependent on the value at 1 second, the CMS will become the dotted line ( $\varepsilon = 1.5$ ). Figure D.4 presents the values of  $\rho_{\ln Sa(T_1), \ln Sa(T_2)}$  used to compute the CMS in Figure D.3a. Since the CMS is scaled to a given spectral acceleration at a period of 1 second, the value of the correlation coefficient is 1.0 at 1 second and is smaller than 1.0 at other periods. The variation of correlation coefficient with period shown in Figure D.4 forces the ordinates of the CMS of Figure D.3a below the dotted line at all periods other than 1 second trending towards those of the solid line and produces a relative peak at 1 second. The analysis of Figure D.3a was repeated for  $\varepsilon = -1.5$  and results are presented in Figure D.3b. The CMS is scaled to the dotted line ( $\varepsilon = -1.5$ ) at a period of 1 second. For periods other than 1 second, the correlation coefficient is smaller than 1 and the ordinates of the CMS are greater than that of the dotted line and trend towards the solid line ( $\varepsilon = 0$ ): a negative value of  $\varepsilon$  tends to indicate a relative valley in the spectrum at 1 second. The trends predicted by the use of the Baker and Cornell CMS are supported by the ground motion data presented in Figure D.2.

### D.3 An Example of Selecting Ground Motions Using $M_w$ , $r$ and $\varepsilon$

A study was performed to identify the differences between a Uniform Hazard Spectrum (UHS) and a CMS and to reflect on procedures for selecting and scaling ground motions based on  $M_w$ ,  $r$  and  $\varepsilon$ . The study uses 3 families of three spectra generated for a sample Site Class B site in the San Francisco Bay Area at longitude 122.2°W and latitude 37.8°N. The three spectra are

1. Spectrum 1: Uniform Hazard Spectrum
2. Spectrum 2: Conditional Mean Spectrum scaled to the UHS (Spectrum 1) at a period of 1 second.
3. Spectrum 3: The geometric-mean spectrum of a set of records selected from Table D.1 considering the  $M_w$ ,  $r$  and  $\varepsilon$  governing the UHS of Spectrum 1 at a period of 1 second; all selected records were scaled to the spectral ordinate of the UHS at a period of 1 second.

The three spectra were generated for each of three earthquake shaking return periods: 2475, 475 and 108 years, which correspond to a 2% probability of exceedance (PE) in 50 years, 10% PE in 50 years and 50% PE in 75 years, respectively. Results are presented in Figure D.5a, Figure D.5b and Figure D.5c for the return periods of 2475, 475 and 108 years, respectively.

The UHS of Spectrum 1 presented in Figure D.5a and Figure D.5b were generated using the USGS ground-motion calculator (USGS 2007). The USGS ground-motion calculator does not provide values for a return period of 108 years. The UHS presented in Figure D.5c was obtained through the USGS website using the 2002 Deaggregation Data (<http://eqint.cr.usgs.gov/deaggint/2002/index.php>), where information is available at periods of 0, 0.2 and 1 seconds.

The CMS was computed using (D.1), where  $\mu_{\ln Sa}$ ,  $\sigma_{\ln Sa}$  and  $\varepsilon$  were computed using the Chiou-Youngs NGA relationship and  $\rho_{\ln Sa(T_1), \ln Sa(T_2)}$  was computed using the correlation-coefficient model by Baker and Jayaram. The correlation coefficients used for the computations of Figure D.5 are the same as those presented in Figure D.4. The CMS computation requires values of mean magnitude and distance ( $\bar{M}$  and  $\bar{r}$ ) for the seismic hazard of interest, which can be identified using the hazard deaggregation. Figure D.6, Figure D.7 and Figure D.8 present the USGS deaggregation results at a period of 1-second for return periods of 2475, 475 and 108 years, respectively. Table D.5 summarizes the values of  $\bar{M}$  and  $\bar{r}$  identified from Figure D.6, Figure D.7 and Figure D.8, the UHS spectral ordinates computed using the USGS ground-motion calculator and the corresponding  $\varepsilon$  at a period of 1 second calculated using the

Chiou-Youngs NGA relationship and the values of  $\bar{M}$  and  $\bar{r}$  shown in Table D.5 for the three return periods. The UHS spectral ordinates reported by the USGS ground-motion calculator are different from those shown in Figure D.6 through Figure D.8. However, the differences are small and ignored here. The values of  $\varepsilon$  shown in Table D.5 are different from those shown in Figure D.6 through Figure D.8 because those reported in the figures were based on the results of PSHA using several pre-2002 attenuation models and the tabulated values were computed using the Chiou-Youngs NGA model. Since the values of  $\varepsilon$  shown in Table D.2 were computed using NGA relationships, the values of  $\varepsilon$  shown in Table D.5 were used to compute CMS, instead of the values identified from the deaggregation results.

Four bins of ground motions are listed in Table D.6, where Bin D1 and Bin D2 were used to compute the geometric-mean spectra (Spectrum 3) presented in Figure D.5a and Figure D.5b, respectively, and Bin D3 and D4 were used to compute Spectrum 3 presented in Figure D.5c. The ground motions in each bin of Table D.6 were selected from the ground motion dataset of Table D.1 using the ranges of  $M_w$  and  $\varepsilon$  shown in Table D.6, which were determined based on the values of  $\bar{M}$  and  $\varepsilon$  shown in Table D.5 for the corresponding return period. No limitation on the value of distance was used for the selection of ground motions because a) all records in the dataset of Table D.1 have site-to-source distances smaller than 15 km and b) if narrow ranges are applied on all three parameters during the selection process, the number of ground motions in each bin will be too small to deliver reasonable results. The ranges of  $r$  shown in Table D.6 were identified after the ground motions for each bin had been selected. Bin D3 and Bin D4 have different ranges of  $M_w$  and  $r$ . The lower bounds on  $M_w$  and  $r$  for Bin D3 are 6.7 and 3 km, respectively, and those for Bin D4 are 6.6 and 7 km, respectively. Bin D4 was established to study the sensitivity of spectral shape on the ranges of the parameters used to select ground motions. The key observations are:

- a. For return periods of 2475 and 475 years, the spectral demand of the UHS is greater than that of the CMS at periods other than 1 second. In Figure D.5a, the ratio of the spectral ordinate of the UHS to that of the CMS at a period of 0.2 second is 1.62; in Figure D.5b, the ratio is 1.29. For the return period of 108 years (Figure D.5c), the spectral demand of the CMS is similar to that of the UHS.
- b. The geometric spectra for the ground motions of Bins D1, D2 and D3 agree well with the CMS of Figure D.5a, Figure D.5b and Figure D.5c, respectively, at periods greater than 0.4 second and implies that a CMS can reasonably represent the average spectral demand for a combination of  $M_w$ ,  $r$  and  $\varepsilon$ .

- c. For long-return-period (475+ years) earthquake shaking, a CMS is a more reasonable representation of earthquake shaking than a UHS since the former is generated using an attenuation model and considers the correlation of spectral ordinates at different periods, whereas the UHS ordinates at different periods are generally governed by different scenario events.
  
- d. The ordinates of the geomean spectrum for the Bin D4 ground motions are significantly smaller than those of the CMS of Figure D.5c in the short period range. If the number of ground motions used in an analysis is as small as that for Bin D3, the resultant geomean spectral shape will be sensitive to the selected ranges of  $M_w$ ,  $r$  and  $\varepsilon$ . It is appropriate to compare the shapes of the geomean spectrum and the CMS and then to adjust the ground motions in the bin if the shapes are substantially different.

**Table D.1. Earthquake ground motion record pairs from PEER NGA Database**

Record sequence number	Earthquake name	Station name	Year	$M_w$	$r$ (km)	$V_{S30}$ (m/s)
6	Imp. Valley-02	El Centro #9	1940	6.95	6.09	213.4
77	San Fernando	Pacoima Dam	1971	6.61	1.81	2016.1
126	Gazli, USSR	Karakyr	1976	6.80	5.46	659.6
158	Imp. Valley-06	Aeropuerto Mexicali	1979	6.53	0.34	274.5
159	Imp. Valley-06	Agrarias	1979	6.53	0.65	274.5
160	Imp. Valley-06	Bonds Corner	1979	6.53	2.68	223.0
161	Imp. Valley-06	Brawley Airport	1979	6.53	10.42	208.7
162	Imp. Valley-06	Calexico Fire St.	1979	6.53	10.45	231.2
165	Imp. Valley-06	Chihuahua	1979	6.53	7.29	274.5
170	Imp. Valley-06	EC County Center FF	1979	6.53	7.31	192.1
171	Imp. Valley-06	EC Meloland Overpass FF	1979	6.53	0.07	186.2
173	Imp. Valley-06	El Centro #10	1979	6.53	6.17	202.9
174	Imp. Valley-06	El Centro #11	1979	6.53	12.45	196.3
178	Imp. Valley-06	El Centro #3	1979	6.53	12.85	162.9
179	Imp. Valley-06	El Centro #4	1979	6.53	7.05	208.9
180	Imp. Valley-06	El Centro #5	1979	6.53	3.95	205.6
181	Imp. Valley-06	El Centro #6	1979	6.53	1.35	203.2
182	Imp. Valley-06	El Centro #7	1979	6.53	0.56	210.5
183	Imp. Valley-06	El Centro #8	1979	6.53	3.86	206.1
184	Imp. Valley-06	El Centro Differential Array	1979	6.53	5.09	202.3
185	Imp. Valley-06	Holtville Post Office	1979	6.53	7.65	202.9
187	Imp. Valley-06	Parachute Test Site	1979	6.53	12.69	348.7
189	Imp. Valley-06	SAHOP Casa Flores	1979	6.53	9.64	338.6
284	Irpinia, Italy-01	Auletta	1980	6.90	9.55	1000.0
285	Irpinia, Italy-01	Bagnoli Irpinio	1980	6.90	8.18	1000.0
292	Irpinia, Italy-01	Sturno	1980	6.90	10.84	1000.0
495	Nahanni, Canada	Site 1	1985	6.76	9.60	659.6
496	Nahanni, Canada	Site 2	1985	6.76	4.93	659.6
497	Nahanni, Canada	Site 3	1985	6.76	5.32	659.6
723	Superst. Hills-02	Parachute Test Site	1987	6.54	0.95	348.7
725	Superst. Hills-02	Poe Road	1987	6.54	11.16	207.5
727	Superst. Hills-02	Superstition Mtn. Camera	1987	6.54	5.61	362.4
728	Superst. Hills-02	Westmorland Fire Sta.	1987	6.54	13.03	193.7
741	Loma Prieta	BRAN	1989	6.93	10.72	376.1

**Table D.1. Earthquake ground motion record pairs from PEER NGA Database (continued)**

Record sequence number	Earthquake name	Station name	Year	$M_w$	$r$ (km)	$V_{S30}$ (m/s)
753	Loma Prieta	Corralitos	1989	6.93	3.85	462.2
763	Loma Prieta	Gilroy - Gavilan Coll.	1989	6.93	9.96	729.7
764	Loma Prieta	Gilroy - Historic Bldg.	1989	6.93	10.97	338.5
765	Loma Prieta	Gilroy Array #1	1989	6.93	9.64	1428.0
766	Loma Prieta	Gilroy Array #2	1989	6.93	11.07	270.8
767	Loma Prieta	Gilroy Array #3	1989	6.93	12.82	349.9
768	Loma Prieta	Gilroy Array #4	1989	6.93	14.34	221.8
779	Loma Prieta	LGPC	1989	6.93	3.88	477.7
801	Loma Prieta	San Jose - Santa Teresa Hills	1989	6.93	14.69	671.8
802	Loma Prieta	Saratoga - Aloha Ave	1989	6.93	8.50	370.8
803	Loma Prieta	Saratoga - W Valley Coll.	1989	6.93	9.31	370.8
821	Erzican, Turkey	Erzincan	1992	6.69	4.38	274.5
825	Cape Mendocino	Cape Mendocino	1992	7.01	6.96	513.7
828	Cape Mendocino	Petrolia	1992	7.01	8.18	712.8
829	Cape Mendocino	Rio Dell Overpass - FF	1992	7.01	14.33	311.8
864	Landers	Joshua Tree	1992	7.28	11.03	379.3
879	Landers	Lucerne	1992	7.28	2.19	684.9
949	Northridge-01	Arleta - Nordhoff Fire Sta.	1994	6.69	8.66	297.7
959	Northridge-01	Canoga Park - Topanga Can	1994	6.69	14.70	267.5
960	Northridge-01	Canyon Country - W Lost Cany	1994	6.69	12.44	308.6
982	Northridge-01	Jensen Filter Plant	1994	6.69	5.43	373.1
983	Northridge-01	Jensen Filter Plant Generator	1994	6.69	5.43	525.8
1004	Northridge-01	LA - Sepulveda VA Hospital	1994	6.69	8.44	380.1
1013	Northridge-01	LA Dam	1994	6.69	5.92	629.0
1042	Northridge-01	N Hollywood - Coldwater Can	1994	6.69	12.51	446.0
1044	Northridge-01	Newhall - Fire Sta.	1994	6.69	5.92	269.1
1045	Northridge-01	Newhall - W Pico Canyon Rd.	1994	6.69	5.48	285.9
1048	Northridge-01	Northridge - 17645 Saticoy St	1994	6.69	12.09	280.9
1050	Northridge-01	Pacoima Dam (downstr)	1994	6.69	7.01	2016.1
1051	Northridge-01	Pacoima Dam (upper left)	1994	6.69	7.01	2016.1
1052	Northridge-01	Pacoima Kagel Canyon	1994	6.69	7.26	508.1
1063	Northridge-01	Rinaldi Receiving Sta.	1994	6.69	6.50	282.3
1080	Northridge-01	Simi Valley - Katherine Rd	1994	6.69	13.42	557.4
1082	Northridge-01	Sun Valley - Roscoe Blvd	1994	6.69	10.05	308.6

**Table D.1. Earthquake ground motion record pairs from PEER NGA Database (continued)**

Record sequence number	Earthquake name	Station name	Year	$M_w$	$r$ (km)	$V_{S30}$ (m/s)
1083	Northridge-01	Sunland - Mt Gleason Ave	1994	6.69	13.35	446.0
1084	Northridge-01	Sylmar - Converter Sta.	1994	6.69	5.35	251.2
1085	Northridge-01	Sylmar - Converter Sta. East	1994	6.69	5.19	370.5
1086	Northridge-01	Sylmar - Olive View Med FF	1994	6.69	5.30	440.5
1106	Kobe, Japan	KJMA	1995	6.90	0.96	312.0
1111	Kobe, Japan	Nishi-Akashi	1995	6.90	7.08	609.0
1119	Kobe, Japan	Takarazuka	1995	6.90	0.27	312.0
1120	Kobe, Japan	Takatori	1995	6.90	1.47	256.0
1148	Kocaeli, Turkey	Arcelik	1999	7.51	13.49	523.0
1161	Kocaeli, Turkey	Gebze	1999	7.51	10.92	792.0
1165	Kocaeli, Turkey	Izmit	1999	7.51	7.21	811.0
1176	Kocaeli, Turkey	Yarimca	1999	7.51	4.83	297.0
1178	Chi-Chi, Taiwan	ALS	1999	7.62	10.80	553.4
1182	Chi-Chi, Taiwan	CHY006	1999	7.62	9.77	438.2
1193	Chi-Chi, Taiwan	CHY024	1999	7.62	9.64	427.7
1197	Chi-Chi, Taiwan	CHY028	1999	7.62	3.14	542.6
1198	Chi-Chi, Taiwan	CHY029	1999	7.62	10.97	544.7
1201	Chi-Chi, Taiwan	CHY034	1999	7.62	14.82	378.8
1202	Chi-Chi, Taiwan	CHY035	1999	7.62	12.65	473.9
1227	Chi-Chi, Taiwan	CHY074	1999	7.62	10.80	553.4
1231	Chi-Chi, Taiwan	CHY080	1999	7.62	2.69	553.4
1244	Chi-Chi, Taiwan	CHY101	1999	7.62	9.96	258.9
1403	Chi-Chi, Taiwan	NSY	1999	7.62	13.15	599.6
1462	Chi-Chi, Taiwan	TCU	1999	7.62	5.18	472.8
1488	Chi-Chi, Taiwan	TCU048	1999	7.62	13.55	473.9
1489	Chi-Chi, Taiwan	TCU049	1999	7.62	3.78	487.3
1490	Chi-Chi, Taiwan	TCU050	1999	7.62	9.51	272.6
1491	Chi-Chi, Taiwan	TCU051	1999	7.62	7.66	272.6
1492	Chi-Chi, Taiwan	TCU052	1999	7.62	0.66	393.2
1493	Chi-Chi, Taiwan	TCU053	1999	7.62	5.97	454.6
1494	Chi-Chi, Taiwan	TCU054	1999	7.62	5.30	460.7
1495	Chi-Chi, Taiwan	TCU055	1999	7.62	6.36	272.6
1496	Chi-Chi, Taiwan	TCU056	1999	7.62	10.50	272.6
1497	Chi-Chi, Taiwan	TCU057	1999	7.62	11.84	473.9

**Table D.1. Earthquake ground motion record pairs from PEER NGA Database (continued)**

Record sequence number	Earthquake name	Station name	Year	$M_w$	$r$ (km)	$V_{S30}$ (m/s)
1499	Chi-Chi, Taiwan	TCU060	1999	7.62	8.53	272.6
1501	Chi-Chi, Taiwan	TCU063	1999	7.62	9.80	272.6
1503	Chi-Chi, Taiwan	TCU065	1999	7.62	0.59	305.9
1504	Chi-Chi, Taiwan	TCU067	1999	7.62	0.64	433.6
1505	Chi-Chi, Taiwan	TCU068	1999	7.62	0.32	487.3
1507	Chi-Chi, Taiwan	TCU071	1999	7.62	5.31	624.9
1508	Chi-Chi, Taiwan	TCU072	1999	7.62	7.03	468.1
1509	Chi-Chi, Taiwan	TCU074	1999	7.62	13.46	549.4
1510	Chi-Chi, Taiwan	TCU075	1999	7.62	0.91	573.0
1511	Chi-Chi, Taiwan	TCU076	1999	7.62	2.76	615.0
1512	Chi-Chi, Taiwan	TCU078	1999	7.62	8.20	443.0
1513	Chi-Chi, Taiwan	TCU079	1999	7.62	10.97	364.0
1515	Chi-Chi, Taiwan	TCU082	1999	7.62	5.18	472.8
1517	Chi-Chi, Taiwan	TCU084	1999	7.62	11.24	553.4
1519	Chi-Chi, Taiwan	TCU087	1999	7.62	7.00	473.9
1521	Chi-Chi, Taiwan	TCU089	1999	7.62	8.88	553.4
1527	Chi-Chi, Taiwan	TCU100	1999	7.62	11.39	473.9
1528	Chi-Chi, Taiwan	TCU101	1999	7.62	2.13	272.6
1529	Chi-Chi, Taiwan	TCU102	1999	7.62	1.51	714.3
1530	Chi-Chi, Taiwan	TCU103	1999	7.62	6.10	494.1
1531	Chi-Chi, Taiwan	TCU104	1999	7.62	12.89	473.9
1533	Chi-Chi, Taiwan	TCU106	1999	7.62	14.99	473.9
1535	Chi-Chi, Taiwan	TCU109	1999	7.62	13.08	473.9
1536	Chi-Chi, Taiwan	TCU110	1999	7.62	11.60	212.7
1541	Chi-Chi, Taiwan	TCU116	1999	7.62	12.40	493.1
1545	Chi-Chi, Taiwan	TCU120	1999	7.62	7.41	459.3
1546	Chi-Chi, Taiwan	TCU122	1999	7.62	9.35	475.5
1547	Chi-Chi, Taiwan	TCU123	1999	7.62	14.93	272.6
1548	Chi-Chi, Taiwan	TCU128	1999	7.62	13.15	599.6
1549	Chi-Chi, Taiwan	TCU129	1999	7.62	1.84	664.4
1550	Chi-Chi, Taiwan	TCU136	1999	7.62	8.29	473.9
1551	Chi-Chi, Taiwan	TCU138	1999	7.62	9.79	652.9
1595	Chi-Chi, Taiwan	WGK	1999	7.62	9.96	258.9
1596	Chi-Chi, Taiwan	WNT	1999	7.62	1.84	664.4



**Table D.1. Earthquake ground motion record pairs from PEER NGA Database (continued)**

Record sequence number	Earthquake name	Station name	Year	$M_w$	$r$ (km)	$V_{s30}$ (m/s)
1602	Duzce, Turkey	Bolu	1999	7.14	12.04	326.0
1605	Duzce, Turkey	Duzce	1999	7.14	6.58	276.0
1611	Duzce, Turkey	Lamont 1058	1999	7.14	0.21	424.8
1612	Duzce, Turkey	Lamont 1059	1999	7.14	4.17	424.8
1614	Duzce, Turkey	Lamont 1061	1999	7.14	11.46	481.0
1615	Duzce, Turkey	Lamont 1062	1999	7.14	9.15	338.0
1617	Duzce, Turkey	Lamont 375	1999	7.14	3.93	424.8
1618	Duzce, Turkey	Lamont 531	1999	7.14	8.03	659.6
1787	Hector Mine	Hector	1999	7.13	11.66	684.9
2114	Denali, Alaska	TAPS Pump Station #10	2002	7.90	2.74	329.4
3548	Loma Prieta	Los Gatos-Lexington Dam	1989	6.93	5.02	1070.3

**Table D.2. Epsilon ( $\varepsilon$ ) and spectral shape for the records of Table D.1**

Record sequence number	Direction of record	$\varepsilon$					Type of spectral shape				
		0.2 s	0.5 s	1 s	2 s	4 s	P1	P2	P3	P4	P5
6	FN	-0.31	-0.41	-0.68	-1.27	-1.92	4	2	2	2	2
77	FN	1.01	2.58	2.80	2.68	2.22	5	2	2	2	2
126	FN	0.16	0.42	1.40	0.65	2.12	1	2	2	2	2
158	FN	-1.07	-0.96	-0.87	-0.62	-1.32	5	2	2	2	2
159	FN	-1.66	-0.74	-1.17	-0.10	-1.01	5	4	2	2	2
160	FN	1.85	0.78	-0.49	-0.98	-1.66	3	2	2	2	2
161	FN	-0.31	-1.84	-0.56	0.17	0.72	4	5	4	2	2
162	FN	0.30	0.66	-0.63	-1.19	-0.87	3	2	2	2	2
165	FN	-0.34	0.47	0.29	-0.62	-0.17	3	4	2	2	2
170	FN	-0.67	0.36	-0.99	-0.06	1.03	3	4	2	4	2
171	FN	-0.59	-0.22	-0.33	0.56	0.49	3	4	2	4	2
173	FN	-0.73	0.08	-1.14	0.04	0.71	5	2	5	4	2
174	FN	1.16	1.13	-0.31	-0.30	0.31	4	2	2	2	2
178	FN	0.79	0.26	-1.28	-0.91	0.78	2	2	2	5	2
179	FN	0.31	0.22	0.41	0.74	1.77	4	2	2	2	2
180	FN	0.16	0.60	0.48	0.26	1.46	3	2	2	2	2
181	FN	-0.16	-0.30	-0.63	0.20	1.41	3	2	2	1	2
182	FN	-0.08	-0.02	0.02	0.26	0.95	3	3	2	2	2
183	FN	0.40	0.13	-0.50	-0.85	0.70	2	2	2	5	2
184	FN	0.57	0.44	-0.13	0.17	0.62	2	2	2	2	2
185	FN	-0.28	0.26	-0.09	-0.53	1.05	3	2	2	5	2
187	FN	-0.69	-0.30	-0.72	-0.06	0.77	2	2	2	2	2
189	FN	1.11	0.93	0.12	-1.04	-2.09	4	2	2	2	2
284	FN	-1.57	-1.60	-0.95	-0.99	-0.20	1	2	2	2	2
285	FN	-0.53	0.14	1.43	1.74	0.57	2	1	4	2	2
292	FN	0.99	0.91	1.12	2.36	2.50	4	2	5	4	2
495	FN	0.27	0.09	0.87	0.61	1.42	2	2	2	2	2
496	FN	-2.25	-1.01	-1.68	-1.30	-1.29	3	2	2	2	2
497	FN	-2.77	-4.14	-3.62	-2.14	-1.14	2	2	2	2	2
723	FN	-0.42	-0.25	0.83	1.66	0.71	4	1	1	2	2
725	FN	0.96	0.89	-0.35	-0.60	-0.07	3	2	2	2	2
727	FN	1.20	0.93	-0.45	-0.13	-1.21	4	2	2	2	2
728	FN	0.50	0.22	0.71	-0.02	0.08	5	2	4	2	2

**Table D.2. Epsilon ( $\varepsilon$ ) and spectral shape for the records of Table D.1 (continued)**

Record sequence number	Direction of record	$\varepsilon$					Type of spectral shape				
		0.2 s	0.5 s	1 s	2 s	4 s	P1	P2	P3	P4	P5
741	FN	0.19	1.50	0.46	-0.61	-0.59	5	4	2	2	2
753	FN	-0.37	-0.40	-0.31	-0.52	-0.61	3	2	2	2	2
763	FN	0.19	-0.10	-0.15	0.20	0.06	3	2	2	2	2
764	FN	-0.75	0.17	0.18	-0.72	-2.06	3	2	2	2	2
765	FN	1.24	1.26	0.78	1.01	1.00	3	2	2	2	2
766	FN	-0.23	0.32	0.36	0.64	-0.52	3	2	2	2	2
767	FN	1.23	1.25	0.43	0.61	-0.10	4	2	2	2	2
768	FN	0.26	0.85	0.34	0.35	0.08	3	2	2	2	2
779	FN	-0.01	0.68	0.52	1.25	2.02	1	4	2	2	2
801	FN	0.56	0.29	0.00	-0.12	0.26	2	4	2	2	2
802	FN	0.26	-0.22	0.27	0.91	0.92	4	2	2	2	2
803	FN	-0.44	-0.65	1.04	1.08	0.43	3	5	4	2	2
821	FN	-0.03	-0.50	0.60	0.99	0.47	4	5	4	2	2
825	FN	-0.24	-1.12	-0.40	0.58	-0.09	2	2	2	2	2
828	FN	-0.94	0.69	1.31	1.44	1.27	5	4	2	2	2
829	FN	-0.18	0.53	0.61	-0.15	-1.31	3	2	2	2	2
864	FN	-0.45	-0.35	0.90	0.34	0.16	4	1	4	2	2
879	FN	0.30	-0.47	0.03	0.55	1.84	2	2	2	2	2
949	FN	-0.92	-0.79	-0.71	-0.75	-0.98	4	4	2	2	2
959	FN	0.14	-0.29	0.02	1.20	0.32	3	2	2	2	2
960	FN	1.17	1.54	1.00	1.42	0.18	4	4	2	2	2
982	FN	-0.53	-1.25	-0.52	0.64	1.20	3	2	2	4	2
983	FN	-0.75	-1.12	-0.17	1.04	1.62	3	2	2	4	2
1004	FN	1.12	0.36	0.21	0.34	0.24	4	2	2	2	2
1013	FN	-1.00	-0.49	0.85	1.10	0.61	1	1	2	2	2
1042	FN	1.06	-0.20	0.11	1.03	0.45	4	2	2	2	2
1044	FN	0.76	1.36	1.46	0.81	1.10	4	4	2	2	2
1045	FN	-0.93	-0.39	0.47	1.37	1.22	3	5	4	2	2
1048	FN	0.23	0.60	0.81	1.11	0.43	3	4	2	2	2
1050	FN	0.47	2.15	1.24	0.76	1.44	3	2	2	2	2
1051	FN	1.96	2.93	3.22	2.34	2.42	2	4	2	2	2
1052	FN	-0.15	1.13	1.11	0.55	0.50	3	4	2	2	2
1063	FN	0.41	0.82	1.62	1.05	0.63	3	1	2	2	2

**Table D.2. Epsilon ( $\varepsilon$ ) and spectral shape for the records of Table D.1 (continued)**

Record sequence number	Direction of record	$\varepsilon$					Type of spectral shape				
		0.2 s	0.5 s	1 s	2 s	4 s	P1	P2	P3	P4	P5
1080	FN	-0.06	1.54	1.66	-0.07	-0.72	3	4	2	2	2
1082	FN	-0.01	-0.22	0.30	-0.35	-0.67	4	2	2	2	2
1083	FN	-0.72	0.09	0.81	0.27	0.29	4	4	2	2	2
1084	FN	0.10	-0.12	0.92	0.68	1.03	3	3	4	2	2
1085	FN	0.34	0.00	-0.02	0.63	1.06	4	2	2	2	2
1086	FN	-0.29	-0.08	0.67	1.59	1.10	3	2	4	2	2
1106	FN	0.08	0.82	1.48	0.23	-0.48	3	1	2	2	2
1111	FN	1.09	2.34	0.02	0.57	-0.30	3	4	2	2	2
1119	FN	0.86	-0.15	0.25	-0.02	-1.20	4	1	2	2	2
1120	FN	0.44	0.37	1.33	1.96	0.19	3	3	4	2	2
1148	FN	0.11	-1.15	-1.33	-1.63	-0.76	4	2	2	2	2
1161	FN	-0.62	0.34	0.05	-0.18	1.76	5	2	2	5	4
1165	FN	-1.26	-0.27	0.07	0.00	-0.01	4	2	2	2	2
1176	FN	-0.72	-0.85	-0.92	-0.86	0.15	3	4	4	2	2
1178	FN	-3.05	-1.18	-0.90	-0.12	-0.36	3	4	2	2	2
1182	FN	-0.33	1.26	0.10	1.28	0.38	3	4	2	2	2
1193	FN	-0.39	0.03	0.51	0.13	1.38	3	2	2	2	2
1197	FN	0.51	1.24	1.22	0.82	-0.35	3	2	2	2	2
1198	FN	-0.65	0.90	0.04	0.36	0.61	3	4	2	2	2
1201	FN	-0.57	0.91	1.01	-0.06	-0.59	3	4	2	2	2
1202	FN	-0.80	-0.06	0.80	0.66	-0.74	3	1	4	2	2
1227	FN	-2.83	-1.00	-0.74	0.11	-0.06	3	4	2	2	2
1231	FN	-1.02	-0.50	0.79	0.66	-1.02	3	3	2	2	2
1244	FN	-0.16	-0.48	0.65	0.05	0.92	1	3	2	2	2
1403	FN	-1.57	-0.75	-0.13	0.69	1.91	3	2	2	1	2
1462	FN	-1.33	-0.16	-0.29	-0.40	-0.34	3	4	2	2	2
1488	FN	-1.89	-1.54	-0.39	-0.23	1.31	1	1	2	5	4
1489	FN	-0.67	-0.72	-0.36	-0.95	-0.34	4	2	2	2	2
1490	FN	-1.00	-0.99	-0.85	-0.75	-0.40	3	1	2	2	2
1491	FN	-0.58	-0.61	-0.64	-0.76	-0.94	4	2	2	2	2
1492	FN	-1.84	-1.43	0.20	0.88	1.00	3	3	4	2	2
1493	FN	-1.33	-0.20	-0.66	-0.89	-0.63	3	2	2	2	2
1494	FN	-2.16	-1.23	-0.39	-0.72	0.17	3	4	2	2	4

**Table D.2. Epsilon ( $\varepsilon$ ) and spectral shape for the records of Table D.1 (continued)**

Record sequence number	Direction of record	$\varepsilon$					Type of spectral shape				
		0.2 s	0.5 s	1 s	2 s	4 s	P1	P2	P3	P4	P5
1495	FN	-0.52	-0.03	-1.04	-0.54	-0.34	3	2	2	2	2
1496	FN	-1.35	-0.44	-0.53	-0.45	-0.55	3	1	2	2	2
1497	FN	-1.69	-1.05	-0.11	0.11	0.76	3	5	2	2	2
1499	FN	-1.16	-0.61	-1.32	-1.51	-0.89	3	2	2	2	2
1501	FN	-0.72	-0.21	0.14	0.57	0.72	3	4	2	2	2
1503	FN	-0.12	-0.92	0.57	0.66	1.14	4	5	4	2	2
1504	FN	-0.46	-0.35	0.21	0.44	-0.06	3	4	2	2	2
1505	FN	-0.93	-0.10	0.06	0.71	1.65	3	2	2	2	2
1507	FN	-0.19	-0.09	0.42	-0.16	0.35	4	2	2	2	2
1508	FN	-0.40	-0.07	0.69	-0.56	-0.14	3	1	2	2	2
1509	FN	-0.35	0.76	1.85	1.07	0.85	3	3	2	2	2
1510	FN	-1.01	-1.00	-0.92	0.30	1.16	3	2	5	4	2
1511	FN	-0.18	-0.88	-0.16	-0.16	0.47	3	2	2	2	2
1512	FN	-0.39	-0.47	-0.23	-0.74	-1.40	2	2	2	2	2
1513	FN	0.79	0.22	-0.02	-0.58	-1.05	4	4	2	2	2
1515	FN	-1.40	-0.19	-0.24	-0.19	-0.34	3	2	2	2	2
1517	FN	0.30	1.09	2.61	2.55	0.53	4	3	4	2	2
1519	FN	-1.88	-1.67	-1.54	-0.91	0.76	4	2	2	2	4
1521	FN	-0.68	-0.90	-0.41	-0.81	-0.58	3	2	2	2	2
1527	FN	-1.43	-0.83	-0.40	-0.28	0.81	3	2	2	2	2
1528	FN	-0.67	-1.17	-1.50	-1.83	-0.60	4	2	2	2	2
1529	FN	-2.36	-0.44	0.31	0.98	1.24	3	4	2	2	2
1530	FN	-2.26	-0.79	-0.11	-0.13	0.58	3	2	2	2	2
1531	FN	-1.81	-1.08	-0.05	-0.54	0.21	5	4	4	2	2
1533	FN	-0.77	0.58	0.40	0.78	1.26	3	4	2	2	2
1535	FN	-1.74	-0.09	-0.19	1.11	1.26	3	4	2	4	2
1536	FN	-1.46	-0.53	0.08	1.22	0.08	3	3	1	4	2
1541	FN	-0.70	-0.20	1.13	0.32	1.09	4	5	4	2	2
1545	FN	-0.96	-0.71	0.24	1.13	0.50	4	5	2	2	2
1546	FN	-0.59	-0.71	-0.63	-0.47	1.17	1	4	2	5	4
1547	FN	-1.53	-0.83	-0.17	0.59	0.54	3	4	3	2	2
1548	FN	-1.39	-0.54	0.13	1.14	2.33	3	2	2	5	4
1549	FN	0.55	0.82	0.24	-0.23	-0.09	4	2	2	2	2

**Table D.2. Epsilon ( $\varepsilon$ ) and spectral shape for the records of Table D.1 (continued)**

Record sequence number	Direction of record	$\varepsilon$					Type of spectral shape				
		0.2 s	0.5 s	1 s	2 s	4 s	P1	P2	P3	P4	P5
1550	FN	-1.59	-1.20	0.66	0.04	-0.38	3	3	4	2	2
1551	FN	-0.96	-0.11	0.53	0.54	1.53	3	2	2	2	2
1595	FN	0.03	-0.15	-0.77	0.01	1.29	2	4	2	3	2
1596	FN	0.43	0.68	0.13	-0.32	-0.43	4	2	2	2	2
1602	FN	1.63	2.00	1.34	0.71	0.25	3	2	2	2	2
1605	FN	-0.72	0.19	-0.35	-0.48	0.19	3	2	2	2	2
1611	FN	-3.87	-4.01	-3.58	-2.45	-1.77	4	2	1	2	2
1612	FN	-0.90	-2.29	-2.57	-3.62	-1.64	4	2	2	5	1
1614	FN	-0.90	-1.24	-0.90	-1.93	-1.57	4	2	2	2	5
1615	FN	-1.15	-1.27	-2.08	-2.67	-2.17	4	2	2	2	5
1617	FN	0.69	0.45	-2.21	-2.75	-1.83	3	2	2	2	2
1618	FN	-0.84	-0.97	-2.11	-2.38	-1.30	4	2	2	2	2
1787	FN	0.61	2.12	0.69	1.17	0.43	3	2	2	2	2
2114	FN	-1.04	-1.40	-0.43	-0.33	-0.68	4	3	2	2	2
3548	FN	-3.20	-3.45	-2.41	-2.33	-0.98	2	2	2	2	2
6	FP	0.21	0.10	-0.50	-0.37	-1.32	4	4	2	2	2
77	FP	0.78	1.32	-0.23	0.40	1.29	1	2	2	2	2
126	FP	0.43	1.24	0.36	1.54	1.98	2	4	5	2	2
158	FP	-0.80	-1.50	-2.03	-2.28	-3.52	2	2	2	2	2
159	FP	-2.25	-1.27	-2.17	-3.06	-3.32	5	4	2	2	2
160	FP	0.68	0.94	-0.50	-0.48	-1.36	5	4	2	2	2
161	FP	-0.05	-0.05	-0.09	-0.44	-0.33	4	2	2	2	2
162	FP	-0.19	-0.38	-0.96	-0.99	-0.73	2	2	2	2	2
165	FP	-0.78	-0.58	0.10	-0.59	-0.50	4	1	2	2	2
170	FP	0.00	0.02	0.65	0.06	-0.09	4	3	4	2	2
171	FP	-0.89	-0.11	-1.66	-1.35	-0.80	3	4	2	2	2
173	FP	-0.04	-0.78	-0.37	0.33	-0.43	4	2	4	2	2
174	FP	1.71	0.49	-0.04	0.92	0.29	4	2	5	2	2
178	FP	0.95	0.51	-0.05	0.84	0.53	4	2	2	2	2
179	FP	0.96	0.38	0.55	0.47	-0.73	3	2	2	2	2
180	FP	0.90	0.65	-0.45	-0.36	-0.06	1	2	2	2	2
181	FP	-0.29	-0.73	-0.10	0.02	0.07	5	5	2	2	2
182	FP	-0.58	-0.66	-0.01	-0.84	-0.86	4	3	2	2	2

**Table D.2. Epsilon ( $\varepsilon$ ) and spectral shape for the records of Table D.1 (continued)**

Record sequence number	Direction of record	$\varepsilon$					Type of spectral shape				
		0.2 s	0.5 s	1 s	2 s	4 s	P1	P2	P3	P4	P5
183	FP	0.87	0.23	-0.38	0.11	-0.13	2	2	2	2	2
184	FP	0.91	0.77	0.41	0.31	-0.35	4	2	2	2	2
185	FP	0.79	-0.58	-0.72	-0.31	0.61	4	2	2	2	2
187	FP	-0.17	-0.24	-0.71	-0.22	0.42	4	2	2	2	2
189	FP	1.10	0.45	-0.24	0.29	-1.46	4	2	2	2	2
284	FP	-1.95	-1.70	-1.08	-0.98	-0.76	4	2	2	2	2
285	FP	-0.75	0.48	0.94	1.27	1.32	2	4	2	2	2
292	FP	1.27	1.65	1.89	2.58	2.69	3	2	2	2	2
495	FP	1.88	0.52	-0.05	0.00	-0.60	4	2	2	2	2
496	FP	-1.79	-0.30	-0.78	-0.41	-1.06	2	4	2	2	2
497	FP	-2.87	-4.22	-4.05	-3.43	-2.53	2	2	4	2	2
723	FP	-0.68	-0.03	-0.20	0.25	0.27	3	4	2	2	2
725	FP	0.06	1.07	0.40	0.45	-0.09	5	4	2	2	2
727	FP	1.34	0.93	1.23	-0.25	-1.70	3	2	2	2	2
728	FP	0.03	0.30	0.30	0.00	0.37	3	2	2	2	2
741	FP	0.10	0.67	0.12	-0.95	-0.23	4	2	2	2	2
753	FP	-0.35	-0.08	-0.39	-0.86	-1.48	3	2	2	2	2
763	FP	0.76	0.88	-0.28	-0.24	-0.84	2	2	2	2	2
764	FP	-0.75	0.23	-0.05	0.40	-0.80	3	2	2	2	2
765	FP	0.96	1.88	0.67	0.62	0.09	3	2	2	2	2
766	FP	0.80	0.16	-0.19	-0.55	-1.33	4	2	2	2	2
767	FP	1.66	0.44	0.08	1.04	0.31	4	2	2	2	2
768	FP	-0.06	1.03	-0.24	-0.88	-1.23	3	4	2	2	2
779	FP	-0.86	-0.05	-0.27	0.50	1.17	1	4	2	2	2
801	FP	-0.27	0.56	0.84	0.28	-0.43	2	2	2	2	2
802	FP	0.36	-0.27	-0.30	0.27	0.38	4	2	2	2	2
803	FP	-0.35	-0.23	0.21	0.31	1.46	3	2	2	2	4
821	FP	0.12	-0.24	-0.95	0.38	-0.51	4	2	5	4	2
825	FP	0.74	0.48	0.45	0.24	1.46	4	2	2	2	2
828	FP	-0.77	0.31	0.87	0.53	0.59	1	4	2	2	2
829	FP	0.79	1.56	-0.16	-1.28	-0.91	3	2	2	2	2
864	FP	-0.75	0.48	0.46	-0.19	-0.72	3	4	2	2	2
879	FP	-0.04	-0.94	-0.36	-0.63	-1.05	2	2	2	2	2

**Table D.2. Epsilon ( $\varepsilon$ ) and spectral shape for the records of Table D.1 (continued)**

Record sequence number	Direction of record	$\varepsilon$					Type of spectral shape				
		0.2 s	0.5 s	1 s	2 s	4 s	P1	P2	P3	P4	P5
949	FP	0.04	-0.58	0.21	-0.26	-0.28	4	2	2	2	2
959	FP	0.38	0.50	-0.30	0.51	-0.50	4	4	2	2	2
960	FP	0.85	0.70	0.69	1.15	-0.03	3	4	2	2	2
982	FP	0.75	0.19	1.02	0.84	-0.37	3	2	2	2	2
983	FP	0.54	0.31	1.37	1.23	-0.02	3	2	2	2	2
1004	FP	0.59	0.69	0.95	0.27	0.08	4	2	2	2	2
1013	FP	-1.48	-0.37	-0.27	1.10	0.88	1	2	2	2	2
1042	FP	-0.61	-0.29	0.53	0.73	1.03	1	2	2	2	2
1044	FP	0.87	-0.06	-0.35	-0.16	-0.86	4	2	2	2	2
1045	FP	-1.26	0.07	0.09	0.76	0.05	3	4	2	2	2
1048	FP	0.08	0.12	-0.30	0.66	0.23	3	2	2	2	2
1050	FP	-0.01	0.24	0.81	0.00	-0.09	4	2	2	2	2
1051	FP	2.15	2.91	1.29	0.91	0.97	1	2	2	2	2
1052	FP	-1.16	-0.39	-0.33	0.13	1.27	3	2	2	2	2
1063	FP	0.26	-0.50	-0.65	0.31	0.08	3	2	2	2	2
1080	FP	-0.19	1.41	0.69	-0.28	-1.11	5	2	2	2	2
1082	FP	0.34	-0.38	0.61	0.18	-0.25	4	1	2	2	2
1083	FP	-1.38	-0.40	0.44	0.18	-0.74	3	1	2	2	2
1084	FP	0.23	0.33	0.59	1.17	-0.57	4	1	2	2	2
1085	FP	-0.06	-1.01	0.66	0.93	-0.59	4	5	4	2	2
1086	FP	-0.01	1.05	0.16	0.47	-1.05	3	4	2	2	2
1106	FP	-0.10	0.59	-0.78	-1.43	-2.00	3	2	2	2	2
1111	FP	0.45	1.30	0.52	0.76	-0.29	4	4	2	2	2
1119	FP	0.11	1.28	0.07	0.29	-0.92	3	4	2	2	2
1120	FP	1.58	0.74	0.28	0.17	-0.26	3	2	2	2	2
1148	FP	-0.69	-1.49	-1.26	-0.72	0.64	4	2	2	2	4
1161	FP	-0.79	0.11	-0.27	-0.05	0.83	2	4	2	2	4
1165	FP	-0.53	-0.64	0.01	0.48	0.46	4	2	2	2	2
1176	FP	-1.01	-0.54	-1.03	-0.54	0.99	4	4	2	5	2
1178	FP	-1.64	-0.99	-1.09	-0.68	0.47	3	2	2	2	2
1182	FP	-0.42	0.38	1.38	0.22	-0.53	3	3	2	2	2
1193	FP	-0.89	-1.01	0.08	0.33	0.72	4	5	1	2	2
1197	FP	0.80	0.81	0.82	0.68	-0.81	3	2	2	2	2



**Table D.2. Epsilon ( $\varepsilon$ ) and spectral shape for the records of Table D.1 (continued)**

Record sequence number	Direction of record	$\varepsilon$					Type of spectral shape				
		0.2 s	0.5 s	1 s	2 s	4 s	P1	P2	P3	P4	P5
1198	FP	-1.29	0.29	0.78	0.03	0.71	3	4	2	2	2
1201	FP	-0.52	0.21	1.94	0.62	-0.37	5	5	4	2	2
1202	FP	-0.49	0.47	1.26	-0.39	-0.35	3	4	2	2	2
1227	FP	-1.52	-1.00	-1.18	-0.54	0.62	3	2	2	2	2
1231	FP	0.11	0.86	2.07	0.62	-0.24	3	3	2	2	2
1244	FP	0.04	0.59	0.92	0.82	1.69	5	5	2	2	2
1403	FP	-1.75	0.04	-0.16	-0.03	0.57	3	4	2	2	2
1462	FP	-1.81	-1.17	-0.59	0.01	0.47	3	4	2	2	2
1488	FP	-1.60	-0.58	-0.15	0.01	1.49	1	1	2	5	4
1489	FP	-0.86	-0.82	-0.67	-0.80	0.31	4	2	2	2	4
1490	FP	-1.48	-0.95	-1.45	-0.94	-0.17	4	2	2	2	2
1491	FP	-0.71	-1.15	-1.31	-0.58	-0.09	4	4	2	2	2
1492	FP	-1.30	-1.48	-0.03	0.64	-0.06	3	5	4	2	5
1493	FP	-2.20	-1.29	-1.21	-0.94	0.09	3	4	2	2	2
1494	FP	-2.08	-1.17	-0.84	0.03	-0.15	3	4	2	2	2
1495	FP	-0.79	-1.05	-0.93	-0.84	0.06	1	4	2	2	2
1496	FP	-1.40	-1.17	-0.84	-1.04	-0.14	3	2	2	2	2
1497	FP	-2.19	-0.90	-0.76	0.06	0.77	3	4	2	2	1
1499	FP	-1.77	-1.35	-1.43	-1.76	-0.26	3	2	2	5	4
1501	FP	-1.50	-1.50	-0.29	0.57	1.08	4	3	1	1	2
1503	FP	-0.57	-0.39	0.27	0.15	-0.40	1	4	2	2	2
1504	FP	-1.59	-0.43	-0.83	-0.48	-0.47	3	4	2	2	2
1505	FP	-1.22	-1.03	-0.41	0.51	0.53	5	4	1	2	5
1507	FP	0.47	-0.83	0.42	-0.66	-0.07	4	5	2	2	2
1508	FP	-0.55	-0.31	0.37	0.15	-0.42	1	3	2	2	2
1509	FP	-0.97	-0.10	0.72	-0.17	-0.65	1	4	2	2	2
1510	FP	-2.13	-1.11	-0.94	-1.24	0.10	3	2	2	5	2
1511	FP	-0.57	0.30	0.64	0.02	0.11	3	2	2	2	2
1512	FP	-0.67	-0.46	-1.14	-1.45	-1.11	4	2	2	2	2
1513	FP	-0.20	-0.78	0.06	-1.14	-1.48	4	2	2	2	2
1515	FP	-1.83	-1.25	-0.46	-0.10	0.60	3	4	2	2	2
1517	FP	-1.10	-0.14	0.90	-0.09	0.24	3	5	2	2	2
1519	FP	-2.36	-0.81	-0.61	-0.52	0.50	3	4	2	5	2

**Table D.2. Epsilon ( $\varepsilon$ ) and spectral shape for the records of Table D.1 (continued)**

Record sequence number	Direction of record	$\varepsilon$					Type of spectral shape				
		0.2 s	0.5 s	1 s	2 s	4 s	P1	P2	P3	P4	P5
1521	FP	-1.58	-1.33	-0.78	-1.26	-0.09	4	2	2	2	2
1527	FP	-1.79	-1.07	-0.81	0.40	0.87	3	4	5	2	4
1528	FP	-1.89	-1.32	-1.43	-1.55	-0.93	3	4	2	2	2
1529	FP	-2.92	-1.49	0.26	1.06	0.91	3	3	2	4	2
1530	FP	-2.20	-0.94	-1.14	-0.90	-0.07	3	4	2	2	2
1531	FP	-2.49	-1.13	-0.75	-0.14	1.03	3	2	4	2	4
1533	FP	-0.91	-0.28	0.39	0.86	1.60	3	1	2	1	2
1535	FP	-1.53	0.31	0.73	1.35	1.70	3	4	2	1	2
1536	FP	-1.63	-0.35	0.40	1.05	0.73	3	3	1	2	2
1541	FP	-0.71	-0.09	0.21	1.01	1.40	4	1	2	2	2
1545	FP	-0.69	-1.31	-0.80	-0.20	0.44	4	2	2	2	2
1546	FP	-0.52	-0.19	0.19	0.65	0.12	3	2	2	2	2
1547	FP	-1.54	-0.52	0.05	0.29	0.91	3	4	4	2	2
1548	FP	-1.56	0.33	0.09	0.34	1.65	3	4	2	2	2
1549	FP	0.32	-0.97	0.22	-0.53	-0.34	4	5	2	2	2
1550	FP	-2.21	-0.70	0.48	-0.41	0.65	3	3	4	5	2
1551	FP	-0.92	0.02	1.03	1.06	1.06	3	5	4	2	2
1595	FP	0.39	0.73	1.15	0.81	1.04	5	3	2	2	2
1596	FP	0.27	-1.06	0.10	-0.68	-0.75	4	5	2	2	2
1602	FP	0.82	1.38	2.09	1.11	-0.31	5	3	2	2	2
1605	FP	0.43	-0.23	0.14	0.30	0.75	3	1	2	2	2
1611	FP	-3.23	-3.32	-2.71	-2.92	-1.90	2	2	4	2	2
1612	FP	-0.80	-2.87	-2.71	-3.77	-2.90	4	2	2	2	1
1614	FP	-0.93	-1.29	-1.48	-1.87	-1.38	3	2	2	2	2
1615	FP	-0.02	-0.86	-1.06	-1.81	-2.62	3	2	2	2	5
1617	FP	0.21	-1.56	-1.91	-2.63	-2.63	4	2	2	2	2
1618	FP	-1.04	-0.10	-0.67	-1.77	-1.51	3	2	2	2	2
1787	FP	0.11	0.72	1.17	0.57	0.08	4	2	2	2	2
2114	FP	-1.78	-1.59	-0.16	0.16	-0.40	3	3	4	2	2
3548	FP	-2.97	-3.20	-2.28	-2.10	-1.43	2	2	2	2	2

**Table D.3. Number of records from Table D.1 in  $\varepsilon$  bins at periods of 0.2, 0.5, 1, 2 and 4 seconds**

		Period (second)				
		0.2	0.5	1.0	2.0	4.0
Bin	$\varepsilon \geq 3$	0	0	1	0	0
	$3 > \varepsilon \geq 2$	1	6	4	5	7
	$2 > \varepsilon \geq 1$	20	24	29	36	48
	$1 > \varepsilon \geq 0$	81	92	112	118	98
	$0 > \varepsilon \geq -1$	113	114	110	100	97
	$-1 > \varepsilon \geq -2$	57	50	25	21	34
	$-2 > \varepsilon \geq -3$	18	2	10	10	8
	$\varepsilon < -3$	4	6	3	4	2

**Table D.4. Number of records from Table D.1 as a function of the period bin and type of spectral shape**

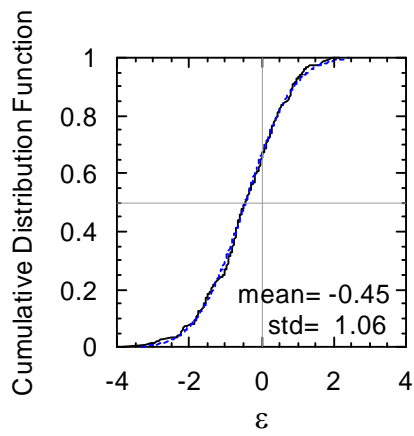
		Period bin				
		P1	P2	P3	P4	P5
Type of spectral shape	1	19	20	7	5	3
	2	27	155	249	263	272
	3	140	23	1	1	0
	4	89	77	30	11	14
	5	19	19	7	14	5

**Table D.5. Spectral accelerations and governing events of 1-second seismic hazard with return periods of 2475, 475 and 108 years for a rock site at 122.2°W, 37.8°N**

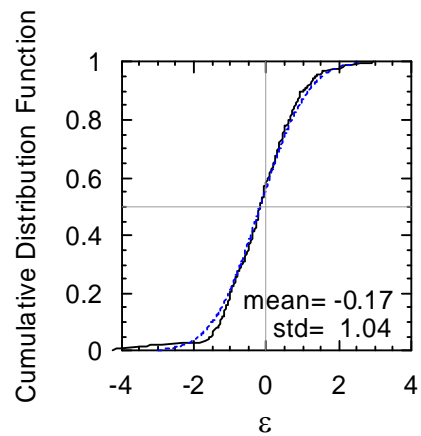
Probability of exceedance	Return period (year)	Spectral acceleration (g)	$\bar{M}$	$\bar{r}$ (km)	$\varepsilon$
2% in 50 years	2475	1.28	6.8	1.6	1.79
10% in 50 years	475	0.74	6.8	3.2	1.24
50% in 75 years	108	0.34	6.9	8.4	0.75

**Table D.6. Ground motion bins D1 through D4**

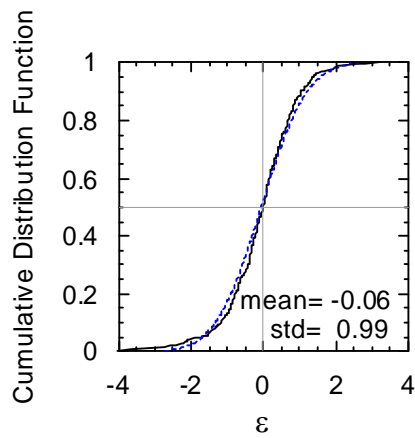
Bin	Range of $M_w$	Range of $r$ (km)	Range of $\varepsilon$	Number of ground motions	Record sequence number
D1	(6.6, 7.2)	(1, 12)	> 1.5	6	FN: 77, 1051, 1063, 1080 FP: 292, 1602
D2	(6.6, 7.2)	(1, 13)	(1, 1.5)	16	FN: 126, 285, 292, 803, 828, 960, 1044, 1050, 1052, 1106, 1120, 1602 FP: 982, 983, 1051, 1787
D3	(6.7, 7.3)	(7, 15)	(0.5, 1)	11	FN: 495, 765, 779, 829, 864, 1787 FP: 285, 765, 801, 828, 1111
D4	(6.6, 7.3)	(3, 15)	(0.5, 1)	25	FN: 495, 765, 779, 821, 829, 864, 1013, 1048, 1083, 1084, 1086, 1787 FP: 285, 765, 801, 828, 960, 1004, 1042, 1050, 1080, 1082, 1084, 1085, 1111



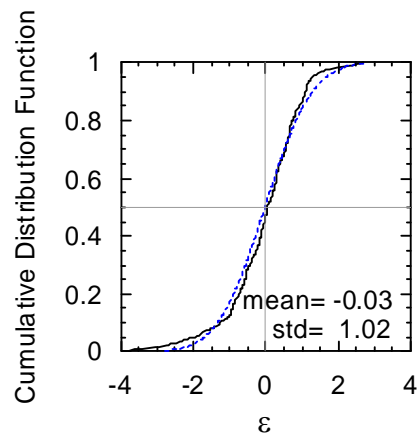
a. 0.2 s



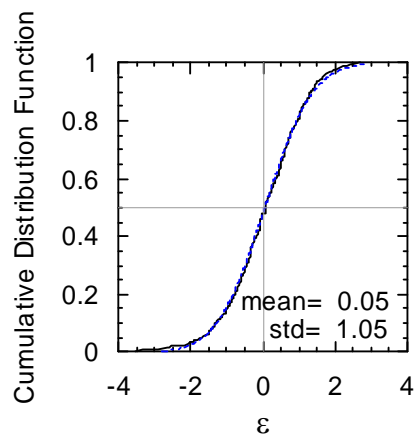
b. 0.5 s



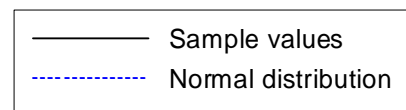
c. 1 s



d. 2 s



e. 4 s



f. legend

**Figure D.1. Good-of-fit test for the distribution of  $\varepsilon$**

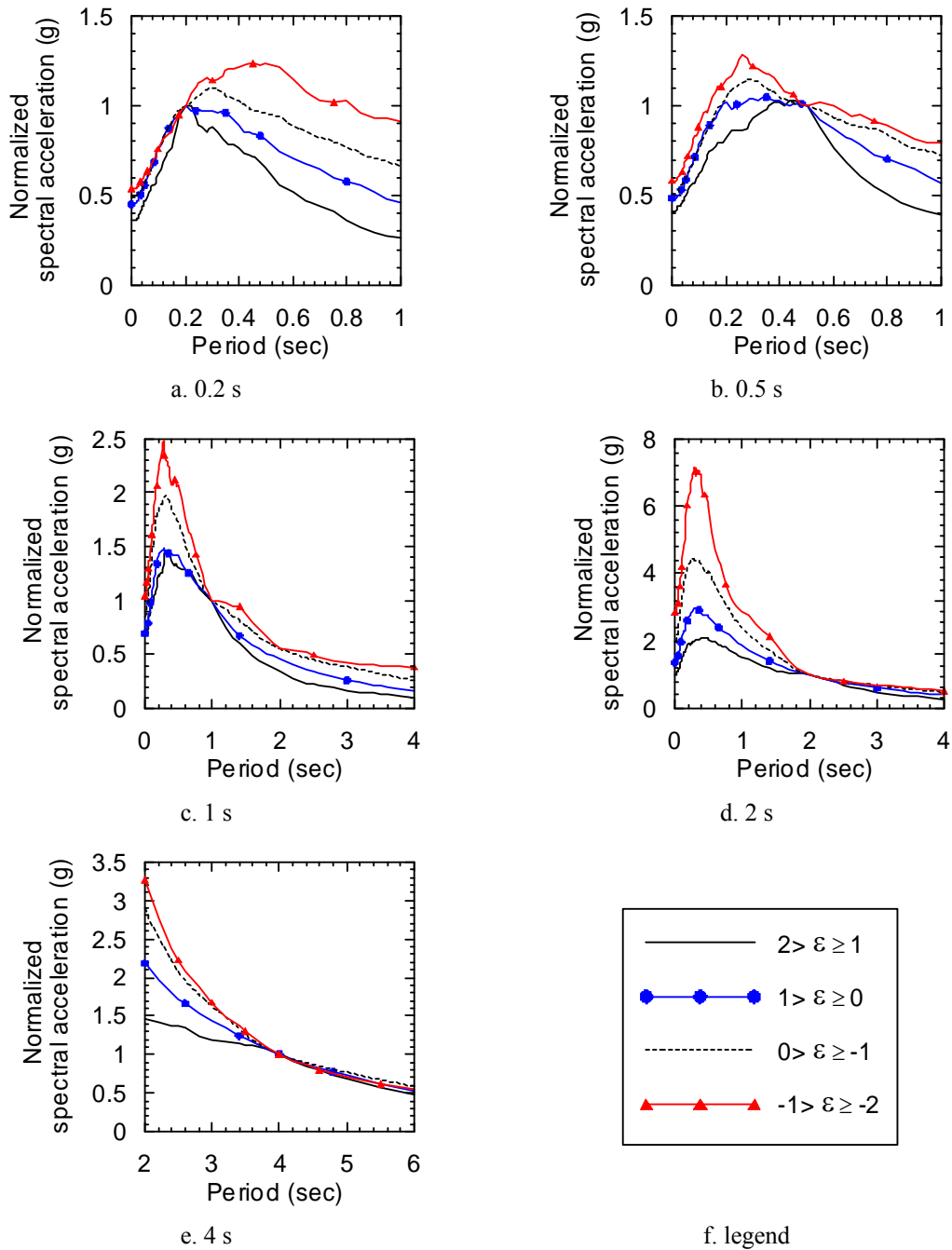
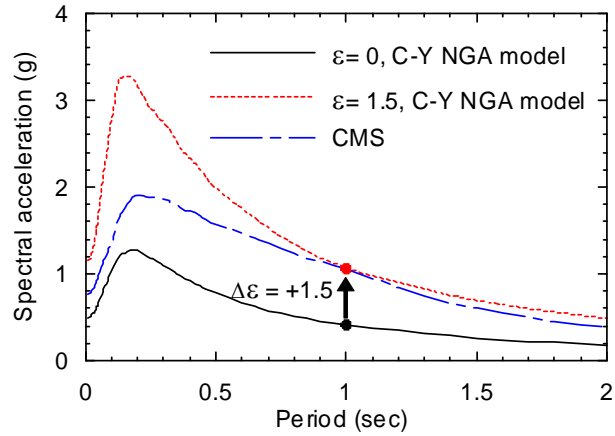
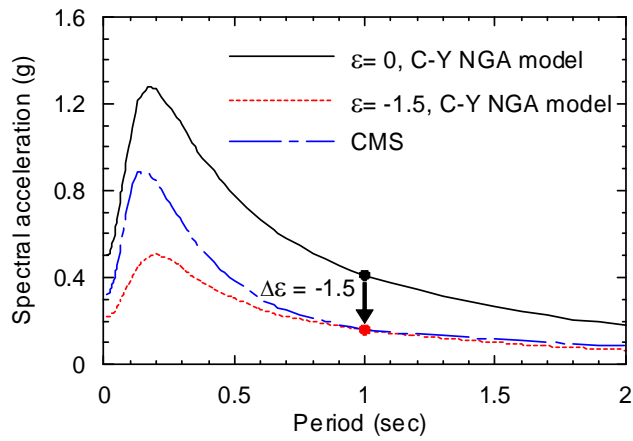


Figure D.2. Geometric-mean spectra for the records in the period bins P1 through P5 and the  $\epsilon$  bins of (2, 1), (1, 0), (0, -1) and (-1, -2)



a. positive  $\varepsilon$



b. negative  $\varepsilon$

**Figure D.3. Spectral accelerations predicted by Chiou-Youngs NGA relationship for a moment magnitude of 6.8, a site-to-source distance of 1.6 km and  $\varepsilon$  of 1.5, 0 and -1.5, and the corresponding CMS for  $\varepsilon$  of 1.5 and -1.5**

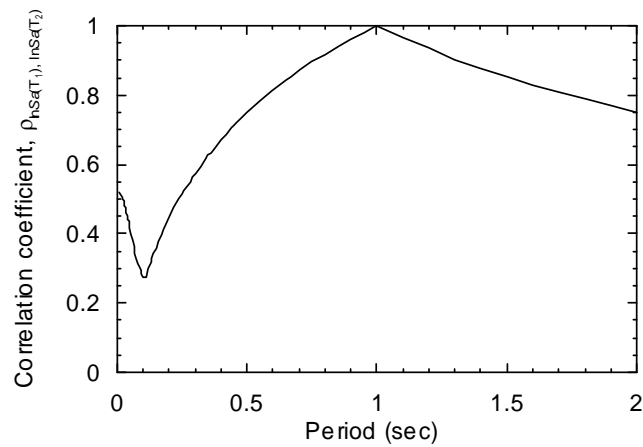
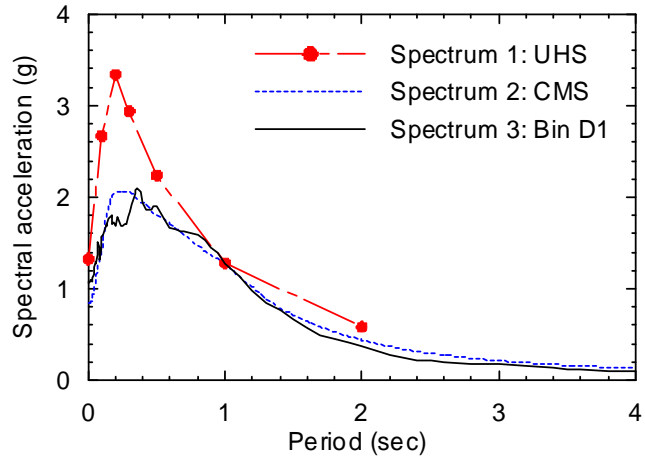
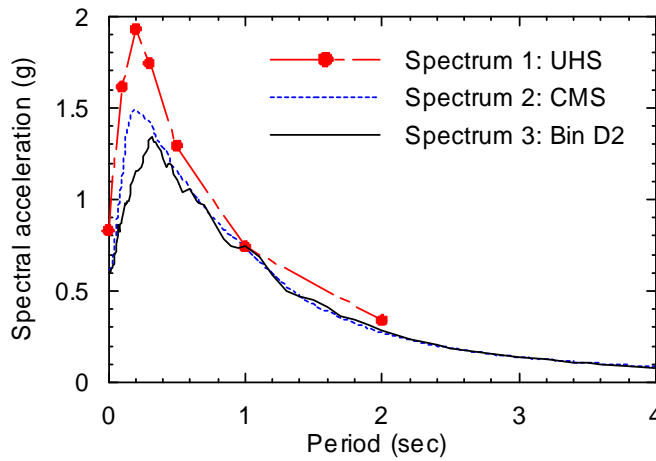


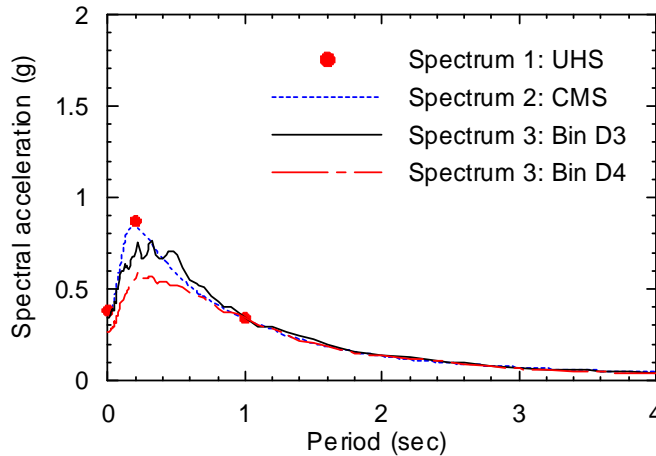
**Figure D.4. The correlation coefficient used to generate the CMS of Figure D.3**



a. 2% probability of exceedance in 50 years



b. 10% probability of exceedance in 50 years



c. 50% probability of exceedance in 75 years

**Figure D.5. UHS, CMS and the geomean spectral accelerations for sample earthquake records for a rock site at 122.2°W, 37.8°N and earthquake shaking return periods of 2475, 475 and 108 years**



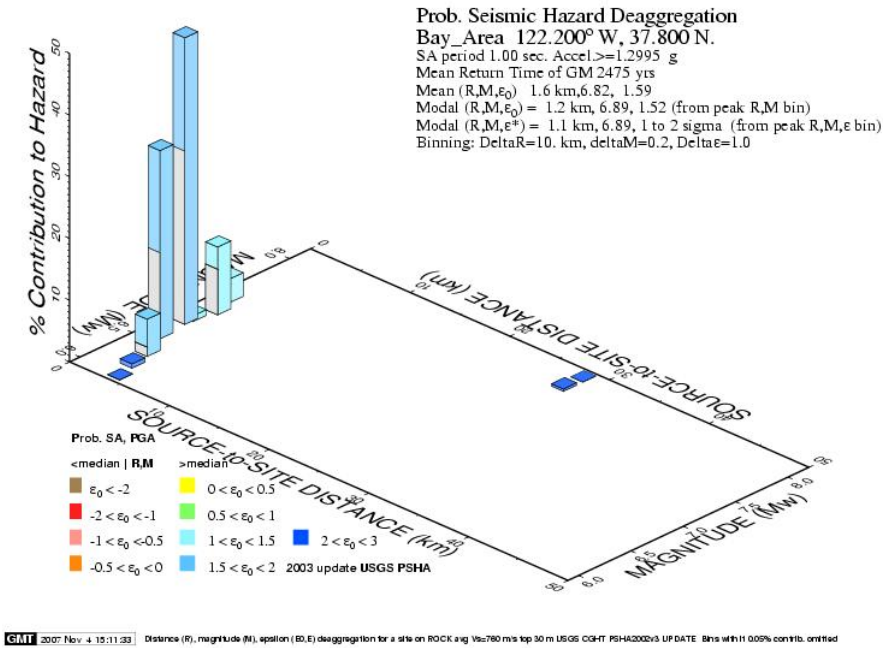


Figure D.6. Deaggregation of 1-second seismic hazard with 2% probability of exceedance in 50 years for a rock site at 122.2°W, 37.8°N

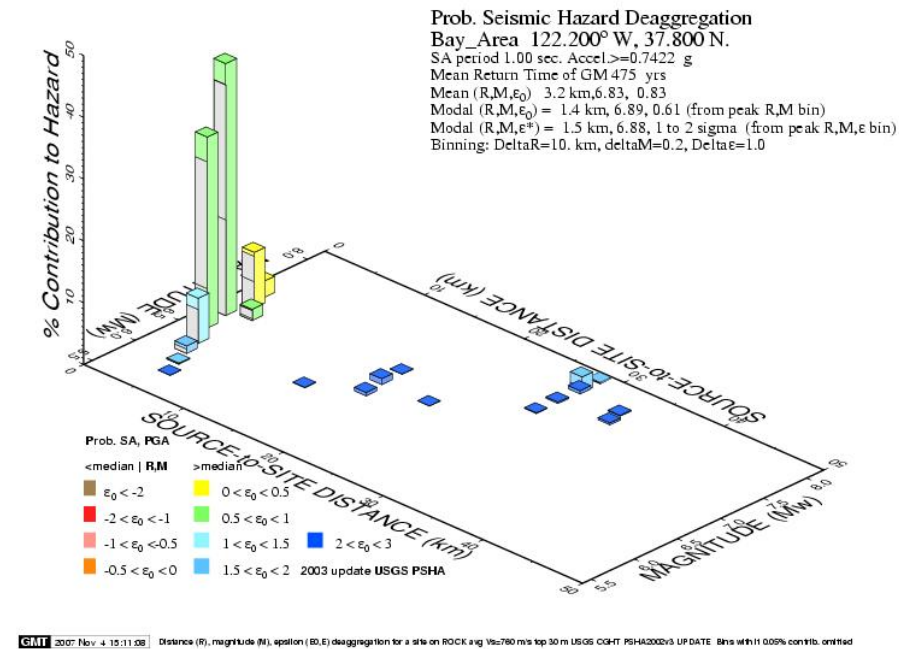


Figure D.7. Deaggregation of 1-second seismic hazard with 10% probability of exceedance in 50 years for a rock site at 122.2°W, 37.8°N

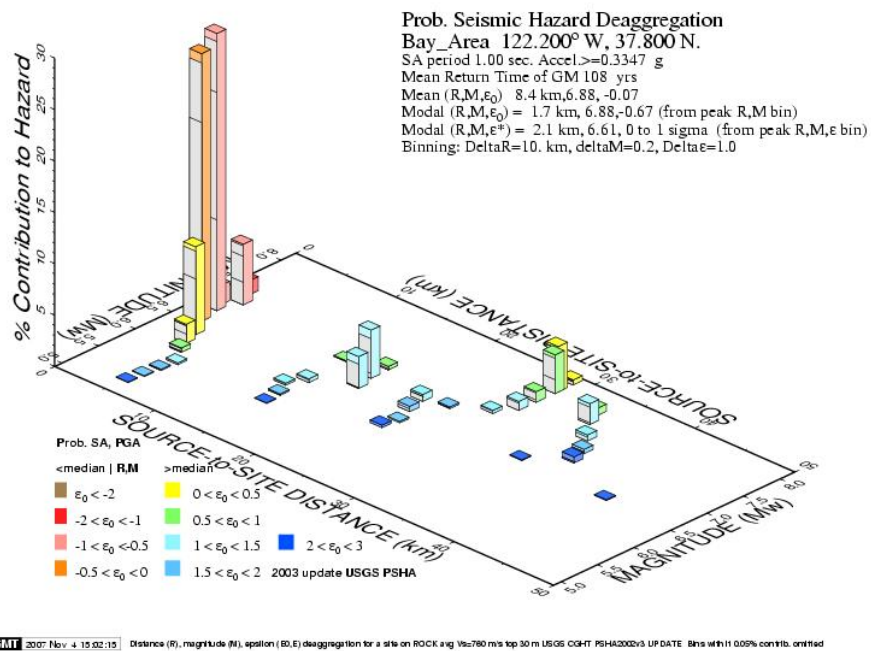


Figure D.8. Deaggregation of 1-second seismic hazard with 50% probability of exceedance in 75 years for a rock site at 122.2°W, 37.8°N

## APPENDIX E

### GEOMETRIC-MEAN SCALING METHOD

The geometric mean scaling method involves amplitude scaling a pair of ground motions by a single factor to minimize the sum of the squared errors between the target spectral values and the scaled geometric mean of the spectral ordinates for the pair,  $Q$

$$Q = \sum_{i=1}^n b_i (a \cdot y_i - \bar{y}_{T_i})^2 \quad (\text{E.1})$$

where  $b_i$  is the weighting factor for the residual value at period  $T_i$ ;  $a$  is the scaling factor for the pair of ground motions of interest;  $y_i$  is the geometric mean of the spectral ordinates for the pair at period  $T_i$ ;  $\bar{y}_{T_i}$  is the target spectral ordinate at period  $T_i$ ; and  $n$  is the number of target spectral values. The scaling factor,  $a$ , that minimizes the value of  $Q$  is computed as follows:

$$\frac{\partial Q}{\partial a} = 0 \Rightarrow \sum_{i=1}^n 2b_i y_i (a \cdot y_i - \bar{y}_{T_i}) = 0 \quad (\text{E.2})$$

$$a = \frac{\sum_{i=1}^n b_i \cdot y_i \cdot \bar{y}_{T_i}}{\sum_{i=1}^n b_i \cdot y_i^2} \quad (\text{E.3})$$

For the case with equal weighting factors,  $b_i$ , for all target periods

$$a = \frac{\sum_{i=1}^n y_i \cdot \bar{y}_{T_i}}{\sum_{i=1}^n y_i^2} \quad (\text{E.4})$$

Five pairs of far-field ground motions from Table 4.2 (termed Bin E0) and two sets of target spectral ordinates were selected to illustrate both the scaling procedure and the importance of selecting seed motions with the same spectral shape as the target spectrum. The five pairs of Bin E0 motions were scaled a) using the target spectral values of 1.34, 1.34 and 0.34g at periods of 0.3, 0.6 and 2 seconds, respectively, to produce Bin E1 motions, and b) using the target spectral values of 1.34, 0.8 and 0.34g at periods of 0.3, 0.6 and 2 seconds, respectively, to produce Bin E2 motions.

The median values of the 10 spectral accelerations for Bin E0 (5 pairs of motions times two components per motion), calculated using (A.5), at periods of 0.3, 0.6 and 2 seconds were 0.82, 0.79 and 0.27g, respectively. Amplitude scaling of these spectral ordinates by 1.6 produces accelerations of 1.31, 1.26 and 0.43g, respectively, and a spectral shape that is more consistent with the target spectrum for Bin E1 (1.34, 1.34 and 0.34g) than for Bin E2 (1.34, 0.80 and 0.34g).

Table E.1 and Table E.2 present calculations that illustrate the scaling process for Bins E1 and E2, respectively. The scaling factor,  $a$ , for each pair of ground motions was calculated using (E.4). The median  $\theta$  and dispersion  $\beta$  of the spectral accelerations for the ground motion bins E0, E1 and E2, calculated using (A.5) and (A.6), respectively, are listed in Table E.3. Figure E.1 presents the median spectral accelerations for the three ground motion bins. The change in the target spectral ordinate at 0.6 second period from 1.34g to 0.8g lowers the median spectral acceleration at all three periods but the shape of the median spectrum is unchanged as shown in Table E.4. Table E.4 shows the median spectral ordinates of the original, Bin E1 and Bin E2 ground motions at periods of 0.3, 0.6 and 2 seconds with the spectral values at 0.3 second normalized to 1.34g. The three normalized spectra are the same.

The dispersion  $\beta$  in the spectral accelerations is reduced by this scaling method. The reduction in  $\beta$  in the short period range (0.3 and 0.6 second) is greater than that at the long period range. This implies that the scaling is dominated by the target spectral ordinates in the short period range. Both  $y_i$  and  $\bar{y}_{T_i}$  in (E.4) are generally larger in the short period range than at long periods, which serves to reduce the quality of the match at longer periods. Table E.5 presents values of  $a$  using the target spectral values for Bin E1 motions at periods of a) 0.3, 0.6 and 2 seconds; b) 0.3 second only; and c) 2 seconds only. The values of  $a$  for case a) are much closer to those of case b) than case c), except for pair 4, in which the spectral ordinate at 0.6 second is greater than that at 0.3 second (see Table E.1) and dominates the scaling. Schemes that more heavily weight the residual value  $b_i$  at period  $T_i$  can be employed to improve the median match at  $T_i$  but at the expense of reducing the dispersion at  $T_i$ .

The advantages of the geometric mean scaling procedure to scale ground motions to a target spectrum include:

1. The scaling procedure is consistent with the methods used to process recorded ground motions for the purpose of developing attenuation relationships.
2. The correlation between the components of a ground motion pair is retained.

3. Some dispersion is retained in the ground motions.

The shortcomings of the procedure include:

1. The shape of the median spectrum of the seed motions must match that of the target spectrum, which substantially limits the general utility of the procedure if the target spectrum has a shape different from most recorded ground motions. The use of a period-limited target spectrum will enhance the utility of this scaling method.
2. Some of the dispersion in the seed ground motions is lost, with significant loss of dispersion at the periods associated with the matching procedure (0.3, 0.6 and 2 seconds in this instance).

**Table E.1 Spectral accelerations for the ground motion bins E0 and E1 at periods of 0.3, 0.6 and 2 seconds**

Pair no.	Spectral accelerations for original ground motions: Bin E0 (g)									$a$	Spectral accelerations for scaled ground motions: Bin E1 (g)								
	T= 0.3 sec			T= 0.6 sec			T= 2 secs				T= 0.3 sec			T= 0.6 sec			T= 2 secs		
	EQ1	EQ2	Geo. mean	EQ1	EQ2	Geo. mean	EQ1	EQ2	Geo. mean		EQ1	EQ2	Geo. mean	EQ1	EQ2	Geo. mean	EQ1	EQ2	Geo. mean
1	1.31	0.96	1.12	0.86	0.89	0.88	0.34	0.48	0.41	1.28	1.68	1.23	1.44	1.11	1.14	1.13	0.44	0.62	0.52
2	0.78	0.69	0.73	0.61	0.63	0.62	0.44	0.36	0.40	1.80	1.41	1.24	1.32	1.11	1.14	1.13	0.79	0.65	0.71
3	0.79	0.46	0.60	0.46	0.52	0.49	0.10	0.10	0.10	2.44	1.93	1.12	1.47	1.13	1.26	1.20	0.25	0.25	0.25
4	0.51	0.56	0.54	0.75	0.99	0.86	0.34	0.25	0.29	1.77	0.91	1.00	0.95	1.33	1.75	1.52	0.60	0.45	0.52
5	1.42	1.29	1.35	1.17	1.48	1.32	0.29	0.33	0.31	1.01	1.43	1.29	1.36	1.18	1.49	1.33	0.29	0.33	0.31

**Table E.2 Spectral accelerations for the ground motion bins E0 and E2 at periods of 0.3, 0.6 and 2 seconds**

Pair no.	Spectral accelerations for original ground motions: Bin E0 (g)									$a$	Spectral accelerations for scaled ground motions: Bin E2 (g)								
	T= 0.3 sec			T= 0.6 sec			T= 2 secs				T= 0.3 sec			T= 0.6 sec			T= 2 secs		
	EQ1	EQ2	Geo. mean	EQ1	EQ2	Geo. mean	EQ1	EQ2	Geo. mean		EQ1	EQ2	Geo. mean	EQ1	EQ2	Geo. mean	EQ1	EQ2	Geo. mean
1	1.31	0.96	1.12	0.86	0.89	0.88	0.34	0.48	0.41	1.07	1.40	1.03	1.20	0.92	0.95	0.94	0.36	0.52	0.43
2	0.78	0.69	0.73	0.61	0.63	0.62	0.44	0.36	0.40	1.49	1.17	1.03	1.10	0.92	0.94	0.93	0.65	0.53	0.59
3	0.79	0.46	0.60	0.46	0.52	0.49	0.10	0.10	0.10	2.01	1.59	0.93	1.21	0.93	1.04	0.98	0.21	0.21	0.21
4	0.51	0.56	0.54	0.75	0.99	0.86	0.34	0.25	0.29	1.35	0.69	0.76	0.73	1.01	1.34	1.16	0.46	0.34	0.40
5	1.42	1.29	1.35	1.17	1.48	1.32	0.29	0.33	0.31	0.81	1.16	1.04	1.10	0.95	1.20	1.07	0.23	0.27	0.25

**Table E.3. Median ( $\theta$ ) and  $\beta$  for spectral accelerations for all bins of ground motion**

Ground motion bin		$\theta$ for spectral acceleration (g)			$\beta$ for spectral acceleration		
		T= 0.3 sec	T= 0.6 sec	T= 2 secs	T= 0.3 sec	T= 0.6 sec	T= 2 secs
Original ground motions: Bin E0		0.82	0.79	0.27	0.41	0.36	0.54
Scaled motions: Bin E1	Target spectral ordinates	1.34	1.34	0.34	--	--	--
	Statistical results	1.30	1.25	0.43	0.23	0.15	0.42
Scaled motions: Bin E2	Target spectral ordinates	1.34	0.8	0.34	--	--	--
	Statistical results	1.05	1.01	0.35	0.25	0.13	0.42

**Table E.4. Normalized median spectral accelerations for all ground motion bins**

Ground motion bin	$\theta$ of spectral acceleration (g) (normalized to 1.34 g at T=0.3 sec)		
	T= 0.3 sec	T= 0.6 sec	T= 2 secs
Bin E0	1.34	1.29	0.45
Bin E1	1.34	1.29	0.45
Bin E2	1.34	1.29	0.45

**Table E.5. Variation in scale factor  $a$  as a function of spectrum matching periods**

Pair no.	$a$		
	Match at 0.3, 0.6 and 2 seconds	Match at 0.3 second only	Match at 2 seconds only
1	1.28	1.19	0.84
2	1.80	1.82	0.86
3	2.44	2.22	3.27
4	1.77	2.49	1.16
5	1.01	0.99	1.11



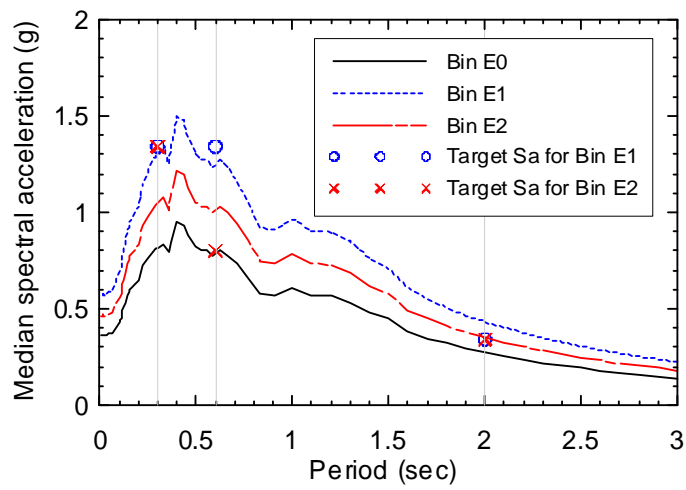


**Figure E.1. Median spectral accelerations for the ground motions bins E0, E1 and E2 and the target spectral accelerations for Bins E1 and E2**



## **APPENDIX F**

### **PERFORMANCE ASSESSMENT CONSIDERING VARIATIONS IN ISOLATOR MECHANICAL PROPERTIES**

#### **F.1 Treatment of Uncertainty of Isolator Properties for Performance Assessment**

Uncertainty in the numerical models used for response-history analysis of conventional and isolated NPPs was addressed in Chapter 3 but not included in the subsequent analysis because the uncertainties are unknown but likely much smaller than that associated with the earthquake ground motion.

Direct and indirect procedures to account for uncertainty in modeling of structural components such as shear walls were introduced in Chapter 3. The treatment of uncertainty in models of seismic isolators is discussed below. The impact of changes in key isolator mechanical properties (e.g., zero-displacement force intercept, yield displacement and post-yield stiffness in bilinear isolators) on demands on secondary systems in isolated NPPs is discussed in Section F.2.

Two direct and one indirect procedure for treating uncertainty in isolator mathematical models are presented here. All three procedures involve nonlinear response-history analysis. Regardless of the procedure chosen, it must be consistent with that used to treat uncertainty in the models of the structural components. The two direct procedures are

1. Develop a large family of numerical models of isolated NPPs with alternate isolator properties that capture the expected distributions of isolator properties over time.
2. Develop a smaller family of numerical models of isolated NPPs with upper (84th percentile) and lower (16th percentile) bound values for the isolator properties.

The second approach, albeit in the absence of explicit percentiles, has been incorporated in the AASHTO Guide Specification for Seismic Isolation Design (AASHTO, 1999) and the 2003 NEHRP Recommended Provisions (FEMA, 2004). Property modification factors are used to bound key material properties. Values for the factors are based on the studies of Constantinou et al. (1999) and Thompson et al. (2000).

The indirect procedure uses a best estimate mathematical model of the isolated NPP and adjusts the dispersions in the computed responses by a single value to account indirectly for uncertainty in isolator and superstructure mechanical characteristics. The implementation of this procedure, which is the least

computationally expensive of the three, would require estimation of the modeling dispersion by analysis of archetype isolated NPPs equipped with isolators that are appropriate for nuclear construction.

## **F.2 Impact of Choice of Isolator Properties on the Results of a Performance Assessment**

Section F.1 introduced direct and indirect procedures to account for uncertainty in isolator models. The discussion is extended below to a) identify how isolator properties can be selected to minimize seismic demands on secondary systems in NPPs, and b) show the impact of variations in isolator properties on the performance of an isolated NPP.

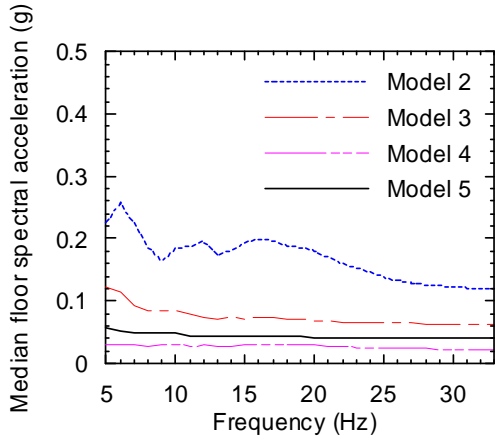
Of the three key isolator mechanical properties identified in Section F.1, variations in yield displacement will likely have the greatest impact on the response of secondary systems in isolated NPPs. In lieu of conducting an extensive Monte Carlo analysis to assess the impact of changes in yield displacement on floor spectra in isolated NPPs, the scenario analysis of Section 5.3 was repeated using Model 3 with an upper bound estimate of yield displacement of 25 mm (Model 5). Such a displacement could be achieved in FP bearings using the triple concave construction (Fenz and Constantinou, 2008). A 25-mm yield displacement could be achieved by adjusting the dimensions of the lead core and the rubber in the LR bearing.

The results of the analysis are presented in Figure F.1 and Figure F.2 using median floor spectral acceleration and AFSA in the X and Y directions, respectively, at nodes 201, 1009 and 216. For FP bearings, the impact of the increase in yield displacement from 1 mm (conventional FP bearings) to 25 mm (triple concave FP bearings) can be seen by comparing results for Models 2 and 5, namely, the increase in yield displacement leads to a significant reduction in the median floor spectral acceleration at all three nodes and dispersion in the acceleration response. For LR bearings, the impact of the increase in yield displacement from 7 mm to 25 mm can be seen by comparing results for Models 3 and 5; the increase in yield displacement also reduces the median floor spectral acceleration at all three nodes; the dispersion in the acceleration response is similar in both cases. The ratio of median AFSA of Model 5 to Model 2 and of Model 5 to Model 3 at nodes 201, 1009 and 216 are presented in Table F.1.

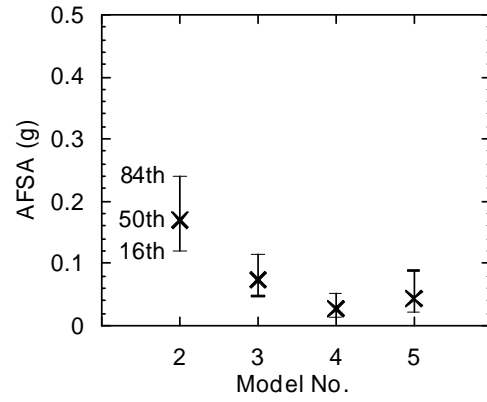
Analysis 3e of Section 5.3.4.1 was repeated for Model 5. The value of the reduction factor  $R_a$  for a probability of unacceptable performance of 0.51 conditioned on the scenario event is 0.027, equal to 23% of the value for Model 2 and 57% of the value for Model 3.

**Table F.1. Ratios of median AFSA of Models 5 and 2 and those of Models 5 and 3 in the X direction for the scenario-based assessment**

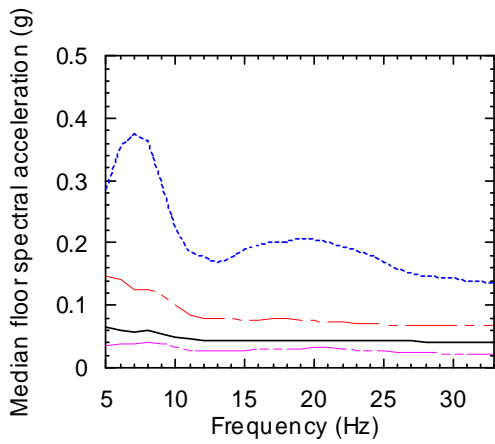
Orientation	$\frac{\text{Model 5}}{\text{Model 2}}$			$\frac{\text{Model 5}}{\text{Model 3}}$		
	Node 201	Node 1009	Node 216	Node 201	Node 1009	Node 216
X	0.26	0.23	0.15	0.59	0.55	0.45
Y	0.26	0.22	0.13	0.60	0.56	0.44



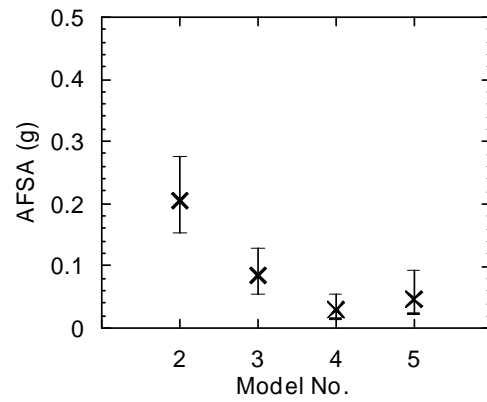
a. Median floor spectral accelerations, Node 201



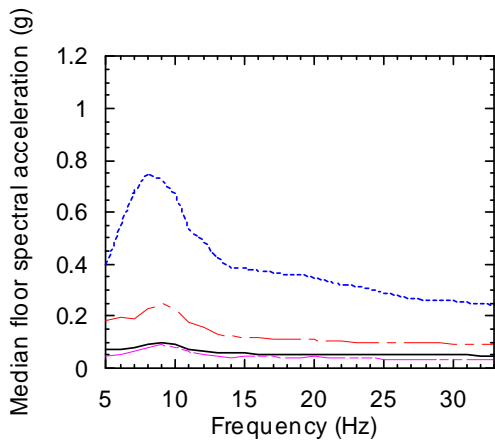
b. AFSA, Node 201



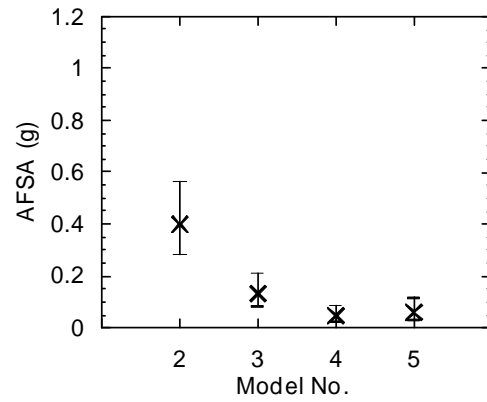
c. Median floor spectral accelerations, Node 1009



d. AFSA, Node 1009

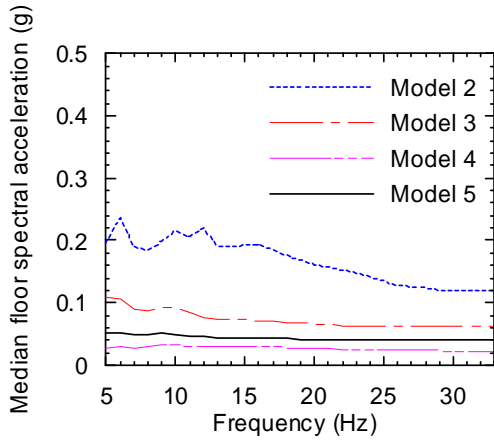


e. Median floor spectral accelerations, Node 216

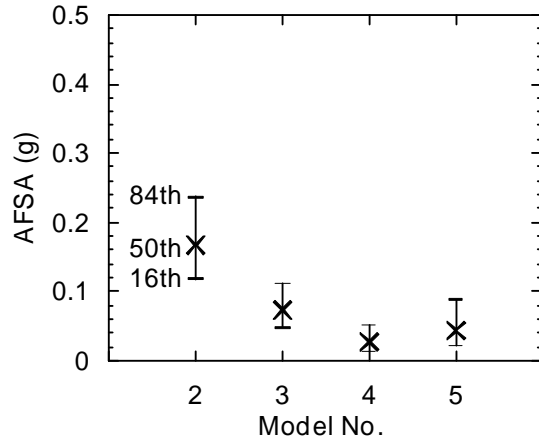


f. AFSA, Node 216

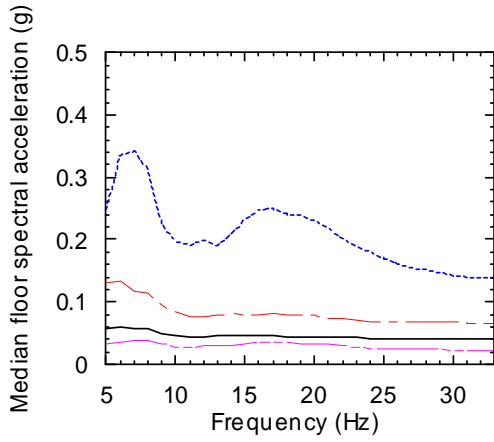
**Figure F.1. Floor spectral accelerations at Nodes 201, 1009 and 216 in the X direction for the scenario-based assessment of Models 2, 3, 4 and 5**



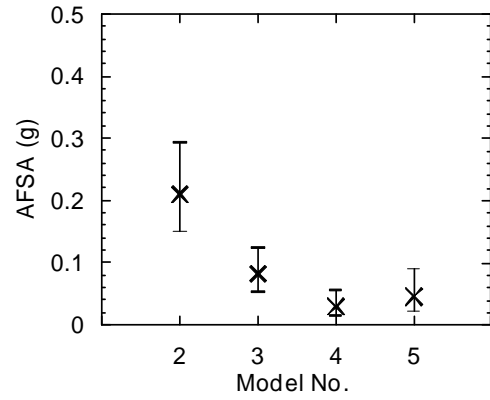
a. Median floor spectral accelerations, Node 201



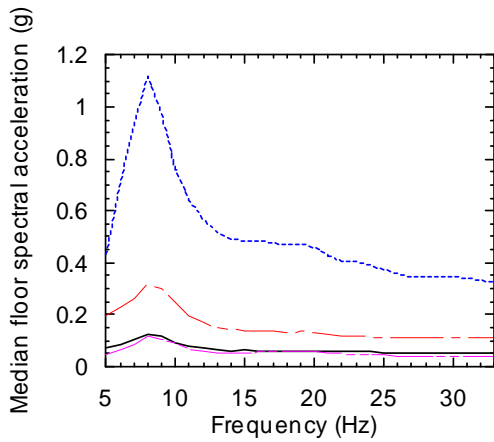
b. AFSA, Node 201



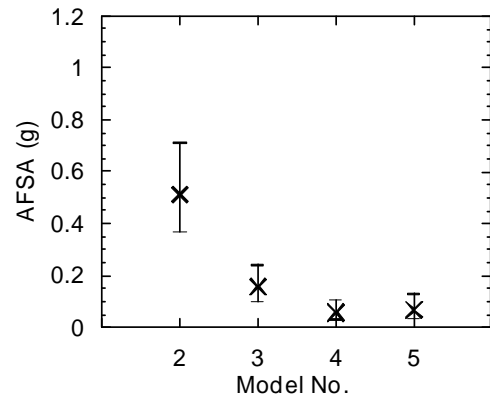
c. Median floor spectral accelerations, Node 1009



d. AFSA, Node 1009



e. Median floor spectral accelerations, Node 216



f. AFSA, Node 216

**Figure F.2. Floor spectral accelerations at Nodes 201, 1009 and 216 in the Y direction for the scenario-based assessment of Models 2, 3, 4 and 5**

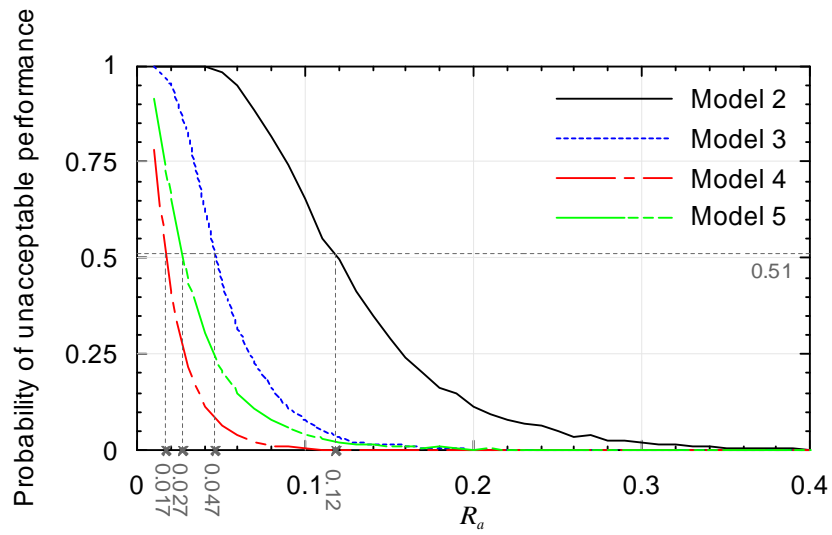


**Figure F.3. Probability of unacceptable performance as a function of the median-capacity ratio of fragility curves using Analysis 3e of Section 5.3.4.1 for the scenario-based assessment of Models 2, 3, 4 and 5**



# APPENDIX G

## AIR BLAST LOADS ON SIMPLE AND COMPLEX OBJECTS

### G.1 Introduction

Hydrocodes (or CFD codes) can be used to compute pressure and loading histories on buildings of regular and irregular geometry. Examples of hydrocodes are LSDYNA (LSTC 2003) and Autodyn ([www.ansys.com](http://www.ansys.com)); examples of CFD codes are Air3D (Rose 2006) and STAR ([www.cd-adapco.com](http://www.cd-adapco.com)). Two examples of CFD analysis were performed using Air3D and the results are presented below to identify the need to perform a CFD or hydrocode analysis for capturing a blast-induced loading environment on structural shape or framing system. For pressure and temperature analysis in the fireball (or near-field), CFD analysis is approximate because the flow field is dominated by the expanding detonation products. Rigorous analysis in the near-field should be performed with a hydrocode.

### G.2 Simple Objects

#### G.2.1 Two-Dimensional Case

The example of Section G.2.1 addresses two-dimensional flow around a 30×30 m object subjected to a rigid surface detonation of 300.8 kg of TNT (hemispherical surface burst explosion) at 30 m from the front face of the object, centered on the object.

Figure G.1 presents the geometry of this example. As shown in Figure G.1, twenty five monitoring locations were specified; location 1 is at the center of the object (seeing normal reflection) and all other 24 monitoring locations were equally spaced across the front face. Figure G.2 presents overpressure contour plots for this example at selected times. The reflection of the incident wave, the interaction between the incident wave, reflected wave and square object can be clearly observed in Figure G.2.

Figure G.3 presents two translational loading histories (kN per meter of height) for the object analyzed in this example: one was computed using the pressure history at location 1 multiplied by 30 m and the other was computed using the sum of the product of the pressure history at each of the other 24 monitoring locations and its tributary length on the front face of the object. It is clear that discretization of the front face of the building produces substantially smaller translational forces and modestly smaller impulses than those conservatively computed using the maximum reflected pressure and impulse.

### ***G.2.2 Three-Dimensional Cases***

The example of this subsection adds height to the object of Section G.2.1 to model a regular building with a rigid, infinitely strong facade. Assume that the building is 20 m in height and that the explosion is again a hemispherical surface burst. The geometry of this example is presented in Figure G.4, where the standoff distance,  $R$ , is 30 m. Twenty-four monitoring locations were distributed across the face of the building in 4 equally spaced rows over the height (2.5, 7.5, 12.5 and 17.5 m) for a total of 96 monitoring locations as shown in Figure G.5. Three monitoring locations are identified in Figure G.5 for the purpose of data presentation. Location 1 is closest to the explosive and locations 2 and 3 are at the left lower and left upper corner of the front face, respectively. Figure G.6 presents translational load histories based on a) monitoring location 1 of Figure G.5 only, and b) all 96 monitoring locations. The differences in the peak net translational load and impulse are substantial.

The above analysis was repeated but for a standoff distance of 15 m. Results are presented in Figure G.7. The two loading regimes in the figure are substantially different and indicate the need to consider target geometry and complex loading environment in the calculation of structural response.

The difference in the two translational load histories of Figure G.7 can be explained using Figure G.8a, which presents the overpressure histories at locations 1, 2 and 3. The peak reflected overpressures, impulses and arrival times for the pressure histories of Figure G.8a are presented in Table G.1. The peak reflected pressure and impulse drops quickly as the distance and angle of incidence from the explosive to the monitoring point increase. This observation explains the significant differences in peak translational load and impulse for the two curves of Figure G.7.

Figure G.8a also shows that the positive overpressure at location 1 had almost diminished before the shock wave reached location 2. When the shock wave arrived at location 3, the reflected overpressures at location 1 and 2 had entered the negative phase. This loading environment explains the differences in shape and positive phase duration for the two curves of Figure G.7.

To compare the shapes of the pressure histories of Figure G.8a, the pressure histories at locations 2 and 3 were shifted in time and amplitude scaled to have the same arrival time and peak reflected overpressure as that at location 1. The shapes of the curves at locations 2 and 3 are very similar although that at location 1 decays faster. One might expect near instantaneous clearing of the reflected pressure to the stagnation pressure at locations 2 and 3 per traditional computations such as TM5-1300, but the rarefaction wave cannot propagate from these two locations back towards location 1 and clearing cannot occur.

### G.3 Complex Objects

The flow of a blast wave around a solid tube is most complex, as identified by Baker (1973) and as shown in Figure G.9. In this figure I is the incident wave, R is the reflected wave, M is the Mach stem, and S denotes a slipstream (divides flows of same pressures but different densities). Figure G.9 chronicles the interaction of a shock front with a cylinder over time, including the reflection of the incident wave, the development of Mach stems and the formation and growth of vortices.

This subsection presents a two-dimensional analysis of 0.5 m diameter tube subjected to a free-air burst of 10 kg of TNT at a (clear) standoff distance of 5 m. Figure G.10 presents overpressure contour plots at selected times, illustrates the complexity of the loading regime and identifies some of the features shown in Figure G.9. The detonation was initiated at (0, 7.5 m) for radial distance and vertical height, respectively, as shown in the figure.

Panel a of Figure G.10 presents the overpressure contour plot when the shock wave first reached the solid tube. Figure G.10a shows high pressures near the point of detonation, which are due to the implosion of the rarefaction wave and its subsequent reflection. As a point of reference, the overpressure associated with the primary shock front at a distance of 2 m was 1.4 MPa (see Figure G.11): approximately 70 times greater than the overpressure associated with the secondary shock front of approximately 20 kPa. In panels b through h of Figure G.10, the reflection of the incident wave and the formation of Mach stems can be seen.

The net translational pressure history in the direction of the flow is presented in Figure G.12. For this example, the peak translational load (impulse) per unit width in the direction of the flow is 0.114 MN (0.098 MN-msec). As a point of comparison, the peak translational load (impulse) per unit length of tube, assuming a plane projected width of 500 mm at 5 m, is 0.21 MN (0.213 MN-msec) ignoring clearing and 0.21 MN (0.124 MN-msec) including the effects of clearing per TM5-1300: a negligible reduction in the peak translational load but a 42% reduction in the impulse. The consideration of shape (circular vs. plane) leads to a 46% reduction in the load and a 54% reduction in the impulse, with respect to the benchmark analysis of a plane front with an infinite reflecting surface.

**Table G.1. Peak reflected overpressures, impulses and arrival times for the pressure histories of Figure G.8a**

Location	Peak reflected overpressure (kPa)	Reflected impulse (kPa-msec)	Arrival time (msec)
1	580	2200	13
2	272	1110	23
3	153	697	37

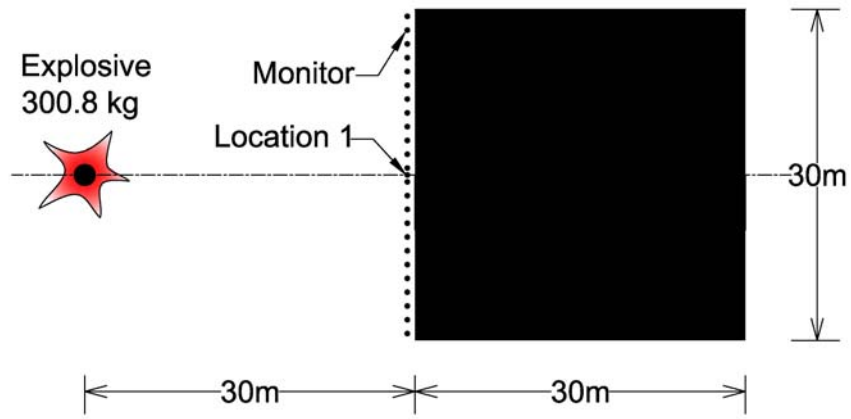
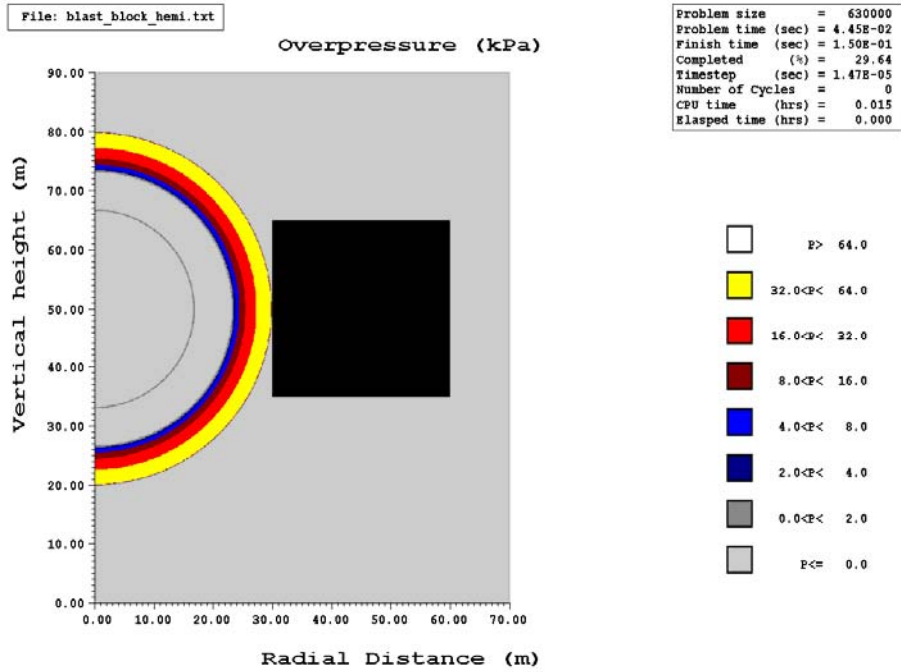
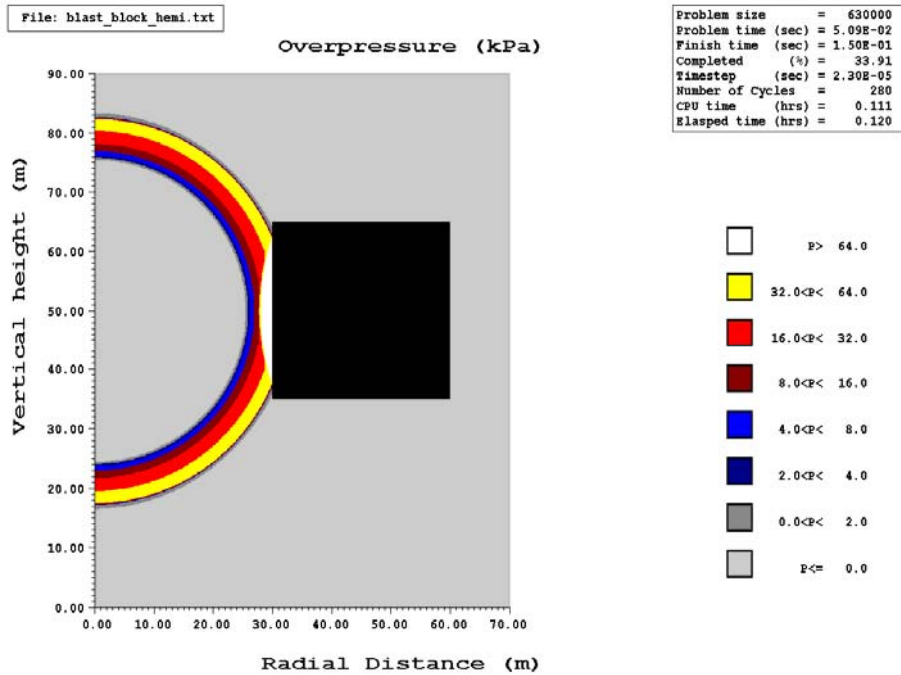


**Figure G.1. Blast analysis of Section G.2.1 for a 30×30 m object**

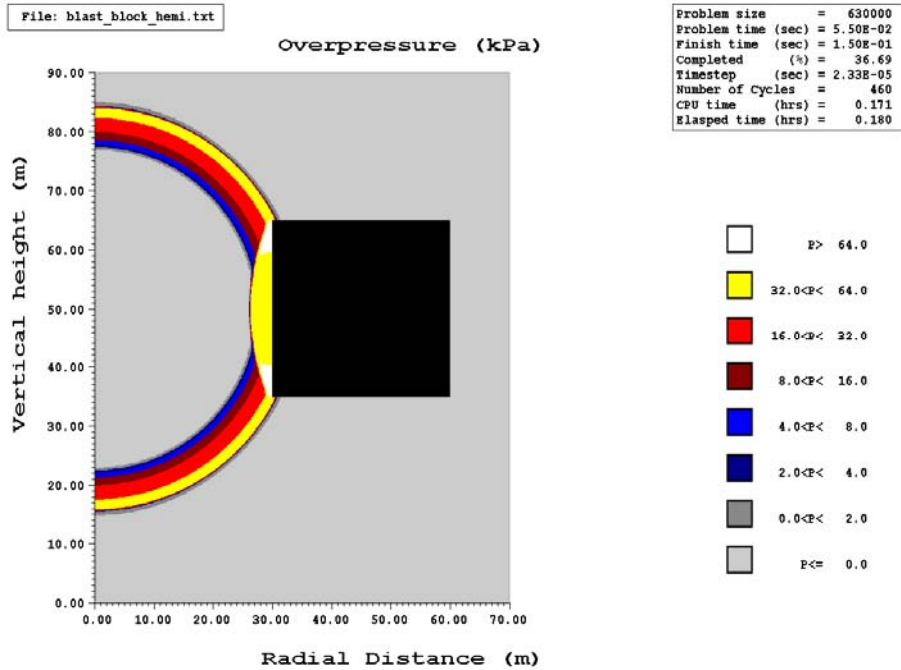


a. Time = 45.5 msec after detonation

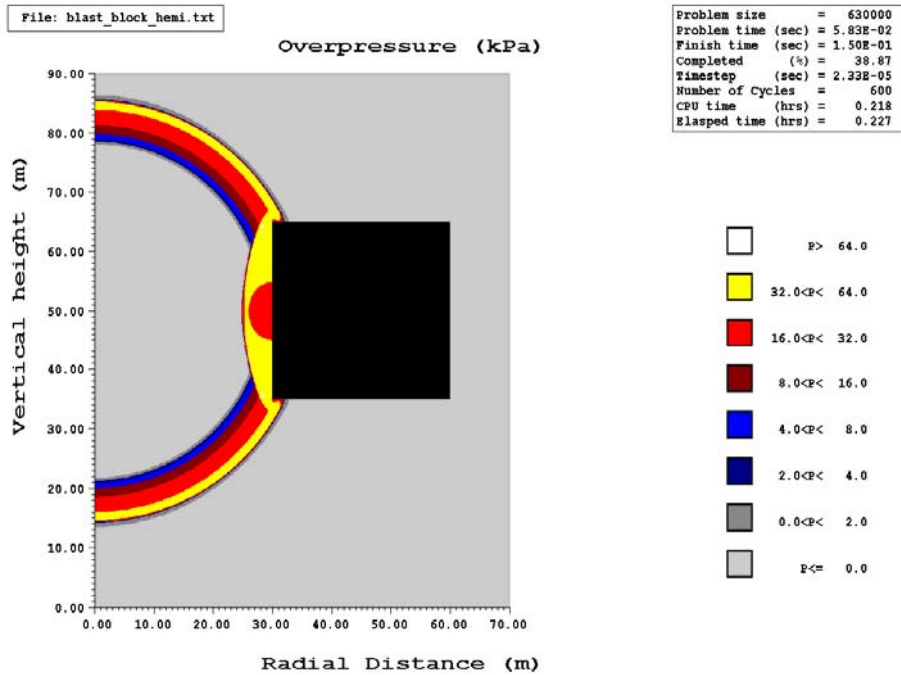


b. Time = 50.9 msec after detonation

Figure G.2. Pressure contour plots for the blast analysis of Section G.2.1

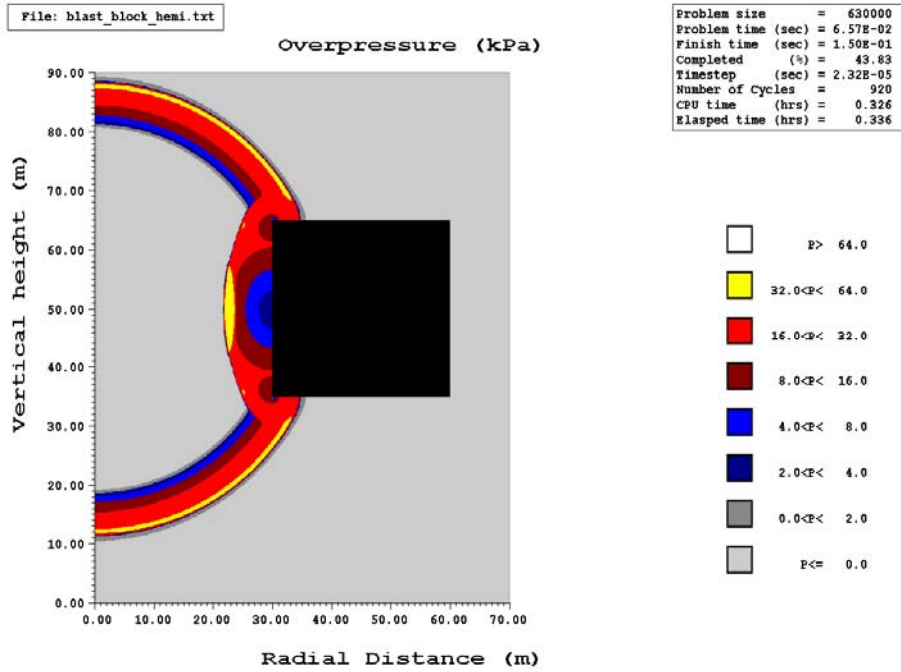


c. Time = 55.0 msec after detonation

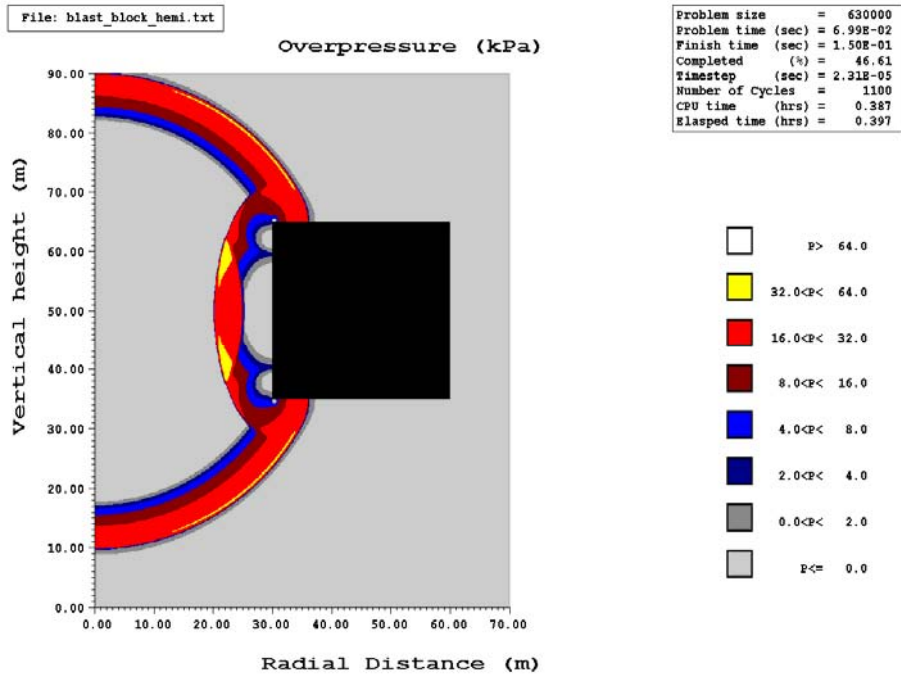


d. Time = 58.3 msec after detonation

Figure G.2. Pressure contour plots for the blast analysis of Section G.2.1 (continued)



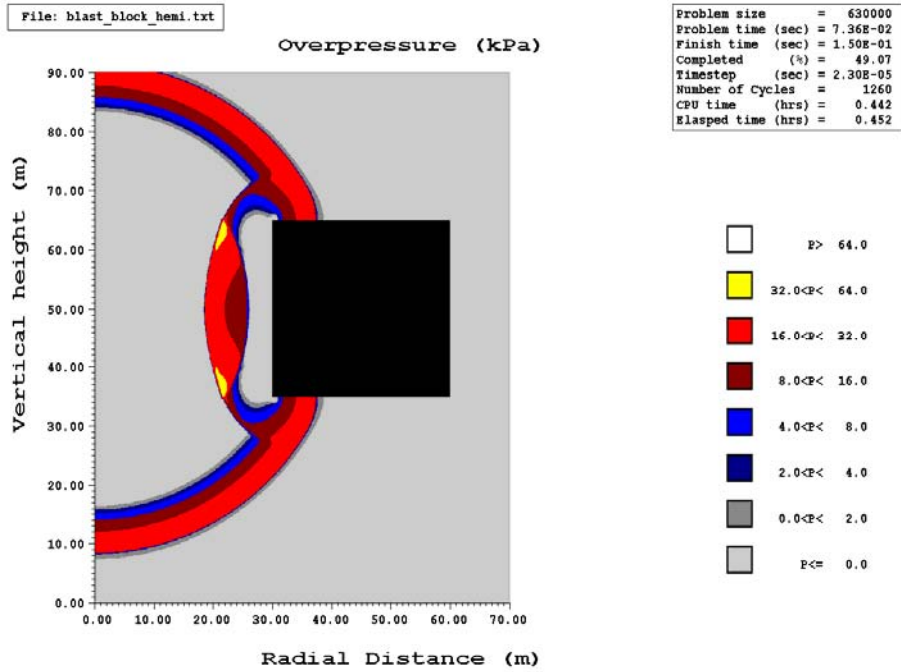
e. Time = 65.7 msec after detonation



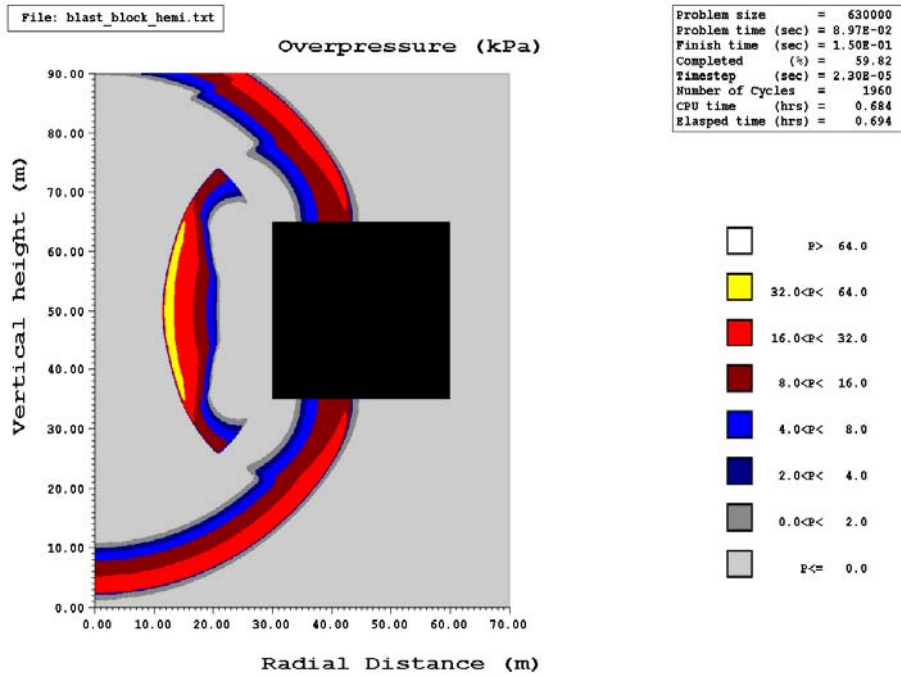
f. Time = 69.9 msec after detonation

Figure G.2. Pressure contour plots for the blast analysis of Section G.2.1 (continued)





g. Time = 73.6 msec after detonation



h. Time = 89.7 msec after detonation

Figure G.2. Pressure contour plots for the blast analysis of Section G.2.1 (continued)

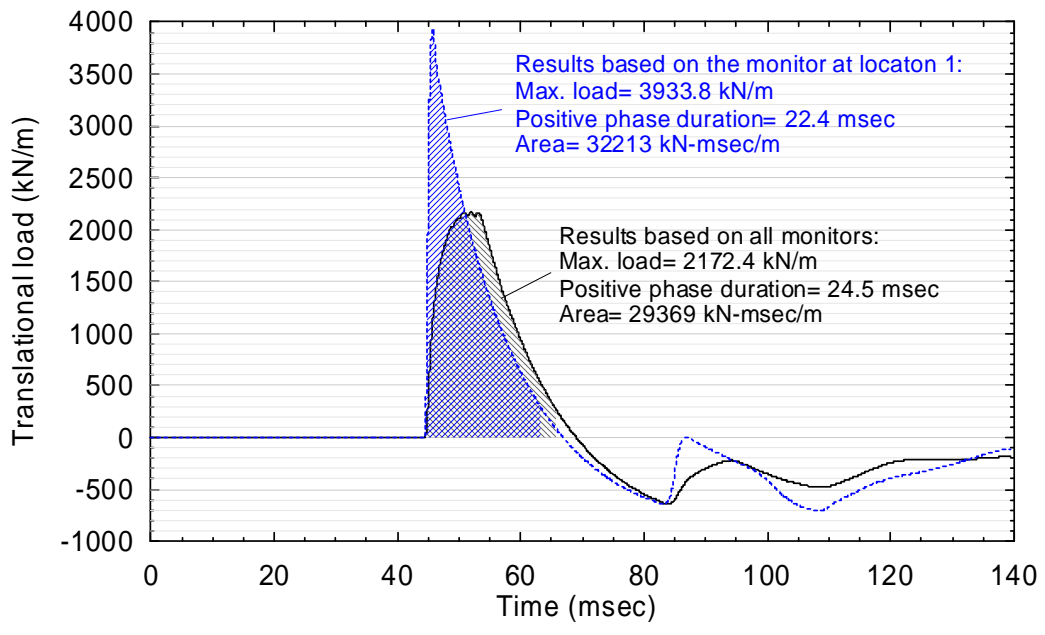


**Figure G.3. Translational load histories for the analysis of Section G.2.1**

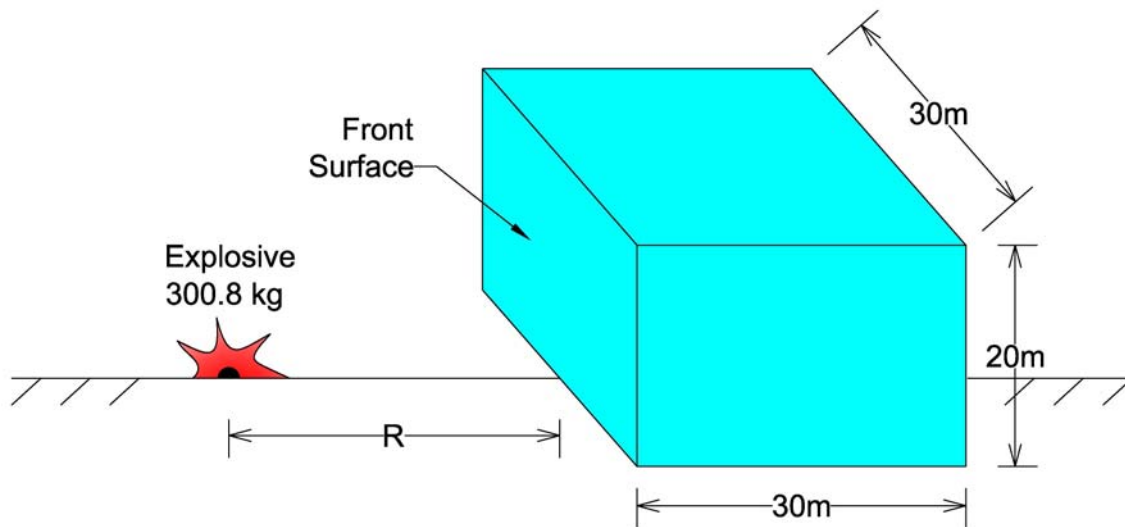


Figure G.4. Blast analysis of Section G.2.2 for a 30×30×20 m object

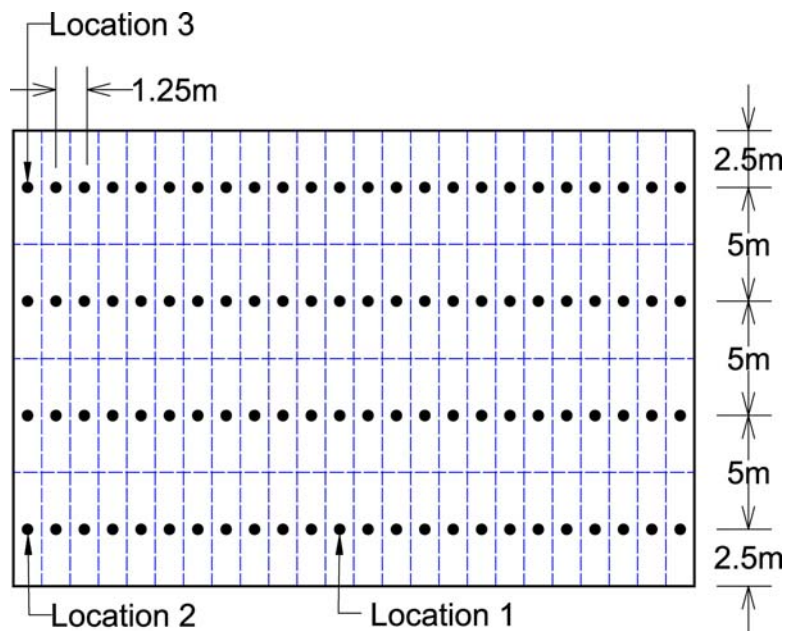


Figure G.5. Distribution of pressure monitors on the front surface of the object of Figure G.4

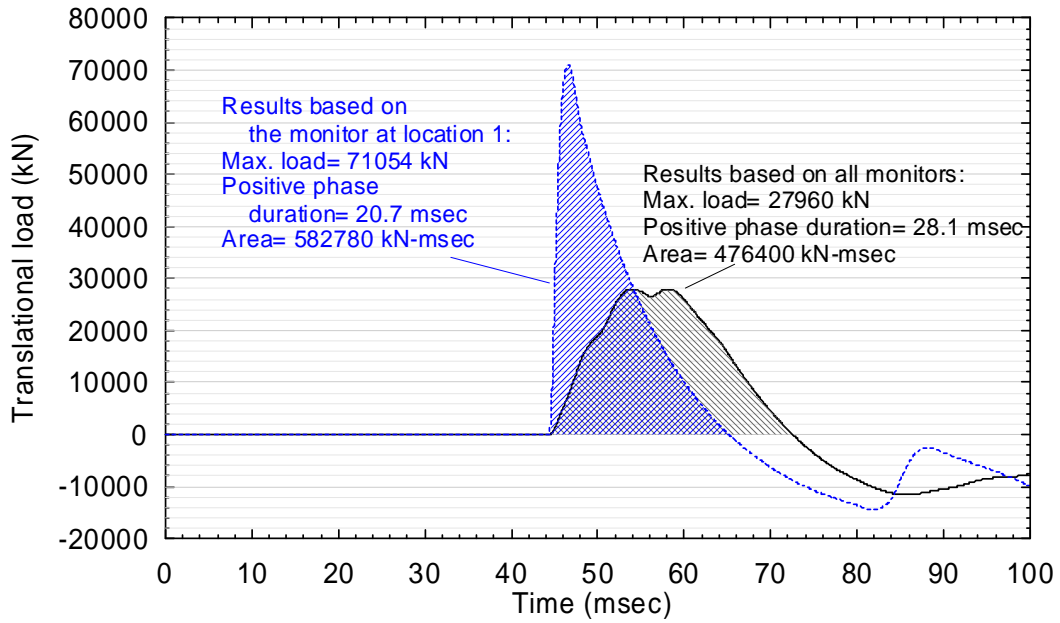


Figure G.6. Translational load histories for the analysis of Figure G.4 with R= 30 meters

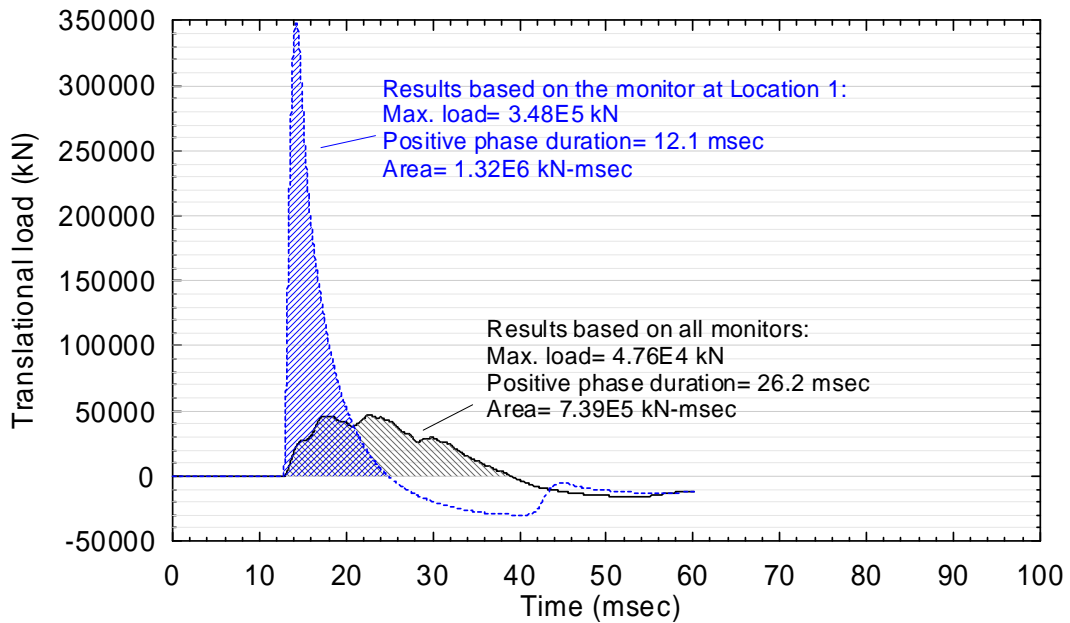
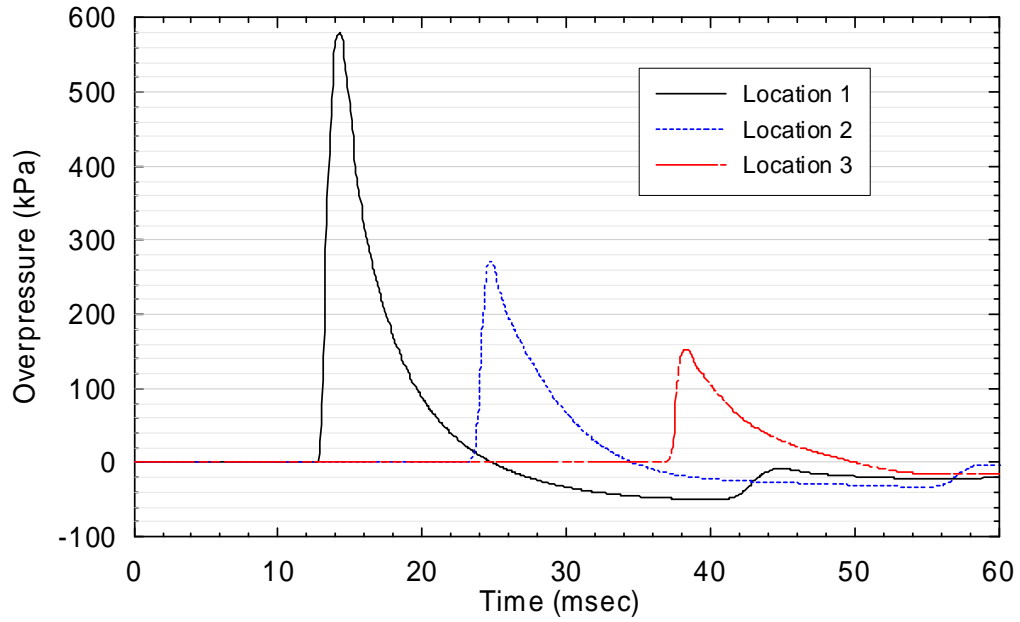
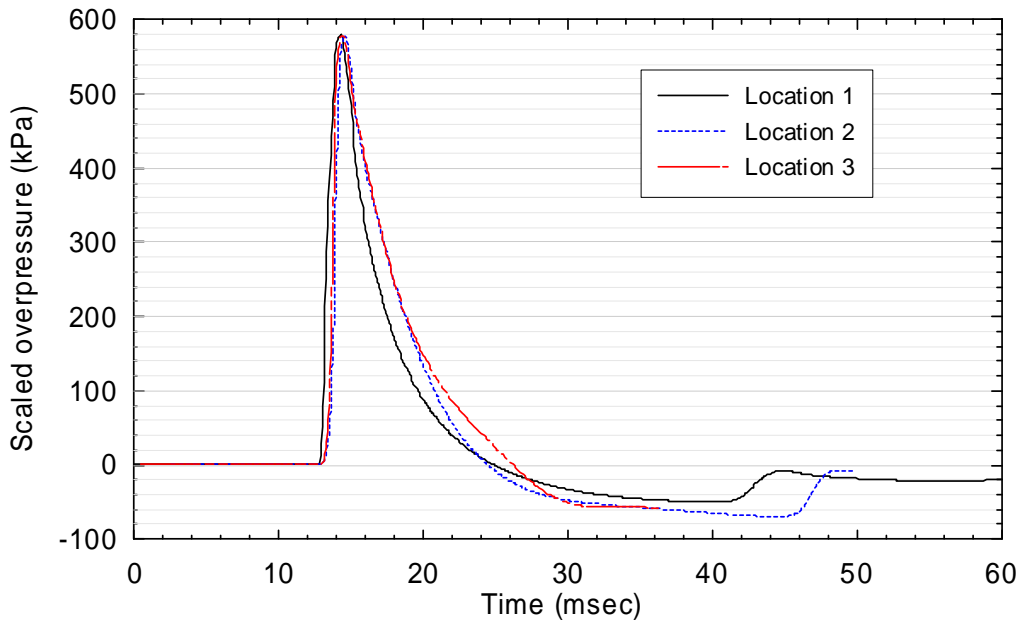


Figure G.7. Translational load histories for the analysis of Figure G.4 with R= 15 meters



a. Original results



b. Scaled results for shape comparison

**Figure G.8. Pressure histories for the analysis of Figure G.4 with R= 15 meters at locations 1, 2 and 3 of Figure G.5**

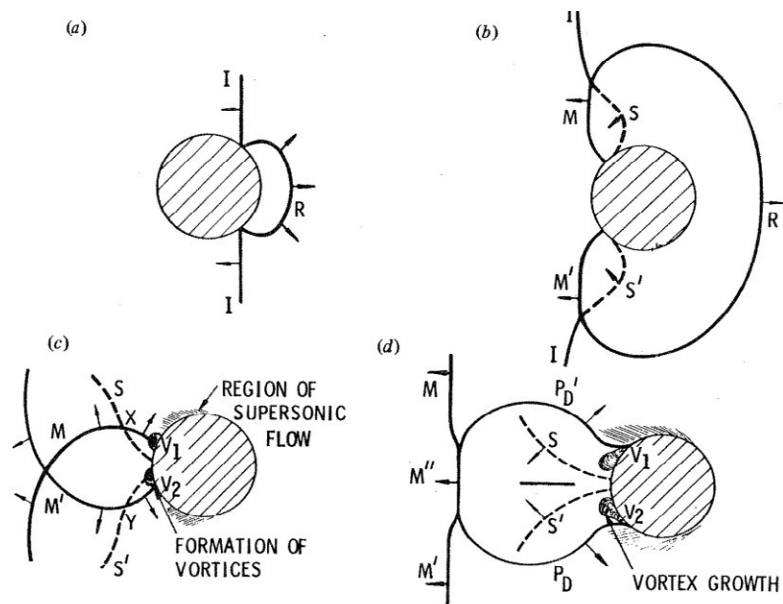
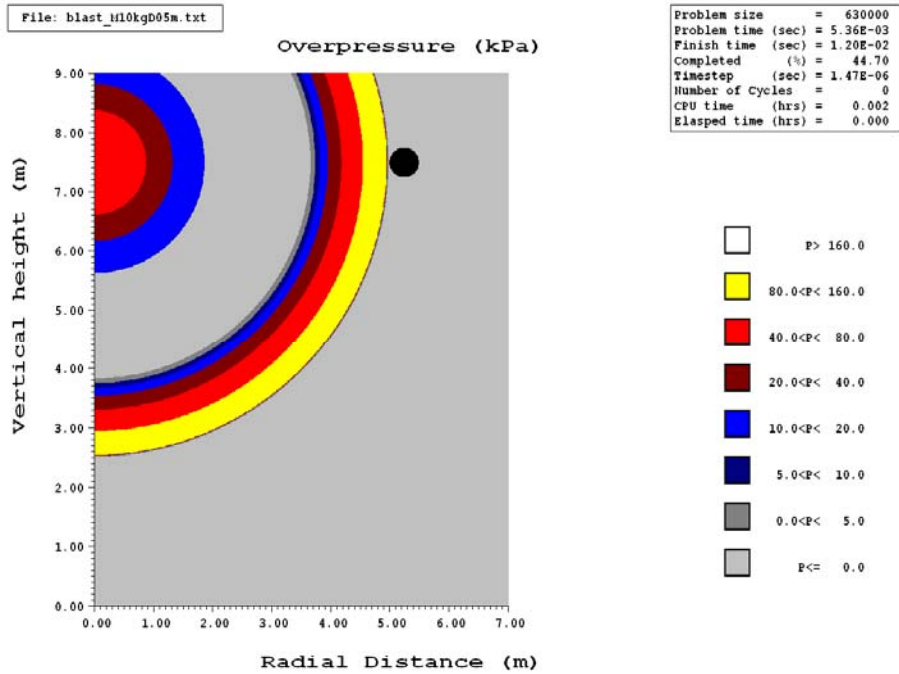
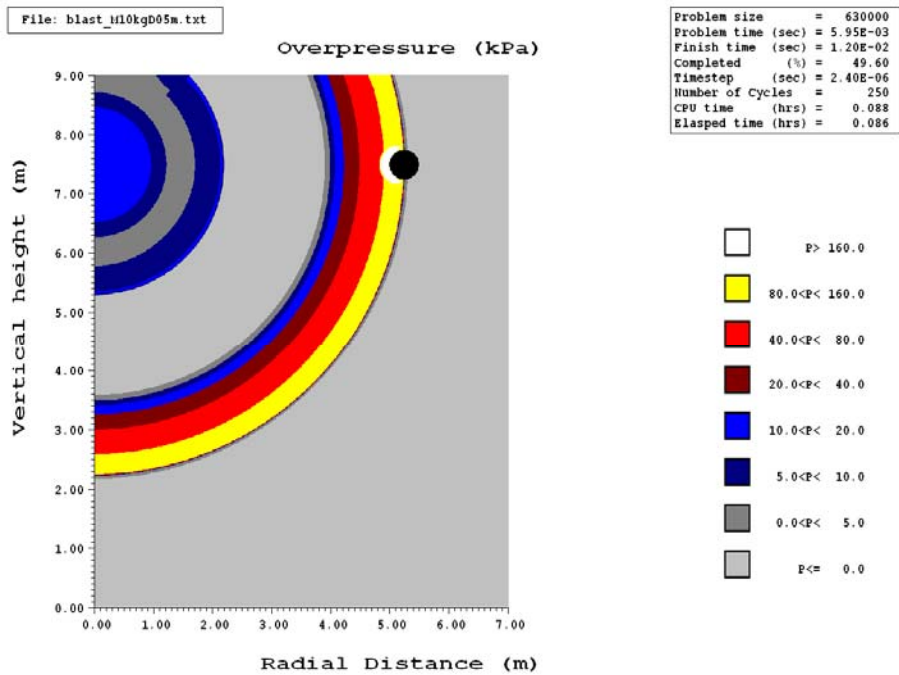


Figure G.9. Interaction of a shock front with a cylinder (Baker 1973)

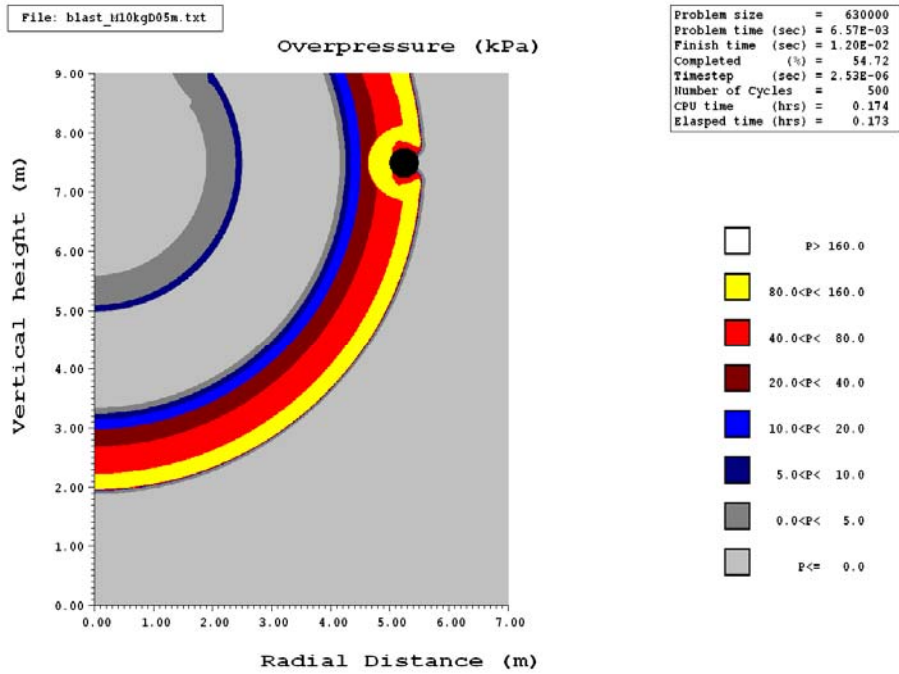


a. Time = 5.36 msec after detonation

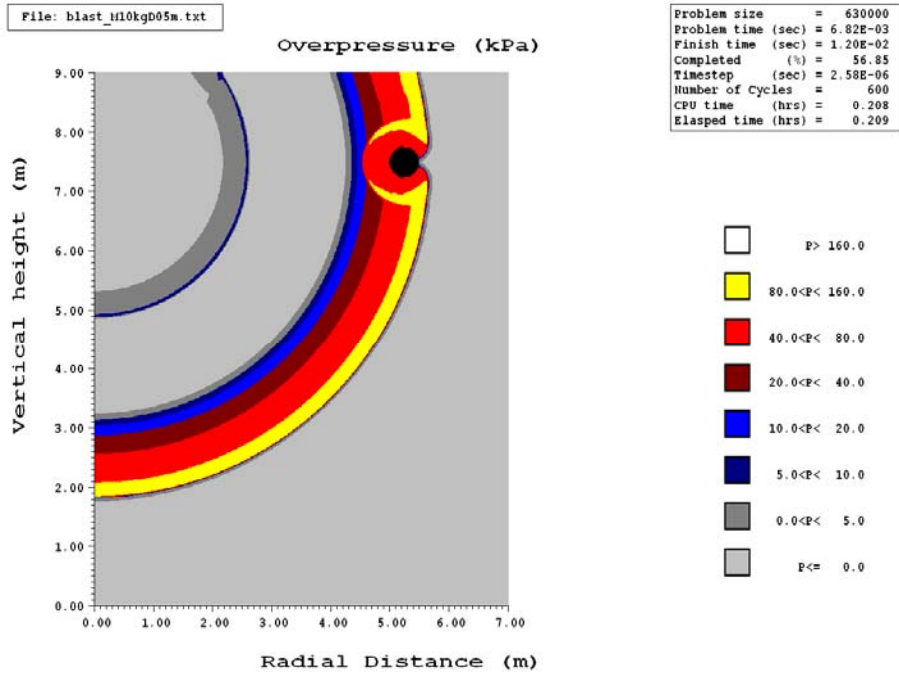


b. Time = 5.95 msec after detonation

**Figure G.10. Pressure contour plot for the blast analysis of Section G.3**



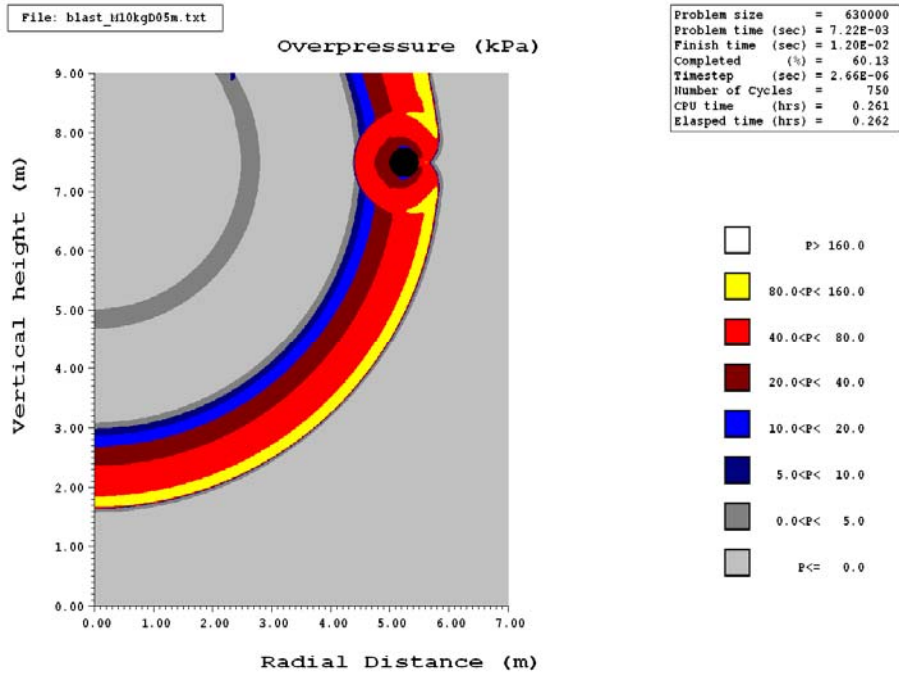
c. Time = 6.57 msec after detonation



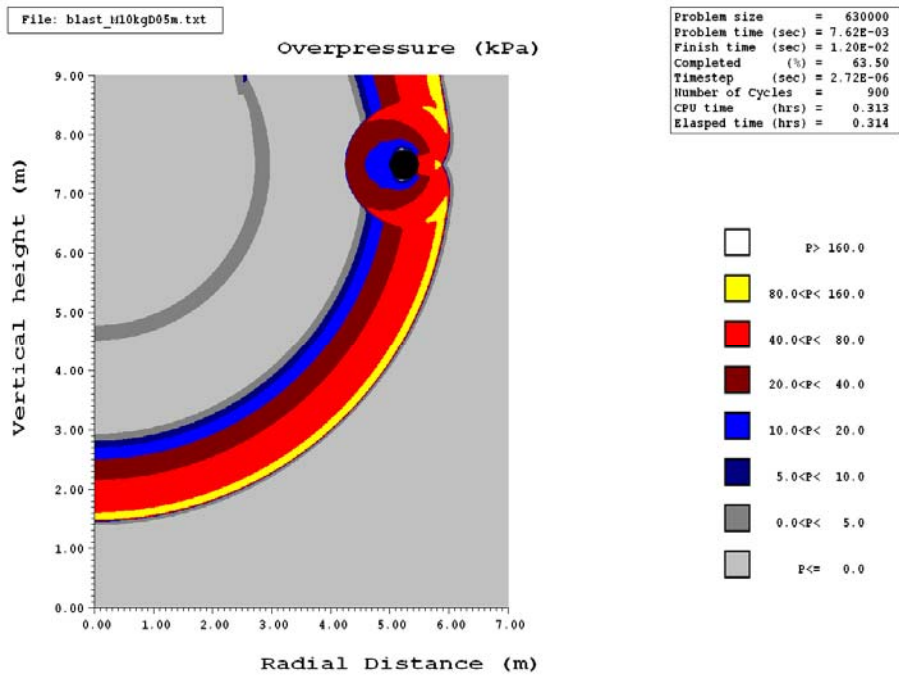
d. Time = 6.82 msec after detonation

Figure G.10. Pressure contour plot for the blast analysis of Section G.3 (continued)



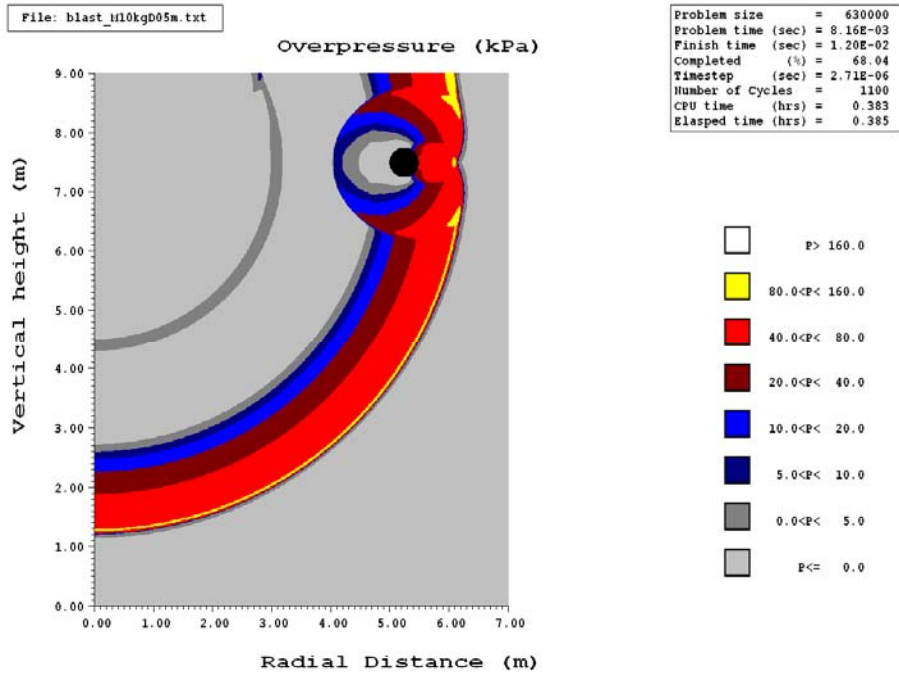


e. Time = 7.22 msec after detonation

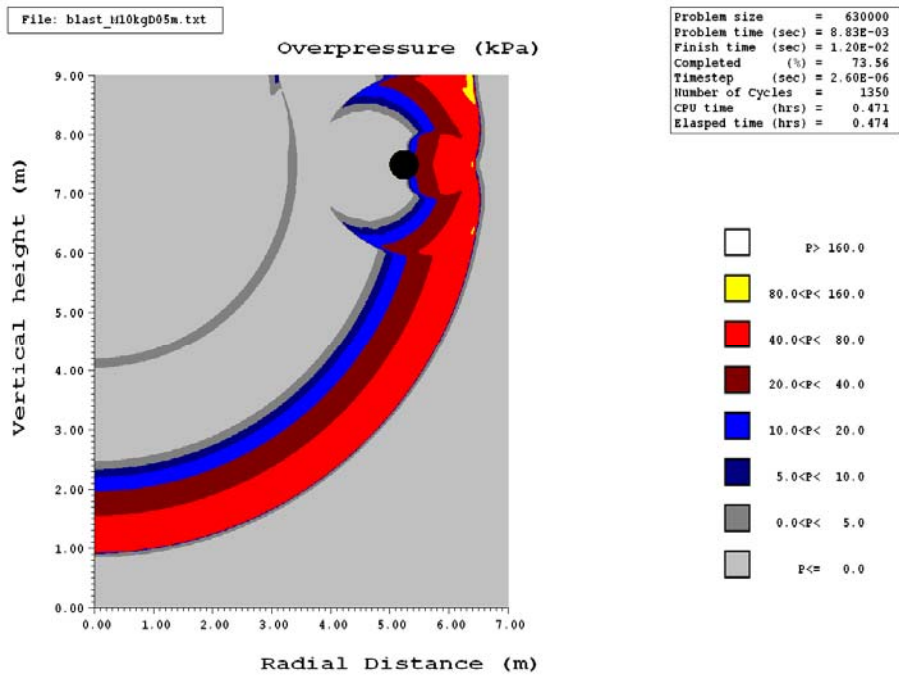


f. Time = 7.62 msec after detonation

Figure G.10. Pressure contour plot for the blast analysis of Section G.3 (continued)



g. Time = 8.16 msec after detonation



h. Time = 8.83 msec after detonation

Figure G.10. Pressure contour plot for the blast analysis of Section G.3 (continued)

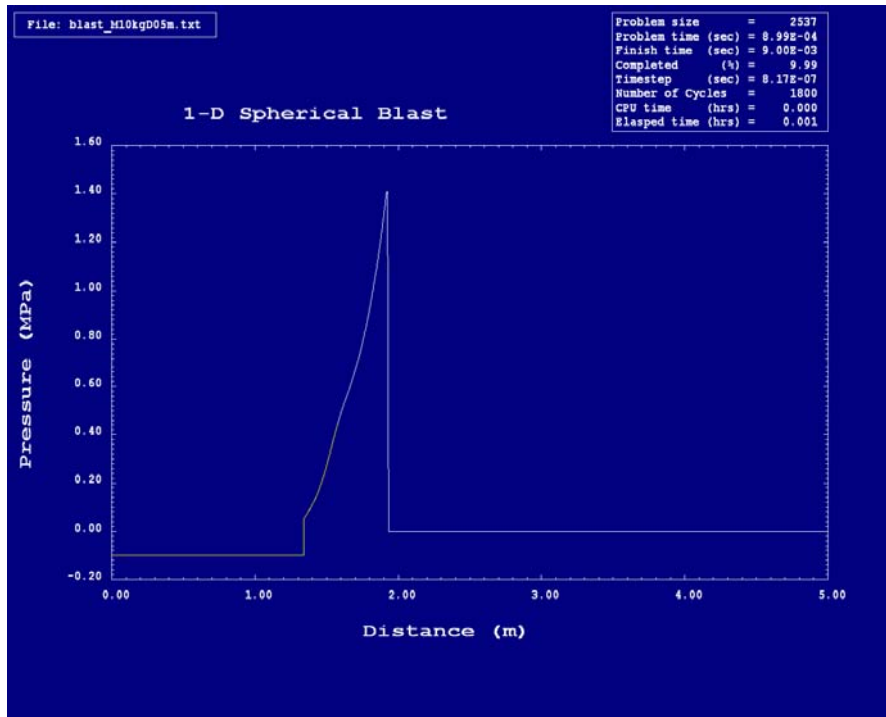


Figure G.11. Sample pressure results for the analysis of Section G.3 at 0.9 msec after detonation

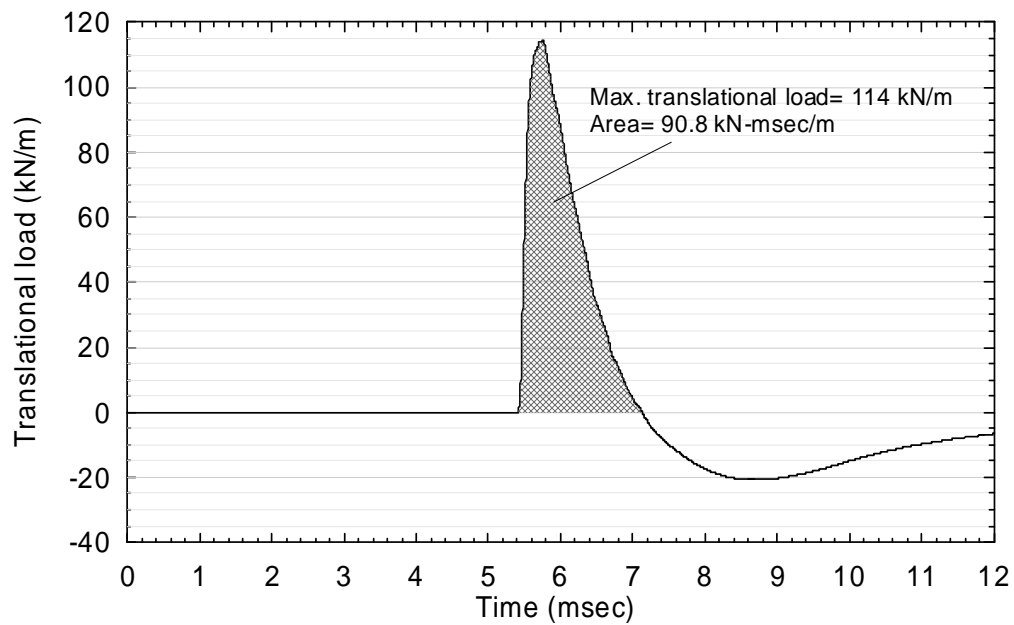


Figure G.12. Translational load histories for the analysis of Section G.3



## MCEER Technical Reports

MCEER publishes technical reports on a variety of subjects written by authors funded through MCEER. These reports are available from both MCEER Publications and the National Technical Information Service (NTIS). Requests for reports should be directed to MCEER Publications, MCEER, University at Buffalo, State University of New York, Red Jacket Quadrangle, Buffalo, New York 14261. Reports can also be requested through NTIS, 5285 Port Royal Road, Springfield, Virginia 22161. NTIS accession numbers are shown in parenthesis, if available.

- NCEER-87-0001 "First-Year Program in Research, Education and Technology Transfer," 3/5/87, (PB88-134275, A04, MF-A01).
- NCEER-87-0002 "Experimental Evaluation of Instantaneous Optimal Algorithms for Structural Control," by R.C. Lin, T.T. Soong and A.M. Reinhorn, 4/20/87, (PB88-134341, A04, MF-A01).
- NCEER-87-0003 "Experimentation Using the Earthquake Simulation Facilities at University at Buffalo," by A.M. Reinhorn and R.L. Ketter, to be published.
- NCEER-87-0004 "The System Characteristics and Performance of a Shaking Table," by J.S. Hwang, K.C. Chang and G.C. Lee, 6/1/87, (PB88-134259, A03, MF-A01). This report is available only through NTIS (see address given above).
- NCEER-87-0005 "A Finite Element Formulation for Nonlinear Viscoplastic Material Using a Q Model," by O. Gyebe and G. Dasgupta, 11/2/87, (PB88-213764, A08, MF-A01).
- NCEER-87-0006 "Symbolic Manipulation Program (SMP) - Algebraic Codes for Two and Three Dimensional Finite Element Formulations," by X. Lee and G. Dasgupta, 11/9/87, (PB88-218522, A05, MF-A01).
- NCEER-87-0007 "Instantaneous Optimal Control Laws for Tall Buildings Under Seismic Excitations," by J.N. Yang, A. Akbarpour and P. Ghaemmaghami, 6/10/87, (PB88-134333, A06, MF-A01). This report is only available through NTIS (see address given above).
- NCEER-87-0008 "IDARC: Inelastic Damage Analysis of Reinforced Concrete Frame - Shear-Wall Structures," by Y.J. Park, A.M. Reinhorn and S.K. Kunnath, 7/20/87, (PB88-134325, A09, MF-A01). This report is only available through NTIS (see address given above).
- NCEER-87-0009 "Liquefaction Potential for New York State: A Preliminary Report on Sites in Manhattan and Buffalo," by M. Budhu, V. Vijayakumar, R.F. Giese and L. Baumgras, 8/31/87, (PB88-163704, A03, MF-A01). This report is available only through NTIS (see address given above).
- NCEER-87-0010 "Vertical and Torsional Vibration of Foundations in Inhomogeneous Media," by A.S. Veletsos and K.W. Dotson, 6/1/87, (PB88-134291, A03, MF-A01). This report is only available through NTIS (see address given above).
- NCEER-87-0011 "Seismic Probabilistic Risk Assessment and Seismic Margins Studies for Nuclear Power Plants," by Howard H.M. Hwang, 6/15/87, (PB88-134267, A03, MF-A01). This report is only available through NTIS (see address given above).
- NCEER-87-0012 "Parametric Studies of Frequency Response of Secondary Systems Under Ground-Acceleration Excitations," by Y. Yong and Y.K. Lin, 6/10/87, (PB88-134309, A03, MF-A01). This report is only available through NTIS (see address given above).
- NCEER-87-0013 "Frequency Response of Secondary Systems Under Seismic Excitation," by J.A. HoLung, J. Cai and Y.K. Lin, 7/31/87, (PB88-134317, A05, MF-A01). This report is only available through NTIS (see address given above).
- NCEER-87-0014 "Modelling Earthquake Ground Motions in Seismically Active Regions Using Parametric Time Series Methods," by G.W. Ellis and A.S. Cakmak, 8/25/87, (PB88-134283, A08, MF-A01). This report is only available through NTIS (see address given above).
- NCEER-87-0015 "Detection and Assessment of Seismic Structural Damage," by E. DiPasquale and A.S. Cakmak, 8/25/87, (PB88-163712, A05, MF-A01). This report is only available through NTIS (see address given above).

- NCEER-87-0016 "Pipeline Experiment at Parkfield, California," by J. Isenberg and E. Richardson, 9/15/87, (PB88-163720, A03, MF-A01). This report is available only through NTIS (see address given above).
- NCEER-87-0017 "Digital Simulation of Seismic Ground Motion," by M. Shinozuka, G. Deodatis and T. Harada, 8/31/87, (PB88-155197, A04, MF-A01). This report is available only through NTIS (see address given above).
- NCEER-87-0018 "Practical Considerations for Structural Control: System Uncertainty, System Time Delay and Truncation of Small Control Forces," J.N. Yang and A. Akbarpour, 8/10/87, (PB88-163738, A08, MF-A01). This report is only available through NTIS (see address given above).
- NCEER-87-0019 "Modal Analysis of Nonclassically Damped Structural Systems Using Canonical Transformation," by J.N. Yang, S. Sarkani and F.X. Long, 9/27/87, (PB88-187851, A04, MF-A01).
- NCEER-87-0020 "A Nonstationary Solution in Random Vibration Theory," by J.R. Red-Horse and P.D. Spanos, 11/3/87, (PB88-163746, A03, MF-A01).
- NCEER-87-0021 "Horizontal Impedances for Radially Inhomogeneous Viscoelastic Soil Layers," by A.S. Veletsos and K.W. Dotson, 10/15/87, (PB88-150859, A04, MF-A01).
- NCEER-87-0022 "Seismic Damage Assessment of Reinforced Concrete Members," by Y.S. Chung, C. Meyer and M. Shinozuka, 10/9/87, (PB88-150867, A05, MF-A01). This report is available only through NTIS (see address given above).
- NCEER-87-0023 "Active Structural Control in Civil Engineering," by T.T. Soong, 11/11/87, (PB88-187778, A03, MF-A01).
- NCEER-87-0024 "Vertical and Torsional Impedances for Radially Inhomogeneous Viscoelastic Soil Layers," by K.W. Dotson and A.S. Veletsos, 12/87, (PB88-187786, A03, MF-A01).
- NCEER-87-0025 "Proceedings from the Symposium on Seismic Hazards, Ground Motions, Soil-Liquefaction and Engineering Practice in Eastern North America," October 20-22, 1987, edited by K.H. Jacob, 12/87, (PB88-188115, A23, MF-A01). This report is available only through NTIS (see address given above).
- NCEER-87-0026 "Report on the Whittier-Narrows, California, Earthquake of October 1, 1987," by J. Pantelic and A. Reinhorn, 11/87, (PB88-187752, A03, MF-A01). This report is available only through NTIS (see address given above).
- NCEER-87-0027 "Design of a Modular Program for Transient Nonlinear Analysis of Large 3-D Building Structures," by S. Srivastav and J.F. Abel, 12/30/87, (PB88-187950, A05, MF-A01). This report is only available through NTIS (see address given above).
- NCEER-87-0028 "Second-Year Program in Research, Education and Technology Transfer," 3/8/88, (PB88-219480, A04, MF-A01).
- NCEER-88-0001 "Workshop on Seismic Computer Analysis and Design of Buildings With Interactive Graphics," by W. McGuire, J.F. Abel and C.H. Conley, 1/18/88, (PB88-187760, A03, MF-A01). This report is only available through NTIS (see address given above).
- NCEER-88-0002 "Optimal Control of Nonlinear Flexible Structures," by J.N. Yang, F.X. Long and D. Wong, 1/22/88, (PB88-213772, A06, MF-A01).
- NCEER-88-0003 "Substructuring Techniques in the Time Domain for Primary-Secondary Structural Systems," by G.D. Manolis and G. Juhn, 2/10/88, (PB88-213780, A04, MF-A01).
- NCEER-88-0004 "Iterative Seismic Analysis of Primary-Secondary Systems," by A. Singhal, L.D. Lutes and P.D. Spanos, 2/23/88, (PB88-213798, A04, MF-A01).
- NCEER-88-0005 "Stochastic Finite Element Expansion for Random Media," by P.D. Spanos and R. Ghanem, 3/14/88, (PB88-213806, A03, MF-A01).

- NCEER-88-0006 "Combining Structural Optimization and Structural Control," by F.Y. Cheng and C.P. Pantelides, 1/10/88, (PB88-213814, A05, MF-A01).
- NCEER-88-0007 "Seismic Performance Assessment of Code-Designed Structures," by H.H-M. Hwang, J-W. Jaw and H-J. Shau, 3/20/88, (PB88-219423, A04, MF-A01). This report is only available through NTIS (see address given above).
- NCEER-88-0008 "Reliability Analysis of Code-Designed Structures Under Natural Hazards," by H.H-M. Hwang, H. Ushiba and M. Shinozuka, 2/29/88, (PB88-229471, A07, MF-A01). This report is only available through NTIS (see address given above).
- NCEER-88-0009 "Seismic Fragility Analysis of Shear Wall Structures," by J-W Jaw and H.H-M. Hwang, 4/30/88, (PB89-102867, A04, MF-A01).
- NCEER-88-0010 "Base Isolation of a Multi-Story Building Under a Harmonic Ground Motion - A Comparison of Performances of Various Systems," by F-G Fan, G. Ahmadi and I.G. Tadjbakhsh, 5/18/88, (PB89-122238, A06, MF-A01). This report is only available through NTIS (see address given above).
- NCEER-88-0011 "Seismic Floor Response Spectra for a Combined System by Green's Functions," by F.M. Lavelle, L.A. Bergman and P.D. Spanos, 5/1/88, (PB89-102875, A03, MF-A01).
- NCEER-88-0012 "A New Solution Technique for Randomly Excited Hysteretic Structures," by G.Q. Cai and Y.K. Lin, 5/16/88, (PB89-102883, A03, MF-A01).
- NCEER-88-0013 "A Study of Radiation Damping and Soil-Structure Interaction Effects in the Centrifuge," by K. Weissman, supervised by J.H. Prevost, 5/24/88, (PB89-144703, A06, MF-A01).
- NCEER-88-0014 "Parameter Identification and Implementation of a Kinematic Plasticity Model for Frictional Soils," by J.H. Prevost and D.V. Griffiths, to be published.
- NCEER-88-0015 "Two- and Three- Dimensional Dynamic Finite Element Analyses of the Long Valley Dam," by D.V. Griffiths and J.H. Prevost, 6/17/88, (PB89-144711, A04, MF-A01).
- NCEER-88-0016 "Damage Assessment of Reinforced Concrete Structures in Eastern United States," by A.M. Reinhorn, M.J. Seidel, S.K. Kunnath and Y.J. Park, 6/15/88, (PB89-122220, A04, MF-A01). This report is only available through NTIS (see address given above).
- NCEER-88-0017 "Dynamic Compliance of Vertically Loaded Strip Foundations in Multilayered Viscoelastic Soils," by S. Ahmad and A.S.M. Israil, 6/17/88, (PB89-102891, A04, MF-A01).
- NCEER-88-0018 "An Experimental Study of Seismic Structural Response With Added Viscoelastic Dampers," by R.C. Lin, Z. Liang, T.T. Soong and R.H. Zhang, 6/30/88, (PB89-122212, A05, MF-A01). This report is available only through NTIS (see address given above).
- NCEER-88-0019 "Experimental Investigation of Primary - Secondary System Interaction," by G.D. Manolis, G. Juhn and A.M. Reinhorn, 5/27/88, (PB89-122204, A04, MF-A01).
- NCEER-88-0020 "A Response Spectrum Approach For Analysis of Nonclassically Damped Structures," by J.N. Yang, S. Sarkani and F.X. Long, 4/22/88, (PB89-102909, A04, MF-A01).
- NCEER-88-0021 "Seismic Interaction of Structures and Soils: Stochastic Approach," by A.S. Veletsos and A.M. Prasad, 7/21/88, (PB89-122196, A04, MF-A01). This report is only available through NTIS (see address given above).
- NCEER-88-0022 "Identification of the Serviceability Limit State and Detection of Seismic Structural Damage," by E. DiPasquale and A.S. Cakmak, 6/15/88, (PB89-122188, A05, MF-A01). This report is available only through NTIS (see address given above).
- NCEER-88-0023 "Multi-Hazard Risk Analysis: Case of a Simple Offshore Structure," by B.K. Bhartia and E.H. Vanmarcke, 7/21/88, (PB89-145213, A05, MF-A01).

- NCEER-88-0024 "Automated Seismic Design of Reinforced Concrete Buildings," by Y.S. Chung, C. Meyer and M. Shinozuka, 7/5/88, (PB89-122170, A06, MF-A01). This report is available only through NTIS (see address given above).
- NCEER-88-0025 "Experimental Study of Active Control of MDOF Structures Under Seismic Excitations," by L.L. Chung, R.C. Lin, T.T. Soong and A.M. Reinhorn, 7/10/88, (PB89-122600, A04, MF-A01).
- NCEER-88-0026 "Earthquake Simulation Tests of a Low-Rise Metal Structure," by J.S. Hwang, K.C. Chang, G.C. Lee and R.L. Ketter, 8/1/88, (PB89-102917, A04, MF-A01).
- NCEER-88-0027 "Systems Study of Urban Response and Reconstruction Due to Catastrophic Earthquakes," by F. Kozin and H.K. Zhou, 9/22/88, (PB90-162348, A04, MF-A01).
- NCEER-88-0028 "Seismic Fragility Analysis of Plane Frame Structures," by H.H-M. Hwang and Y.K. Low, 7/31/88, (PB89-131445, A06, MF-A01).
- NCEER-88-0029 "Response Analysis of Stochastic Structures," by A. Kardara, C. Bucher and M. Shinozuka, 9/22/88, (PB89-174429, A04, MF-A01).
- NCEER-88-0030 "Nonnormal Accelerations Due to Yielding in a Primary Structure," by D.C.K. Chen and L.D. Lutes, 9/19/88, (PB89-131437, A04, MF-A01).
- NCEER-88-0031 "Design Approaches for Soil-Structure Interaction," by A.S. Veletsos, A.M. Prasad and Y. Tang, 12/30/88, (PB89-174437, A03, MF-A01). This report is available only through NTIS (see address given above).
- NCEER-88-0032 "A Re-evaluation of Design Spectra for Seismic Damage Control," by C.J. Turkstra and A.G. Tallin, 11/7/88, (PB89-145221, A05, MF-A01).
- NCEER-88-0033 "The Behavior and Design of Noncontact Lap Splices Subjected to Repeated Inelastic Tensile Loading," by V.E. Sagan, P. Gergely and R.N. White, 12/8/88, (PB89-163737, A08, MF-A01).
- NCEER-88-0034 "Seismic Response of Pile Foundations," by S.M. Mamoon, P.K. Banerjee and S. Ahmad, 11/1/88, (PB89-145239, A04, MF-A01).
- NCEER-88-0035 "Modeling of R/C Building Structures With Flexible Floor Diaphragms (IDARC2)," by A.M. Reinhorn, S.K. Kunnath and N. Panahshahi, 9/7/88, (PB89-207153, A07, MF-A01).
- NCEER-88-0036 "Solution of the Dam-Reservoir Interaction Problem Using a Combination of FEM, BEM with Particular Integrals, Modal Analysis, and Substructuring," by C-S. Tsai, G.C. Lee and R.L. Ketter, 12/31/88, (PB89-207146, A04, MF-A01).
- NCEER-88-0037 "Optimal Placement of Actuators for Structural Control," by F.Y. Cheng and C.P. Pantelides, 8/15/88, (PB89-162846, A05, MF-A01).
- NCEER-88-0038 "Teflon Bearings in Aseismic Base Isolation: Experimental Studies and Mathematical Modeling," by A. Mokha, M.C. Constantinou and A.M. Reinhorn, 12/5/88, (PB89-218457, A10, MF-A01). This report is available only through NTIS (see address given above).
- NCEER-88-0039 "Seismic Behavior of Flat Slab High-Rise Buildings in the New York City Area," by P. Weidlinger and M. Ettouney, 10/15/88, (PB90-145681, A04, MF-A01).
- NCEER-88-0040 "Evaluation of the Earthquake Resistance of Existing Buildings in New York City," by P. Weidlinger and M. Ettouney, 10/15/88, to be published.
- NCEER-88-0041 "Small-Scale Modeling Techniques for Reinforced Concrete Structures Subjected to Seismic Loads," by W. Kim, A. El-Attar and R.N. White, 11/22/88, (PB89-189625, A05, MF-A01).
- NCEER-88-0042 "Modeling Strong Ground Motion from Multiple Event Earthquakes," by G.W. Ellis and A.S. Cakmak, 10/15/88, (PB89-174445, A03, MF-A01).



- NCEER-88-0043 "Nonstationary Models of Seismic Ground Acceleration," by M. Grigoriu, S.E. Ruiz and E. Rosenblueth, 7/15/88, (PB89-189617, A04, MF-A01).
- NCEER-88-0044 "SARCF User's Guide: Seismic Analysis of Reinforced Concrete Frames," by Y.S. Chung, C. Meyer and M. Shinozuka, 11/9/88, (PB89-174452, A08, MF-A01).
- NCEER-88-0045 "First Expert Panel Meeting on Disaster Research and Planning," edited by J. Pantelic and J. Stoyke, 9/15/88, (PB89-174460, A05, MF-A01).
- NCEER-88-0046 "Preliminary Studies of the Effect of Degrading Infill Walls on the Nonlinear Seismic Response of Steel Frames," by C.Z. Chrysostomou, P. Gergely and J.F. Abel, 12/19/88, (PB89-208383, A05, MF-A01).
- NCEER-88-0047 "Reinforced Concrete Frame Component Testing Facility - Design, Construction, Instrumentation and Operation," by S.P. Pessiki, C. Conley, T. Bond, P. Gergely and R.N. White, 12/16/88, (PB89-174478, A04, MF-A01).
- NCEER-89-0001 "Effects of Protective Cushion and Soil Compliancy on the Response of Equipment Within a Seismically Excited Building," by J.A. HoLung, 2/16/89, (PB89-207179, A04, MF-A01).
- NCEER-89-0002 "Statistical Evaluation of Response Modification Factors for Reinforced Concrete Structures," by H.H-M. Hwang and J-W. Jaw, 2/17/89, (PB89-207187, A05, MF-A01).
- NCEER-89-0003 "Hysteretic Columns Under Random Excitation," by G-Q. Cai and Y.K. Lin, 1/9/89, (PB89-196513, A03, MF-A01).
- NCEER-89-0004 "Experimental Study of 'Elephant Foot Bulge' Instability of Thin-Walled Metal Tanks," by Z-H. Jia and R.L. Ketter, 2/22/89, (PB89-207195, A03, MF-A01).
- NCEER-89-0005 "Experiment on Performance of Buried Pipelines Across San Andreas Fault," by J. Isenberg, E. Richardson and T.D. O'Rourke, 3/10/89, (PB89-218440, A04, MF-A01). This report is available only through NTIS (see address given above).
- NCEER-89-0006 "A Knowledge-Based Approach to Structural Design of Earthquake-Resistant Buildings," by M. Subramani, P. Gergely, C.H. Conley, J.F. Abel and A.H. Zaghaw, 1/15/89, (PB89-218465, A06, MF-A01).
- NCEER-89-0007 "Liquefaction Hazards and Their Effects on Buried Pipelines," by T.D. O'Rourke and P.A. Lane, 2/1/89, (PB89-218481, A09, MF-A01).
- NCEER-89-0008 "Fundamentals of System Identification in Structural Dynamics," by H. Imai, C-B. Yun, O. Maruyama and M. Shinozuka, 1/26/89, (PB89-207211, A04, MF-A01).
- NCEER-89-0009 "Effects of the 1985 Michoacan Earthquake on Water Systems and Other Buried Lifelines in Mexico," by A.G. Ayala and M.J. O'Rourke, 3/8/89, (PB89-207229, A06, MF-A01).
- NCEER-89-R010 "NCEER Bibliography of Earthquake Education Materials," by K.E.K. Ross, Second Revision, 9/1/89, (PB90-125352, A05, MF-A01). This report is replaced by NCEER-92-0018.
- NCEER-89-0011 "Inelastic Three-Dimensional Response Analysis of Reinforced Concrete Building Structures (IDARC-3D), Part I - Modeling," by S.K. Kunnath and A.M. Reinhorn, 4/17/89, (PB90-114612, A07, MF-A01). This report is available only through NTIS (see address given above).
- NCEER-89-0012 "Recommended Modifications to ATC-14," by C.D. Poland and J.O. Malley, 4/12/89, (PB90-108648, A15, MF-A01).
- NCEER-89-0013 "Repair and Strengthening of Beam-to-Column Connections Subjected to Earthquake Loading," by M. Corazao and A.J. Durrani, 2/28/89, (PB90-109885, A06, MF-A01).
- NCEER-89-0014 "Program EXKAL2 for Identification of Structural Dynamic Systems," by O. Maruyama, C-B. Yun, M. Hoshiya and M. Shinozuka, 5/19/89, (PB90-109877, A09, MF-A01).

- NCEER-89-0015 "Response of Frames With Bolted Semi-Rigid Connections, Part I - Experimental Study and Analytical Predictions," by P.J. DiCorso, A.M. Reinhorn, J.R. Dickerson, J.B. Radzinski and W.L. Harper, 6/1/89, to be published.
- NCEER-89-0016 "ARMA Monte Carlo Simulation in Probabilistic Structural Analysis," by P.D. Spanos and M.P. Mignolet, 7/10/89, (PB90-109893, A03, MF-A01).
- NCEER-89-P017 "Preliminary Proceedings from the Conference on Disaster Preparedness - The Place of Earthquake Education in Our Schools," Edited by K.E.K. Ross, 6/23/89, (PB90-108606, A03, MF-A01).
- NCEER-89-0017 "Proceedings from the Conference on Disaster Preparedness - The Place of Earthquake Education in Our Schools," Edited by K.E.K. Ross, 12/31/89, (PB90-207895, A012, MF-A02). This report is available only through NTIS (see address given above).
- NCEER-89-0018 "Multidimensional Models of Hysteretic Material Behavior for Vibration Analysis of Shape Memory Energy Absorbing Devices, by E.J. Graesser and F.A. Cozzarelli, 6/7/89, (PB90-164146, A04, MF-A01).
- NCEER-89-0019 "Nonlinear Dynamic Analysis of Three-Dimensional Base Isolated Structures (3D-BASIS)," by S. Nagarajaiah, A.M. Reinhorn and M.C. Constantinou, 8/3/89, (PB90-161936, A06, MF-A01). This report has been replaced by NCEER-93-0011.
- NCEER-89-0020 "Structural Control Considering Time-Rate of Control Forces and Control Rate Constraints," by F.Y. Cheng and C.P. Pantelides, 8/3/89, (PB90-120445, A04, MF-A01).
- NCEER-89-0021 "Subsurface Conditions of Memphis and Shelby County," by K.W. Ng, T-S. Chang and H-H.M. Hwang, 7/26/89, (PB90-120437, A03, MF-A01).
- NCEER-89-0022 "Seismic Wave Propagation Effects on Straight Jointed Buried Pipelines," by K. Elhadi and M.J. O'Rourke, 8/24/89, (PB90-162322, A10, MF-A02).
- NCEER-89-0023 "Workshop on Serviceability Analysis of Water Delivery Systems," edited by M. Grigoriu, 3/6/89, (PB90-127424, A03, MF-A01).
- NCEER-89-0024 "Shaking Table Study of a 1/5 Scale Steel Frame Composed of Tapered Members," by K.C. Chang, J.S. Hwang and G.C. Lee, 9/18/89, (PB90-160169, A04, MF-A01).
- NCEER-89-0025 "DYNA1D: A Computer Program for Nonlinear Seismic Site Response Analysis - Technical Documentation," by Jean H. Prevost, 9/14/89, (PB90-161944, A07, MF-A01). This report is available only through NTIS (see address given above).
- NCEER-89-0026 "1:4 Scale Model Studies of Active Tendon Systems and Active Mass Dampers for Aseismic Protection," by A.M. Reinhorn, T.T. Soong, R.C. Lin, Y.P. Yang, Y. Fukao, H. Abe and M. Nakai, 9/15/89, (PB90-173246, A10, MF-A02). This report is available only through NTIS (see address given above).
- NCEER-89-0027 "Scattering of Waves by Inclusions in a Nonhomogeneous Elastic Half Space Solved by Boundary Element Methods," by P.K. Hadley, A. Askar and A.S. Cakmak, 6/15/89, (PB90-145699, A07, MF-A01).
- NCEER-89-0028 "Statistical Evaluation of Deflection Amplification Factors for Reinforced Concrete Structures," by H.H.M. Hwang, J-W. Jaw and A.L. Ch'ng, 8/31/89, (PB90-164633, A05, MF-A01).
- NCEER-89-0029 "Bedrock Accelerations in Memphis Area Due to Large New Madrid Earthquakes," by H.H.M. Hwang, C.H.S. Chen and G. Yu, 11/7/89, (PB90-162330, A04, MF-A01).
- NCEER-89-0030 "Seismic Behavior and Response Sensitivity of Secondary Structural Systems," by Y.Q. Chen and T.T. Soong, 10/23/89, (PB90-164658, A08, MF-A01).
- NCEER-89-0031 "Random Vibration and Reliability Analysis of Primary-Secondary Structural Systems," by Y. Ibrahim, M. Grigoriu and T.T. Soong, 11/10/89, (PB90-161951, A04, MF-A01).

- NCEER-89-0032 "Proceedings from the Second U.S. - Japan Workshop on Liquefaction, Large Ground Deformation and Their Effects on Lifelines, September 26-29, 1989," Edited by T.D. O'Rourke and M. Hamada, 12/1/89, (PB90-209388, A22, MF-A03).
- NCEER-89-0033 "Deterministic Model for Seismic Damage Evaluation of Reinforced Concrete Structures," by J.M. Bracci, A.M. Reinhorn, J.B. Mander and S.K. Kunnath, 9/27/89, (PB91-108803, A06, MF-A01).
- NCEER-89-0034 "On the Relation Between Local and Global Damage Indices," by E. DiPasquale and A.S. Cakmak, 8/15/89, (PB90-173865, A05, MF-A01).
- NCEER-89-0035 "Cyclic Undrained Behavior of Nonplastic and Low Plasticity Silts," by A.J. Walker and H.E. Stewart, 7/26/89, (PB90-183518, A10, MF-A01).
- NCEER-89-0036 "Liquefaction Potential of Surficial Deposits in the City of Buffalo, New York," by M. Budhu, R. Giese and L. Baumgrass, 1/17/89, (PB90-208455, A04, MF-A01).
- NCEER-89-0037 "A Deterministic Assessment of Effects of Ground Motion Incoherence," by A.S. Veletsos and Y. Tang, 7/15/89, (PB90-164294, A03, MF-A01).
- NCEER-89-0038 "Workshop on Ground Motion Parameters for Seismic Hazard Mapping," July 17-18, 1989, edited by R.V. Whitman, 12/1/89, (PB90-173923, A04, MF-A01).
- NCEER-89-0039 "Seismic Effects on Elevated Transit Lines of the New York City Transit Authority," by C.J. Costantino, C.A. Miller and E. Heymsfield, 12/26/89, (PB90-207887, A06, MF-A01).
- NCEER-89-0040 "Centrifugal Modeling of Dynamic Soil-Structure Interaction," by K. Weissman, Supervised by J.H. Prevost, 5/10/89, (PB90-207879, A07, MF-A01).
- NCEER-89-0041 "Linearized Identification of Buildings With Cores for Seismic Vulnerability Assessment," by I-K. Ho and A.E. Aktan, 11/1/89, (PB90-251943, A07, MF-A01).
- NCEER-90-0001 "Geotechnical and Lifeline Aspects of the October 17, 1989 Loma Prieta Earthquake in San Francisco," by T.D. O'Rourke, H.E. Stewart, F.T. Blackburn and T.S. Dickerman, 1/90, (PB90-208596, A05, MF-A01).
- NCEER-90-0002 "Nonnormal Secondary Response Due to Yielding in a Primary Structure," by D.C.K. Chen and L.D. Lutes, 2/28/90, (PB90-251976, A07, MF-A01).
- NCEER-90-0003 "Earthquake Education Materials for Grades K-12," by K.E.K. Ross, 4/16/90, (PB91-251984, A05, MF-A05). This report has been replaced by NCEER-92-0018.
- NCEER-90-0004 "Catalog of Strong Motion Stations in Eastern North America," by R.W. Busby, 4/3/90, (PB90-251984, A05, MF-A01).
- NCEER-90-0005 "NCEER Strong-Motion Data Base: A User Manual for the GeoBase Release (Version 1.0 for the Sun3)," by P. Friberg and K. Jacob, 3/31/90 (PB90-258062, A04, MF-A01).
- NCEER-90-0006 "Seismic Hazard Along a Crude Oil Pipeline in the Event of an 1811-1812 Type New Madrid Earthquake," by H.H.M. Hwang and C-H.S. Chen, 4/16/90, (PB90-258054, A04, MF-A01).
- NCEER-90-0007 "Site-Specific Response Spectra for Memphis Sheahan Pumping Station," by H.H.M. Hwang and C.S. Lee, 5/15/90, (PB91-108811, A05, MF-A01).
- NCEER-90-0008 "Pilot Study on Seismic Vulnerability of Crude Oil Transmission Systems," by T. Ariman, R. Dobry, M. Grigoriu, F. Kozin, M. O'Rourke, T. O'Rourke and M. Shinozuka, 5/25/90, (PB91-108837, A06, MF-A01).
- NCEER-90-0009 "A Program to Generate Site Dependent Time Histories: EQGEN," by G.W. Ellis, M. Srinivasan and A.S. Cakmak, 1/30/90, (PB91-108829, A04, MF-A01).
- NCEER-90-0010 "Active Isolation for Seismic Protection of Operating Rooms," by M.E. Talbott, Supervised by M. Shinozuka, 6/8/9, (PB91-110205, A05, MF-A01).

- NCEER-90-0011 "Program LINEARID for Identification of Linear Structural Dynamic Systems," by C-B. Yun and M. Shinozuka, 6/25/90, (PB91-110312, A08, MF-A01).
- NCEER-90-0012 "Two-Dimensional Two-Phase Elasto-Plastic Seismic Response of Earth Dams," by A.N. Yiagos, Supervised by J.H. Prevost, 6/20/90, (PB91-110197, A13, MF-A02).
- NCEER-90-0013 "Secondary Systems in Base-Isolated Structures: Experimental Investigation, Stochastic Response and Stochastic Sensitivity," by G.D. Manolis, G. Juhn, M.C. Constantinou and A.M. Reinhorn, 7/1/90, (PB91-110320, A08, MF-A01).
- NCEER-90-0014 "Seismic Behavior of Lightly-Reinforced Concrete Column and Beam-Column Joint Details," by S.P. Pessiki, C.H. Conley, P. Gergely and R.N. White, 8/22/90, (PB91-108795, A11, MF-A02).
- NCEER-90-0015 "Two Hybrid Control Systems for Building Structures Under Strong Earthquakes," by J.N. Yang and A. Daniellians, 6/29/90, (PB91-125393, A04, MF-A01).
- NCEER-90-0016 "Instantaneous Optimal Control with Acceleration and Velocity Feedback," by J.N. Yang and Z. Li, 6/29/90, (PB91-125401, A03, MF-A01).
- NCEER-90-0017 "Reconnaissance Report on the Northern Iran Earthquake of June 21, 1990," by M. Mehrain, 10/4/90, (PB91-125377, A03, MF-A01).
- NCEER-90-0018 "Evaluation of Liquefaction Potential in Memphis and Shelby County," by T.S. Chang, P.S. Tang, C.S. Lee and H. Hwang, 8/10/90, (PB91-125427, A09, MF-A01).
- NCEER-90-0019 "Experimental and Analytical Study of a Combined Sliding Disc Bearing and Helical Steel Spring Isolation System," by M.C. Constantinou, A.S. Mokha and A.M. Reinhorn, 10/4/90, (PB91-125385, A06, MF-A01). This report is available only through NTIS (see address given above).
- NCEER-90-0020 "Experimental Study and Analytical Prediction of Earthquake Response of a Sliding Isolation System with a Spherical Surface," by A.S. Mokha, M.C. Constantinou and A.M. Reinhorn, 10/11/90, (PB91-125419, A05, MF-A01).
- NCEER-90-0021 "Dynamic Interaction Factors for Floating Pile Groups," by G. Gazetas, K. Fan, A. Kaynia and E. Kausel, 9/10/90, (PB91-170381, A05, MF-A01).
- NCEER-90-0022 "Evaluation of Seismic Damage Indices for Reinforced Concrete Structures," by S. Rodriguez-Gomez and A.S. Cakmak, 9/30/90, PB91-171322, A06, MF-A01).
- NCEER-90-0023 "Study of Site Response at a Selected Memphis Site," by H. Desai, S. Ahmad, E.S. Gazetas and M.R. Oh, 10/11/90, (PB91-196857, A03, MF-A01).
- NCEER-90-0024 "A User's Guide to Strongmo: Version 1.0 of NCEER's Strong-Motion Data Access Tool for PCs and Terminals," by P.A. Friberg and C.A.T. Susch, 11/15/90, (PB91-171272, A03, MF-A01).
- NCEER-90-0025 "A Three-Dimensional Analytical Study of Spatial Variability of Seismic Ground Motions," by L-L. Hong and A.H.-S. Ang, 10/30/90, (PB91-170399, A09, MF-A01).
- NCEER-90-0026 "MUMOID User's Guide - A Program for the Identification of Modal Parameters," by S. Rodriguez-Gomez and E. DiPasquale, 9/30/90, (PB91-171298, A04, MF-A01).
- NCEER-90-0027 "SARCF-II User's Guide - Seismic Analysis of Reinforced Concrete Frames," by S. Rodriguez-Gomez, Y.S. Chung and C. Meyer, 9/30/90, (PB91-171280, A05, MF-A01).
- NCEER-90-0028 "Viscous Dampers: Testing, Modeling and Application in Vibration and Seismic Isolation," by N. Makris and M.C. Constantinou, 12/20/90 (PB91-190561, A06, MF-A01).
- NCEER-90-0029 "Soil Effects on Earthquake Ground Motions in the Memphis Area," by H. Hwang, C.S. Lee, K.W. Ng and T.S. Chang, 8/2/90, (PB91-190751, A05, MF-A01).

- NCEER-91-0001 "Proceedings from the Third Japan-U.S. Workshop on Earthquake Resistant Design of Lifeline Facilities and Countermeasures for Soil Liquefaction, December 17-19, 1990," edited by T.D. O'Rourke and M. Hamada, 2/1/91, (PB91-179259, A99, MF-A04).
- NCEER-91-0002 "Physical Space Solutions of Non-Proportionally Damped Systems," by M. Tong, Z. Liang and G.C. Lee, 1/15/91, (PB91-179242, A04, MF-A01).
- NCEER-91-0003 "Seismic Response of Single Piles and Pile Groups," by K. Fan and G. Gazetas, 1/10/91, (PB92-174994, A04, MF-A01).
- NCEER-91-0004 "Damping of Structures: Part 1 - Theory of Complex Damping," by Z. Liang and G. Lee, 10/10/91, (PB92-197235, A12, MF-A03).
- NCEER-91-0005 "3D-BASIS - Nonlinear Dynamic Analysis of Three Dimensional Base Isolated Structures: Part II," by S. Nagarajaiah, A.M. Reinhorn and M.C. Constantinou, 2/28/91, (PB91-190553, A07, MF-A01). This report has been replaced by NCEER-93-0011.
- NCEER-91-0006 "A Multidimensional Hysteretic Model for Plasticity Deforming Metals in Energy Absorbing Devices," by E.J. Graesser and F.A. Cozzarelli, 4/9/91, (PB92-108364, A04, MF-A01).
- NCEER-91-0007 "A Framework for Customizable Knowledge-Based Expert Systems with an Application to a KBES for Evaluating the Seismic Resistance of Existing Buildings," by E.G. Ibarra-Anaya and S.J. Fennes, 4/9/91, (PB91-210930, A08, MF-A01).
- NCEER-91-0008 "Nonlinear Analysis of Steel Frames with Semi-Rigid Connections Using the Capacity Spectrum Method," by G.G. Deierlein, S-H. Hsieh, Y-J. Shen and J.F. Abel, 7/2/91, (PB92-113828, A05, MF-A01).
- NCEER-91-0009 "Earthquake Education Materials for Grades K-12," by K.E.K. Ross, 4/30/91, (PB91-212142, A06, MF-A01). This report has been replaced by NCEER-92-0018.
- NCEER-91-0010 "Phase Wave Velocities and Displacement Phase Differences in a Harmonically Oscillating Pile," by N. Makris and G. Gazetas, 7/8/91, (PB92-108356, A04, MF-A01).
- NCEER-91-0011 "Dynamic Characteristics of a Full-Size Five-Story Steel Structure and a 2/5 Scale Model," by K.C. Chang, G.C. Yao, G.C. Lee, D.S. Hao and Y.C. Yeh," 7/2/91, (PB93-116648, A06, MF-A02).
- NCEER-91-0012 "Seismic Response of a 2/5 Scale Steel Structure with Added Viscoelastic Dampers," by K.C. Chang, T.T. Soong, S-T. Oh and M.L. Lai, 5/17/91, (PB92-110816, A05, MF-A01).
- NCEER-91-0013 "Earthquake Response of Retaining Walls; Full-Scale Testing and Computational Modeling," by S. Alampalli and A-W.M. Elgamal, 6/20/91, to be published.
- NCEER-91-0014 "3D-BASIS-M: Nonlinear Dynamic Analysis of Multiple Building Base Isolated Structures," by P.C. Tsopelas, S. Nagarajaiah, M.C. Constantinou and A.M. Reinhorn, 5/28/91, (PB92-113885, A09, MF-A02).
- NCEER-91-0015 "Evaluation of SEAOC Design Requirements for Sliding Isolated Structures," by D. Theodossiou and M.C. Constantinou, 6/10/91, (PB92-114602, A11, MF-A03).
- NCEER-91-0016 "Closed-Loop Modal Testing of a 27-Story Reinforced Concrete Flat Plate-Core Building," by H.R. Somaprasad, T. Toksoy, H. Yoshiyuki and A.E. Aktan, 7/15/91, (PB92-129980, A07, MF-A02).
- NCEER-91-0017 "Shake Table Test of a 1/6 Scale Two-Story Lightly Reinforced Concrete Building," by A.G. El-Attar, R.N. White and P. Gergely, 2/28/91, (PB92-222447, A06, MF-A02).
- NCEER-91-0018 "Shake Table Test of a 1/8 Scale Three-Story Lightly Reinforced Concrete Building," by A.G. El-Attar, R.N. White and P. Gergely, 2/28/91, (PB93-116630, A08, MF-A02).
- NCEER-91-0019 "Transfer Functions for Rigid Rectangular Foundations," by A.S. Veletsos, A.M. Prasad and W.H. Wu, 7/31/91, to be published.

- NCEER-91-0020 "Hybrid Control of Seismic-Excited Nonlinear and Inelastic Structural Systems," by J.N. Yang, Z. Li and A. Daniellians, 8/1/91, (PB92-143171, A06, MF-A02).
- NCEER-91-0021 "The NCEER-91 Earthquake Catalog: Improved Intensity-Based Magnitudes and Recurrence Relations for U.S. Earthquakes East of New Madrid," by L. Seeber and J.G. Armbruster, 8/28/91, (PB92-176742, A06, MF-A02).
- NCEER-91-0022 "Proceedings from the Implementation of Earthquake Planning and Education in Schools: The Need for Change - The Roles of the Changemakers," by K.E.K. Ross and F. Winslow, 7/23/91, (PB92-129998, A12, MF-A03).
- NCEER-91-0023 "A Study of Reliability-Based Criteria for Seismic Design of Reinforced Concrete Frame Buildings," by H.H.M. Hwang and H-M. Hsu, 8/10/91, (PB92-140235, A09, MF-A02).
- NCEER-91-0024 "Experimental Verification of a Number of Structural System Identification Algorithms," by R.G. Ghanem, H. Gavin and M. Shinozuka, 9/18/91, (PB92-176577, A18, MF-A04).
- NCEER-91-0025 "Probabilistic Evaluation of Liquefaction Potential," by H.H.M. Hwang and C.S. Lee, 11/25/91, (PB92-143429, A05, MF-A01).
- NCEER-91-0026 "Instantaneous Optimal Control for Linear, Nonlinear and Hysteretic Structures - Stable Controllers," by J.N. Yang and Z. Li, 11/15/91, (PB92-163807, A04, MF-A01).
- NCEER-91-0027 "Experimental and Theoretical Study of a Sliding Isolation System for Bridges," by M.C. Constantinou, A. Kartoum, A.M. Reinhorn and P. Bradford, 11/15/91, (PB92-176973, A10, MF-A03).
- NCEER-92-0001 "Case Studies of Liquefaction and Lifeline Performance During Past Earthquakes, Volume 1: Japanese Case Studies," Edited by M. Hamada and T. O'Rourke, 2/17/92, (PB92-197243, A18, MF-A04).
- NCEER-92-0002 "Case Studies of Liquefaction and Lifeline Performance During Past Earthquakes, Volume 2: United States Case Studies," Edited by T. O'Rourke and M. Hamada, 2/17/92, (PB92-197250, A20, MF-A04).
- NCEER-92-0003 "Issues in Earthquake Education," Edited by K. Ross, 2/3/92, (PB92-222389, A07, MF-A02).
- NCEER-92-0004 "Proceedings from the First U.S. - Japan Workshop on Earthquake Protective Systems for Bridges," Edited by I.G. Buckle, 2/4/92, (PB94-142239, A99, MF-A06).
- NCEER-92-0005 "Seismic Ground Motion from a Haskell-Type Source in a Multiple-Layered Half-Space," A.P. Theoharis, G. Deodatis and M. Shinozuka, 1/2/92, to be published.
- NCEER-92-0006 "Proceedings from the Site Effects Workshop," Edited by R. Whitman, 2/29/92, (PB92-197201, A04, MF-A01).
- NCEER-92-0007 "Engineering Evaluation of Permanent Ground Deformations Due to Seismically-Induced Liquefaction," by M.H. Baziar, R. Dobry and A-W.M. Elgamal, 3/24/92, (PB92-222421, A13, MF-A03).
- NCEER-92-0008 "A Procedure for the Seismic Evaluation of Buildings in the Central and Eastern United States," by C.D. Poland and J.O. Malley, 4/2/92, (PB92-222439, A20, MF-A04).
- NCEER-92-0009 "Experimental and Analytical Study of a Hybrid Isolation System Using Friction Controllable Sliding Bearings," by M.Q. Feng, S. Fujii and M. Shinozuka, 5/15/92, (PB93-150282, A06, MF-A02).
- NCEER-92-0010 "Seismic Resistance of Slab-Column Connections in Existing Non-Ductile Flat-Plate Buildings," by A.J. Durrani and Y. Du, 5/18/92, (PB93-116812, A06, MF-A02).
- NCEER-92-0011 "The Hysteretic and Dynamic Behavior of Brick Masonry Walls Upgraded by Ferrocement Coatings Under Cyclic Loading and Strong Simulated Ground Motion," by H. Lee and S.P. Prawl, 5/11/92, to be published.
- NCEER-92-0012 "Study of Wire Rope Systems for Seismic Protection of Equipment in Buildings," by G.F. Demetriades, M.C. Constantinou and A.M. Reinhorn, 5/20/92, (PB93-116655, A08, MF-A02).

- NCEER-92-0013 "Shape Memory Structural Dampers: Material Properties, Design and Seismic Testing," by P.R. Witting and F.A. Cozzarelli, 5/26/92, (PB93-116663, A05, MF-A01).
- NCEER-92-0014 "Longitudinal Permanent Ground Deformation Effects on Buried Continuous Pipelines," by M.J. O'Rourke, and C. Nordberg, 6/15/92, (PB93-116671, A08, MF-A02).
- NCEER-92-0015 "A Simulation Method for Stationary Gaussian Random Functions Based on the Sampling Theorem," by M. Grigoriu and S. Balopoulou, 6/11/92, (PB93-127496, A05, MF-A01).
- NCEER-92-0016 "Gravity-Load-Designed Reinforced Concrete Buildings: Seismic Evaluation of Existing Construction and Detailing Strategies for Improved Seismic Resistance," by G.W. Hoffmann, S.K. Kunnath, A.M. Reinhorn and J.B. Mander, 7/15/92, (PB94-142007, A08, MF-A02).
- NCEER-92-0017 "Observations on Water System and Pipeline Performance in the Limón Area of Costa Rica Due to the April 22, 1991 Earthquake," by M. O'Rourke and D. Ballantyne, 6/30/92, (PB93-126811, A06, MF-A02).
- NCEER-92-0018 "Fourth Edition of Earthquake Education Materials for Grades K-12," Edited by K.E.K. Ross, 8/10/92, (PB93-114023, A07, MF-A02).
- NCEER-92-0019 "Proceedings from the Fourth Japan-U.S. Workshop on Earthquake Resistant Design of Lifeline Facilities and Countermeasures for Soil Liquefaction," Edited by M. Hamada and T.D. O'Rourke, 8/12/92, (PB93-163939, A99, MF-E11).
- NCEER-92-0020 "Active Bracing System: A Full Scale Implementation of Active Control," by A.M. Reinhorn, T.T. Soong, R.C. Lin, M.A. Riley, Y.P. Wang, S. Aizawa and M. Higashino, 8/14/92, (PB93-127512, A06, MF-A02).
- NCEER-92-0021 "Empirical Analysis of Horizontal Ground Displacement Generated by Liquefaction-Induced Lateral Spreads," by S.F. Bartlett and T.L. Youd, 8/17/92, (PB93-188241, A06, MF-A02).
- NCEER-92-0022 "IDARC Version 3.0: Inelastic Damage Analysis of Reinforced Concrete Structures," by S.K. Kunnath, A.M. Reinhorn and R.F. Lobo, 8/31/92, (PB93-227502, A07, MF-A02).
- NCEER-92-0023 "A Semi-Empirical Analysis of Strong-Motion Peaks in Terms of Seismic Source, Propagation Path and Local Site Conditions, by M. Kamiyama, M.J. O'Rourke and R. Flores-Berrones, 9/9/92, (PB93-150266, A08, MF-A02).
- NCEER-92-0024 "Seismic Behavior of Reinforced Concrete Frame Structures with Nonductile Details, Part I: Summary of Experimental Findings of Full Scale Beam-Column Joint Tests," by A. Beres, R.N. White and P. Gergely, 9/30/92, (PB93-227783, A05, MF-A01).
- NCEER-92-0025 "Experimental Results of Repaired and Retrofitted Beam-Column Joint Tests in Lightly Reinforced Concrete Frame Buildings," by A. Beres, S. El-Borgi, R.N. White and P. Gergely, 10/29/92, (PB93-227791, A05, MF-A01).
- NCEER-92-0026 "A Generalization of Optimal Control Theory: Linear and Nonlinear Structures," by J.N. Yang, Z. Li and S. Vongchavalitkul, 11/2/92, (PB93-188621, A05, MF-A01).
- NCEER-92-0027 "Seismic Resistance of Reinforced Concrete Frame Structures Designed Only for Gravity Loads: Part I - Design and Properties of a One-Third Scale Model Structure," by J.M. Bracci, A.M. Reinhorn and J.B. Mander, 12/1/92, (PB94-104502, A08, MF-A02).
- NCEER-92-0028 "Seismic Resistance of Reinforced Concrete Frame Structures Designed Only for Gravity Loads: Part II - Experimental Performance of Subassemblages," by L.E. Aycaardi, J.B. Mander and A.M. Reinhorn, 12/1/92, (PB94-104510, A08, MF-A02).
- NCEER-92-0029 "Seismic Resistance of Reinforced Concrete Frame Structures Designed Only for Gravity Loads: Part III - Experimental Performance and Analytical Study of a Structural Model," by J.M. Bracci, A.M. Reinhorn and J.B. Mander, 12/1/92, (PB93-227528, A09, MF-A01).

- NCEER-92-0030 "Evaluation of Seismic Retrofit of Reinforced Concrete Frame Structures: Part I - Experimental Performance of Retrofitted Subassemblages," by D. Choudhuri, J.B. Mander and A.M. Reinhorn, 12/8/92, (PB93-198307, A07, MF-A02).
- NCEER-92-0031 "Evaluation of Seismic Retrofit of Reinforced Concrete Frame Structures: Part II - Experimental Performance and Analytical Study of a Retrofitted Structural Model," by J.M. Bracci, A.M. Reinhorn and J.B. Mander, 12/8/92, (PB93-198315, A09, MF-A03).
- NCEER-92-0032 "Experimental and Analytical Investigation of Seismic Response of Structures with Supplemental Fluid Viscous Dampers," by M.C. Constantinou and M.D. Symans, 12/21/92, (PB93-191435, A10, MF-A03). This report is available only through NTIS (see address given above).
- NCEER-92-0033 "Reconnaissance Report on the Cairo, Egypt Earthquake of October 12, 1992," by M. Khater, 12/23/92, (PB93-188621, A03, MF-A01).
- NCEER-92-0034 "Low-Level Dynamic Characteristics of Four Tall Flat-Plate Buildings in New York City," by H. Gavin, S. Yuan, J. Grossman, E. Pekelis and K. Jacob, 12/28/92, (PB93-188217, A07, MF-A02).
- NCEER-93-0001 "An Experimental Study on the Seismic Performance of Brick-Infilled Steel Frames With and Without Retrofit," by J.B. Mander, B. Nair, K. Wojtkowski and J. Ma, 1/29/93, (PB93-227510, A07, MF-A02).
- NCEER-93-0002 "Social Accounting for Disaster Preparedness and Recovery Planning," by S. Cole, E. Pantoja and V. Razak, 2/22/93, (PB94-142114, A12, MF-A03).
- NCEER-93-0003 "Assessment of 1991 NEHRP Provisions for Nonstructural Components and Recommended Revisions," by T.T. Soong, G. Chen, Z. Wu, R-H. Zhang and M. Grigoriu, 3/1/93, (PB93-188639, A06, MF-A02).
- NCEER-93-0004 "Evaluation of Static and Response Spectrum Analysis Procedures of SEAOC/UBC for Seismic Isolated Structures," by C.W. Winters and M.C. Constantinou, 3/23/93, (PB93-198299, A10, MF-A03).
- NCEER-93-0005 "Earthquakes in the Northeast - Are We Ignoring the Hazard? A Workshop on Earthquake Science and Safety for Educators," edited by K.E.K. Ross, 4/2/93, (PB94-103066, A09, MF-A02).
- NCEER-93-0006 "Inelastic Response of Reinforced Concrete Structures with Viscoelastic Braces," by R.F. Lobo, J.M. Bracci, K.L. Shen, A.M. Reinhorn and T.T. Soong, 4/5/93, (PB93-227486, A05, MF-A02).
- NCEER-93-0007 "Seismic Testing of Installation Methods for Computers and Data Processing Equipment," by K. Kosar, T.T. Soong, K.L. Shen, J.A. HoLung and Y.K. Lin, 4/12/93, (PB93-198299, A07, MF-A02).
- NCEER-93-0008 "Retrofit of Reinforced Concrete Frames Using Added Dampers," by A. Reinhorn, M. Constantinou and C. Li, to be published.
- NCEER-93-0009 "Seismic Behavior and Design Guidelines for Steel Frame Structures with Added Viscoelastic Dampers," by K.C. Chang, M.L. Lai, T.T. Soong, D.S. Hao and Y.C. Yeh, 5/1/93, (PB94-141959, A07, MF-A02).
- NCEER-93-0010 "Seismic Performance of Shear-Critical Reinforced Concrete Bridge Piers," by J.B. Mander, S.M. Waheed, M.T.A. Chaudhary and S.S. Chen, 5/12/93, (PB93-227494, A08, MF-A02).
- NCEER-93-0011 "3D-BASIS-TABS: Computer Program for Nonlinear Dynamic Analysis of Three Dimensional Base Isolated Structures," by S. Nagarajaiah, C. Li, A.M. Reinhorn and M.C. Constantinou, 8/2/93, (PB94-141819, A09, MF-A02).
- NCEER-93-0012 "Effects of Hydrocarbon Spills from an Oil Pipeline Break on Ground Water," by O.J. Helweg and H.H.M. Hwang, 8/3/93, (PB94-141942, A06, MF-A02).
- NCEER-93-0013 "Simplified Procedures for Seismic Design of Nonstructural Components and Assessment of Current Code Provisions," by M.P. Singh, L.E. Suarez, E.E. Matheu and G.O. Maldonado, 8/4/93, (PB94-141827, A09, MF-A02).
- NCEER-93-0014 "An Energy Approach to Seismic Analysis and Design of Secondary Systems," by G. Chen and T.T. Soong, 8/6/93, (PB94-142767, A11, MF-A03).



- NCEER-93-0015 "Proceedings from School Sites: Becoming Prepared for Earthquakes - Commemorating the Third Anniversary of the Loma Prieta Earthquake," Edited by F.E. Winslow and K.E.K. Ross, 8/16/93, (PB94-154275, A16, MF-A02).
- NCEER-93-0016 "Reconnaissance Report of Damage to Historic Monuments in Cairo, Egypt Following the October 12, 1992 Dahshur Earthquake," by D. Sykora, D. Look, G. Croci, E. Karaesmen and E. Karaesmen, 8/19/93, (PB94-142221, A08, MF-A02).
- NCEER-93-0017 "The Island of Guam Earthquake of August 8, 1993," by S.W. Swan and S.K. Harris, 9/30/93, (PB94-141843, A04, MF-A01).
- NCEER-93-0018 "Engineering Aspects of the October 12, 1992 Egyptian Earthquake," by A.W. Elgamal, M. Amer, K. Adalier and A. Abul-Fadl, 10/7/93, (PB94-141983, A05, MF-A01).
- NCEER-93-0019 "Development of an Earthquake Motion Simulator and its Application in Dynamic Centrifuge Testing," by I. Krstelj, Supervised by J.H. Prevost, 10/23/93, (PB94-181773, A-10, MF-A03).
- NCEER-93-0020 "NCEER-Taisei Corporation Research Program on Sliding Seismic Isolation Systems for Bridges: Experimental and Analytical Study of a Friction Pendulum System (FPS)," by M.C. Constantinou, P. Tsopelas, Y-S. Kim and S. Okamoto, 11/1/93, (PB94-142775, A08, MF-A02).
- NCEER-93-0021 "Finite Element Modeling of Elastomeric Seismic Isolation Bearings," by L.J. Billings, Supervised by R. Shepherd, 11/8/93, to be published.
- NCEER-93-0022 "Seismic Vulnerability of Equipment in Critical Facilities: Life-Safety and Operational Consequences," by K. Porter, G.S. Johnson, M.M. Zadeh, C. Scawthorn and S. Eder, 11/24/93, (PB94-181765, A16, MF-A03).
- NCEER-93-0023 "Hokkaido Nansei-oki, Japan Earthquake of July 12, 1993, by P.I. Yanev and C.R. Scawthorn, 12/23/93, (PB94-181500, A07, MF-A01).
- NCEER-94-0001 "An Evaluation of Seismic Serviceability of Water Supply Networks with Application to the San Francisco Auxiliary Water Supply System," by I. Markov, Supervised by M. Grigoriu and T. O'Rourke, 1/21/94, (PB94-204013, A07, MF-A02).
- NCEER-94-0002 "NCEER-Taisei Corporation Research Program on Sliding Seismic Isolation Systems for Bridges: Experimental and Analytical Study of Systems Consisting of Sliding Bearings, Rubber Restoring Force Devices and Fluid Dampers," Volumes I and II, by P. Tsopelas, S. Okamoto, M.C. Constantinou, D. Ozaki and S. Fujii, 2/4/94, (PB94-181740, A09, MF-A02 and PB94-181757, A12, MF-A03).
- NCEER-94-0003 "A Markov Model for Local and Global Damage Indices in Seismic Analysis," by S. Rahman and M. Grigoriu, 2/18/94, (PB94-206000, A12, MF-A03).
- NCEER-94-0004 "Proceedings from the NCEER Workshop on Seismic Response of Masonry Infills," edited by D.P. Abrams, 3/1/94, (PB94-180783, A07, MF-A02).
- NCEER-94-0005 "The Northridge, California Earthquake of January 17, 1994: General Reconnaissance Report," edited by J.D. Goltz, 3/11/94, (PB94-193943, A10, MF-A03).
- NCEER-94-0006 "Seismic Energy Based Fatigue Damage Analysis of Bridge Columns: Part I - Evaluation of Seismic Capacity," by G.A. Chang and J.B. Mander, 3/14/94, (PB94-219185, A11, MF-A03).
- NCEER-94-0007 "Seismic Isolation of Multi-Story Frame Structures Using Spherical Sliding Isolation Systems," by T.M. Al-Hussaini, V.A. Zayas and M.C. Constantinou, 3/17/94, (PB94-193745, A09, MF-A02).
- NCEER-94-0008 "The Northridge, California Earthquake of January 17, 1994: Performance of Highway Bridges," edited by I.G. Buckle, 3/24/94, (PB94-193851, A06, MF-A02).
- NCEER-94-0009 "Proceedings of the Third U.S.-Japan Workshop on Earthquake Protective Systems for Bridges," edited by I.G. Buckle and I. Friedland, 3/31/94, (PB94-195815, A99, MF-A06).

- NCEER-94-0010 "3D-BASIS-ME: Computer Program for Nonlinear Dynamic Analysis of Seismically Isolated Single and Multiple Structures and Liquid Storage Tanks," by P.C. Tsopelas, M.C. Constantinou and A.M. Reinhorn, 4/12/94, (PB94-204922, A09, MF-A02).
- NCEER-94-0011 "The Northridge, California Earthquake of January 17, 1994: Performance of Gas Transmission Pipelines," by T.D. O'Rourke and M.C. Palmer, 5/16/94, (PB94-204989, A05, MF-A01).
- NCEER-94-0012 "Feasibility Study of Replacement Procedures and Earthquake Performance Related to Gas Transmission Pipelines," by T.D. O'Rourke and M.C. Palmer, 5/25/94, (PB94-206638, A09, MF-A02).
- NCEER-94-0013 "Seismic Energy Based Fatigue Damage Analysis of Bridge Columns: Part II - Evaluation of Seismic Demand," by G.A. Chang and J.B. Mander, 6/1/94, (PB95-18106, A08, MF-A02).
- NCEER-94-0014 "NCEER-Taisei Corporation Research Program on Sliding Seismic Isolation Systems for Bridges: Experimental and Analytical Study of a System Consisting of Sliding Bearings and Fluid Restoring Force/Damping Devices," by P. Tsopelas and M.C. Constantinou, 6/13/94, (PB94-219144, A10, MF-A03).
- NCEER-94-0015 "Generation of Hazard-Consistent Fragility Curves for Seismic Loss Estimation Studies," by H. Hwang and J-R. Huo, 6/14/94, (PB95-181996, A09, MF-A02).
- NCEER-94-0016 "Seismic Study of Building Frames with Added Energy-Absorbing Devices," by W.S. Pong, C.S. Tsai and G.C. Lee, 6/20/94, (PB94-219136, A10, A03).
- NCEER-94-0017 "Sliding Mode Control for Seismic-Excited Linear and Nonlinear Civil Engineering Structures," by J. Yang, J. Wu, A. Agrawal and Z. Li, 6/21/94, (PB95-138483, A06, MF-A02).
- NCEER-94-0018 "3D-BASIS-TABS Version 2.0: Computer Program for Nonlinear Dynamic Analysis of Three Dimensional Base Isolated Structures," by A.M. Reinhorn, S. Nagarajaiah, M.C. Constantinou, P. Tsopelas and R. Li, 6/22/94, (PB95-182176, A08, MF-A02).
- NCEER-94-0019 "Proceedings of the International Workshop on Civil Infrastructure Systems: Application of Intelligent Systems and Advanced Materials on Bridge Systems," Edited by G.C. Lee and K.C. Chang, 7/18/94, (PB95-252474, A20, MF-A04).
- NCEER-94-0020 "Study of Seismic Isolation Systems for Computer Floors," by V. Lambrou and M.C. Constantinou, 7/19/94, (PB95-138533, A10, MF-A03).
- NCEER-94-0021 "Proceedings of the U.S.-Italian Workshop on Guidelines for Seismic Evaluation and Rehabilitation of Unreinforced Masonry Buildings," Edited by D.P. Abrams and G.M. Calvi, 7/20/94, (PB95-138749, A13, MF-A03).
- NCEER-94-0022 "NCEER-Taisei Corporation Research Program on Sliding Seismic Isolation Systems for Bridges: Experimental and Analytical Study of a System Consisting of Lubricated PTFE Sliding Bearings and Mild Steel Dampers," by P. Tsopelas and M.C. Constantinou, 7/22/94, (PB95-182184, A08, MF-A02).
- NCEER-94-0023 "Development of Reliability-Based Design Criteria for Buildings Under Seismic Load," by Y.K. Wen, H. Hwang and M. Shinozuka, 8/1/94, (PB95-211934, A08, MF-A02).
- NCEER-94-0024 "Experimental Verification of Acceleration Feedback Control Strategies for an Active Tendon System," by S.J. Dyke, B.F. Spencer, Jr., P. Quast, M.K. Sain, D.C. Kaspari, Jr. and T.T. Soong, 8/29/94, (PB95-212320, A05, MF-A01).
- NCEER-94-0025 "Seismic Retrofitting Manual for Highway Bridges," Edited by I.G. Buckle and I.F. Friedland, published by the Federal Highway Administration (PB95-212676, A15, MF-A03).
- NCEER-94-0026 "Proceedings from the Fifth U.S.-Japan Workshop on Earthquake Resistant Design of Lifeline Facilities and Countermeasures Against Soil Liquefaction," Edited by T.D. O'Rourke and M. Hamada, 11/7/94, (PB95-220802, A99, MF-E08).

- NCEER-95-0001 “Experimental and Analytical Investigation of Seismic Retrofit of Structures with Supplemental Damping: Part 1 - Fluid Viscous Damping Devices,” by A.M. Reinhorn, C. Li and M.C. Constantinou, 1/3/95, (PB95-266599, A09, MF-A02).
- NCEER-95-0002 “Experimental and Analytical Study of Low-Cycle Fatigue Behavior of Semi-Rigid Top-And-Seat Angle Connections,” by G. Pekcan, J.B. Mander and S.S. Chen, 1/5/95, (PB95-220042, A07, MF-A02).
- NCEER-95-0003 “NCEER-ATC Joint Study on Fragility of Buildings,” by T. Anagnos, C. Rojahn and A.S. Kiremidjian, 1/20/95, (PB95-220026, A06, MF-A02).
- NCEER-95-0004 “Nonlinear Control Algorithms for Peak Response Reduction,” by Z. Wu, T.T. Soong, V. Gattulli and R.C. Lin, 2/16/95, (PB95-220349, A05, MF-A01).
- NCEER-95-0005 “Pipeline Replacement Feasibility Study: A Methodology for Minimizing Seismic and Corrosion Risks to Underground Natural Gas Pipelines,” by R.T. Eguchi, H.A. Seligson and D.G. Honegger, 3/2/95, (PB95-252326, A06, MF-A02).
- NCEER-95-0006 “Evaluation of Seismic Performance of an 11-Story Frame Building During the 1994 Northridge Earthquake,” by F. Naeim, R. DiSulio, K. Benuska, A. Reinhorn and C. Li, to be published.
- NCEER-95-0007 “Prioritization of Bridges for Seismic Retrofitting,” by N. Basöz and A.S. Kiremidjian, 4/24/95, (PB95-252300, A08, MF-A02).
- NCEER-95-0008 “Method for Developing Motion Damage Relationships for Reinforced Concrete Frames,” by A. Singhal and A.S. Kiremidjian, 5/11/95, (PB95-266607, A06, MF-A02).
- NCEER-95-0009 “Experimental and Analytical Investigation of Seismic Retrofit of Structures with Supplemental Damping: Part II - Friction Devices,” by C. Li and A.M. Reinhorn, 7/6/95, (PB96-128087, A11, MF-A03).
- NCEER-95-0010 “Experimental Performance and Analytical Study of a Non-Ductile Reinforced Concrete Frame Structure Retrofitted with Elastomeric Spring Dampers,” by G. Pekcan, J.B. Mander and S.S. Chen, 7/14/95, (PB96-137161, A08, MF-A02).
- NCEER-95-0011 “Development and Experimental Study of Semi-Active Fluid Damping Devices for Seismic Protection of Structures,” by M.D. Symans and M.C. Constantinou, 8/3/95, (PB96-136940, A23, MF-A04).
- NCEER-95-0012 “Real-Time Structural Parameter Modification (RSPM): Development of Innervated Structures,” by Z. Liang, M. Tong and G.C. Lee, 4/11/95, (PB96-137153, A06, MF-A01).
- NCEER-95-0013 “Experimental and Analytical Investigation of Seismic Retrofit of Structures with Supplemental Damping: Part III - Viscous Damping Walls,” by A.M. Reinhorn and C. Li, 10/1/95, (PB96-176409, A11, MF-A03).
- NCEER-95-0014 “Seismic Fragility Analysis of Equipment and Structures in a Memphis Electric Substation,” by J-R. Huo and H.H.M. Hwang, 8/10/95, (PB96-128087, A09, MF-A02).
- NCEER-95-0015 “The Hanshin-Awaji Earthquake of January 17, 1995: Performance of Lifelines,” Edited by M. Shinozuka, 11/3/95, (PB96-176383, A15, MF-A03).
- NCEER-95-0016 “Highway Culvert Performance During Earthquakes,” by T.L. Youd and C.J. Beckman, available as NCEER-96-0015.
- NCEER-95-0017 “The Hanshin-Awaji Earthquake of January 17, 1995: Performance of Highway Bridges,” Edited by I.G. Buckle, 12/1/95, to be published.
- NCEER-95-0018 “Modeling of Masonry Infill Panels for Structural Analysis,” by A.M. Reinhorn, A. Madan, R.E. Valles, Y. Reichmann and J.B. Mander, 12/8/95, (PB97-110886, MF-A01, A06).
- NCEER-95-0019 “Optimal Polynomial Control for Linear and Nonlinear Structures,” by A.K. Agrawal and J.N. Yang, 12/11/95, (PB96-168737, A07, MF-A02).

- NCEER-95-0020 "Retrofit of Non-Ductile Reinforced Concrete Frames Using Friction Dampers," by R.S. Rao, P. Gergely and R.N. White, 12/22/95, (PB97-133508, A10, MF-A02).
- NCEER-95-0021 "Parametric Results for Seismic Response of Pile-Supported Bridge Bents," by G. Mylonakis, A. Nikolaou and G. Gazetas, 12/22/95, (PB97-100242, A12, MF-A03).
- NCEER-95-0022 "Kinematic Bending Moments in Seismically Stressed Piles," by A. Nikolaou, G. Mylonakis and G. Gazetas, 12/23/95, (PB97-113914, MF-A03, A13).
- NCEER-96-0001 "Dynamic Response of Unreinforced Masonry Buildings with Flexible Diaphragms," by A.C. Costley and D.P. Abrams, 10/10/96, (PB97-133573, MF-A03, A15).
- NCEER-96-0002 "State of the Art Review: Foundations and Retaining Structures," by I. Po Lam, to be published.
- NCEER-96-0003 "Ductility of Rectangular Reinforced Concrete Bridge Columns with Moderate Confinement," by N. Wehbe, M. Saiidi, D. Sanders and B. Douglas, 11/7/96, (PB97-133557, A06, MF-A02).
- NCEER-96-0004 "Proceedings of the Long-Span Bridge Seismic Research Workshop," edited by I.G. Buckle and I.M. Friedland, to be published.
- NCEER-96-0005 "Establish Representative Pier Types for Comprehensive Study: Eastern United States," by J. Kulicki and Z. Prucz, 5/28/96, (PB98-119217, A07, MF-A02).
- NCEER-96-0006 "Establish Representative Pier Types for Comprehensive Study: Western United States," by R. Imbsen, R.A. Schamber and T.A. Osterkamp, 5/28/96, (PB98-118607, A07, MF-A02).
- NCEER-96-0007 "Nonlinear Control Techniques for Dynamical Systems with Uncertain Parameters," by R.G. Ghanem and M.I. Bujakov, 5/27/96, (PB97-100259, A17, MF-A03).
- NCEER-96-0008 "Seismic Evaluation of a 30-Year Old Non-Ductile Highway Bridge Pier and Its Retrofit," by J.B. Mander, B. Mahmoodzadegan, S. Bhadra and S.S. Chen, 5/31/96, (PB97-110902, MF-A03, A10).
- NCEER-96-0009 "Seismic Performance of a Model Reinforced Concrete Bridge Pier Before and After Retrofit," by J.B. Mander, J.H. Kim and C.A. Ligozio, 5/31/96, (PB97-110910, MF-A02, A10).
- NCEER-96-0010 "IDARC2D Version 4.0: A Computer Program for the Inelastic Damage Analysis of Buildings," by R.E. Valles, A.M. Reinhorn, S.K. Kunnath, C. Li and A. Madan, 6/3/96, (PB97-100234, A17, MF-A03).
- NCEER-96-0011 "Estimation of the Economic Impact of Multiple Lifeline Disruption: Memphis Light, Gas and Water Division Case Study," by S.E. Chang, H.A. Seligson and R.T. Eguchi, 8/16/96, (PB97-133490, A11, MF-A03).
- NCEER-96-0012 "Proceedings from the Sixth Japan-U.S. Workshop on Earthquake Resistant Design of Lifeline Facilities and Countermeasures Against Soil Liquefaction, Edited by M. Hamada and T. O'Rourke, 9/11/96, (PB97-133581, A99, MF-A06).
- NCEER-96-0013 "Chemical Hazards, Mitigation and Preparedness in Areas of High Seismic Risk: A Methodology for Estimating the Risk of Post-Earthquake Hazardous Materials Release," by H.A. Seligson, R.T. Eguchi, K.J. Tierney and K. Richmond, 11/7/96, (PB97-133565, MF-A02, A08).
- NCEER-96-0014 "Response of Steel Bridge Bearings to Reversed Cyclic Loading," by J.B. Mander, D-K. Kim, S.S. Chen and G.J. Premus, 11/13/96, (PB97-140735, A12, MF-A03).
- NCEER-96-0015 "Highway Culvert Performance During Past Earthquakes," by T.L. Youd and C.J. Beckman, 11/25/96, (PB97-133532, A06, MF-A01).
- NCEER-97-0001 "Evaluation, Prevention and Mitigation of Pounding Effects in Building Structures," by R.E. Valles and A.M. Reinhorn, 2/20/97, (PB97-159552, A14, MF-A03).
- NCEER-97-0002 "Seismic Design Criteria for Bridges and Other Highway Structures," by C. Rojahn, R. Mayes, D.G. Anderson, J. Clark, J.H. Hom, R.V. Nutt and M.J. O'Rourke, 4/30/97, (PB97-194658, A06, MF-A03).

- NCEER-97-0003 "Proceedings of the U.S.-Italian Workshop on Seismic Evaluation and Retrofit," Edited by D.P. Abrams and G.M. Calvi, 3/19/97, (PB97-194666, A13, MF-A03).
- NCEER-97-0004 "Investigation of Seismic Response of Buildings with Linear and Nonlinear Fluid Viscous Dampers," by A.A. Seleemah and M.C. Constantinou, 5/21/97, (PB98-109002, A15, MF-A03).
- NCEER-97-0005 "Proceedings of the Workshop on Earthquake Engineering Frontiers in Transportation Facilities," edited by G.C. Lee and I.M. Friedland, 8/29/97, (PB98-128911, A25, MR-A04).
- NCEER-97-0006 "Cumulative Seismic Damage of Reinforced Concrete Bridge Piers," by S.K. Kunnath, A. El-Bahy, A. Taylor and W. Stone, 9/2/97, (PB98-108814, A11, MF-A03).
- NCEER-97-0007 "Structural Details to Accommodate Seismic Movements of Highway Bridges and Retaining Walls," by R.A. Imbsen, R.A. Schamber, E. Thorkildsen, A. Kartoum, B.T. Martin, T.N. Rosser and J.M. Kulicki, 9/3/97, (PB98-108996, A09, MF-A02).
- NCEER-97-0008 "A Method for Earthquake Motion-Damage Relationships with Application to Reinforced Concrete Frames," by A. Singhal and A.S. Kiremidjian, 9/10/97, (PB98-108988, A13, MF-A03).
- NCEER-97-0009 "Seismic Analysis and Design of Bridge Abutments Considering Sliding and Rotation," by K. Fishman and R. Richards, Jr., 9/15/97, (PB98-108897, A06, MF-A02).
- NCEER-97-0010 "Proceedings of the FHWA/NCEER Workshop on the National Representation of Seismic Ground Motion for New and Existing Highway Facilities," edited by I.M. Friedland, M.S. Power and R.L. Mayes, 9/22/97, (PB98-128903, A21, MF-A04).
- NCEER-97-0011 "Seismic Analysis for Design or Retrofit of Gravity Bridge Abutments," by K.L. Fishman, R. Richards, Jr. and R.C. Divito, 10/2/97, (PB98-128937, A08, MF-A02).
- NCEER-97-0012 "Evaluation of Simplified Methods of Analysis for Yielding Structures," by P. Tsopelas, M.C. Constantinou, C.A. Kircher and A.S. Whittaker, 10/31/97, (PB98-128929, A10, MF-A03).
- NCEER-97-0013 "Seismic Design of Bridge Columns Based on Control and Repairability of Damage," by C-T. Cheng and J.B. Mander, 12/8/97, (PB98-144249, A11, MF-A03).
- NCEER-97-0014 "Seismic Resistance of Bridge Piers Based on Damage Avoidance Design," by J.B. Mander and C-T. Cheng, 12/10/97, (PB98-144223, A09, MF-A02).
- NCEER-97-0015 "Seismic Response of Nominally Symmetric Systems with Strength Uncertainty," by S. Balopoulou and M. Grigoriu, 12/23/97, (PB98-153422, A11, MF-A03).
- NCEER-97-0016 "Evaluation of Seismic Retrofit Methods for Reinforced Concrete Bridge Columns," by T.J. Wipf, F.W. Klaiber and F.M. Russo, 12/28/97, (PB98-144215, A12, MF-A03).
- NCEER-97-0017 "Seismic Fragility of Existing Conventional Reinforced Concrete Highway Bridges," by C.L. Mullen and A.S. Cakmak, 12/30/97, (PB98-153406, A08, MF-A02).
- NCEER-97-0018 "Loss Assessment of Memphis Buildings," edited by D.P. Abrams and M. Shinozuka, 12/31/97, (PB98-144231, A13, MF-A03).
- NCEER-97-0019 "Seismic Evaluation of Frames with Infill Walls Using Quasi-static Experiments," by K.M. Mosalam, R.N. White and P. Gergely, 12/31/97, (PB98-153455, A07, MF-A02).
- NCEER-97-0020 "Seismic Evaluation of Frames with Infill Walls Using Pseudo-dynamic Experiments," by K.M. Mosalam, R.N. White and P. Gergely, 12/31/97, (PB98-153430, A07, MF-A02).
- NCEER-97-0021 "Computational Strategies for Frames with Infill Walls: Discrete and Smeared Crack Analyses and Seismic Fragility," by K.M. Mosalam, R.N. White and P. Gergely, 12/31/97, (PB98-153414, A10, MF-A02).

- NCEER-97-0022 "Proceedings of the NCEER Workshop on Evaluation of Liquefaction Resistance of Soils," edited by T.L. Youd and I.M. Idriss, 12/31/97, (PB98-155617, A15, MF-A03).
- MCEER-98-0001 "Extraction of Nonlinear Hysteretic Properties of Seismically Isolated Bridges from Quick-Release Field Tests," by Q. Chen, B.M. Douglas, E.M. Maragakis and I.G. Buckle, 5/26/98, (PB99-118838, A06, MF-A01).
- MCEER-98-0002 "Methodologies for Evaluating the Importance of Highway Bridges," by A. Thomas, S. Eshenaur and J. Kulicki, 5/29/98, (PB99-118846, A10, MF-A02).
- MCEER-98-0003 "Capacity Design of Bridge Piers and the Analysis of Overstrength," by J.B. Mander, A. Dutta and P. Goel, 6/1/98, (PB99-118853, A09, MF-A02).
- MCEER-98-0004 "Evaluation of Bridge Damage Data from the Loma Prieta and Northridge, California Earthquakes," by N. Basoz and A. Kiremidjian, 6/2/98, (PB99-118861, A15, MF-A03).
- MCEER-98-0005 "Screening Guide for Rapid Assessment of Liquefaction Hazard at Highway Bridge Sites," by T. L. Youd, 6/16/98, (PB99-118879, A06, not available on microfiche).
- MCEER-98-0006 "Structural Steel and Steel/Concrete Interface Details for Bridges," by P. Ritchie, N. Kauh and J. Kulicki, 7/13/98, (PB99-118945, A06, MF-A01).
- MCEER-98-0007 "Capacity Design and Fatigue Analysis of Confined Concrete Columns," by A. Dutta and J.B. Mander, 7/14/98, (PB99-118960, A14, MF-A03).
- MCEER-98-0008 "Proceedings of the Workshop on Performance Criteria for Telecommunication Services Under Earthquake Conditions," edited by A.J. Schiff, 7/15/98, (PB99-118952, A08, MF-A02).
- MCEER-98-0009 "Fatigue Analysis of Unconfined Concrete Columns," by J.B. Mander, A. Dutta and J.H. Kim, 9/12/98, (PB99-123655, A10, MF-A02).
- MCEER-98-0010 "Centrifuge Modeling of Cyclic Lateral Response of Pile-Cap Systems and Seat-Type Abutments in Dry Sands," by A.D. Gadre and R. Dobry, 10/2/98, (PB99-123606, A13, MF-A03).
- MCEER-98-0011 "IDARC-BRIDGE: A Computational Platform for Seismic Damage Assessment of Bridge Structures," by A.M. Reinhorn, V. Simeonov, G. Mylonakis and Y. Reichman, 10/2/98, (PB99-162919, A15, MF-A03).
- MCEER-98-0012 "Experimental Investigation of the Dynamic Response of Two Bridges Before and After Retrofitting with Elastomeric Bearings," by D.A. Wendichansky, S.S. Chen and J.B. Mander, 10/2/98, (PB99-162927, A15, MF-A03).
- MCEER-98-0013 "Design Procedures for Hinge Restrainers and Hinge Sear Width for Multiple-Frame Bridges," by R. Des Roches and G.L. Fenves, 11/3/98, (PB99-140477, A13, MF-A03).
- MCEER-98-0014 "Response Modification Factors for Seismically Isolated Bridges," by M.C. Constantinou and J.K. Quarshie, 11/3/98, (PB99-140485, A14, MF-A03).
- MCEER-98-0015 "Proceedings of the U.S.-Italy Workshop on Seismic Protective Systems for Bridges," edited by I.M. Friedland and M.C. Constantinou, 11/3/98, (PB2000-101711, A22, MF-A04).
- MCEER-98-0016 "Appropriate Seismic Reliability for Critical Equipment Systems: Recommendations Based on Regional Analysis of Financial and Life Loss," by K. Porter, C. Scawthorn, C. Taylor and N. Blais, 11/10/98, (PB99-157265, A08, MF-A02).
- MCEER-98-0017 "Proceedings of the U.S. Japan Joint Seminar on Civil Infrastructure Systems Research," edited by M. Shinozuka and A. Rose, 11/12/98, (PB99-156713, A16, MF-A03).
- MCEER-98-0018 "Modeling of Pile Footings and Drilled Shafts for Seismic Design," by I. PoLam, M. Kapuskar and D. Chaudhuri, 12/21/98, (PB99-157257, A09, MF-A02).

- MCEER-99-0001 "Seismic Evaluation of a Masonry Infilled Reinforced Concrete Frame by Pseudodynamic Testing," by S.G. Buonopane and R.N. White, 2/16/99, (PB99-162851, A09, MF-A02).
- MCEER-99-0002 "Response History Analysis of Structures with Seismic Isolation and Energy Dissipation Systems: Verification Examples for Program SAP2000," by J. Scheller and M.C. Constantinou, 2/22/99, (PB99-162869, A08, MF-A02).
- MCEER-99-0003 "Experimental Study on the Seismic Design and Retrofit of Bridge Columns Including Axial Load Effects," by A. Dutta, T. Kokorina and J.B. Mander, 2/22/99, (PB99-162877, A09, MF-A02).
- MCEER-99-0004 "Experimental Study of Bridge Elastomeric and Other Isolation and Energy Dissipation Systems with Emphasis on Uplift Prevention and High Velocity Near-source Seismic Excitation," by A. Kasalanati and M. C. Constantinou, 2/26/99, (PB99-162885, A12, MF-A03).
- MCEER-99-0005 "Truss Modeling of Reinforced Concrete Shear-flexure Behavior," by J.H. Kim and J.B. Mander, 3/8/99, (PB99-163693, A12, MF-A03).
- MCEER-99-0006 "Experimental Investigation and Computational Modeling of Seismic Response of a 1:4 Scale Model Steel Structure with a Load Balancing Supplemental Damping System," by G. Pekcan, J.B. Mander and S.S. Chen, 4/2/99, (PB99-162893, A11, MF-A03).
- MCEER-99-0007 "Effect of Vertical Ground Motions on the Structural Response of Highway Bridges," by M.R. Button, C.J. Cronin and R.L. Mayes, 4/10/99, (PB2000-101411, A10, MF-A03).
- MCEER-99-0008 "Seismic Reliability Assessment of Critical Facilities: A Handbook, Supporting Documentation, and Model Code Provisions," by G.S. Johnson, R.E. Sheppard, M.D. Quilici, S.J. Eder and C.R. Scawthorn, 4/12/99, (PB2000-101701, A18, MF-A04).
- MCEER-99-0009 "Impact Assessment of Selected MCEER Highway Project Research on the Seismic Design of Highway Structures," by C. Rojahn, R. Mayes, D.G. Anderson, J.H. Clark, D'Appolonia Engineering, S. Gloyd and R.V. Nutt, 4/14/99, (PB99-162901, A10, MF-A02).
- MCEER-99-0010 "Site Factors and Site Categories in Seismic Codes," by R. Dobry, R. Ramos and M.S. Power, 7/19/99, (PB2000-101705, A08, MF-A02).
- MCEER-99-0011 "Restrainer Design Procedures for Multi-Span Simply-Supported Bridges," by M.J. Randall, M. Saiidi, E. Maragakis and T. Isakovic, 7/20/99, (PB2000-101702, A10, MF-A02).
- MCEER-99-0012 "Property Modification Factors for Seismic Isolation Bearings," by M.C. Constantinou, P. Tsopelas, A. Kasalanati and E. Wolff, 7/20/99, (PB2000-103387, A11, MF-A03).
- MCEER-99-0013 "Critical Seismic Issues for Existing Steel Bridges," by P. Ritchie, N. Kauh and J. Kulicki, 7/20/99, (PB2000-101697, A09, MF-A02).
- MCEER-99-0014 "Nonstructural Damage Database," by A. Kao, T.T. Soong and A. Vender, 7/24/99, (PB2000-101407, A06, MF-A01).
- MCEER-99-0015 "Guide to Remedial Measures for Liquefaction Mitigation at Existing Highway Bridge Sites," by H.G. Cooke and J. K. Mitchell, 7/26/99, (PB2000-101703, A11, MF-A03).
- MCEER-99-0016 "Proceedings of the MCEER Workshop on Ground Motion Methodologies for the Eastern United States," edited by N. Abrahamson and A. Becker, 8/11/99, (PB2000-103385, A07, MF-A02).
- MCEER-99-0017 "Quindío, Colombia Earthquake of January 25, 1999: Reconnaissance Report," by A.P. Asfura and P.J. Flores, 10/4/99, (PB2000-106893, A06, MF-A01).
- MCEER-99-0018 "Hysteretic Models for Cyclic Behavior of Deteriorating Inelastic Structures," by M.V. Sivaselvan and A.M. Reinhorn, 11/5/99, (PB2000-103386, A08, MF-A02).

- MCEER-99-0019 "Proceedings of the 7<sup>th</sup> U.S.- Japan Workshop on Earthquake Resistant Design of Lifeline Facilities and Countermeasures Against Soil Liquefaction," edited by T.D. O'Rourke, J.P. Bardet and M. Hamada, 11/19/99, (PB2000-103354, A99, MF-A06).
- MCEER-99-0020 "Development of Measurement Capability for Micro-Vibration Evaluations with Application to Chip Fabrication Facilities," by G.C. Lee, Z. Liang, J.W. Song, J.D. Shen and W.C. Liu, 12/1/99, (PB2000-105993, A08, MF-A02).
- MCEER-99-0021 "Design and Retrofit Methodology for Building Structures with Supplemental Energy Dissipating Systems," by G. Pekcan, J.B. Mander and S.S. Chen, 12/31/99, (PB2000-105994, A11, MF-A03).
- MCEER-00-0001 "The Marmara, Turkey Earthquake of August 17, 1999: Reconnaissance Report," edited by C. Scawthorn; with major contributions by M. Bruneau, R. Eguchi, T. Holzer, G. Johnson, J. Mander, J. Mitchell, W. Mitchell, A. Papageorgiou, C. Scaethorn, and G. Webb, 3/23/00, (PB2000-106200, A11, MF-A03).
- MCEER-00-0002 "Proceedings of the MCEER Workshop for Seismic Hazard Mitigation of Health Care Facilities," edited by G.C. Lee, M. Ettouney, M. Grigoriu, J. Hauer and J. Nigg, 3/29/00, (PB2000-106892, A08, MF-A02).
- MCEER-00-0003 "The Chi-Chi, Taiwan Earthquake of September 21, 1999: Reconnaissance Report," edited by G.C. Lee and C.H. Loh, with major contributions by G.C. Lee, M. Bruneau, I.G. Buckle, S.E. Chang, P.J. Flores, T.D. O'Rourke, M. Shinozuka, T.T. Soong, C-H. Loh, K-C. Chang, Z-J. Chen, J-S. Hwang, M-L. Lin, G-Y. Liu, K-C. Tsai, G.C. Yao and C-L. Yen, 4/30/00, (PB2001-100980, A10, MF-A02).
- MCEER-00-0004 "Seismic Retrofit of End-Sway Frames of Steel Deck-Truss Bridges with a Supplemental Tendon System: Experimental and Analytical Investigation," by G. Pekcan, J.B. Mander and S.S. Chen, 7/1/00, (PB2001-100982, A10, MF-A02).
- MCEER-00-0005 "Sliding Fragility of Unrestrained Equipment in Critical Facilities," by W.H. Chong and T.T. Soong, 7/5/00, (PB2001-100983, A08, MF-A02).
- MCEER-00-0006 "Seismic Response of Reinforced Concrete Bridge Pier Walls in the Weak Direction," by N. Abo-Shadi, M. Saiidi and D. Sanders, 7/17/00, (PB2001-100981, A17, MF-A03).
- MCEER-00-0007 "Low-Cycle Fatigue Behavior of Longitudinal Reinforcement in Reinforced Concrete Bridge Columns," by J. Brown and S.K. Kunnath, 7/23/00, (PB2001-104392, A08, MF-A02).
- MCEER-00-0008 "Soil Structure Interaction of Bridges for Seismic Analysis," I. PoLam and H. Law, 9/25/00, (PB2001-105397, A08, MF-A02).
- MCEER-00-0009 "Proceedings of the First MCEER Workshop on Mitigation of Earthquake Disaster by Advanced Technologies (MEDAT-1), edited by M. Shinozuka, D.J. Inman and T.D. O'Rourke, 11/10/00, (PB2001-105399, A14, MF-A03).
- MCEER-00-0010 "Development and Evaluation of Simplified Procedures for Analysis and Design of Buildings with Passive Energy Dissipation Systems, Revision 01," by O.M. Ramirez, M.C. Constantinou, C.A. Kircher, A.S. Whittaker, M.W. Johnson, J.D. Gomez and C. Chrysostomou, 11/16/01, (PB2001-105523, A23, MF-A04).
- MCEER-00-0011 "Dynamic Soil-Foundation-Structure Interaction Analyses of Large Caissons," by C-Y. Chang, C-M. Mok, Z-L. Wang, R. Settgast, F. Waggoner, M.A. Ketchum, H.M. Gonnermann and C-C. Chin, 12/30/00, (PB2001-104373, A07, MF-A02).
- MCEER-00-0012 "Experimental Evaluation of Seismic Performance of Bridge Restrainers," by A.G. Vlassis, E.M. Maragakis and M. Saiid Saiidi, 12/30/00, (PB2001-104354, A09, MF-A02).
- MCEER-00-0013 "Effect of Spatial Variation of Ground Motion on Highway Structures," by M. Shinozuka, V. Saxena and G. Deodatis, 12/31/00, (PB2001-108755, A13, MF-A03).
- MCEER-00-0014 "A Risk-Based Methodology for Assessing the Seismic Performance of Highway Systems," by S.D. Werner, C.E. Taylor, J.E. Moore, II, J.S. Walton and S. Cho, 12/31/00, (PB2001-108756, A14, MF-A03).



- MCEER-01-0001 “Experimental Investigation of P-Delta Effects to Collapse During Earthquakes,” by D. Vian and M. Bruneau, 6/25/01, (PB2002-100534, A17, MF-A03).
- MCEER-01-0002 “Proceedings of the Second MCEER Workshop on Mitigation of Earthquake Disaster by Advanced Technologies (MEDAT-2),” edited by M. Bruneau and D.J. Inman, 7/23/01, (PB2002-100434, A16, MF-A03).
- MCEER-01-0003 “Sensitivity Analysis of Dynamic Systems Subjected to Seismic Loads,” by C. Roth and M. Grigoriu, 9/18/01, (PB2003-100884, A12, MF-A03).
- MCEER-01-0004 “Overcoming Obstacles to Implementing Earthquake Hazard Mitigation Policies: Stage 1 Report,” by D.J. Alesch and W.J. Petak, 12/17/01, (PB2002-107949, A07, MF-A02).
- MCEER-01-0005 “Updating Real-Time Earthquake Loss Estimates: Methods, Problems and Insights,” by C.E. Taylor, S.E. Chang and R.T. Eguchi, 12/17/01, (PB2002-107948, A05, MF-A01).
- MCEER-01-0006 “Experimental Investigation and Retrofit of Steel Pile Foundations and Pile Bents Under Cyclic Lateral Loadings,” by A. Shama, J. Mander, B. Blabac and S. Chen, 12/31/01, (PB2002-107950, A13, MF-A03).
- MCEER-02-0001 “Assessment of Performance of Bolu Viaduct in the 1999 Duzce Earthquake in Turkey” by P.C. Roussis, M.C. Constantinou, M. Erdik, E. Durukal and M. Dicleli, 5/8/02, (PB2003-100883, A08, MF-A02).
- MCEER-02-0002 “Seismic Behavior of Rail Counterweight Systems of Elevators in Buildings,” by M.P. Singh, Rildova and L.E. Suarez, 5/27/02. (PB2003-100882, A11, MF-A03).
- MCEER-02-0003 “Development of Analysis and Design Procedures for Spread Footings,” by G. Mylonakis, G. Gazetas, S. Nikolaou and A. Chauncey, 10/02/02, (PB2004-101636, A13, MF-A03, CD-A13).
- MCEER-02-0004 “Bare-Earth Algorithms for Use with SAR and LIDAR Digital Elevation Models,” by C.K. Huyck, R.T. Eguchi and B. Houshmand, 10/16/02, (PB2004-101637, A07, CD-A07).
- MCEER-02-0005 “Review of Energy Dissipation of Compression Members in Concentrically Braced Frames,” by K.Lee and M. Bruneau, 10/18/02, (PB2004-101638, A10, CD-A10).
- MCEER-03-0001 “Experimental Investigation of Light-Gauge Steel Plate Shear Walls for the Seismic Retrofit of Buildings” by J. Berman and M. Bruneau, 5/2/03, (PB2004-101622, A10, MF-A03, CD-A10).
- MCEER-03-0002 “Statistical Analysis of Fragility Curves,” by M. Shinozuka, M.Q. Feng, H. Kim, T. Uzawa and T. Ueda, 6/16/03, (PB2004-101849, A09, CD-A09).
- MCEER-03-0003 “Proceedings of the Eighth U.S.-Japan Workshop on Earthquake Resistant Design of Lifeline Facilities and Countermeasures Against Liquefaction,” edited by M. Hamada, J.P. Bardet and T.D. O’Rourke, 6/30/03, (PB2004-104386, A99, CD-A99).
- MCEER-03-0004 “Proceedings of the PRC-US Workshop on Seismic Analysis and Design of Special Bridges,” edited by L.C. Fan and G.C. Lee, 7/15/03, (PB2004-104387, A14, CD-A14).
- MCEER-03-0005 “Urban Disaster Recovery: A Framework and Simulation Model,” by S.B. Miles and S.E. Chang, 7/25/03, (PB2004-104388, A07, CD-A07).
- MCEER-03-0006 “Behavior of Underground Piping Joints Due to Static and Dynamic Loading,” by R.D. Meis, M. Maragakis and R. Siddharthan, 11/17/03, (PB2005-102194, A13, MF-A03, CD-A00).
- MCEER-04-0001 “Experimental Study of Seismic Isolation Systems with Emphasis on Secondary System Response and Verification of Accuracy of Dynamic Response History Analysis Methods,” by E. Wolff and M. Constantinou, 1/16/04 (PB2005-102195, A99, MF-E08, CD-A00).
- MCEER-04-0002 “Tension, Compression and Cyclic Testing of Engineered Cementitious Composite Materials,” by K. Kesner and S.L. Billington, 3/1/04, (PB2005-102196, A08, CD-A08).

- MCEER-04-0003 “Cyclic Testing of Braces Laterally Restrained by Steel Studs to Enhance Performance During Earthquakes,” by O.C. Celik, J.W. Berman and M. Bruneau, 3/16/04, (PB2005-102197, A13, MF-A03, CD-A00).
- MCEER-04-0004 “Methodologies for Post Earthquake Building Damage Detection Using SAR and Optical Remote Sensing: Application to the August 17, 1999 Marmara, Turkey Earthquake,” by C.K. Huyck, B.J. Adams, S. Cho, R.T. Eguchi, B. Mansouri and B. Houshmand, 6/15/04, (PB2005-104888, A10, CD-A00).
- MCEER-04-0005 “Nonlinear Structural Analysis Towards Collapse Simulation: A Dynamical Systems Approach,” by M.V. Sivaselvan and A.M. Reinhorn, 6/16/04, (PB2005-104889, A11, MF-A03, CD-A00).
- MCEER-04-0006 “Proceedings of the Second PRC-US Workshop on Seismic Analysis and Design of Special Bridges,” edited by G.C. Lee and L.C. Fan, 6/25/04, (PB2005-104890, A16, CD-A00).
- MCEER-04-0007 “Seismic Vulnerability Evaluation of Axially Loaded Steel Built-up Laced Members,” by K. Lee and M. Bruneau, 6/30/04, (PB2005-104891, A16, CD-A00).
- MCEER-04-0008 “Evaluation of Accuracy of Simplified Methods of Analysis and Design of Buildings with Damping Systems for Near-Fault and for Soft-Soil Seismic Motions,” by E.A. Pavlou and M.C. Constantinou, 8/16/04, (PB2005-104892, A08, MF-A02, CD-A00).
- MCEER-04-0009 “Assessment of Geotechnical Issues in Acute Care Facilities in California,” by M. Lew, T.D. O’Rourke, R. Dobry and M. Koch, 9/15/04, (PB2005-104893, A08, CD-A00).
- MCEER-04-0010 “Scissor-Jack-Damper Energy Dissipation System,” by A.N. Sigaher-Boyle and M.C. Constantinou, 12/1/04 (PB2005-108221).
- MCEER-04-0011 “Seismic Retrofit of Bridge Steel Truss Piers Using a Controlled Rocking Approach,” by M. Pollino and M. Bruneau, 12/20/04 (PB2006-105795).
- MCEER-05-0001 “Experimental and Analytical Studies of Structures Seismically Isolated with an Uplift-Restraint Isolation System,” by P.C. Roussis and M.C. Constantinou, 1/10/05 (PB2005-108222).
- MCEER-05-0002 “A Versatile Experimentation Model for Study of Structures Near Collapse Applied to Seismic Evaluation of Irregular Structures,” by D. Kusumastuti, A.M. Reinhorn and A. Rutenberg, 3/31/05 (PB2006-101523).
- MCEER-05-0003 “Proceedings of the Third PRC-US Workshop on Seismic Analysis and Design of Special Bridges,” edited by L.C. Fan and G.C. Lee, 4/20/05, (PB2006-105796).
- MCEER-05-0004 “Approaches for the Seismic Retrofit of Braced Steel Bridge Piers and Proof-of-Concept Testing of an Eccentrically Braced Frame with Tubular Link,” by J.W. Berman and M. Bruneau, 4/21/05 (PB2006-101524).
- MCEER-05-0005 “Simulation of Strong Ground Motions for Seismic Fragility Evaluation of Nonstructural Components in Hospitals,” by A. Wanitkorkul and A. Filiatrault, 5/26/05 (PB2006-500027).
- MCEER-05-0006 “Seismic Safety in California Hospitals: Assessing an Attempt to Accelerate the Replacement or Seismic Retrofit of Older Hospital Facilities,” by D.J. Alesch, L.A. Arendt and W.J. Petak, 6/6/05 (PB2006-105794).
- MCEER-05-0007 “Development of Seismic Strengthening and Retrofit Strategies for Critical Facilities Using Engineered Cementitious Composite Materials,” by K. Kesner and S.L. Billington, 8/29/05 (PB2006-111701).
- MCEER-05-0008 “Experimental and Analytical Studies of Base Isolation Systems for Seismic Protection of Power Transformers,” by N. Murota, M.Q. Feng and G-Y. Liu, 9/30/05 (PB2006-111702).
- MCEER-05-0009 “3D-BASIS-ME-MB: Computer Program for Nonlinear Dynamic Analysis of Seismically Isolated Structures,” by P.C. Tsopelas, P.C. Roussis, M.C. Constantinou, R. Buchanan and A.M. Reinhorn, 10/3/05 (PB2006-111703).
- MCEER-05-0010 “Steel Plate Shear Walls for Seismic Design and Retrofit of Building Structures,” by D. Vian and M. Bruneau, 12/15/05 (PB2006-111704).


- MCEER-05-0011 "The Performance-Based Design Paradigm," by M.J. Astrella and A. Whittaker, 12/15/05 (PB2006-111705).
- MCEER-06-0001 "Seismic Fragility of Suspended Ceiling Systems," H. Badillo-Almaraz, A.S. Whittaker, A.M. Reinhorn and G.P. Cimellaro, 2/4/06 (PB2006-111706).
- MCEER-06-0002 "Multi-Dimensional Fragility of Structures," by G.P. Cimellaro, A.M. Reinhorn and M. Bruneau, 3/1/06 (PB2007-106974, A09, MF-A02, CD A00).
- MCEER-06-0003 "Built-Up Shear Links as Energy Dissipators for Seismic Protection of Bridges," by P. Dusicka, A.M. Itani and I.G. Buckle, 3/15/06 (PB2006-111708).
- MCEER-06-0004 "Analytical Investigation of the Structural Fuse Concept," by R.E. Vargas and M. Bruneau, 3/16/06 (PB2006-111709).
- MCEER-06-0005 "Experimental Investigation of the Structural Fuse Concept," by R.E. Vargas and M. Bruneau, 3/17/06 (PB2006-111710).
- MCEER-06-0006 "Further Development of Tubular Eccentrically Braced Frame Links for the Seismic Retrofit of Braced Steel Truss Bridge Piers," by J.W. Berman and M. Bruneau, 3/27/06 (PB2007-105147).
- MCEER-06-0007 "REDARS Validation Report," by S. Cho, C.K. Huyck, S. Ghosh and R.T. Eguchi, 8/8/06 (PB2007-106983).
- MCEER-06-0008 "Review of Current NDE Technologies for Post-Earthquake Assessment of Retrofitted Bridge Columns," by J.W. Song, Z. Liang and G.C. Lee, 8/21/06 (PB2007-106984).
- MCEER-06-0009 "Liquefaction Remediation in Silty Soils Using Dynamic Compaction and Stone Columns," by S. Thevanayagam, G.R. Martin, R. Nashed, T. Shenthan, T. Kanagalingam and N. Ecemis, 8/28/06 (PB2007-106985).
- MCEER-06-0010 "Conceptual Design and Experimental Investigation of Polymer Matrix Composite Infill Panels for Seismic Retrofitting," by W. Jung, M. Chiewanichakorn and A.J. Aref, 9/21/06 (PB2007-106986).
- MCEER-06-0011 "A Study of the Coupled Horizontal-Vertical Behavior of Elastomeric and Lead-Rubber Seismic Isolation Bearings," by G.P. Warn and A.S. Whittaker, 9/22/06 (PB2007-108679).
- MCEER-06-0012 "Proceedings of the Fourth PRC-US Workshop on Seismic Analysis and Design of Special Bridges: Advancing Bridge Technologies in Research, Design, Construction and Preservation," Edited by L.C. Fan, G.C. Lee and L. Ziang, 10/12/06 (PB2007-109042).
- MCEER-06-0013 "Cyclic Response and Low Cycle Fatigue Characteristics of Plate Steels," by P. Dusicka, A.M. Itani and I.G. Buckle, 11/1/06 06 (PB2007-106987).
- MCEER-06-0014 "Proceedings of the Second US-Taiwan Bridge Engineering Workshop," edited by W.P. Yen, J. Shen, J-Y. Chen and M. Wang, 11/15/06 (PB2008-500041).
- MCEER-06-0015 "User Manual and Technical Documentation for the REDARS<sup>TM</sup> Import Wizard," by S. Cho, S. Ghosh, C.K. Huyck and S.D. Werner, 11/30/06 (PB2007-114766).
- MCEER-06-0016 "Hazard Mitigation Strategy and Monitoring Technologies for Urban and Infrastructure Public Buildings: Proceedings of the China-US Workshops," edited by X.Y. Zhou, A.L. Zhang, G.C. Lee and M. Tong, 12/12/06 (PB2008-500018).
- MCEER-07-0001 "Static and Kinetic Coefficients of Friction for Rigid Blocks," by C. Kafali, S. Fathali, M. Grigoriu and A.S. Whittaker, 3/20/07 (PB2007-114767).
- MCEER-07-0002 "Hazard Mitigation Investment Decision Making: Organizational Response to Legislative Mandate," by L.A. Arendt, D.J. Alesch and W.J. Petak, 4/9/07 (PB2007-114768).
- MCEER-07-0003 "Seismic Behavior of Bidirectional-Resistant Ductile End Diaphragms with Unbonded Braces in Straight or Skewed Steel Bridges," by O. Celik and M. Bruneau, 4/11/07 (PB2008-105141).

- MCEER-07-0004 “Modeling Pile Behavior in Large Pile Groups Under Lateral Loading,” by A.M. Dodds and G.R. Martin, 4/16/07(PB2008-105142).
- MCEER-07-0005 “Experimental Investigation of Blast Performance of Seismically Resistant Concrete-Filled Steel Tube Bridge Piers,” by S. Fujikura, M. Bruneau and D. Lopez-Garcia, 4/20/07 (PB2008-105143).
- MCEER-07-0006 “Seismic Analysis of Conventional and Isolated Liquefied Natural Gas Tanks Using Mechanical Analogs,” by I.P. Christovasilis and A.S. Whittaker, 5/1/07.
- MCEER-07-0007 “Experimental Seismic Performance Evaluation of Isolation/Restraint Systems for Mechanical Equipment – Part 1: Heavy Equipment Study,” by S. Fathali and A. Filiatrault, 6/6/07 (PB2008-105144).
- MCEER-07-0008 “Seismic Vulnerability of Timber Bridges and Timber Substructures,” by A.A. Sharma, J.B. Mander, I.M. Friedland and D.R. Allicock, 6/7/07 (PB2008-105145).
- MCEER-07-0009 “Experimental and Analytical Study of the XY-Friction Pendulum (XY-FP) Bearing for Bridge Applications,” by C.C. Marin-Artieda, A.S. Whittaker and M.C. Constantinou, 6/7/07 (PB2008-105191).
- MCEER-07-0010 “Proceedings of the PRC-US Earthquake Engineering Forum for Young Researchers,” Edited by G.C. Lee and X.Z. Qi, 6/8/07.
- MCEER-07-0011 “Design Recommendations for Perforated Steel Plate Shear Walls,” by R. Purba and M. Bruneau, 6/18/07, (PB2008-105192).
- MCEER-07-0012 “Performance of Seismic Isolation Hardware Under Service and Seismic Loading,” by M.C. Constantinou, A.S. Whittaker, Y. Kalpakidis, D.M. Fenz and G.P. Warn, 8/27/07, (PB2008-105193).
- MCEER-07-0013 “Experimental Evaluation of the Seismic Performance of Hospital Piping Subassemblies,” by E.R. Goodwin, E. Maragakis and A.M. Itani, 9/4/07, (PB2008-105194).
- MCEER-07-0014 “A Simulation Model of Urban Disaster Recovery and Resilience: Implementation for the 1994 Northridge Earthquake,” by S. Miles and S.E. Chang, 9/7/07, (PB2008-106426).
- MCEER-07-0015 “Statistical and Mechanistic Fragility Analysis of Concrete Bridges,” by M. Shinozuka, S. Banerjee and S-H. Kim, 9/10/07, (PB2008-106427).
- MCEER-07-0016 “Three-Dimensional Modeling of Inelastic Buckling in Frame Structures,” by M. Schachter and AM. Reinhorn, 9/13/07, (PB2008-108125).
- MCEER-07-0017 “Modeling of Seismic Wave Scattering on Pile Groups and Caissons,” by I. Po Lam, H. Law and C.T. Yang, 9/17/07 (PB2008-108150).
- MCEER-07-0018 “Bridge Foundations: Modeling Large Pile Groups and Caissons for Seismic Design,” by I. Po Lam, H. Law and G.R. Martin (Coordinating Author), 12/1/07 (PB2008-111190).
- MCEER-07-0019 “Principles and Performance of Roller Seismic Isolation Bearings for Highway Bridges,” by G.C. Lee, Y.C. Ou, Z. Liang, T.C. Niu and J. Song, 12/10/07.
- MCEER-07-0020 “Centrifuge Modeling of Permeability and Pinning Reinforcement Effects on Pile Response to Lateral Spreading,” by L.L Gonzalez-Lagos, T. Abdoun and R. Dobry, 12/10/07 (PB2008-111191).
- MCEER-07-0021 “Damage to the Highway System from the Pisco, Perú Earthquake of August 15, 2007,” by J.S. O’Connor, L. Mesa and M. Nykamp, 12/10/07, (PB2008-108126).
- MCEER-07-0022 “Experimental Seismic Performance Evaluation of Isolation/Restraint Systems for Mechanical Equipment – Part 2: Light Equipment Study,” by S. Fathali and A. Filiatrault, 12/13/07 (PB2008-111192).
- MCEER-07-0023 “Fragility Considerations in Highway Bridge Design,” by M. Shinozuka, S. Banerjee and S.H. Kim, 12/14/07 (PB2008-111193).

- MCEER-07-0024 "Performance Estimates for Seismically Isolated Bridges," by G.P. Warn and A.S. Whittaker, 12/30/07 (PB2008-112230).
- MCEER-08-0001 "Seismic Performance of Steel Girder Bridge Superstructures with Conventional Cross Frames," by L.P. Carden, A.M. Itani and I.G. Buckle, 1/7/08, (PB2008-112231).
- MCEER-08-0002 "Seismic Performance of Steel Girder Bridge Superstructures with Ductile End Cross Frames with Seismic Isolators," by L.P. Carden, A.M. Itani and I.G. Buckle, 1/7/08 (PB2008-112232).
- MCEER-08-0003 "Analytical and Experimental Investigation of a Controlled Rocking Approach for Seismic Protection of Bridge Steel Truss Piers," by M. Pollino and M. Bruneau, 1/21/08 (PB2008-112233).
- MCEER-08-0004 "Linking Lifeline Infrastructure Performance and Community Disaster Resilience: Models and Multi-Stakeholder Processes," by S.E. Chang, C. Pasion, K. Tatebe and R. Ahmad, 3/3/08 (PB2008-112234).
- MCEER-08-0005 "Modal Analysis of Generally Damped Linear Structures Subjected to Seismic Excitations," by J. Song, Y-L. Chu, Z. Liang and G.C. Lee, 3/4/08 (PB2009-102311).
- MCEER-08-0006 "System Performance Under Multi-Hazard Environments," by C. Kafali and M. Grigoriu, 3/4/08 (PB2008-112235).
- MCEER-08-0007 "Mechanical Behavior of Multi-Spherical Sliding Bearings," by D.M. Fenz and M.C. Constantinou, 3/6/08 (PB2008-112236).
- MCEER-08-0008 "Post-Earthquake Restoration of the Los Angeles Water Supply System," by T.H.P. Tabucchi and R.A. Davidson, 3/7/08 (PB2008-112237).
- MCEER-08-0009 "Fragility Analysis of Water Supply Systems," by A. Jacobson and M. Grigoriu, 3/10/08.
- MCEER-08-0010 "Experimental Investigation of Full-Scale Two-Story Steel Plate Shear Walls with Reduced Beam Section Connections," by B. Qu, M. Bruneau, C-H. Lin and K-C. Tsai, 3/17/08.
- MCEER-08-0011 "Seismic Evaluation and Rehabilitation of Critical Components of Electrical Power Systems," S. Ersoy, B. Feizi, A. Ashrafi and M. Ala Saadeghvaziri, 3/17/08.
- MCEER-08-0012 "Seismic Behavior and Design of Boundary Frame Members of Steel Plate Shear Walls," by B. Qu and M. Bruneau, 4/26/08.
- MCEER-08-0013 "Development and Appraisal of a Numerical Cyclic Loading Protocol for Quantifying Building System Performance," by A. Filiatrault, A. Wanitkorkul and M. Constantinou, 4/27/08.
- MCEER-08-0014 "Structural and Nonstructural Earthquake Design: The Challenge of Integrating Specialty Areas in Designing Complex, Critical Facilities," by W.J. Petak and D.J. Alesch, 4/30/08.
- MCEER-08-0015 "Seismic Performance Evaluation of Water Systems," by Y. Wang and T.D. O'Rourke, 5/5/08.
- MCEER-08-0016 "Seismic Response Modeling of Water Supply Systems," by P. Shi and T.D. O'Rourke, 5/5/08.
- MCEER-08-0017 "Numerical and Experimental Studies of Self-Centering Post-Tensioned Steel Frames," by D. Wang and A. Filiatrault, 5/12/08.
- MCEER-08-0018 "Development, Implementation and Verification of Dynamic Analysis Models for Multi-Spherical Sliding Bearings," by D.M. Fenz and M.C. Constantinou, 8/15/08.
- MCEER-08-0019 "Performance Assessment of Conventional and Base Isolated Nuclear Power Plants for Earthquake Blast Loadings," by Y.N. Huang, A.S. Whittaker and N. Luco, 10/28/08.








**EARTHQUAKE ENGINEERING TO EXTREME EVENTS**

University at Buffalo, The State University of New York  
Red Jacket Quadrangle ■ Buffalo, New York 14261  
Phone: (716) 645-3391 ■ Fax: (716) 645-3399  
E-mail: [mceer@buffalo.edu](mailto:mceer@buffalo.edu) ■ WWW Site <http://mceer.buffalo.edu>



University at Buffalo *The State University of New York*

ISSN 1520-295X